NUREG/CR-6685
SAND2000-2093

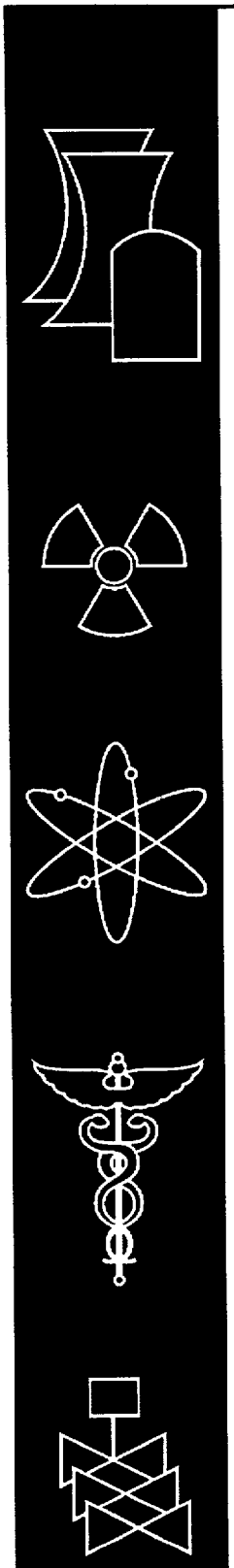

# Pretest Analysis of a 1:4-Scale Prestressed Concrete Containment Vessel Model

**Sandia National Laboratories**

**U.S. Nuclear Regulatory Commission**
**Office of Nuclear Regulatory Research**
**Washington, DC 20555-0001**

## AVAILABILITY OF REFERENCE MATERIALS IN NRC PUBLICATIONS

### NRC Reference Material

As of November 1999, you may electronically access NUREG-series publications and other NRC records at NRC's Public Electronic Reading Room at www.nrc.gov/NRC/ADAMS/index.html. Publicly released records include, to name a few, NUREG-series publications; *Federal Register* notices; applicant, licensee, and vendor documents and correspondence; NRC correspondence and internal memoranda; bulletins and information notices; inspection and investigative reports; licensee event reports; and Commission papers and their attachments.

NRC publications in the NUREG series, NRC regulations, and *Title 10, Energy*, in the Code of *Federal Regulations* may also be purchased from one of these two sources.

1. The Superintendent of Documents
   U.S. Government Printing Office
   P. O. Box 37082
   Washington, DC 20402–9328
   www.access.gpo.gov/su_docs
   202–512–1800
2. The National Technical Information Service
   Springfield, VA 22161–0002
   www.ntis.gov
   1–800–533–6847 or, locally, 703–805–6000

A single copy of each NRC draft report for comment is available free, to the extent of supply, upon written request as follows:

Address: Office of the Chief Information Officer,
Reproduction and Distribution
Services Section
U.S. Nuclear Regulatory Commission
Washington, DC 20555-0001
E-mail: DISTRIBUTION@nrc.gov
Facsimile: 301–415–2289

Some publications in the NUREG series that are posted at NRC's Web site address www.nrc.gov/NRC/NUREGS/indexnum.html are updated periodically and may differ from the last printed version. Although references to material found on a Web site bear the date the material was accessed, the material available on the date cited may subsequently be removed from the site.

### Non-NRC Reference Material

Documents available from public and special technical libraries include all open literature items, such as books, journal articles, and transactions, *Federal Register* notices, Federal and State legislation, and congressional reports. Such documents as theses, dissertations, foreign reports and translations, and non-NRC conference proceedings may be purchased from their sponsoring organization.

Copies of industry codes and standards used in a substantive manner in the NRC regulatory process are maintained at—

The NRC Technical Library
Two White Flint North
11545 Rockville Pike
Rockville, MD 20852–2738

These standards are available in the library for reference use by the public. Codes and standards are usually copyrighted and may be purchased from the originating organization or, if they are American National Standards, from—

American National Standards Institute
11 West 42nd Street
New York, NY 10036–8002
www.ansi.org
212–642–4900

The NUREG series comprises (1) technical and administrative reports and books prepared by the staff (NUREG–XXXX) or agency contractors (NUREG/CR–XXXX), (2) proceedings of conferences (NUREG/CP–XXXX), (3) reports resulting from international agreements (NUREG/IA–XXXX), (4) brochures (NUREG/BR–XXXX), and (5) compilations of legal decisions and orders of the Commission and Atomic and Safety Licensing Boards and of Directors' decisions under Section 2.206 of NRC's regulations (NUREG–0750).

NUREG/CR-6685
SAND2000-2093

# Pretest Analysis of a 1:4-Scale Prestressed Concrete Containment Vessel Model

Manuscript Completed: August 2000
Date Published: October 2000

Prepared by
R. A. Dameron,* L. Zhang,*
Y. R. Rashid,* M. S. Vargas*

Sandia National Laboratories, Principal Contractor
P.O. Box 5800
Albuquerque, NM 87185-0744

Subcontractor:
*ANATECH Corporation
5435 Oberlin Drive
San Diego, CA 92121

J. F. Costello, NRC Project Manager

**Prepared for**
**Division of Engineering Technology**
**Office of Nuclear Regulatory Research**
**U.S. Nuclear Regulatory Commission**
**Washington, DC 20555-0001**
**NRC Job Code Y6131**

**NUREG/CR-6685 has been reproduced from the best available copy.**

# Abstract

The Nuclear Power Engineering Corporation of Japan and the U.S. Nuclear Regulatory Commission, Office of Nuclear Regulatory Research, are co-sponsoring and jointly funding a Cooperative Containment Research Program at Sandia National Laboratories in Albuquerque, New Mexico. As a part of the program, a prestressed concrete containment vessel model will be tested to failure at Sandia in September 2000. The model, uniformly scaled at 1:4, is representative of the containment structure of an actual pressurized-water reactor plan (OHI-3) in Japan. The objectives of the internal pressurization test are to obtain measurement data of the structural response of the model to pressure loading beyond design basis accident in order to validate analytical modeling, to find pressure capacity of the model, and to observe its failure mechanisms.

This report describes results of pretest analytical studies of the prestressed concrete containment vessel model performed by ANATECH Corp. under contract with Sandia National Laboratories. Construction is being commissioned by the Nuclear Power Engineering Corporation in Japan. The pretest analysis represents the second phase of a comprehensive analysis effort. The first phase consisted of preliminary analyses to determine what finite element models would be necessary for the pretest prediction analyses.

The principal objectives of the pretest analyses are to (1) obtain validation of analytical methods for predicting the structural response and failure modes of a prestressed concrete containment and (2) provide information useful for planning test procedures and instrumentation.

In addition to documenting the predicted behavior of the liner, concrete, rebar, and tendons, a variety of failure modes and locations have been investigated. Global analysis was used to help identify possible failure modes; other analyses investigated localized failure modes or modes specifically associated with 3D behavior. Liner-tearing failure at the cylinder's midheight near penetrations and a shear/bending failure at the base of the cylinder wall were found to be competing failure modes. More detailed modeling of these locations placed a higher likelihood of failure on the liner tearing mode at the cylinder midheight near a major penetration. The most likely location for the liner-tearing failure was found to be near the equipment hatch at the ending point of a vertical T-anchor, near where the liner is attached to the thickened liner insert plate. Using a strain-based failure criteria that considers the triaxiality of stress and a reduction in ductility in the vicinity of a weld, the failure strain was 0.162. The failure pressure at which the local analysis computed strain that reached the failure strain, is 3.2 times the design pressure of 0.4 MPa, or 1.28 MPa.

The pretest analyses, which were completed one year prior to completion of model construction and testing, did not include certain as-built features, actual prestress losses, creep and temperature conditions that may affect the PCCV model behavior during the test. An assessment of the possible uncertainties these as-built conditions may introduce and an approximate analysis of temperature and creep effects are described in the closing chapters of this report.

# Contents

# Figures

**Figure** **Page**

# Tables

# Executive Summary

This report describes pretest analyses of a 1:4-scale model of a prestressed concrete containment vessel (PCCV) being constructed by the Nuclear Power Engineering Corporation (NUPEC)[a] in Japan. The work was performed for Sandia National Laboratories (SNL)[b] as part of a cooperative effort between the United States Nuclear Regulatory Commission and NUPEC. The pretest analyses represent the second of three analysis phases for the PCCV test program. The first phase, Preliminary Analysis, was used to determine what finite element models and what level of modeling detail would be necessary for the pretest prediction analyses. The third analysis phase will focus on posttest comparison of test measurements to analytical predictions and on refined analysis of the observed failure mechanism. The principal objectives of the pretest analyses are to (1) validate the analytical methods for predicting the global structural response of a prestressed concrete containment, (2) gain insight into the potential structural failure modes of a prestressed concrete containment, and (3) provide information useful for planning of test procedures and instrumentation. Because pretest analyses were completed one year prior to completion of model construction and testing, they did not include certain as-built features, actual measured prestress losses, creep and temperature conditions. Prestress losses due to friction, anchor set, and concrete creep were included in the pretest analysis but only from the assumptions used in the PCCV model design.

In the pretest analysis phase, the first model developed and analyzed was a 2D axisymmetric global model with discrete representation of concrete, liner, rebar, and tendons. The typical azimuth chosen for the modeling plane was 135°, which is remote from major penetrations and buttresses. The ABAQUS general purpose finite element program with the ANACAP-U concrete and steel constitutive modeling modules were used for the analysis. Tendons and their prestressing were modeled to replicate expected tendon stress-strain behavior and friction effects. Concrete cracking was simulated with the "smeared crack" approach where cracking is introduced at the finite element integration points.

A list of possible failure modes and failure locations was developed in the preliminary analysis phase prior to conducting the global analyses. Only some of the potential failure modes are specifically addressed by the global analysis; others are addressed by local models. A liner failure at the midheight of the cylinder near a penetration and a shear/bending failure at the base of the cylinder wall were both found to have significant probability of occurrence. After preliminary analyses, recommendations were made for analysis refinements and for local models that could better predict the sequence of competing failure modes that were identified. The local models developed for the pretest prediction analysis were the equipment hatch region, the personnel airlock region, and the mainsteam penetration region. A detailed 3D model of the entire cylinder midheight region (3DCM) was also developed to investigate, in detail, tendon behavior in the cylinder and 3D effects that drive the local strain concentrations near the penetrations.

A study of potential shear failure at the wall-basemat juncture showed that while wall-basemat outer surface concrete spalling is predicted to occur by $3.2P_d$, a through-wall shear failure is not likely until at least $4.0P_d$, and other failure modes are judged to be more likely to occur prior to reaching this pressure.

Tendon modeling tasks described herein demonstrated the utility of a new tendon modeling approach in which friction losses are explicitly represented by friction truss tie elements. Improved tendon stress distributions at various pressures are provided as benchmarks of expected tendon behavior. Capturing the tendon stress distributions in more detail has improved the prediction of displacement response and liner strains, especially near the E/H where this distribution is very complex. The 3DCM model with its detailed tendon representation, predicted a rupture of the hoop tendon closest to the E/H at a model pressure of about $3.5P_d$, and if this occurred prior to earlier depressurization associated with liner tearing/leakage, rupture of other tendons and large deformations of the vessel would quickly follow. However, this mode is predicted to be precluded by the liner tearing and leakage failure mode.

---

[a] The work of the Nuclear Power Engineering Corporation is performed under contract by the Ministry of International Trade and Industry, Japan.

[b] Sandia National Laboratories is a multiprogram laboratory operated by Sandia Corporation, a Lockheed Martin Company, for the United States Department of Energy under contract DE-AC04-94AL85000.

Using a strain-based failure criteria that considers the triaxiality of stress and a reduction in ductility in the vicinity of a weld, the liner failure strain was 0.162. The failure pressure at which a local analysis computed effective plastic strain that reached the failure strain, was $3.2P_d$, or 1.28 MPa. The location for this liner-tearing failure was near the equipment hatch (E/H), adjacent to a vertical liner anchor that terminates near the E/H insert plate transition. Other local models showed other candidate liner tear locations, several of which may occur during the pressure range $3.2P_d$ to $3.5P_d$, if they are not precluded first by the growth of the first tear and subsequent depressurization of the vessel. A significant candidate tear location was also found near the 90° buttress where hoop strains are elevated due to bending, and a weld seam and hoop stiffener "rat-hole" is coincidentally located.

The analysis work comprising the pretest predictions was based on several major assumptions necessitated by project schedule constraints and the diminishing returns associated with increasing refinements to analytical detail. Thus, most of the predictive analyses documented herein were conducted about a year before the scheduled pressure test. These limitations made it impossible to consider in the pretest predictions, the geometric and structural imperfections, actual prestressing (as opposed to designers' planned values), temperature effects, material property variability, and the as-built stress and strain state in the model at test time, including time-dependent effects. The closing chapter of this report discusses these items and places them in perspective relative to the analytical predictions of the earlier chapters. It also presents the results of an axisymmetric analysis of temperature and creep effects. Conclusions of the time-dependent effects analysis showed:

1. creep displacements in the cylinder of about 0.6 cm radially and 1.2 cm vertically;

2. creep strains (in hoop direction) of 0.1% in the liner and rebar at the cylinder midheight;

3. total hoop strains at the cylinder midheight, including the results of prestress and creep, that cause the liner to nearly reach yield;

4. prestress losses attributable to creep that are significantly larger than was originally anticipated by the designers, i.e., losses attributable to creep of approximately 10% of initial tendon stress.

While the scope and objectives of the pretest analysis work for the 1:4-scale PCCV did not include a probabilistic risk assessment of the failure (leakage) pressure prediction, an evaluation framework for conducting one is presented. An illustration of how the final probability of leakage versus pressure might look for the 1:4-scale PCCV model is shown. The final probability of liner tearing/leakage versus pressure is constructed with reference to the final list of candidate tearing locations, and it combines probabilities by location. Combining probabilities and locations produces the leakage pressure predictions and confidence intervals summarized below:

Best estimate (P=0.5), $p_{leakage}=3.2P_d=1.28MPa$

Upper bound (P=0.9), $p_{leakage}=3.51P_d=1.38MPa$

Lower bound (P=0.1), $p_{leakage}=2.75P_d = 1.08MPa$

# Acknowledgments

This pretest analysis effort was sponsored by the U.S. Nuclear Regulatory Commission. The authors would first like to thank Dr. James F. Costello of the Nuclear Regulatory Commission for his technical interaction and support throughout the program.

The work described herein was performed by ANATECH for Sandia National Laboratories in Albuquerque under Contract No. AO-5464. Reviews of the analysis plan and the analysis results have been conducted by Vincent Luk, Mike Hessheimer, and other Sandia personnel. The valuable discussions and guidance received during those reviews were critical to the development and presentation of the results. It should also be noted that the analytical models and software developed by ANATECH for the Electric Power Research Institute in their Containment Integrity Program were made freely available by the institute and proved to be indispensable in the performance of this work.

# Acronyms and Initialisms

| | |
|---|---|
| 3DCM | 3D cylinder midheight (model) |
| A/L | airlock |
| ABAQUS | general purpose finite element program |
| ANACAP-U | concrete and steel constitutive modeling modules |
| ANAGEN | mesh generator serving as preprocessor to ABAQUS |
| CTL | Construction Technology Laboratories |
| DOF | Degree of Freedom |
| E/H | equipment hatch |
| EPRI | Electric Power Research Institute (United States) |
| F/W | feedwater |
| FE | finite element |
| HAZ | heat-affected zone |
| ILRT | Integrated Leak Rate Test |
| LWR | light-water reactor |
| M/S | mainsteam |
| NRC | Nuclear Regulatory Commission (United States) |
| NUPEC | Nuclear Power Engineering Corporation (Japan) |
| PCCV | prestressed concrete containment vessel |
| SCL | strain concentration location |
| SFT | System Functionality Test |
| SIT | Structural Integrity Test |
| SNL | Sandia National Laboratories (United States) |
| SOL | Standard Output Location |

# 1. INTRODUCTION

This report describes the pretest analyses of a 1:4-scale model of a prestressed concrete containment vessel (PCCV) constructed by Nuclear Power Engineering Corporation (NUPEC)[c] at Sandia National Laboratories (SNL).[d] The model is shown in Figure 1-1. The analysis work was performed for SNL as part of a cooperative effort between the Nuclear Regulatory Commission (NRC) and NUPEC. The principal objectives of the pretest analyses were to (1) obtain validation of analytical methods for predicting the global structural response of a steel-lined, prestressed concrete containment, (2) gain insight into the potential structural failure modes of a prestressed concrete containment, and (3) provide information useful for planning test procedures and instrumentation.

## 1.1 Program Background

In reactor containment research conducted in recent years, concrete containment structures have attracted special attention because of their complex behavior and the critical function they perform: to prevent the release of radioactive material to the atmosphere as a byproduct of a severe accident occurring in the primary nuclear steam supply system.

Studies on the use of concrete structures as pressure boundaries began in the 1960s during the early stages of development of gas-cooled reactors. Material and model experiments conducted in the United States and Europe[e] (Hessheimer et al. 1997) provide extensive experience upon which to draw to assess the overpressure capabilities of light-water reactor (LWR) containment structures. In large-scale tests of concrete pressure vessels in which steel liners were included, leakage developed because of liner tearing at lower than anticipated pressures and, more significantly, at low uniform deformations.

Given this historical evidence, it has been postulated in recent years that, for a gradually increasing pressure, leakage at a pressure less than the burst pressure is the most likely failure mode.[f] Thus, research in recent years has been directed toward not only the prediction of containment global response, but also at the study of liner tearing behavior. The pretest analyses described herein focus on both global and local aspects of behavior.

The testing of the 1:4-scale prestressed concrete containment vessel (PCCV) model represents a valuable opportunity to examine the ultimate pressure capacity of a steel-lined, prestressed concrete containment model in a manner similar to SNL's NRC-sponsored 1:6-scale model of a reinforced concrete containment (Clauss 1987; 1989). Pretest predictions and posttest analysis of the 1:6-scale model were carried out by ANATECH as part of the Electric Power Research Institute's (EPRI's) participation in SNL's Round Robin Analysis program. In that effort, concrete-analysis methodology and liner-tearing criteria developed under EPRI's sponsorship were utilized to obtain reasonably close predictions of the failure pressure and failure modes of the 1:6-scale model. The analysis methodology used in the present work is similar to that employed in the analysis of the 1:6-scale model. However, the 1:4-scale PCCV model introduces new elements into the analysis because of the prestressed design.

While there is extensive evidence supporting liner tear and leak-before-break as the dominant failure mode of steel-lined concrete containments, some containment research[g] (Dameron et al., 1990; Hessheimer et al. 1997) has indicated that prestressed containments may be more prone to a structural failure (rather than leak) than reinforced containments primarily because of two reasons:

1. the generally narrower pressure range between liner tearing and structural failure that exists in prestressed containments (and lower ductility due to lower failure strains in tendons versus rebar); and

2. prestressed containments have generally thinner walls and rely more heavily on concrete as

---

[c] The work of the Nuclear Power Engineering Corporation is performed under contract by the Ministry of International Trade and Industry, Japan.

[d] Sandia National Laboratories is a multiprogram laboratory operated by Sandia Corporation, a Lockheed Martin Company for the United States Department of Energy under contract DE-AC04-94AL85000.

[e] Conference on Prestressed Concrete Pressure Vessels. 1967. London, England: The Institute of Civil Engineers.

[f] Dameron, R.A., R.S. Dunham, and Y.R. Rashid. 1989. Methods for Ultimate Load Analysis of Concrete Containments, Phase 3: Developing Criteria and Guidelines for Predicting Concrete Containment Leakage. EPRI NP6260SD, ANATECH Report to EPRI. February 1989.

[g] Dameron, R.A., R-S. Dunham, Y.R. Rashid. 1987. Methods for Ultimate Load Analysis of Concrete Containments, Phase 2. EPRI NP-4869M, ANATECH Report to EPRI. March 1987.

a structural component (i.e., higher shear stresses at the same level of pressure).

The former issue becomes relevant for accident scenarios with high rates of loading (rates that could "leap frog" beyond a liner tearing pressure) and the latter issue suggests the possibility of a shear or other brittle concrete failure.

The Sizewell B test of a 1:10-Scale PCCV in England and associated analyses emphasized structural failure modes because the test was loaded with a water-filled rubber bladder that precluded leak-before-break failure. The issues stated above make the 1:4-scale PCCV model test particularly interesting for purposes of addressing competing structural and liner-tearing failure modes. In the current work, prediction of ultimate capacities and of gross structural failure modes are, therefore, of at least equal importance to predicting liner-tearing failure.

In summary, some unique aspects of studying the 1:4-scale PCCV are:

1. Different over-pressure behavior: At high pressures approaching global failure, prestressed containments may have less residual strength than reinforced containments.

2. Higher potential for shear failure: Shear failure at the base of the wall-basemat region is judged to be of relatively higher probability than in a reinforced containment. The Conference on Prestressed Concrete Pressure Vessels[h] yielded examples of shear failures.

## 1.2 Preliminary Analysis Phase

The pretest analysis work that is the focus of the document was preceded by a preliminary analysis phase in which modeling and analysis were performed with limited material property information in order to guide the selection of modeling extent and level of detail necessary to perform pretest prediction analyses.

The pretest prediction analyses must provide the progression of elevated liner strains as a function of the pressure applied to the model. The location with strains reaching the strain-failure criteria first is the most likely to fail; the location with strains reaching the criteria second is the second-most likely to fail, and so forth. This is how the failure modes are ultimately ranked, especially among the different penetration discontinuities in the structure.

Preliminary analysis included axisymmetric and some 3D local modeling, including preliminary studies of the equipment hatch (E/H) and personnel airlocks (A/L). The preliminary E/H analysis showed that peak liner-strain results from analysis are significantly influenced by the nature of the representation of the concrete wall, rebar, and tendons, the extent of the local model, and the boundary condition assumptions. As evidence of this, a liner-only study that relied on a shell model of the wall with smeared concrete, rebar, and tendons showed much higher strains near the E/H than a more detailed 3D representation. There was also considerable lack of agreement between the radial displacement behavior of the E/H and A/L models. At equal pressure milestones, an E/H model was found to expand radially more than the personnel A/L model. Some of this difference is from differences in wall thickening and tendon and rebar layout near the E/H, and some is from the proximity of the E/H to the nearest buttress (the buttresses significantly restrict radial movement and the E/H is farther from a buttress than the A/L). Thus, in addition to identifying which penetration might have the most severe strain concentration, the final local penetration analyses must rely on a consistent method for comparing the general strain fields in the vicinity of the penetrations to the far-field strains in the global analysis. To address this and to address the need for detailed behavior information in the prestressing tendons, a detailed 3D model of the cylinder midheight region was also shown to be needed.

## 1.3 Pretest Analysis: Scope and Objectives

The objectives of the pretest analyses are to:

1. obtain a database for the validation of analytical models for predicting the global structural response of a prestressed concrete containment;

2. gain insight, through pretest predictions, into the potential structural failure modes of a prestressed concrete containment;

3. aid in the design, gage placement, and planning of the pressurization test.

The blind prediction format for participating in the experiment enhances the credibility of the analytical

[h] Conference on Prestressed Concrete Pressure Vessels. 1967. London, England: The Institute of Civil Engineers.

model validation. Predictions of possible failures near all penetrations in the PCCV model are provided with a suite of local models that includes the E/H and A/L models, and a model of the mainsteam (M/S) penetration group. Inspection of the liner/anchor details near the M/S penetrations indicates that the local-liner strain discontinuities may be the strongest of the three geometries. Further, the strain concentration geometry at the feedwater (F/W) group is no worse than that at the M/S group, and the "driving strain" (the strain field near the penetration that is the base strain to which the strain concentration is applied) is lower than that at the M/S because of its lower elevation on the model (proximity to the basemat). Thus, the M/S location governs the F/W location by inspection. These observations were the impetus for choosing the local models.

In preliminary analyses, there was difficulty accurately ranking the penetrations by likelihood of failure because of large variation in radial response around the circumference of the model. The global axisymmetric model predicts a radial displacement versus pressure at the cylinder midheight that may serve as a reasonable average displacement, but the radial displacement around the circumference was found to vary by a factor of three or more, depending on proximity to a buttress or wall embossment. Final failure mode ranking, therefore, requires prediction of the 3D response of the midheight region (Figure 1-2) of the cylinder. A 3D cylinder midheight (3DCM) model was developed that extends 360° circumferentially. Both buttresses were modeled. The model was constructed with the help of the tendon, concrete, and rebar mesh generators already in place for the E/H, A/L, buttress, and M/S geometries. The primary objectives of the 3DCM model are to:

1. provide a 3D prediction of the radial displacement around the midheight of the cylinder;

2. capture the behavior of prestressing tendons including friction losses and anchor-set effects; and

3. provide correlation of the response of the local models to model pressure on the basis of the deformations experienced at boundaries of the local models.

Additionally, the scope of the work was to cover all areas of investigation that pertain to the prediction of the structure's failure modes. These modes and their behavior are described in the next section.

## 1.4 Failure Modes and Behavior Investigated

The general objectives of all of the pretest analyses are to predict possible failure modes. Prior to starting the analyses, a list of potential failure mechanisms and vulnerable regions and components of the model were developed. Additional details of the 1:4-scale PCCV model are shown in Figures 1-3 and 1-4. The list was intended to be as comprehensive as possible, regardless of the relative likelihood of the events in the list. Subsequently, a detailed plan was developed for systematically eliminating or investigating each of the failure mechanisms and vulnerable components. Table 1-1 lists these items and the method proposed at the outset of the pretest analysis to evaluate each item.

Many items in the table are identified as either "free-field" or localized behavior. Free-field behavior refers to a failure mechanism that is possible at a reasonable distance away from discrete stiffness discontinuities such as penetrations or the wall-basemat juncture. Local failure mechanisms are those near stiffness discontinuities that are caused by local stress or strain concentration from the presence of the discontinuity or a connection detail. In general, global analyses, such as those reported in Chapter 5, only specifically predict free-field behavior. However, based on experience from prior structural testing, inferences can be made from free-field behavior about local behavior. This issue is detailed in the discussion of failure criteria and failure predictions. Some examples of potential local failure locations (particularly liner-tearing failure) are shown in Figures 1-3 and 1-4.

Each of the local penetration analyses investigated and ranked the potential for liner-tearing failure mode. The potential for liner tearing near penetrations is increased by strain concentrations:

1. near the edges or ends of vertical T-anchors;

2. near the edges or ends of horizontal stiffeners;

3. near liner thickness discontinuities;

4. near liner bending points (edges of embossments where a liner angle change occurs);

5. near weld seams, particularly at a corner where a vertical seam meets a horizontal seam.

The local analysis models described herein investigate strain concentrations 1 through 4, but not 5. Strain

concentration is addressed through judgment and test data applied to the liner-strain failure criteria.

The local analysis models also investigate shear and bending in the containment wall, elevated rebar strain, elevated tendon strain, and will predict failure in these modes, if it were to occur. The only significant local deformations and strains other than in the liner are the wall bending near the buttresses and the elevated wall membrane strains at local rebar termination points. These modes were all investigated using the 3DCM model.

## 1.5 Computational Tools

Over the past two decades, ANATECH has developed a constitutive modeling approach for the nonlinear analysis of reinforced concrete structures. This constitutive model is based on pioneering work by Rashid, the original developer of the smeared-cracking finite element methodology in the 1960s (Rashid 1968). During the 1980s it was used successfully to predict large nuclear containment structural behavior[i] (Clauss 1987) where continuum response was critical to the solution. This methodology has also been successfully applied to a wide variety of standard beams and slabs and to successfully predict results of laboratory tests of numerous bridge structure components. These predictions have included characterization of cracking, crushing, compressive plasticity (softening), cyclic hysteresis, stiffness degradation, rebar fracture, and ultimate structural failure.[j] This nonlinear modeling methodology uses the nonlinear finite element programs ANACAP-U[j,k] and ABAQUS (ABAQUS User's Manual 1988).[l]

The ANACAP-U concrete constitutive (material) model is based on the smeared-cracking methodology developed by Rashid (1968) and a $J_2$-plasticity theory that permits the incorporation of cracking and other significant concrete response characteristics. The theoretical basis for this model is fully described in the ANACAP Theory Manual.[j] Within the concrete constitutive model, cracking and all other forms of material nonlinearity are treated at the finite element integration points. Thus, the cracking and stress/strain state can vary within an element. Cracks are assumed to form perpendicularly to the principal strain directions in which the cracking criterion is exceeded. Multiple cracks are allowed to form, but they must be mutually orthogonal. When cracking occurs, the stress normal to the crack direction is reduced to zero resulting in redistribution of stresses around the crack. Once a crack forms, the direction of the crack remains fixed, and it can never "heal." However, cracks may close and reopen under load reversals. The shear stiffness is also reduced upon cracking and further decays as the crack opens. This effect is known as "shear retention," and it is attributed to crack roughness and aggregate interlock.

Rebar reinforcement is modeled as individual subelements within the concrete elements. Rebar subelement stiffness is superimposed on the concrete element stiffness in which the rebar resides (ABAQUS User's Manual 1998). The rebar material behavior is handled with a separate constitutive model that treats the steel plasticity, strain hardening, and bond-slip behavior (if bond slip is expected to be significant). The theoretical basis for the rebar model and computational aspects of the rebar plasticity algorithm are described in Rashid et al.[j] The concrete and rebar formulations can handle arbitrary strain reversals at any point in the response, whether in tension or compression.

The ANACAP-U material modeling modules are called by ABAQUS through ABAQUS's subroutine UMAT utility. More information about how this utility works is available in the ABAQUS User's Manual (1988). For all of the analyses described herein, ABAQUS Version 5.6 and ANACAP-U Version 2.5 were used.

---

[i] Dameron, R.A., R.S. Dunham, and Y.R. Rashid. 1989. Methods for Ultimate Load Analysis of Concrete Containments, Phase 3: Developing Criteria and Guidelines for Predicting Concrete Containment Leakage. EPRI NP6260SD, ANATECH Report to EPRI. February 1989.

[j] Rashid, Y.R., R.S. Dunham, R.J. James, and R.A. Dameron. 1998. "ANAMAT Concrete, Rebar, and Steel Material Models," ANA-98-0243, ANATECH Report, ANACAP Theory Manual. April 1998.

[k] James, R.J., R.S. Dunham, and R.A. Dameron. 1997. ANACAP-U User's Manual, Version 2.5. ANA-97-0221, ANATECH Report. September 1997.

**Table 1-1. Potential Failure Modes, Failure Mechanisms, and Analysis Methods for the 1:4-Scale Prestressed Concrete Containment Vessel Model**

| Failure Mode | Failure Mechanism | Evaluation Method |
|---|---|---|
| Loss of Prestressing | Tendon rupture in free-field | Global axisymmetric model |
| | Tendon rupture near a penetration | 3DCM model |
| | Crushing or shear cone failure of concrete adjacent to tendon anchorage | Local buttress analysis (Preliminary Analysis Phase) |
| | Tendon grip or other mechanical anchorage failure | Ancillary tests by tendon supplier and/or NUPEC and SNL |
| Failure of Reinforcement | Rebar rupture in free-field | Global axisymmetric and 3DCM models |
| | Rupture of rebar around personnel A/L, E/H, or other penetration | Local 3D and 3DCM models |
| | Rebar bond slip or anchorage failure | Detailed axisymmetric wall-basemat model |
| Shear/Bending Failure | Wall-basemat juncture | Global axisymmetric model with detailed wall-basemat |
| | Through-basemat | Global axisymmetric model with detailed wall-basemat |
| | Springline | Global axisymmetric analysis and 3D wedge model (Preliminary Analysis Phase) |
| | In wall adjacent to E/H personnel A/L | Local 3D models of penetrations |
| Pressure Loss from Liner Tearing | Tear in free-field liner | Global axisymmetric model |
| | Horizontal tear at wall-basemat juncture | Global axisymmetric model and detailed liner-only wall-basemat model (Preliminary Analysis Phase) |
| | Horizontal tear at springline | Global axisymmetric model and 3D wedge model (Preliminary Analysis) |
| | Horizontal tear near penetrations or other liner anchor discontinuity | Global axisymmetric and local 3D penetration models |
| | Vertical tear near penetrations | Global axisymmetric and local 3D penetration models |
| | Vertical tear at edges of buttress | 3DCM and local 3D models |

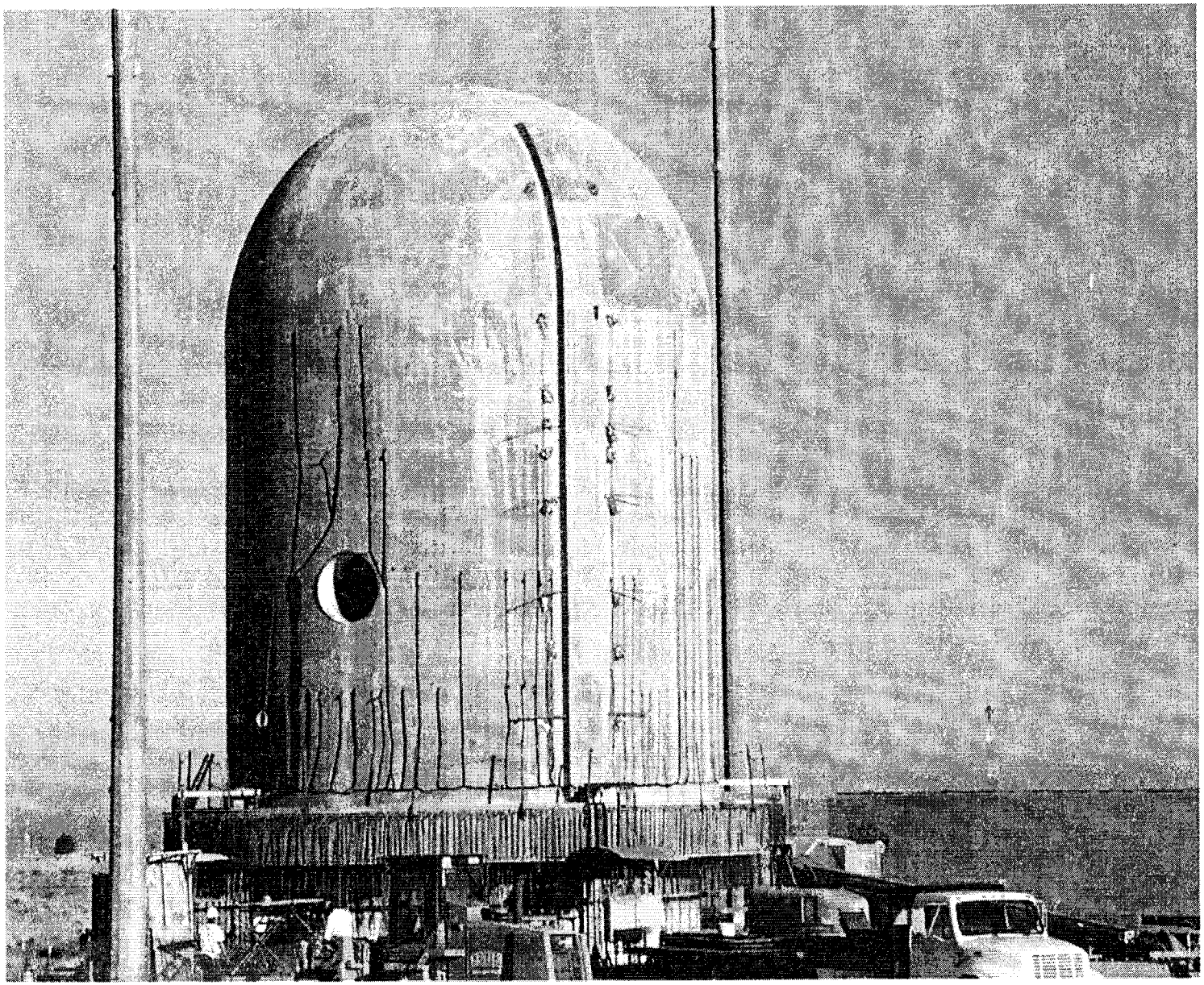

Figure 1-1. NUPEC/NRC 1:4-Scale Prestressed Concrete Containment Vessel (PCCV) Model Built at Sandia National Laboratories

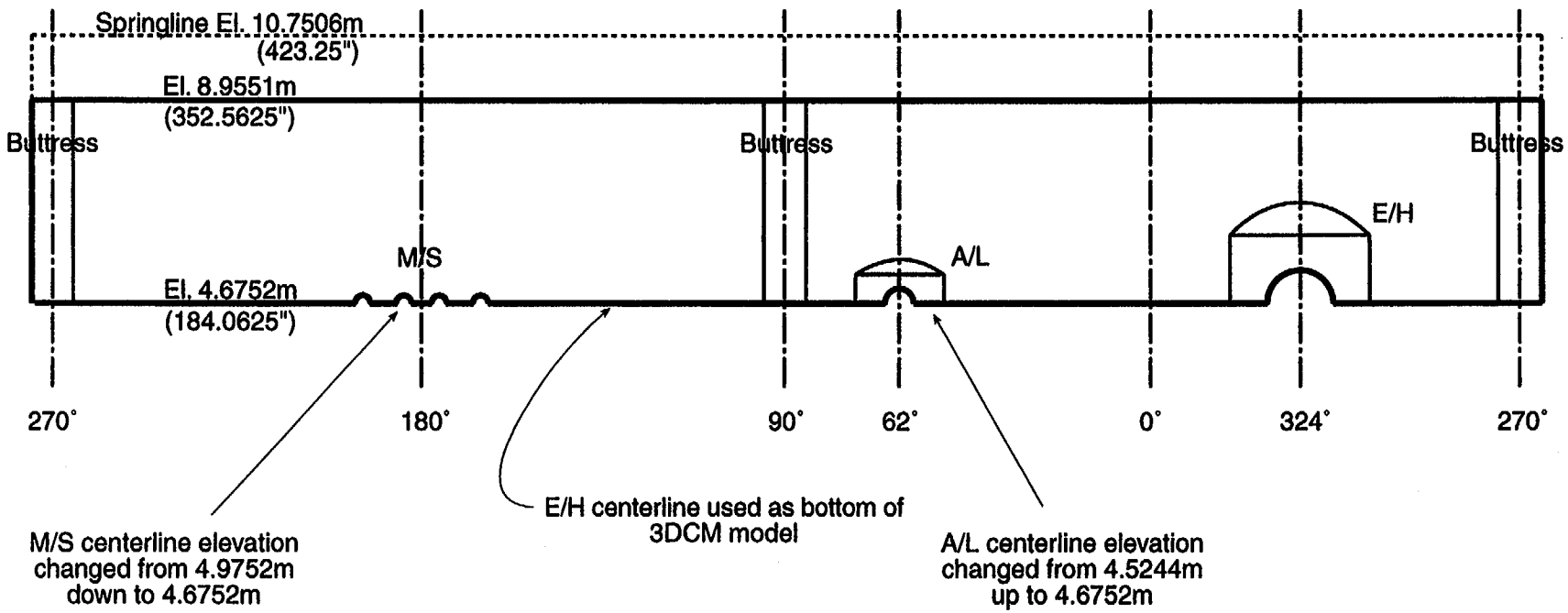


Figure 1-2. Region Represented in 3DCM Model

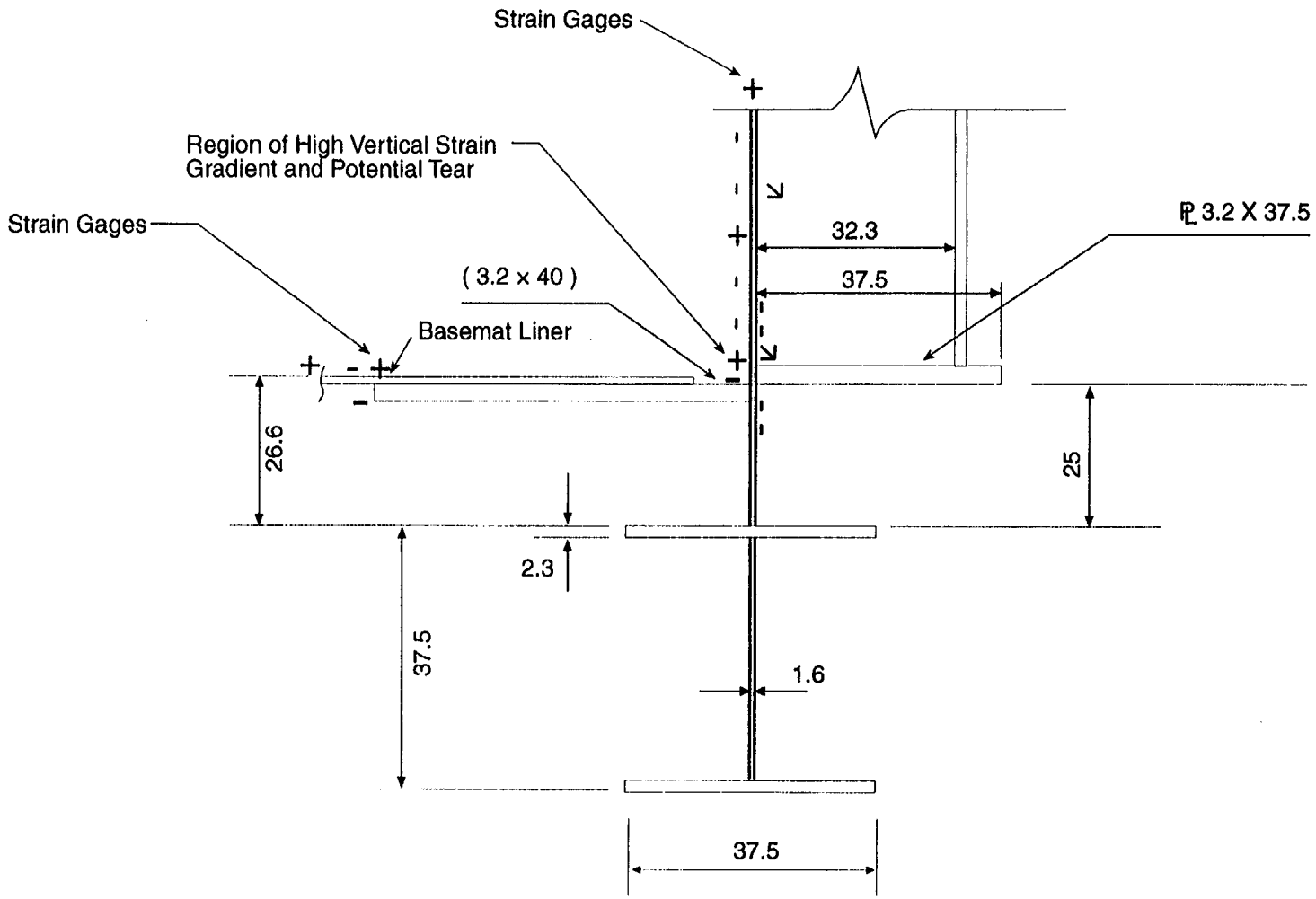


Figure 1-3. Wall - Basemat Liner Connection Detail-Regions of High Strains, Predicted by Analysis, and Gages Placed

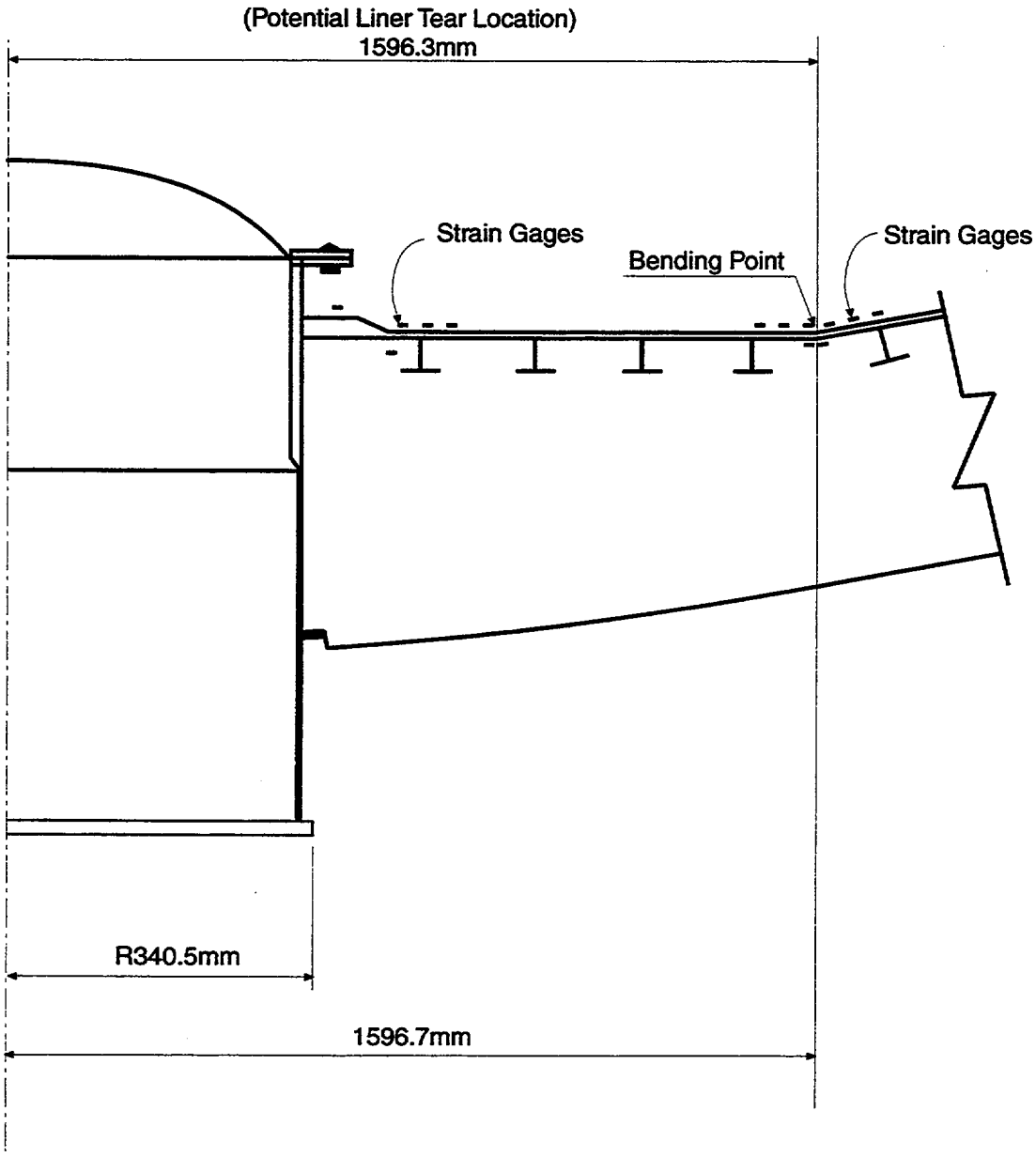


Figure 1-4. Plan Section View of Equipment Hatch Showing Typical Liner Strain Gages at Potential High Strain Locations

# 2. PCCV MODEL DESCRIPTION

## 2.1 Geometry and Loading

Geometry and material property information for the prestressed concrete containment vessel (PCCV) model was provided by Sandia National Laboratories (SNL) (Appendix A). The model shown in Figure 2-1 consists of a 10.8m diameter cylinder with a wall thickness of 325mm, a 3.5m-thick basemat, and a hemispherical dome of thickness 275mm. The rebar for axisymmetric modeling layout is itemized in Figures 2-2a, 2-2b, 2-2c, and 2-2d. The model rests on a 15cm-thick mudmat built over engineered backfill. There is no bond between the basemat and the mudmat, so the model is free to lift up. A partial plan view of the basemat geometry is shown in Figure 2-2d; the basemat reinforcement consists of radial, hoop, and orthogonal rebar patterns.

The meridional tendons are a hairpin design laid out parallel to one of two orthogonal planes (nominally east-west and north-south) (Figure 2-3) and anchored in the tendon gallery. The hoop tendons, as shown in Figure 2-3, span 360°, and the anchorages are staggered between the two buttresses located at 90° and 270°.

The cylinder wall contains a scaled version of an equipment hatch, a personnel airlock, and several smaller penetrations as shown in Figure 2-1 and in the liner stretchout shown in Figure 2-4. The two main openings (equipment hatch and personnel airlock) are located at azimuth 324° and 62°, respectively.

Because of the existence of buttresses and penetrations, the azimuth of the model that is believed to be influenced the least by non-axisymmetric features of the PCCV model is at 135°. This azimuth is located no closer than 45° from any perturbation in free-field stiffness. Thus, this azimuth of the model was adopted specifically for predicting "global" response.

The test calls for nitrogen pressurization. The design pressure $P_d$ of the model is 0.4 MPa. The planned loading sequence is a loading cycle to $0.5P_d$ for the System Functionality Test (SFT), $1.125P_d$ for the Structural Integrity Test (SIT), $0.9\ P_d$ for the Integrated Leak Rate Test (ILRT) prior to ultimate pressurization of the model. The loading used in the prediction analyses includes the SIT as shown in Figure 2-5.

## 2.2 Material Properties

The material property input to the analyses was based on data measured by the model constructor and summarized by SNL (Appendix A). Assumed properties were used for preliminary analysis, and more precise data based on concrete cylinder and steel coupon tests made during model construction were used for the pretest analysis. The pretest analysis models use the properties outlined in the following subsections.

### 2.2.1 Concrete Properties

The concrete properties used in the analysis were based on stress versus strain data of the trial mix concrete given in Table 2-1 and on a few measurements that were available from construction prior to January 1999. In the preliminary analysis, concrete strength of 10% higher than specified on the drawings was assumed. The 10% increase was added to account for additional strength associated with aging of the material between the time of placement and the time of testing.

The NUPEC report, JPN-22-T-1 (Rev. 1), March 9, 1998, provided data for Series A and Series B of the trial mix and gave the following definitions:

Series A: Specimens were taken out of plastic bags at the age of seven days.

Series B: Specimens were kept in plastic bags until tests were performed.

In the process of selecting a representative concrete material curve, it was noted in SNL's final information package released to Round Robin participants (Appendix A) that the actual concrete poured was generally weaker than that used in the trial mix tests. Based on this information, the trial mix data were not used directly for the $f_c' = 44.13$ MPa concrete. The data were used, however, to calibrate the shape of the stress-strain curve and to establish parameters such as $\varepsilon_{crush}$ (the uniaxial strain at maximum compressive strength), $\varepsilon_{fracture}$ (the cracking strain), Young's modulus, and Poisson's ratio. For the compressive strength, the specified strength plus 10% for aging was used. The stress-strain curve that was assumed and the various data provided by SNL are plotted in Figure 2-6.

For the $f_c' = 29.42$ MPa concrete, tests taken at the time of construction showed better correlation to the trial mix data, so these data (Table 2-1) were used to establish $f_c'$ and the other material parameters. From past experience with the 1:6 scale reinforced concrete containment model and other test models, actual strength corresponds best to field cured specimens. This is because the PCCV model itself is subjected to the same atmospheric elements and temperature variations as the field cured specimens. The stress-strain curve used in the analysis is shown in Figure 2-7. All inputs to the analytical material models are summarized in Table 2-1.

### 2.2.2 Reinforcement

Stress-strain data from rebar pull tests were provided in the SNL information packages sent to all Round Robin participants (Appendix A). In general, three test curves were provided for each bar size and specified strength. For some bar sizes, results of pull tests on dumb-bell shaped specimens fabricated from the standard bars were also provided. It was generally observed that the dumb-bell specimens produced significantly higher yield and ultimate strengths than the unaltered bar specimens. Based on experience and on some additional qualitative information provided by SNL, it was deduced that the yield curve for the standard (unaltered) specimens provided the best representation of engineering stress versus engineering strain to use in the analysis, but that the dumb-bell specimens provided the best representation of Young's modulus. This rule was followed in the generation of the idealized curves for analysis, plotted in Figures 2-8 through 2-17. In each case, one dataset that appeared to represent the average of three reliable datasets, was selected as the representative stress-strain data. Single "outlier" curves which deviated significantly from the other two curves were ignored. The yield curve data input to the analysis is also tabulated in Table 2-2b. In all cases Young's modulus was set equal to 200,000 MPa.

It should be noted that since the measured stress-strain data are based on a measured force divided by nominal area, it is mathematically appropriate to input nominal areas to the finite element model, regardless of the presence of the "ribs" or irregularities on the deformed bars.

### 2.2.3 Tendons

Strand and tendon stress and strain data in SNL's information package (Appendix A) were obtained by testing both individual strands and tendon assemblies (including anchor hardware) according to Japanese test standards JIS G 3536 and JISZ 2241. Engineering stress was calculated from the applied force and the initial cross-sectional areas. Elongation was determined from the stroke of the testing machine, and strain was obtained by averaging the data from strain gages mounted on individual strand wires. It should be noted that the strain gage data were not corrected to account for the pitch of the wires in the strand that affect the accuracy of the strain readings by as much as 20%. Consequently, the most appropriate data to use directly in finite element representation of the tendons are tendon system load versus elongation data provided in the PCCV Material Property Report.[1] The load cell data are then divided by the nominal area (3.393 $cm^2$) to get engineering stress. The final idealizations of the data are plotted in Figures 2-18 and 2-19. The data input to the analysis is tabulated in Table 2-2a. Young's modulus was set equal to 195,200 MPa, based on the tendon pull tests.

### 2.2.4 Liner

Six sets of liner stress-strain measurements were provided by SNL: three for the hoop direction and three for the vertical direction. Because the differences in the hoop and vertical properties were too small to warrant the added complexities of using an anisotropic plasticity model, the data were averaged.

[1] Pace, D. W., E.W. Klamerus, and M. F. Hessheimer. 1999. "PCCV Material Property Report," Project Report No. R-SN-P-004, Rev. A. Albuquerque, NM: Sandia National Laboratories, January 1999.

## Table 2-1. Material Data for Trial Mix Concrete

### Series A

| Test Items | | $f_c'$ = 29.42 MPa* | | $f_c'$ = 44.13 MPa* | |
|---|---|---|---|---|---|
| | | **Standard Curing** | **Field Curing** | **Standard Curing** | **Field Curing** |
| Comprehensive Strength (MPa) | (1 week) | 33.64 | 29.42 | 39.13 | 40.99 |
| Compressive Strength (MPa) | (4 weeks) | 40.31 | 33.44 | 49.72 | 48.25 |
| Compressive Strength (MPa) | (13 weeks) | 51.39 | 41.68 | 60.21 | 48.84 |
| Tensile Strength (MPa) | (13 weeks) | 3.93 | 3.37 | 4.21 | 3.45 |
| Flexural Strength (MPa) | (13 weeks) | 5.37 | 4.00 | 5.58 | 5.51 |
| Young's modulus ($\times 10^3$ MPa) | (13 weeks) | 29.03 | 27.95 | 31.97 | 26.97 |
| Poisson's ratio | (13 weeks) | 0.20 | 0.18 | 0.20 | 0.18 |
| Density (ton/m$^3$) | (13 weeks) | 2.25 | 2.21 | 2.26 | 2.19 |

### Series B

| Test Items | | $f_c'$ = 29.42 MPa | | $f_c'$ = 44.13 MPa | |
|---|---|---|---|---|---|
| | | **Standard Curing** | **Field Curing** | **Standard Curing** | **Field Curing** |
| Comprehensive Strength (MPa) | (1 week) | N/A | N/A | N/A | N/A |
| Compressive Strength (MPa) | (4 weeks) | 47.46 | 41.78 | 53.46 | 53.35 |
| Compressive Strength (MPa) | (13 weeks) | 58.94 | 47.07 | 64.43 | 61.78 |
| Tensile Strength (MPa) | (13 weeks) | 3.98 | 3.98 | 4.46 | 3.84 |
| Flexural Strength (MPa) | (13 weeks) | 5.63 | 5.90 | 5.77 | 4.39 |
| Young's modulus (x$10^3$ MPa) | (13 weeks) | 29.81 | 26.77 | 29.62 | 29.13 |
| Poisson's ratio | (13 weeks) | 0.22 | 0.23 | 0.23 | 0.23 |
| Density (ton/m$^3$) | (13 weeks) | 2.25 | 2.23 | 2.24 | 2.23 |

* Designates the specified 91 day minimum strength (used for design).

### Summary

| | Spec. $f_c'$ = 29.42 MPa | Spec. $f_c'$ = 44.13 MPa |
|---|---|---|
| Uniaxial Compressive Strength | 48.81 MPa<br>(1.1 × Avg. of Series A, Series B at 13 weeks, Field Cured) | 48.54 MPa<br>(1.1 × Spec. Value) |
| Uniaxial Tensile Strength** | 2.65 MPa<br>(assumed $\varepsilon_{fracture} = 80 \times 10^{-6}$) | 2.64 MPa<br>(assumed $\varepsilon_{fracture} = 80 \times 10^{-6}$) |
| Initial Young's modulus** | 33,071 MPa<br>(57,000 $\sqrt{f_c'}$, with $f_c'$ in psi) | 32,979 MPa<br>(57,000 $\sqrt{f_c'}$, with $f_c'$ in psi) |
| Poisson's ratio** | 0.2 | 0.2 |
| Density | 2.2 ton/m$^3$ | 2.2 ton/m$^3$ |

** Tensile Strength, Young's modulus, and Poisson's ratio were based on experience and on formulae built-into the ANACAP-U constitutive model, but they all compare fairly well to the trial mix data.

## Table 2-2a. Input Data to Analytical Models for Liner and Tendon Properties

| Liner Stress vs. Plastic Strain Input | | Tendon Stress vs. Plastic Strain Input | |
|---|---|---|---|
| $\sigma_y$ = 376.2 MPa | | $\sigma_y$ = 1592.7 MPa | |
| **Plastic Strain (mm/mm)** | **Stress (MPa)** | **Plastic Strain (mm/mm)** | **Stress (MPa)** |
| 0.06% | 378.2 | 0.05% | 1621.7 |
| 0.10% | 375.9 | 0.07% | 1647.2 |
| 0.22% | 375.2 | 0.11% | 1676.2 |
| 0.30% | 374.9 | 0.16% | 1702.4 |
| 0.42% | 374.2 | 0.24% | 1728.6 |
| 0.50% | 374.1 | 0.27% | 1734.1 |
| 0.62% | 373.8 | 0.33% | 1743.1 |
| 0.70% | 373.6 | 0.40% | 1748.6 |
| 0.82% | 373.0 | 0.47% | 1754.8 |
| 0.90% | 372.5 | 0.53% | 1757.5 |
| 1.02% | 372.3 | 0.60% | 1760.3 |
| 1.10% | 372.4 | 0.67% | 1763.1 |
| 1.22% | 373.5 | 0.74% | 1765.8 |
| 1.42% | 379.4 | 0.81% | 1769.3 |
| 1.62% | 384.1 | 0.88% | 1774.8 |
| 1.74% | 386.1 | 0.94% | 1777.5 |
| 1.84% | 390.5 | 1.02% | 1783.0 |
| 2.14% | 402.3 | 1.08% | 1783.0 |
| 2.54% | 414.3 | 1.15% | 1789.3 |
| 2.94% | 424.6 | 1.22% | 1792.0 |
| 3.02% | 426.4 | 1.29% | 1794.8 |
| 3.34% | 432.9 | 1.35% | 1801.0 |
| 3.42% | 434.5 | 1.42% | 1803.7 |
| 3.74% | 440.4 | 1.49% | 1809.2 |
| 3.82% | 441.8 | 1.62% | 1815.5 |
| 4.14% | 446.8 | 1.69% | 1821.0 |
| 4.22% | 447.9 | 1.76% | 1823.7 |
| 4.54% | 452.0 | 1.83% | 1829.9 |
| 4.62% | 452.8 | 1.89% | 1832.7 |
| 4.82% | 455.1 | 1.96% | 1835.4 |
| 4.84% | 455.3 | 2.03% | 1838.2 |
| 5.21% | 456.2 | 2.10% | 1844.4 |
| 32.82% | 497.7 | 2.16% | 1847.2 |
| 35.00% | 498.2 | 2.23% | 1849.9 |
| 40.00% | 49.8 | 2.30% | 1852.7 |
| | | 2.37% | 1855.4 |
| | | 2.44% | 1858.2 |
| | | 2.57% | 1864.4 |
| | | 2.64% | 1867.2 |
| | | 2.71% | 1869.9 |
| | | 2.78% | 1872.7 |
| | | 2.84% | 1876.1 |
| | | 2.91% | 1876.1 |
| | | 5.00% | 1875.4 |
| | | 10.00% | 187.5 |

## Table 2-2b. Stress-Strain Input Data to Analytical Models for Rebar

| SD6 Stress-Strain Input | | SD345D10 Stress-Strain Input | | SD390D10 Stress-Strain Input | | SD390D13 Stress-Strain | |
|---|---|---|---|---|---|---|---|
| $\sigma_y$ = 382.0MPa | | $\sigma_y$ = 373.3MPa | | $\sigma_y$ = 481.9MPa | | $\sigma_y$ = 434.6MPa | |
| **Strain (mm/mm)** | **Stress (MPa)** | **Strain (mm/mm)** | **Stress (MPa)** | **Strain (mm/mm)** | **Stress (MPa)** | **Strain (mm/mm)** | **Stress (MPa)** |
| 1.30% | 352.4 | 0.74% | 356.9 | 1.15% | 462.2 | 0.73% | 420.2 |
| 1.78% | 354.1 | 1.45% | 367.7 | 1.47% | 475.3 | 1.06% | 428.1 |
| 2.29% | 355.3 | 1.59% | 376.0 | 1.65% | 484.3 | 1.20% | 431.2 |
| 2.70% | 359.8 | 1.78% | 384.3 | 1.71% | 489.8 | 1.27% | 434.6 |
| 3.11% | 368.7 | 1.93% | 389.6 | 1.85% | 495.3 | 1.33% | 437.9 |
| 3.38% | 377.2 | 2.11% | 397.1 | 1.96% | 497.4 | 1.41% | 440.7 |
| 3.50% | 380.3 | 2.30% | 405.4 | 2.11% | 510.7 | 1.52% | 449.7 |
| 3.78% | 383.9 | 2.51% | 413.2 | 2.34% | 520.4 | 1.68% | 456.8 |
| 4.22% | 395.0 | 2.71% | 420.7 | 2.55% | 528.4 | 1.85% | 463.8 |
| 4.59% | 398.1 | 2.91% | 427.2 | 2.75% | 535.1 | 2.02% | 470.3 |
| 4.97% | 404.7 | 3.11% | 434.0 | 2.96% | 543.4 | 2.18% | 476.4 |
| 5.42% | 410.1 | 3.33% | 440.5 | 3.12% | 548.4 | 2.34% | 482.6 |
| 5.78% | 413.2 | 3.54% | 446.7 | 3.37% | 556.0 | 2.51% | 488.6 |
| 6.23% | 418.0 | 3.77% | 452.8 | 3.54% | 560.9 | 2.69% | 494.4 |
| 6.60% | 420.6 | 4.00% | 458.5 | 3.72% | 565.7 | 2.87% | 500.0 |
| 7.04% | 423.3 | 4.45% | 468.1 | 4.19% | 576.6 | 3.05% | 505.4 |
| 7.68% | 425.3 | 4.82% | 475.3 | 4.57% | 584.4 | 3.23% | 510.6 |
| 8.08% | 425.8 | 5.26% | 482.9 | 4.96% | 591.0 | 3.42% | 515.6 |
| 9.12% | 426.4 | 5.65% | 489.0 | 5.39% | 597.4 | 3.61% | 520.3 |
| 2.86% | 426.7 | 6.07% | 494.4 | 5.76% | 601.8 | 3.90% | 527.1 |
| 0.17% | 489.3 | 6.40% | 498.1 | 6.27% | 607.6 | 4.30% | 535.6 |
| 2.00% | 0.1 | 6.80% | 502.2 | 6.89% | 612.9 | 4.72% | 543.2 |
| | | 7.21% | 505.0 | 7.53% | 615.4 | 5.16% | 550.2 |
| | | 7.91% | 508.5 | 10.43% | 616.6 | 5.52% | 555.1 |
| | | 10.15% | 509.3 | 20.20% | 652.7 | 5.90% | 559.7 |
| | | 23.60% | 552.7 | 25.00% | 0.1 | 6.33% | 563.9 |
| | | 25.00% | 0.1 | | | 6.84% | 567.9 |
| | | | | | | 7.11% | 569.1 |
| | | | | | | 12.46% | 570.3 |
| | | | | | | 23.88% | 610.5 |
| | | | | | | 25.00% | 0.1 |

## Table 2-2c. Stress-Strain Input Data to Analytical Models for Rebar

| SDS16 Stress-Strain Input | | SD390D19 Stress-Strain Input | | SD390D22 Stress-Strain Input | | SD490D10 Stress-Strain | |
|---|---|---|---|---|---|---|---|
| $\sigma_y$ = 454.7MPa | | $\sigma_y$ = 477.6MPa | | $\sigma_y$ = 461.0MPa | | $\sigma_y$ = 491.8MPa | |
| Strain (mm/mm) | Stress (MPa) | Strain (mm/mm) | Stress (MPa) | Strain (mm/mm) | Stress (MPa) | Strain (mm/mm) | Stress (MPa) |
| 0.15% | 450.0 | 1.10% | 467.6 | 0.32% | 456.0 | 1.35% | 481.2 |
| 0.90% | 445.6 | 1.71% | 478.7 | 0.67% | 458.1 | 1.59% | 490.3 |
| 1.30% | 443.3 | 1.89% | 489.5 | 0.79% | 459.8 | 1.66% | 493.3 |
| 1.49% | 455.2 | 2.25% | 504.0 | 0.81% | 459.5 | 1.84% | 506.1 |
| 1.64% | 462.5 | 2.48% | 513.0 | 0.83% | 460.4 | 2.09% | 517.9 |
| 1.83% | 470.2 | 2.72% | 521.7 | 0.90% | 469.5 | 2.28% | 526.0 |
| 2.07% | 479.2 | 2.96% | 530.3 | 0.99% | 475.4 | 2.47% | 533.8 |
| 2.23% | 485.4 | 3.22% | 538.4 | 1.08% | 481.3 | 2.67% | 541.1 |
| 2.45% | 493.4 | 3.47% | 545.9 | 1.18% | 487.1 | 2.85% | 547.4 |
| 2.65% | 500.3 | 3.73% | 553.0 | 1.27% | 492.9 | 3.04% | 553.7 |
| 2.85% | 506.6 | 4.12% | 562.8 | 1.37% | 498.6 | 3.22% | 559.5 |
| 3.03% | 512.1 | 4.52% | 571.4 | 1.47% | 504.1 | 3.41% | 565.3 |
| 3.27% | 518.9 | 4.91% | 579.0 | 1.56% | 509.6 | 3.60% | 570.6 |
| 3.45% | 523.5 | 5.41% | 587.5 | 1.66% | 515.0 | 3.80% | 575.8 |
| 3.63% | 528.2 | 5.69% | 591.9 | 1.76% | 520.4 | 4.11% | 583.7 |
| 3.96% | 535.6 | 6.15% | 598.1 | 1.97% | 530.9 | 4.57% | 593.5 |
| 4.36% | 543.5 | 6.64% | 603.7 | 2.18% | 541.0 | 4.18% | 598.0 |
| 4.76% | 550.5 | 7.02% | 607.1 | 2.39% | 550.6 | 5.18 | 604.0 |
| 5.32% | 559.1 | 7.52% | 610.3 | 2.55% | 557.5 | 5.67% | 610.5 |
| 5.55% | 562.1 | 7.94% | 613.3 | 2.76% | 566.3 | 5.92% | 613.1 |
| 5.95% | 566.5 | 8.35% | 614.8 | 2.98% | 574.5 | 6.50% | 619.7 |
| 6.36% | 570.5 | 20.79% | 658.2 | 3.15% | 580.4 | 7.24% | 621.4 |
| 6.71% | 572.9 | 22.00% | 0.1 | 3.38% | 587.9 | 21.11% | 665.8 |
| 7.18% | 575.4 | | | 3.55% | 593.1 | 23.00% | 0.1 |
| 7.59% | 576.1 | | | 3.79% | 599.7 | | |
| 21.85% | 616.4 | | | 4.19% | 609.6 | | |
| 23.00% | 0.1 | | | 4.57% | 617.7 | | |
| | | | | 4.80% | 622.0 | | |
| | | | | 5.16% | 628.3 | | |
| | | | | 5.56% | 634.4 | | |
| | | | | 5.78% | 637.2 | | |
| | | | | 6.17% | 641.5 | | |
| | | | | 6.58% | 645.3 | | |
| | | | | 7.01% | 648.6 | | |
| | | | | 7.59% | 651.4 | | |
| | | | | 9.00% | 652.0 | | |
| | | | | 18.45% | 680.6 | | |
| | | | | 20.00 | 0.1 | | |

## Table 2-2d. Stress-Strain Input Data to Analytical Models for Rebar

| SD13 Stress-Strain Input | | SD490D16 Stress-Strain Input | | SD490D19 Stress-Strain | |
|---|---|---|---|---|---|
| $\sigma_y$ = 545.7MPa | | $\sigma_y$ = 500.0MPa | | $\sigma_y$ = 512.2MPa | |
| **Strain (mm/mm)** | **Stress (MPa)** | **Strain (mm/mm)** | **Stress (MPa)** | **Strain (mm/mm)** | **Stress (MPa)** |
| 0.57% | 524.1 | 1.01% | 485.1 | 0.08% | 509.0 |
| 0.99% | 538.7 | 1.38% | 499.0 | 1.45% | 505.9 |
| 1.13% | 542.7 | 1.44% | 500.9 | 1.64% | 520.3 |
| 1.20% | 547.2 | 1.53% | 501.1 | 1.77% | 526.3 |
| 1.30% | 549.5 | 1.64% | 513.8 | 1.87% | 530.9 |
| 1.44% | 564.7 | 1.78% | 521.4 | 1.95% | 535.5 |
| 1.60% | 573.9 | 1.92% | 528.7 | 2.05% | 540.2 |
| 1.82% | 586.4 | 2.15% | 539.5 | 2.25% | 549.8 |
| 2.04% | 598.1 | 2.37% | 549.5 | 2.45% | 558.6 |
| 2.21% | 606.8 | 2.52% | 556.0 | 2.64% | 566.8 |
| 2.44% | 617.8 | 2.75% | 565.5 | 2.84% | 574.9 |
| 2.61% | 625.5 | 2.99% | 574.4 | 3.04% | 582.6 |
| 2.83% | 635.0 | 3.37% | 588.3 | 3.25% | 590.2 |
| 3.00% | 641.5 | 3.76% | 602.8 | 3.48% | 597.5 |
| 3.17% | 647.7 | 4.00% | 611.4 | 3.71% | 604.5 |
| 3.37% | 655.0 | 4.60% | 628.2 | 4.18% | 617.4 |
| 3.50% | 659.4 | 5.43% | 643.7 | 4.55% | 626.0 |
| 3.71% | 665.7 | 16.82% | 688.1 | 4.93% | 633.8 |
| 4.12% | 676.8 | 18.00% | 0.1 | 5.20% | 638.5 |
| 4.33% | 681.8 | | | 5.46% | 642.8 |
| 4.70% | 689.6 | | | 5.93% | 649.3 |
| 5.00% | 694.8 | | | 6.24% | 653.2 |
| 5.29% | 699.7 | | | 6.62% | 565.8 |
| 5.70% | 705.8 | | | 6.99% | 658.5 |
| 6.15% | 711.2 | | | 17.51% | 709.5 |
| 6.50% | 714.2 | | | 10.00% | 0.1 |
| 6.99% | 718.6 | | | | |
| 7.41% | 720.8 | | | | |
| 7.95% | 722.7 | | | | |
| 11.73% | 722.9 | | | | |
| 16.10% | 751.2 | | | | |
| 18.00% | 0.1 | | | | |

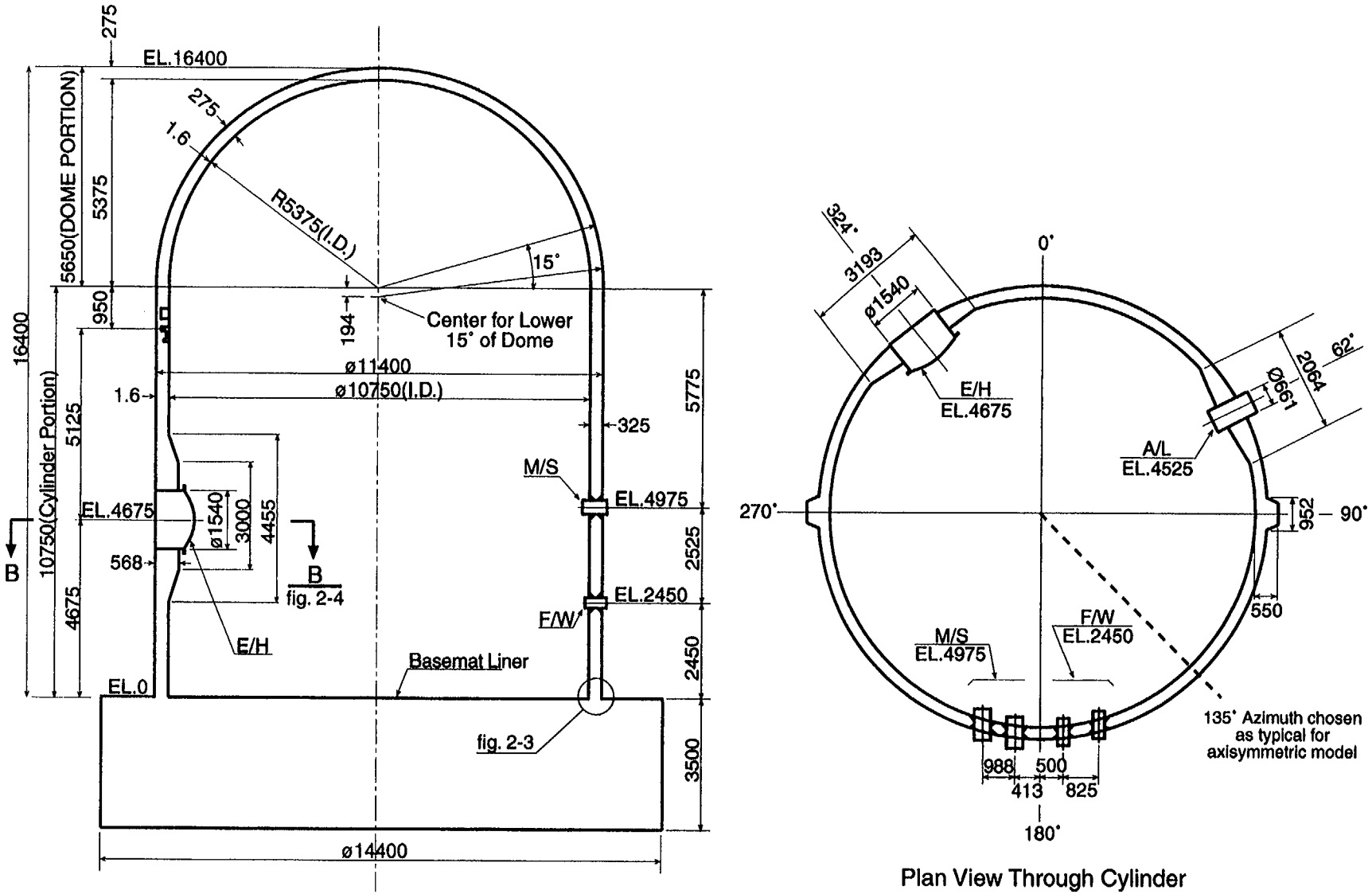


Figure 2-1. 1:4-Scale Prestressed Concrete Containment Vessel (PCCV) Model Geometry (Dimensions in mm)

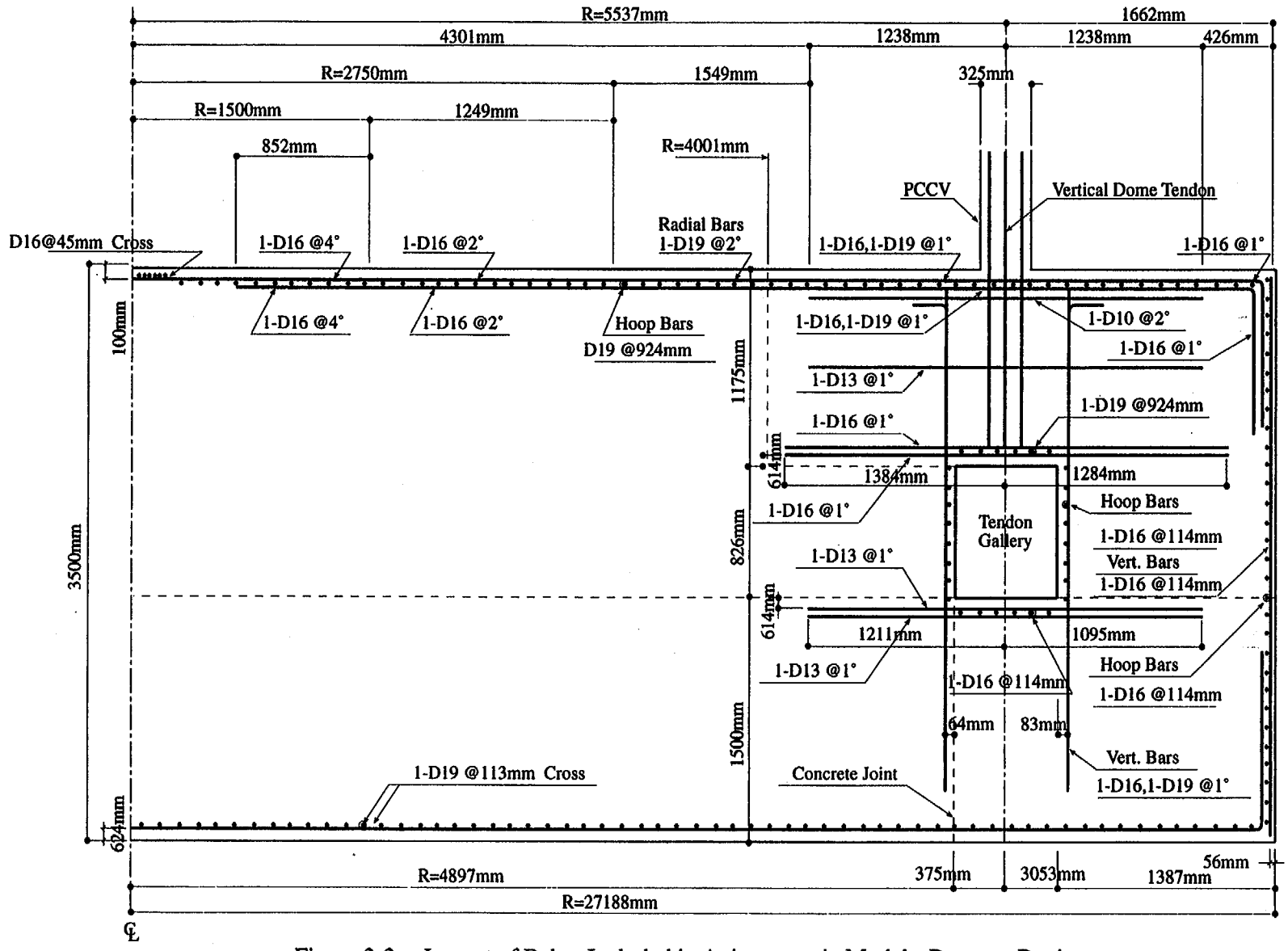


Figure 2-2a. Layout of Rebar Included in Axisymmetric Model - Basemat Region

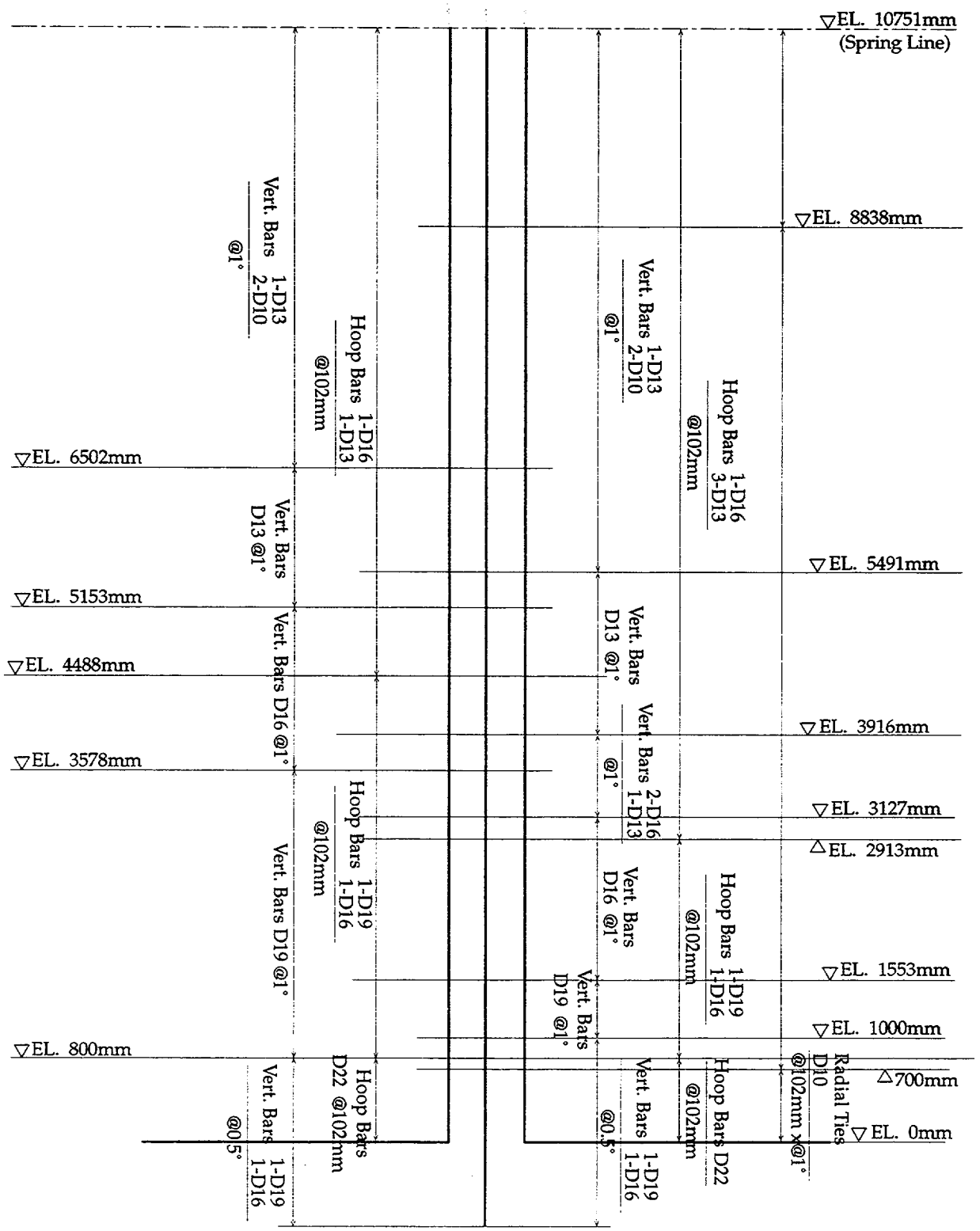


Figure 2-2b. Layout of Rebar Included in Axisymmetric Model - Cylinder Wall Region

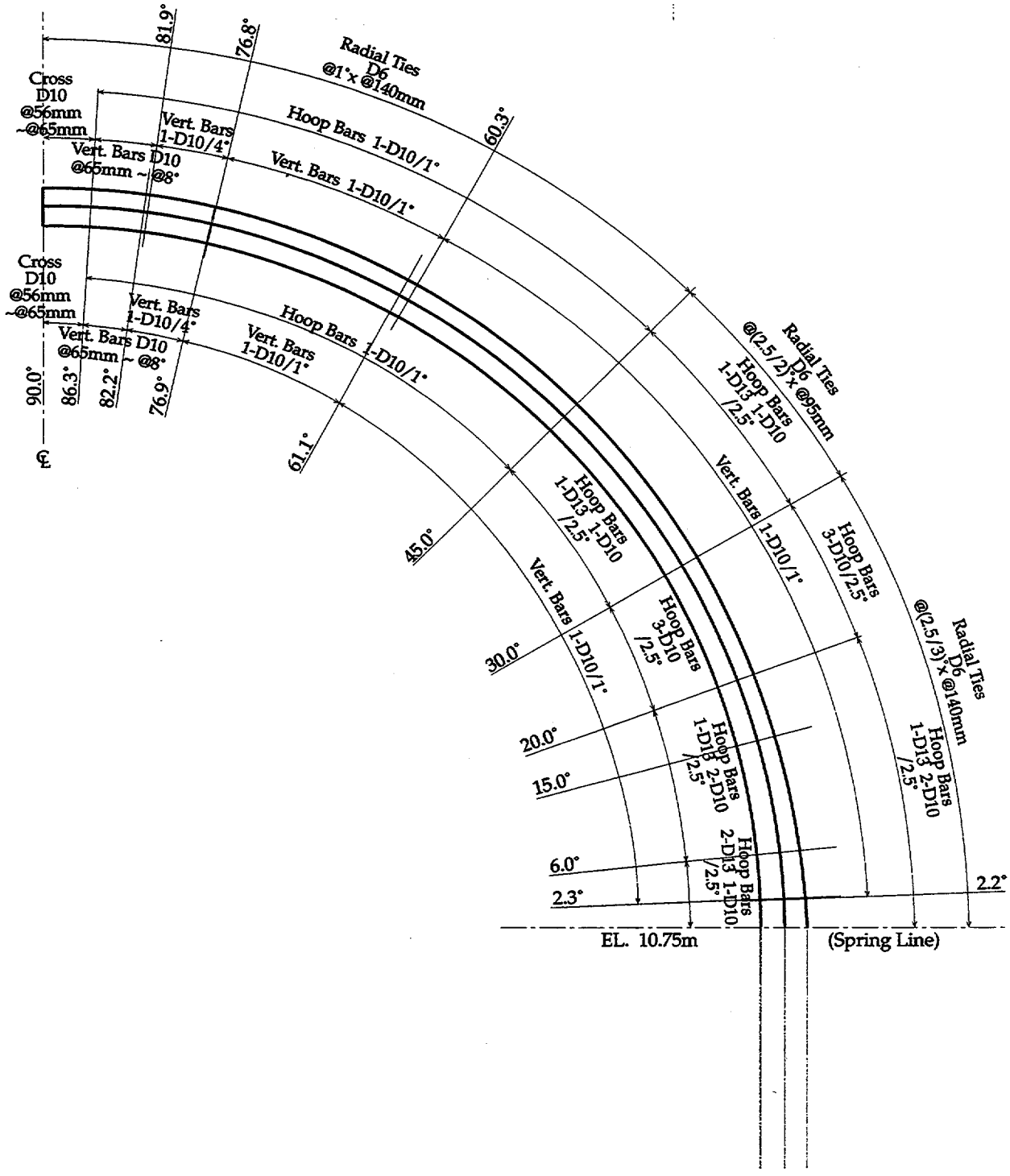


Figure 2-2c. Layout of Rebar Included in Axisymmetric Model - Dome Region

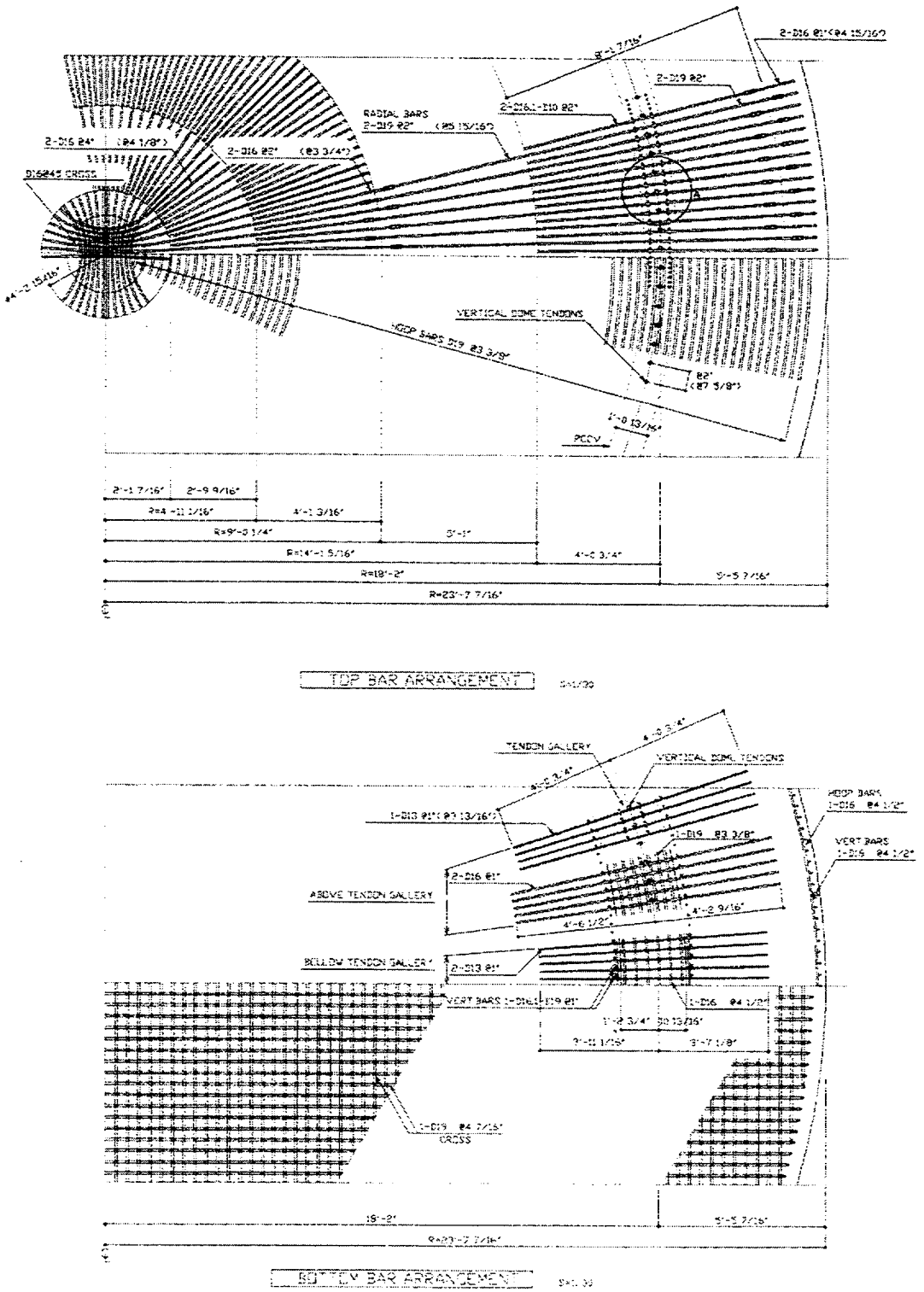


Figure 2-2d. 1:4-Scale Model-Basemat Reinforcement

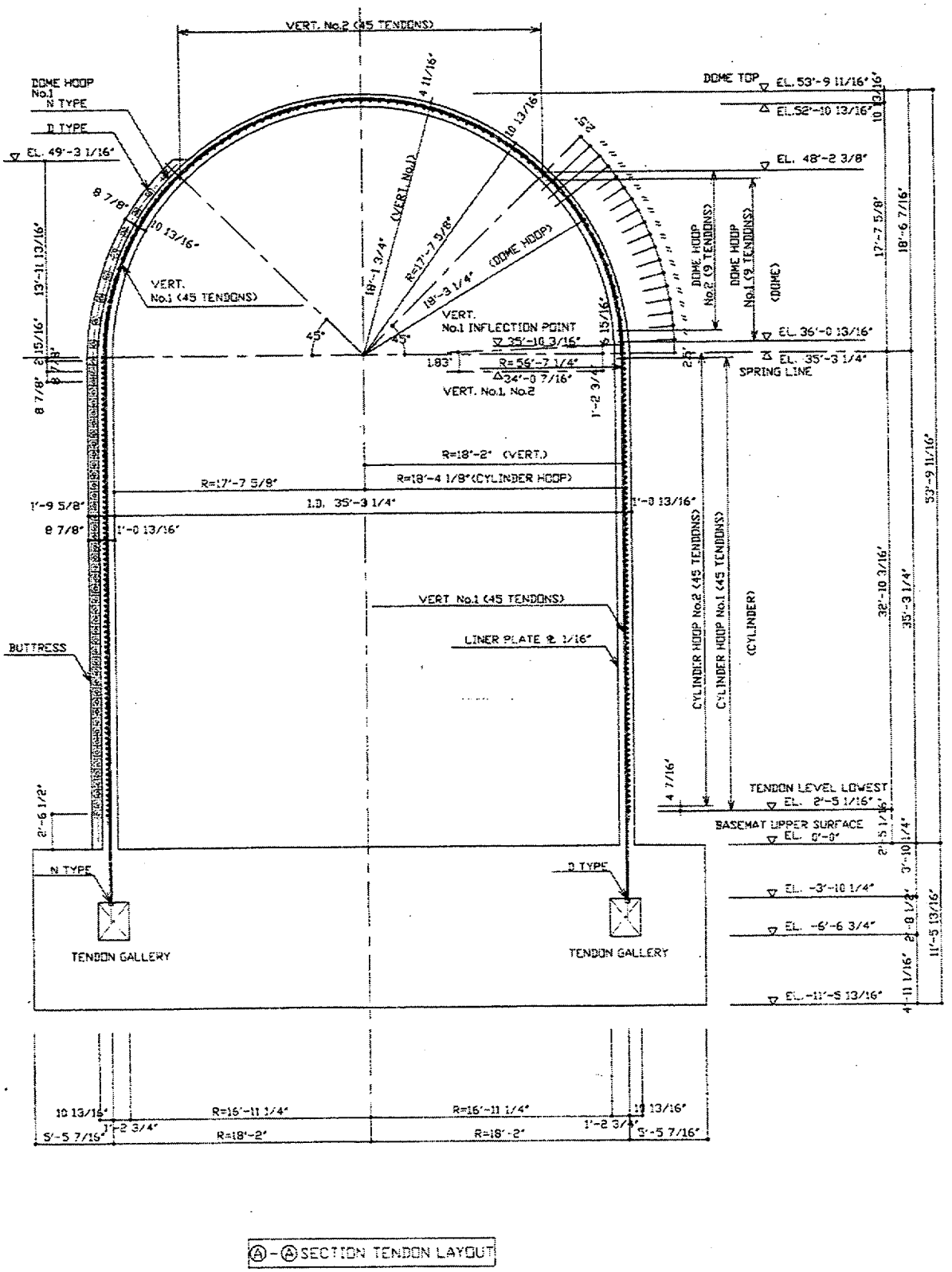


Figure 2-3. 1:4-Scale Model Tendon Layout

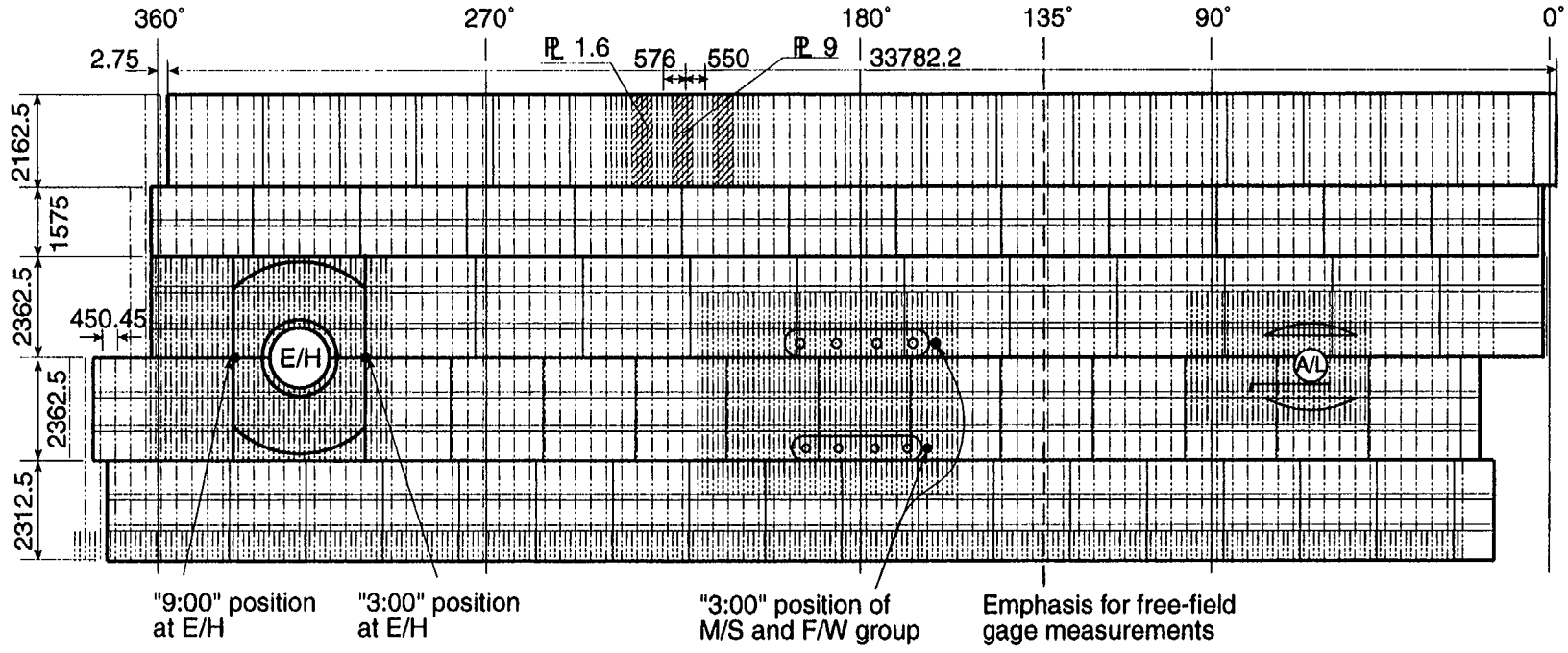


Figure 2-4. 1:4-Scale Prestressed Concrete Containment Vessel (PCCV) Model - Liner Stretchout, with Initial Guesses of High-Strain Locations

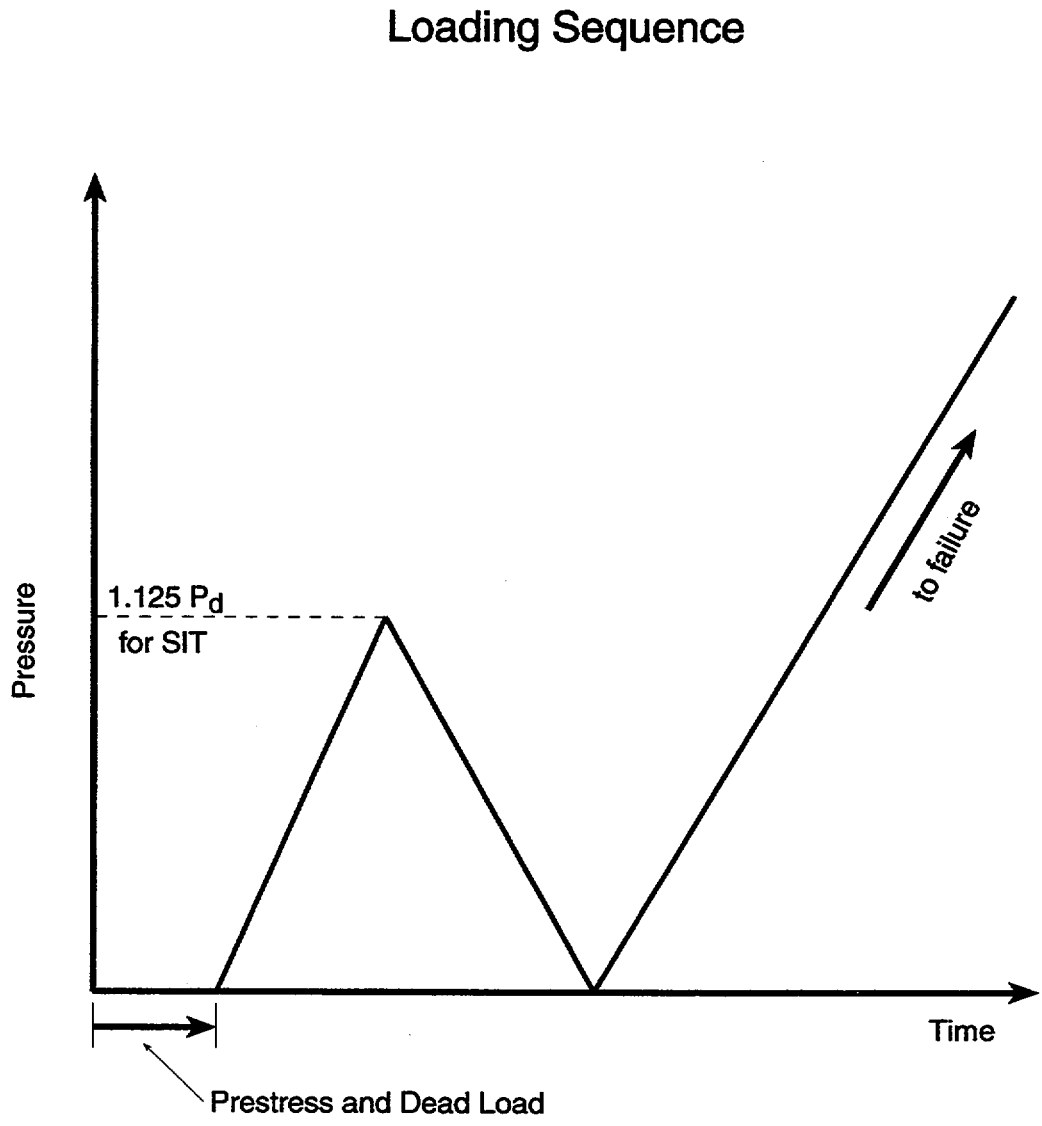


Figure 2-5. Pressurization Sequence Applied in Analysis

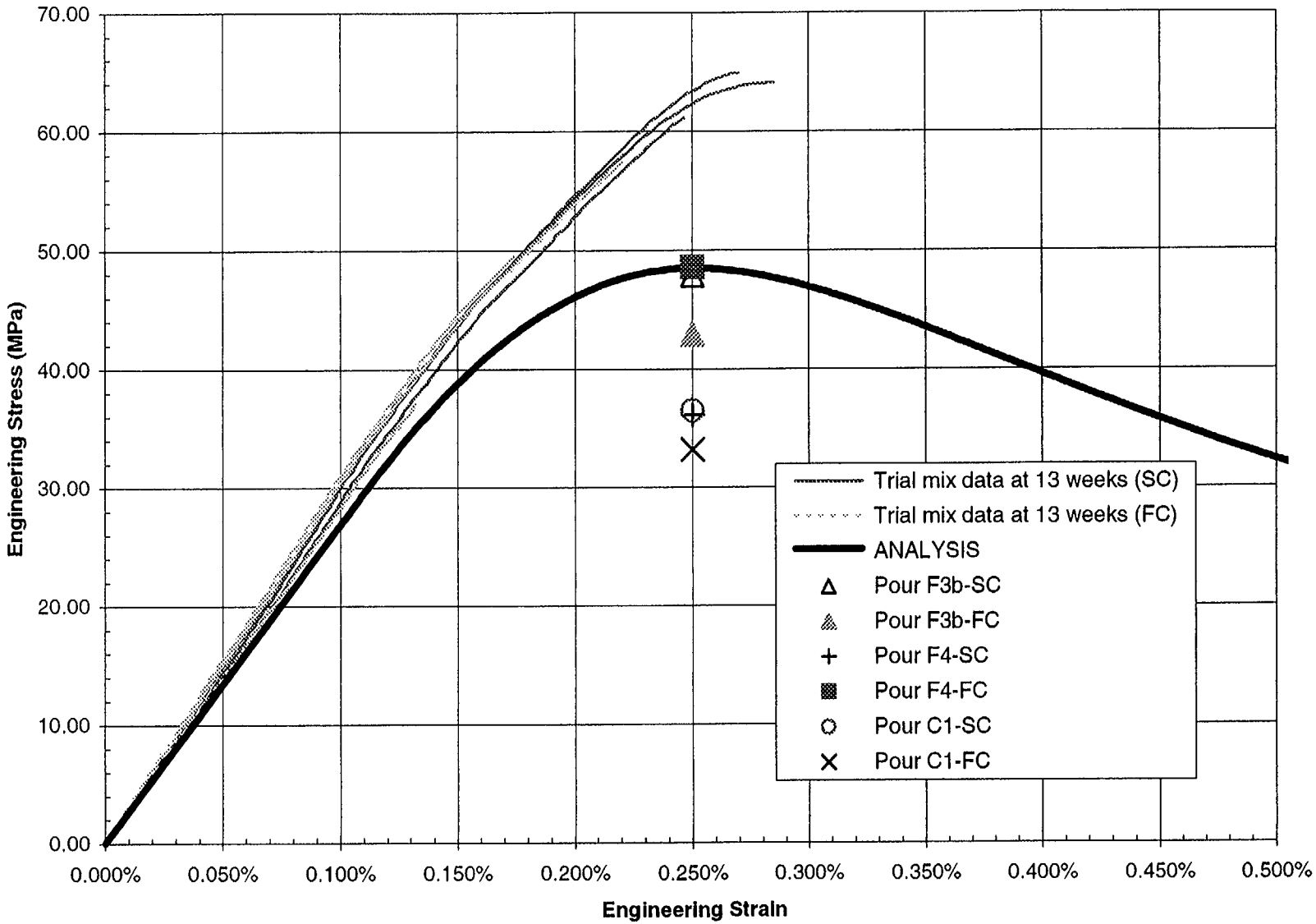


Figure 2-6. Cylinder Concrete (spec. $f_c'$ = 48.55 MPa) Stress-Strain Idealization and Sample Measurements

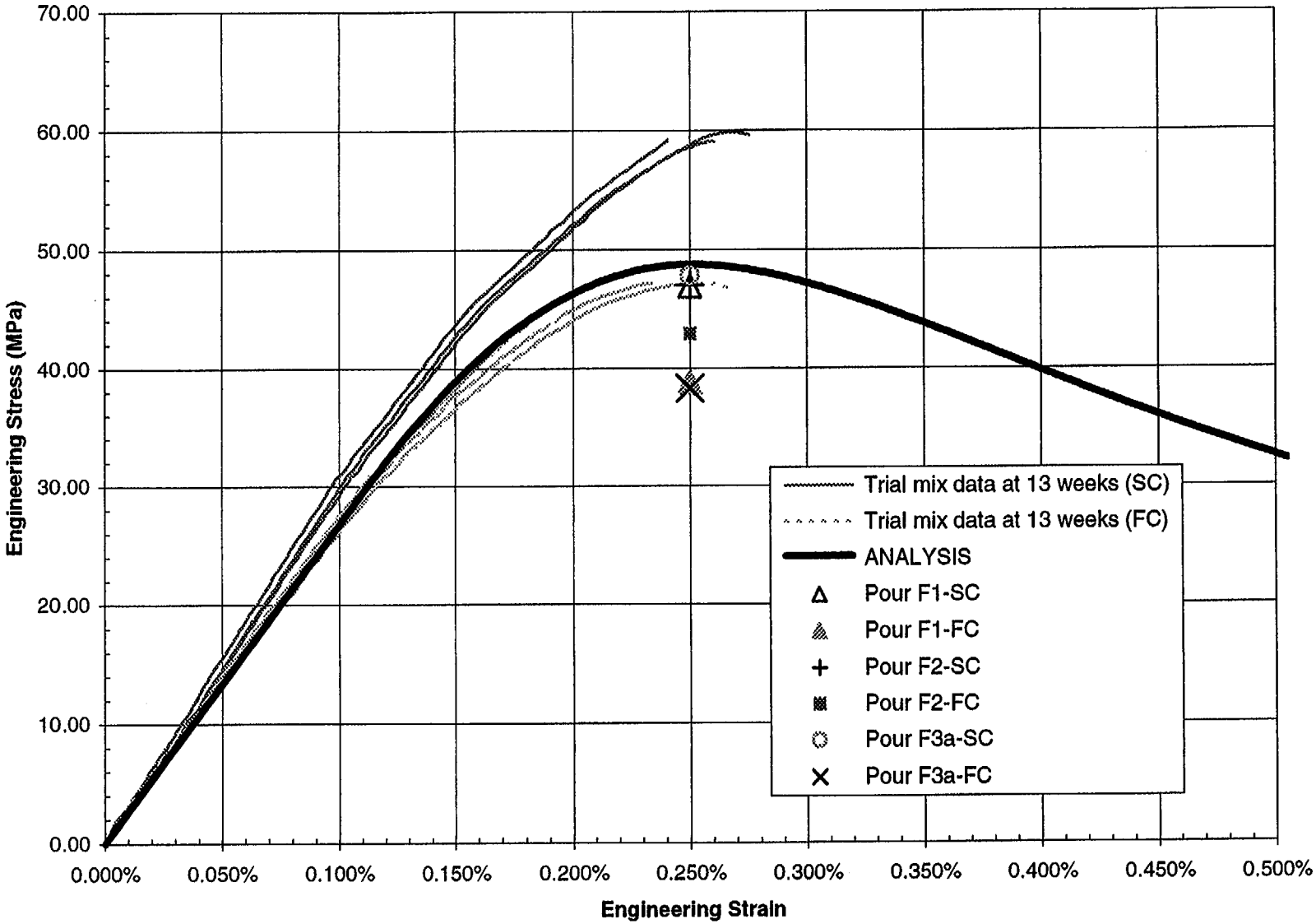


Figure 2-7. Basemat Concrete (spec. $f_c'$ = 48.80 MPa) Stress-Strain Idealization and Sample Measurements

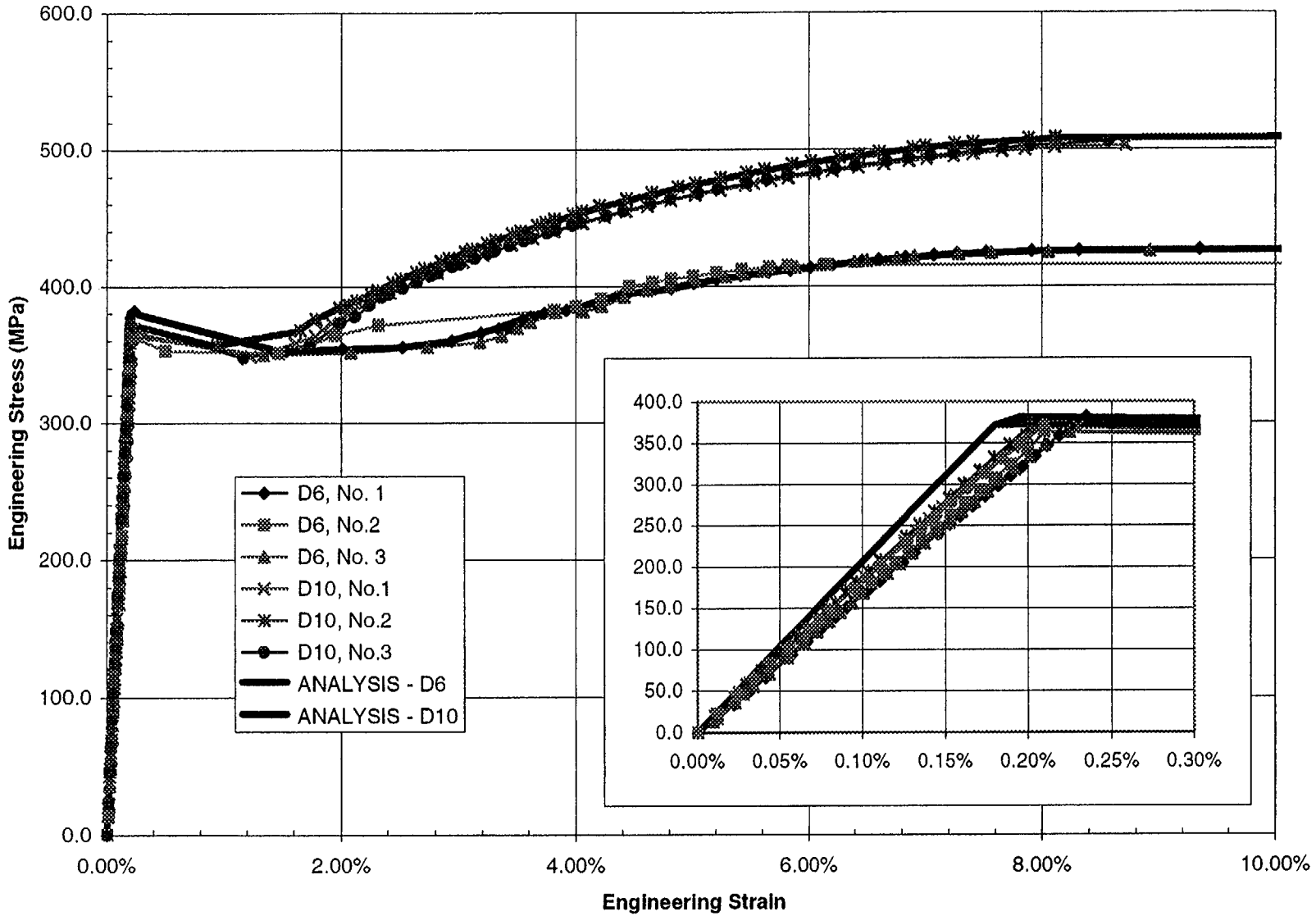


Figure 2-8. Idealized and Measured Stress-Strain for SD345 Size D6 and D10 Rebar

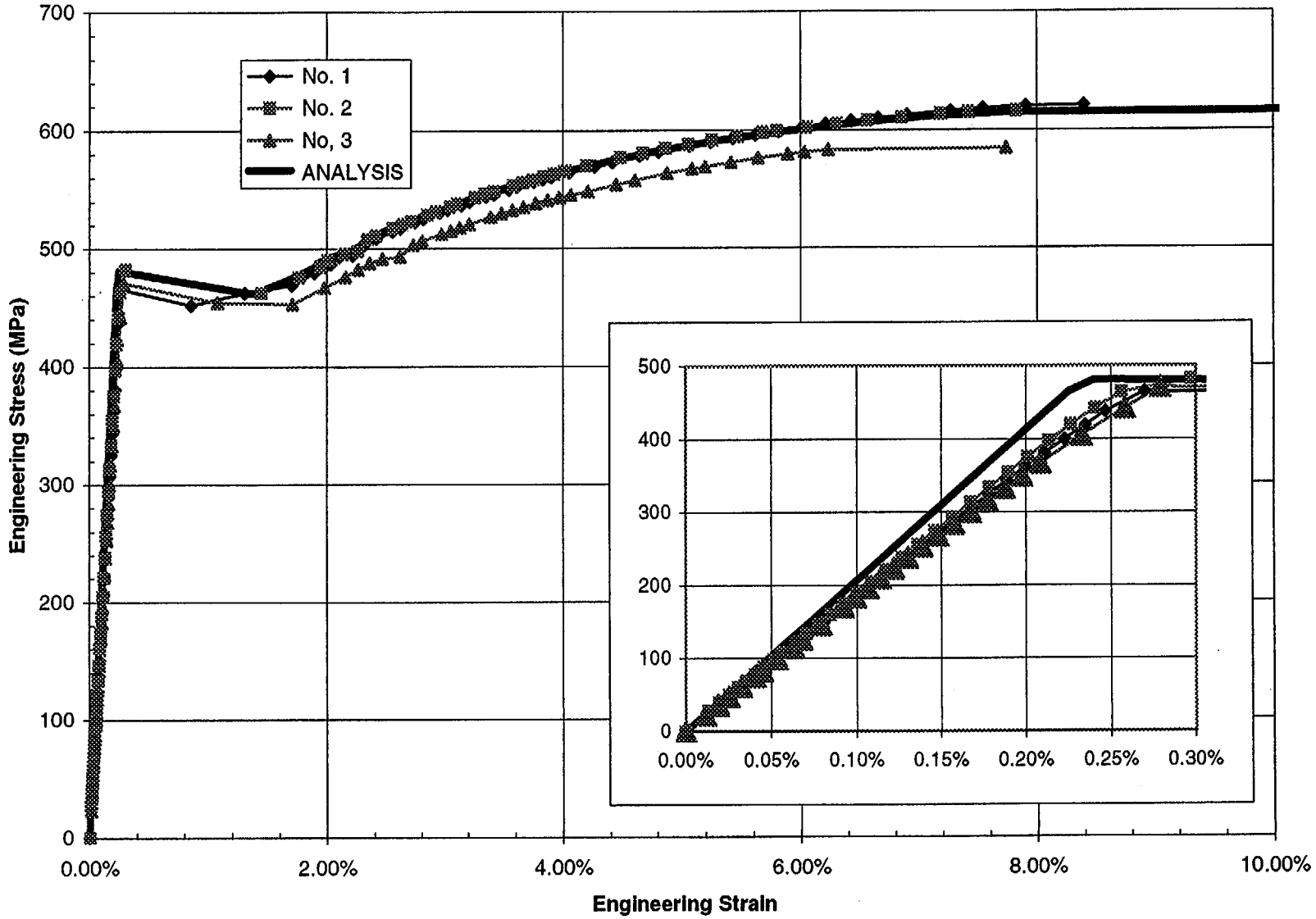


Figure 2-9. Idealized and Measured Stress-Strain for SD390 Size D10 Rebar

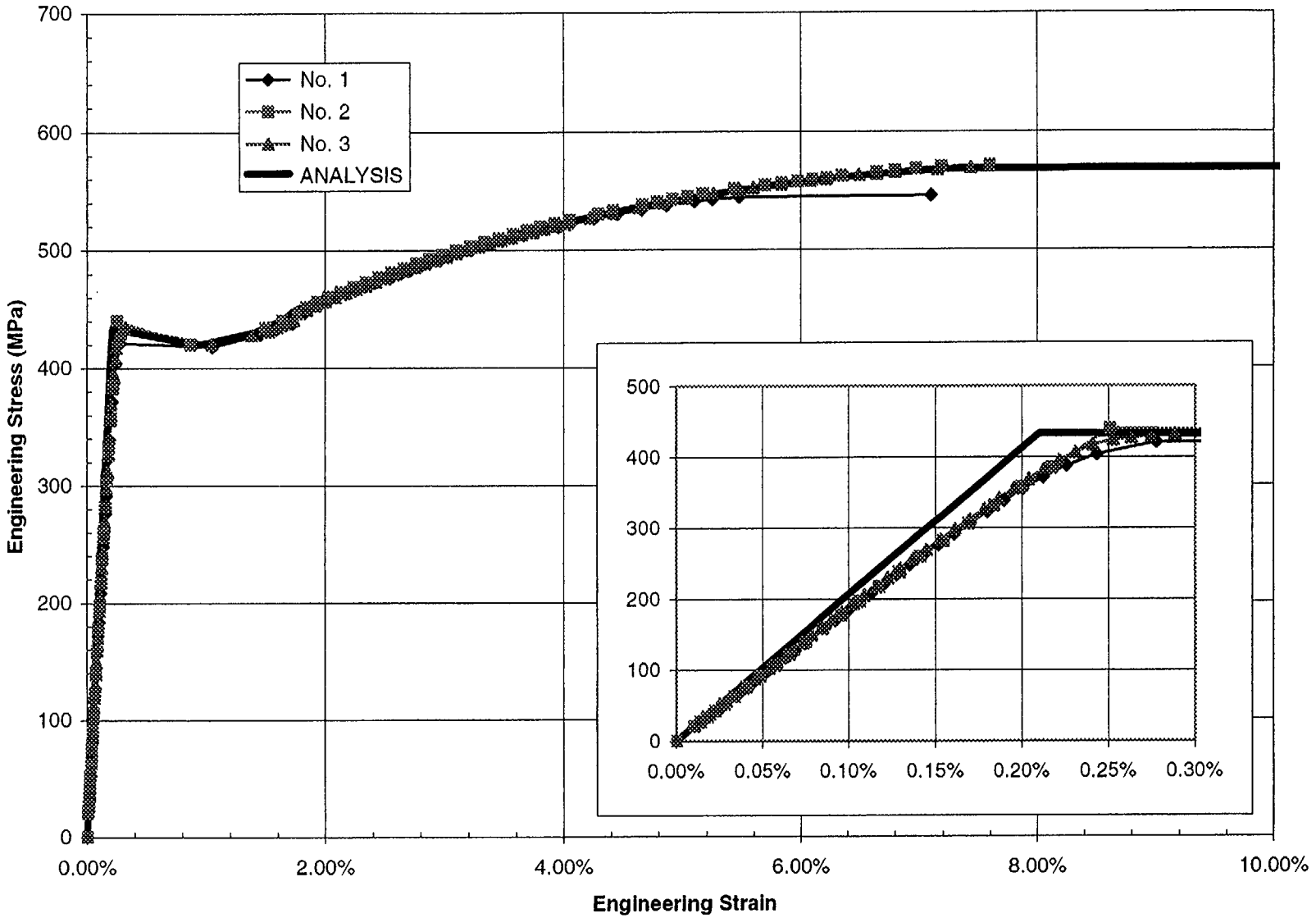


Figure 2-10. Idealized and Measured Stress-Strain for SD390 D13 Rebar

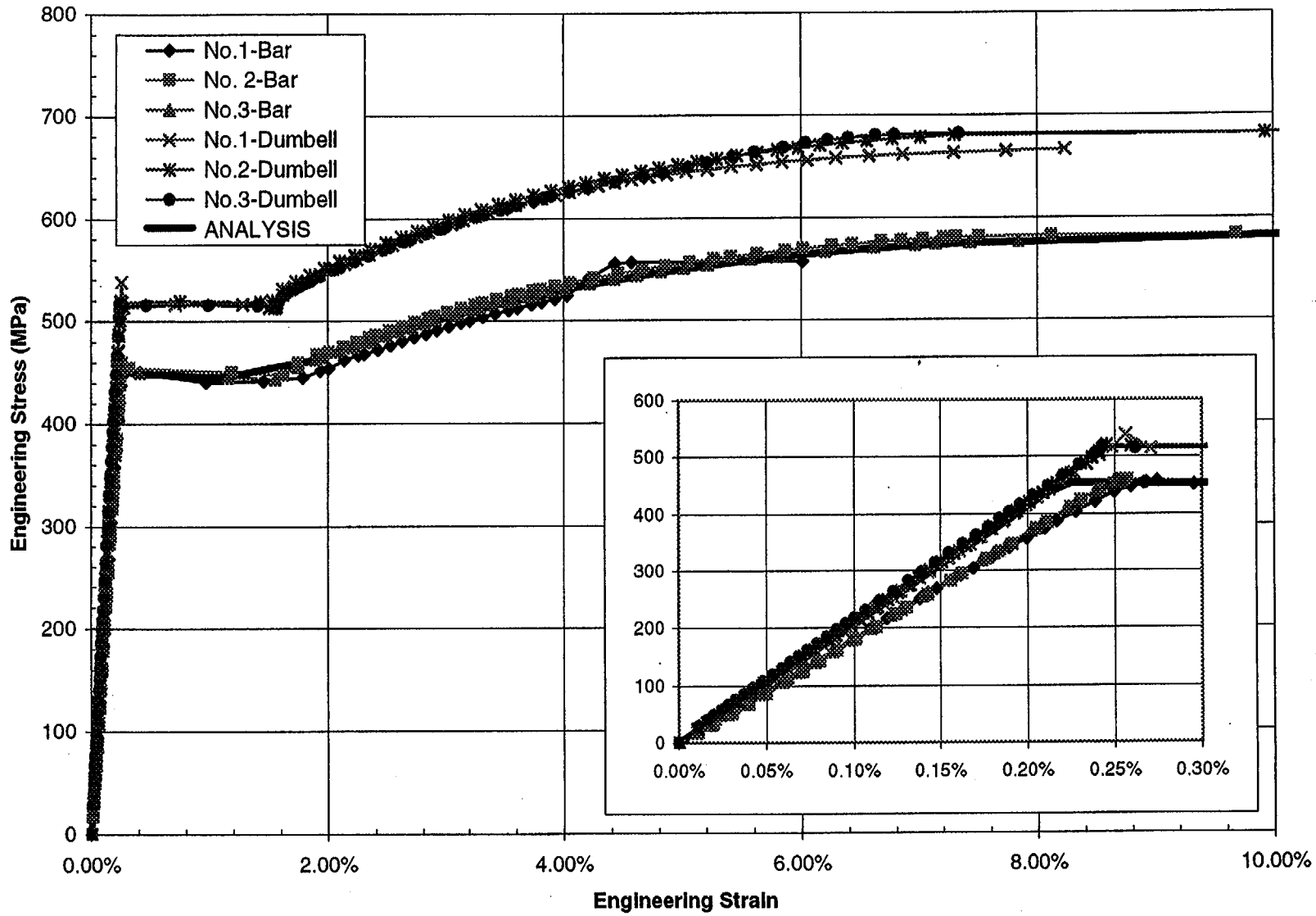


Figure 2-11. Idealized and Measured Stress-Strain for SD390 Size D16 Rebar

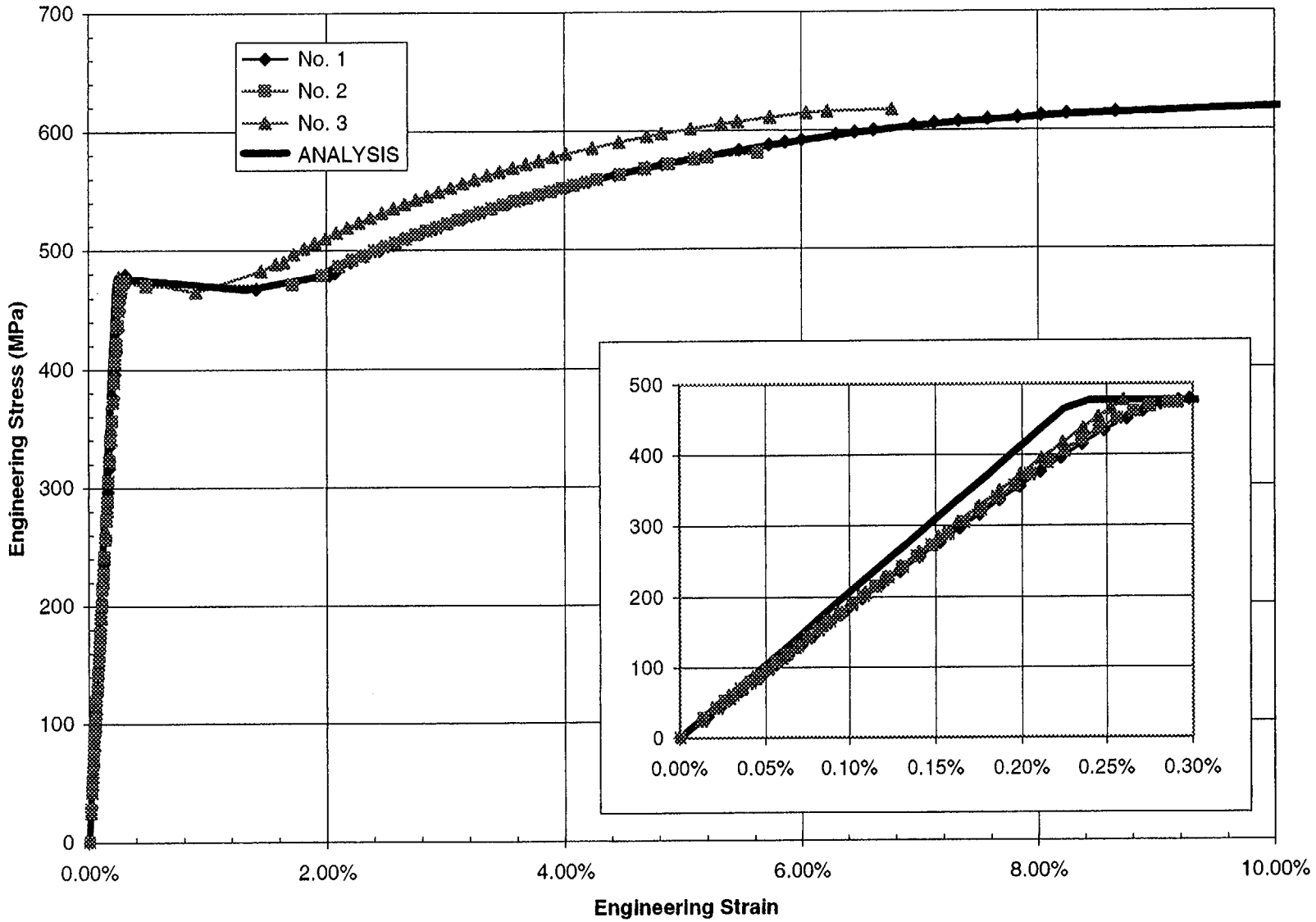


Figure 2-12. Idealized and Measured Stress-Strain for SD390 Size D19 Rebar

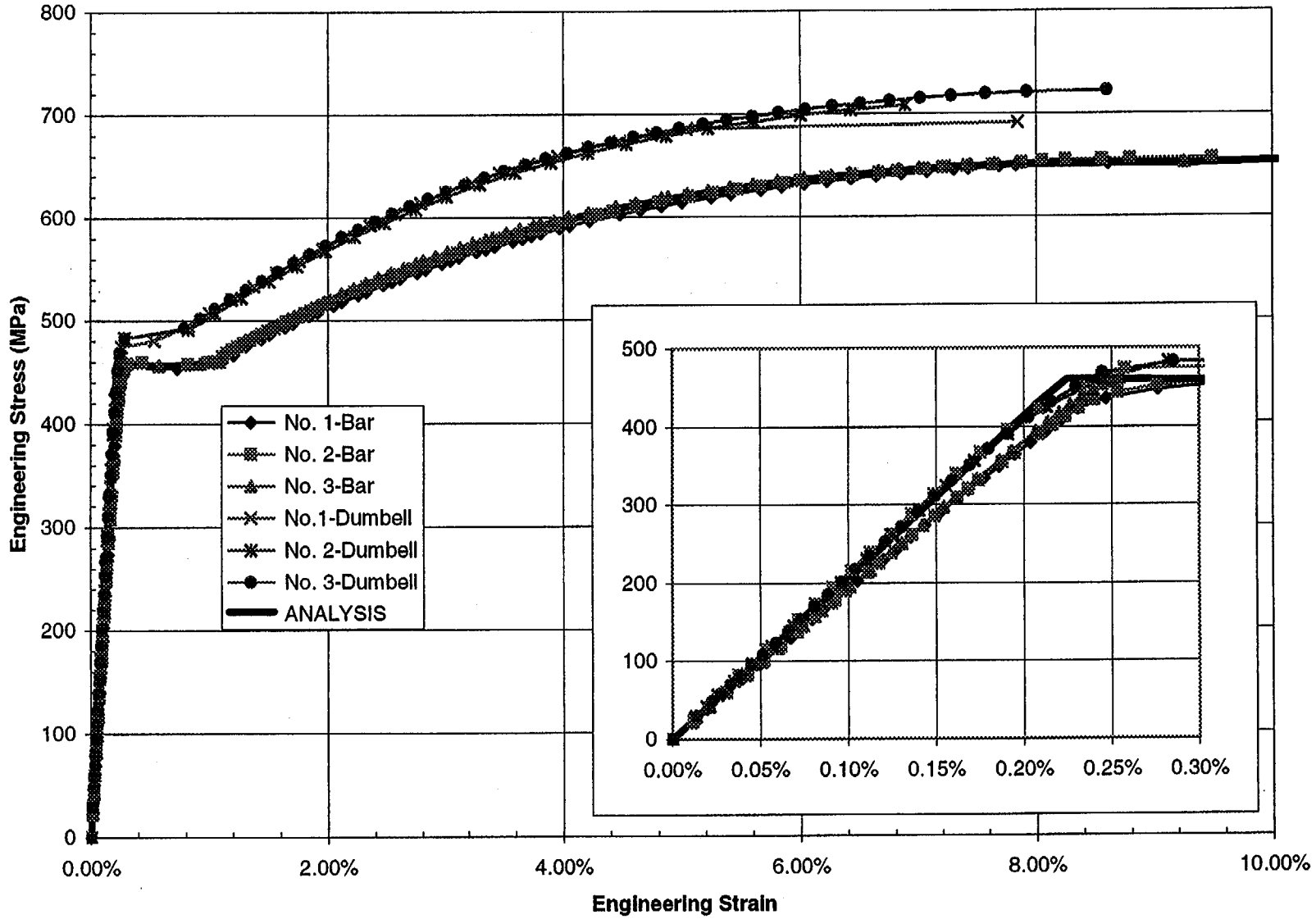


Figure 2-13. Idealized and Measured Stress-Strain for SD390 Size D22 Rebar

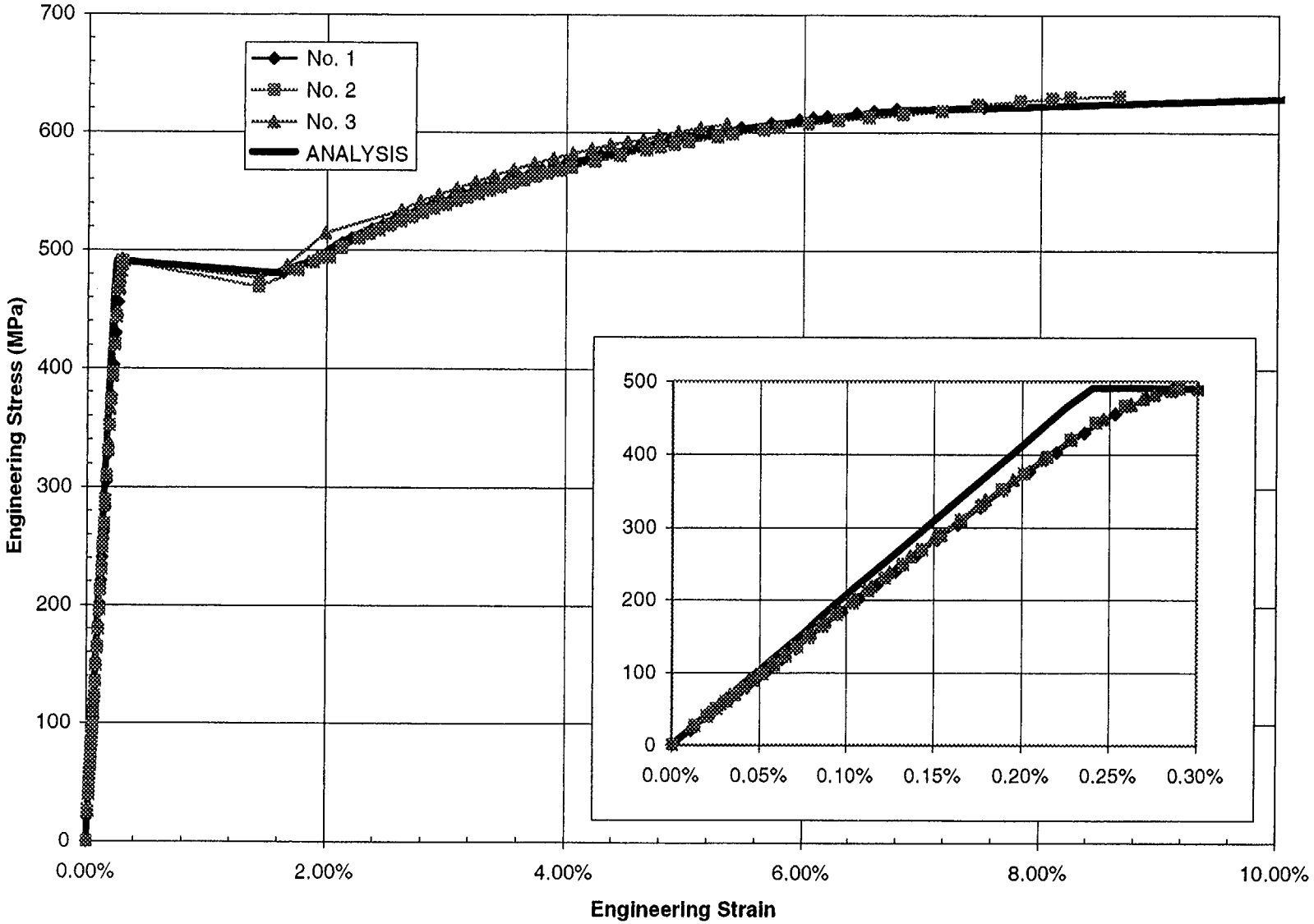


Figure 2-14. Idealized and Measured Stress-Strain for SD490 Size D10 Rebar

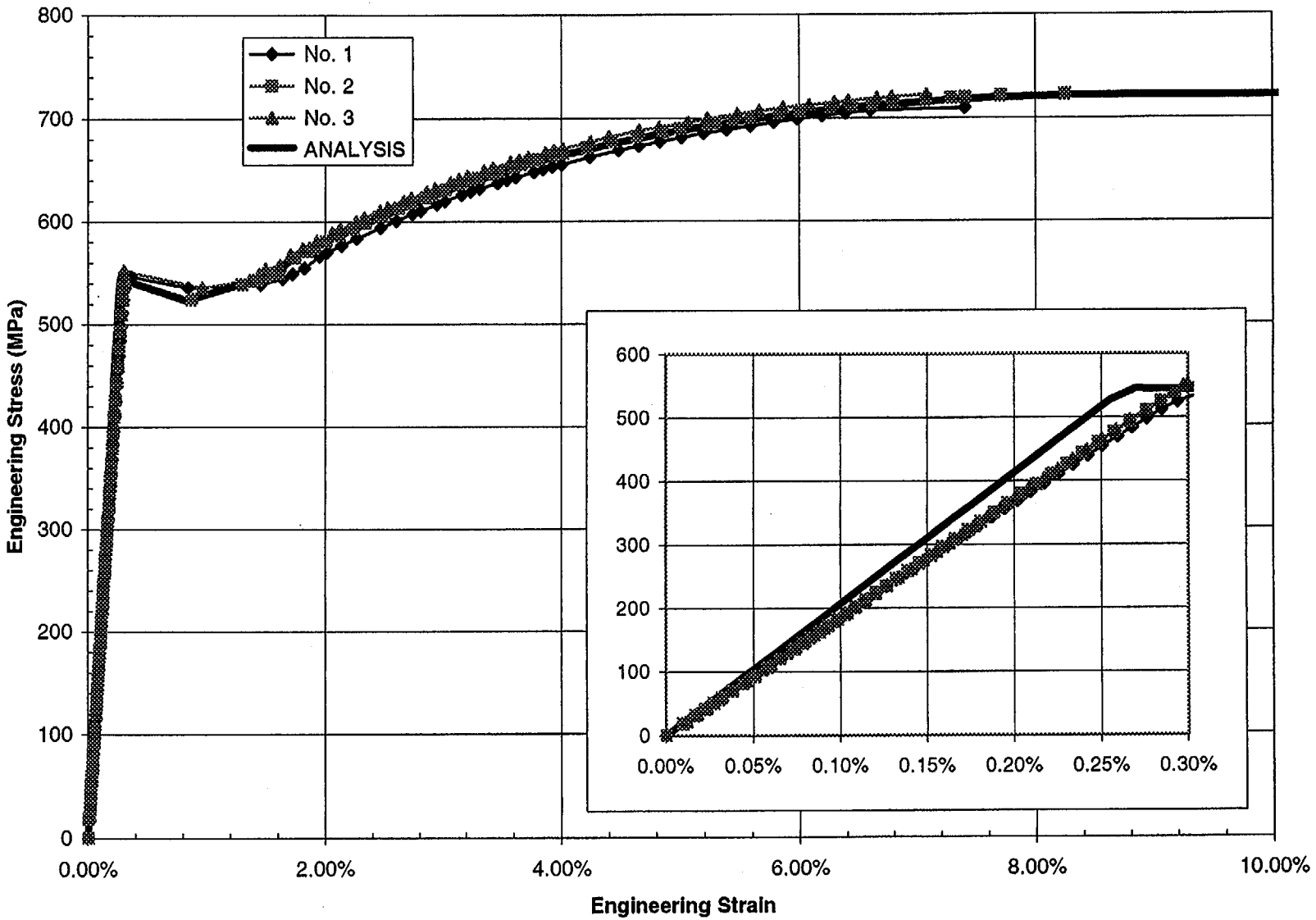


Figure 2-15. Idealized and Measured Stress-Strain for SD490 Size D13 Rebar

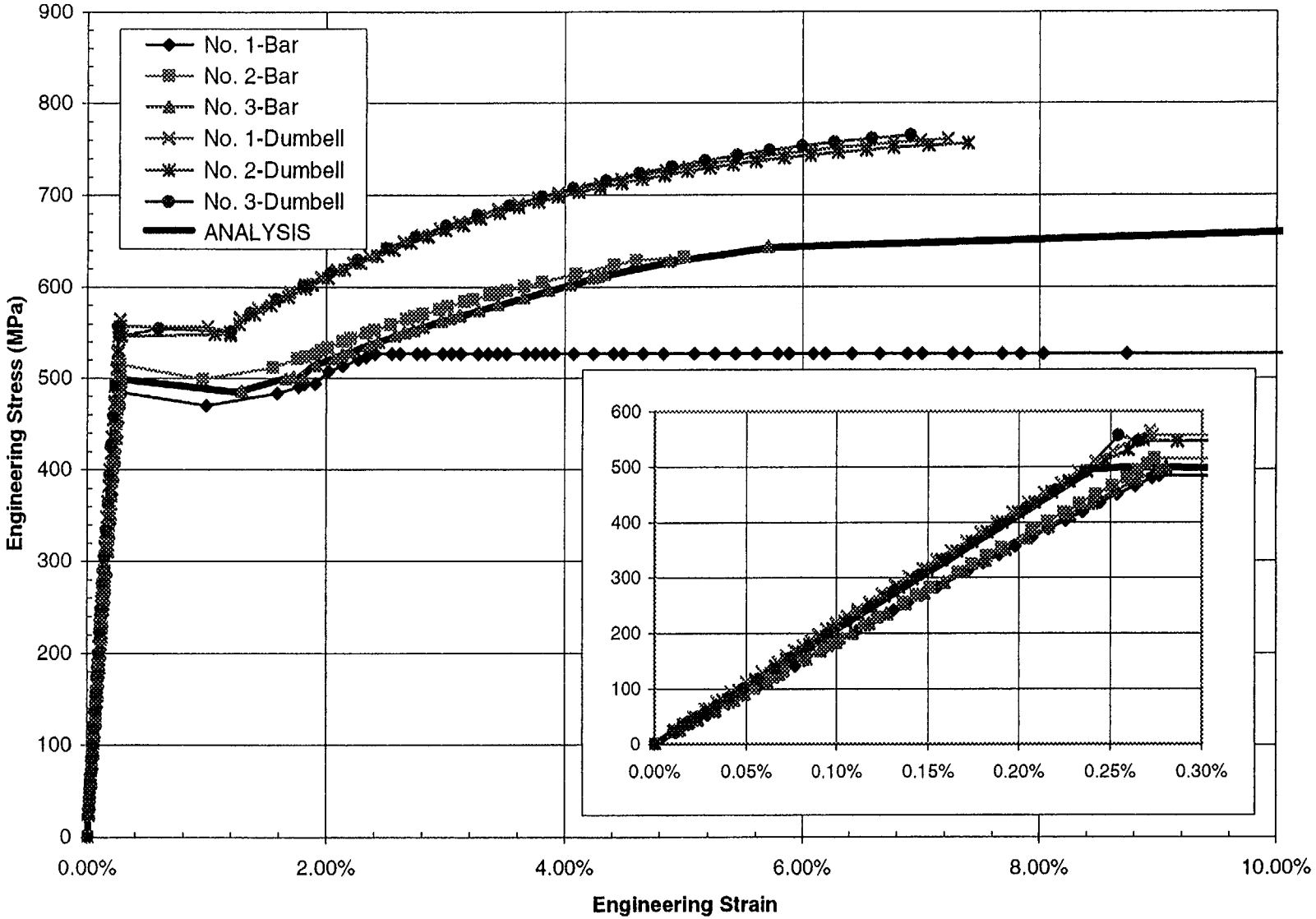


Figure 2-16. Idealized and Measured Stress-Strain for SD490 Size D16 Rebar

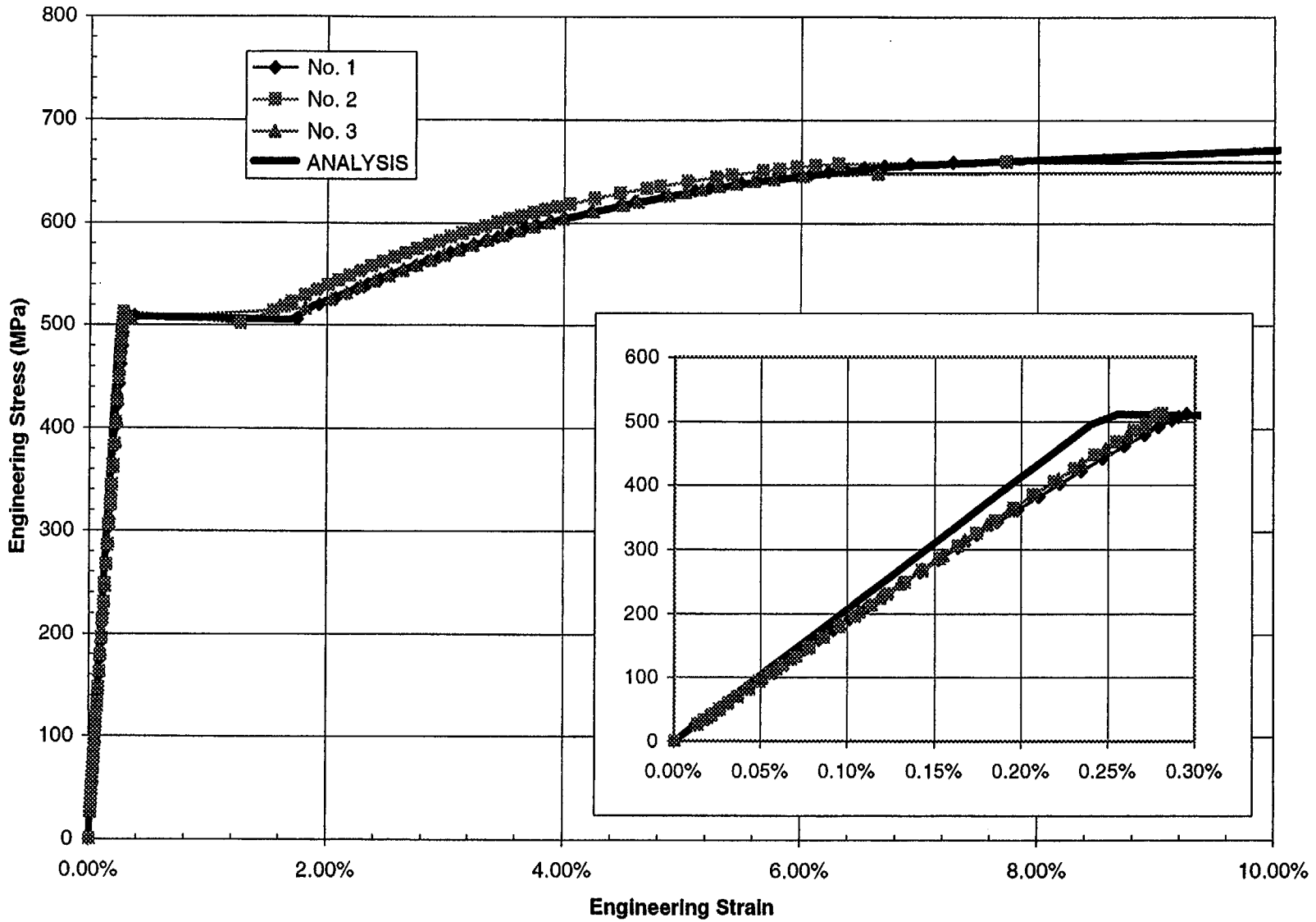


Figure 2-17. Idealized and Measured Stress-Strain for SD490 Size D19 Rebar

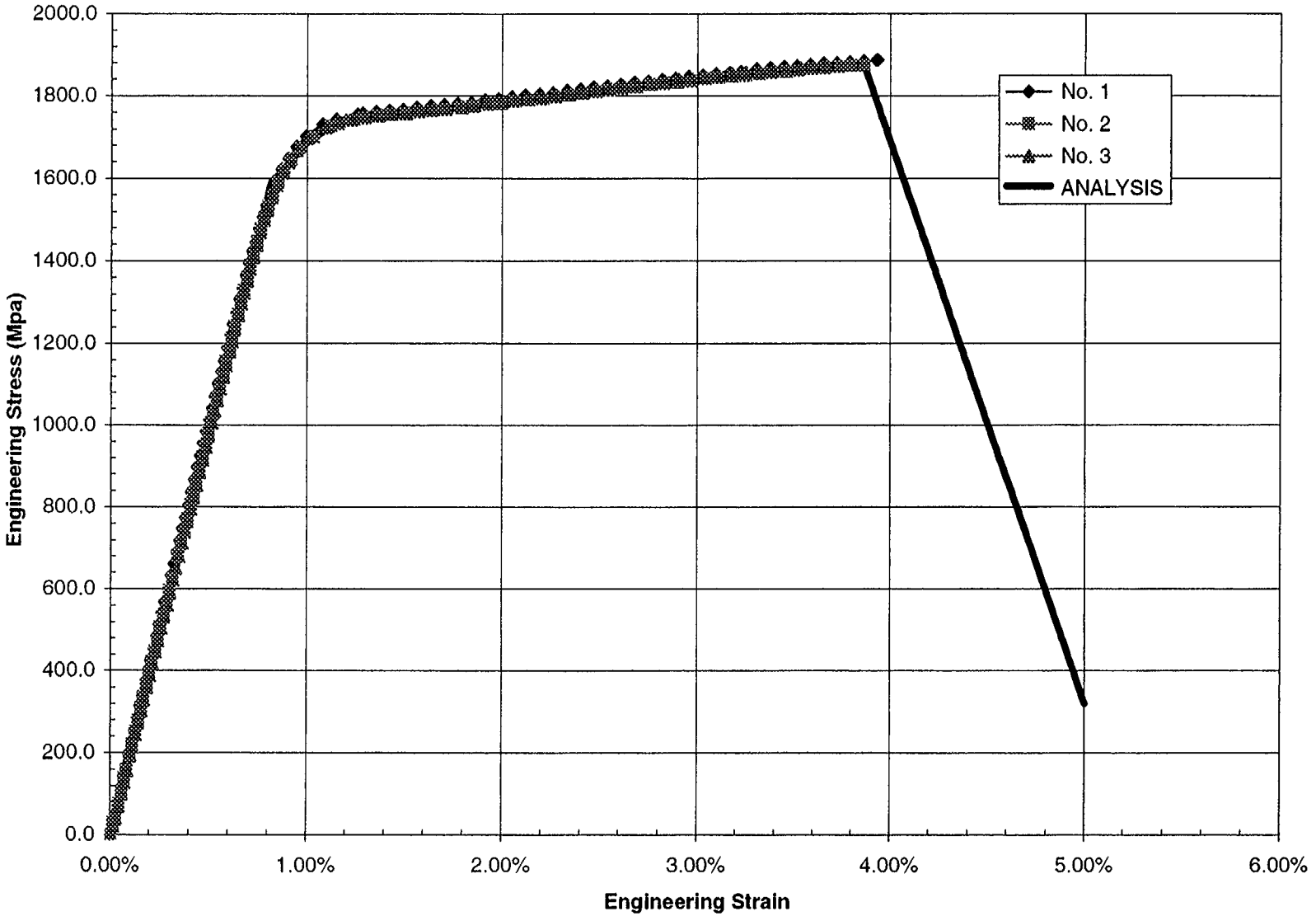


Figure 2-18. Idealized and Measured Stress-Strain for Tendons

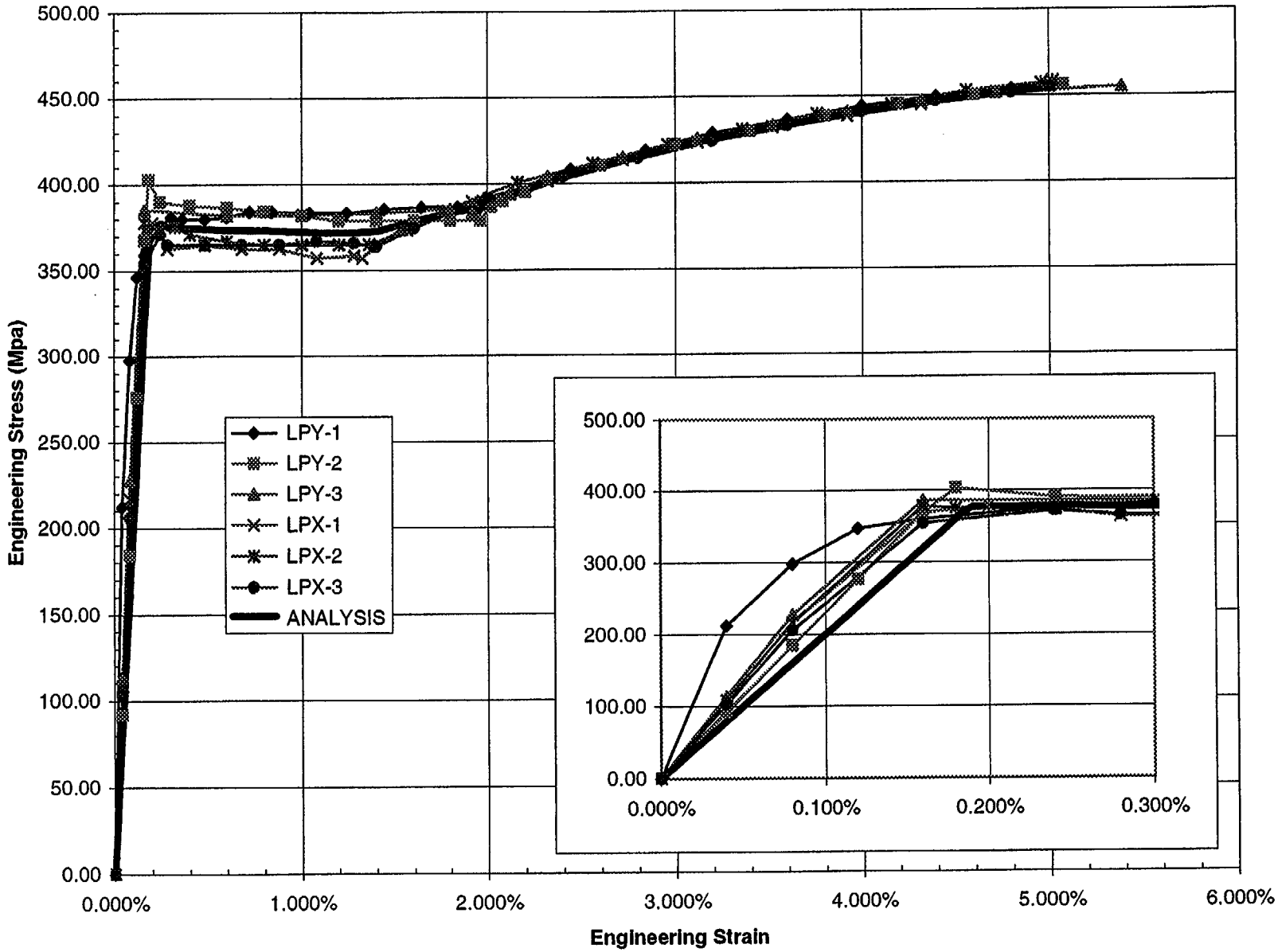


Figure 2-19. Idealized and Measured Stress-Strain for Liner

# 3. LINER ANCHOR BEHAVIOR STUDIES

## 3.1 Potential for Liner Buckling

Liner anchors used in an actual containment establish a mechanical connection between the liner and the concrete and prevent liner buckling, under normal conditions (including initial post-tensioning loads). One aspect of the liner anchor studies examined the potential for liner buckling. The check is warranted because in areas of the prestressed concrete containment vessel (PCCV) model away from penetrations, the anchors are only scaled three-for-one, so the scaled unsupported length is longer than in a full-scale prototype.

For the liner buckling study, a shell element liner grid of one "span" between anchors was developed, including the specified "true" curvature of the PCCV model. Each node of the grid had a contact element tying the liner to an idealized rigid (but movable) surface, simulating the concrete. Symmetry boundary conditions were applied as shown in Figure 3-1. To simulate a possible buckling condition, the contact surface was moved toward the center of curvature (to the left in Figure 3-1), which puts the liner into hoop compression. Figure 3-1 shows the deformed shape at a strain of $-1.5 \times 10^{-4}$, which is equivalent to the hoop liner strain that occurs during prestress. After observing no buckling instability at this load, the boundary was moved 30 times further, to a strain of $-4.7 \times 10^{-3}$ in an effort to induce buckling. However, no buckle was introduced (as shown in Figures 3-2 and 3-3). The strain field shown in Figure 3-3 is uniform except for a minor strain gradient at the edge of the model that is only a boundary-condition effect.

After finding no buckling instability for a perfectly curved liner, a model was made with curvature reduced to zero to evaluate the possibility of local "out-of-roundness" in the liner construction. The first stage of loading is shown in Figure 3-4a. In this case, the liner does begin to bow inward, away from the concrete as shown by the "open" contact elements. Upon magnifying the prestress load by 12, the liner with out-of-straightness formed a fairly large bulge, and the response became unstable (Figure 3-4b). The hoop strains for the prestress condition are shown in Figure 3-5. At the point of instability, a general yield condition in the liner ($\varepsilon \cong 1.5 \times 10^{-3}$) was reached.

The buckling study showed that there is no tendency for the liner to locally buckle. The only buckling mode that could be induced was for a segment with large initial imperfection (zero curvature), and this case did not reach a general yield condition until about 12 times the initial precompression due to prestress.

## 3.2 Characterization of Liner Anchor Behavior

Several 3D models were generated to analyze the penetration areas, including the equipment hatch (E/H), personnel airlock (A/L), and mainsteam (M/S) locations. A detail common to each model is the interaction between the T-anchors and the surrounding concrete. The T-anchors and concrete move together in the radial direction during pressurization, but the liner can "slide" along the liner concrete interaction surfaces in the tangential direction. This relative sliding is resisted by the T-anchors. Nonlinear behavior occurs as the concrete is crushed and the liner and the T-anchors are strained plastically. The liner anchor model analyzes this relationship, and its results have been used to generate the nonlinear force-deflection characteristics for use in the 3D penetration models. The liner anchor behavior simulation was also calibrated to liner anchor pull tests conducted by the Nuclear Power Engineering Corporation (NUPEC) (Appendix A).

Modeling dimensions and boundary conditions for the liner anchor model can be seen in Figure 3-6. Radial model length was determined from half the wall thickness. Tangential distance was determined from mid-distance between T-anchors near penetrations (which were scaled one-for-one from the full-scale prototype). The liner in the liner anchor model was strained tangentially, according to the time-history results from the axisymmetric analysis and in accordance with liner pressurization. Contact surfaces were applied at all interaction areas between the liner/anchor and concrete. A sensitivity study was done on the friction coefficient used on these surfaces using coefficients of $\mu$=0.2 and $\mu$=0.5. The liner end opposite where displacement was applied was fixed from in-plane rotation. A sensitivity study on this boundary condition used parameters that allowed this end to displace tangentially versus a fixed condition.

Force versus displacement history plots can be seen in Figure 3-7. The x-axis refers to the relative displacement between points 1 and 2 from Figure 3-6, the distance over which bending diminishes in the anchor web. Results verify that a larger coefficient of friction creates a greater reaction force. The free-condition model creates a larger relative displacement than the more constrictive fixed condition models. Figure 3-8

shows the deformed shape of the grid, in particular, the case of fixed boundary condition and $\mu = 0.5$. Figure 3-9 shows the radial and hoop strains in the liner and anchor at a liner hoop strain that is representative of global hoop strains in the barrel near 3.5 $P_d$. Figure 3-10 plots strain in the liner and anchor for the free-edge condition. Radial strains reach –0.015 and 0.027, while hoop strains reach -0.026 and 0.016.

Figure 3-11 compares these test cases to a liner anchor pull test performed by NUPEC. The analytical model results show a little larger force than the NUPEC test results, but the general force-deflection behavior is similar. The detailed analytical model of the anchors, therefore, was judged to provide a reasonable simulation.

All local models use a simplified method of modeling the anchors to simulate the behavior exhibited by testing and by more detailed analysis (the liner anchor model). Figure 3-12 shows the geometry of the anchor used in the local models. The anchor depth has been reduced to 12 mm, and the "root" of this 12-mm-high web is the point of fixity. An iterative process of modifying the thickness and shear stiffness of the anchors was used to match the results of the more detailed analysis. The results from the $\mu = 0.2$ and "fixed" case are used as the appropriately conservative approach because their stiffness and ultimate capacity were slightly lower than the two "free" cases. The thickness of the anchor web is 1.6 mm, whereas in the idealized representation in the local models of the penetrations it is 6.6 mm. This method was not intended to produce accurate strains in the anchors themselves. It was intended to accurately simulate the hoop strains in the liner, which is the predicted location of failure. Figure 3-13 shows the correlation between the two methods.

The hoop stiffeners have been modeled with a similar technique in the local E/H and A/L models. It was determined that that there were no regions of critical hoop stiffeners in the M/S model, so none were included. It is required that the depth of the anchor and the stiffener are equal for modeling purposes. The thickness to achieve the actual area for the stiffeners in the local models was calibrated to be 8.4mm as opposed to the actual 3.2mm.

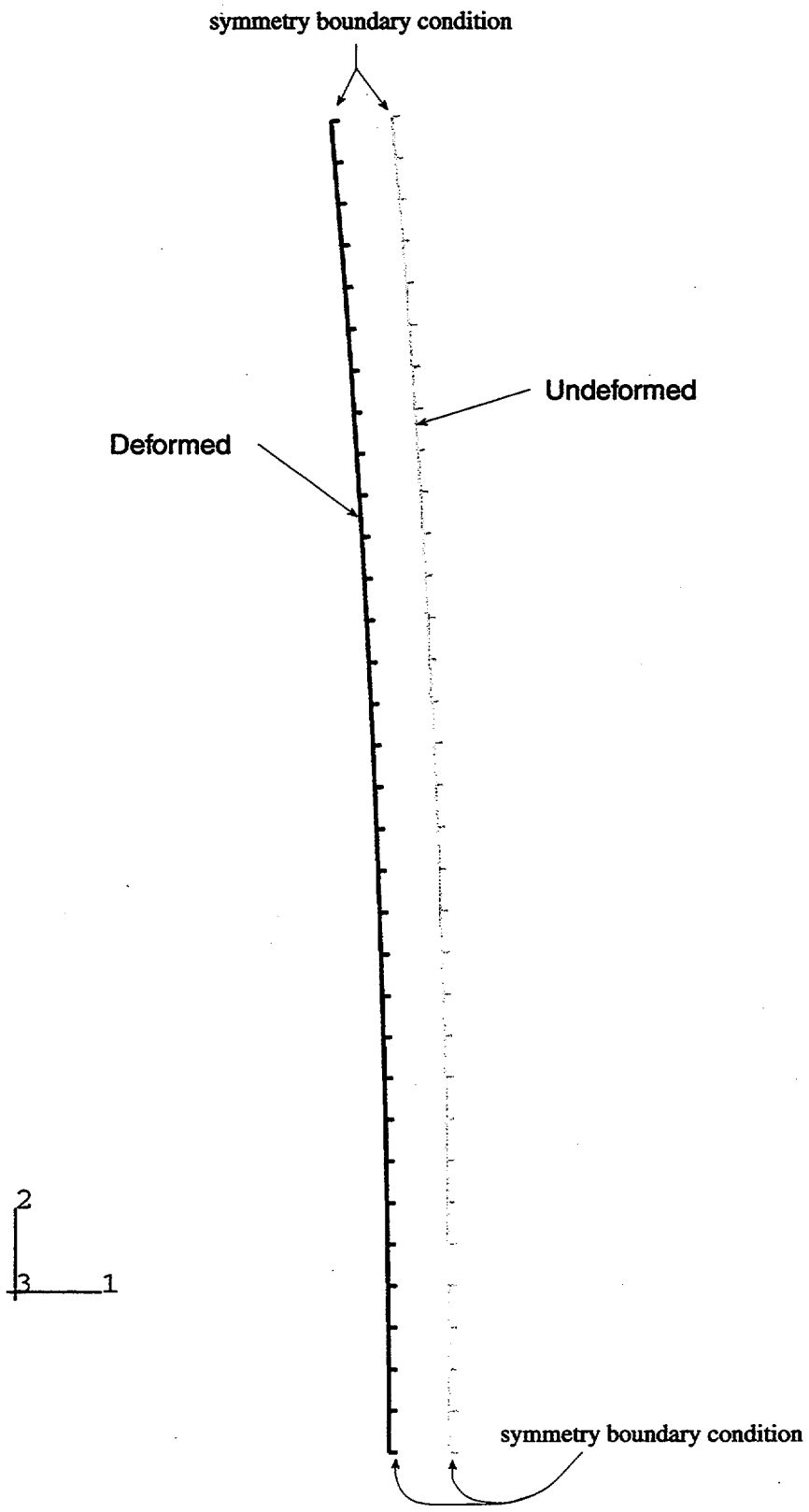


Figure 3-1. Liner Buckling Study Displaced Shape at Far-field Strain of -1.5E-4 (Prestress) for Ideal Buckle Model (mag. factor = 25.0)

*buckle.inp*

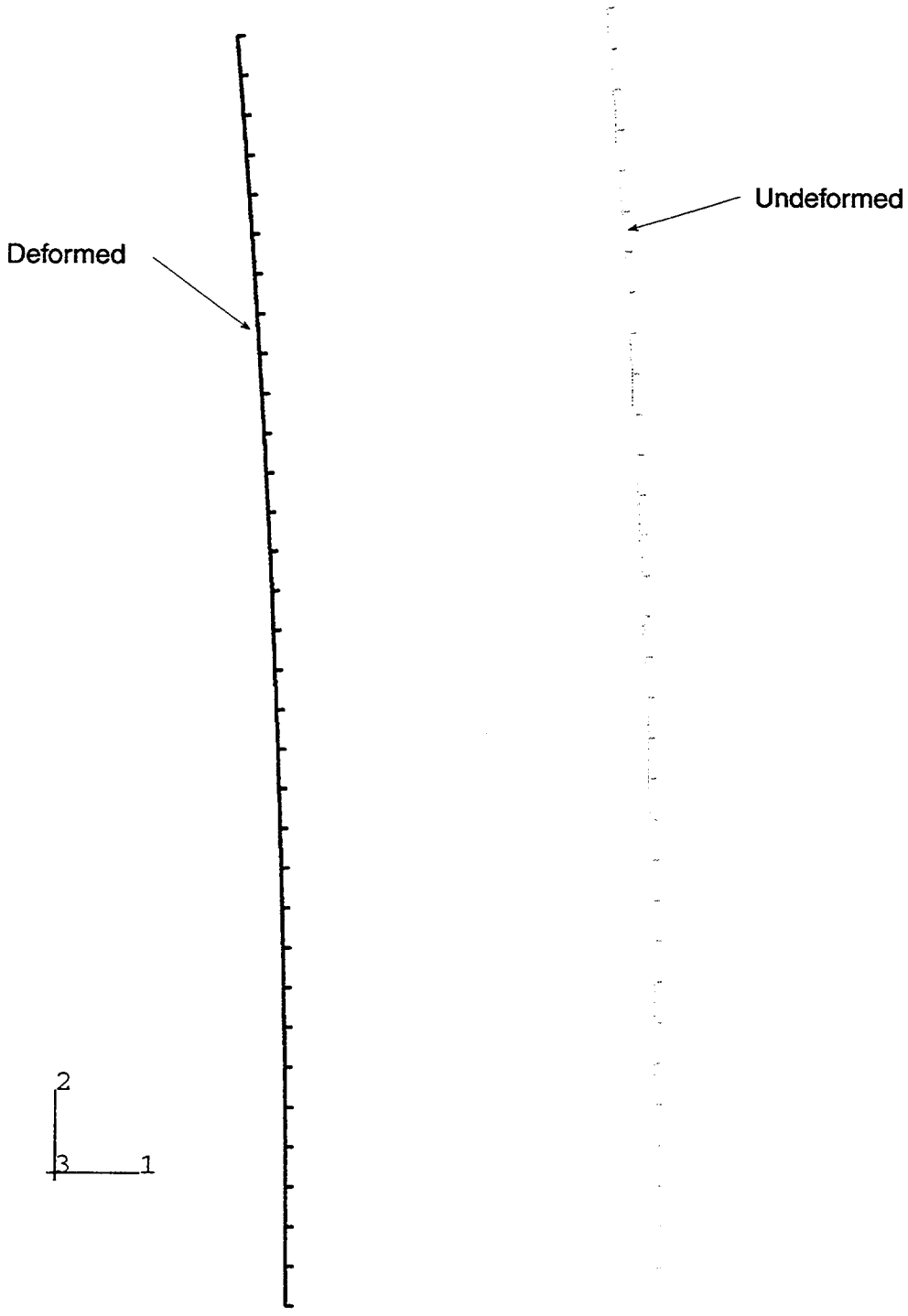


Figure 3-2. Displaced Shape at Far-field Strain of -4.7E-3 for Ideal Buckle Model (mag. factor = 5.0)

*buckle.inp*

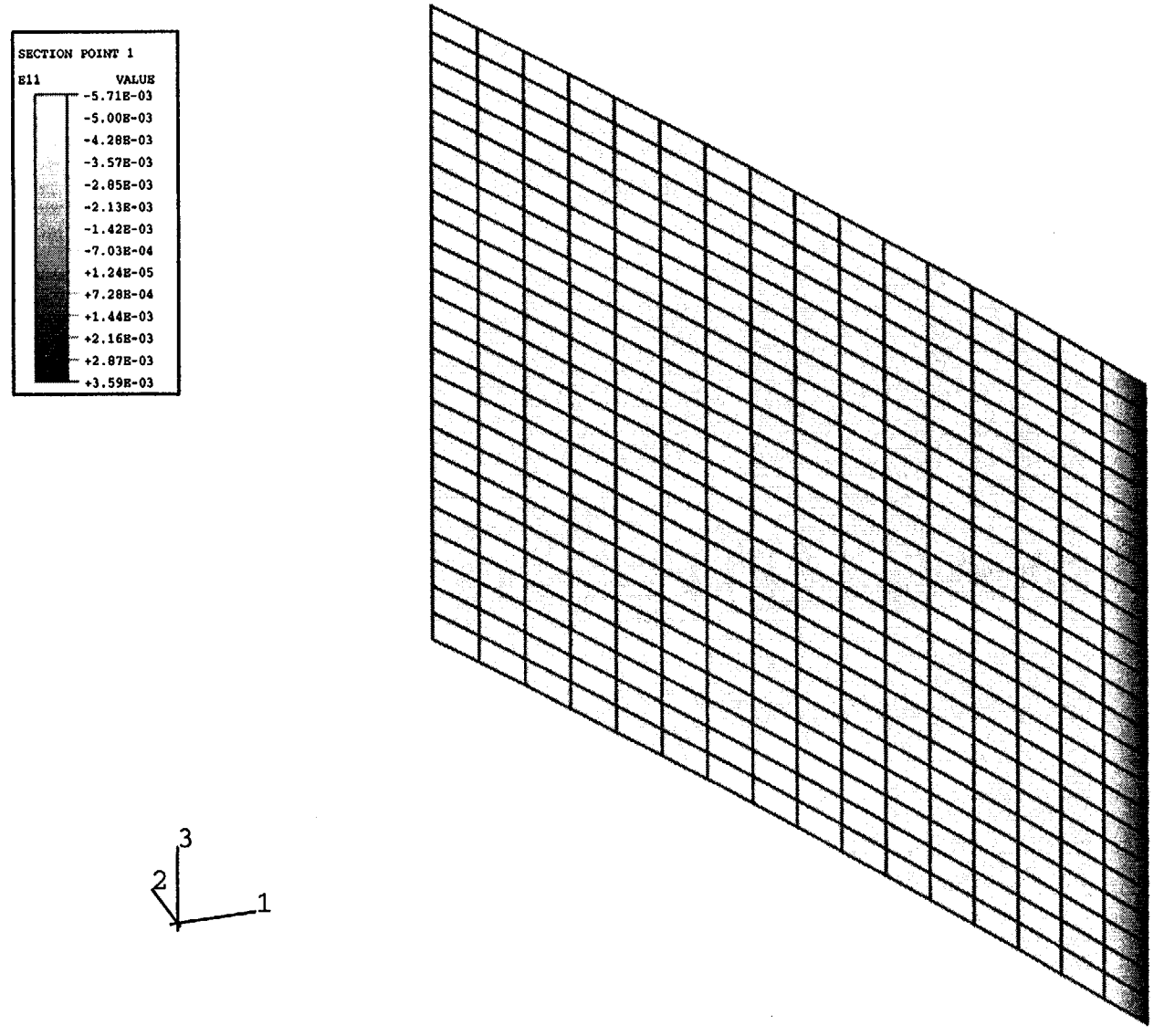


*buckle.inp* Figure 3-3. Hoop Strain Contours at Far-field Strain of 4.7E-3 for Ideal Buckle Model (mag. factor = 5.0)

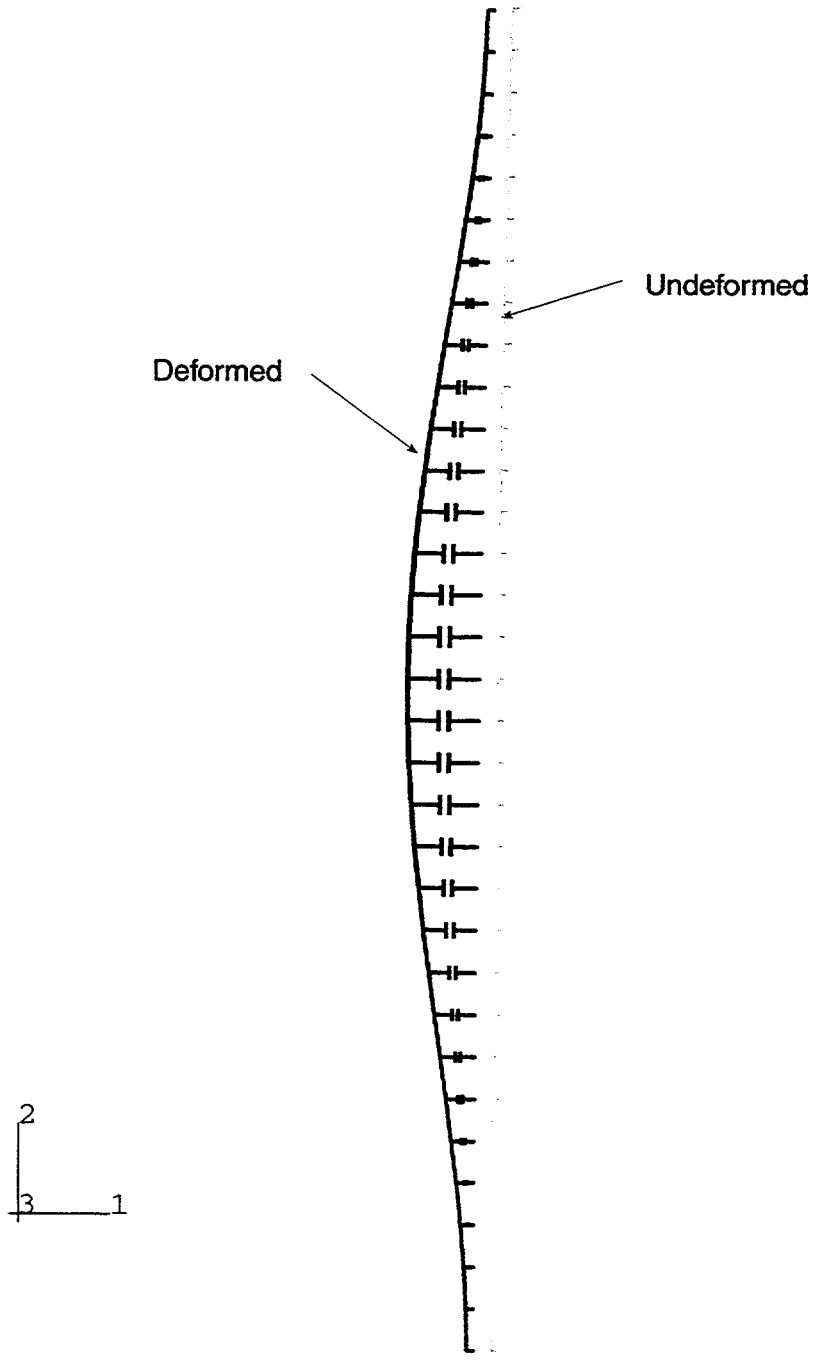


Figure 3-4a. Displaced Shape of Slight Imperfection Buckle Model at Prestress, Far-field Strain = -1.5E-4 (mag. factor = 5.0)

*buckle.inp*

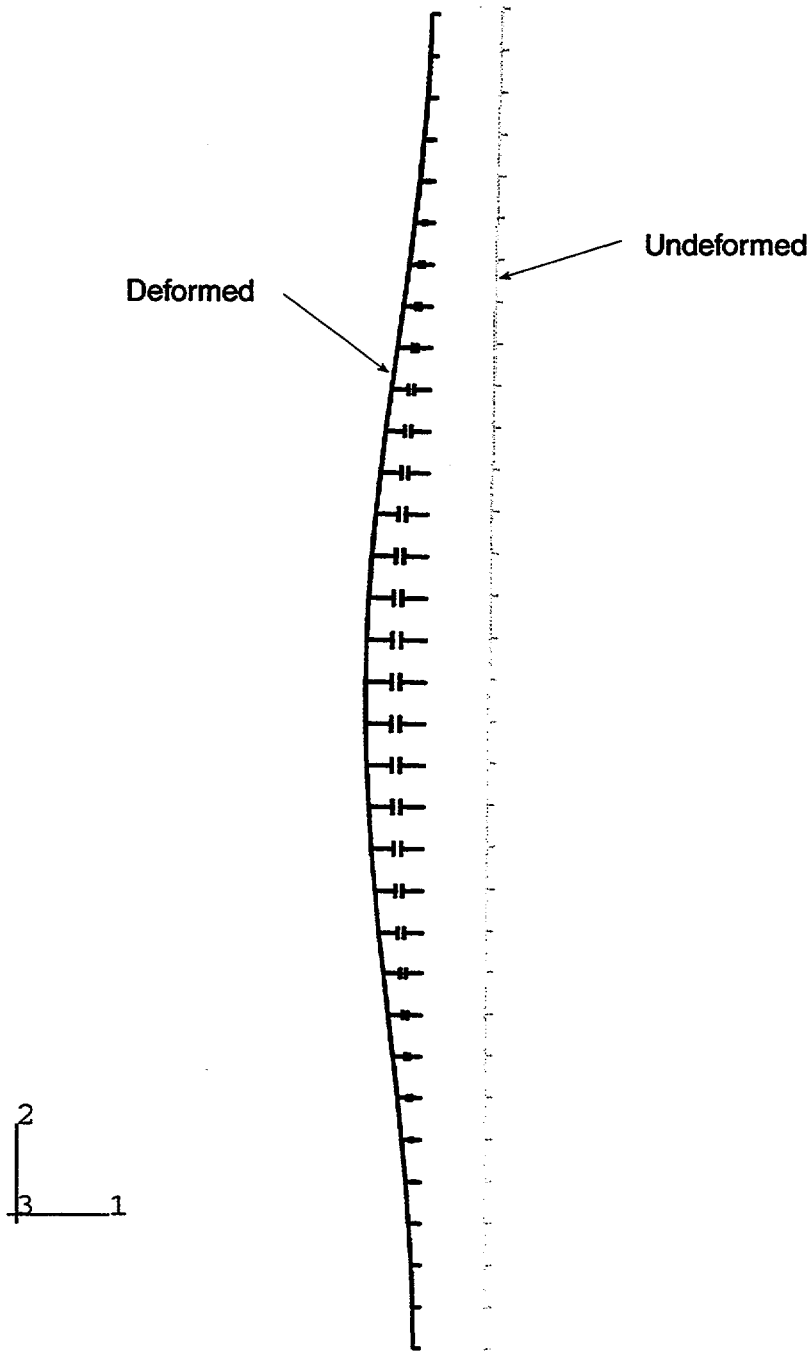


Figure 3-4b. Displaced Shape of Slight Imperfection Buckle Model at Failure (mag. factor = 1.0)
*buckle.inp*

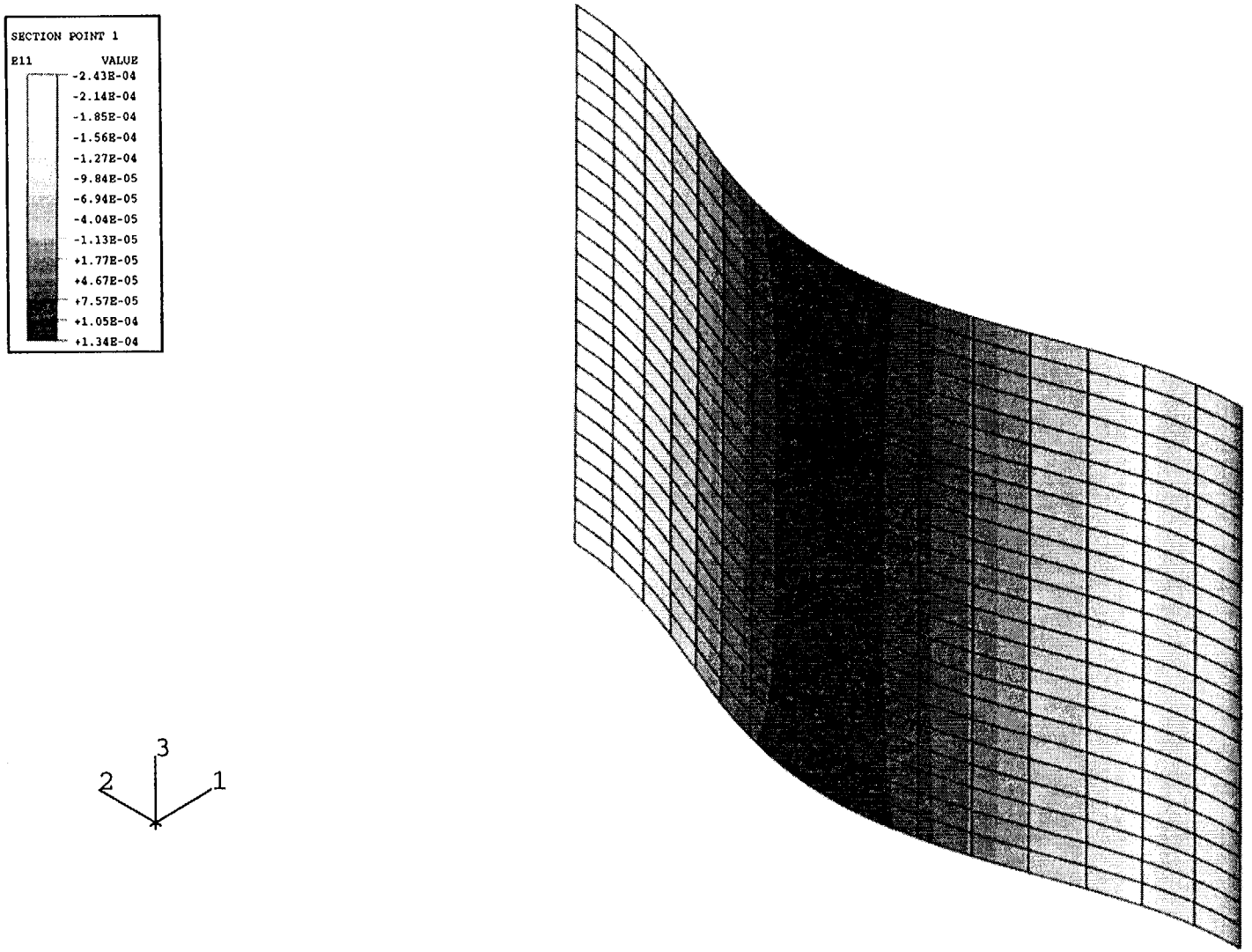


Figure 3-5. Hoop Strain Contours of Slight Imperfection Buckle Model at Prestress, Far-field Strain = -1.5E-4 (mag. factor =25.0)
*buckle.inp*

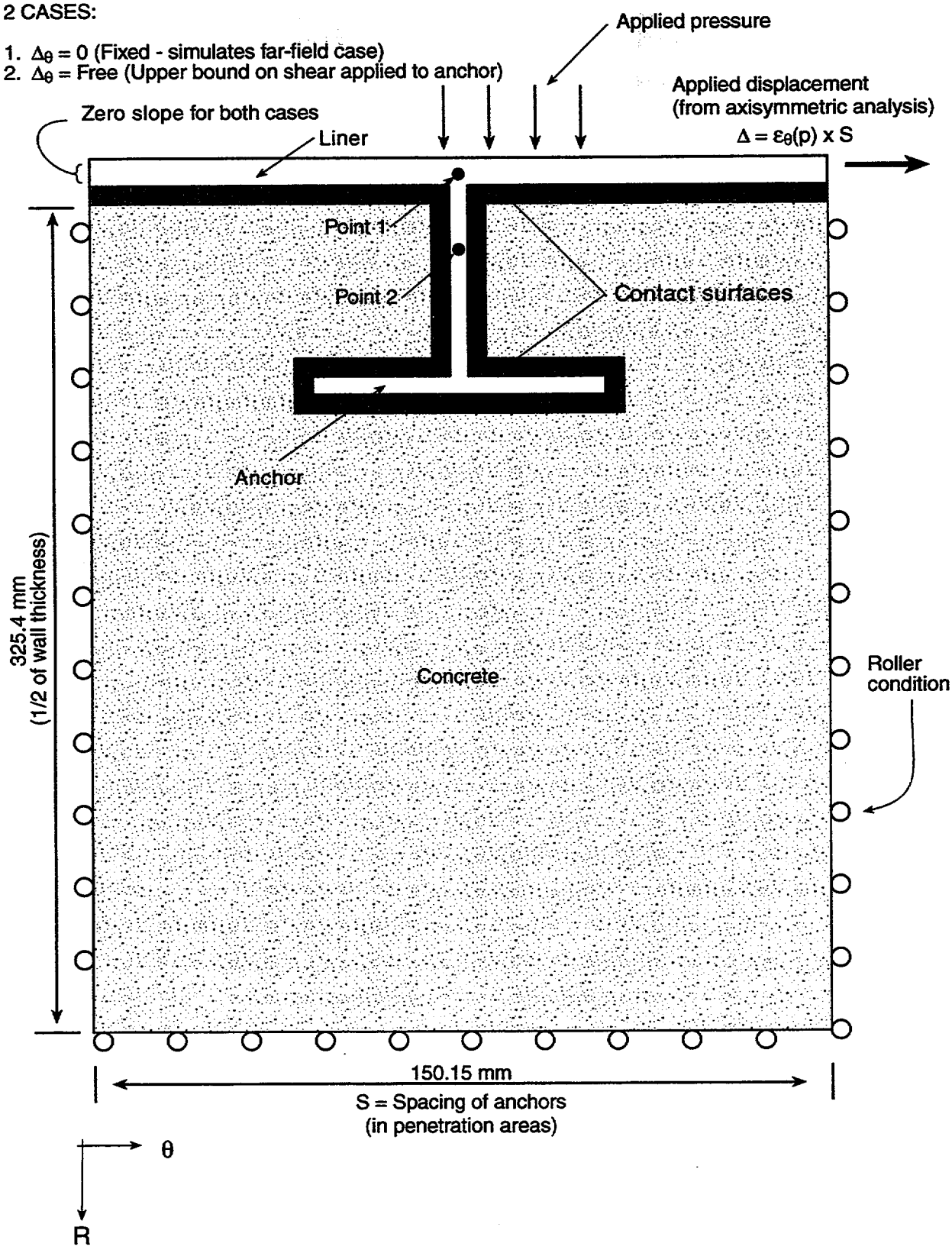


Figure 3-6. Schematic of Liner Anchor Model and Boundary Conditions

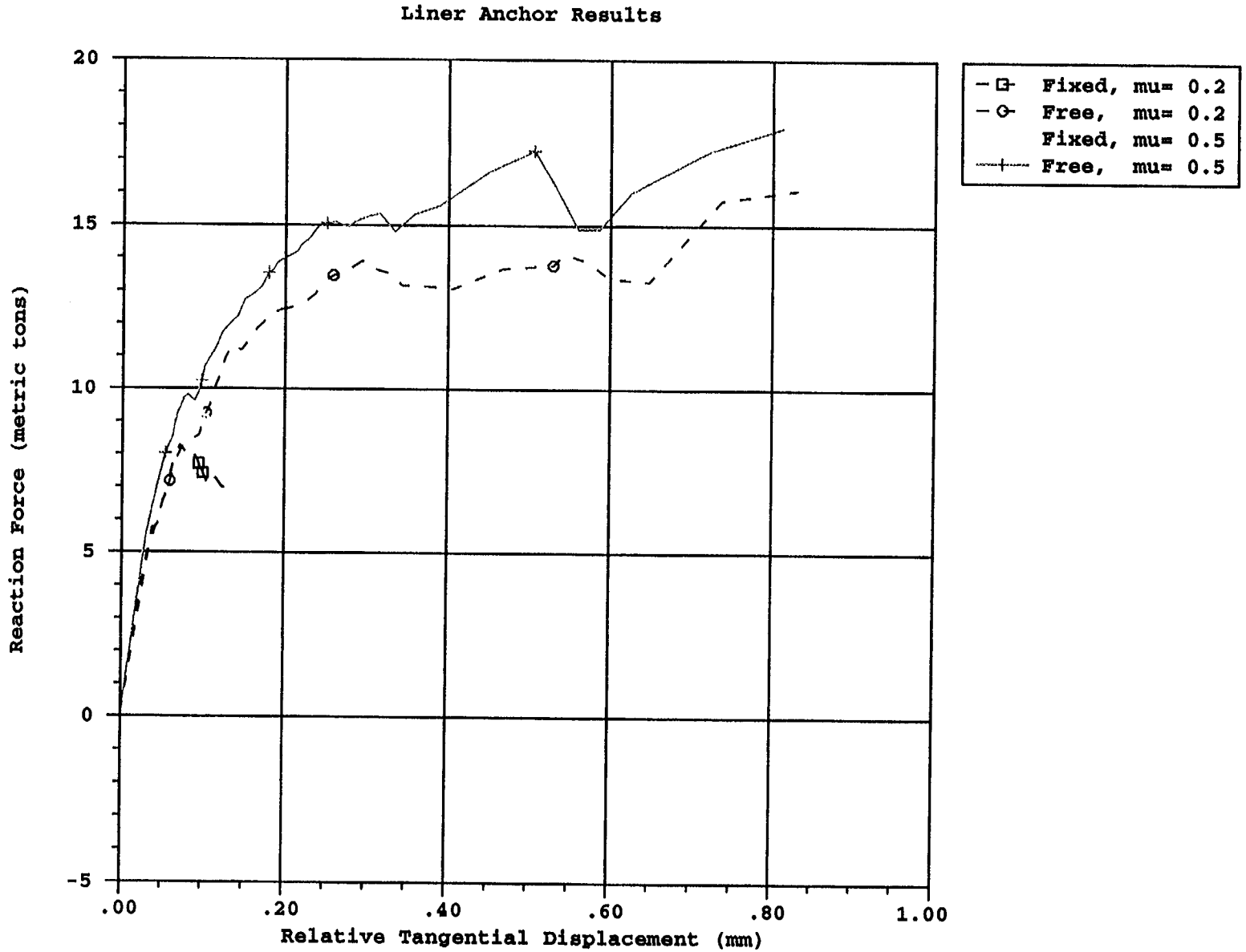


Figure 3-7. Force vs. Displacement Results for Liner Anchor Studies

*fix2.inp, free2.inp, fix5.inp, free5.inp*

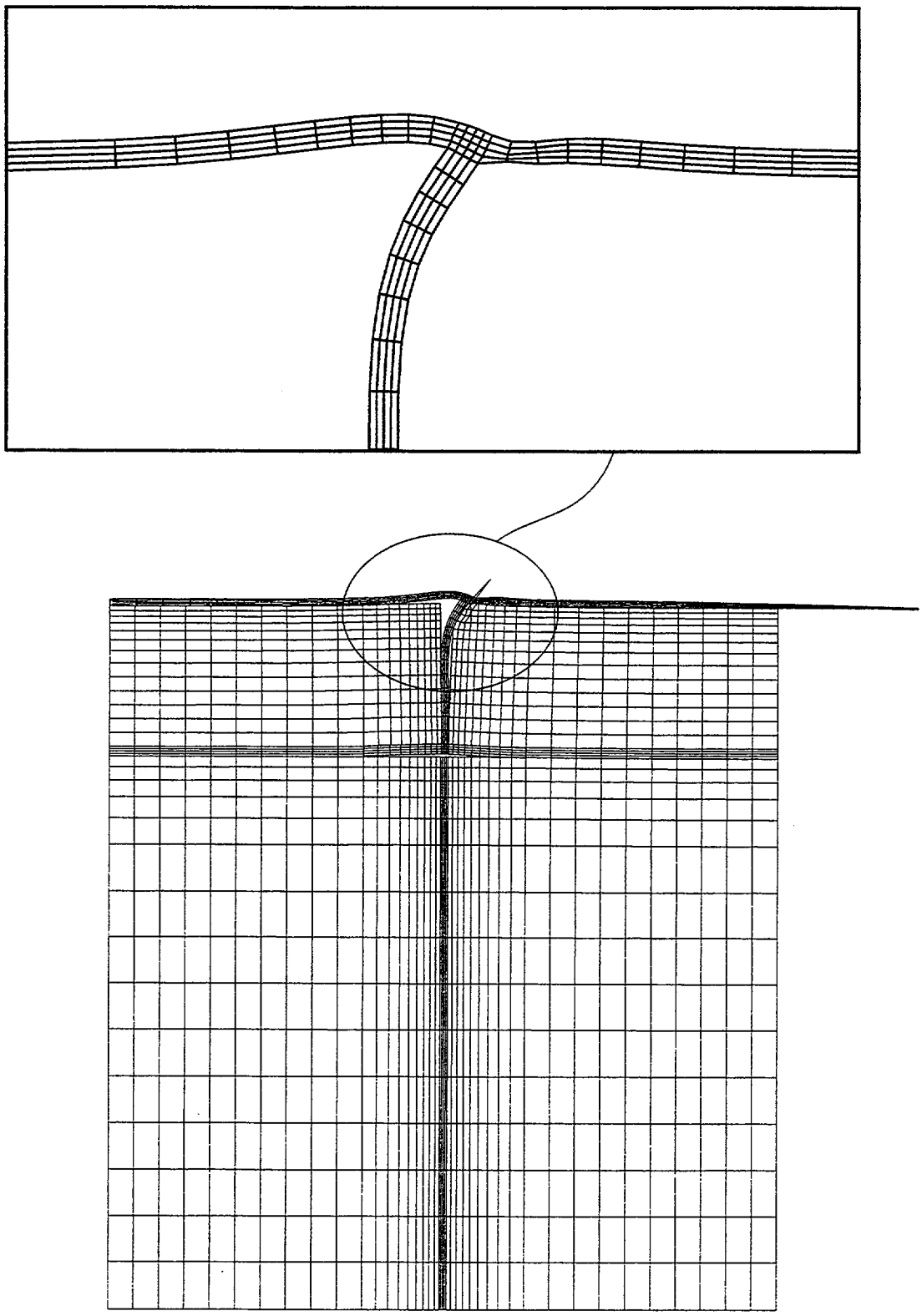

Figure 3-8. Deformed Mesh of Fixed Boundary Condition Case
at Far-field Strain = 8.4E-3 (Pressure = $3.5P_d$), $\mu = 0.5$, Magnification Factor = 50.0
*fix5.inp*

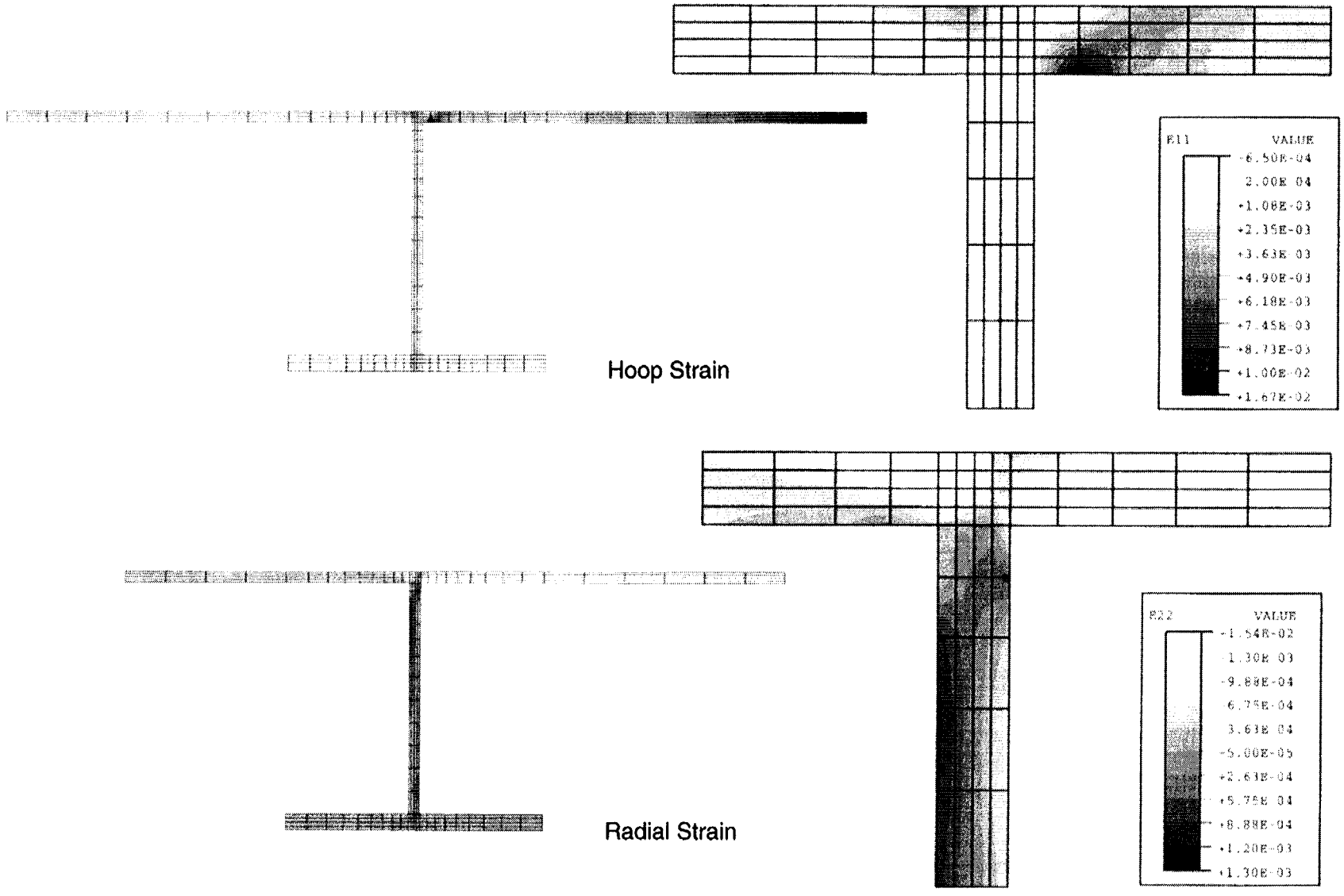


*fix5.inp*

Figure 3-9. Strain Contours for Fixed Edge Case at Far-field Strain = 8.4E-3, $\mu = 0.5$

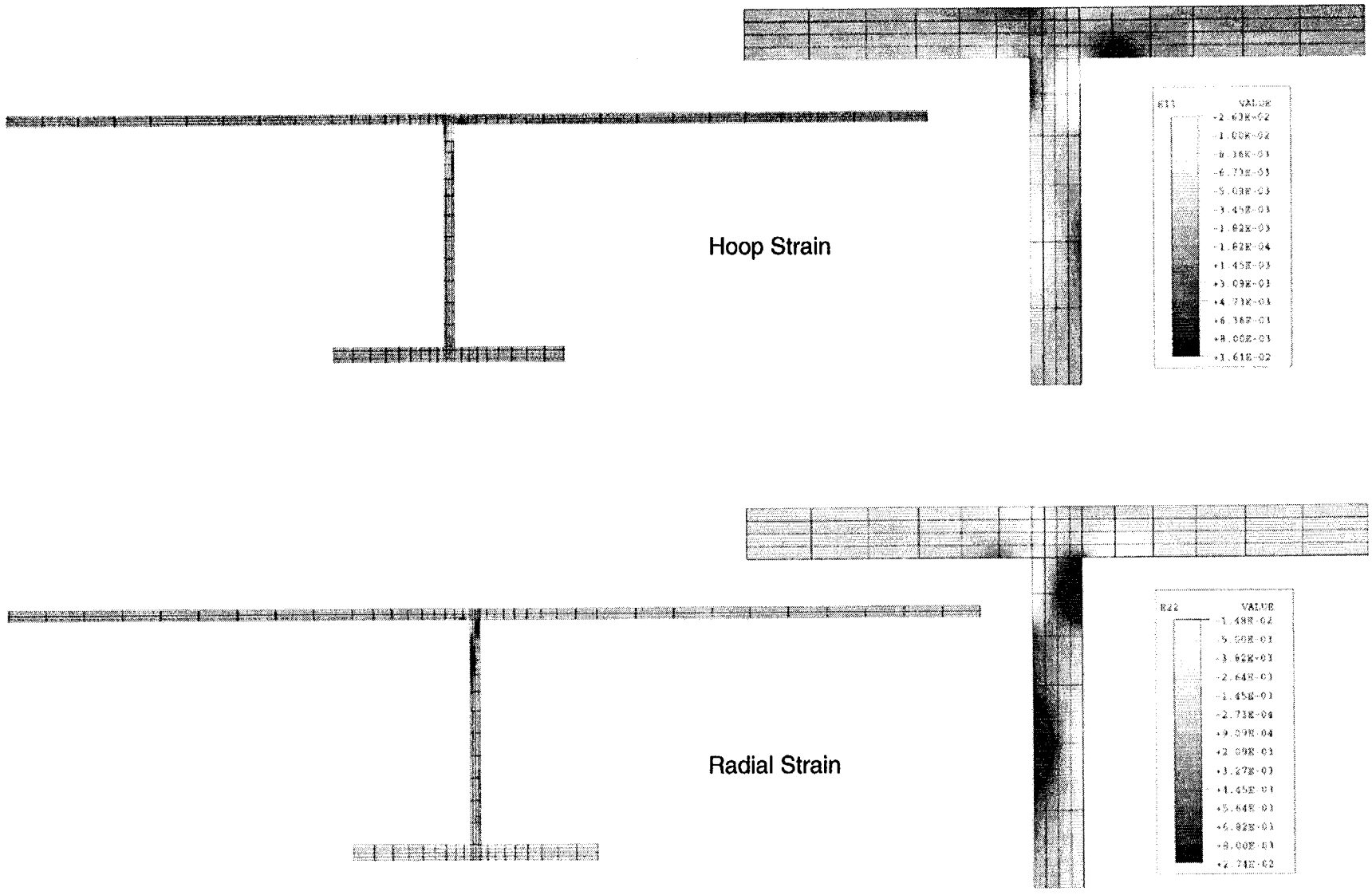


*free5.inp*

Figure 3-10. Strain Contours for Free Edge Case at Far-field Strain = 8.4E-3, $\mu = 0.5$

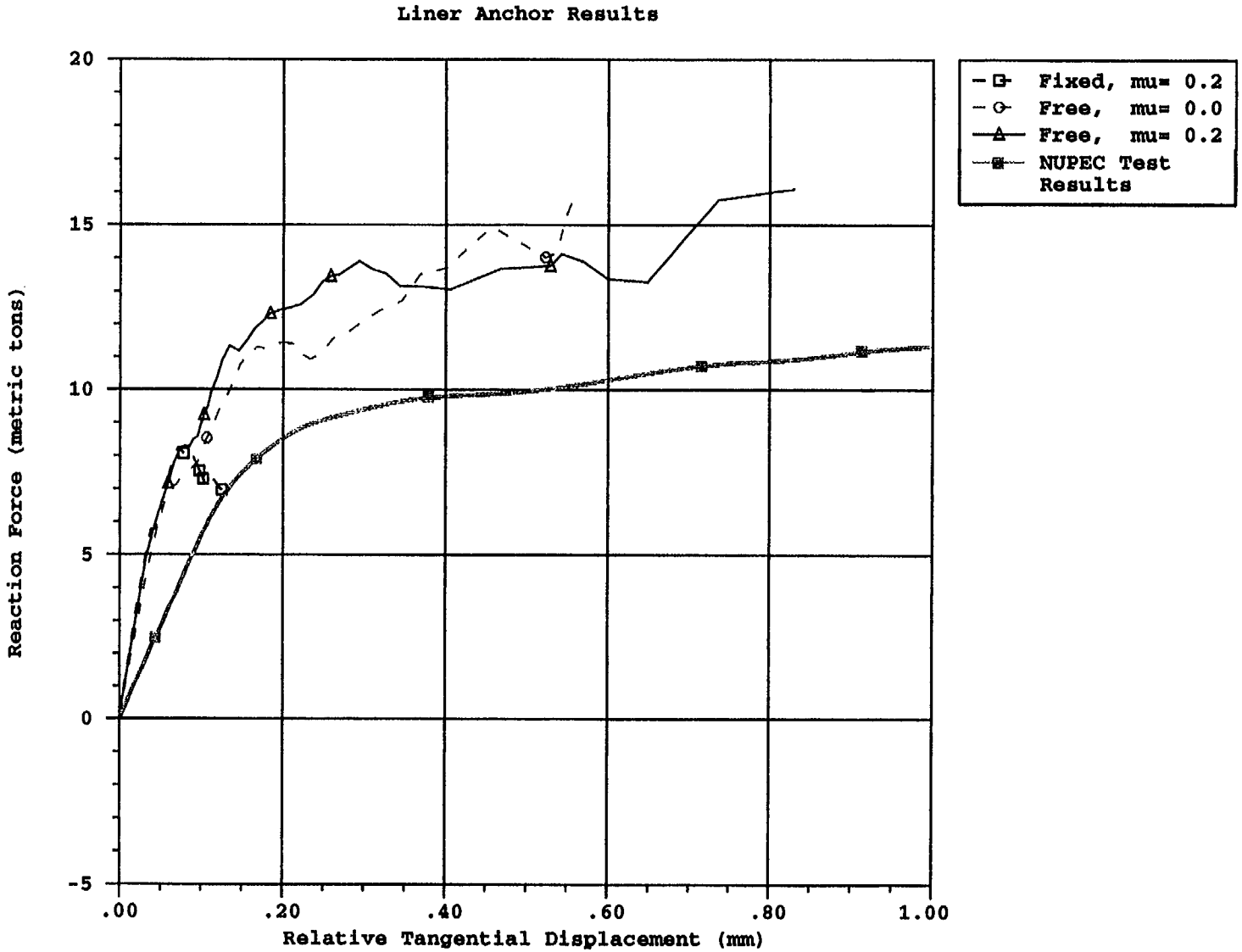


*fix2.inp, free0.inp, free2.inp*

Figure 3-11. Force vs. Displacement Results for Liner Anchor Studies

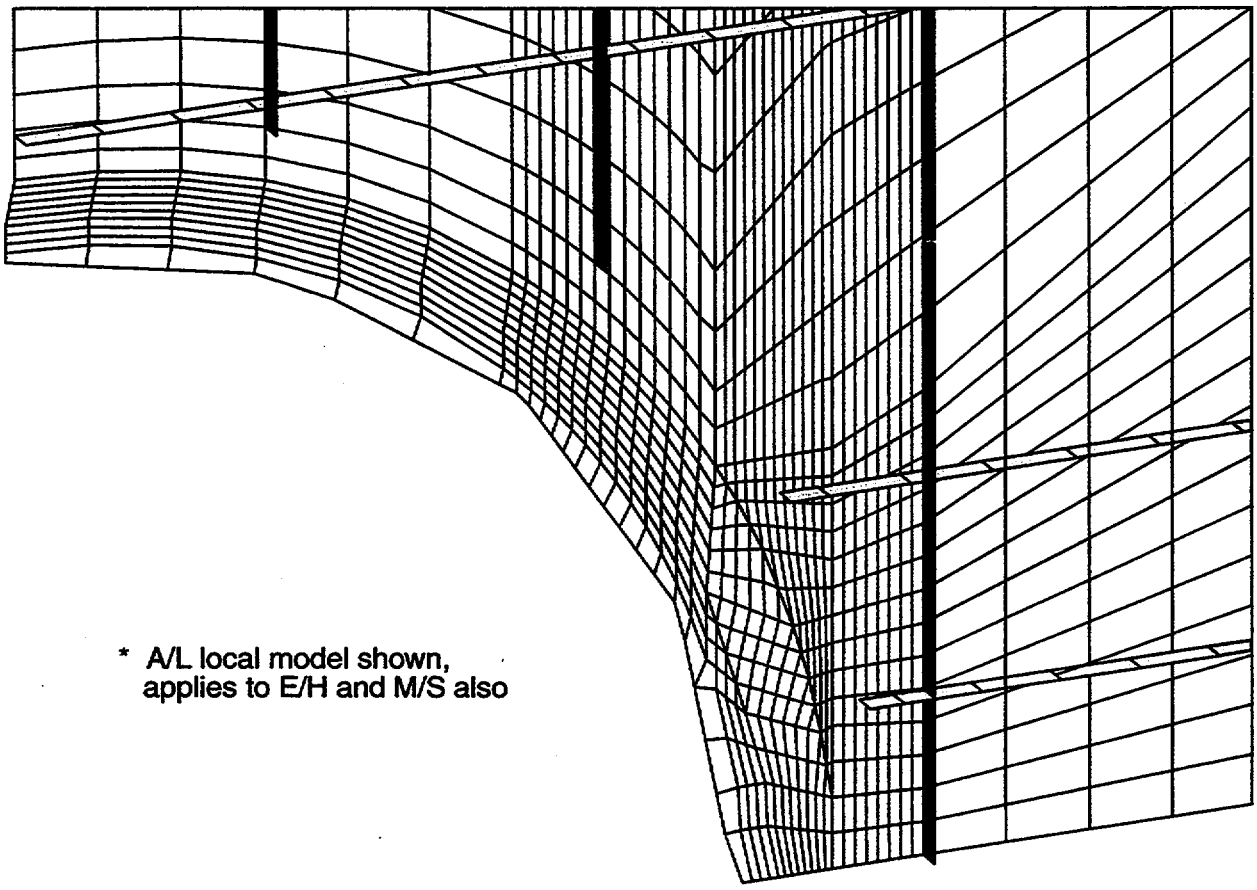


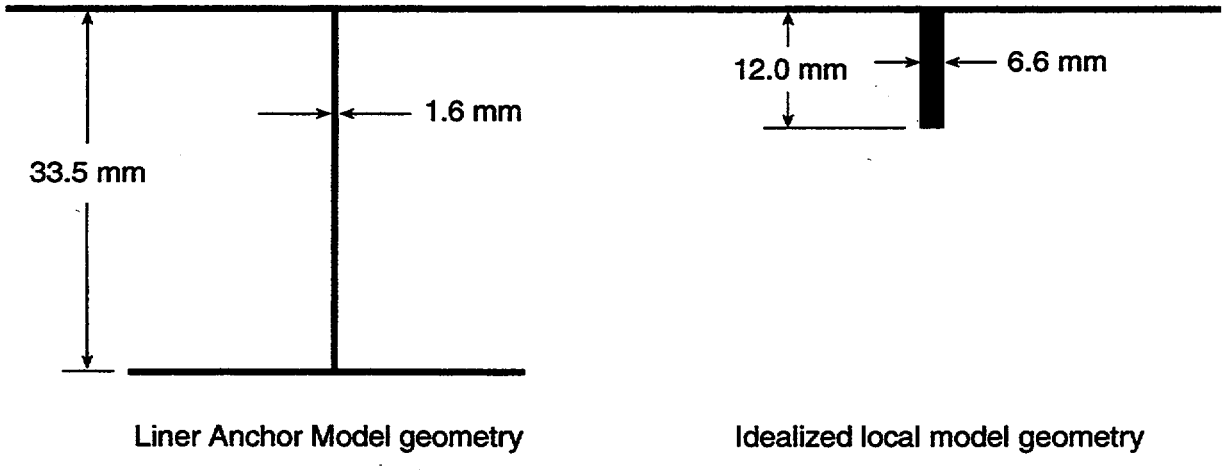


Figure 3-12. Idealized Modeling of Anchors and Stiffeners

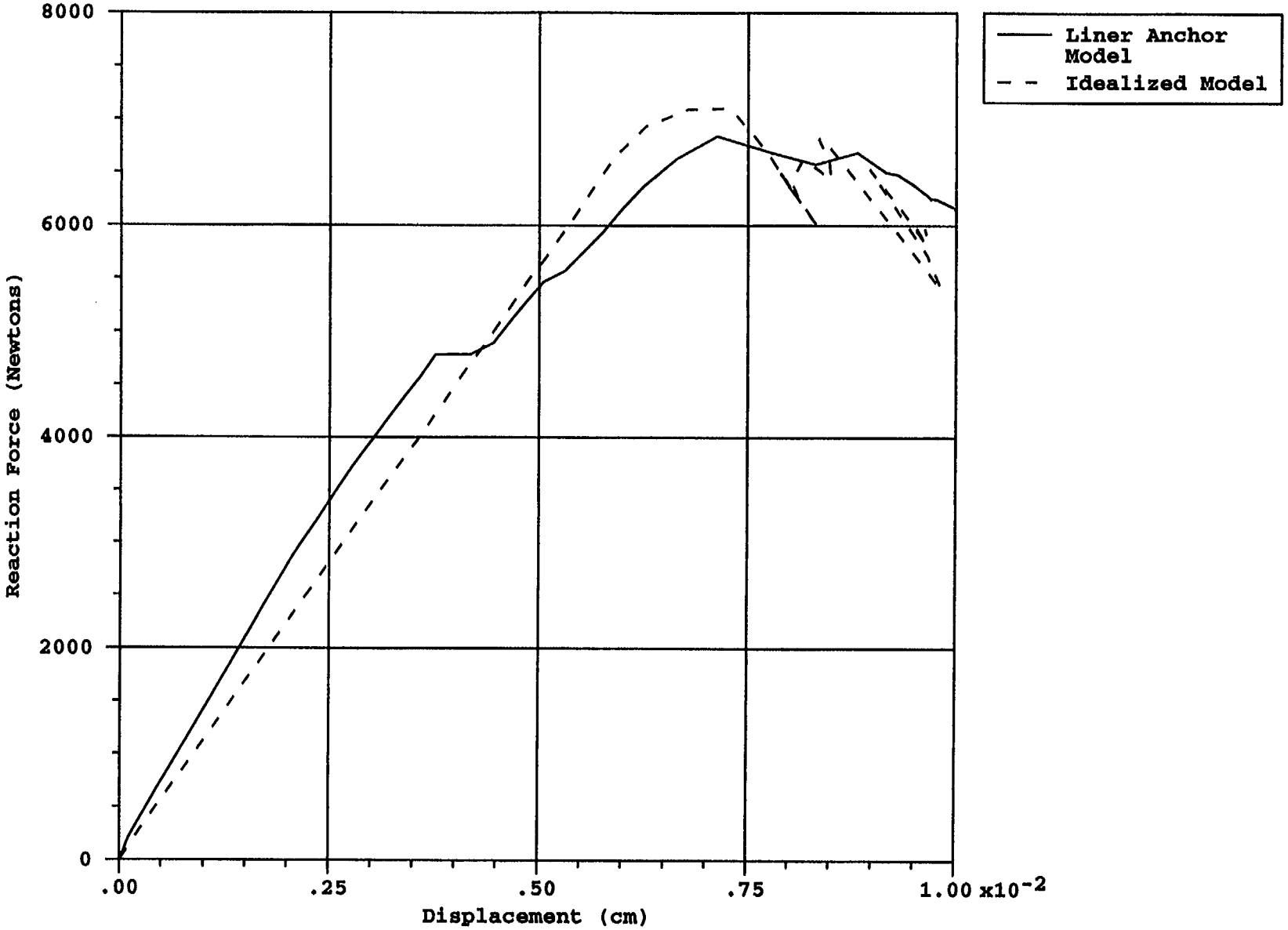


Figure 3-13. Force-Displacement Results of Liner Anchor Model vs. Idealized Model

*fix2.inp, ideal.inp*

# 4. FAILURE CRITERIA

## 4.1 Concrete

For the concrete material, shear failure and compression due to flexure are the only failure modes that have meaningful consequences. Expected failure in direct tension in the form of cracking does not lead to structure failure. It simply results in stress redistribution to steel elements.

Shear-failure criteria found in concrete behavior research are generally dependent on the geometry of the section being considered (depth of section and amount of shear reinforcement) and on the simultaneous presence of bending moment. Thus shear-failure criteria for the prestressed concrete containment vessel (PCCV) model would be location specific. The PCCV preliminary analyses showed elevated shear stresses at various locations in the model, but only the shear stresses of the wall-basemat juncture location are significantly high to warrant detailed consideration.

At the wall-basemat juncture the massive basemat effectively restrains the cylinder wall against radial expansion. Analysis results indicate that circumferential cracks are formed in the wall very close to the juncture under the combined effect of bending and tension. These cracks could extend either across the wall or into the basemat. In the first case, the crack would run into the compressive zone at the outer surface. In the second case the crack would run into the basemat in an area of smaller compression. (More information and illustration of the predicted cracks in this region are provided in Chapter 6.) In both crack formation cases, enough flexural deformation and shear strain exists to warrant further investigation of potential shear failure.

### 4.1.1 Theoretical Considerations

Shear response of concrete has been found to follow three stages of deformation:

1. The concrete resists the deformation with no assistance from the reinforcement or the aggregate; as soon as cracks begin to develop at some angle (between 0 and 45° depending on location) to the direction of the applied shear force, the structural shear stiffness drops suddenly.

2. Frictional resistance increases with further deformations as aggregate interlock begins to mobilize; during this stage the cracks grow wider.

3. The structure reaches its maximum resistance and begins to soften and eventually fail in a mixed mode of shear sliding, crushing and rebar yielding under combined tension and dowel action; the latter mechanisms are attributable to the dilation of the cracks which forces rebars into direct tension and bending beyond their yield limit.

These deformation states vary considerably over the failure "plane," but tests to measure shear behavior generally provide only data in terms of average shear stress across a section versus average shear strain. Experimentalists have developed shear-behavior material models from such tests. However, to apply such models in a continuum analysis approach where the models have to be applied locally (at an integration point) requires consideration of fundamental mechanics and use of damage parameters calibrated to match experimental results. This approach is used in the ANACAP-U modeling.

Explicit shear-failure prediction is made by using an appropriately detailed analytical model and then observing when large shear distortions of the entire wall-basemat section exceed certain prescribed criteria for the reinforcement in the section. Thus, the concrete failure criterion is not a set expression or strain limit but rather a complex continuum response prediction model. The prediction is reasonably good partly because of a recent improvement to ANACAP-U called the shear-shedding model. Background and development of the shear-shedding model is described in the ANACAP Theory Manual.[m] This modification to the old shear-retention model addresses the issue of buildup of shear stress across an open crack in excess of the actual ability of cracked concrete to resist such stresses. Buildup of shear stresses across open cracks in a conventional smeared-crack constitutive model is possible because of the requirement that cracks only form in orthogonal planes. The shear-shedding model addresses such limitations by not only reducing the

[m] Rashid, Y.R., R.S. Dunham, R.J. James, and R.A. Dameron. 1998. "ANAMAT Concrete, Rebar, and Steel Material Models," ANA-98-0243, ANATECH Report, ANACAP Theory Manual. April 1998

shear modulus as a function of crack opening strain (as first suggested by Al-Mahaidi)[n] but also by reducing shear stress at large crack opening and large shear strains.

The shear-shedding model, first introduced into test versions of ANACAP-U in 1996, has now been successfully calibrated to a number of structure component tests,[o] and so has been judged to be a reasonably reliable improvement over the old shear-retention model.

### 4.1.2 Other Shear Criteria

While shear-failure prediction for the project is based on the continuum response prediction coupled with the rebar strain criteria, it is appropriate to turn to the concrete design/performance literature for a check on the final prediction. On the capacity side, criteria can be based on forces or average stresses within the section. The modified compression field theory developed by Collins and Mitchell (1997) provides reasonable stress-based criteria for the PCCV model.

This theory (Collins and Mitchell 1997) is a refined version of a strut-and-tie model which provides a rational basis for calculating compression strut angles of less than 45°, and, with the "modified" theory, the local resistance of concrete in tension between cracks and the effect of aggregate interlock are considered. The difficulty with applying force or stress-based theories to the PCCV is that the shear force is indeterminate, i.e., it is a function of the pressure, the relative hoop stiffness of the cylinder to the basemat, and the flexural stiffness of the cylinder wall. Because of these factors, the shear at the section does not necessarily monotonically increase with pressure. The modified compression field theory is used in Chapter 6 to check for shear failure in the axisymmetric analysis.

Very little is found in the literature for deformation-based criteria that would be useful for FE (finite element) analysis implementation. For the PCCV failure prediction, the primary criterion has been based on strain in the shear reinforcement. If strain in the shear reinforcement at the wall-basemat juncture reaches the failure threshold discussed in Section 4.2, this is judged to lead to shear failure of the section. The modified compression field theory is retained as a backup check to the shear formulations in the constitutive model.

## 4.2 Rebar

The failure criteria used for predicting failure of reinforcement is based on rebar strain, but there are rebar-concrete interaction issues that influence the strain level. Discussion of these issues is provided below.

As described in Chapter 2, the material representation of reinforcement is based on a plastic stress versus strain curve, where the strain is analogous to the "elongation" (engineering strain) measured in a uniaxial tension test of a rebar specimen. Although this procedure does not consider local strain concentrations between the reinforcement "ribs," the elongation data did not deviate substantially from similar tests where strain gages were placed directly on the bars. The other factor to consider in reinforcement, however, is the effect of rebar-concrete interaction. This phenomenon is known to produce a strain pattern in embedded rebars like that shown in Figure 4-1. A good discussion of this phenomenon and some measured strain profiles can be found in Collins and Mitchell (1997). Strains are lowest midway between cracks and are highest at the cracks. No simulation of this phenomenon is attempted in the smeared-crack representation of the PCCV model. The phenomenon can, however, influence the actual strain level at rebar fracture.

The shape of the strain profile in Figure 4-1 is dependent on many factors, including

- bar diameter,
- crack spacing,
- bond characteristics like aggregate size, or
- strain level.

Even though the profile changes with strain level, the fracture strain is the only strain level of interest in the failure criteria. The other parameters will tend to influence the strain profile in the following ways.

- Larger bar diameters will tend to show lower fluctuations between $\varepsilon_0$ and $\varepsilon_{peak}$, where $\varepsilon_0$ and $\varepsilon_{peak}$ are defined in Figure 4-1, because the "development lengths" are longer, so the bar stress fluctuates more gradually.

[n] Al-Mahaidi, R.S.H. 1979. "Nonlinear Finite Element Analysis of Reinforced Concrete Deep Members." Report 79-1. Ithaca, NY: Cornell University, Structural Engineering Department. January 1979.

[o] James, R.J., R.S. Dunham, and R.J. Dameron. 1998. "ANACAP-U Verification and Validation Manual." ANATECH Report. April, 1998.

- Bigger crack spacing will show larger fluctuations between $\varepsilon_0$ and $\varepsilon_{peak}$.

- Higher bond stress will show larger fluctuations than lower bond stress does.

With these known trends, but lacking a specific criterion based on tests, the following criterion was adopted, based on experience and observations of rebar fractures in concrete specimen tests.

$$\varepsilon_{peak} = C_s C_d \varepsilon_{avg} \quad (4\text{-}1)$$

When $\varepsilon_{peak}$ reaches or exceeds the measured rebar fracture elongation, the criterion is exceeded.

$\varepsilon_{avg}$ (shown in Figure 4-1) is the bar strain taken directly from the finite element analysis; $C_s$ is an empirical factor accounting for the crack spacing. $C_d$ is an empirical factor accounting for the bar diameter.

Because the ratio of $\varepsilon_{peak}/\varepsilon_{avg}$ is observed to be no greater than approximately 2, $C_s$ and $C_d$ have been normalized as follows

$$C_s = S^{0.1} \quad (4\text{-}2)$$

where S = crack spacing in mm (obviously S will never be smaller than the bar diameter of the orthogonal rebar and for the PCCV model; it is assumed that S is never larger than 304 mm)

$$C_d = 3.0\, d^{-0.2} \quad (4\text{-}3)$$

The results of this formula for several different crack spacings and bar diameters are shown below. Based on this criterion, rebar strains from the finite element analysis that are in the range of between 5% and 7% will exceed the failure criteria.

| $\varepsilon_{avg}$ | Dia. (mm) | Spacing (mm) | $C_d$ | $C_s$ | $\varepsilon_{peak}$ |
|---|---|---|---|---|---|
| 0.05 | 13 | 100 | 1.80 | 1.58 | 0.14 |
| 0.05 | 16 | 100 | 1.72 | 1.58 | 0.14 |
| 0.05 | 19 | 100 | 1.66 | 1.58 | 0.13 |
| 0.05 | 19 | 200 | 1.66 | 1.70 | 0.14 |
| 0.05 | 24 | 300 | 1.59 | 1.77 | 0.14 |

## 4.3 Tendons

Because unbonded prestressing tendons do not experience bond interaction with concrete as do rebar, the tendon failure criterion is strain, without any applied factors. The material stress-strain curve plotted in Chapter 2 predicts and simulates tendon fracture and post-fracture behavior in the analysis.

It should be noted that tendons can fail in different ways, including failure of strands far from the anchorage, failure near the anchorage, failure of the anchorage itself, and failure of the concrete surrounding the anchorage. For the pretest predictions it has been assumed that since the stress-strain behavior (Chapter 2) is derived from the force-elongation response of the tendon system, this is the correct representation of all tendon system failure modes. This means that no specific consideration was given to the possibility of anchor/bearing failure in the pretest prediction analysis.

## 4.4 Liner Failure Criteria

### 4.4.1 Liner – Away from Welds

The liner failure criterion is also based on strain, but the strain at failure is influenced by the multiaxiality of the stress state and by possible reductions in ductility in the vicinity of welds. If the strain from the strain concentration near a penetration or other stiffness discontinuity exceeds the strain criteria of the liner, the liner will tear and leakage will occur. A literature survey conducted by ANATECH in the early stages of the 1:6-scale model work[p] resulted in adoption of a liner strain-based failure criterion that takes into account the triaxiality of stress when computing the failure strain. This criterion, based on the work of Manjoine[q] and others, has subsequently been used also by Sandia National Laboratories for predicting the ductility capacity of liner and other steel plate material subjected to multiaxial stress. The criteria development is as follows:

The ductility ratio z is defined as

$$z = \frac{\varepsilon_{eff}}{\varepsilon_{ul}} \quad (4\text{-}4)$$

The criteria states that

---

[p] Dameron, R.A., R.S. Dunham, and Y.R. Rashid. 1989. Methods for Ultimate Load Analysis of Concrete Containments, Phase 3: Developing Criteria and Guidelines for Predicting Concrete Containment Leakage. EPRI NP6260SD, ANATECH Report to EPRI. February 1989.

[q] Manjoine, M.J. 1983. "Elevated Temperature Mechanics of Metals," preprints of the 4th International Seminar on Inelastic Analysis and Life Prediction in High-Temperature Environment, 7th International Conference on Structural Mechanics in Reactor Technology (SMiRT), August 1983.

$$z = 2^{(1-TF)}, \quad (4\text{-}5)$$

where TF is the Davis triaxiality factor.

$$TF = \frac{\sqrt{2}(\sigma_1+\sigma_2+\sigma_3)}{\left[(\sigma_1-\sigma_2)^2+(\sigma_2-\sigma_3)^2+(\sigma_3-\sigma_1)^2\right]^{1/2}} \quad (4\text{-}6)$$

$\varepsilon_{eff}$ is the effective plastic strain predicted from analysis including any concentration factors that may be appropriate. $\varepsilon_{uf}$ denotes uniaxial failure strain, which is the standard uniaxial elongation limit that is obtained from a coupon test. In the case of the PCCV model, this average value is 0.34 for liner material uninterrupted by welds. The ductility relationship (Eq. 4-6) has been found to be a reliable formulation, particularly for triaxiality factors which occur in containment liners. While Manjoine proposed Eq. 4-6 for the range 0<TF<5, containment analysts need be concerned only with the range of approximately 1<TF<2. To make this statement it has been assumed that at stress states of interest, no membrane compressive stress exists in the liner and out-of-plane stresses ($\sigma_3$) are small and so have a negligible effect on TF. This reduces Eq. 4-6 to

$$TF = \frac{(\sigma_1+\sigma_2)}{(\sigma_1^2-\sigma_1\sigma_2+\sigma_2^2)^{1/2}} \quad (4\text{-}7)$$

Using this formula, calculating ductility ratios at various liner stress states is straightforward. For example, for uniaxial tension, $\sigma_2$=0, TF=1, and ductility ratio=1. For $\sigma_1$=$\sigma_2$ (for example the approximate stress condition in the containment dome), TF=2, ductility ratio =0.5, which means that the liner will tear at an effective plastic strain of only half the uniaxial failure strain. The following provides a more specific example of application of Equation 4-7.

For the liner local region around the T-anchors and stiffeners (described in the local analysis chapters) that show elevated strain, the state of stress is also strongly biaxial. Over the pressure range near failure the hoop stress in the liner near a liner anchor termination is approximately 410 MPa. The vertical stress is approximately 268 MPa. Because the uniaxial failure strain is 0.34, the biaxial failure strain is $\varepsilon_{eff}^{failure}$, computed by

$$TF = \frac{(\sigma_1+\sigma_2)}{(\sigma_1^2-\sigma_1\sigma_2+\sigma_2^2)^{1/2}} = 1.88 \quad (4\text{-}8)$$

$$z = 2^{(1-1.88)} = 0.543$$

$$\varepsilon_{eff}^{failure} = 0.185$$

When implementing this criterion, experience has shown that *highly* localized strain concentrations may exist (of spatial extent on the order of one or two liner thicknesses) that are not captured by finite element models with insufficient mesh refinement. For the local models used in the PCCV prediction analyses described herein, however, mesh size in the vicinity of critical strain concentrations is reasonably fine, on the order of 4 to 5 mm (about 3 liner thicknesses). Therefore, liner failure predictions have been made without any additional strain concentration or amplification factors.

### 4.4.2 Liner – Near Welds

Based on Nuclear Power Engineering Corporation (NUPEC) testing of dog-bone shaped specimens with and without welds (Appendix A) and based on qualitative observations from other welded steel plate tests, there is evidence to support a reduction in ductility of liner plate material near welds. The test data in (Appendix A) provide some information about how, and at what elongation, the liner may fail near a weld.

Based on test standard JIS-Z-2201, which was used for defining liner plate test specimens (Test Piece No. 5 13a, or 13b), the gage length, L, over which the elongation is measured is 50 mm. Based on the supplementary liner welding test documentation (Document MH-K9-41), the coupon specimens for the liner weld tests were identical to those for the virgin material. These liner weld tests produced the data summarized in Table 4-1.

The tests also recorded where the fractures occurred. In two-thirds of the cases, the fractures were in the virgin parent metal; in the rest of the cases it occurred partly in the heat-affected zone (HAZ) and partly in the parent metal.

Based on the liner reweld test data summarized in Table 4-1, the following conclusions have been drawn and actions taken:

1. There is a small (10% or less) reduction in the apparent yield strength of a welded specimen versus a virgin specimen. This is probably due to a reduction in yield strength of the

**Table 4-1. Summary of Liner Reweld Test Data**

| Root Gap | Weld Classification | With Backing Plate | Yield Stress (MPa) | Ult. Strength (MPa) | Elongation (%) |
|---|---|---|---|---|---|
| 3mm | As welded | Yes | 383 | 505 | 18.9 |
| 3mm | As welded | No | 402 | 519 | 15.3 |
| 3mm | Repaired | Yes | 380 | 506 | 18.9 |
| 3mm | Repaired | No | 380 | 504 | 17.6 |
| 5mm | As welded | Yes | 371 | 499 | 22.9 |
| 5mm | As welded | No | 389 | 506 | 19.4 |
| 5mm | Repaired | Yes | 362 | 506 | 18.1 |
| 5mm | Repaired | No | 366 | 498 | 19.1 |

material in the HAZ. Because liner failure is strain-controlled not strength-controlled and because of the complexities of incorporating this into a finite element model, it was decided to ignore this effect in the pretest prediction analysis.

2. There is very little effect on the ultimate strength of welded versus virgin specimens.

3. There is no consistent trend in the elongation or strength measurements that delineates the as-welded versus repaired specimens; nor is there any consistent trend differentiating the behavior of specimens with or without backing bars.

4. The measured elongations are consistently, significantly lower for welded specimens than for unwelded specimens. This is because gage-length effects, since the weld material undergoes little or no plastic deformation. While this gage-length effect is difficult to quantify, it is addressed, approximately, in the failure criteria.

The above listed observations are incorporated into the liner failure criteria *only at locations where a weld is located* by a general reduction in elongation at fracture, with a small correction factor for gage-length effects of the welded specimens. This is implemented as

$$\varepsilon_{eff_w}^{failure} = K_w \varepsilon_{eff}^{failure} \tag{4-10}$$

where $\varepsilon_{eff_w}^{failure}$ is the effective plastic strain assumed sufficient to cause a fracture where a seam weld of the liner is located. Welds of stiffeners or anchors onto the liner are assumed to have lesser effect on liner ductility than the full-penetration seam welds and so will be ignored.

$$K_w = \left[\frac{(L)}{(L-w)}(\text{Elong. of welded specimens}) / (\text{Avg. Elong. of unwelded specimens})\right] \tag{4-10}$$

where L = liner test specimen gage length (50 mm) and w = root gap of weld.

Averaging the data in Table 4-1 and using 0.34 as the unwelded specimen average elongation gives

$$K_w = 0.60$$

Therefore, a 40% reduction in failure strain will be applied in the failure prediction where high strain concentrations occur at a location coincident with a seam weld.

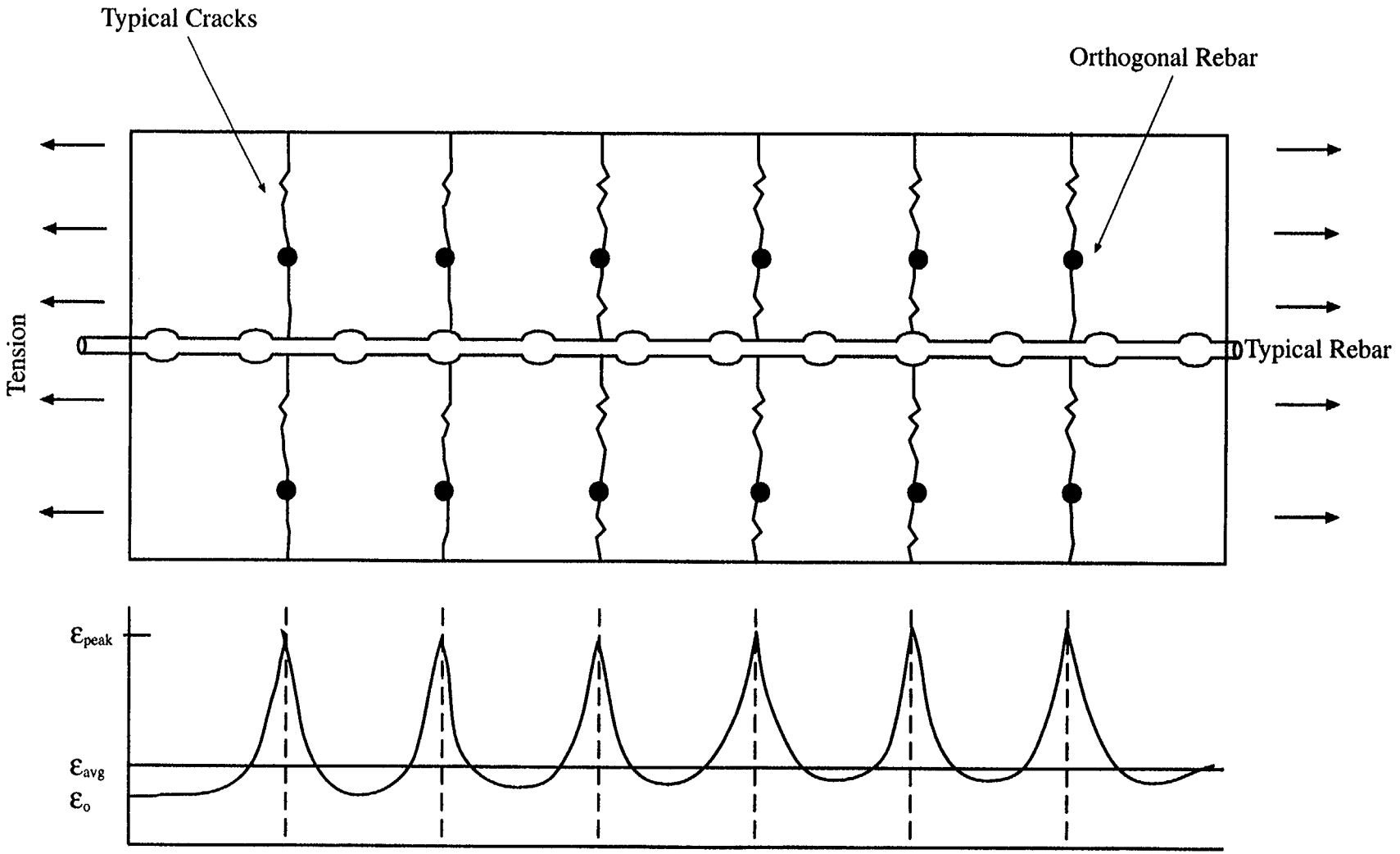


Figure 4-1. Basis for Strain Failure Criteria in Reinforcement

# 5. GLOBAL AXISYMMETRIC ANALYSIS

## 5.1 Hand Calculations

As with any nonlinear analysis of a complex structure, the first step is to identify and categorize structural components and to compute the approximate response behavior to use for guidance in establishing the load-stepping strategy for nonlinear finite element analysis. A summary of the major milestones predicted by hand calculation was developed and is described in this subsection. The following definitions refer to the formulae in this subsection.

$\rho$ = reinforcement ratio

$\rho_{\text{hoop rebar}} = \rho_{hr}$ = area of hoop reinforcement/gross concrete area

$\rho_{\text{liner}}$ = area of liner/gross concrete area

$\rho_{\text{hoop tendons}} = \rho_{ht}$

$t_{\text{liner}}$ = thickness of liner = 0.16cm

$t_{eq}$ = equivalent concrete thickness or transformed section thickness (concrete section area with steel portion transformed by ratio of Young's moduli)

$t'_{eq} = t_{eq}$ including rebar and tendons

$t_c$ = thickness of concrete wall = 32.5cm

$\sigma_o$(concr) = compressive concrete stress after prestressing

R = inside radius of cylinder = 538cm

$E_{rebar}$, $E_c$, $E_{liner}$ = Young's moduli of rebar, concrete, and liner, respectively

$\varepsilon_{cr}$ = concrete cracking strain = $80 \times 10^{-6}$

$\varepsilon_{ry}$ = rebar yield strain

$\sigma_{bar_{ult}}$ = rebar ultimate strength

$\sigma_{tendon_{ult}}$ = tendon ultimate strength (stress at 4.77% strain was used)

**Pressure at which Cylinder Stress Overcomes Prestress, $P_o$**

Because there are three 16mm hoop bars and five 13mm bars every 45cm (measured vertically)

$$\rho_{\text{hoop rebar}} = \frac{3 \times 2.01\text{cm}^2 + 5 \times 1.33\text{cm}^2}{32.5\text{cm} \times 45\text{cm}} = 0.00865 \quad (5\text{-}1)$$

$$\rho_{\text{liner}} = \frac{t_{\text{liner}}}{32.5\text{cm}} = \frac{0.16}{32.5} = 0.00492 \quad (5\text{-}2)$$

$$t_{eq} = \left(1 + \frac{E_{rebar}}{E_c}\rho_{hr} + \frac{E_{liner}}{E_c}\rho_{\text{liner}}\right) t_c = \left(1 + \frac{200}{33}(0.00865) + \frac{200(0.00492)}{33}\right) t_c \quad (5\text{-}3)$$

$$t_{eq} = 35.2\text{cm}$$

There are four hoop tendons of area $3.39\text{cm}^2$ in every 45cm wall segment.

$$\rho_{\text{hoop tendons}} = \frac{4 \times 3.39\text{cm}^2}{32.5 \times 45} = 0.00927 \quad (5\text{-}4)$$

$$\rho_{\text{total}} = 0.00865 + 0.00492 + 0.00927 = 0.0228 \quad (5\text{-}5)$$

In compression under tendon action,

$$\sigma_o(\text{concr}) = -\rho_{\text{tendon}}\,\sigma_{i_{\text{tendon}}} = -0.00927 \times 706\ \text{Mpa} \quad (5\text{-}6)$$

(avg. prestress in hoop tendons including assumed losses)

$\sigma_o$ = -8.83 MPa

pressure to overcome prestress, $P_o$ is

$$P_o = \frac{-\sigma_o t'_{eq}}{R} = \frac{-8.83(35.3)}{538} = 0.580\ \text{MPa} \quad (5\text{-}7)$$

**Cylinder Hoop Cracking Pressure, $P_{hc}$**

Total equivalent t including tendons = $t'_{eq}$

$$t'_{eq} = \left(1 + \frac{E_{steel}}{E_c}\rho_{\text{total}}\right) t_c = \left(1 + \frac{200}{33}(0.0228)\right) 32.5 = 37.0\text{cm} \quad (5\text{-}8)$$

$$P_{hc} = \frac{t'_{cq} E_c \varepsilon_{cr}}{R} + P_o = \frac{37.0 \times (33{,}000) \times 80 \times 10^{-6}}{538} + 0.580 \quad (5\text{-}9)$$

$$P_{hc} = 0.762 \text{ MPa}$$

**Pressure at Rebar Yield, $P_{ry}$**

Assuming the tendons have not yielded, the hoop stiffness after cracking is approximately that of elastic rebar, liner and tendons acting alone. Therefore,

$$\varepsilon_{ry} = \frac{(P_{ry} - P_o)R}{(\rho_{total}) t_c E_s} = \frac{\sigma_y}{E_s} = \frac{455}{200{,}000} = 0.00228 \quad (5\text{-}10)$$

Solving,

$$P_{ry} = \frac{0.00228(0.0228)32.5(200{,}000)}{538} + 0.580 \quad (5\text{-}11)$$

$$P_{ry} = 1.21 \text{ MPa}$$

**Ultimate Barrel Failure Based on Ultimate Strengths of Steel Components, $P_{ult}$**

$$P_{ult} = \frac{\sigma bar_{ult} \rho hr t_c}{R} + \frac{\sigma tendon_{ult} \rho ht t_c}{R} + \frac{\sigma liner_{ult} \rho liner t_c}{R} \quad (5\text{-}12)$$

$$P_{ult} = 32.5\left[658(0.00865) + 1876(0.00927) + 498(0.00492)\right]/538$$
$$= 1.54 \text{ MPa} = 4.0 \text{ Pd}$$

These pressure milestones aid in establishing the increment sizes for the nonlinear solution and in checking for major errors in the finite element computation. Note, however, that this is for the ideal case of an infinite cylinder. Some additional ultimate strength may occur for the PCCV model, from the end-cap effects provided by the dome and the basemat, and some premature deformations may occur in the PCCV model from strain concentrations associated with local and non-axisymmetric details.

## 5.2 Prestressing Loss Assumptions

Care was taken in designing the prestressing system so that losses would be minimized. Thus, actual prestress would be as close as possible to the nominal values expected to exist in the full-scale prototype. (Prestress levels were selected in such a way that the compression in the concrete was matched between the prototype at 40 years and the model at the time of the pressure test.) Nevertheless, prestressing losses must still be estimated to accurately represent the actual stresses that will exist in the prestressed concrete containment vessel (PCCV) model at the time of testing. In general, the philosophy used in applying initial tendon stress was as follows: (1) estimate "test-time" values based on the nominal values targeted by the designers *and* modified for creep or any other in situ conditions; (2) apply tendon stresses according to best-estimate values and allow the model to equilibrate to final tendon stresses that are reasonably close to these best-estimate values, including anchor slip. In the axisymmetric analysis, there is no opportunity to simulate the progression of friction along the tendon path in the hoop tendons, but this phenomenon was included in the meridional tendons.

A consideration of losses was conducted prior to setting up the analysis. Standard prestressing losses (Collins and Mitchell 1997), along with a brief explanation of the basis for their consideration, are listed below:

(1) Elastic Shortening - Considered in the finite element analysis.

(2) Steel Relaxation - Considered by the designers in calculating the "nominal target" values.

(3) Shrinkage of Concrete - Considered only in combination with creep.

(4) Creep of Concrete - A small value of creep (and shrinkage) was included by the designers (see Figure 5-1, combined under "The Tendon Losses"); a larger value was observed in ancillary test measurements. These measurements indicated that approximately (an additional) 5% of the designers final target prestress could be lost by additional concrete creep, so this additional 5% was subtracted from the target values. (This process is summarized in Table 5-1).

(5) Anchorage Slip - Considered explicitly in local model analysis; not relevant for axisymmetric analysis.

(6) Angular Friction - Considered explicitly in local analysis of hoop tendons, and in global axisymmetric analysis of meridional tendons in dome.

(7) Others: Temperature - Not considered.

Therefore, the three types of losses given further specific modeling consideration are elastic shortening, anchorage slip, and angular friction. The modeling considerations related to each of these are described below.

Elastic Shortening: In post-tensioning, the amount and distribution of elastic shortening depend on the order of post-tensioning. From the post-tensioning schedules, it has been assumed that the tendons are jacked in a sequence appropriate to reacting the total desired lock-off force. In ABAQUS, an option called PRESTRESS HOLD allows an initial post-tensioning equilibrium step that holds the tendon stresses at a preset value while the structure iterates to equilibrium and thus maintains a constant stress regardless of elastic shortening. By using the PRESTRESS HOLD option, elastic shortening losses are addressed in the analysis only to the extent that they were considered in the design calculations. This procedure was used for the hoop tendons, with the prestress hold value corresponding to the designers' target values listed in Table 5-1.

Anchorage Loss (lock-off slip): The assumption for these losses comes from hand calculations and from the specifications that the coefficient of tendon friction is equal to 0.21. Anchorage loss calculations are summarized in Figure 5-1. Two methods are illustrated: a triangular integration method and an exact integration method. The exact method was used in the finite element analysis.

Angular Friction: Wobble friction and friction in straight portions of meridional tendons in the barrel below the springline were neglected. From standard prestressed concrete texts (Collins and Mitchell 1997), the angular friction was included in the curved tendon portions with the formula:

$$T_2 = T_1 e^{-(\mu\alpha)} \qquad (5\text{-}13)$$

where $\alpha$ is the angle between $T_1$ and $T_2$, and $\mu$ is the coefficient of static angular friction. $T_1$ is the tendon force next to a jack before friction losses, and $T_2$ is the tendon force at some angle $\alpha$ away from $T_1$.

Example:

Meridional Tendons

$\alpha = 90° = 1.57$ Radians, $\mu = 0.21$ from specifications

$$T_1 = T_2 e^{-1.57 \times 0.21} = T_2 (1.0817) \qquad (5\text{-}14)$$

$T_2 = 92.4\% \, T_1$

which is the percentage loss targeted from the springline up to the dome apex. A summary of these calculations and input to the preliminary analytical models is given in Table 5-1.

**Table 5-1. Initial and Final Tendon Stresses after Losses (in MPa) from Design Package**

| | Hoop Tendons | | Meridional Tendons |
|---|---|---|---|
| | Group 1 | Group 2 | |
| Target prestress force from drawings* | 453kN | 453kN | 503 kN |
| Initial prestress without loss (MPa) | 1337MPa | 1337MPa | 1483 MPa |
| After additional loss assumed due to creep | 1268 MPa | 1268 MPa | 1414 MPa |
| Prestress with friction-dependent loss (MPa) at 135° azimuth | 797 MPa | 1109 MPa | location |
| Stress at anchor after anchor set | 1122 MPa ** | 1122 MPa ** | 1318 MPa |
| Target stress at anchor for FE models | 1122 MPa ** | 1122 MPa ** | 1341 MPa |

| Meridional Tendon Stresses and Losses | | | | | | |
|---|---|---|---|---|---|---|
| Position angle in dome (deg) measured from springline | 0° | 15° | 30° | 45° | 90° | |
| Target prestress after all losses (MPa) | 1334 | 1365 | 1236 | 1170 | 977 | |
| Stress in analytical model after prestress (MPa) | 1342 | 1269 | 1220 | 1139 | 962 | |

* Includes designers' calculations of relaxation and concrete creep and shrinkage. Group 1 tendons are those jacked from the 90° buttress, and Group 2 tendons are those jacked from the 270° buttress.

** Not needed for axisymmetric analysis; value shown is for a 2mm setting loss.

## 5.3 New Tendon Friction Modeling Approach

### 5.3.1 Tendon Friction Loss Representation

In response to questions during the Preliminary Analysis Phase about how tendon friction loss and unbonded tendon behavior would affect the PCCV model response, a methodology was devised to more accurately represent the sliding tendon behavior. Since rebar representation of the prestressing tendons does not account for sliding between the tendon and the concrete, the tendons were modeled explicitly as truss elements in the meridional tendons of the axisymmetric analysis and in all the local models. Initial attempts to model the tendons explicitly and define a contact surface definition with sliding friction in ABAQUS gave unsatisfactory numerical stability. Therefore, the following approach was adopted.

A two-node tendon truss element was included for each row of concrete elements along the tendon path. The resulting grid has a 1:1 ratio of concrete nodes to tendon nodes along the tendon. The concrete nodes were placed at the inside face of the tendon duct so that the reaction force from the tendon would be transmitted to the concrete wall at the appropriate location. The analogous tendon nodes were placed at the center of the tendon duct. To account for the tendon sliding and friction along curved surfaces, tendon nodes were offset from concrete nodes along the tendon path so that the angle between each concrete node and tendon node was equal to the angle of friction. A graphic representation of the modeling technique used in the axisymmetric model is shown in Figures 5-2a and 5-2b. The representation in the local models was similar. As shown in Figure 5-2a, the friction coefficient used was $\mu = 0.21$. The friction force is simulated in a truss element between the concrete and the tendon. Note that the calculations performed with this modeling technique use small displacement theory so that the friction angle remains constant throughout the analysis. Tendon friction is assumed to be negligible over straight surfaces, so the friction angle is set to zero through straight sections of duct.

### 5.3.2 Tendon Prestress Application at Boundaries

Prestress could not be applied as an initial condition when using this modeling approach because the preset friction angle assumes the force comes from the jacking direction (Figure 5-2b). Therefore, a method had to be devised to pull the end of the tendon at the jacking location and cause the reaction force to be imparted into the concrete at the tie down, making the analytical simulation of prestress completely analogous to the physical application. The prestress was applied using an extra, elastic, two-node truss element at the jacking location. One end of this "jacking" element was connected to the end of the tendon, and the other was mathematically constrained to the concrete nodes in the tie-down region. In the first analysis step, the jacking element was loaded with a prestress that produced enough strain to stretch the entire tendon to the target level of prestress. The approximate relationship between the prestress in the jacking element and the prestress in the tendon is given as:

$$\sigma_j = \sigma_t * (l_t/l_j) + \text{jacking and anchoring losses} \quad (5\text{-}15)$$

where,

$\sigma_j$ = prestress applied to jacking element
$\sigma_t$ = prestress transmitted to tendon
$l_t$ = effective tendon length
$l_j$ = length of jacking element

Because the effective tendon length over a curved surface is difficult to calculate, the appropriate jacking prestress was arrived at through iteration. Jacking elements were modeled 31mm long, so the ratio $l_t/l_j$ was large. To accommodate the large stress and strain, the jacking elements were modeled with elastic material properties. The prestress and strain in the jacking elements are large and are not meant to represent physical values. It is important that after reaching equilibrium in the prestress load step, the end of the tendon is loaded with the design stress, after losses.

The ends of the tendons in the opposite direction of force are mathematically connected to the concrete nodes through the wall thickness. As a result, the tendon force is transmitted as an appropriate stress at the boundary locations, which simulates the tendon anchor plate reacting against the concrete.

## 5.4 Computational Grid

### 5.4.1 Element Layout

The axisymmetric model from the Preliminary Analysis Phase[r] (Dameron et al. 1997) was modified to include much more grid refinement at the wall-basemat juncture and an explicit vertical tendon and friction trusses at each concrete tendon node pair. Figures 5-3 and 5-4 illustrate the model. It should be noted that axisymmetric modeling does not allow tendon slip modeling for the hoop tendons. The concrete grid was modified to place a row of concrete nodes along the inside face of the tendon duct. The revised grid has 12 elements through the wall thickness near the basemat, and 10 elements through the wall thickness up the remainder of the wall. The basemat grid was adjusted to accommodate the revised element density in the wall, but remained similar to the grid used in previous analyses. The concrete and liner were represented with 8-node quadrilateral elements (ABAQUS CAX8R) and 3-node axisymmetric shell elements, respectively.

The reinforcement in the structure was represented with ABAQUS rebar subelements as shown in Figure 5-4. These subelement stiffnesses are overlaid onto their parent concrete elements in which they reside, but they do not have separate degrees of freedom, and so have strain compatibility with the concrete. The rebar stress-strain behavior is evaluated separately from the concrete, however. Also added as rebar subelements is steel associated with the "tendon sheath support frame." This frame adds the equivalent of the following to the structure:

- Adds 7 hoops of areas 2.79 $cm^2$ to cylinder
- Adds 35 verticals of areas 4.61 $cm^2$ to cylinder
- Adds extra $\rho$=0.0018 to dome (reinf. ratio)

The bottom of the model is supported by nonlinear contact springs. These springs have "zero" resistance to uplift and have compression stiffness based on the elastic stiffness of the concrete mudmat. The stiffness of the subgrade was not considered in the analysis.

[r] Dameron, R.A., and V.K. Luk.1997. "Preliminary Assessment of Potential Liner Tearing Near the Equipment Hatch of a 1:4 Scale PCCV," from the Post-Conference Seminar, 14th International Conference on Structural Mechanics in Reactor Technology (SMiRT), Saclay, France, August 25–26, 1997.

The total number of elements used in the revised model is 2009. The vertical tendon is modeled with 144 two-node truss elements and 36 two-node axisymmetric shell elements. Axisymmetric shells were used to represent the tendons in the dome above a dome angle of 45° to accommodate the "smeared" hoop and vertical components of the hairpin tendons in the dome. This modeling approach is reasonable because above 45°, the tendons are all vertical (no hoop) and at the 135° azimuth they all intersect the model plane at ± 45°. This avoided the difficulties of terminating the truss elements at the dome apex with finite cross-section area but zero radius.

The liner is constructed of quadratic shell elements and 3 node quadratic beam elements for the liner anchors. The thickness of the liner elements is 1.6 mm as specified in the structural drawings. The cross-section of the T-shaped liner anchor beams was computed in such a way that the thickness of the web and the width of the flange are scaled by the total number of T-anchors in the circumferential direction, namely by 225 from elevation -25 mm to elevation 712.4 mm and by 75 for the rest of the T-anchor beams.

Note that vertical tendon truss elements are allowed to slide relative to the concrete between the two anchor points. Hoop tendons are modeled as rebars and, hence, they are always bonded to the concrete.

The concrete in the PCCV model is made of two different materials as shown in Figure 5-5. One is the higher strength concrete that is used for the dome, the barrel wall and a part of the basemat around the tendon gallery. The other is the normal concrete in the remaining part of the basemat, part of which is poured in place after prestressing.

### 5.4.2 Tendon Stressing and Model Loading

The jacking element described previously was loaded with an initial prestress that resulted in 12mm of tendon elongation and 1342 MPa of tendon stress at the anchor. A contour of the tendon stresses after anchoring is shown in Figure 5-6. As shown, the tendon stress is constant through the straight portion of the tendon and decreases in the dome. Since the included angle of the dome is $\pi/2$ and $\mu = 0.21$, the theoretical friction loss is $1\text{-}e^{(-.21*\pi/2.)} = 28\%$. The loss shown in the Figure 5-6 is near 34%. Since the dome tendons were modeled as axisymmetric shells, the prestress at the 135° azimuth is translated to the hoop direction. Near the top of the dome in this axisymmetric analysis, the tendon

prestress is principally hoop in nature. The tendon prestress in the hoop direction at the top of the dome is 1000 MPa. If we assume that the vertical prestressing is transmitted entirely to the hoop direction at the top of the dome, then the prestress loss is exactly 28% [(1342 - 962)/1342 = 28%].

The model was prestressed with the ABAQUS *INITIAL STRESS command in conjunction with the *PRESTRESS HOLD option (for the hoop tendons) that allows the model stresses to equilibrate while forcing the hoop tendon stresses to remain at predetermined levels. Prestressing losses and initial stress values were given previously.

Pressure load was applied then added to interior model surfaces over 161 increments. As is normally the case for concrete containment analysis, the ABAQUS feature "DIRECT=NOSTOP" was used with five iterations per load step. The five iterations ensure that materials in the plastic range stay on a yield surface, but the "NOSTOP" parameter allows advancement of the solution before achieving full force convergence, which is difficult to achieve in cracked concrete elements. Instead of achieving force convergence, the displacement convergence at each increment was monitored to ensure the quality of the solution.

## 5.5 Global Axisymmetric Analysis Results

Results of the axisymmetric analysis are plotted in Figures 5-7 through 5-22. The first two figures show shear and moment diagrams of the lower 3 m of the cylinder wall at various pressures. Figure 5-9 shows the locations of plotted response history information.

The deformed shapes for four different pressure loads are shown in Figure 5-10.

### 5.5.1 Displacement Behavior

Figures 5-11 through 5-17 plot response information versus pressure. The vertical grid lines on the plots represent multiples of design pressure, $P_d$ = 0.4 MPa. Figures 5-11 and 5-12 show radial and vertical displacement histories at the five locations: cylinder wall-basemat, wall-midheight, dome springline, 45° and 90° dome angle. Comparison of these curves shows the relative response levels of the different portions of the PCCV model. For radial response, different critical milestones can also be noted by the changes in curve slope. Cylinder cracking coincides with the slope jump in the curves at about $1.7P_d$. Progressive yielding of steel elements corresponds to the steadily increasing slope of the displacement versus pressure curves.

### 5.5.2 Liner Strains

Liner strains at various positions are shown in Figures 5-13 through 5-14. Hoop liner strains are maximum at the wall-midheight (Position 2). Meridional liner strains are maximum at the wall-basemat (Position 1). Strain response in the dome is consistently lower than the cylinder, thus indicating prediction of very minimal damage to the dome during the test. The most important observation is that wall-midheight hoop liner strain reaches 2% (a threshold to be discussed later) at nearly the same pressure (3.7 versus $3.9P_d$) as wall-basemat meridional liner strain. This suggests the existence of two closely competing failure mechanisms, which require close evaluation to determine which will occur first.

### 5.5.3 Tendon Behavior

Tendon strain and stress history plots are shown in Figures 5-15 through 5-17. The strain traces begin at P=0 with substantial tensile strain (0.6 to 0.7%) due to their prestressing. Tendon yielding begins to occur between 1% and 2% strain, although the tendons have no sharp yield point as do the liner and rebar. Hoop tendon strains exceed 4% by $4 \times P_d$, so this is judged to be an absolute upper limit on capacity for the 1:4-Scale PCCV. However, for reasons discussed later in this chapter, failure is expected well before the occurrence of free-field tendon rupture.

### 5.5.4 Strain Distributions

Strain distributions plotted onto the deformed model shape are shown in Figures 5-18 through 5-22. The strain contours are maximum and minimum principal strains, which show the general locations and levels of damage predicted to occur. The two primary damage locations are the cylinder midheight and the wall-basemat juncture. The wall-basemat juncture damage is detailed in Chapter 6. Figures 5-18 through 5-21 show maximum principal strains at pressures of $3.0P_d$, $3.4P_d$, and $3.8P_d$, and Figure 5-22 shows minimum principal strains at $3.4P_d$. The largest strains tend to occur near the inner corner of the wall-basemat juncture, in the concrete, near the liner anchor embedment. Maximum principal strains of 0.034, 0.10, and 0.26 are indicated at $3.0P_d$, $3.4P_d$, and $3.8P_d$, respectively.

## 5.6 Potential Failure Modes Evidenced from Global Axisymmetric Analysis

The axisymmetric analysis described in this chapter provides a detailed set of predictions that can eventually be compared to strain and displacement gage readings that will be measured in the test, thereby evaluating the adequacy of the analytical method. The focus of the axisymmetric analysis, however, was also to gain insight on potential failure mechanisms listed in Table 1-1, and to add failure scenarios to that list. The various failure scenarios are discussed below vis-a-vis the global analysis model results and experience from other containment pressure tests.

(1) Tendon Rupture: The straining of the hoop tendons (and rebar) at the midheight of the cylinder to their ductility limits was the final limit state in the global axisymmetric analyses. General tendon rupture is predicted at approximately 4 x $P_d$ with tendon hoop strain exceeding 4%.

(2) Other Loss-of-Prestress Failures: The chance of tendon slippage or other anchorage failure is presumed minimized by design and by verification from the Nuclear Power Engineering Corporation's ancillary tests. Local failure under the tendon-bearing plates is still possible, however. A significant shear path develops passing inward and upward from the meridional tendon anchorage. Stresses are predicted to be severe enough to possibly lead to failure in the basemat. (Bursting of the anchorage zone in the buttress investigated during the Preliminary Analysis Phase was not found to be a likely failure mode.)

(3) Simultaneous Shear Failure and Rupture of Reinforcement at Shear Cracks: Failure of reinforcement crossing major shear cracks can occur simultaneously with shear failure. The possibility of local rebar failure exists wherever large rebar strains in excess of the failure criteria are predicted by analysis. Shear reinforcement also exhibit large strains at the wall-basemat juncture. It is more difficult to predict the behavior associated with a stirrup failure because the surrounding concrete, rebars and adjacent stirrups can pick up the released load. However, a large shear dislocation may form at such a location which would tear the liner. This is evaluated in more detail in Chapter 6.

(4) Loss of Pressure from Liner Tearing and Leakage: This is considered to be the most likely failure mode for this steel-lined vessel. While the uniaxial strains in coupon tests of liner material show elongation of up to 34%, past observations of PCCV and specimen behavior[5] (Hessheimer et al. 1997) indicate the presence of liner strain concentrations of as high as 10 or higher. Based on these observations, reaching global liner strains in the PCCV model beyond approximately 2% is judged to be very unlikely. Strain concentrations at local discontinuities include liner thickness changes, stiffener terminations, and bending points near penetrations. The liner's vulnerability is further amplified by the fact that it experiences highly biaxial stress. Under such conditions, its ductility (or observed engineering strain at fracture) can be reduced by a factor of two or more. Based on this qualitative evidence, failure of the test model is predicted to occur from liner tearing and leakage at global (far-field) strains of between 1% and 2%. Without examining local model results, this places the failure pressure at between 3.5 and 3.7 × $P_d$. Clearly, more detailed analyses are needed to refine this estimate and predict more precisely where the most likely failure location will be.

[5] Dameron, R.A., R.S. Dunham, and Y.R. Rashid. 1989. Methods for Ultimate Load Analysis of Concrete Containments, Phase 3: Developing Criteria and Guidelines for Predicting Concrete Containment Leakage. EPRI NP626OSD, ANATECH Report to EPRI. February 1989.

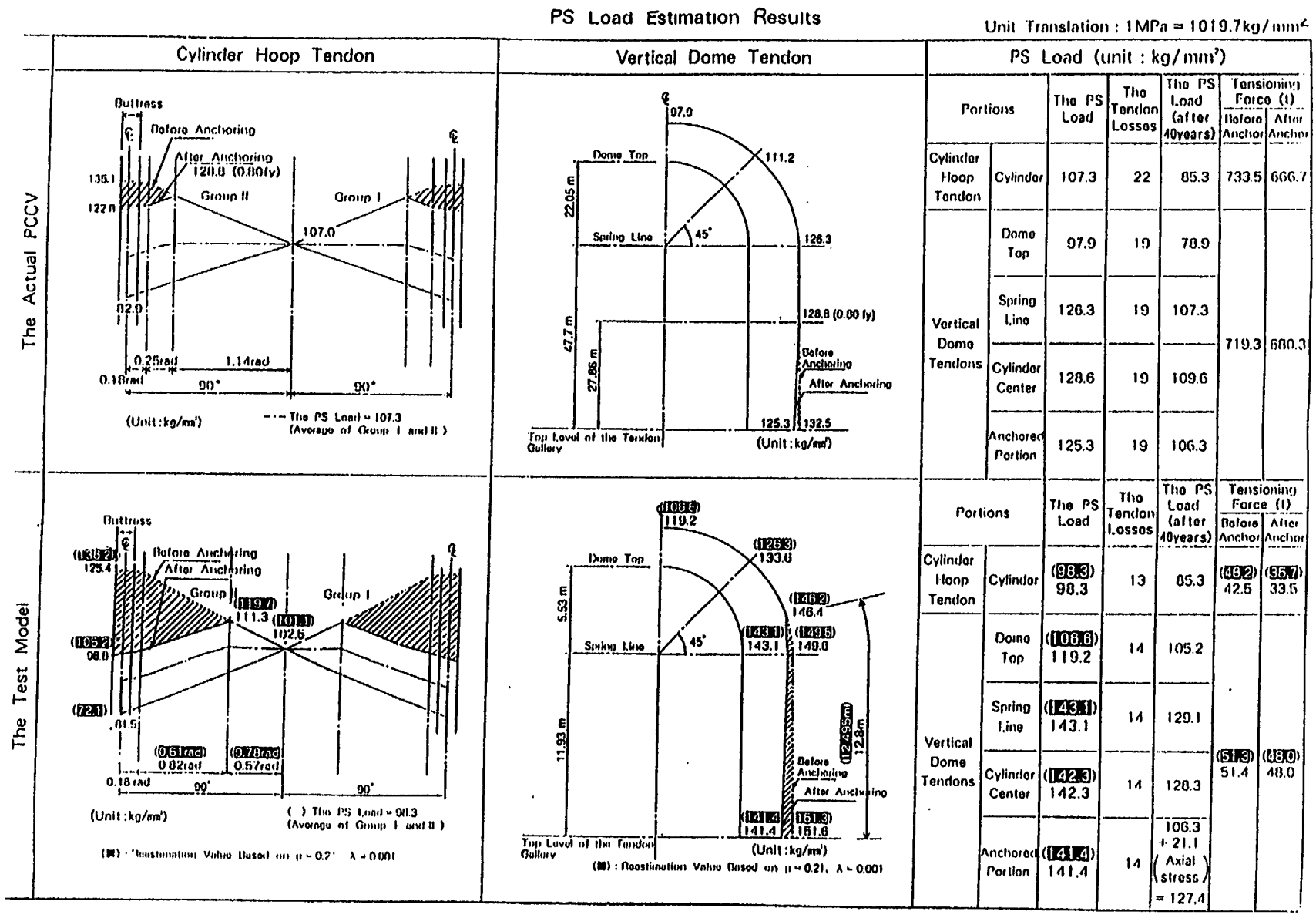


Figure 5-1. Designers' Prestress Force Estimates Including Friction, Anchor Set, and Other Losses

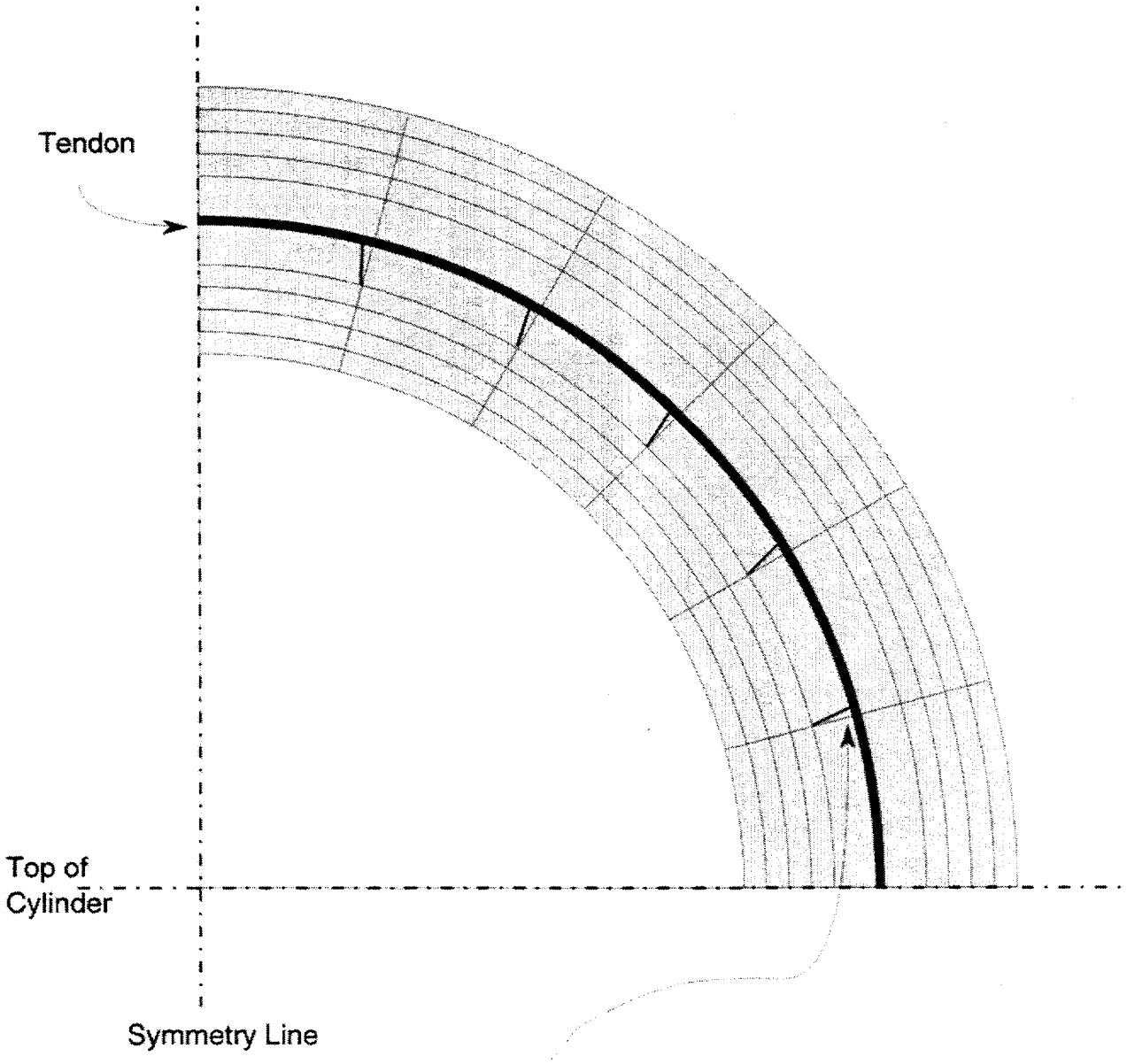


Figure 5-2a. Modeling of Tendon Friction Behavior

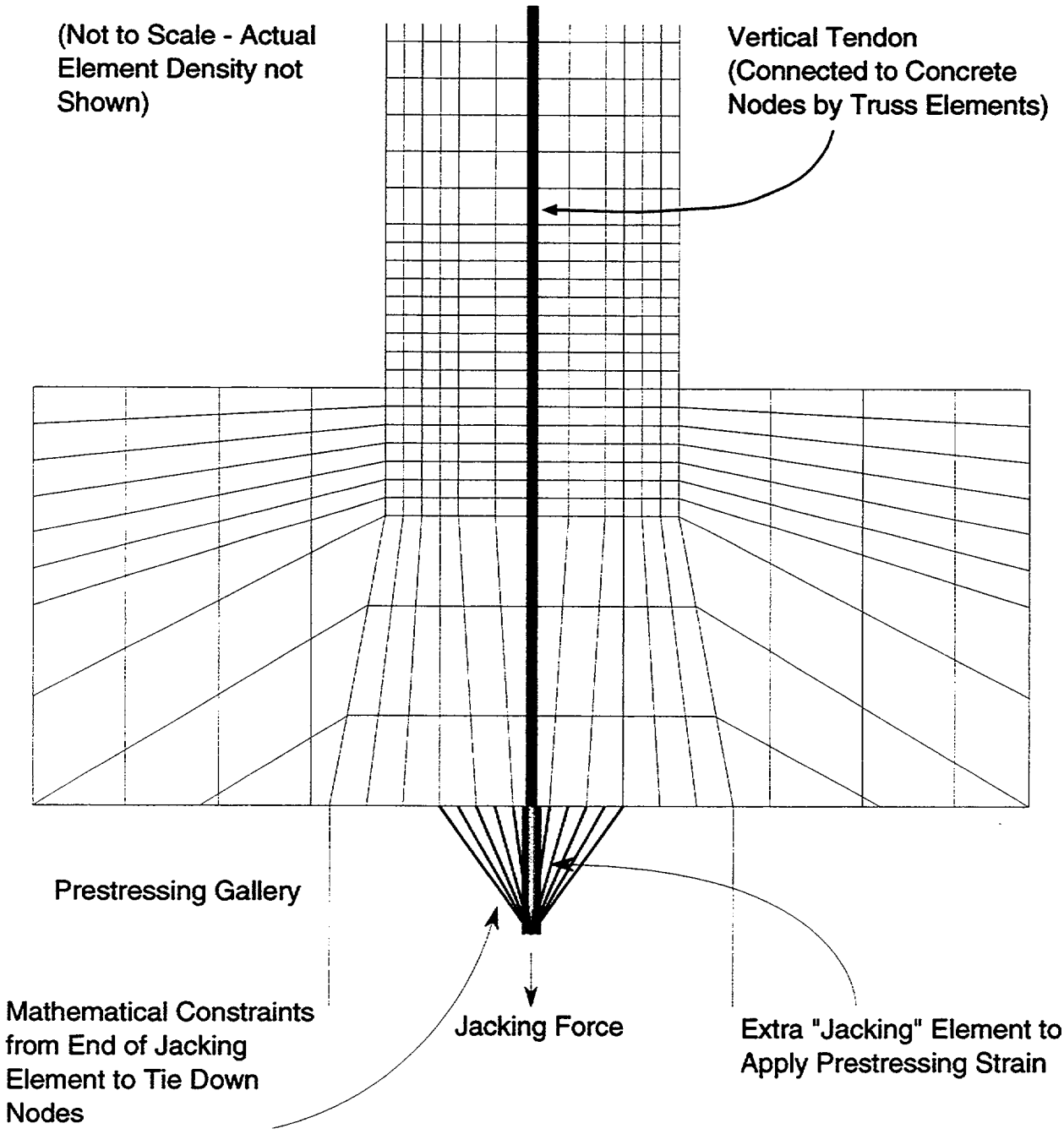


Figure 5–2b. Modeling of Prestress Application with Jacking Element

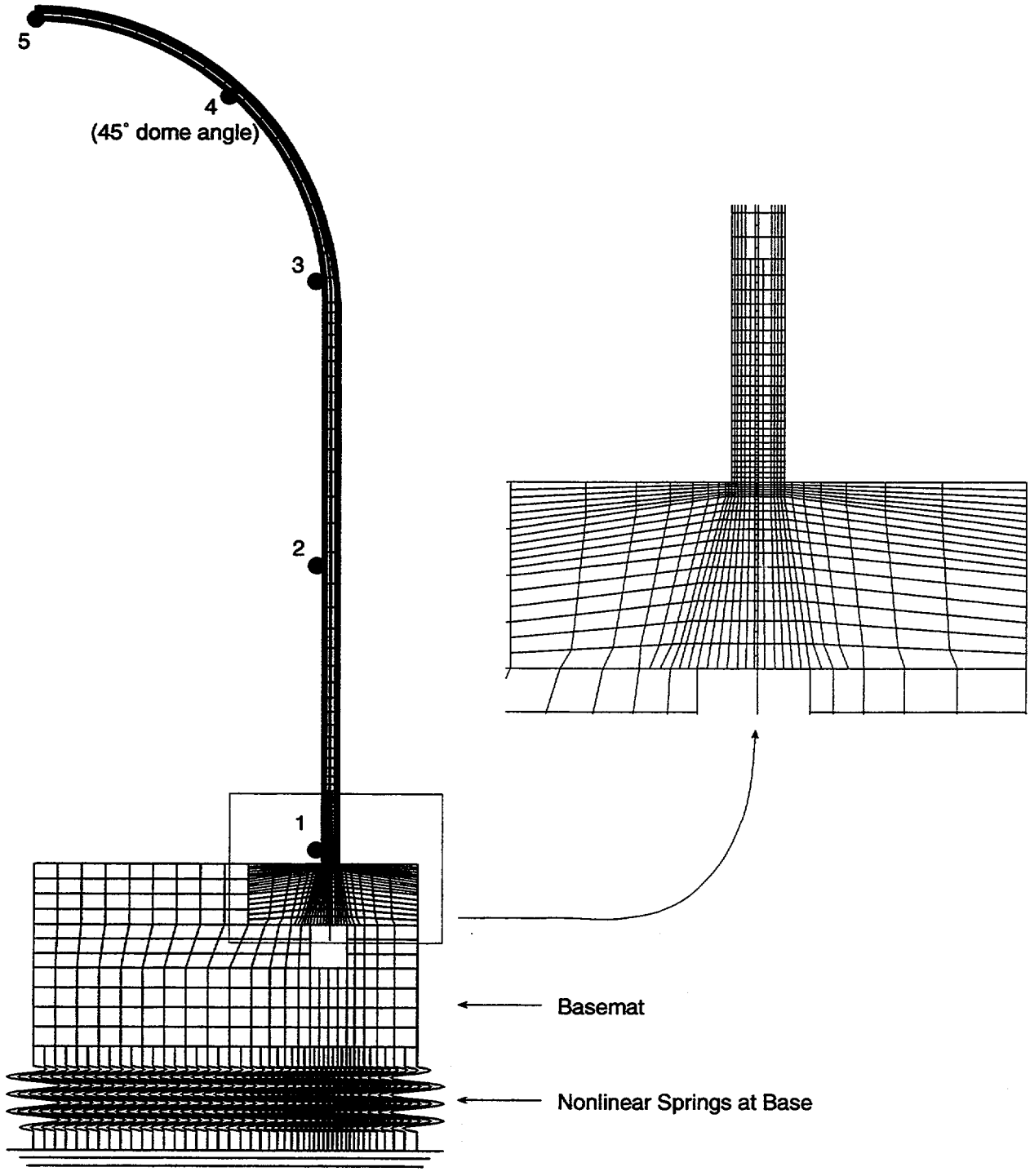


Figure 5-3. Axisymmetric Model of Prestressed Concrete Containment Vessel (PCCV) and Locations for Plotted Output

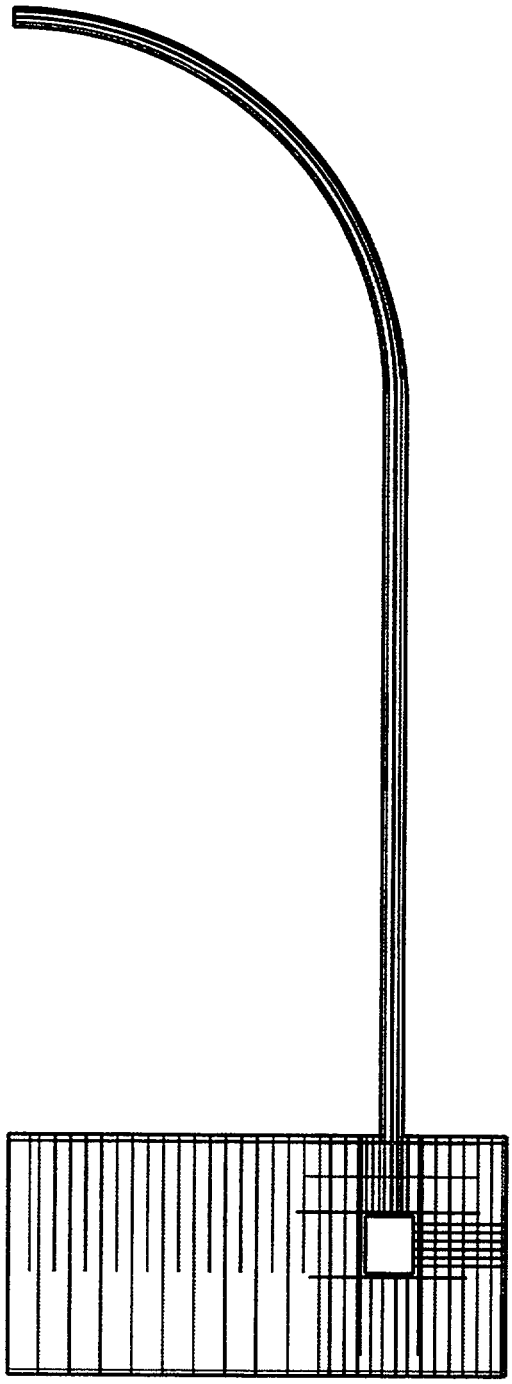

Figure 5-4. 1:4-Scale Prestressed Concrete Containment Vessel (PCCV) Reinforcement Included in Asymmetric Model

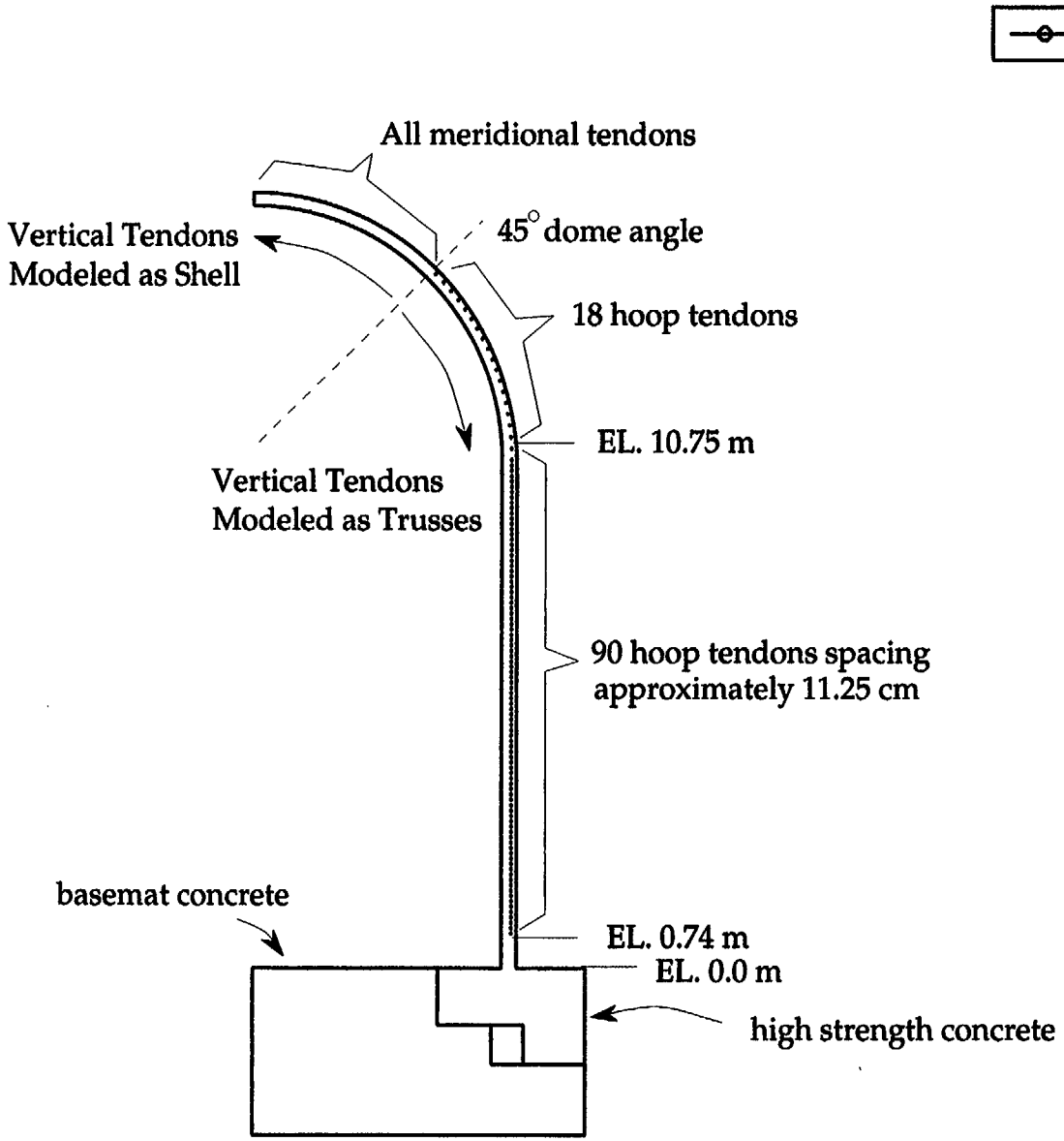


Figure 5-5. Hoop Tendon and Concrete Outlines

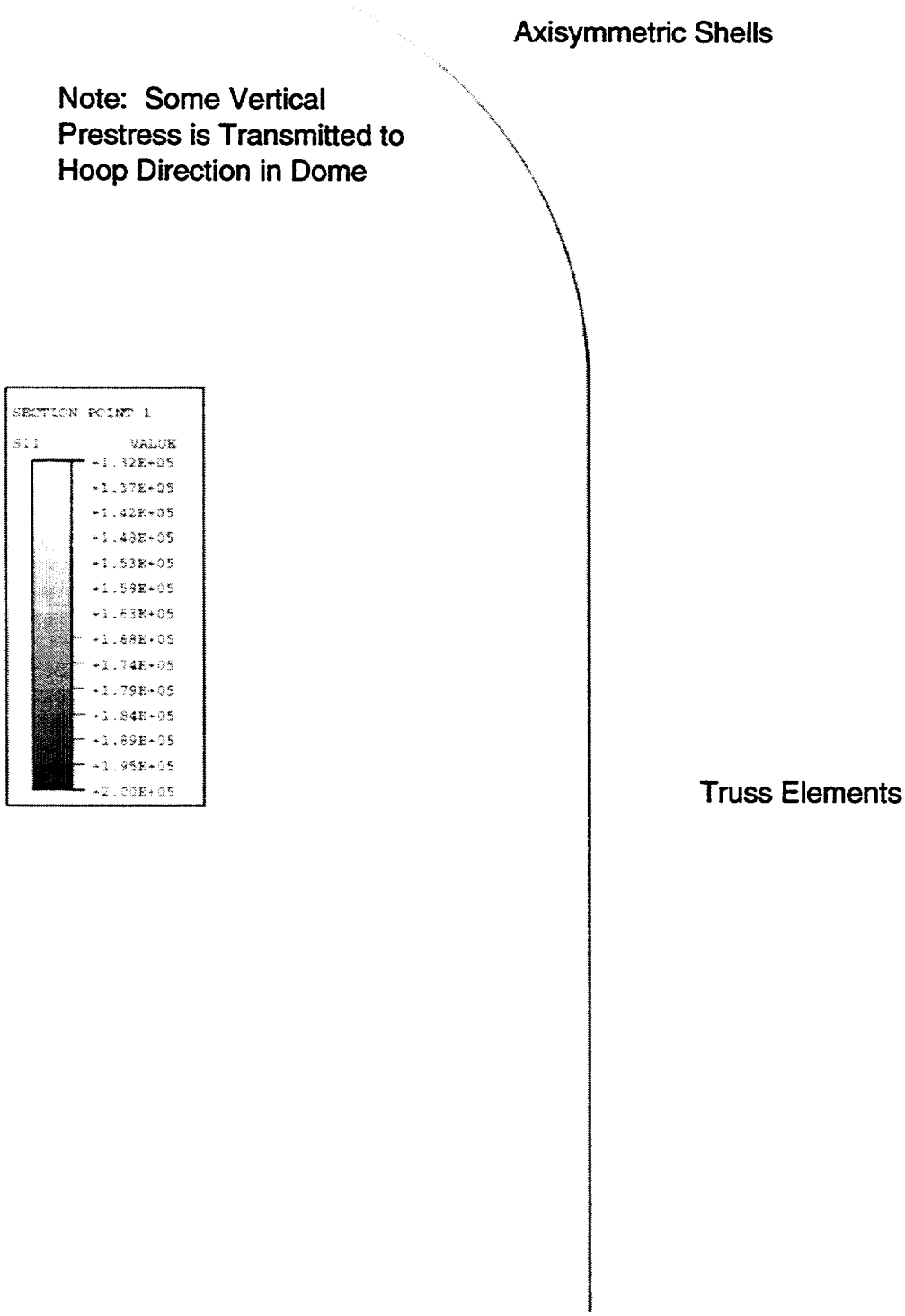


*model14.inp* Figure 5–6. Revised Axisymmetric Model, Tendon Prestress Pattern

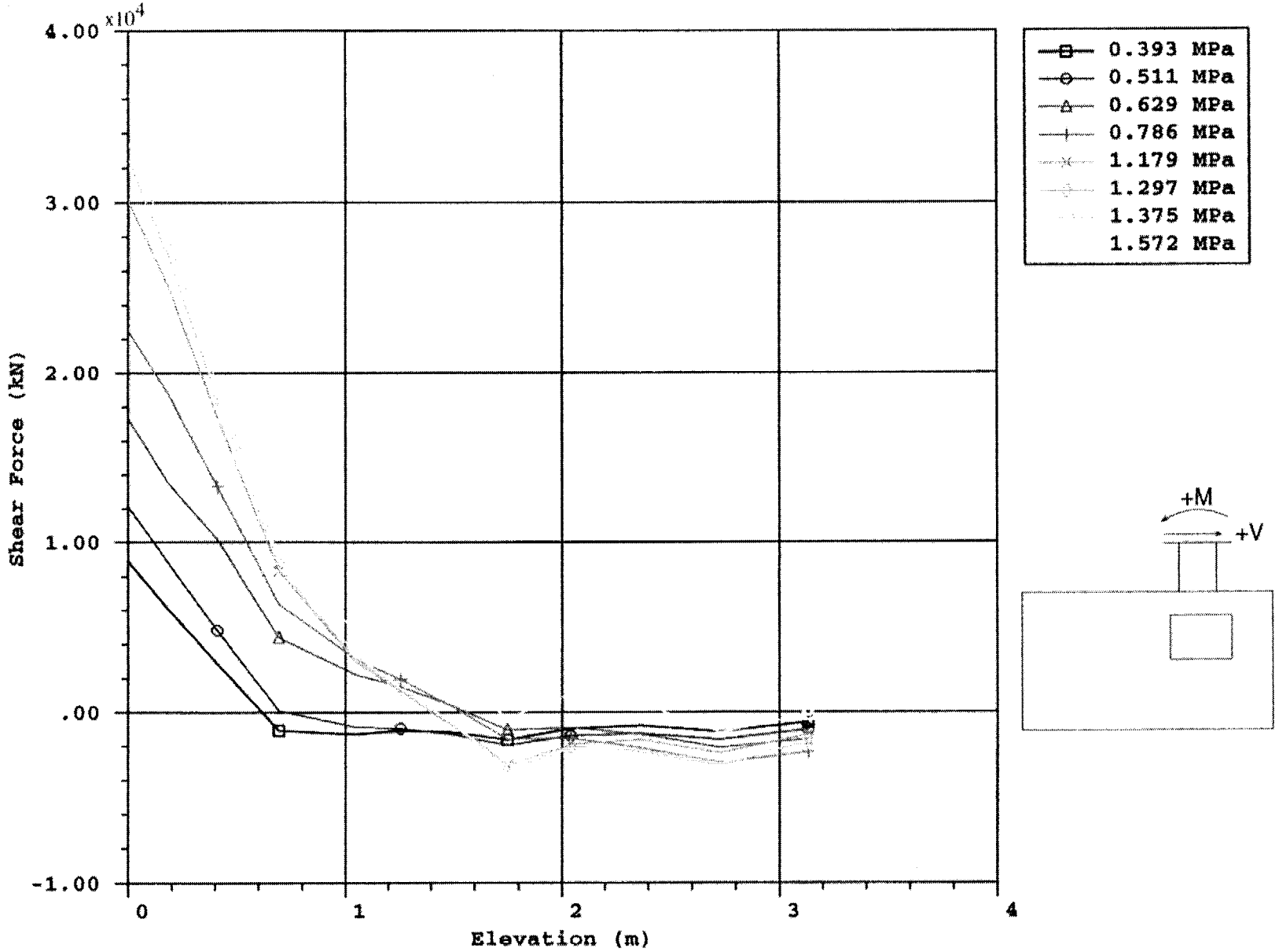


Figure 5-7. Shear Force Profile Along the Wall of the Prestressed Concrete Containment Vessel (PCCV) for Different Pressure Loads

*model14.inp*

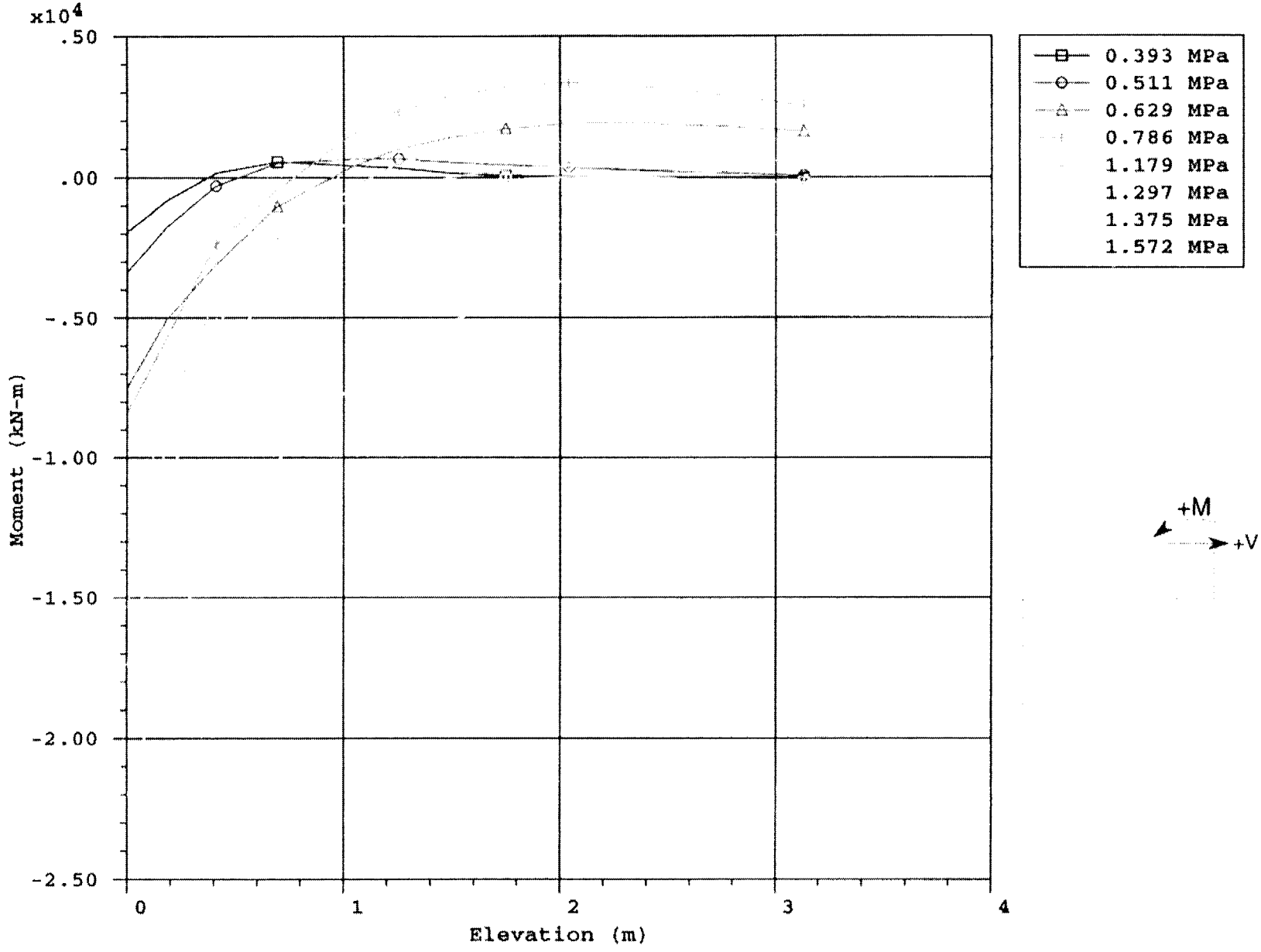


Figure 5-8. Moment Profile Along the Wall of the Prestressed Concrete Containment Vessel (PCCV) for Different Pressure Loads

*model14.inp*

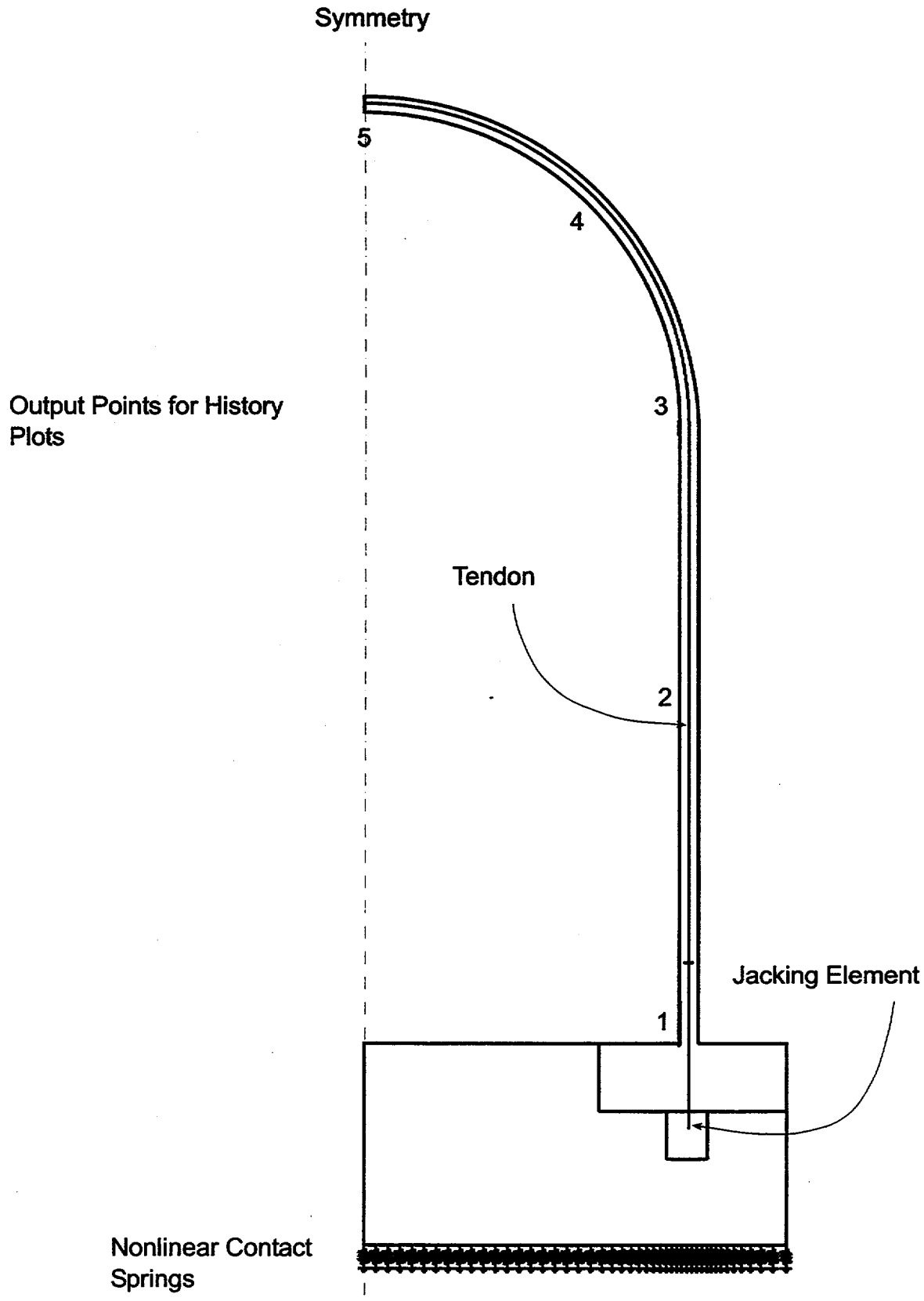


Figure 5-9. Revised Axisymmetric Model with Explicit Tendon Friction Modeling

*model14.inp*

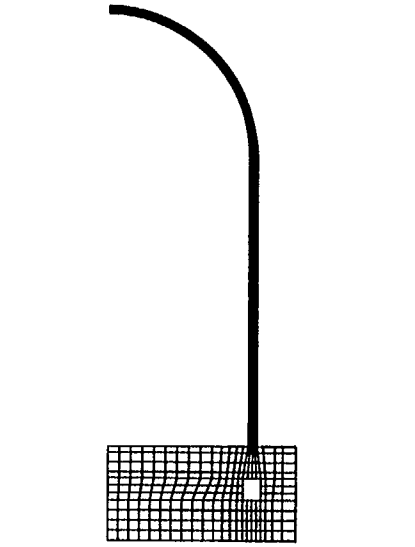

Pressure = 0.393 MPa (1.0 Pd)

Pressure = 0.786 MPa (2.0 Pd)

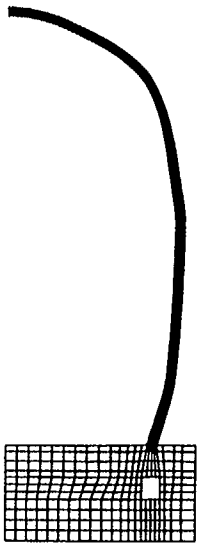

Pressure = 1.179 MPa (3.0 Pd)

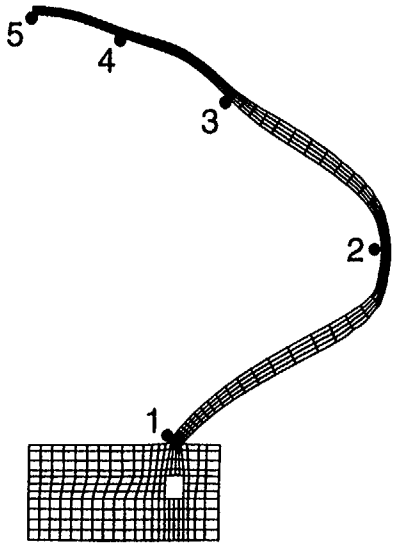


Pressure = 1.572 MPa (4.0 Pd)



*model14.inp*

Figure 5-10. Deformed Shapes, Displacements Magnified by 50

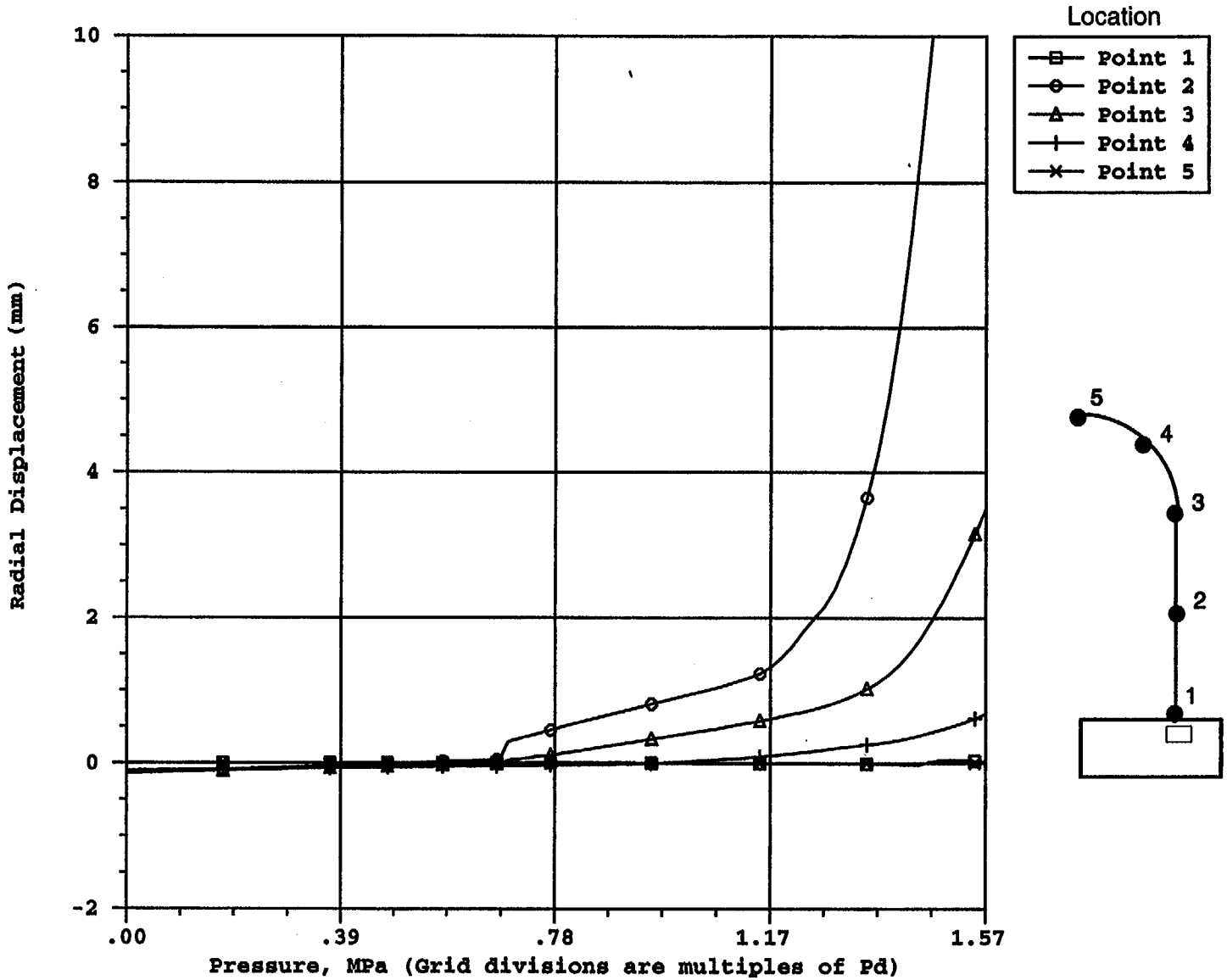


*model14.inp*

Figure 5-11. Axisymmetric Analysis, Radial Displacement as a Function of Pressure

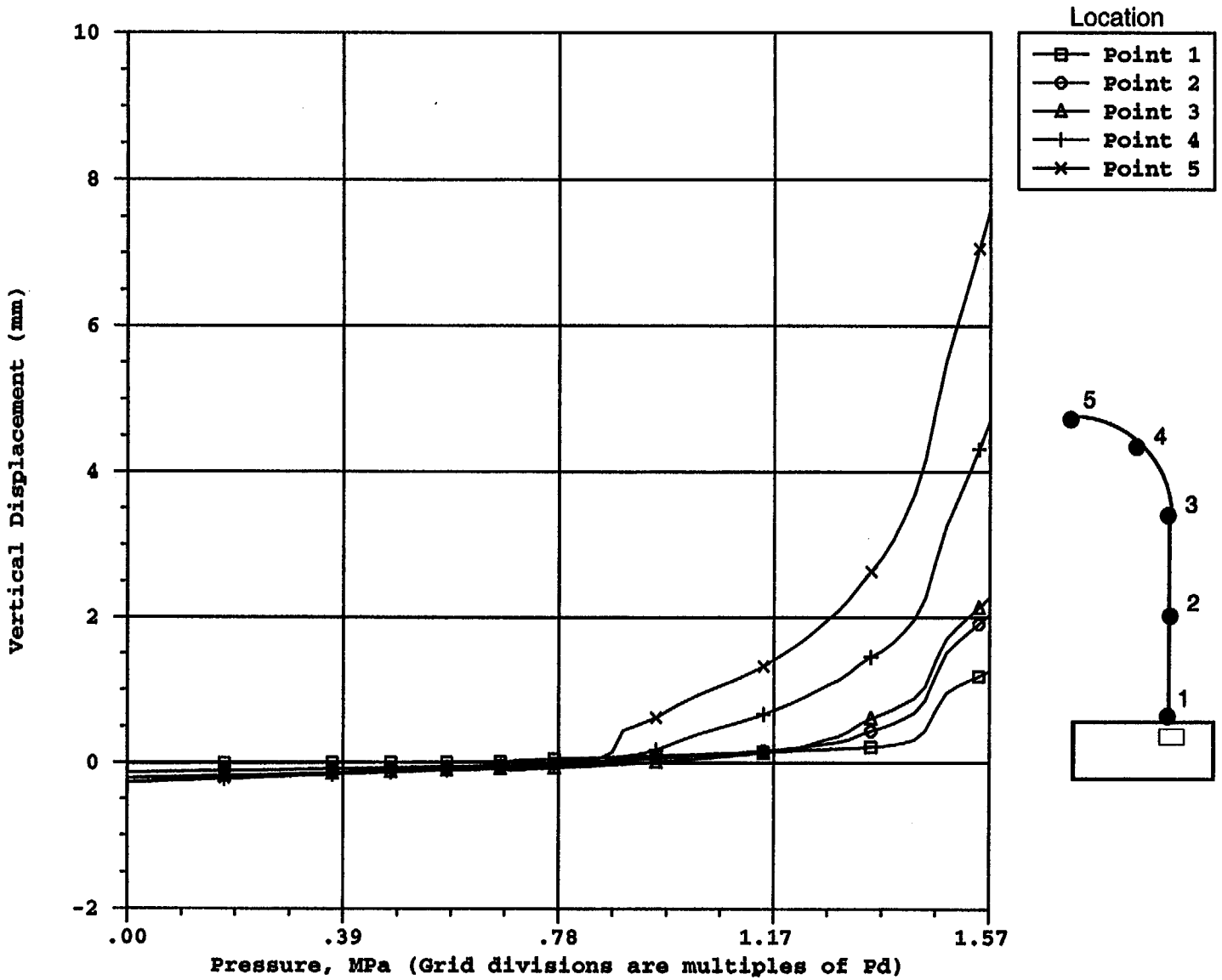


*model14.inp*

Figure 5-12. Axisymmetric Analysis, Vertical Displacement as a Function of Pressure

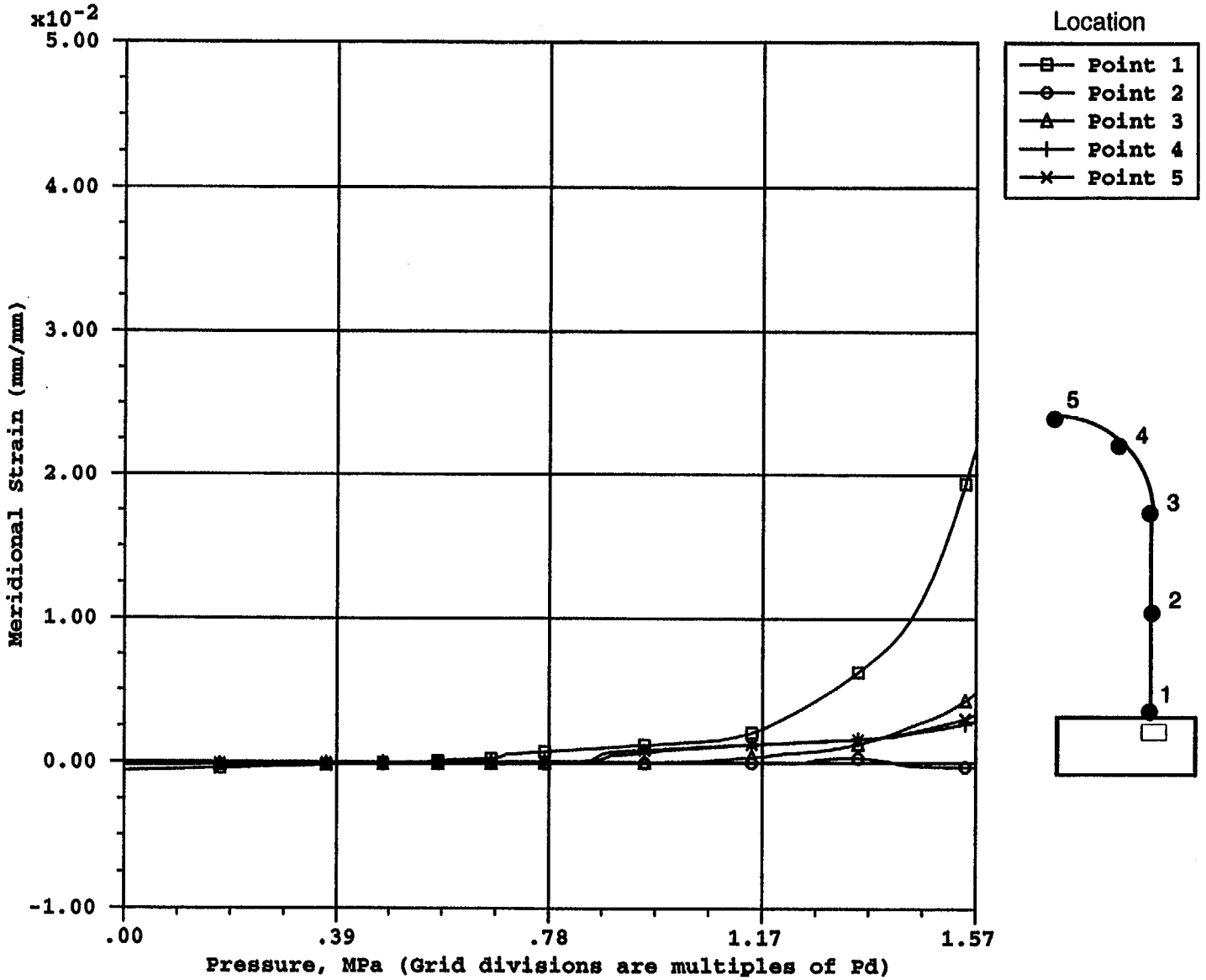


*model14.inp*

Figure 5-13. Axisymmetric Analysis, Meridional Strains in Liner as a Function of Pressure

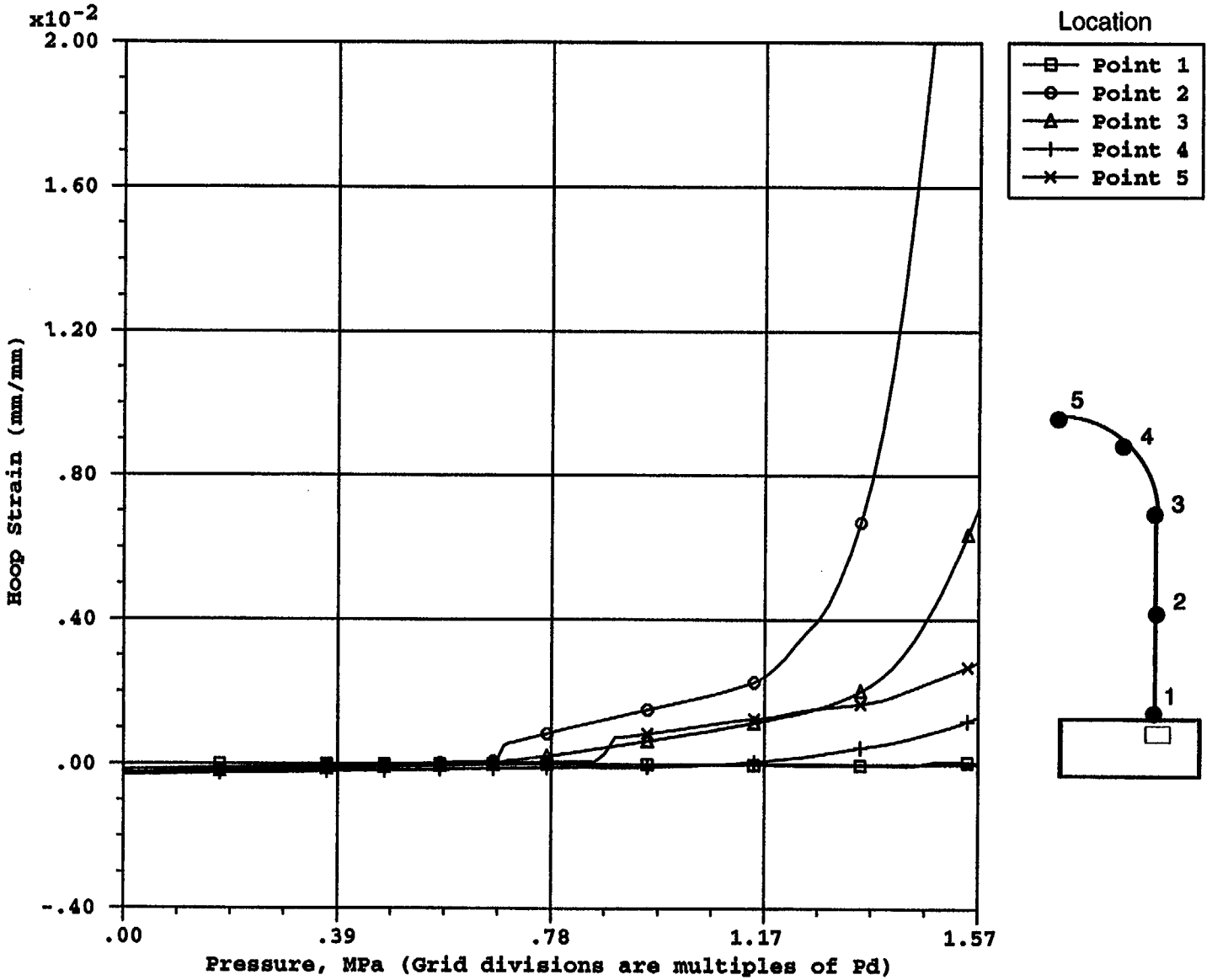


*model14.inp*

Figure 5-14. Axisymmetric Analysis, Hoop Strains in Liner as a Function of Pressure

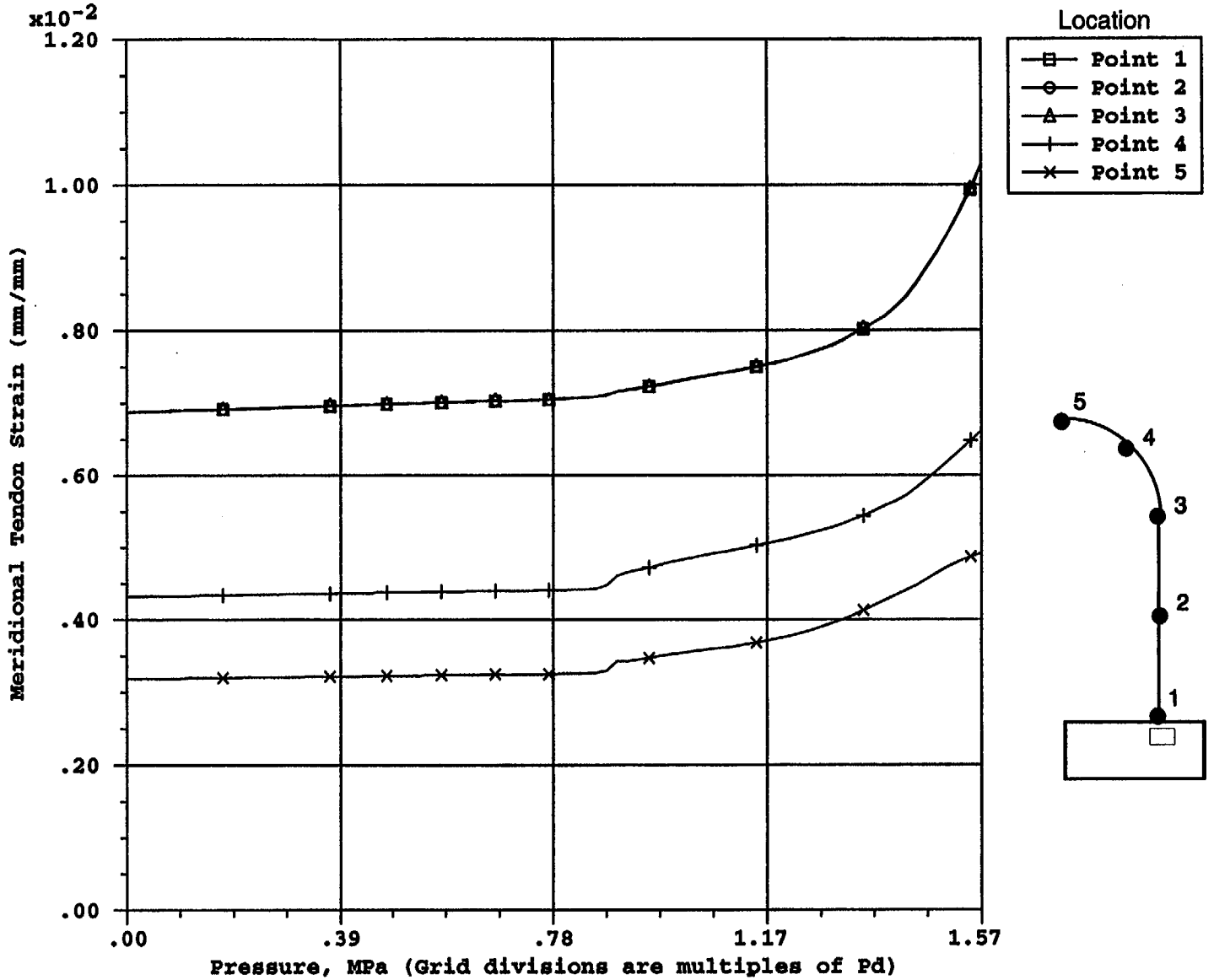


*model14.inp*

Figure 5-15. Axisymmetric Analysis, Meridional Strains as a Function of Pressure

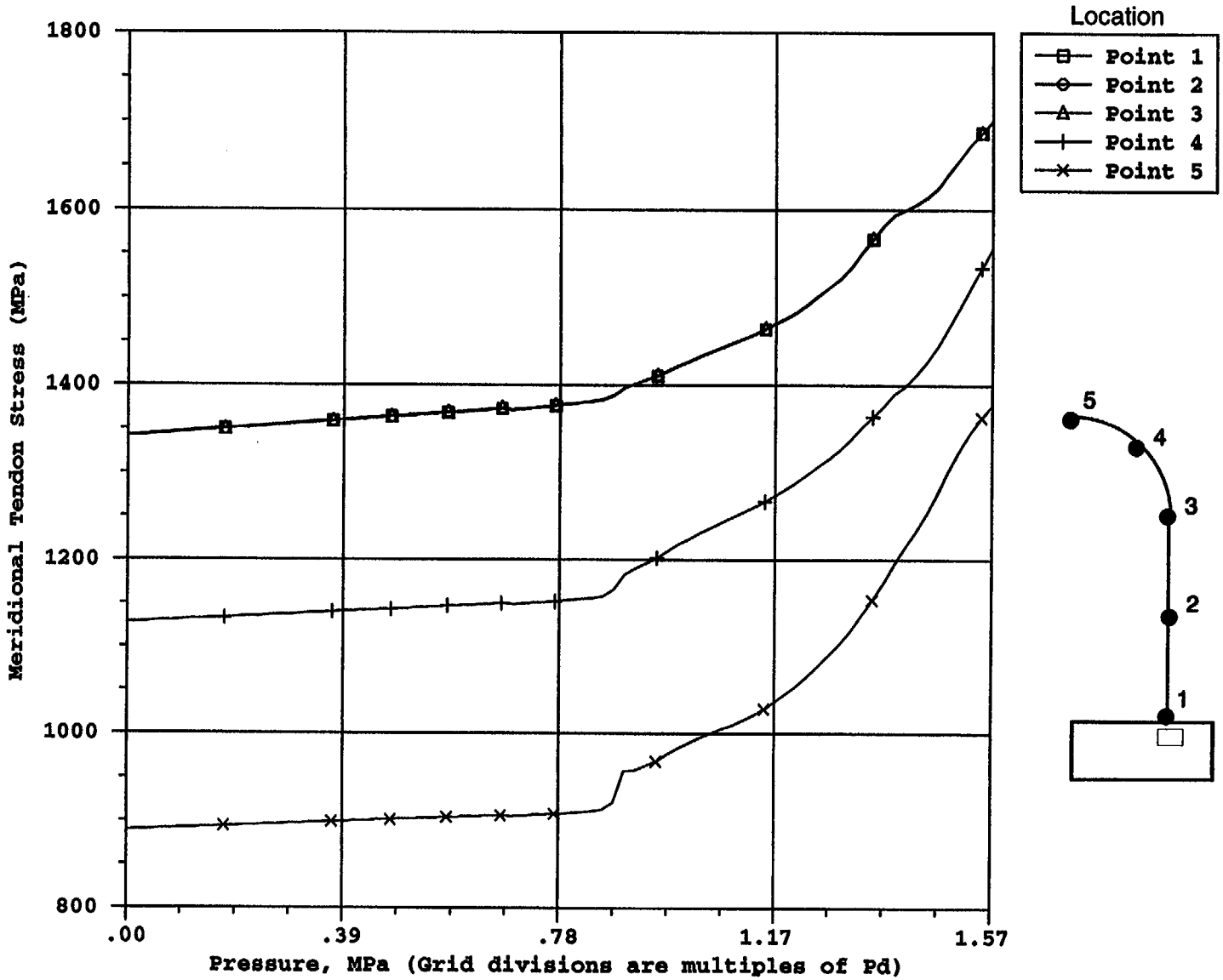


*model14.inp*

Figure 5-16. Axisymmetric Analysis, Meridional Tendon Stresses as a Function of Pressure

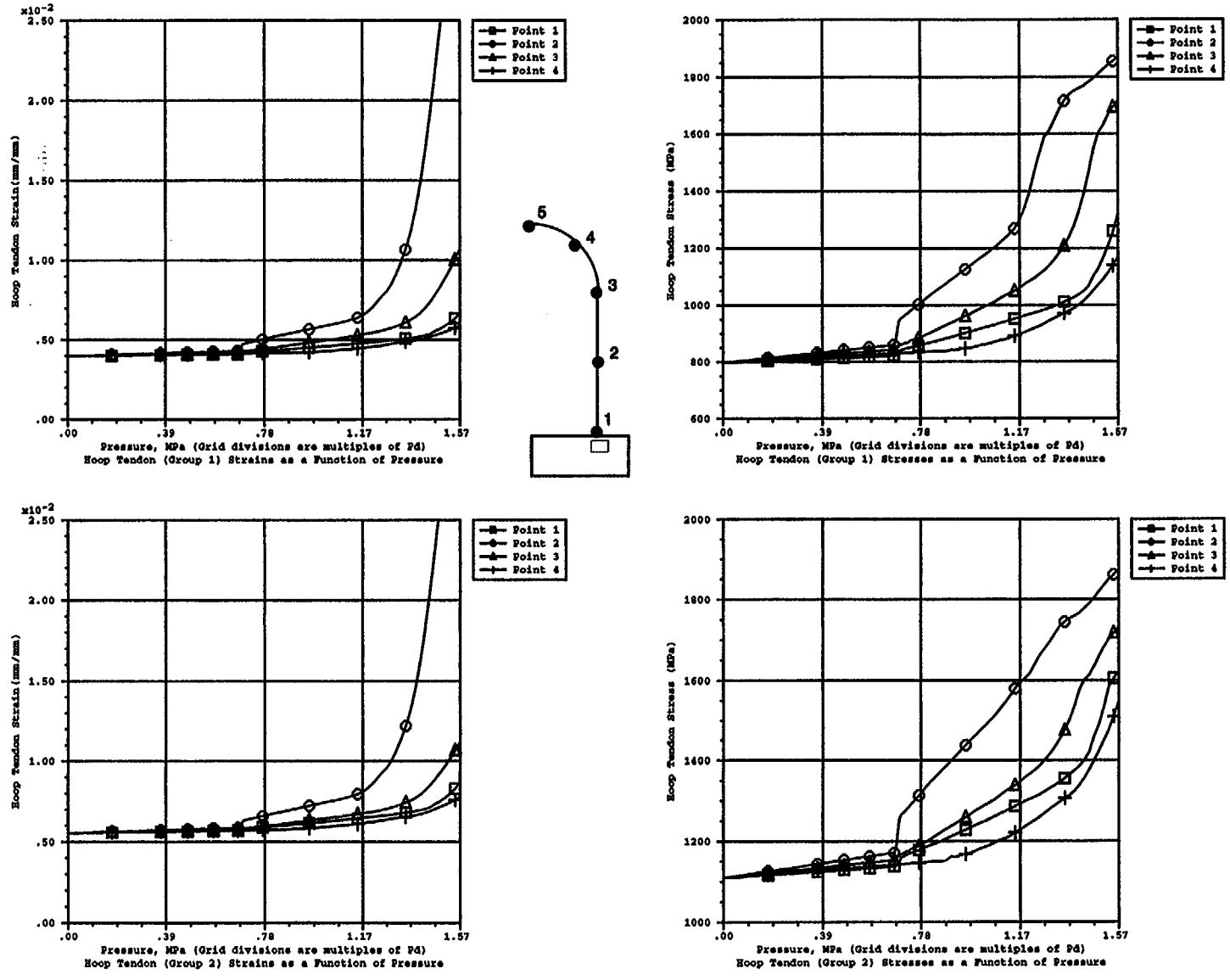


*model14.inp*

Figure 5-17. Axisymmetric Analysis, Hoop Tendon Strain and Stress Histories

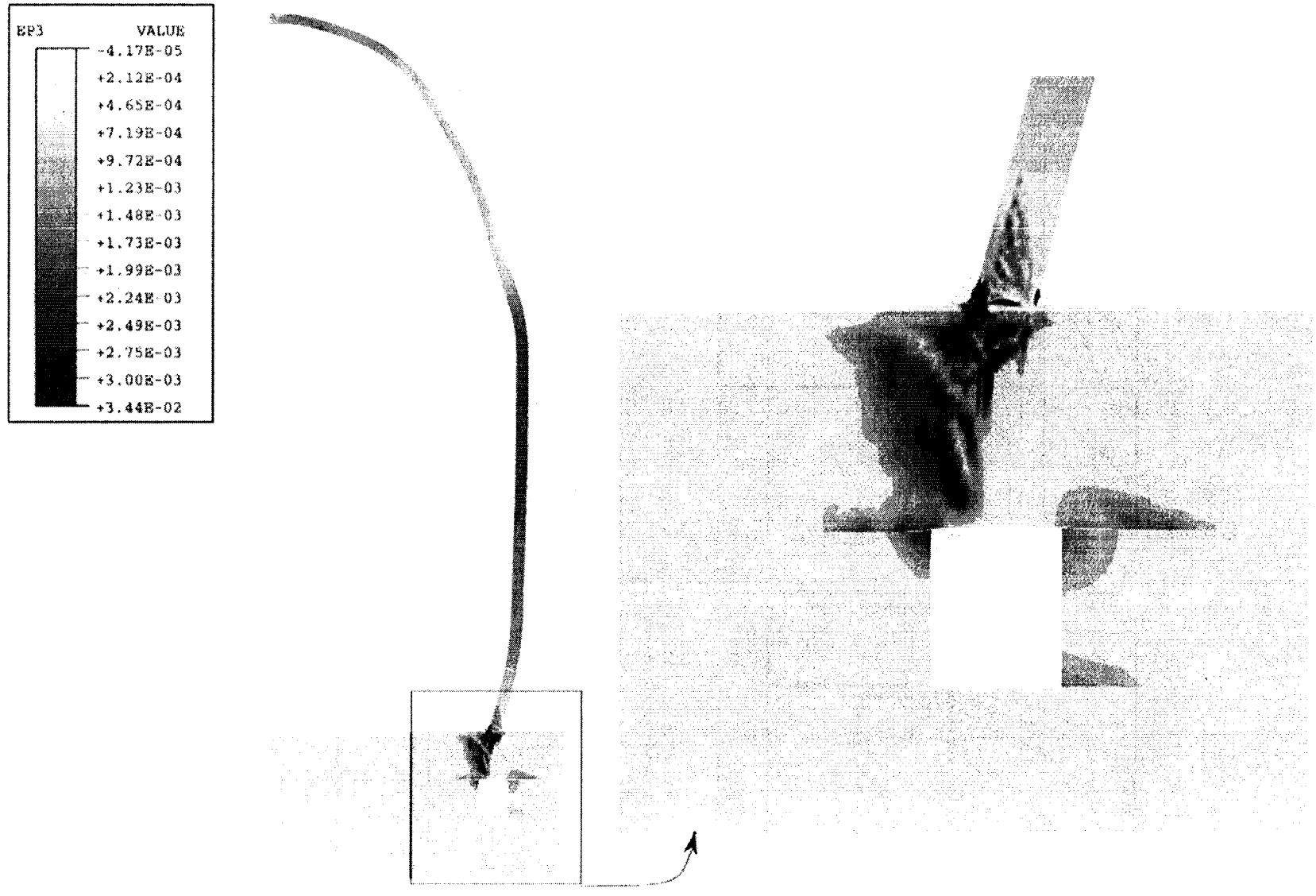


*model14.inp* Figure 5-18. Axisymmetric Model, Maximum Principal Strain Contours (Displacements x 50) at P=3.0 $P_d$

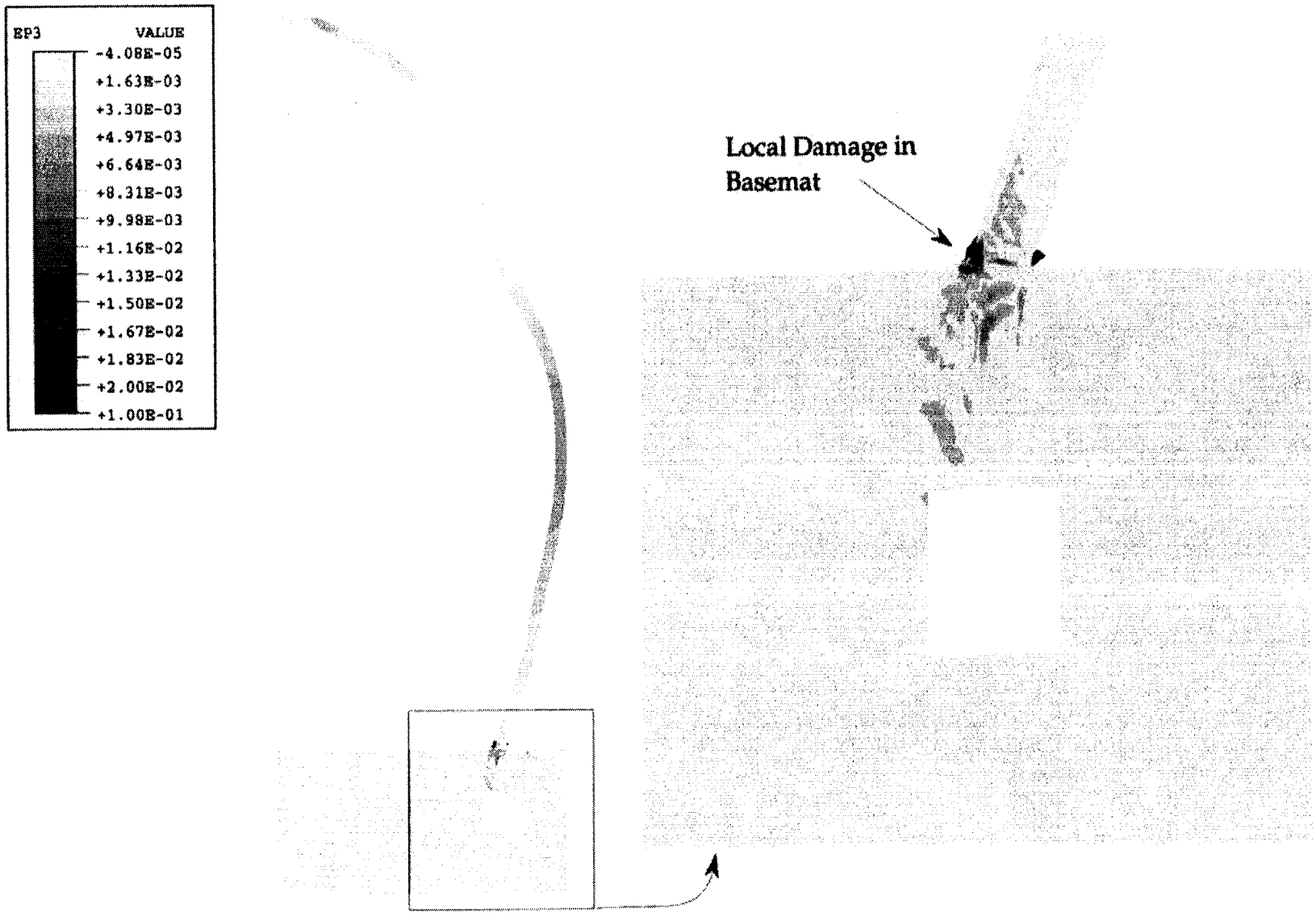


*model14.inp* Figure 5-19. Axisymmetric Model, Maximum Principal Strain Contours (Displacements x 50) at P=3.4 $P_d$

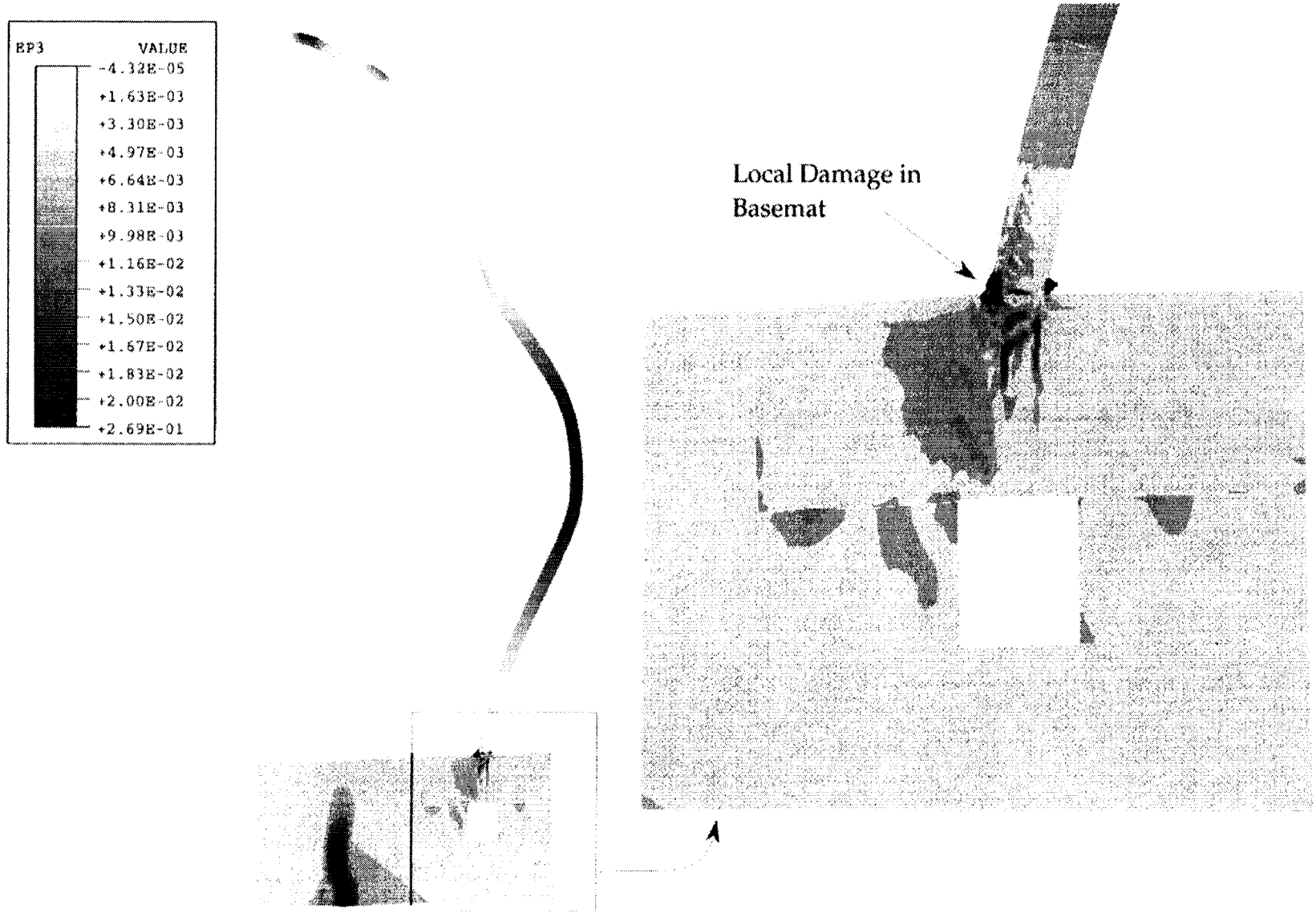


*model14.inp*

Figure 5-20. Axisymmetric Model, Maximum Principal Strain Contours (Displacements x 20) at P=3.8 $P_d$

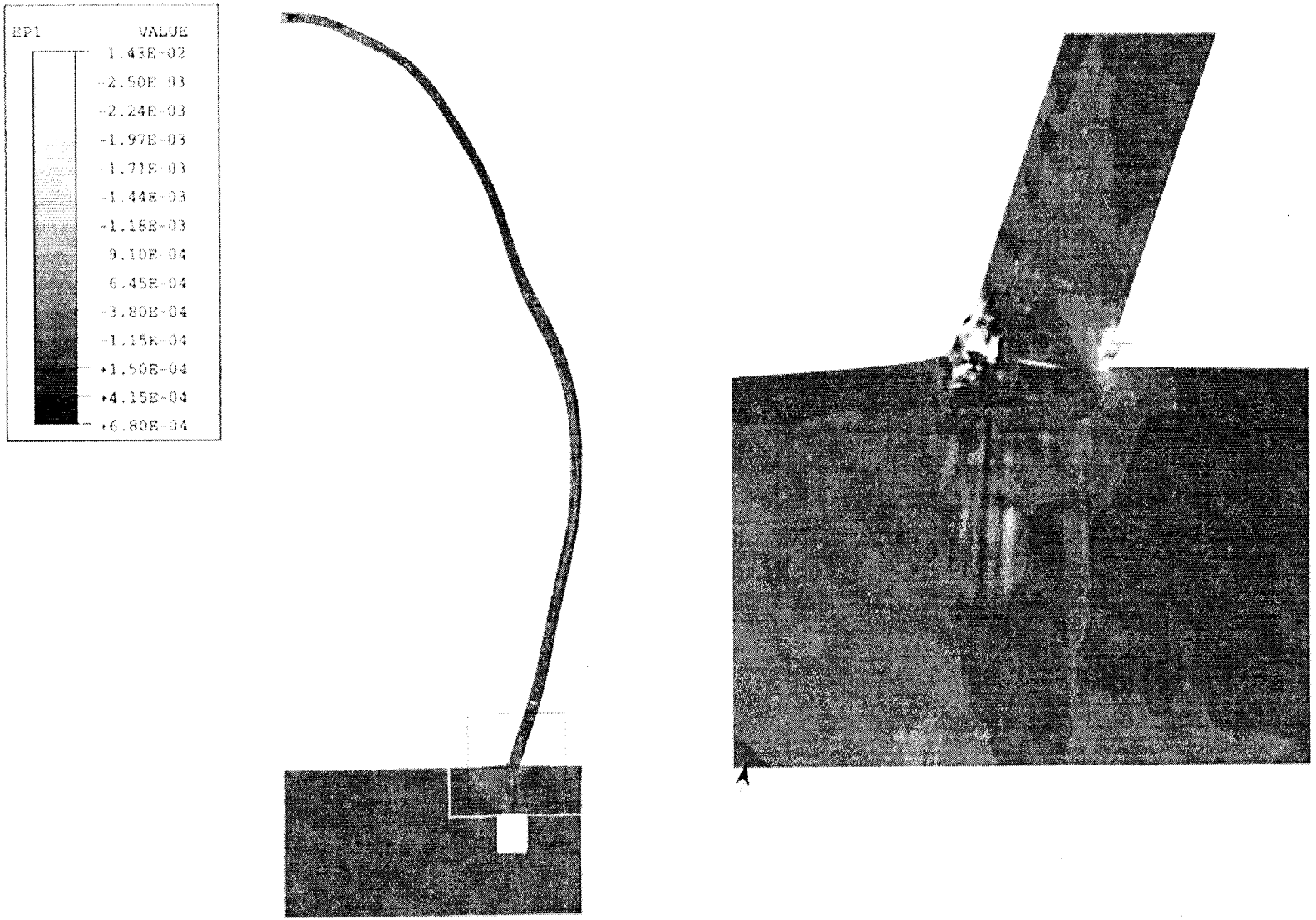


*model14.inp*

Figure 5-21. Axisymmetric Model, Minimum Principal Strain Contours (Displacements x 50) at P=3.4 $P_d$

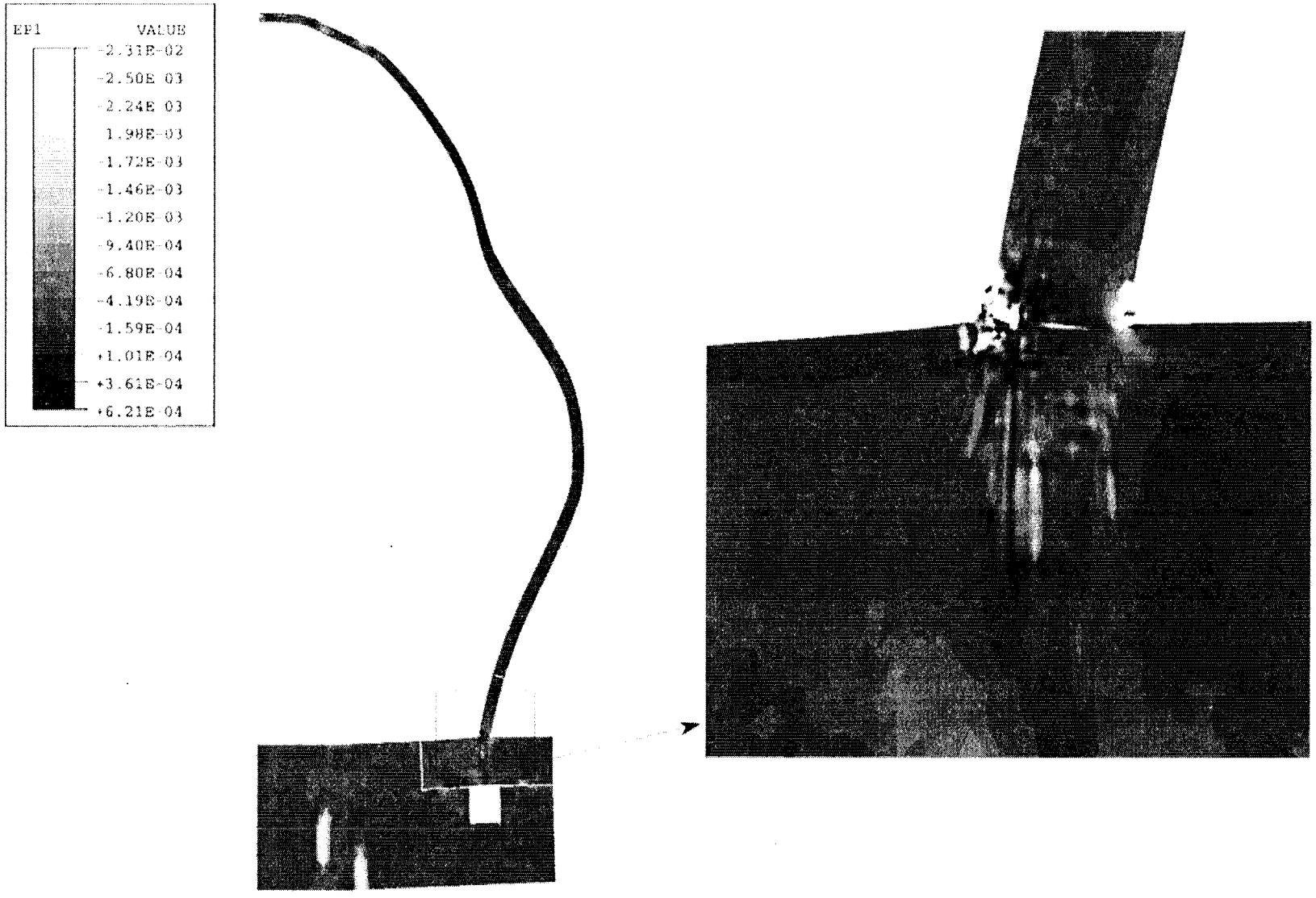


*model14.inp* Figure 5-22. Axisymmetric Model, Minimum Principal Strain Contours (Displacements x 20) at P=3.8 $P_d$

# 6. EVALUATION OF POTENTIAL SHEAR FAILURE

## 6.1 Background on Containment Shear Failure Assessment

Pretest analysis activities described in Chapter 5 have investigated axisymmetric global behavior and have justified the local liner strain concentration close to the wall-basemat juncture. Though liner tearing is emphasized in later chapters, the assumption of a liner-tearing failure mode is largely based on experience with reinforced concrete containments. For the prestressed concrete containment vessel (PCCV) model, the potential for shear failure at or near the liner tearing pressure may be considerable and requires detailed investigation. This chapter examines the behavior of the PCCV model in the region most susceptible to a shear failure, the wall-basemat juncture region.

Discussion of the constitutive modeling aspects of shear behavior and discussion of a shear failure criterion is provided in Chapter 4. This chapter focuses directly on the predicted shear behavior and the evaluation of its failure potential.

### 6.1.1 Potential Shear Failure Locations

Zones of potential shear problems in a concrete structure are generally indicated by cracks, especially cracks inclined to the direction of flexure or primary tension. Figures 6-1 through 6-5 show cracking patterns at pressures of 1.6, 2.0, 3.0, 3.6, and 4.0 times design pressure as predicted by axisymmetric analysis. Definitions of crack orientations are indicated in Figure 6-6. The crack patterns show critical cracking pressure milestones that can be correlated to stiffness changes in the displacement and strain response curves described earlier. The crack symbols occur at each integration point that is cracked, and they show the crack orientation. Lines are drawn in the crack zones to demonstrate the estimation of actual cracks that can be made based on the crack symbols and on the assumption that crack spacing will coincide generally with rebar spacing. Virtually no cracking in the PCCV model is observed until $1.5P_d$. This implies that very little nonlinear behavior or crack "ratcheting" is expected during the preliminary pressure cycles (to the $1.15P_d$ SIT loading). It should be noted that in fact, the model in its unpressurized condition, has been observed to be extensively cracked from routine shrinkage during curing and thermal response. Therefore, a distinct stiffness reduction at $1.5P_d$ is unlikely to be observed. Pretest analyses have not been revised to account for these observations, however. For the cracking that is predicted analytically, radial cracking (due to hoop stress) occurs first in the cylinder and later extends into the dome. Circumferential cracking also occurs, especially at the wall-basemat juncture, but these cracks are plotted as lines at the finite element integration points.

The shear behavior in the PCCV model is highly complex because of the combined effects of internal pressure. The deformation scenario predicted by global analysis for the PCCV model (assuming no leakage up to the point of catastrophic shear failure) follows:

(1) radial cracks from hoop stress will develop first, beginning at some distance up from the basemat;

(2) this development will be followed by circumferential cracks caused by flexure, which start at the pressure side of the wall-basemat juncture.

Significant shear stresses will develop at the wall-basemat juncture. The hatch embossments, the springline, and the buttress/wall junctures are other candidate locations for radial shear stresses to develop. The relative likelihood of shear failure at these candidate locations is discussed below.

The hatch embossment acts as an inclusion with two deformation modes that could affect failure in that region. Local deformations from the discontinuity around the embossed area and a global radial motion that may be different from the wall, cause a discontinuity in the deformation profile. Any possible shear failure there would be a "champagne cork" failure which can occur only if the cracks around the embossed area open sufficiently wide to cause total loss of aggregate interlock. This would require very large deformations and, therefore, is considered the least likely shear failure mode among the four shear locations. A 3D penetration model was studied later in the pretest analysis program (Chapter 7).

The second candidate for a shear failure is the separation of the buttress from the wall. The buttress acts as a beam anchored to the basemat with a softer support at the springline. The differential radial displacement between the buttress and the wall will have to be resisted by the shear in the crack planes. Again, unless the crack opening displacements are sufficiently large to defeat the aggregate interlock, shear failure will not occur. Furthermore, the buttress discontinuity is not

very significant and it will deform enough to defuse any shear failure. This failure mode was also considered unlikely after it was investigated in a subtask on tendon behavior in the Preliminary Analysis Phase of the work.

The springline is the next candidate for shear failure. The stiffness of the dome could exert sufficient constraints on the wall to cause the wall to bend severely and separate azimuthally from the dome. Based on results of the global axisymmetric analyses, the shear and bending that develop at the springline are well below design shear failure thresholds.

The fourth and strongest candidate for shear failure is the wall-basemat juncture. Here the basemat discontinuity completely restrains the wall. Circumferential cracks in the wall either at the corner or a few centimeters up, would form under the combined effect of bending and tension. This crack could extend either across the wall or extend into the basemat as illustrated in Figure 6-7. In the first case, the crack will run into the compressive zone at the outer surface. In the second case the crack will run into the basemat in an area of smaller compression. In both cases enough flexural deformation and shear stress exist to warrant further investigation of shear failure potential.

In the Preliminary Analysis Phase (Dameron et al. 1998) a wall-basemat shear modeling study was conducted as follows:

1. A refined mesh in the wall-basemat region was developed based on the axisymmetric global model of the Preliminary Analysis Phase.

2. The strain field and failure potential near the wall-basemat was evaluated with different constitutive modeling approaches to modeling shear:

   - with the "standard" shear retention concrete model;

   - with a more recently developed concrete model that addresses "shear shedding."

3. Differences in failure mode at this location versus other locations were considered:

   - shear failure of the concrete section increases the local liner strain and causes a small tear and leakage;

   - a brief occurrence of crack pressurization causes a failure here to be more energetic.

4. A brief mesh-size sensitivity was conducted.

### 6.1.2 Effects of Crack Pressurization

In the Preliminary Analysis Phase, crack pressurization was an additional consideration where a crack exists, but a leak path through the containment wall may not exist. In this event, it was postulated that crack pressurization could cause a rapid structural failure that could lead to a rupture that is much larger than that observed in other concrete test models. The influence of crack pressurization on failure potential is estimated as follows. The total blowdown load is $\frac{\pi D t}{2} P x \frac{1}{2}$, where D is the diameter, t is the wall-thickness, P is the pressure and the factor $\frac{1}{2}$ assumes a triangular distribution of pressure in the crack if the crack is open at the outer end. If this failure mode precedes liner failure, P can be assumed to be equal to or less than the failure pressure associated with liner tearing (approximately 1.5 MPa); then the blowdown load is calculated to be 3,400 kN. This must be resisted by the vertical steel. The resulting blowdown stress in the vertical steel is about 21 MPa for an open crack, or 42 MPa for a crack with one end closed. The effect of the additional stress was thought to become significant if the stress in the prestressing steel is already on the plateau of the stress-strain curve. For full crack pressurization to occur, however, the liner has to fail first, and the crack must be closed at the outer edge of the wall (which may be the case, due to bending induced compression). The transient pressure in the crack is assumed to be instantaneously established. More realistic assumptions about the pressure distribution in the crack could reduce the stress in the steel. Even with that, however, the calculated stress warranted an investigation of this mode.

### 6.1.3 Conclusions of Wall-Basemat Shear Parameter Study

Plotted results of the wall-basemat shear study are not included in this report because there was little discernable difference between the failure behavior of the standard and "shear-shedding" concrete models in the PCCV wall-basemat analyses. Secondly, the parameter studies did not show any acceleration of failure from crack pressurization. To address questions of mesh-size sensitivity, preliminary analyses used a local axisymmetric model with different element mesh-sizes in the wall-basemat region. The mesh-size study showed little difference in the computed response of the wall or in the liner strains. Some noticeable differences in the crushing strains at the outer wall surface were ob-

served, so the grid with additional refinement was incorporated into the final global axisymmetric model. The final global axisymmetric model with 12 elements through the wall thickness in the region near the basemat was used to examine the potential shear failure mode near the bottom of the wall.

## 6.2 Discussion of Analysis Results at the Wall-Basemat Juncture

### 6.2.1 Summary of Preliminary Wall-Basemat Juncture Liner Analysis

In the Preliminary Analysis Phase, a detailed liner-only model of the wall-basemat mat juncture region was developed and analyzed. The model was loaded with displacement boundary conditions at key points of contact with the concrete, as obtained from a preliminary axisymmetric analysis. Figures 6-8a and 6-8b show the model and a strain contour of this wall-basemat juncture liner-only model at $4.0 \times P_d$. The principal strains are found to be predominately vertical strains. High strain concentrations were found at two locations:

(1) at the intersection of the interior ring, backing ring, and wall liner; and

(2) at the intersection of the backing ring, web of the T-anchor, and flange of the T-anchor.

The second location is not critical because failure here will probably not depressurize the containment. The magnitude of the peak strain was only 5.9%. This is still well below the strain to exceed the failure criteria.

While this preliminary local liner analysis was limited by not modeling the concrete, the conclusions are thought to be reasonable based on the judgment that the liner deformation state was reasonably simulated. In the actual structure a large crack is predicted to form at the juncture re-entrant corner as sketched in Figure 6-7. This crack will allow the bottom edge of the vertical liner anchor to rotate with the wall concrete while the "I" shape that the vertical liner is anchored to 25 mm below the juncture will essentially move with the basemat.

### 6.2.2 Results with Final Detailed Model

This subsection continues the discussion introduced in Chapter 5 from the analysis to $4.0 \times P_d$ using the shear-shedding ANACAP material model for the concrete.

Figures 6-9 and 6-10 show maximum principal strain contours for the concrete and the liner in the vicinity of the wall-basemat mat juncture. According to the concrete strain plots, by $3.4P_d$, some spalling of the outer concrete wall is predicted. Two liner "hot spots" occur: one just above the Elev. 0.0 juncture and one below, between the juncture and the I-shaped embedment anchor. The strain contours show a local zone of cracking and damage near the juncture (near the I-shaped embedment) and a zone of elevated shear strains along a 45° line through the base of the wall.

## 6.3 Comparison of Shear Damage Predictions to Failure Criteria

Explicit shear failure prediction is associated with large shear distortions of the entire wall-basemat section and large strains in the reinforcement crossing the shear plane. Shear failure of the wall section was not predicted to occur, based on the strains presented in this chapter.

In order to further quantify the shear conditions in the wall-basemat mat juncture region a comparison to the modified compression field theory (Collins and Mitchell 1997) was conducted. First, Figures 6-11 and 6-12 plot shear force and moment versus elevation for selected pressures.

On the capacity side of the comparison, the modified compression field theory evaluation proceeds as follows. The hand analysis presented below is conducted for a two-degree portion of the PCCV model at a given principal tensile strain. For consistency with the methods and equations published in Collins and Mitchell (1997), English units are used.

Step 1: Choose Principal Tensile Strain

The principal tensile strain in the present example is chosen as 0.0136.

Step 2: Estimate Diagonal Shear Crack Angle $\theta$ (to be verified later)

An angle $\theta$ of 30 degrees is assumed.

Step 3: Calculate Crack Width

The crack width is a function of the principal tensile strain and crack spacing. Crack spacing in the diagonal direction ($s_{m\theta}$) can be estimated by the expected crack spacing in the longitudinal and vertical directions (with only direct tension acting) as

$$s_{m\theta} = \left( \frac{1}{\frac{\sin\theta}{s_{mx}} + \frac{\cos\theta}{s_{mv}}} \right) \qquad (6\text{-}1)$$

where $s_{mx}$ and $s_{mv}$ are the crack spacing in the longitudinal and vertical directions. With crack spacings of 4 in. and 16 in. the diagonal crack spacing is found to be 5.58 in. The crack width is determined by multiplying the principal tensile strain of 0.0136 by the spacing of 5.58 in., resulting in a crack width of 0.0759 in.

Step 4: Estimate the Stress in the Shear Reinforcement (to be verified later)

Assume that the shear reinforcement has yielded, $f_v = f_{vy}$ (70.9 ksi).

Step 5: Calculate the Average Tensile Stress $f_1$

Above the cracking strain the tensile stress is taken as the lesser of

$$f_1 = \frac{\alpha_1 \alpha_2 f_{cr}}{1 + \sqrt{500\varepsilon_1}} \qquad (6\text{-}2)$$

and

$$f_1 = v_{ci} \tan\theta + \frac{A_v}{sb_w}\left(f_{vy} - f_v\right) \qquad (6\text{-}3)$$

where

$$v_{ci} = \frac{2.16\sqrt{f_c'}}{0.3 + \frac{24w}{a + 0.63}} \quad \text{in psi and in.} \qquad (6\text{-}4)$$

Because the bars are deformed, $\alpha_1$ and $\alpha_2$ are both 1.0. With a cracking stress of 657 psi ($7.5\sqrt{f_c'}$) the first value results in 174 psi. For the second expression, the local shear stresses along the crack, $v_{ci}$, produce 112 psi, resulting in $f_1$ of 64.5 psi (note that because it was assumed previously that $f_v = f_{vy}$ the second term of the expression dropped out). The lesser of the above expressions is the tensile stress of 64.5 psi.

Step 6: Determine the Shear Force V

The shear force corresponding to a principal tensile strain of 0.0136 is found from the following expression:

$$V = f_1 b_w jd\cot\theta + \frac{A_s f_v}{s} jd\cot\theta = \frac{64.5}{1000}(8.05)(10.24)(1.732) + \frac{(0.24)}{(4.44)}(70.9)(10.24)(1.732) = 77.2k \qquad (6\text{-}5)$$

Step 7: Determine the Principal Compressive Stress

The principal compressive stress is found from

$$f_2 = (\tan\theta + \cot\theta)v - f_1 \qquad (6\text{-}6)$$

where v is the average shear stress found as

$$v = \frac{V}{b_w jd} = \frac{77.2}{(8.05)(10.24)} = 0.936 \text{ ksi (936psi)} \qquad (6\text{-}7)$$

Thus, the principal compressive stress is 1987 psi.

Step 8: Determine the Maximum Allowable Compressive Stress $f_{2max}$

The compressive stress capacity is reduced as a function of the transverse tensile strains, resulting in a maximum allowable compressive stress of

$$f_{2\max} = f_c'\left(\frac{1}{0.8 + 170\varepsilon_1}\right) = 2250 \text{ psi.} \qquad (6\text{-}8)$$

Step 9: Verify that Compressive Stress Is Less than Maximum Allowable

Because $f_2$ is less than $f_{2max}$ (1987 psi < 2250 psi) this step is satisfied. If this were not satisfied, a smaller principal tensile strain would be selected, and a new analysis conducted.

Step 10: Determine the Principal Compressive Strain

The principal compressive strain is found from

$$\varepsilon_2 = \varepsilon_c'\left(1 - \sqrt{1 - \frac{f_2}{f_{2\max}}}\right) = -0.00132 \quad (\varepsilon_c' = -0.002) \qquad (6\text{-}9)$$

Step 11: Find the Longitudinal and Transverse Strains

The longitudinal and transverse strains are found as

$$\varepsilon_x = \frac{\varepsilon_1 \tan^2\theta + \varepsilon_2}{1 + \tan^2\theta} = 0.00241 \qquad (6\text{-}10)$$

$$\varepsilon_t = \frac{\varepsilon_1 + \varepsilon_2 \tan^2\theta}{1+\tan^2\theta} = 0.00987 \qquad (6\text{-}11)$$

Step 12: Compute the Stress in the Transverse Reinforcement

The stress in the shear reinforcement is calculated to be

$$f_v = E_s\varepsilon_t = (29000)(0.009987) = 286 \text{ ksi.}$$

Therefore, $f_v = f_{vy}$.

Step 13: Check Assumed Stress in Transverse Steel

Assumed stress was the yield stress which was verified in Step 12 above, therefore O.K.

Step 14: Check Assumed Longitudinal Steel Stress

Because the longitudinal strain multiplied by $E_s$ is greater than the longitudinal reinforcement yield stress, the assumed stress of yield is correct. The stress in the prestressing steel is equal to E multiplied by the sum of the initial strain plus the longitudinal strain, or 223 ksi.

Step 15: Check the Axial Load

This step verifies that the analysis adds up to the applied section axial load. The axial load is computed as

$$N = A_{sx}f_{sx} + A_{ps}f_p - \frac{V}{\tan\theta} + f_1 b_w jd \qquad (6\text{-}12)$$

$$N = (3)\,(68.6) + (.504)\,(54.7) + (.686)\,(223)$$

$$-77.2/\tan 30 + (64.5)\,(8.05)\,(10.24)\,/1000 = 258 \text{kips}$$

This is close to the modified section axial load of 232 kips (an equivalent axial load which has the same tensile strain at mid-depth as found from the combined flexure and tension, as suggested in Collins and Mitchell [1997]), indicating that the assumed crack angle of 30° is slightly off. At this point an iteration to the above process may be conducted by changing the assumed crack angle in Step 2 and checking the modified section axial load, until the desired convergence is reached. In a computer analysis of the section the shear capacity and diagonal crack angle, at this principal tensile strain, were found to be 78.3 kips and 29.9° compared to 77.2 kips and 30° found by hand above. For the full 360° PCCV, these results are multiplied by 360/2, with shear capacities of 13,896 kips ($6.18^4$ kN) and 14,094 kips ($6.27^4$ kN) for the hand and computer analyses, respectively.

The process described above is conducted at increasing principal tensile strains, with a constant axial load (modified to account for the flexure at the section) until the ultimate shear capacity is found. For each pressure step shown in Figures 6-11 and 6-12, the tension load is found and the corresponding moment is determined from Figure 6-12 at the point of maximum shear demand just above the base of the wall (see Figure 6-11). Results of these analyses are presented in Figures 6-13 and 6-14 which show the compression strut angle and shear capacity under the increasing pressure loads (the example presented above is for the PCCV pressure load of 1.179 MPa with the shear capacity of $6.27^4$ kN from Figure 6-13. These graphs show the shear and crack angle at ultimate as well as at the final load step. A comparison between the ultimate shear capacity from the modified compression field theory and demand from the global model presented in Figure 6-15, indicates that the PCCV has reserved shear strength within the pressure loads applied.

## 6.4 Conclusions

Later chapters will show that a liner tear near a penetration has a high probability of occurring between $3.0P_d$ and $3.3P_d$. Based on this and the results in this section, a liner tear at the wall-basemat juncture can be postulated, but it is judged to have a very low probability of occurrence. By postulating it to occur, however, the current study examined the effects of crack pressurization over the loading range $3.5P_d$ to $4.0P_d$. The study concluded that crack-pressurization effects are very localized and so do not lead to a large strain increment in the tendons. No catastrophic rupture was predicted attributable to crack pressurization.

All sensitivity analyses performed herein showed extensive spalling on the outer, lower edge of the containment wall and extensive cracking associated with shear and flexure. The analysis did not predict a shear failure at less than $4.0P_d$, but the model does predict large flexure and shear deformations in the inner half of the wall and local strains of up to 3% across part of the section. A general decrease in total shear force at a section cut through the wall-basemat was observed at pressures larger than $2.5P_d$. This shows that the concrete becomes heavily damaged at this pressure and that the concrete contribution to the total shear is rapidly declining beyond the $2.5P_d$ pressure. The shear reinforcement is still predicted to have reserve capacity, so a liner tear at a penetration is still judged to precede a structural shear failure or liner tear at the wall-basemat.

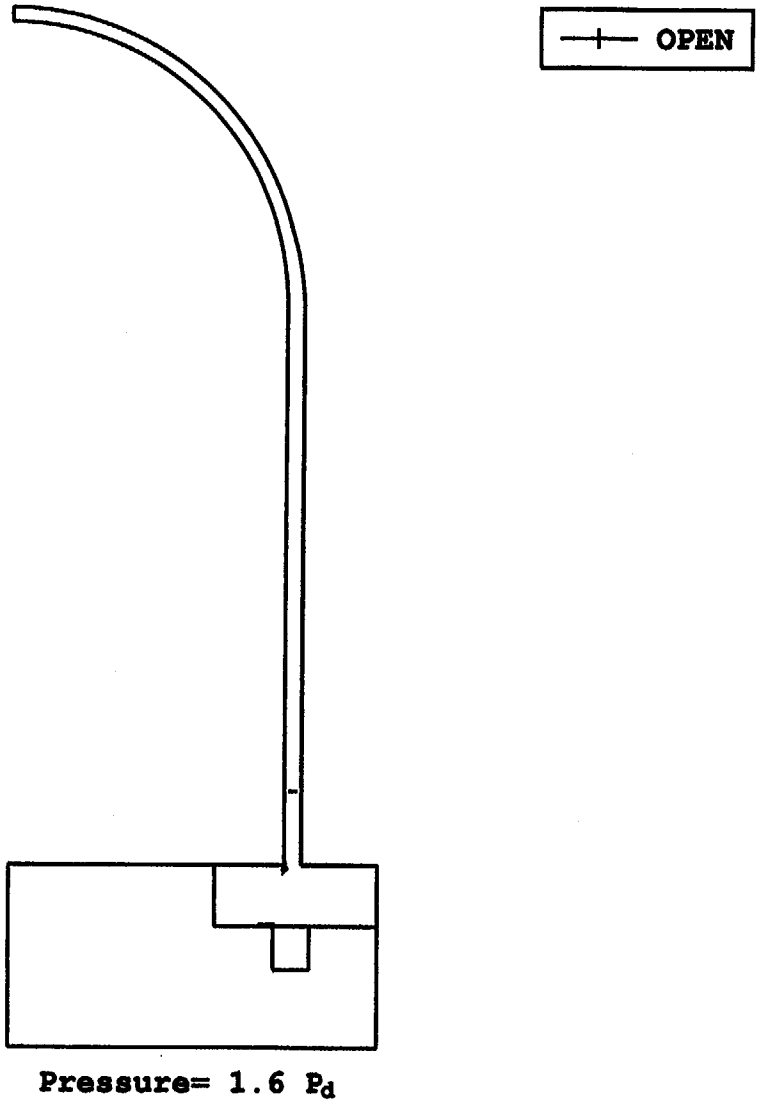


*model14.inp*

Figure 6-1a. Crack Patterns of Axisymmetric Model at 1.6 x $P_d$ Pressure

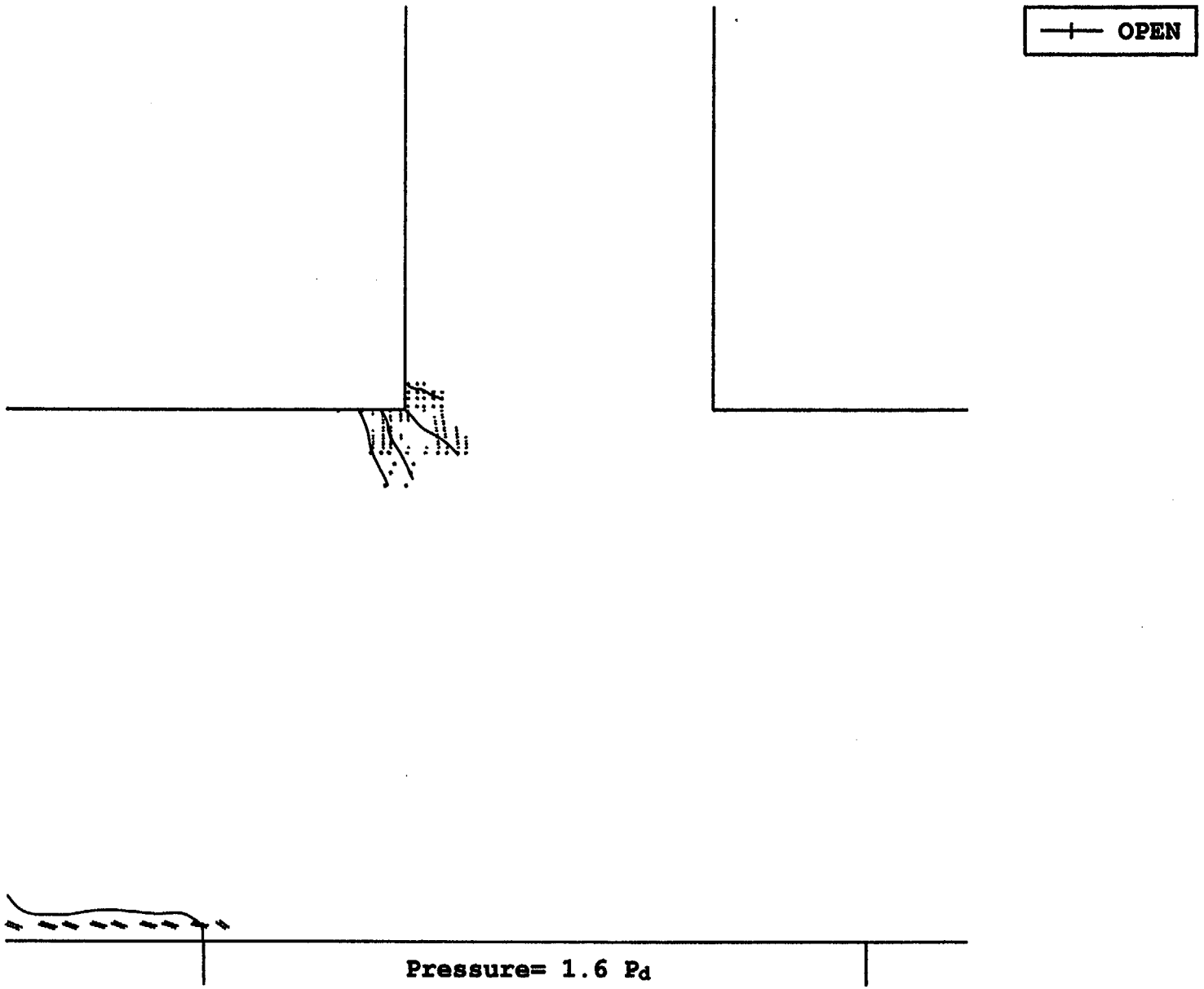


Figure 6-1b. Crack Patterns of Axisymmetric Model at 1.6 x $P_d$ Pressure-Enlarged View



*model14.inp*

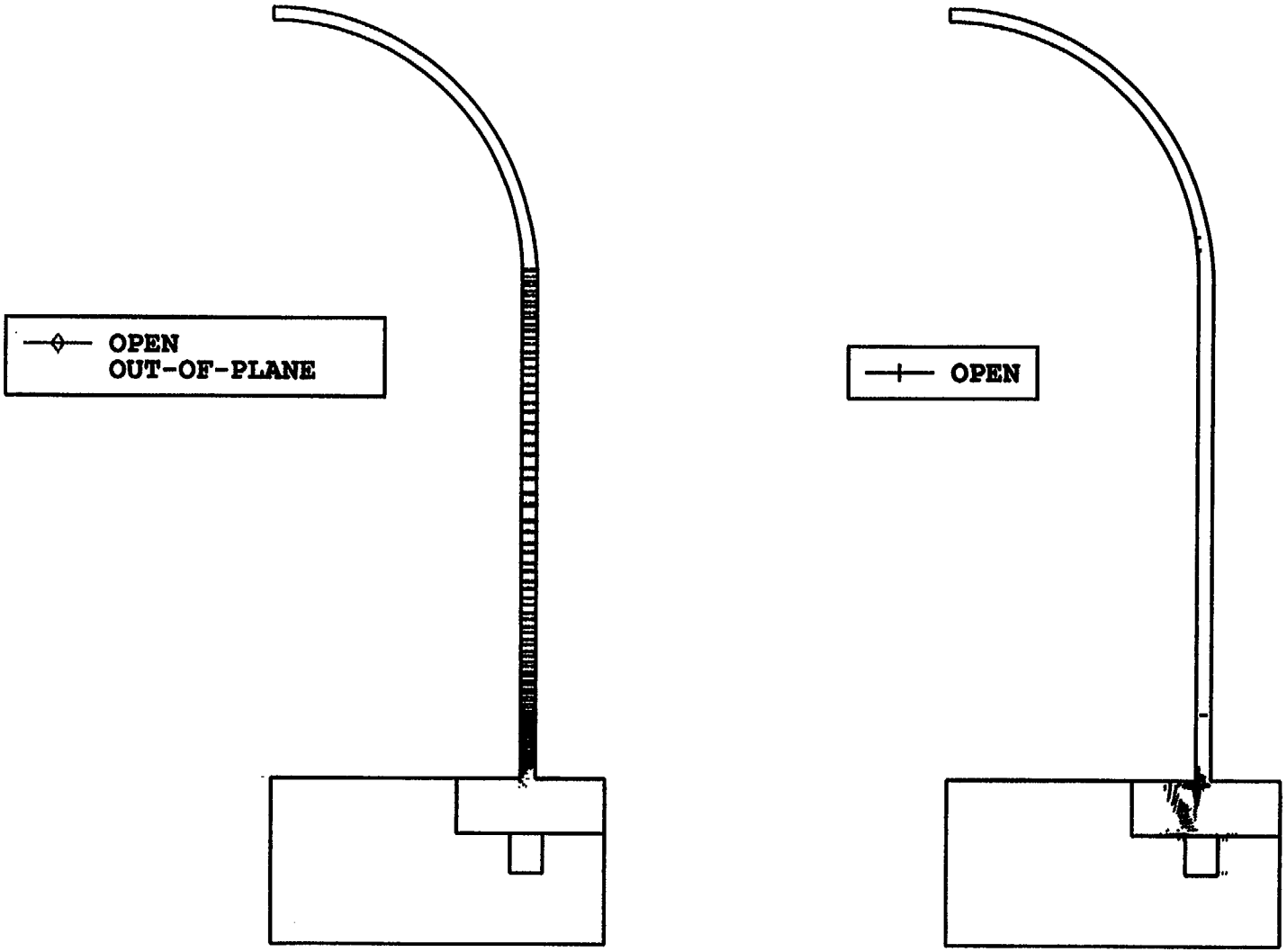


**Pressure= 2.0 $P_d$**

*model14.inp*

Figure 6-2a. Crack Patterns of Axisymmetric Model at 2.0 x $P_d$ Pressure

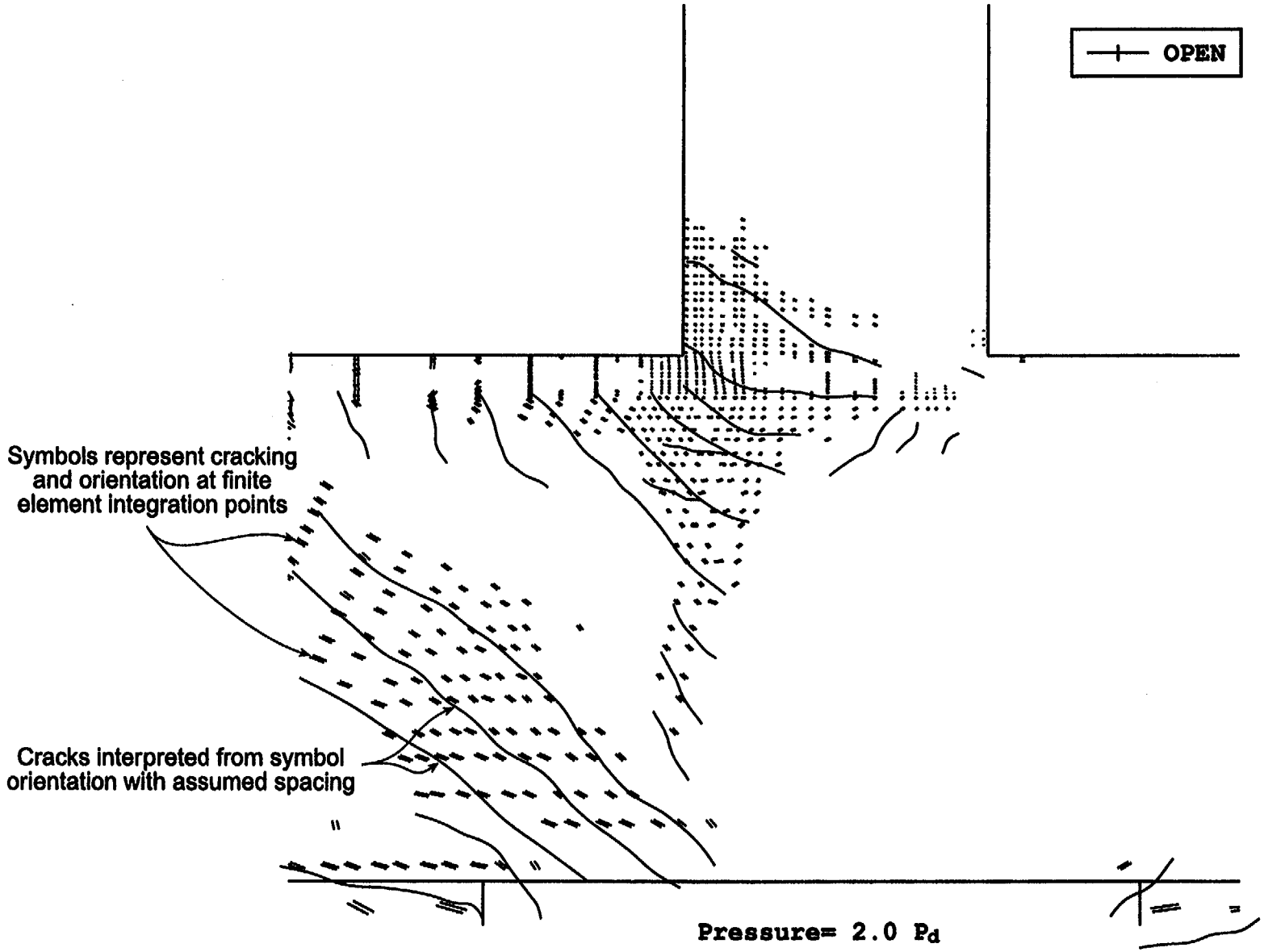


*model14.inp*

Figure 6-2b. Crack Patterns of Axisymmetric Model at 2.0 x $P_d$ Pressure-Enlarged View

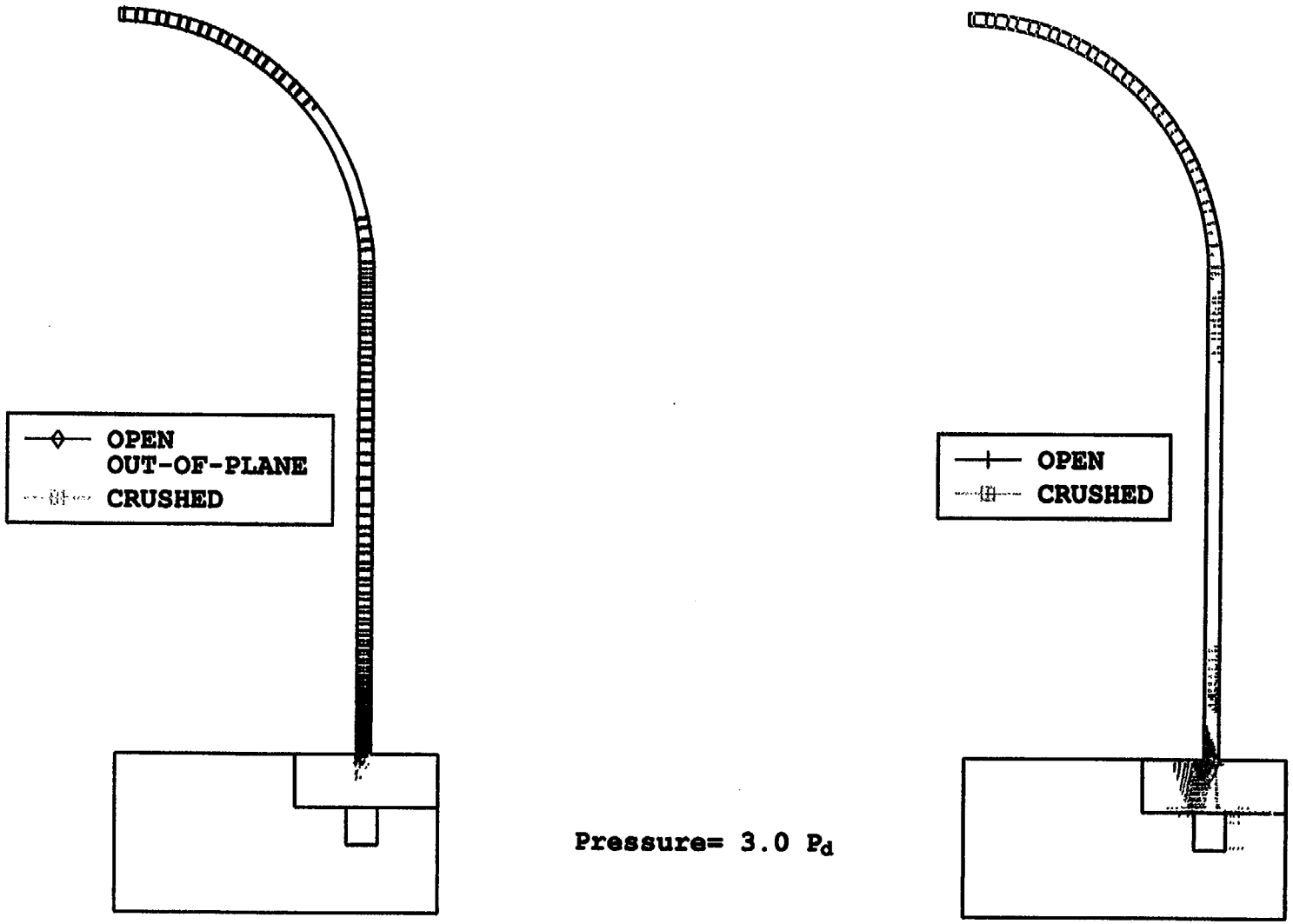


*model14.inp*

Figure 6-3a. Crack Patterns of Axisymmetric Model at 3.0 x $P_d$ Pressure

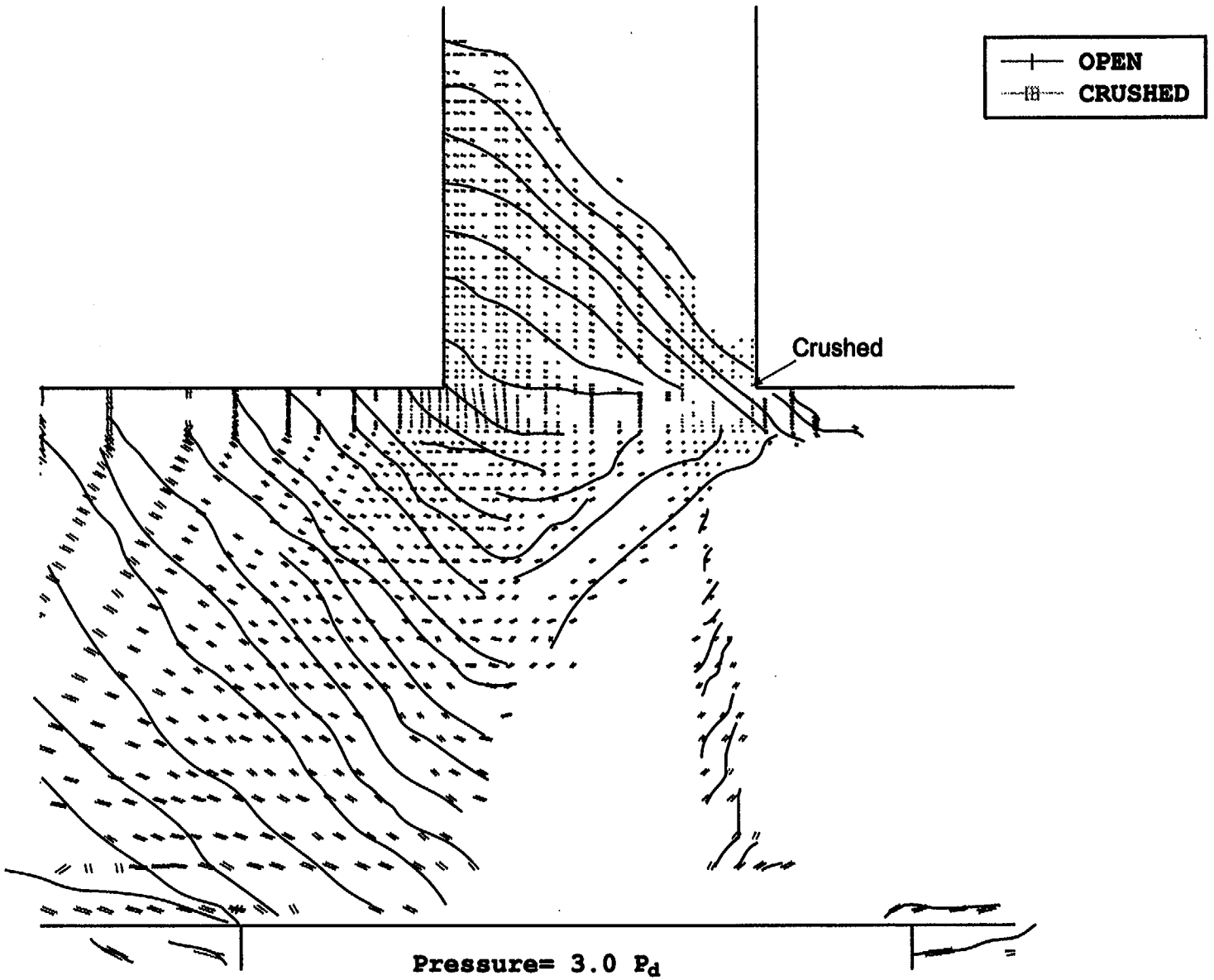


*model14.inp*

Figure 6-3b. Crack Patterns of Axisymmetric Model at 3.0 x $P_d$ Pressure-Enlarged View

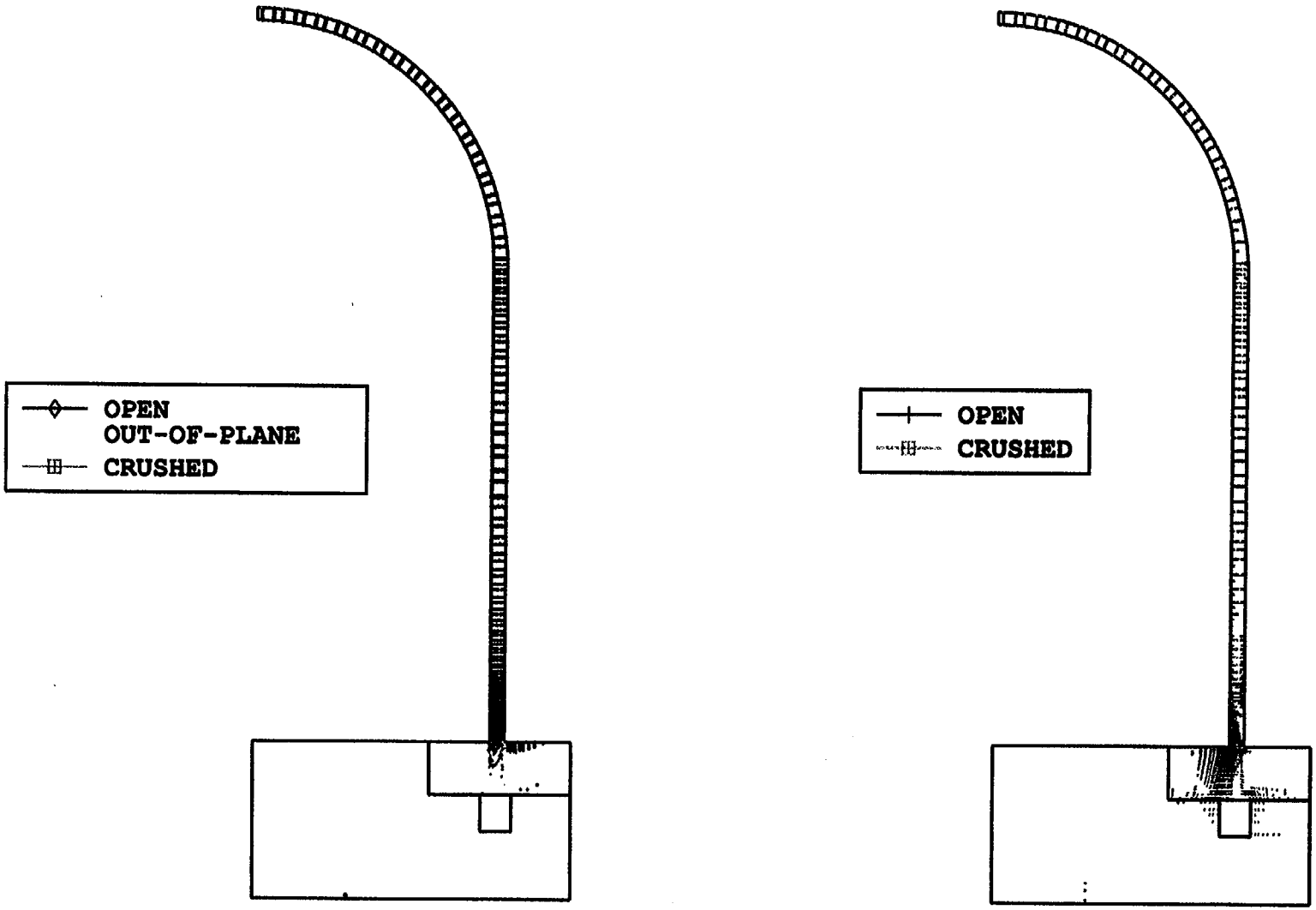


**Pressure= 3.6 $P_d$**

*model14.inp*

Figure 6-4a. Crack Patterns of Axisymmetric Model at 3.6 x $P_d$ Pressure

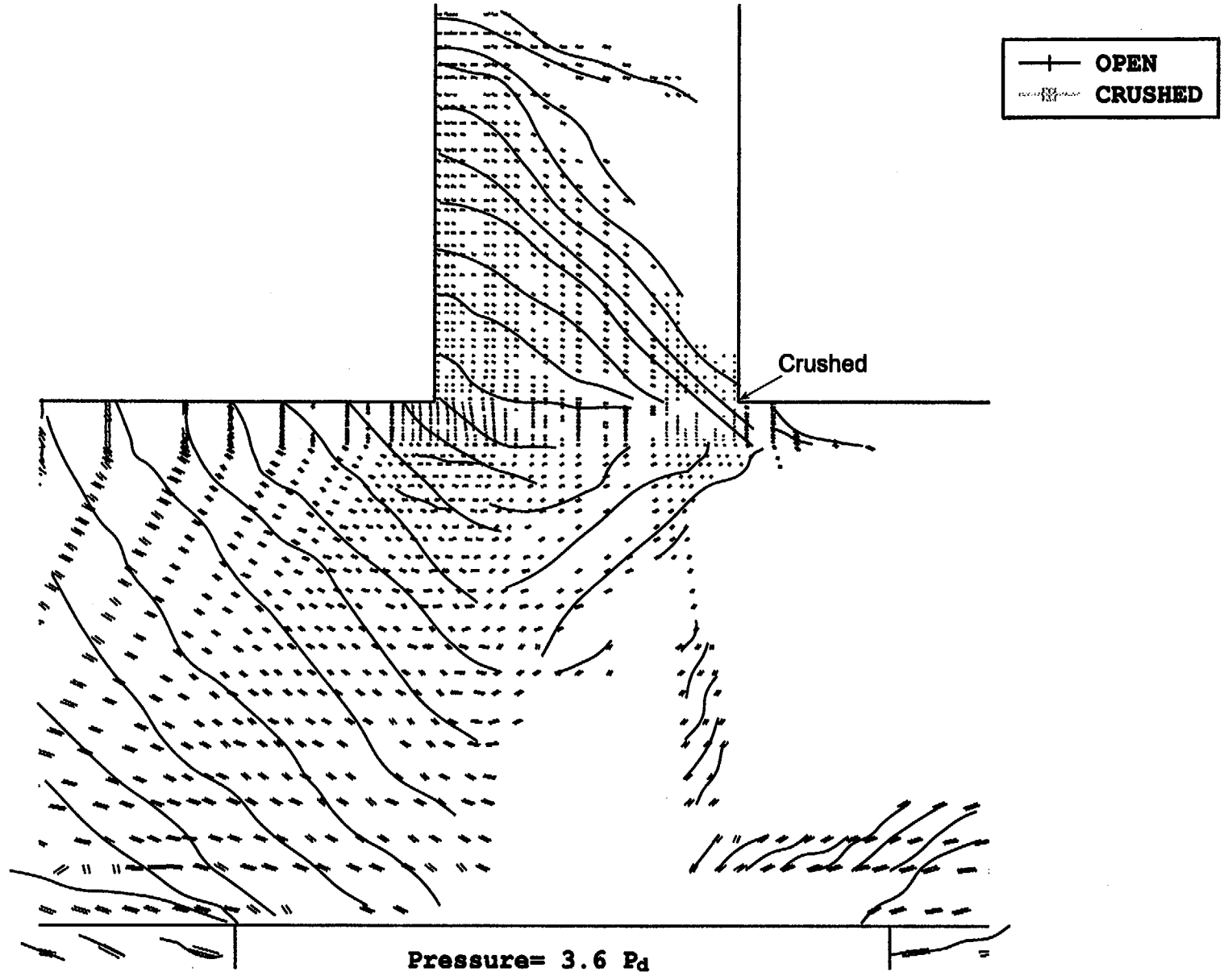


*model14.inp*

Figure 6-4b. Crack Patterns of Axisymmetric Model at 3.6 x $P_d$ Pressure-Enlarged View

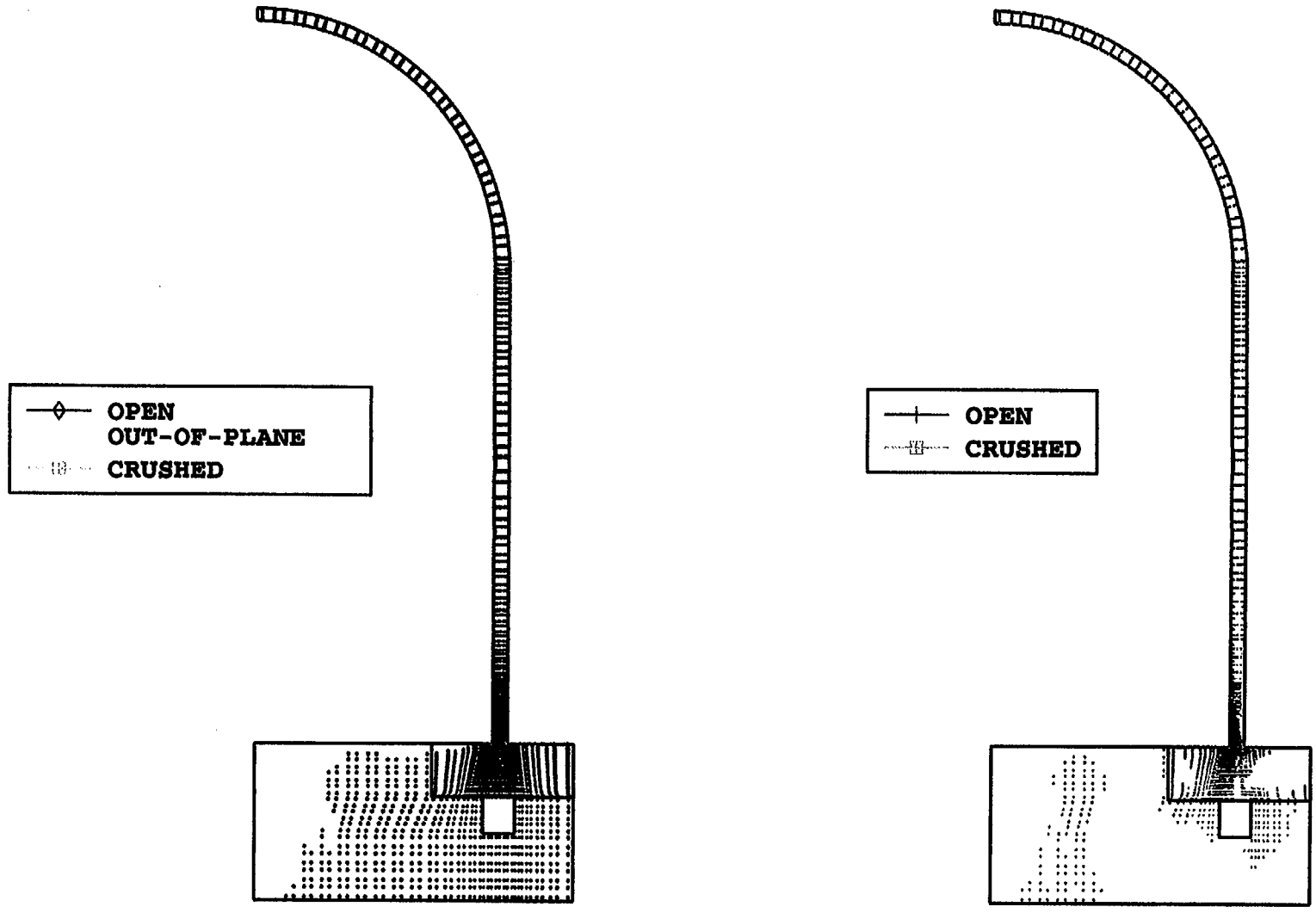


*model14.inp*

Figure 6-5a. Crack Patterns of Axisymmetric Model at 4.0 x $P_d$ Pressure

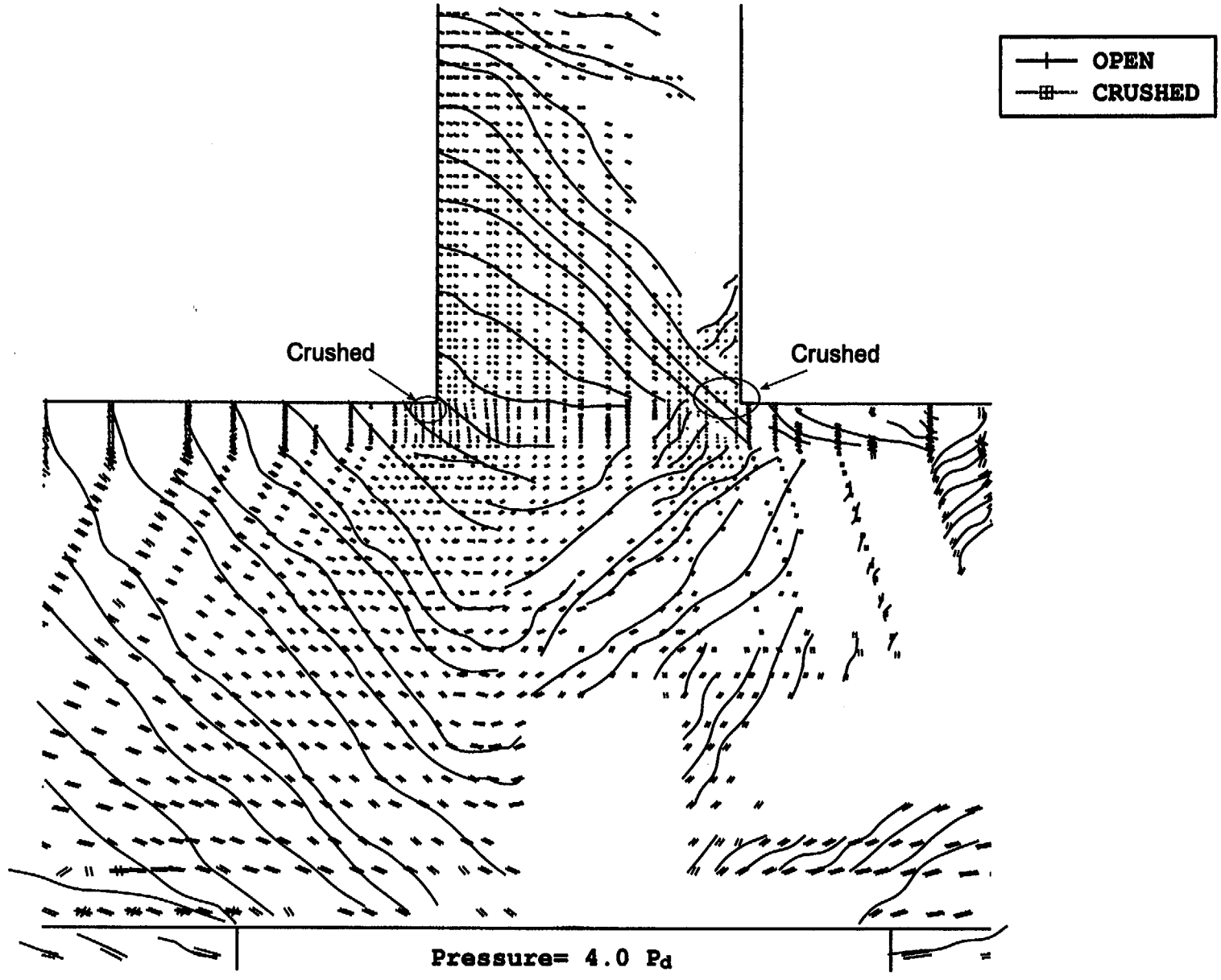


Figure 6-5b. Crack Patterns of Axisymmetric Model at 4.0 x $P_d$ Pressure Enlarged View

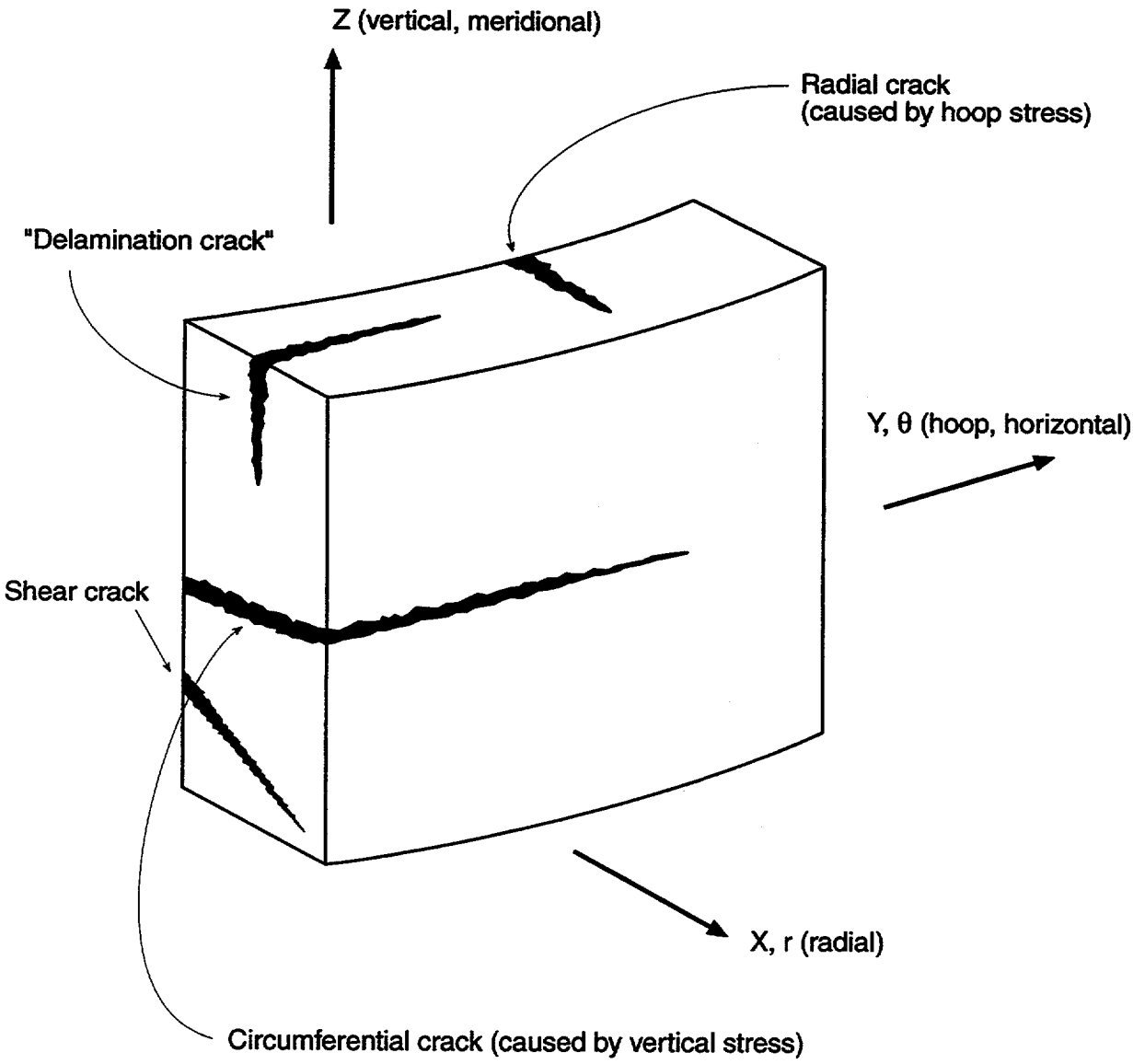


Figure 6-6. Crack Direction Nomenclature

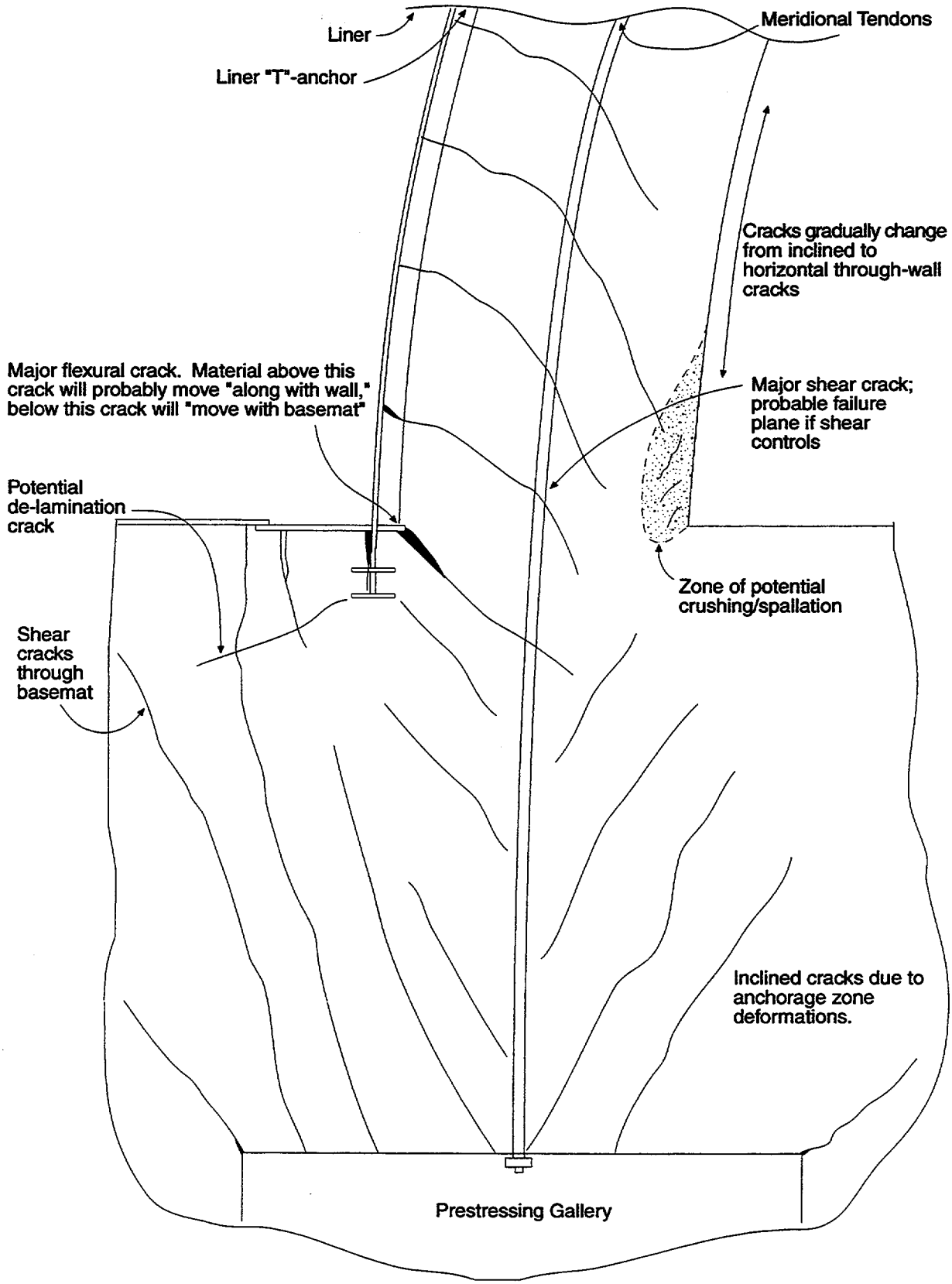


Figure 6-7. Deformed Shape and Crack Patterns of Wall-Basemat Juncture Region

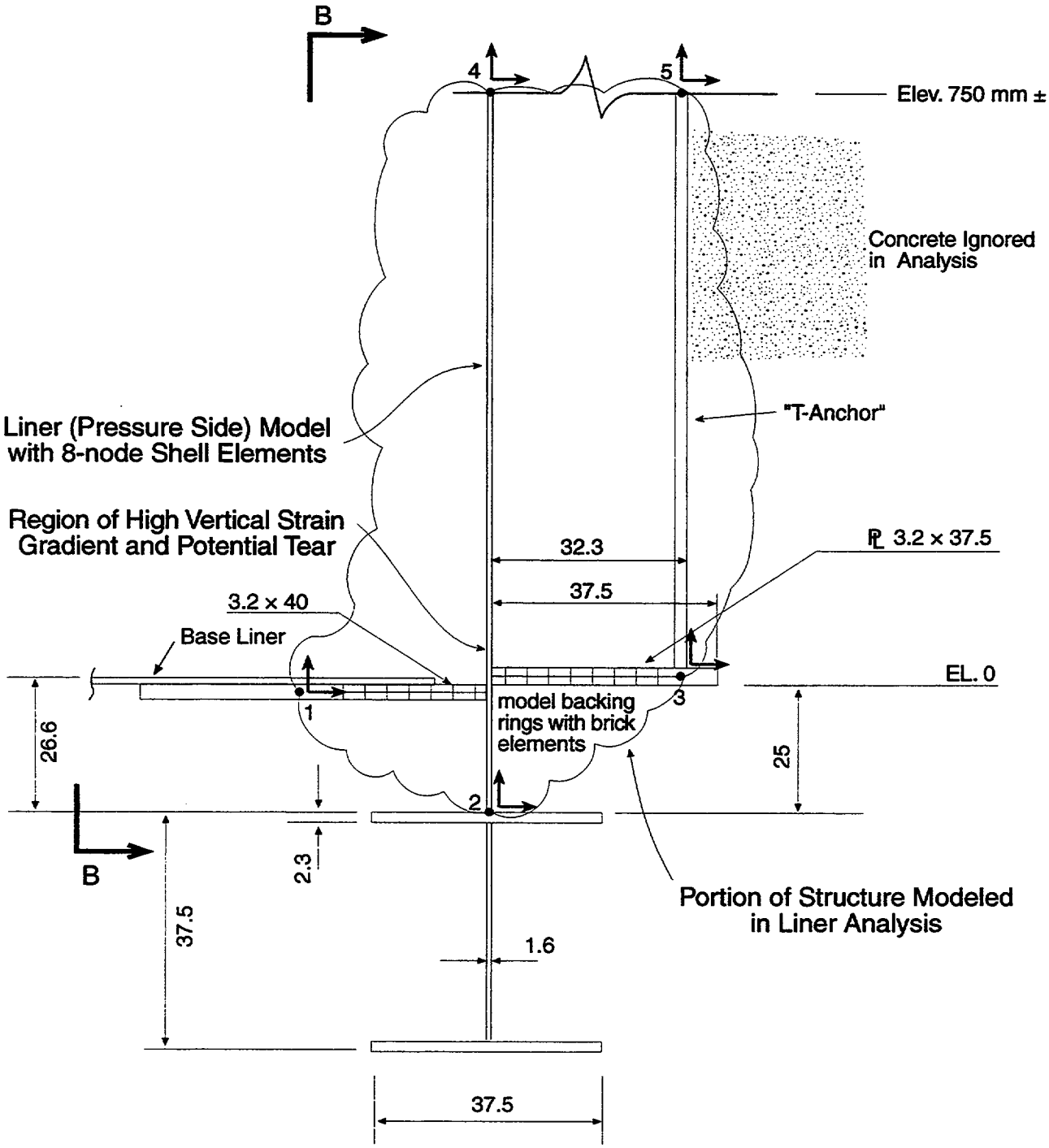


Figure 6-8a. Wall - Basemat Liner Connection Region (Section View)

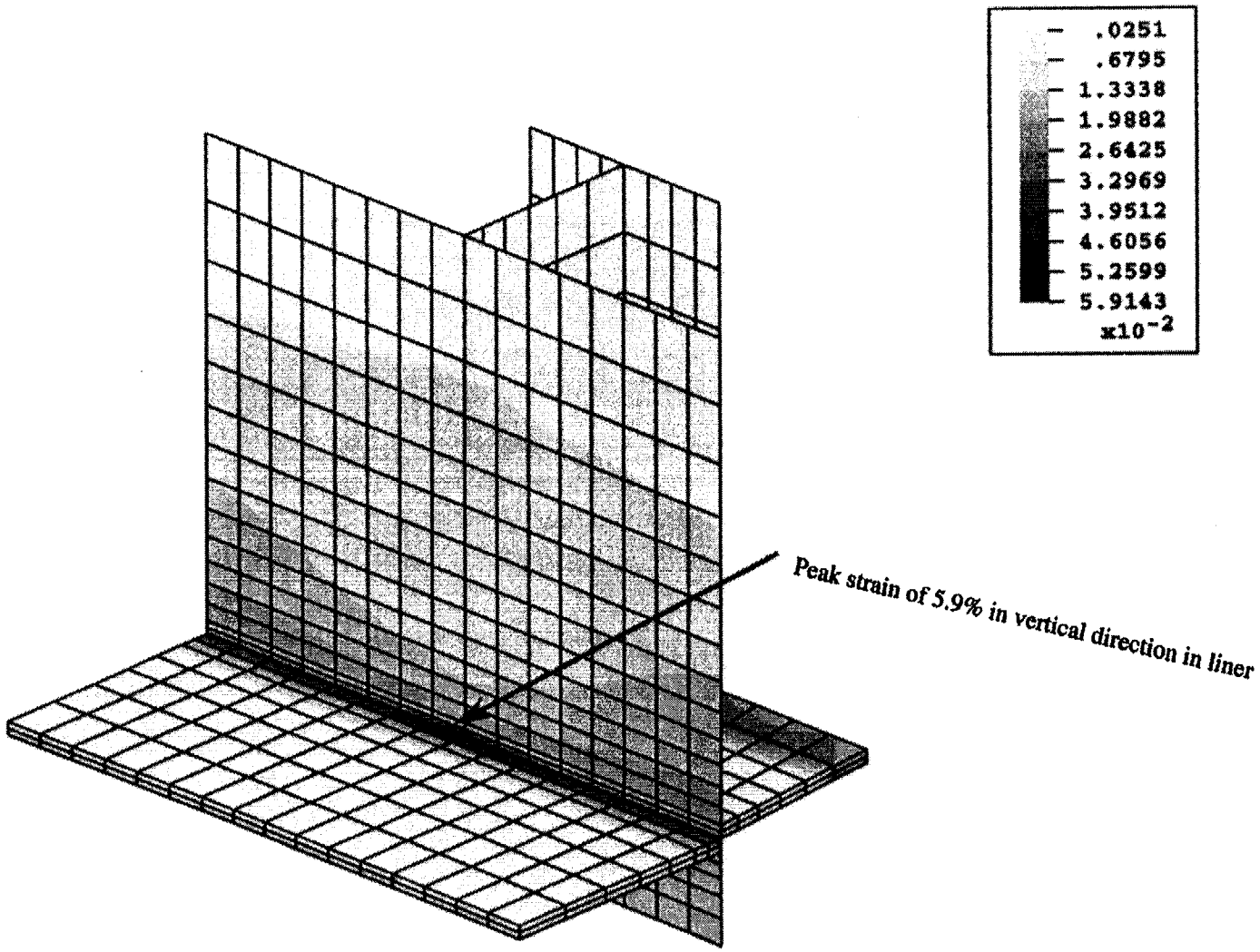


Figure 6-8b. Preliminary Analysis Phase Result of Liner Only Model Study at Pressure of Approximately 4 x $P_d$

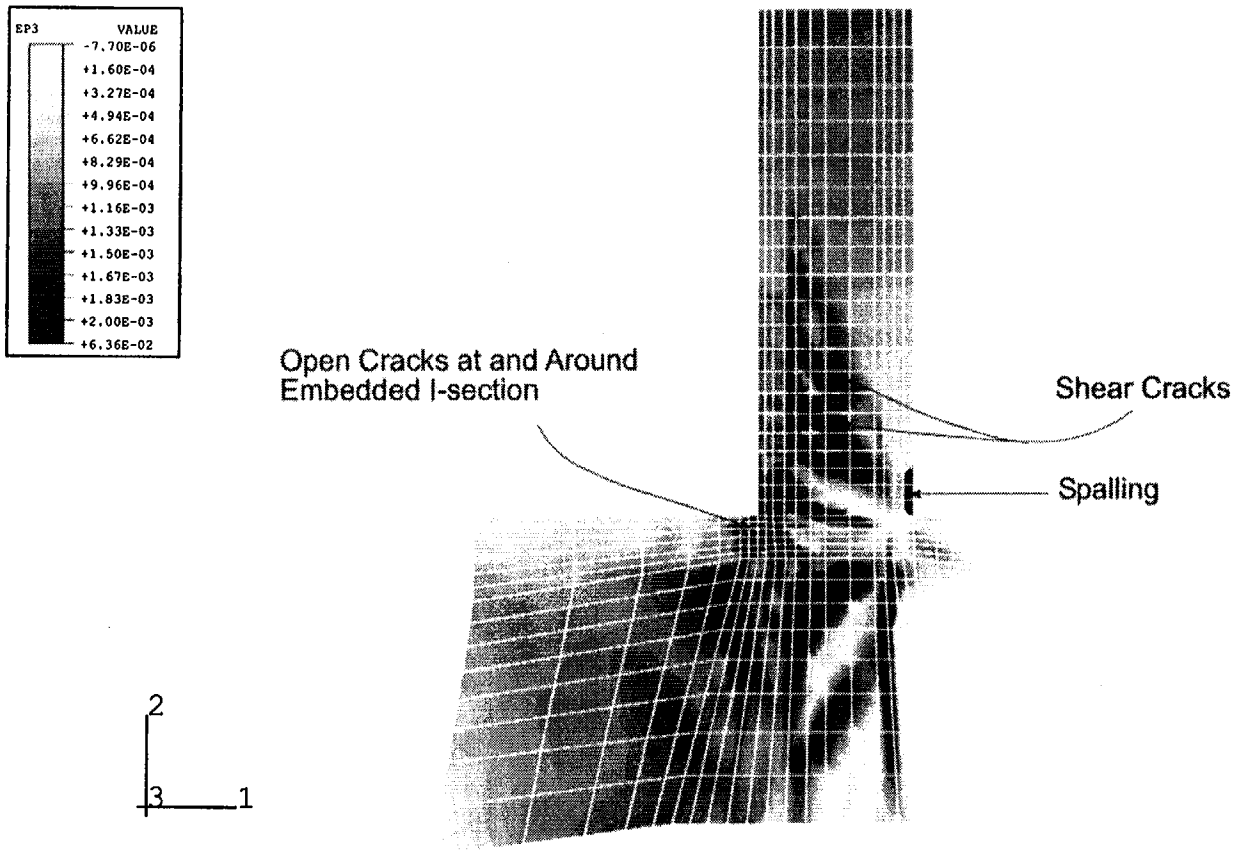


**Figure 6-9. Maximum Principle Strain Contours in Wall-Basemat Region at 3.4 x $P_d$ Showing Damaged Areas**
***model 14.inp***

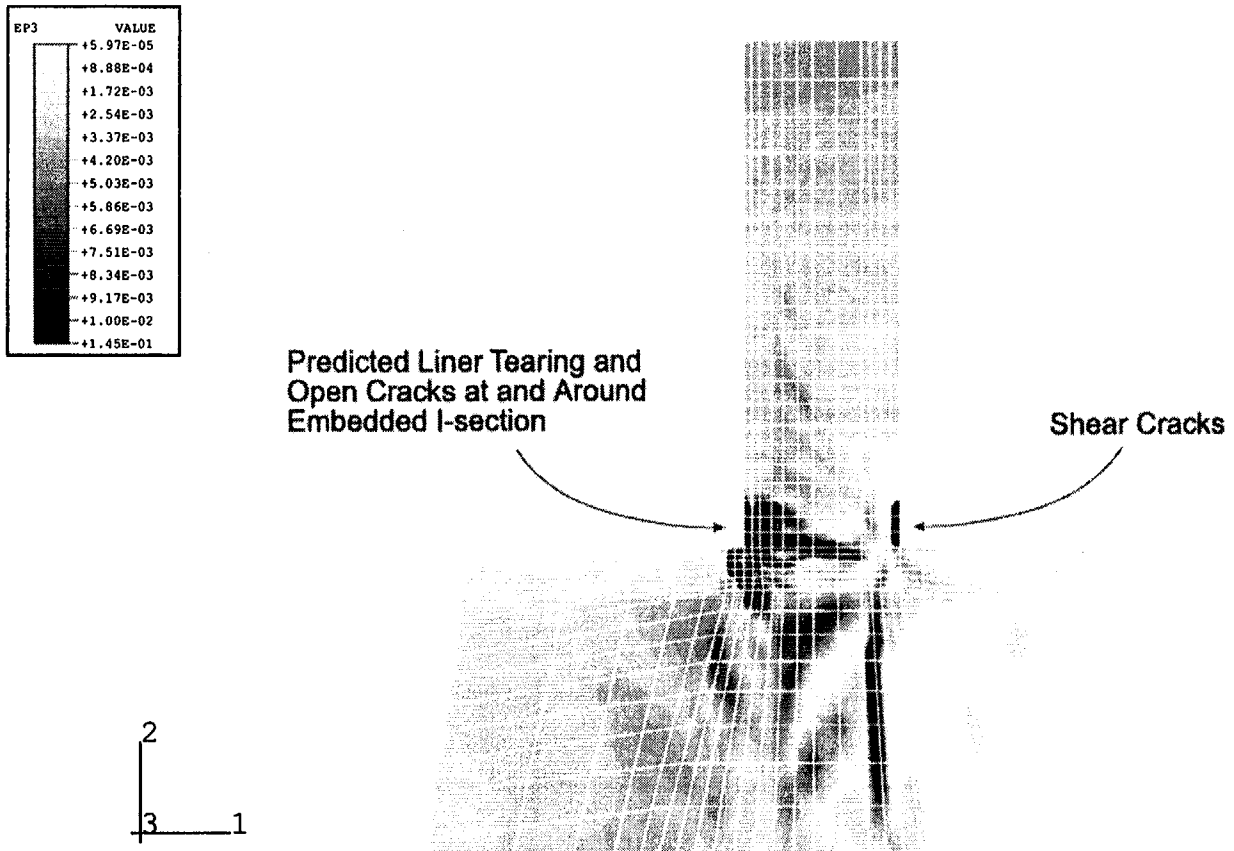


*model 14.inp*

**Figure 6-10. Maximum Principle Strain Contours in Wall-Basemat Region at 3.8 x $P_d$ Showing Damaged Areas and Possible Liner Tearing**

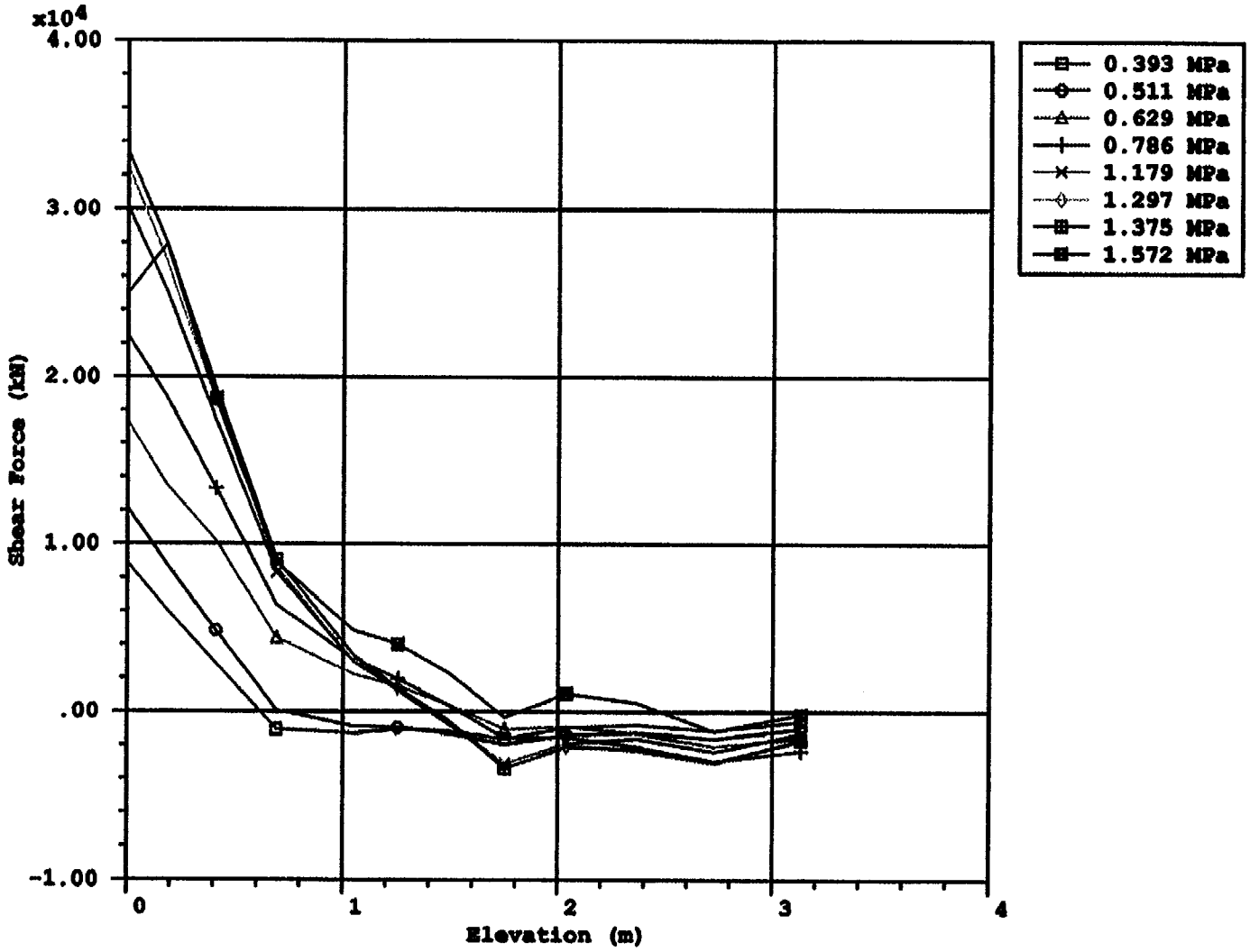


Figure 6-11. Shear Force Profile Along The Wall of the Prestressed Concrete Containment Vessel (PCCV) for Different Pressure Loads

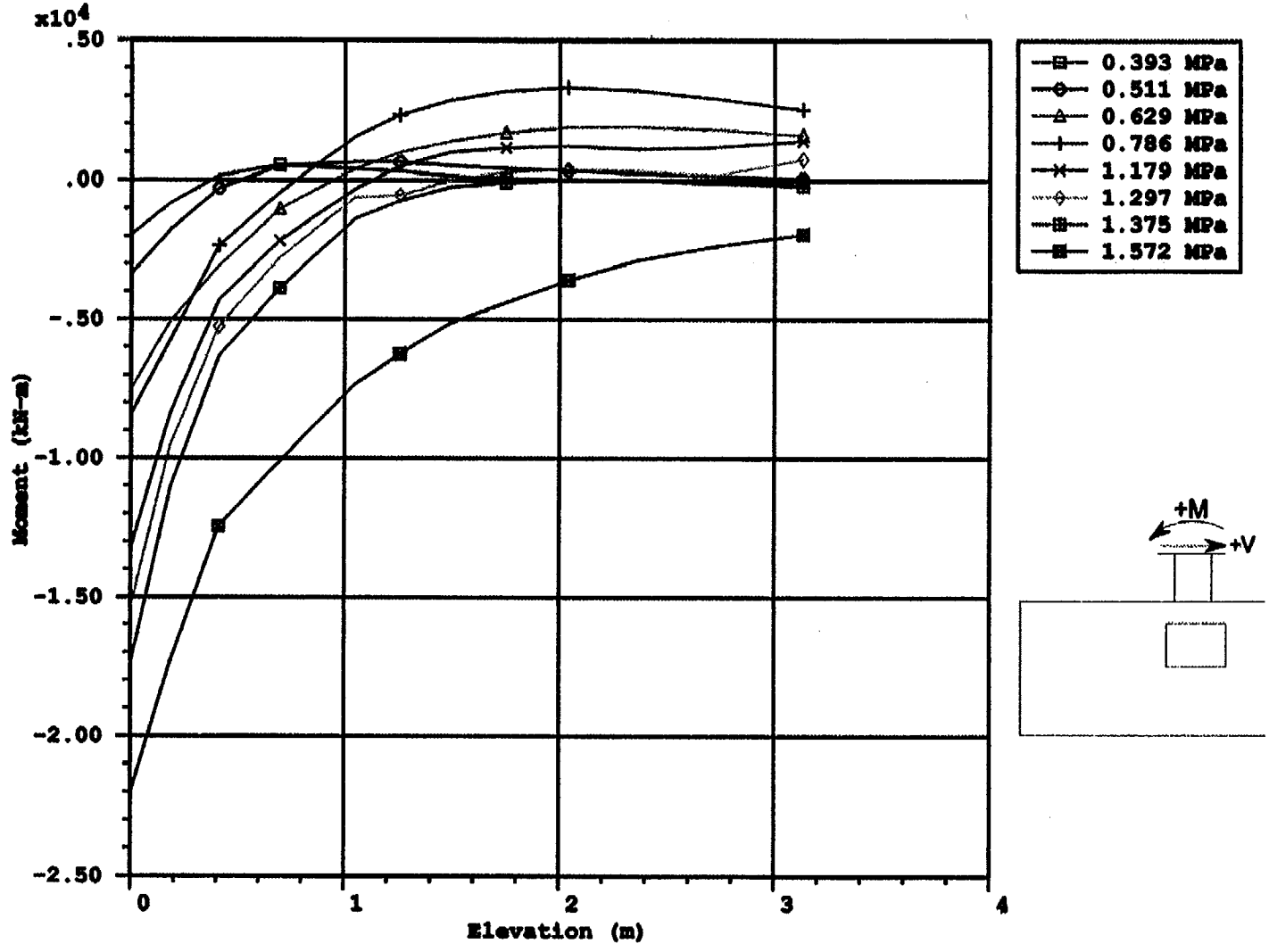


Figure 6-12. Moment Profile Along the Wall of the Prestressed Concrete Containment Vessel (PCCV) for Different Pressure Loads

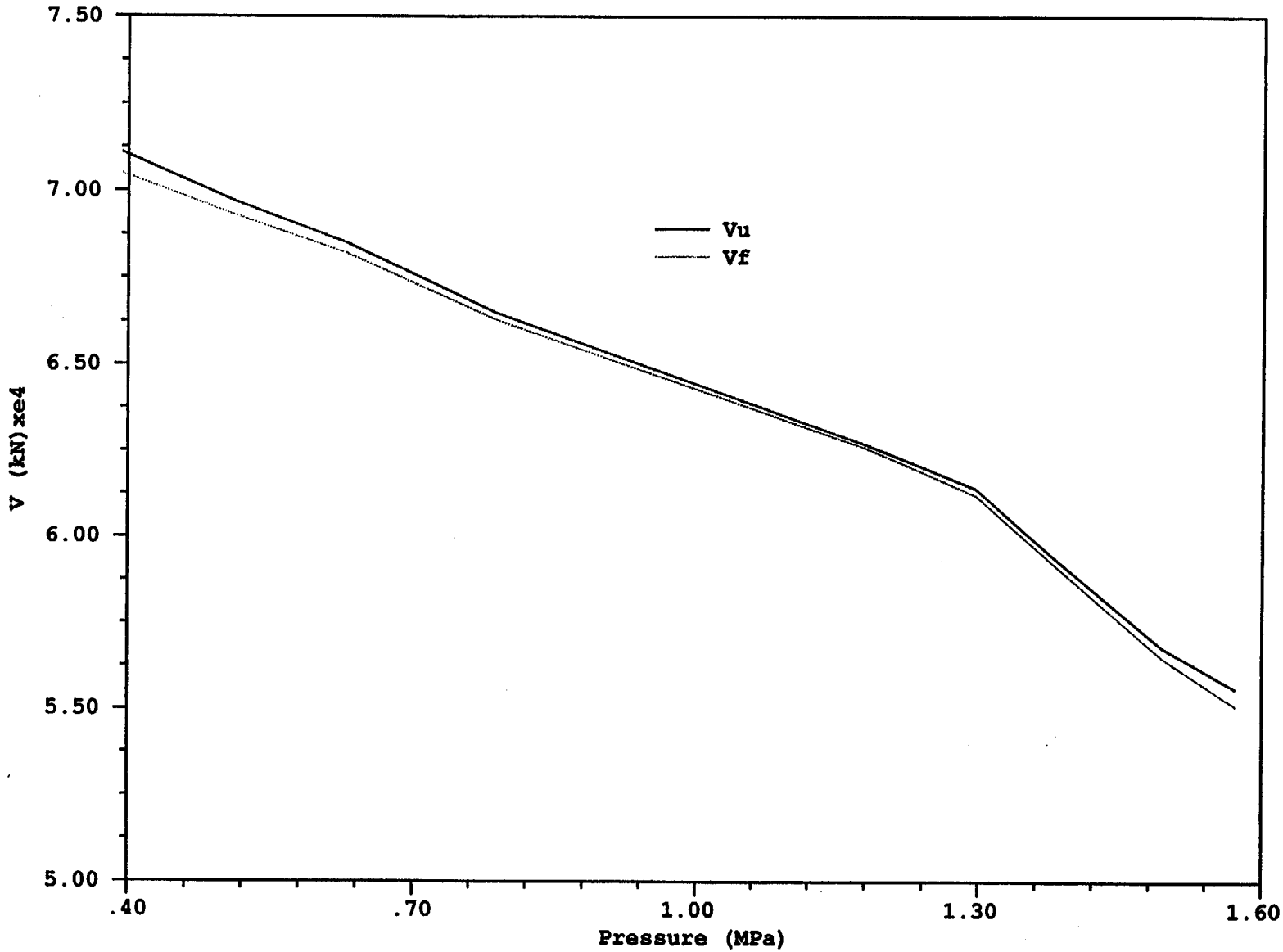


Figure 6-13. Prestressed Concrete Containment Vessel (PCCV) Shear Capacity from Modified Compression Field Theory

*model 14.inp*

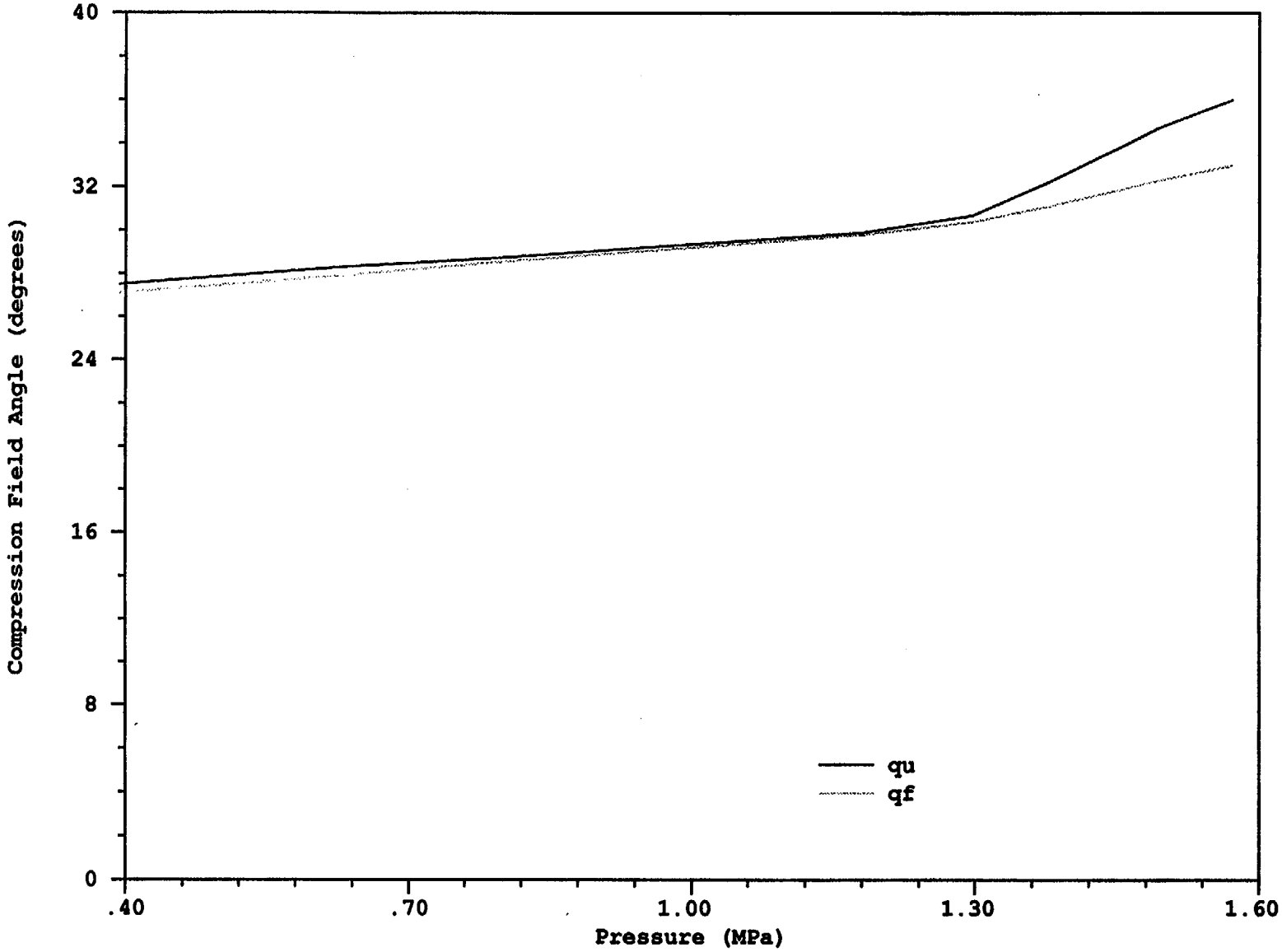


Figure 6-14. Prestressed Concrete Containment Vessel (PCCV) Crack Angle from Modified Compression Field Theory

*model 14.inp*

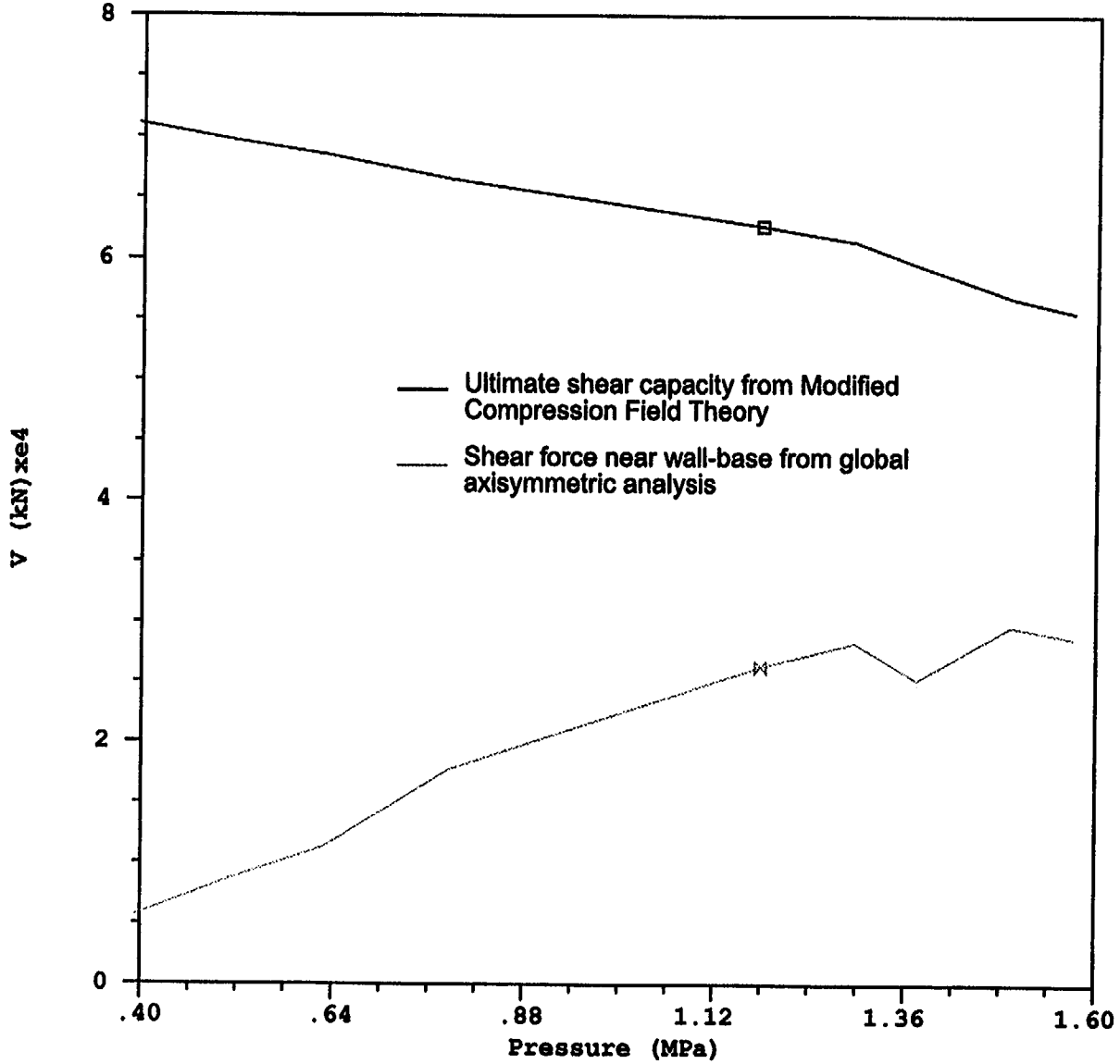


Figure 6-15. Comparison of Prestressed Concrete Containment Vessel (PCCV) Shear Strength from Modified Compression Field Theory to Shear Demand from the Global Analysis Model

*model 14.inp*

# 7. 3DCM MODEL ANALYSIS

## 7.1 Model Geometry

The three-dimensional cylinder midheight (3DCM) model is a detailed representation of a horizontal slice through the prestressed concrete containment vessel (PCCV) cylinder, that extends from Elev. 4.67m to about Elev. 7.62m, and extends 360° circumferentially. For modeling convenience, the centerline elevations of the equipment hatch (E/H) and the personnel airlock (A/L) were assumed to be the same (this required only a few centimeters upward and downward adjustment of these centerlines from their true location). The E/H and A/L, therefore, were modeled in vertical half-symmetry. The mainsteam group also was moved, though a little further (28 cm) so that it, too, could be represented in half-symmetry. Both buttresses were modeled. The model was constructed with the help of the tendon, concrete, and rebar mesh generators already in place for the E/H, A/L, buttress, and mainsteam (M/S) local model geometries. Hoop and meridional tendons were modeled two-for-one. The liner was explicitly modeled with shell elements, and liner anchors were modeled with beam elements. Rebar was modeled one-for-one with the rebar subelement modeling strategy described in earlier chapters. The liner grid density was not as fine as for the individual local models, so the 3DCM model was not used to predict "peak" local liner strains. The grid was considered fine enough to represent the stiffness and yielding behavior of the liner in order to predict reliable displacement versus pressure histories at the boundaries of local models.

The primary objectives of the 3DCM model were to provide:

(1) a 3-D prediction of the radial displacement at the midheight of the cylinder,

(2) prediction of complete tendon stress profiles for critical hoop tendons throughout the test pressure history, and

(3) accurate displacement and "far-field" strain versus pressure prediction for applying boundary conditions to and ranking the peak liner strains of local penetration studies.

The results of the 3DCM model allowed correlation of the response of the local models to model pressure on the basis of the deformations experienced at the boundaries of the local models.

The region represented by the 3DCM model is shown in Figure 7-1.

The finite element model geometry is shown in Figure 7-2. The model consists of 8-node brick elements, four through the wall thickness, 4-node shell elements for the liner, truss elements for tendons and friction ties, subelements for rebar, and 4-node shell elements for the hatch covers.

The material properties of structural elements are the same as for the global axisymmetric analysis described in Chapter 5.

The prestressing tendons in the 3DCM model use the same modeling strategy as in the local penetration models and as in the dome of the axisymmetric analysis (Chapter 5), including the friction truss ties that distribute angular friction along the curved tendon paths. This system is illustrated in Figure 7-3, along with the tendon layout. The hoop tendons are modeled "one-for-two" because of grid size considerations, but the meridional tendons are modeled one-for-one.

The reinforcement in the model is represented with ABAQUS subelements. These are generated in space using the ANAGEN program and plotted as shown in Figures 7-4 through 7-7. The actual rebar represented in the model is the rebar found by the model generator that intersects the concrete brick element boundaries. Thus, rebar shown on Figures 7-4 through 7-7 that falls outside of the concrete boundaries does not become part of the finite element mesh. In addition to the bars shown, through-thickness wall ties are included in all portions of the wall. Note that all rebar included in the model is assumed, by the subelement formulation, to have strain compatibility with the concrete, so it is fully effective, even in rebar anchorage zones.

The added stiffness provided by the "tendon sheath support frame" was also represented by adding rebar of area equivalent to the support frame at the locations of the support frame members. The locations of these additions are shown in Figure 7-8. In the hoop direction the frame adds three hoops of area 2.8 $cm^2$ each to the model, and in the meridional direction it adds 35 verticals of area 4.61 $cm^2$ each to the model.

## 7.2 Boundary Conditions

For any partial model of a pressure vessel, application of the boundary conditions is difficult but critical to the

modeling simulation. The boundary condition assumptions applied to the 3DCM are shown in Figures 7-9a and 7-9b. The goal was to simulate the actual force conditions as closely as possible and apply the minimum of displacement constraints needed to prevent rigid body motion. Conditions applied follow:

1. Apply internal pressure on all interior surfaces, including hatch covers.

2. Apply vertical stress $\sigma_z$ (equal to PR/2t) on the top "cut" surface.

3. Apply $\theta_\theta = 0$ at the top surface (i.e., zero rotation about tangential axis.)

4. Constrain $\Delta_z = 0$ at the concrete nodes on the bottom surface.

5. At only three nodes, near the midheight of the 3DCM model (Elev. 6.823 m) constrain $\Delta_\theta$ (tangential displacement) = 0. Do not apply any radial constraints.

The $\Delta_z = 0$ is required to successfully execute the vertical prestressing step. This also imposes $\theta_\theta = 0$ around the bottom of the model. $\theta_\theta = 0$ at the top and bottom is substantiated by behavior observed in the global axisymmetric analysis, as illustrated in Figures 7-10 and 7-11. At the top and bottom surfaces of the 3DCM model, the global results show nearly zero slope. This is logical at the PCCV cylinder midheight because of being equidistant from the dome and the basemat. The top of the 3DCM model appears to be the highest point of nearly zero slope before the deformed wall curves back inwardly toward the dome springline discontinuity. Though these zero-slope conditions are only approximate, they are numerically convenient, and they help provide numerical stabilization of the edges of the 3DCM model. The displacements that are allowed to move freely are more important to the behavior prediction of interest, namely, radial displacement and, at the top boundary, vertical displacement. Note that the top boundary is free to move vertically, so the model will capture vertical extension or contraction variation with azimuth.

The tangential displacement boundary conditions constrain only three degrees of freedom, the minimum possible to prevent rigid body motion of the model in the R-$\theta$ plane. The constraints are tangential only, and the points are at the two buttresses and at the 180° azimuth. The buttresses are believed to provide tangential stiffness (beam action), so these points will probably have nearly zero tangential displacement in the actual structure. The 0° point also should move only radially because of the symmetry of this side of the wall centered around the M/S group. The 180° point, however, may move some tangentially, as the model deforms, because of the asymmetry of the E/H versus the A/L.

## 7.3 Tendon Prestressing

The methodology for prestressing is analogous to that described in Chapter 5 for the axisymmetric model meridional tendons. The target initial stresses, set by the designers, were shown in Figure 5-1. Also shown are comparisons to what these values would be estimated to be in a full scale prototype. The designers' primary goal in scaling the prestressing system was to match the overall level of prestress in an actual plant after 40 years, but the figure shows some of the difficulties in scaling caused by anchor set and other friction losses which are not easily scaled. The initial stresses applied to tendons were calculated with a procedure similar to that described for the axisymmetric model. At hoop anchorages, the design stress (less an additional 5% for extra anticipated concrete creep loss) after anchoring (1268 MPa) was applied uniformly. Note, however, that because the model and tendons deform during prestress equilibration, the anchor stress application requires several trial iterations to achieve the desired anchor stress at all tendons at the end of the prestress loading step. The vertical tendon stresses (1341 MPa) were applied to the tendon element "tails" at the bottom of the model. The target stress for vertical tendons away from penetrations was the design stress. (Friction along straight tendon segments was ignored). The target stress for tendons with any path deviation caused by penetrations was reduced from the design stress by the angular friction loss encountered between the base of the PCCV wall (Elev. 0) and the base of the 3DCM model. This theoretical loss along portions "outside" the 3DCM model was performed by hand calculation. Performing the hand calculation for this local friction loss also provided a good check on the implementation of the tendon friction trusses in the 3DCM model. The loss in the vertical tendon stress between the equator of the E/H and the top of the 3DCM model, for example, should be half the total loss expected that is caused by the E/H path penetration.

## 7.4 Tendon Anchor Set Loss Sensitivity Study

In the early stages of developing the 3DCM model, the hoop tendon friction modeling was made uniform

around the circumference of the cylinder. This leads to continuous angular friction losses extending from the tendon tangent point all around the circumference, but it ignores the existence of anchor setting losses. After obtaining preliminary results without setting losses, a modeling strategy was introduced to all the setting losses by reversing the orientation of the friction tie elements along the portion of the tendon path that tendon friction theory would predict to be influenced by setting losses. This anchor set modeling strategy is illustrated in Figures 7-12 and 7-13. As illustrated later in this chapter, the introduction of these losses profoundly influenced the three-dimensional deformation behavior of the cylinder, particularly the azimuth distribution of radial displacement. To demonstrate why this might occur, the setting loss concepts are further illustrated in Figure 7-14, which shows that the zone of influence of setting losses is a full 45° from each tendon end. With 360° tendons jacked from both ends this is a total zone of influence of 180°, or *half the circumference*. This is about double the zone of influence that would be found in a full-scale prototype, and the total amount of loss (in terms of stress) is *more than four times* that of the prototype. This occurs in the PCCV model for two reasons

(1) Setting losses act over a length of tendon that is determined by the amount of slip in the jack hardware and by the amount of friction. Because the 1:4-scale PCCV tendons use jacking hardware similar to the full-scale, the length over which setting losses act is similar to the prototype, not scaled. In a 1:4-scale model, this length covers a much larger azimuth.

(2) Ancillary tests of the 1:4-scale PCCV tendons demonstrate an angular friction coefficient of $\mu$=0.21, which is 30% to 50% higher than what commonly is found for full-scale prototypes. This makes the total loss (in terms of stress) larger and exacerbates the influence of the setting losses on the model behavior.

Based on these observations and on the large influence observed from the first setting loss model, a parameter study was conducted to evaluate the sensitivity of the setting losses on behavior. The following cases with setting loss assumptions illustrated in Figure 7-15, were analyzed.

- No setting losses;
- Case 1: designers' calculations (5mm set loss-not scaled) for 1:4-scale PCCV, 10° to tangency + 35°, total of 45° influence zone;
- Case 2: prototypical setting loss (2mm set loss, nominally scaled with consideration of hardware limitations), 10° to tangency +15°, total of 25° influence zone;
- Case 3: small losses, 10° to tangency + 5°, total of 15° influence zone.

Note that the prestress loss calculations that correspond to the figure were shown in Figure 5-1, which corresponds to 3DCM model Case 1.

The results of the sensitivity study are best summarized by comparing the displacement patterns of the 3DCM models. These are shown in deformed shape plots of Figures 7-16 through 7-21, and in the radial displacement versus pressure plots of Figures 7-22a through 7-22d, showing the following:

- At pressures higher than the tendon yield pressure, the cylinder response tends to the "bi-modal," because of the influence of the buttresses and/or the influence of the setting losses.
- The case with no losses and Case 3 show the largest displacement at 0° and 180°, while Case 1 shows largest displacements at 90°.
- Case 2 20° shows the most uniform distribution of radial displacement.
- The "mode" of expansion of the cylinder has a major effect on the response and on the failure prediction.

After extensive review of the analysis results it was concluded that for the larger friction coefficient ($\mu$=0.21), the setting loss assumption may indeed produce the large variations in radial response demonstrated by the analysis. However, it is also possible that because the analytical model presets the sign and magnitude of the friction coefficient, the analysis is incapable of capturing the variations in friction which may occur during pressurization and may reduce the radial response sensitivity to the setting loss. It was also observed that the setting losses used by the designers were probably a conservative upper bound. The anchor slip assumed by the designers was 5mm. Most of the anchor slips were in the range of 3 to 3.5mm in the ancillary tests conducted by the Nuclear Power Engi-

neering Corporation (NUPEC). The anchor slip might be further minimized to as low as 1 to 2mm during jacking by removing the load slowly. The results of detailed anchor slip loss calculations shown in Figure 5-1 are summarized below. These calculations assume angular ($\mu$=0.21) and wobble friction.

| 3DCM Case | Influence Zone of Anchor Slip (Angle) | Angle from Buttress Centerline | Set Loss (mm) |
|---|---|---|---|
| 1 | 35° | 45° | 5mm |
| 2 | 15° | 25° | 2mm |
| 3 | 5° | 15° | 0.5mm |
| 4 | 0° | 10° | 0mm |

While NUPEC's official specification remains a not-to-exceed value of 5mm, because the anchor slip of Case 2 corresponds to the equivalent azimuth zone of influence of a full-scale prototype, it was decided to use Case 2 as the basis for the pretest prediction analysis.

The target applied stresses for the final case (Case 2) are those shown in Table 5-1. The stress contours in all of the tendons at the end of the prestressing step are shown in Figures 7-23 and 7-24.

After prestressing, pressure was applied to the model up to 3.8 times the design pressure ($3.8P_d$). The deformed shapes at Prestress, $1.5P_d$, $2.0P_d$, $2.5P_d$, $3.0P_d$, 3.5, and $3.8P_d$ are shown in Figures 7-25 through 7-31. The radial displacements versus pressure are then shown in Figures 7-32 and 7-33. The most prominent observations of the displacement response are listed below. Note, however, that these observations are made for Case 2, and they differ for other cases.

(1) At prestress, all portions of the cylinder wall move inwardly more than the buttresses.

(2) By $3.0P_d$, all portions of the wall deform outwardly more than the buttresses.

(3) The model deforms radially out more at 4.6752m (cylinder midheight) than at 8.9567m, which is the same trend as in the axisymmetric model.

(4) The largest hoop expansion occurs at the E/H, and the "free-field displacements" (displacement at 0° and 180°) are slightly less and are approximately equal to each other.

(5) At pressures greater than $3.0P_d$, the radial displacements at 135° (and elsewhere) become significantly larger in the 3DCM model than in the axisymmetric analysis. Below $3.0P_d$, the axisymmetric analysis agrees well with the 135° azimuth of the 3DCM model.

The progression of stress and strain in the hoop tendons of the 3DCM model is shown in Figures 7-34 through 7-37 for pressures = $2.0P_d$, 3.0 x $P_d$, and 3.5 x $P_d$. The latter two plots show how tendon yielding starts first at the lowermost tendons near the equipment hatch. By $3.0P_d$, strains in the hoop tendon adjacent to the hatches have reached 1.4%, and at $3.5P_d$, strains exceed 5%, enough to rupture a tendon. By $3.8P_d$, many tendons rupture, which produces the stress and strain contours shown in Figure 7-37, in which tendon stresses drop to zero at the rupture location and the stress drop is propagating around the circumference of the model. In the actual test, this propagation might occur very quickly along the tendon's entire length. In the finite element analysis, however, convergence difficulties dictate a much slower progression. By P = $3.8P_d$, the analysis would have to be run for unreasonably long run times to further propagate the tendon rupture, so the analysis was stopped. It is thought that the analysis up to this point adequately captures the response up to a possible tendon rupture.

Other response measures and indicators of damage are strain contours shown on liner stretchouts at P=$2.0P_d$ and P = $3.0P_d$ in Figures 7-38 and 7-39 and shown in deformed shape perspective views in Figure 7-40 and 7-41. These plots show the elevated strains associated with the following:

1. local circumferential bending adjacent to each buttress,

2. strain concentrations at terminations or step-downs in rebar patterns, and

3. strain concentrations near hatches or near the edges of wall embossments.

One of the key objectives of the 3DCM model was to predict the stress and strain behavior in critical hoop tendons in the cylinder. Three instrumented tendons are identified in Figure 7-42: Tendon # H35, H53, and H68. Figures 7-43, 7-44, and 7-45 show the predicted stresses all along these tendons at seven pressure milestones. These plots show the effectiveness of the friction modeling strategy, the effects of reaching yield over a small portion of the tendon, and the effects of a rupture. Tendon stress and force histories at specific standard output locations are shown in Figures 7-46 and 7-47.

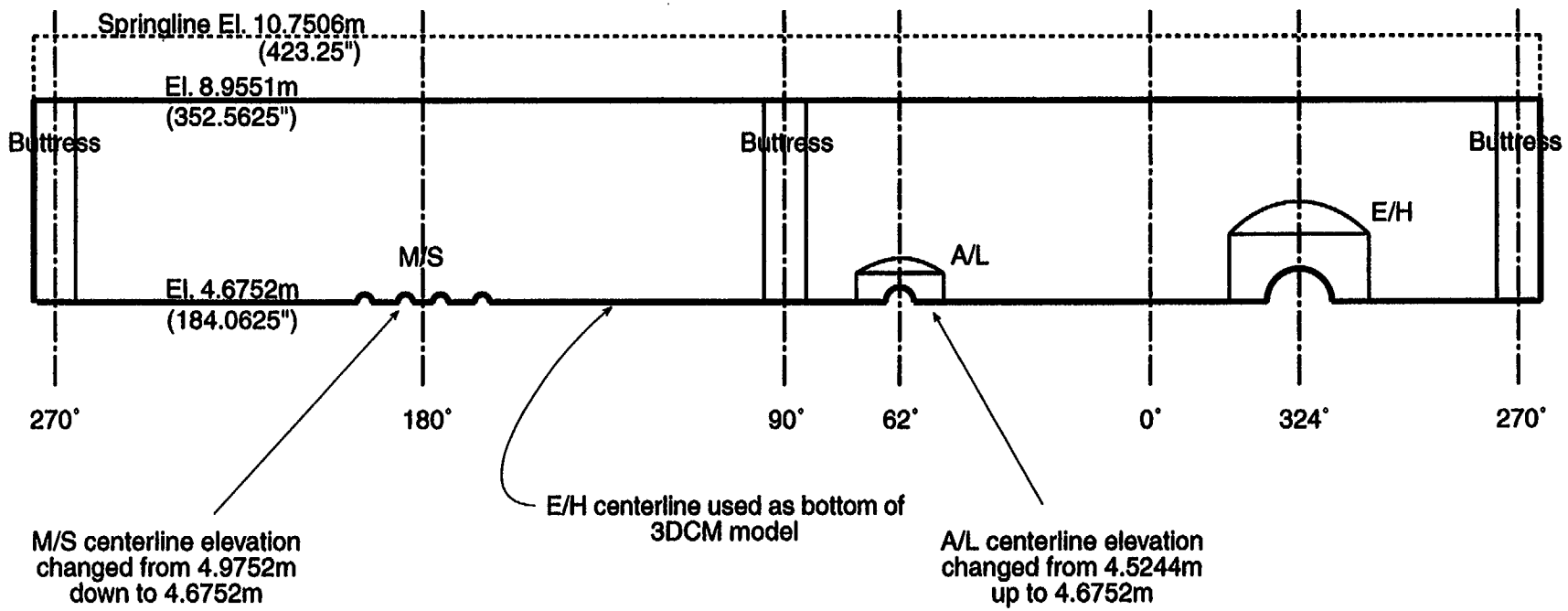


Figure 7-1. Inside "Stretchout" View of Portion of Prestressed Concrete Containment Vessel (PCCV) Modeled in 3DCM Model

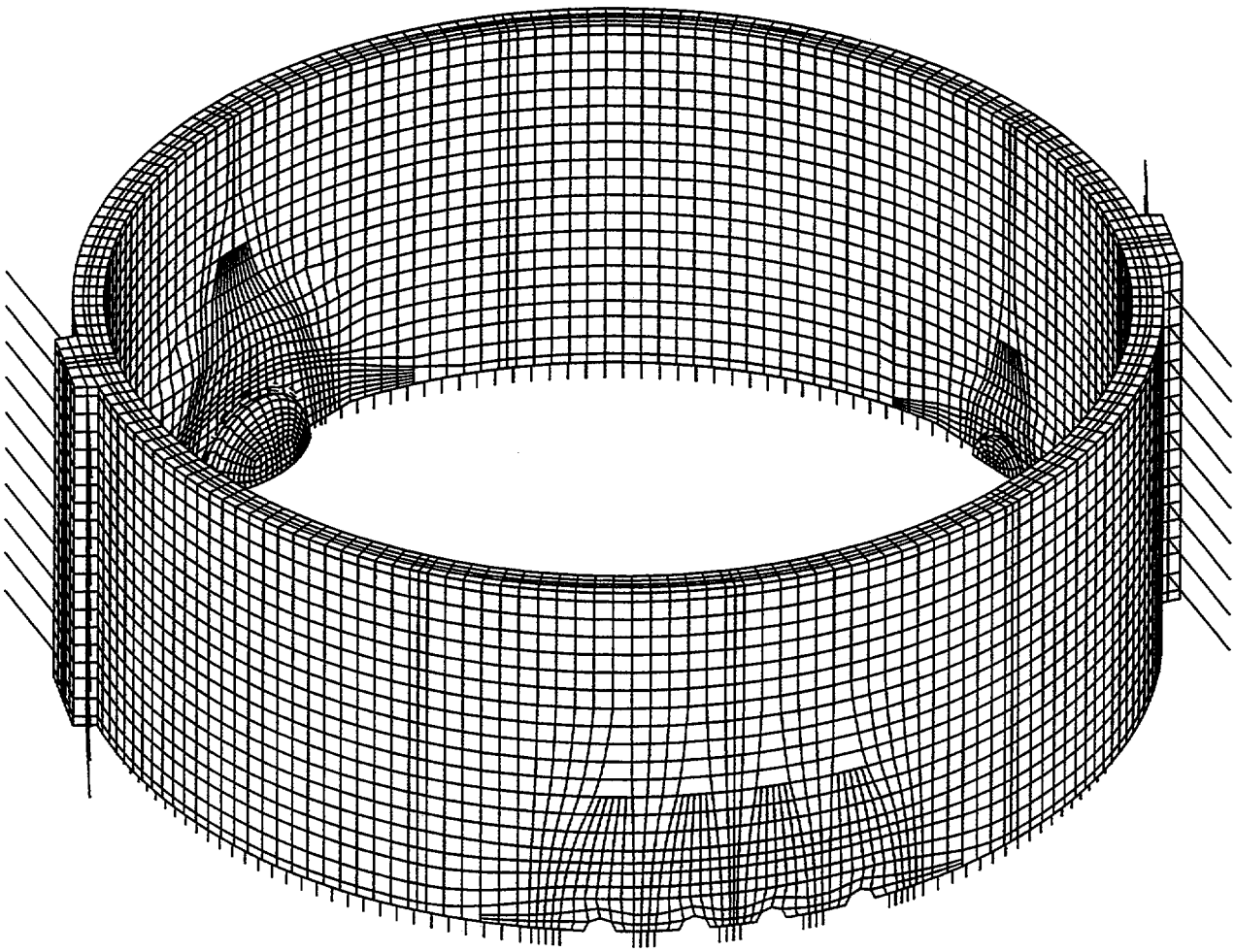

Figure 7-2. Isometric View of 3DCM Model

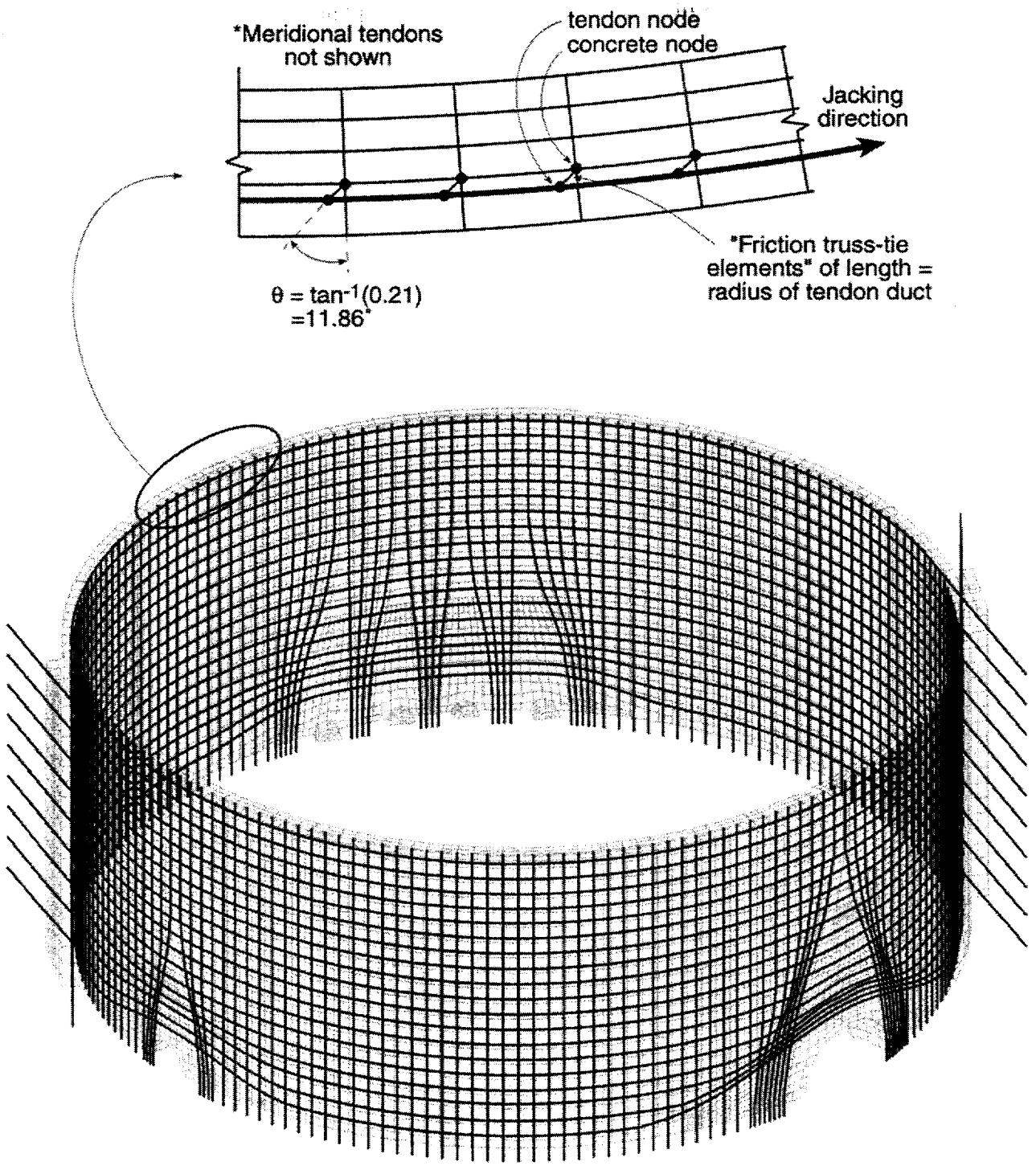


Figure 7-3. Isometric View of 3DCM Model and Tendon Modeling

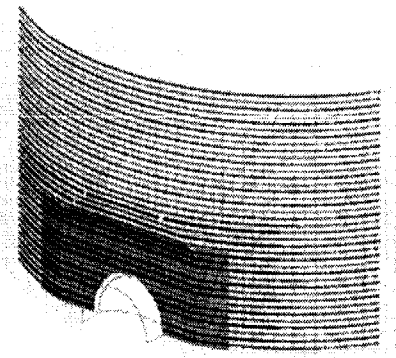

Inner Hoop Rebar

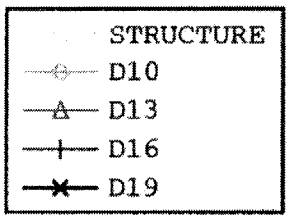


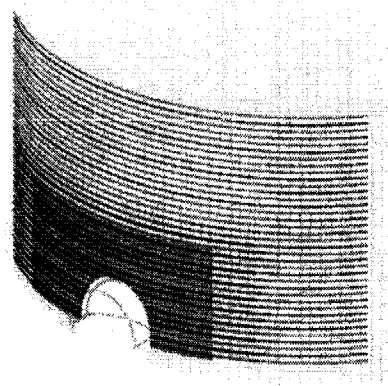

Outer Hoop Rebar

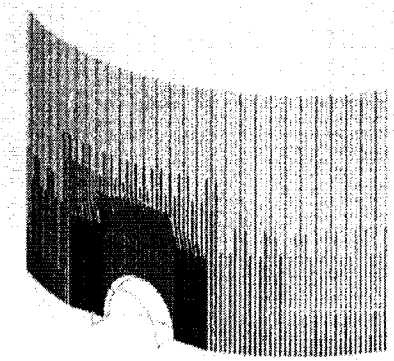

Inner Vertical Rebar

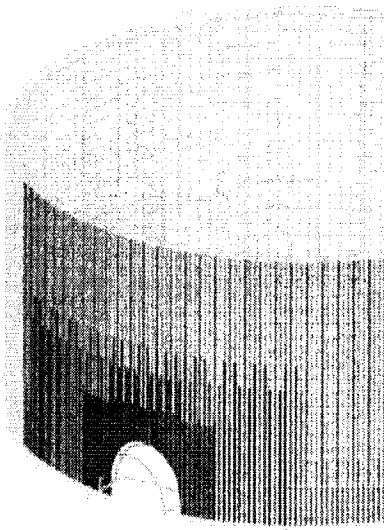

Outer Vertical Rebar

Figure 7-4. 3DCM Rebar for 270° - 360° (E/H)

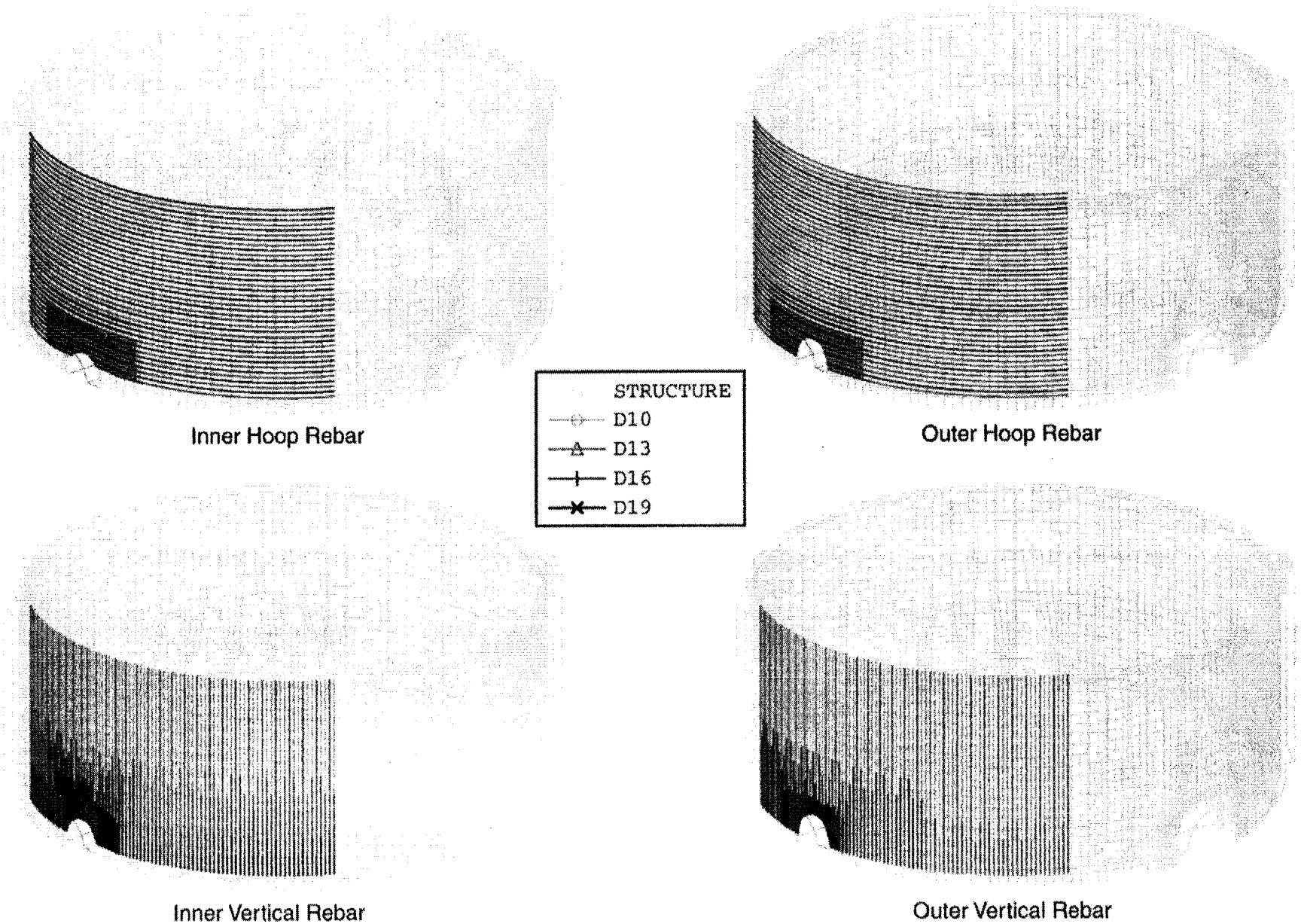


Figure 7-5. 3DCM Rebar for 0° - 90° (A/L)

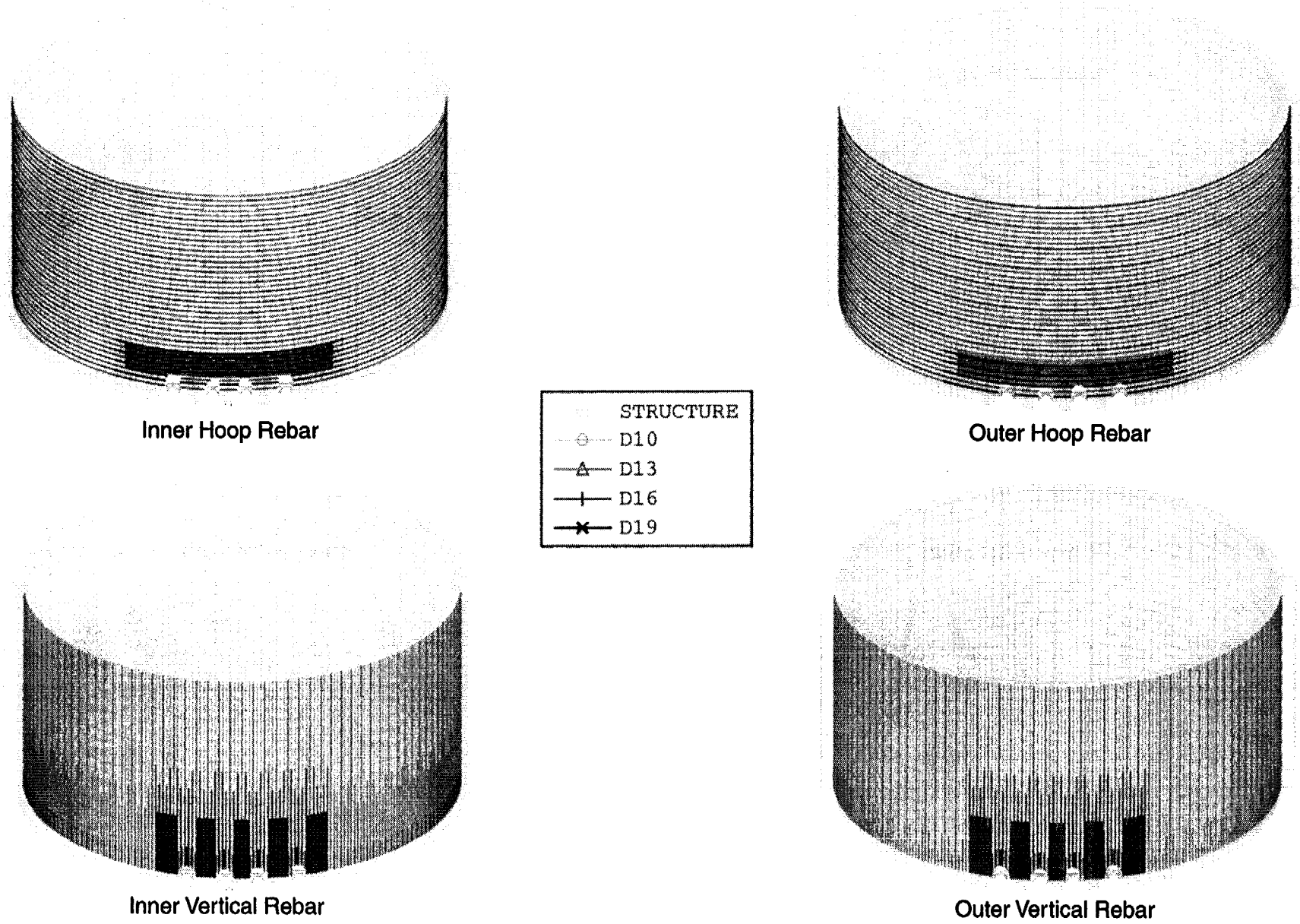


Figure 7-6. 3DCM Rebar for 90° - 270° (M/S)

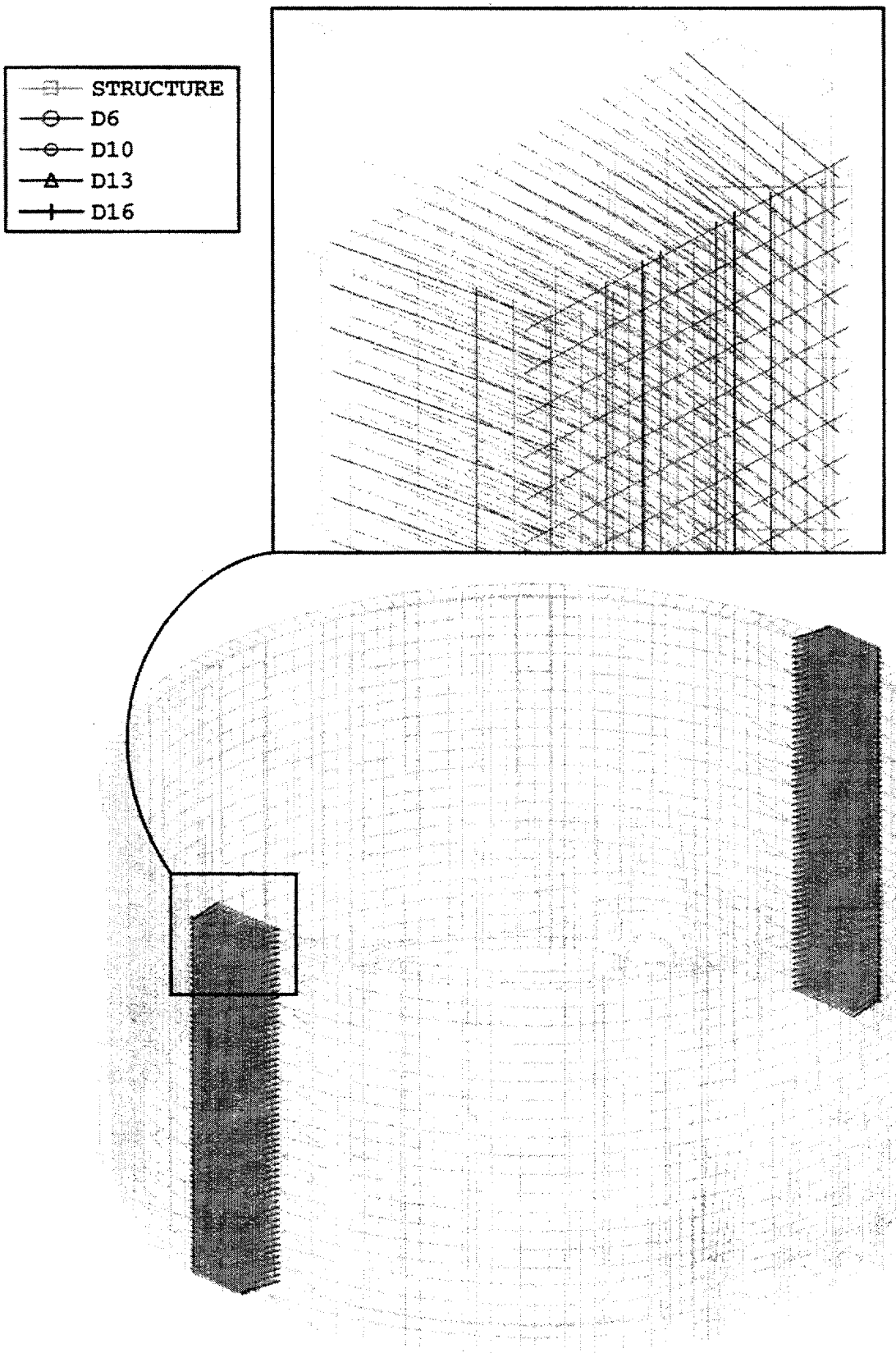


Figure 7-7. 3DCM Rebar for Buttresses

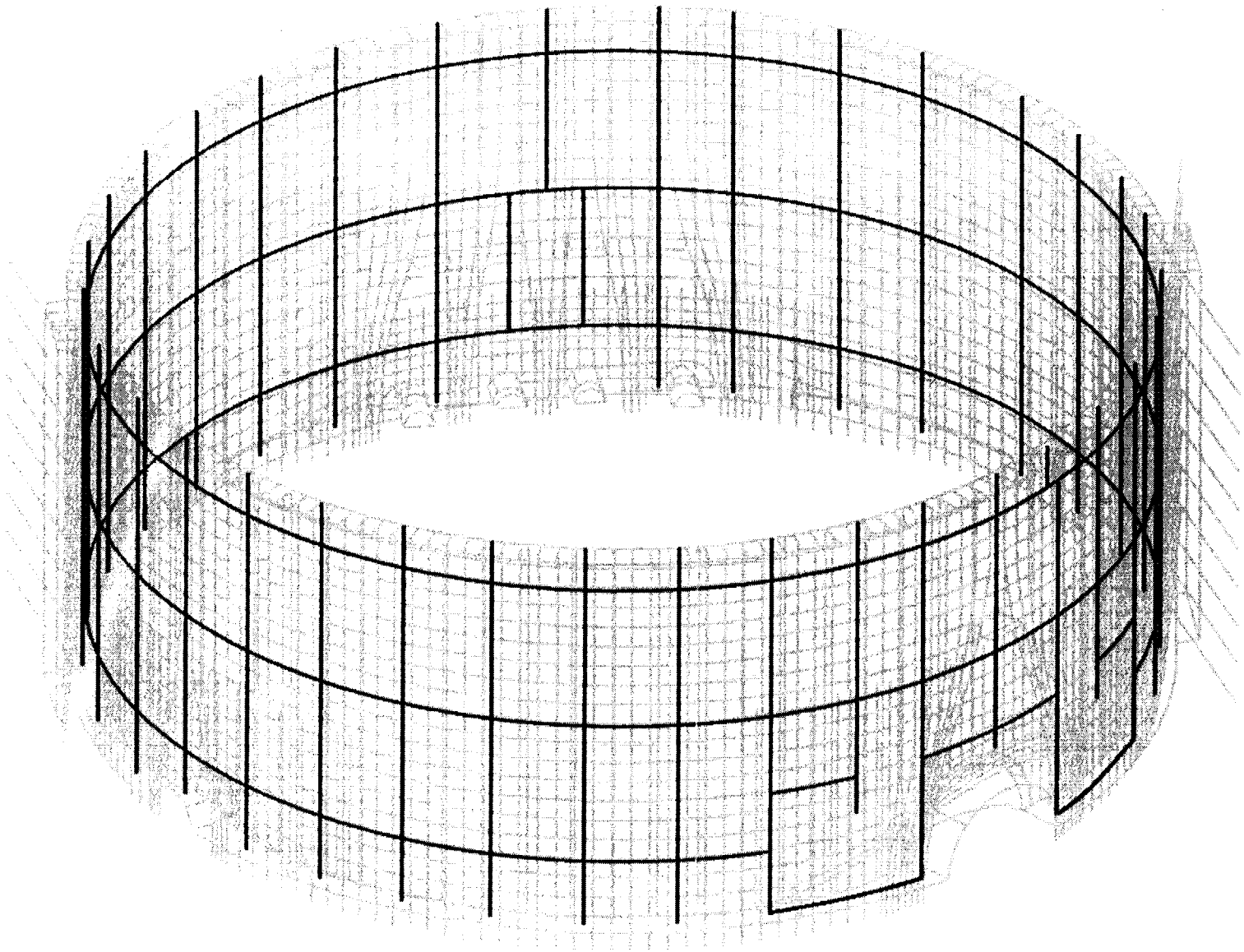

Figure 7-8. Added Rebar Subelements for Idealized Tendon Sheath Support Frame

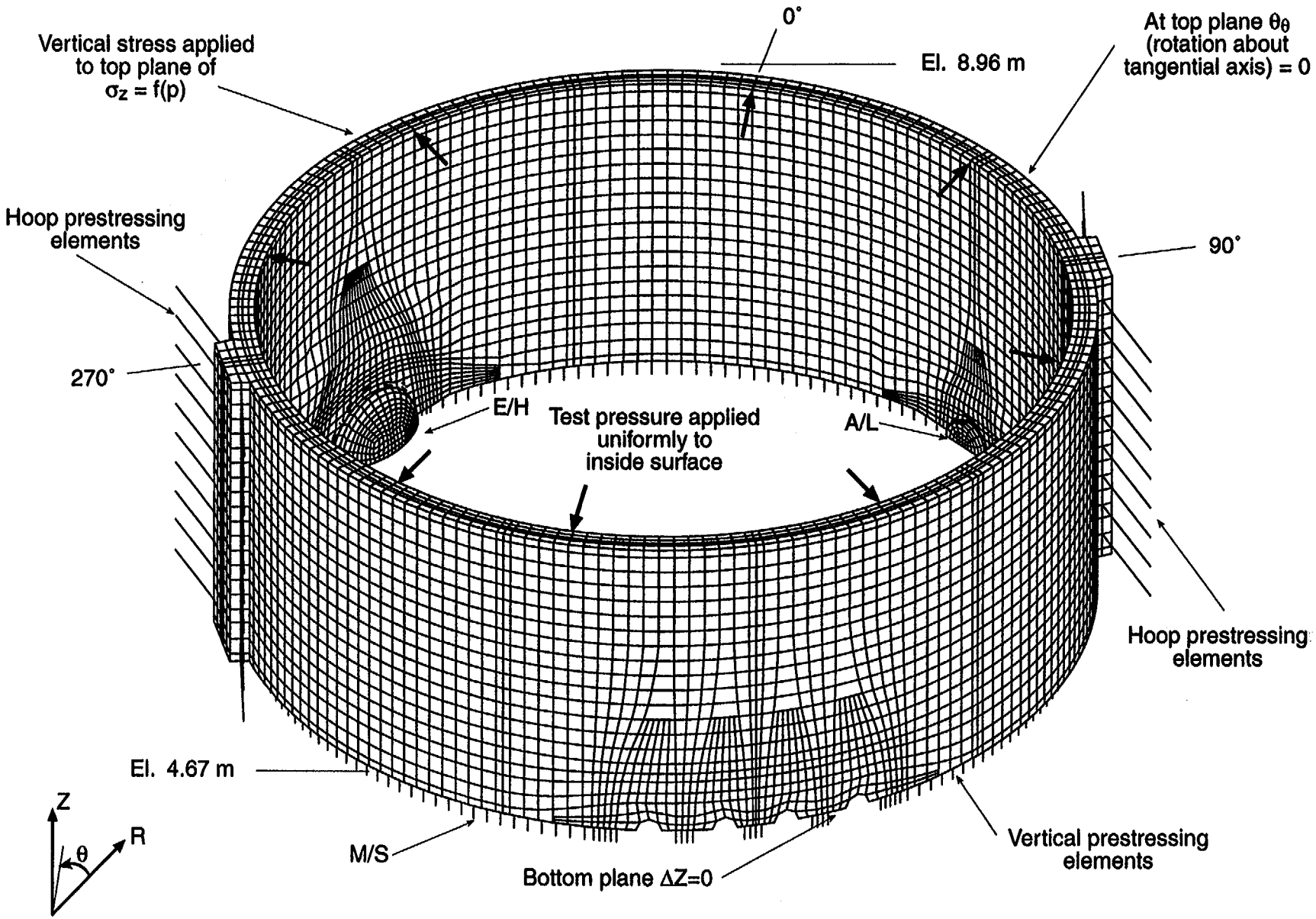


Figure 7-9a. 3DCM Model Vertical Boundary Conditions

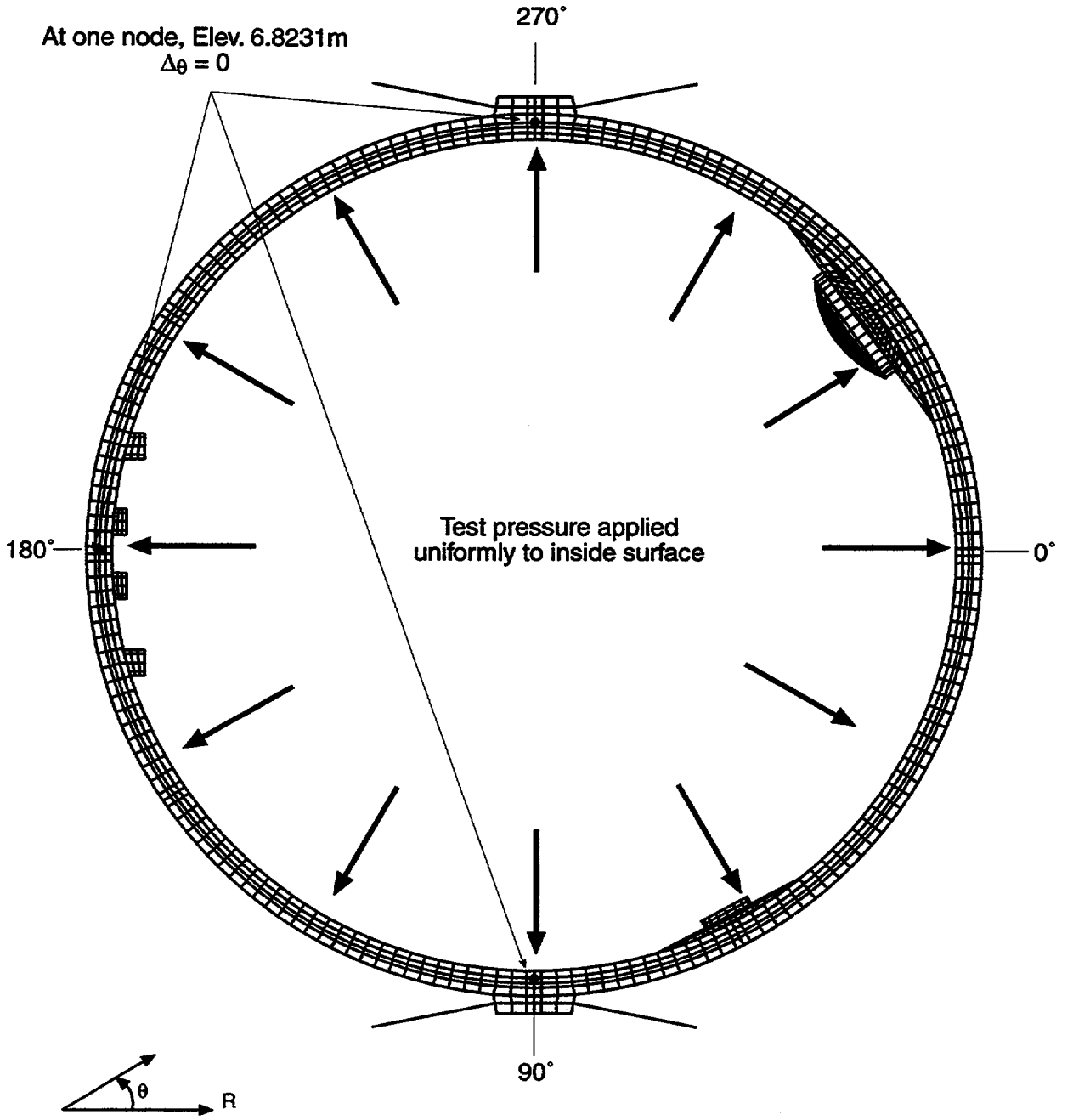


Figure 7-9b. 3DCM Model (Looking Up) Horizontal Boundary Conditions

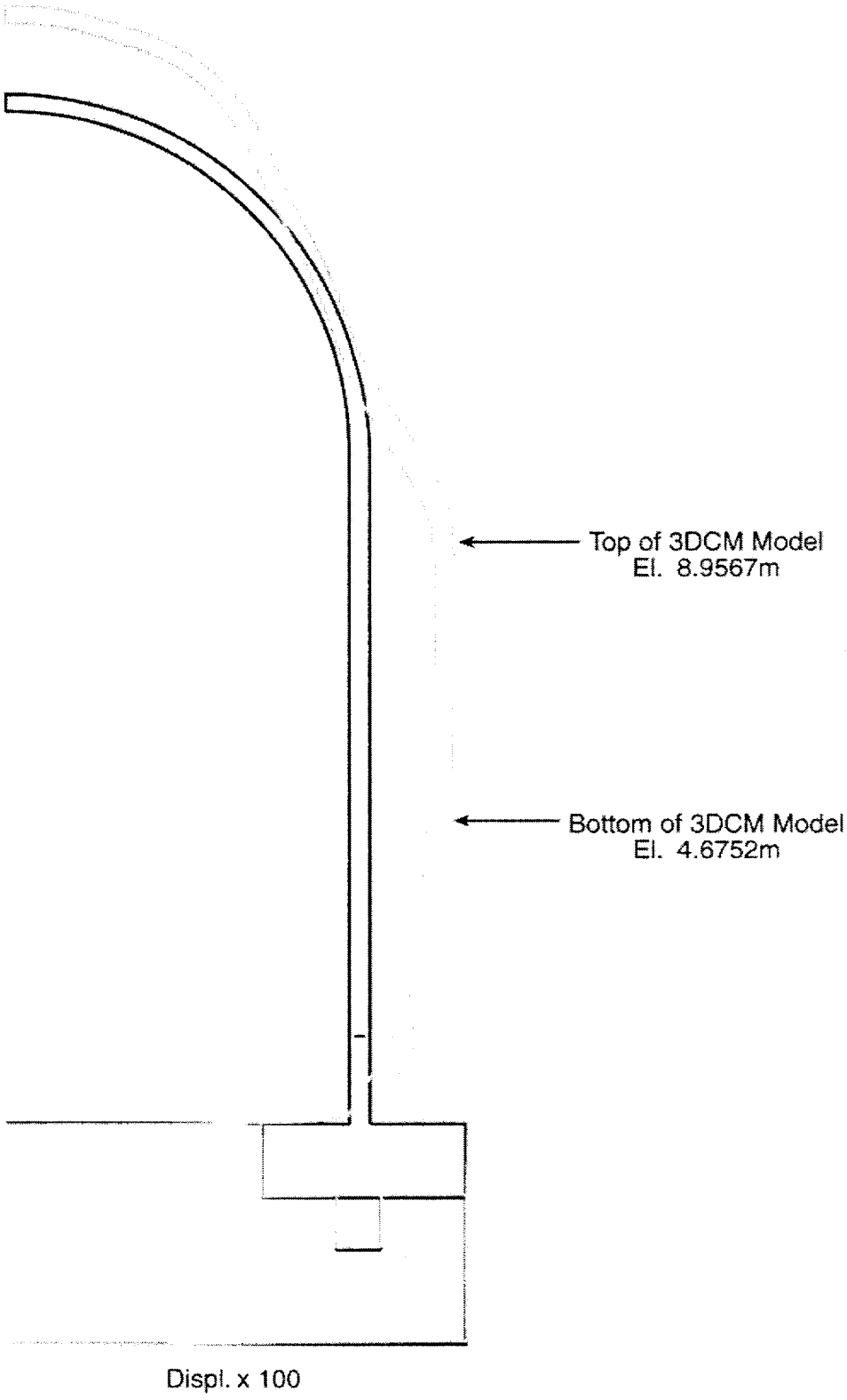


Figure 7-10. Global Axisymmetric Analysis Deformed Shape at P = 3.0 $P_d$ to Demonstrate 3DCM Boundary Conditions

*model14.inp*

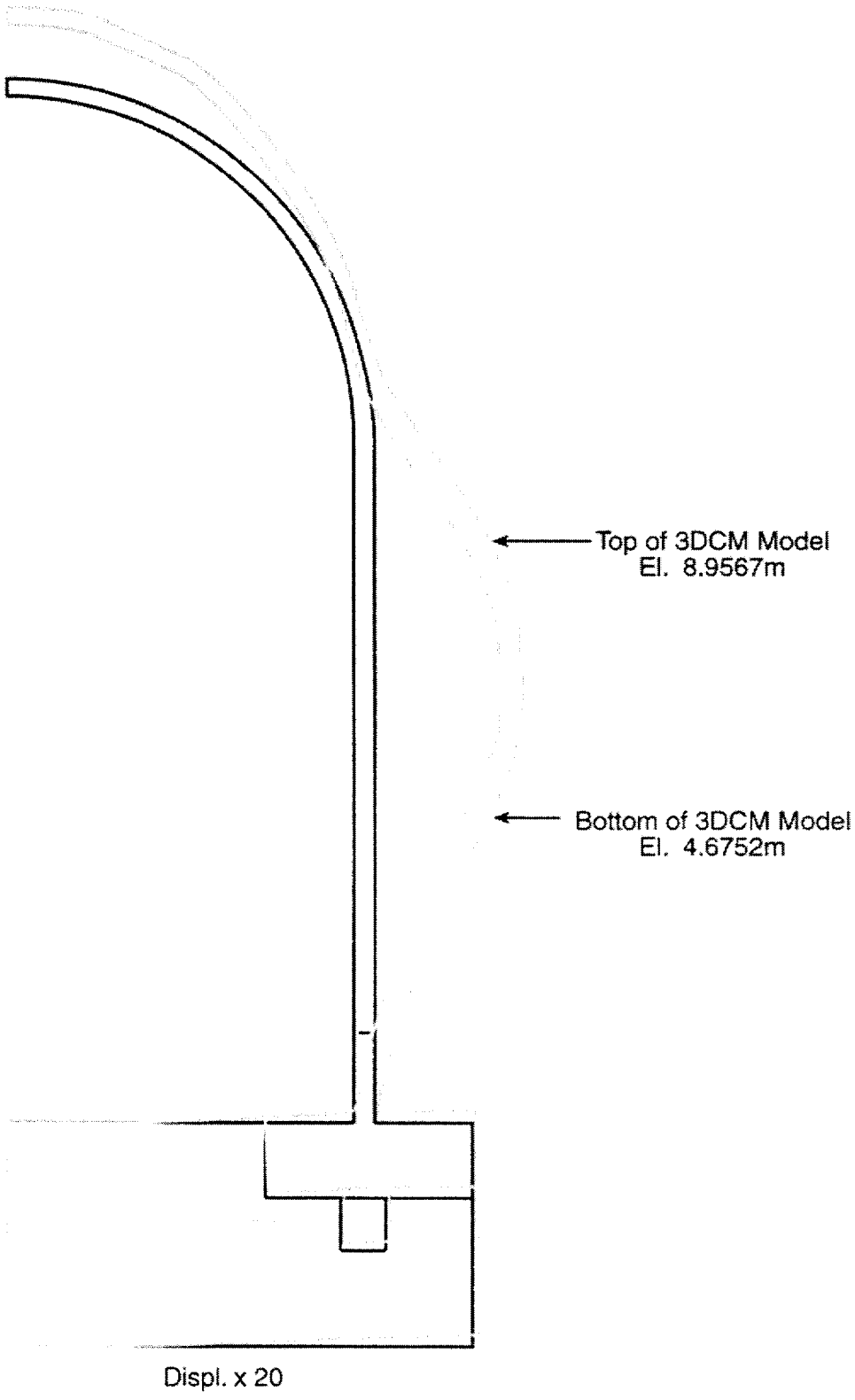


Figure 7-11. Global Axisymmetric Analysis Deformed Shape at P = 3.8 $P_d$ to Demonstrate 3DCM Boundary Conditions

*model14.inp*

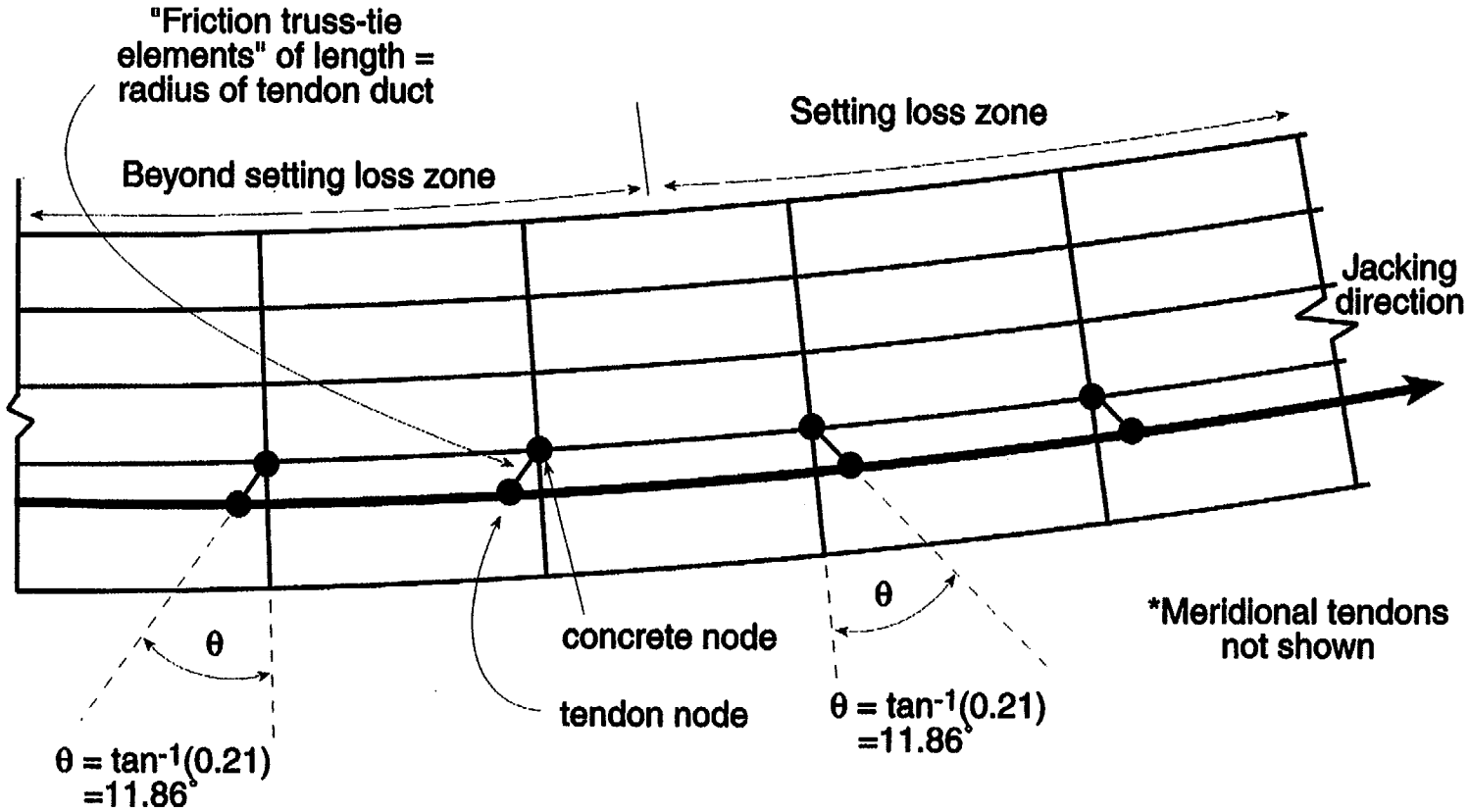


Figure 7-12. Detailed Schematic of Tendon Friction Modeling to Include Setting Losses

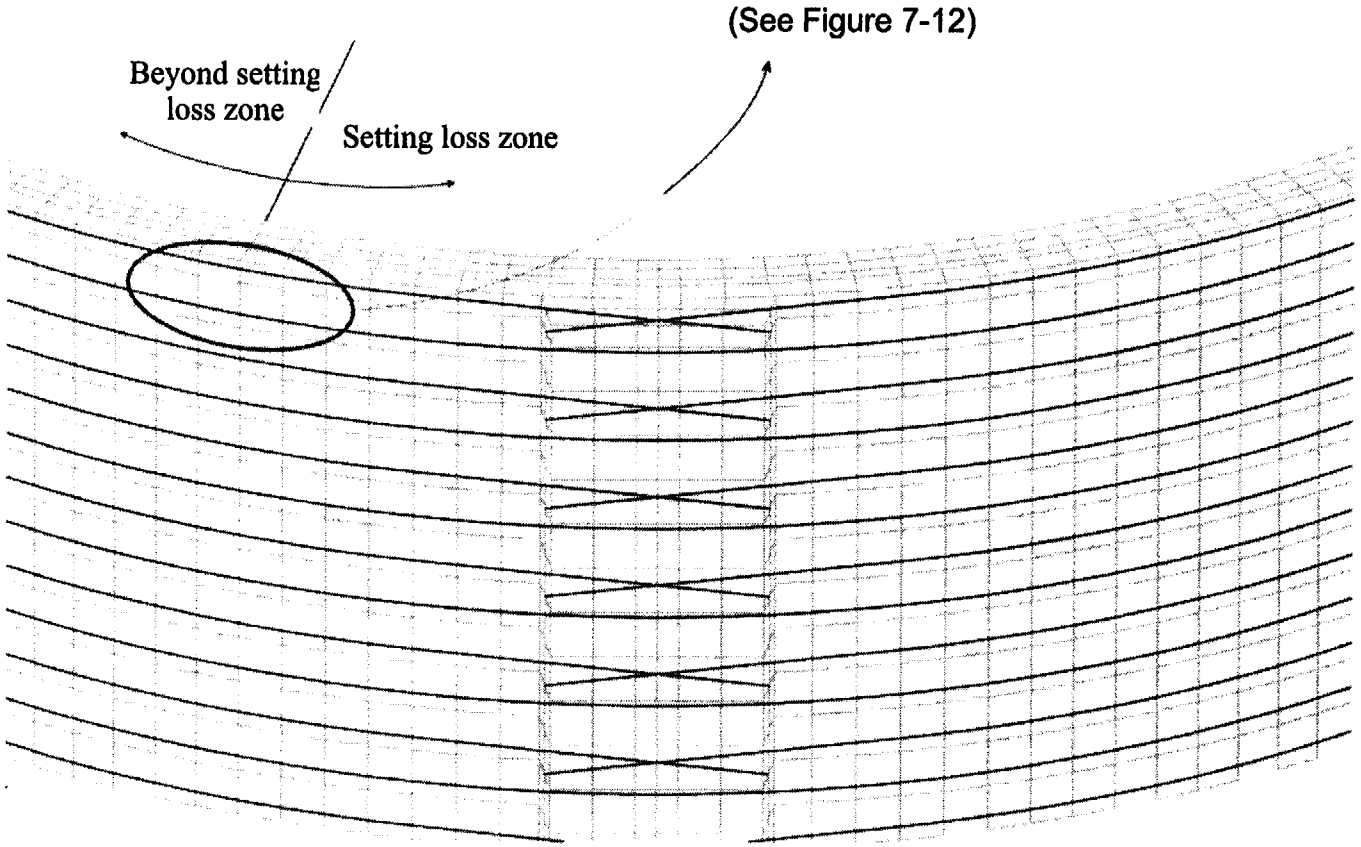


Figure 7-13. Changes to Tendon Friction Modeling to Include Setting Losses

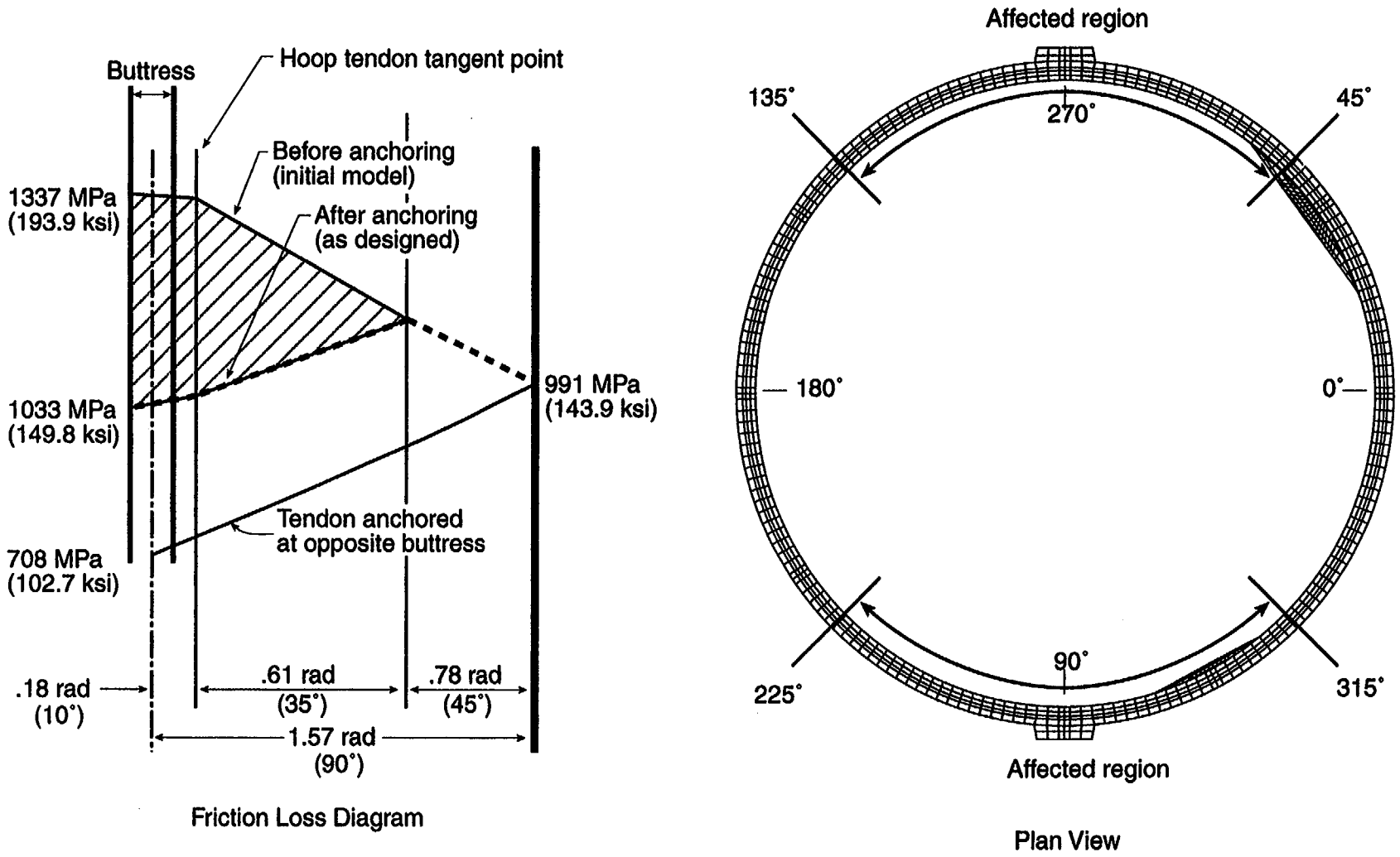


Figure 7-14. As-designed Tendon Anchor Set Losses (Setting Loss Case 1)

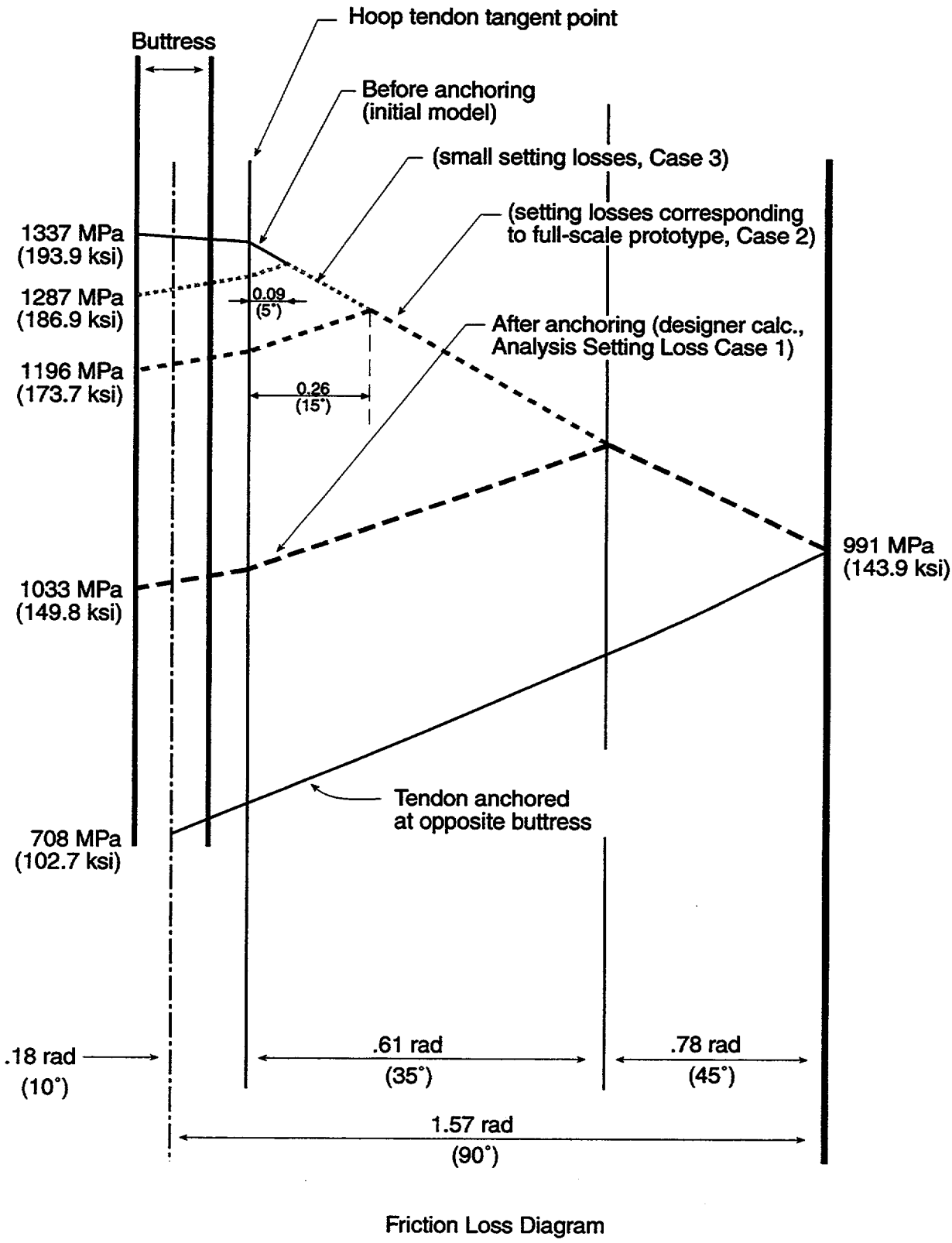


Figure 7-15. Other Setting Loss Cases for Parameter Study

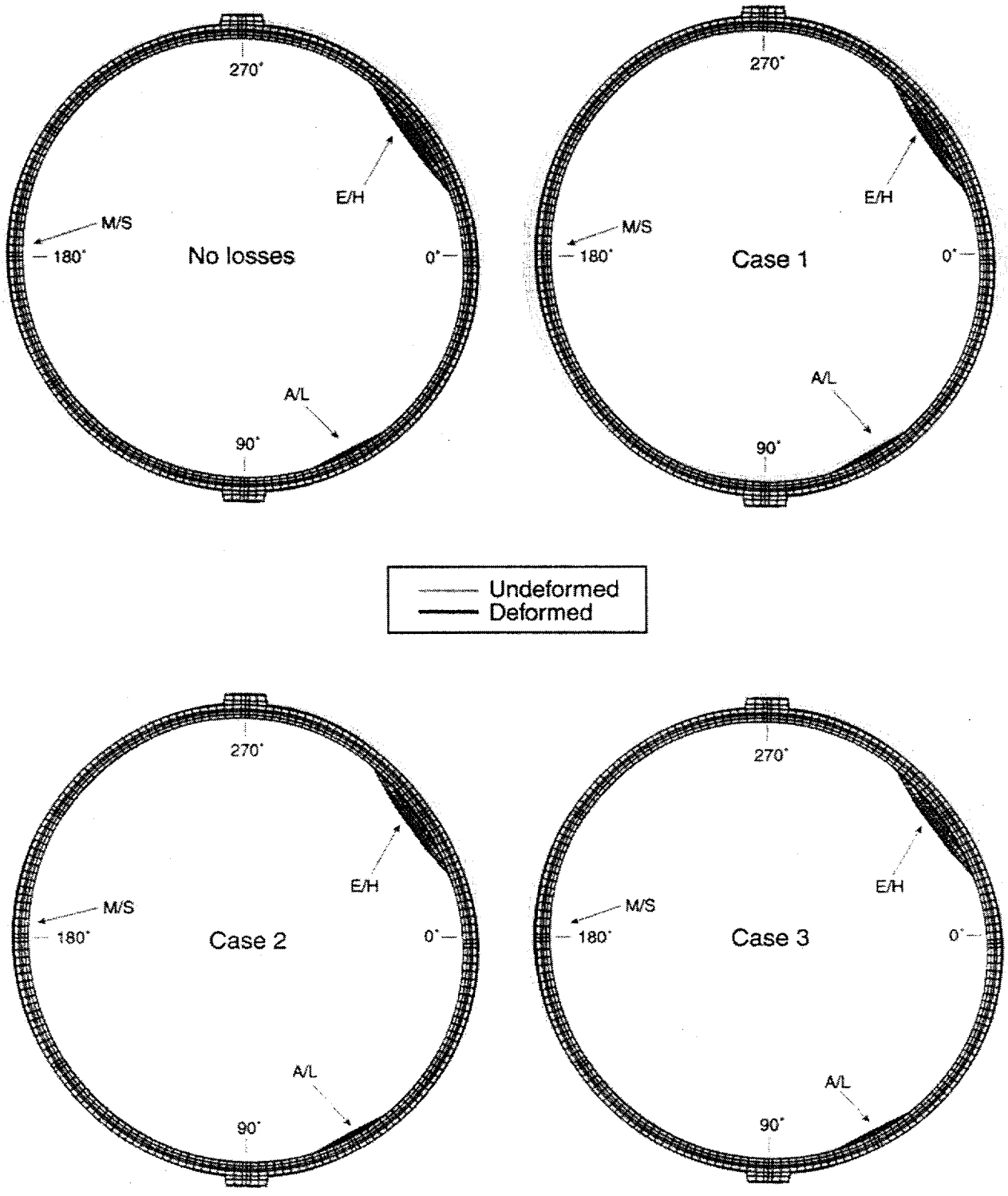


Figure 7-16. 3DCM Model Deformed Shape with Prestress Only (mag. factor = 100x)

*3dcm00.inp, 3dcm15.inp, 3dcm25.inp, 3dcm45.inp*

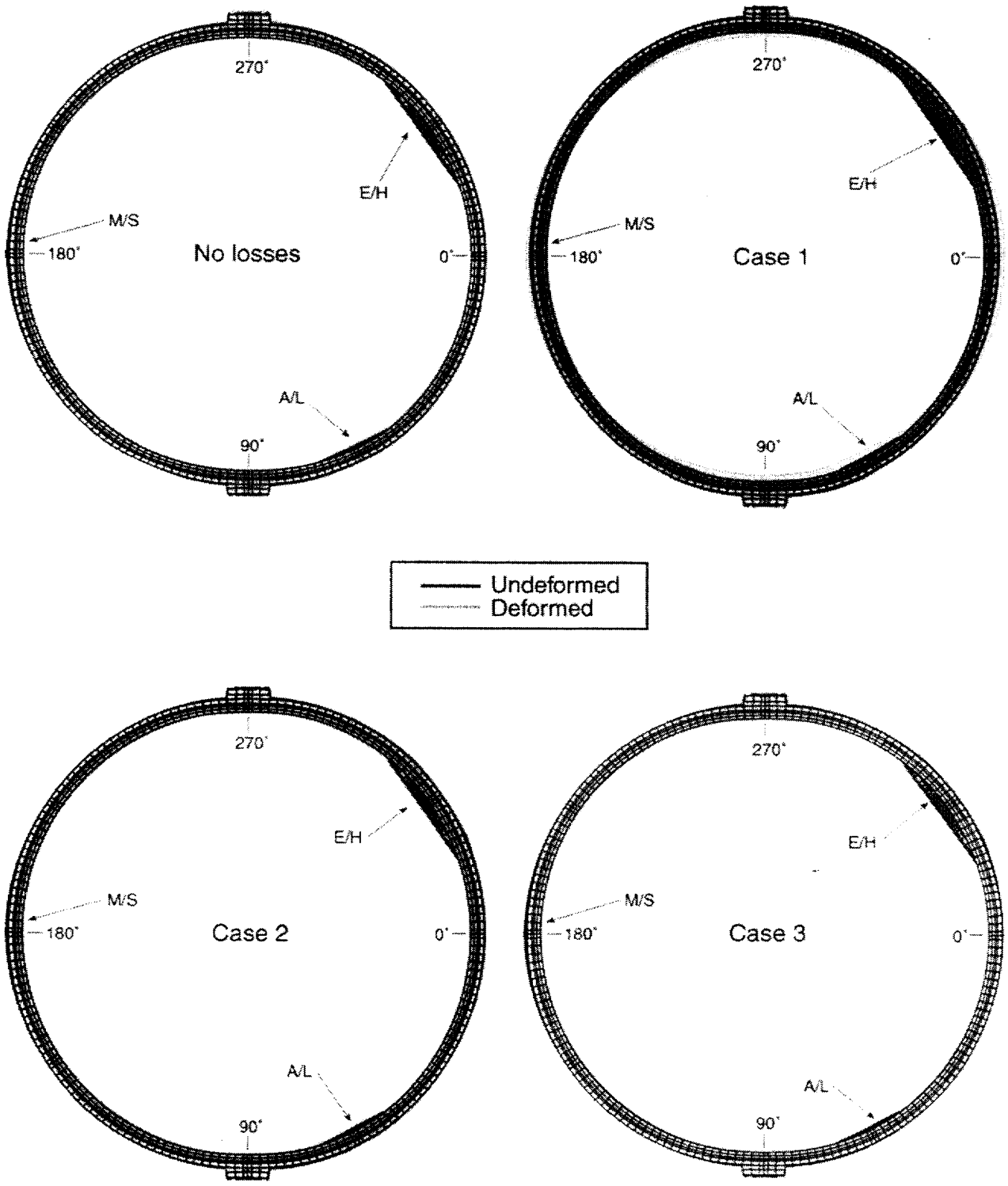


Figure 7-17. 3DCM Model Deformed Shape at Pressure = 1.5 Pd (mag. factor = 100x)

*3dcm00.inp, 3dcm15.inp, 3dcm25.inp, 3dcm45.inp*

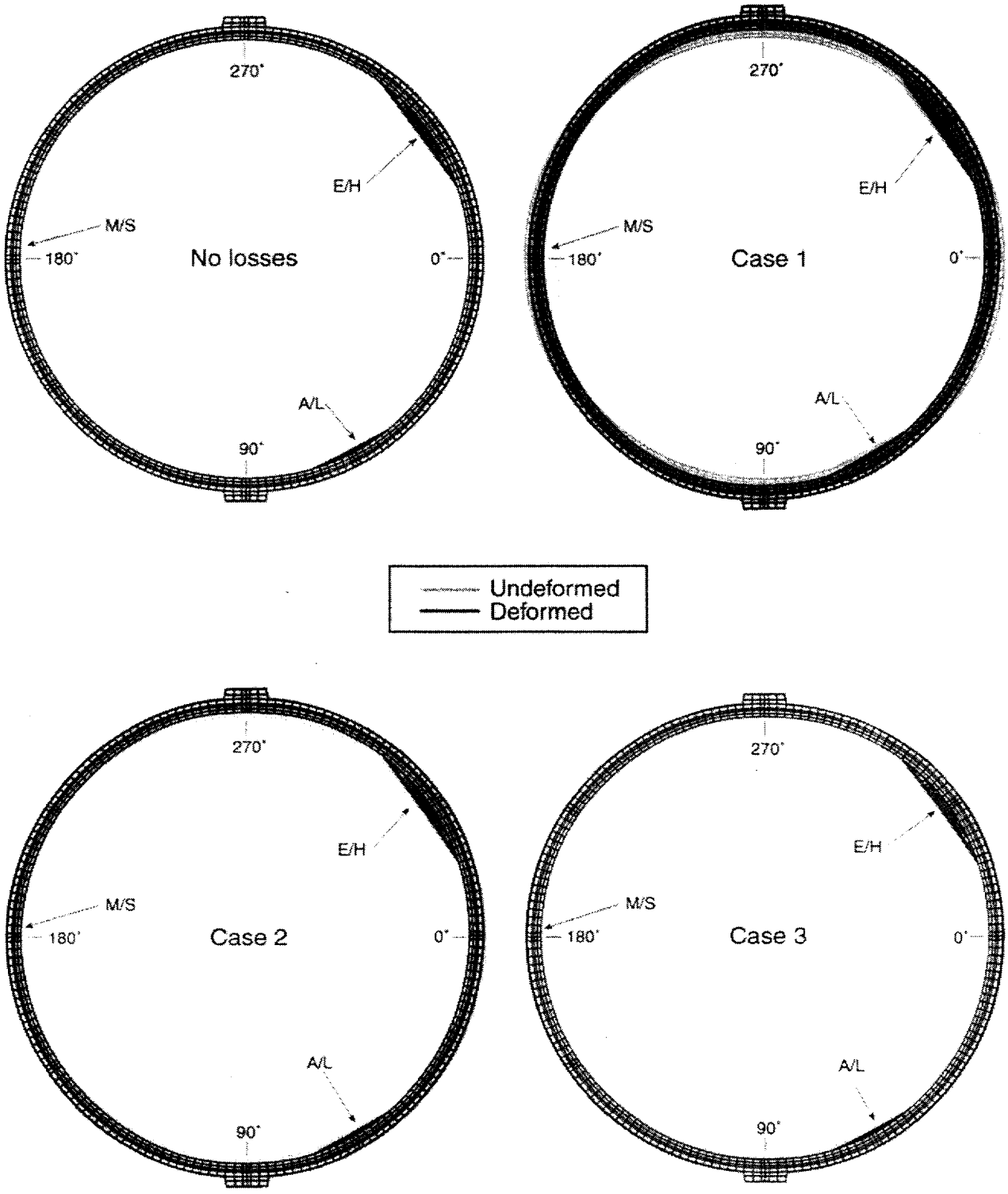


Figure 7-18. 3DCM Model Deformed Shape at Pressure = 2.0 Pd (mag. factor = 10x)
*3dcm00.inp, 3dcm15.inp, 3dcm25.inp, 3dcm45.inp*

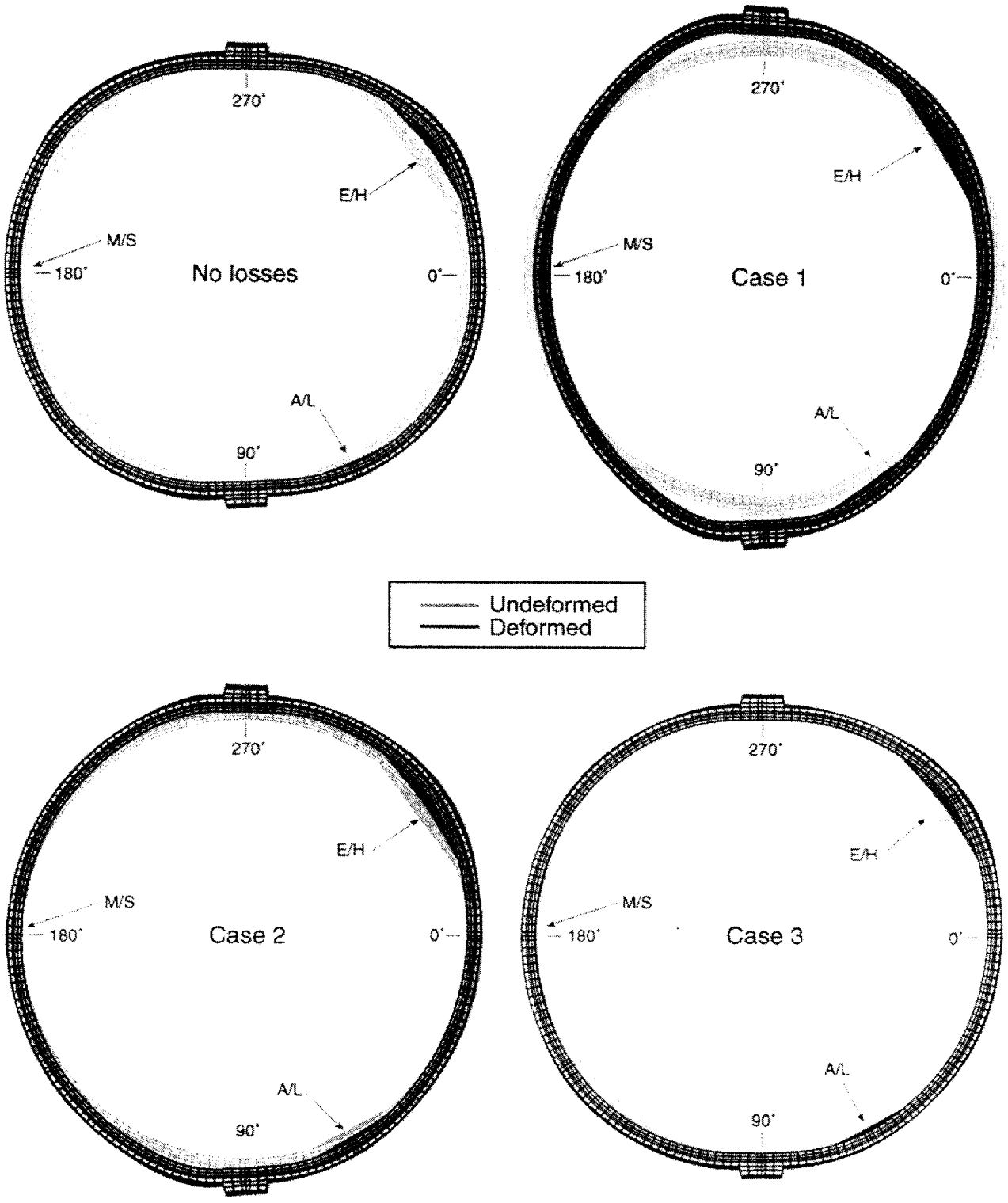


Figure 7-19. 3DCM Model Deformed Shape at Pressure = 3.0 Pd (mag. factor = 10x)

*3dcm00.inp, 3dcm15.inp, 3dcm25.inp, 3dcm45.inp*

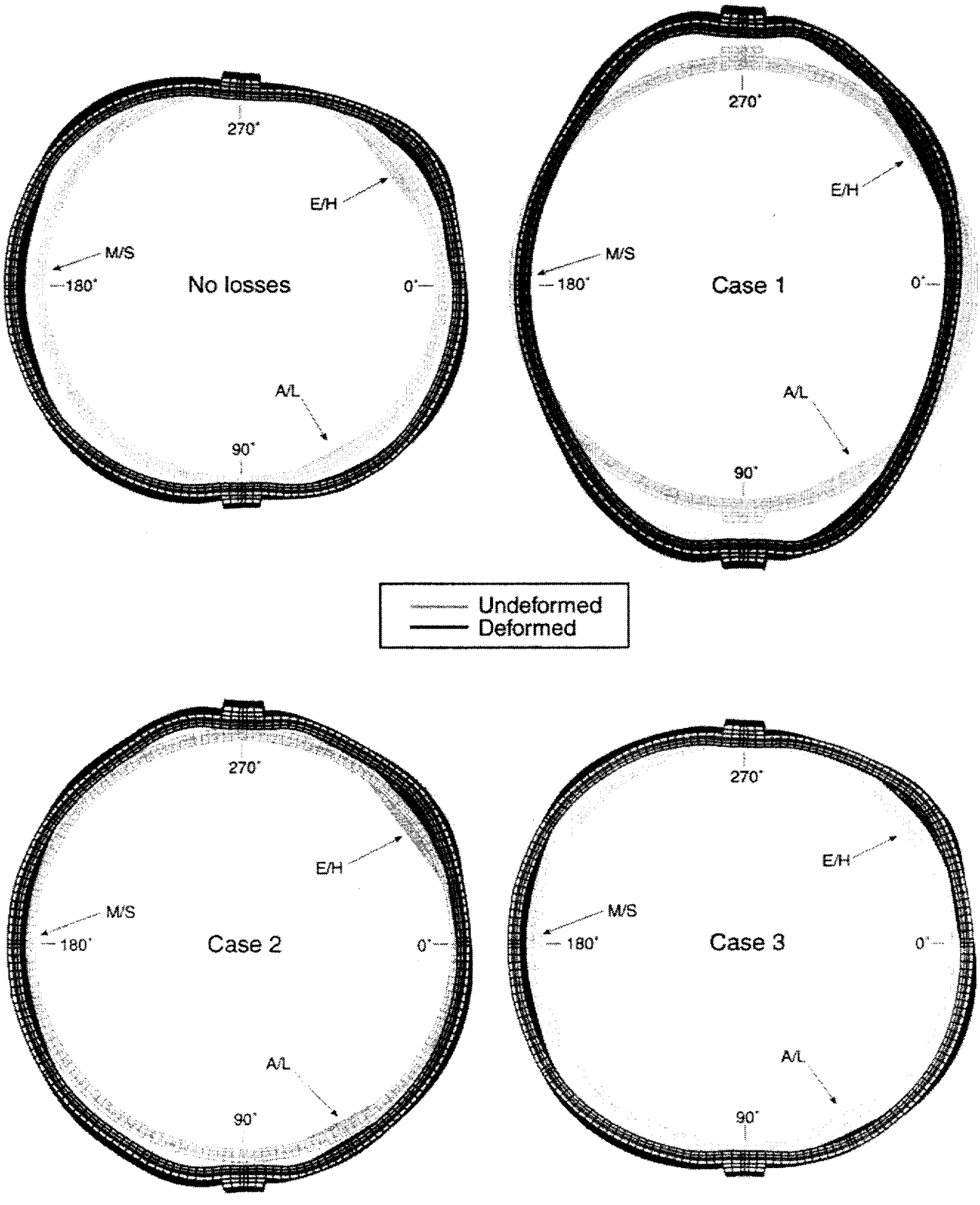


Figure 7-20. 3DCM Model Deformed Shape at Pressure = 3.5 Pd (mag. factor = 10x)

*3dcm00.inp, 3dcm15.inp, 3dcm25.inp, 3dcm45.inp*

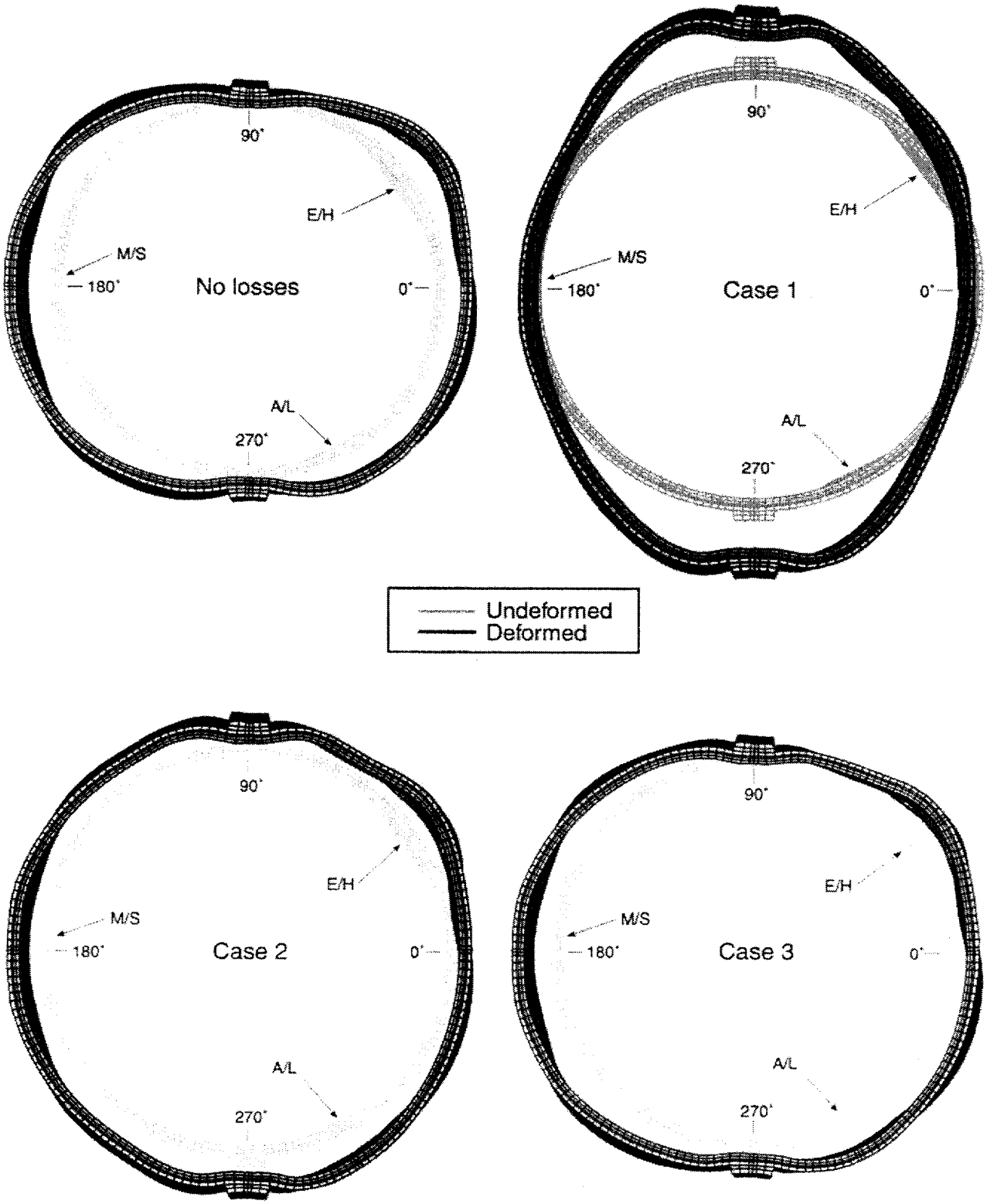


Figure 7-21. 3DCM Model Deformed Shape at Pressure = 3.8 Pd (mag. factor = 10x)

*3dcm00.inp, 3dcm15.inp, 3dcm25.inp, 3dcm45.inp*

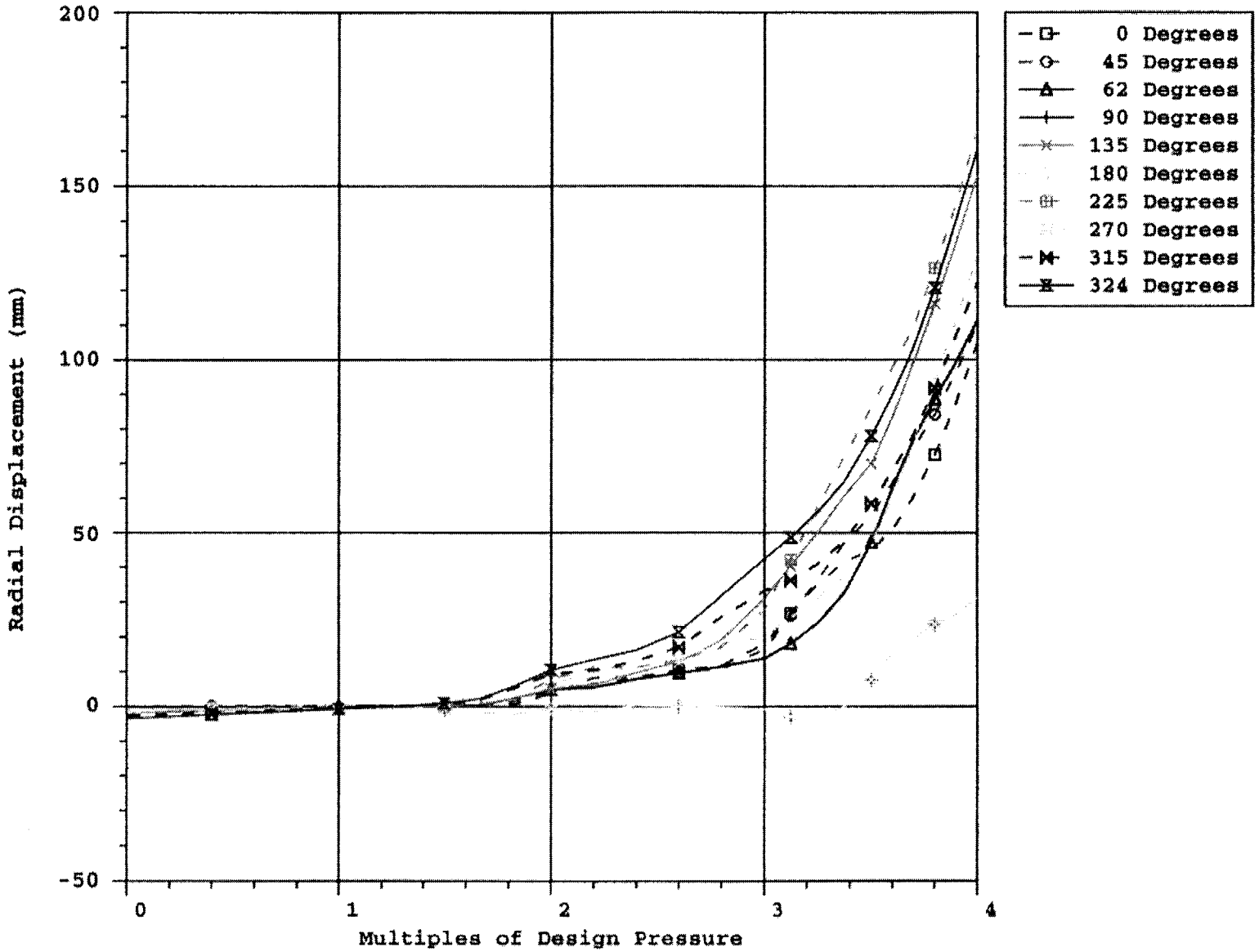


Figure 7-22a. 3DCM Model with No Setting Losses, Radial Displacement Comparisons vs. Pressure at Elevation 4.6725 m

*3dcm00.inp*

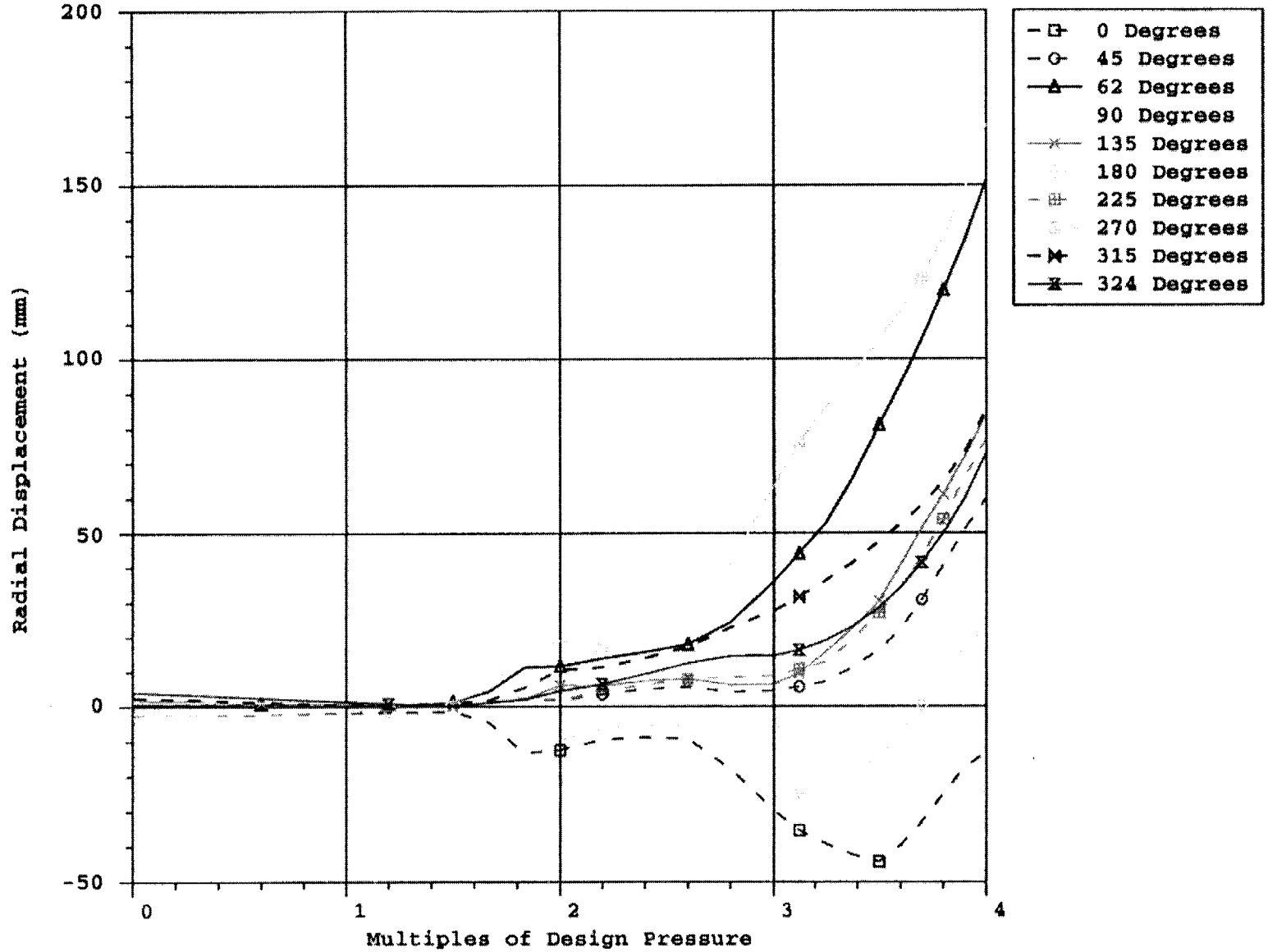


Figure 7-22b. 3DCM Case 1 Model, Radial Displacement Comparisons vs. Pressure at Elevation 4.6752 m

*3dcm45.inp*

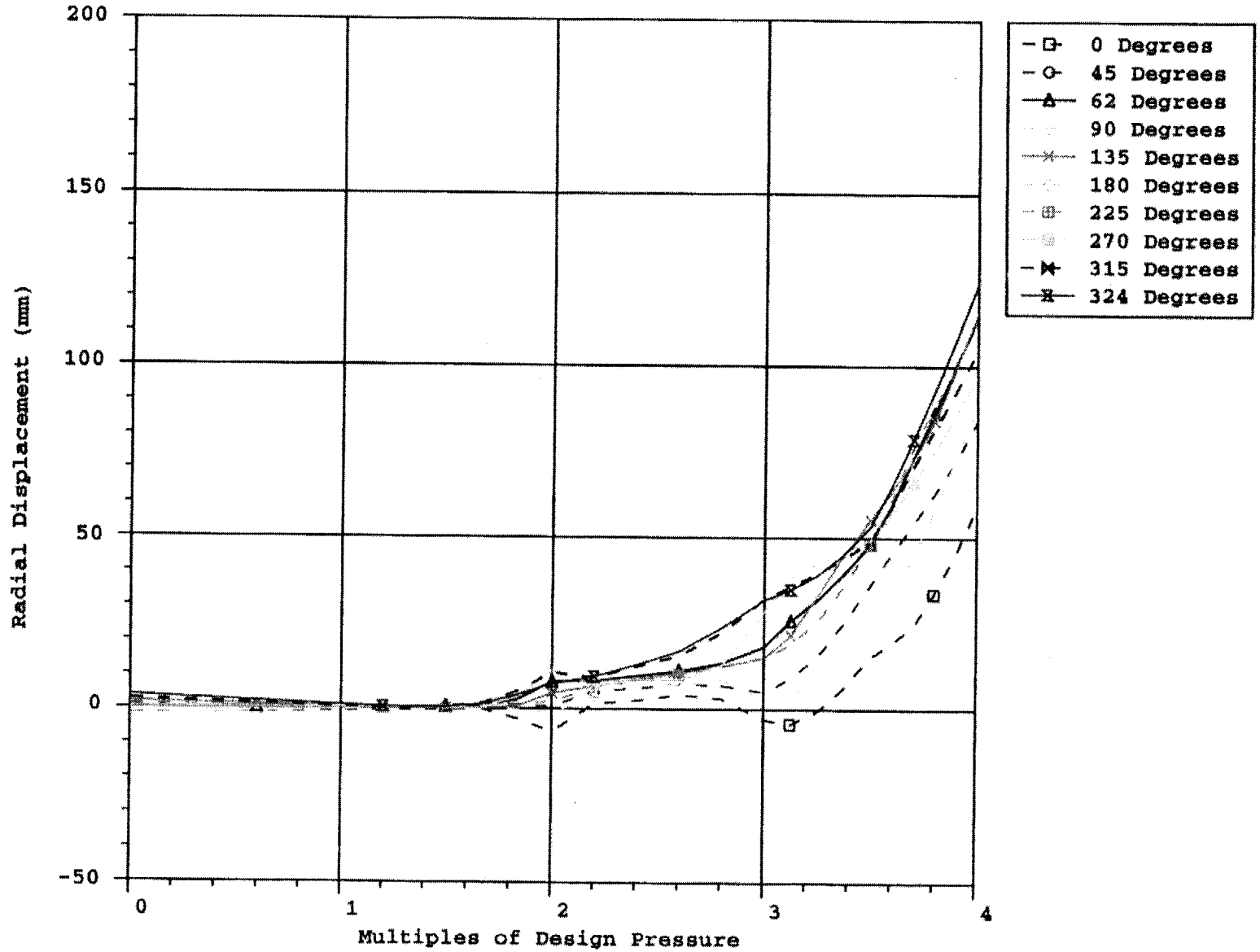


Figure 7-22c. 3DCM Case 2 Model, Radial Displacement Comparisons vs. Pressure at Elevation 4.6752 m

*3dcm25.inp*

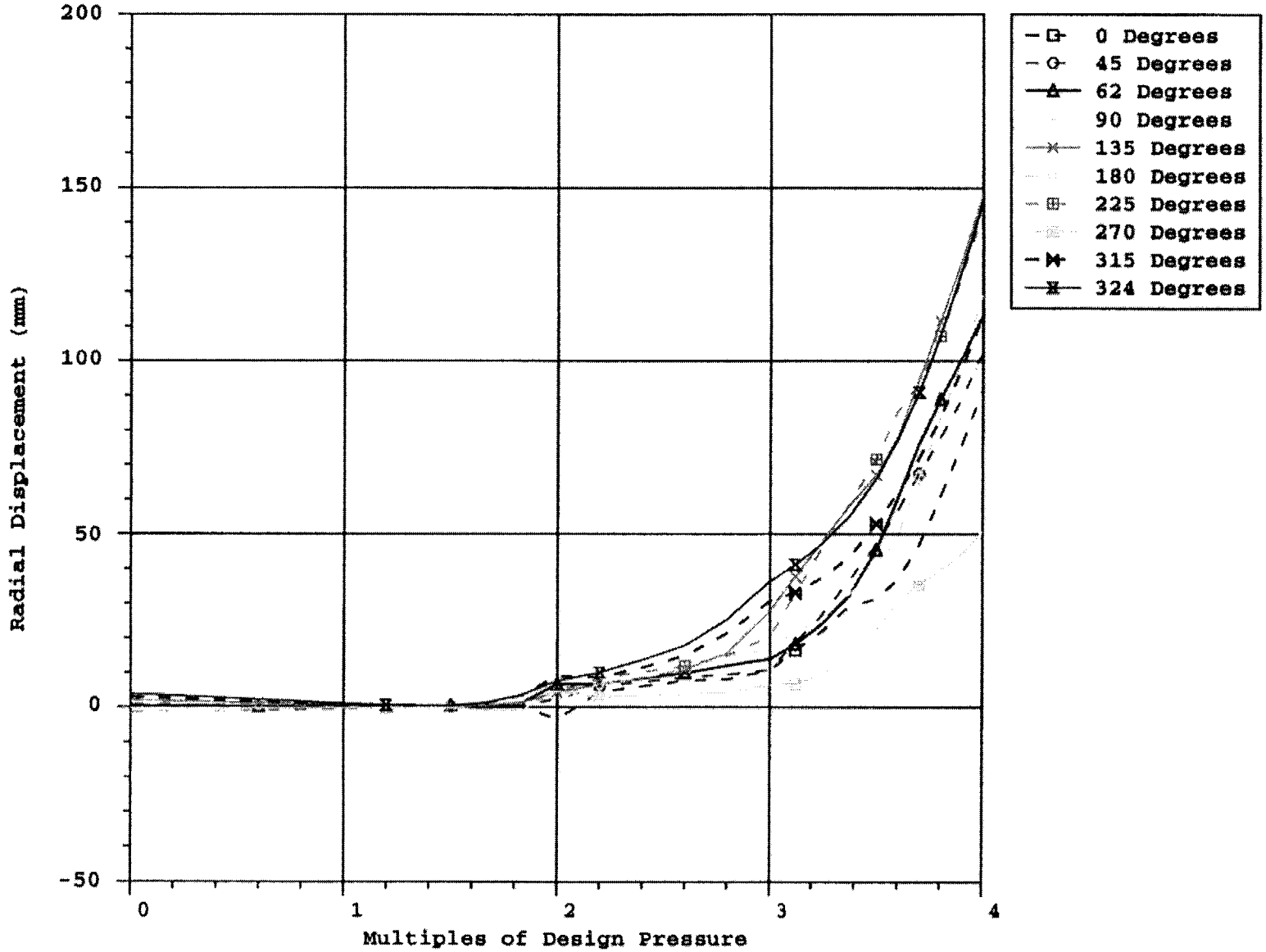


Figure 7-22d. 3DCM Case 3 Model, Radial Displacement Comparisons vs. Pressure at Elevation 4.6752 m

*3dcm15.inp*

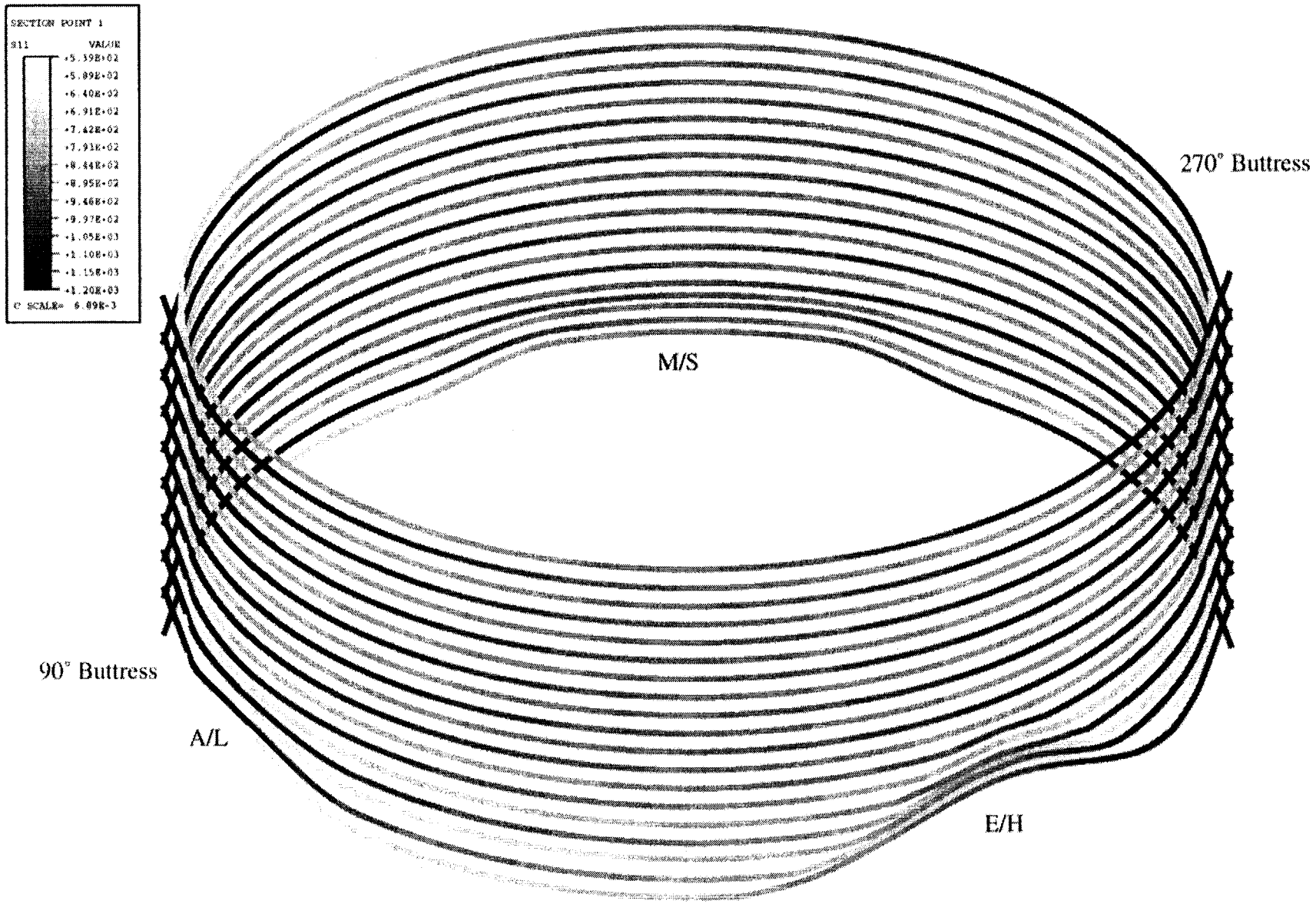


Figure 7-23. Stress Contours in Hoop Tendons After Prestress

*3dcm.inp*

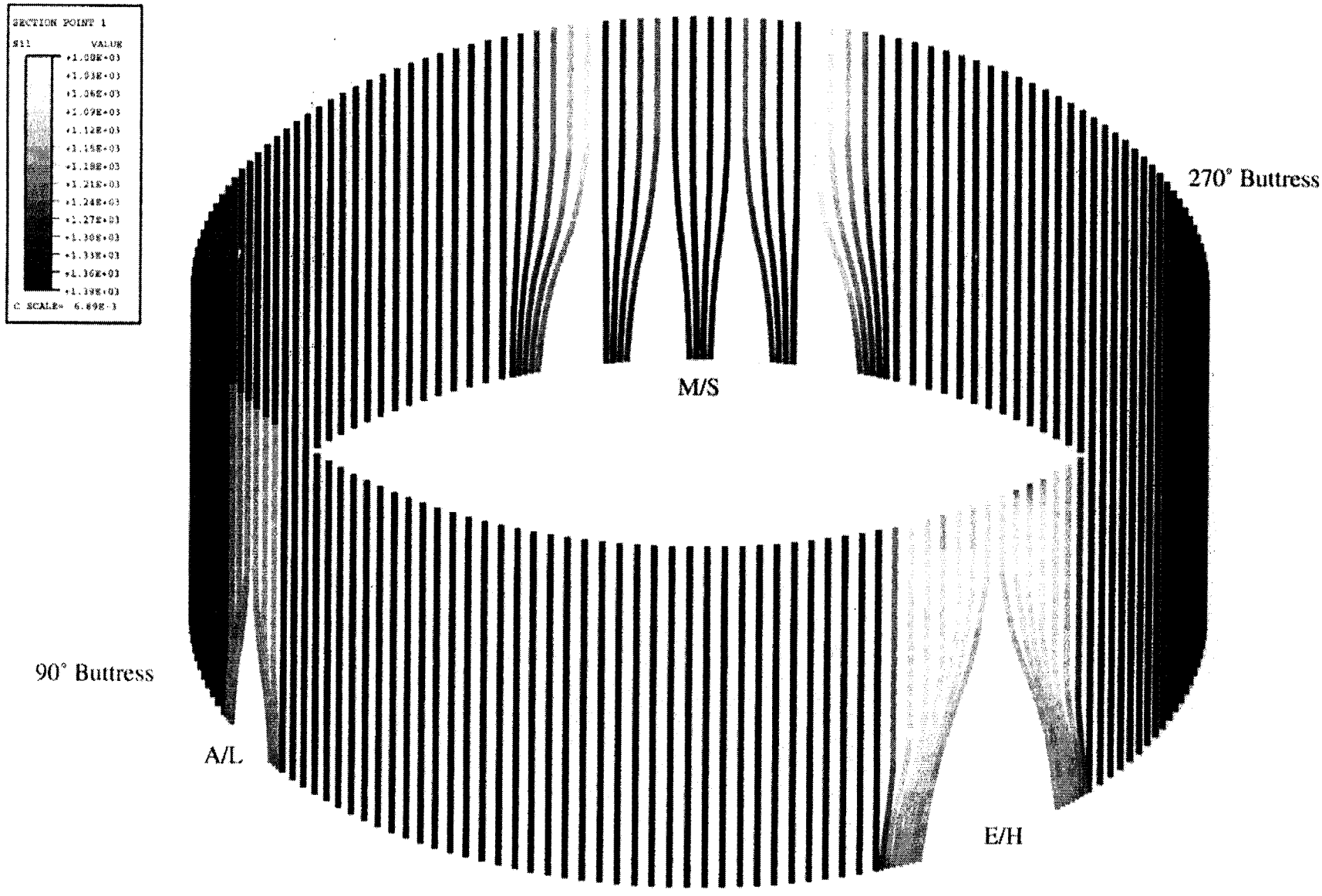


Figure 7-24. Stress Contours in Meridional Tendons After Prestress

*3dcm.inp*

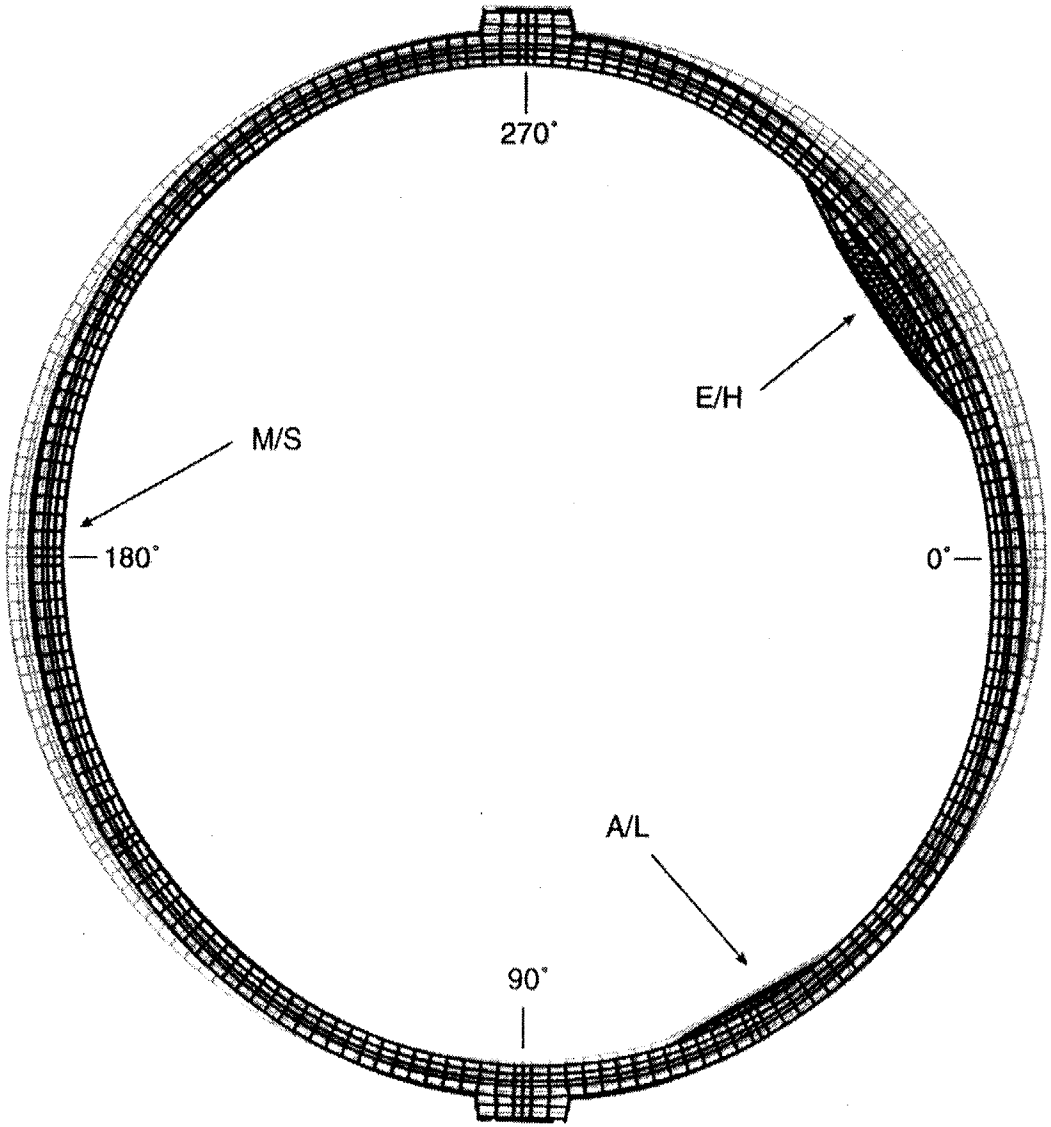


Figure 7-25. 3DCM Deformed Shape at Prestress (mag. factor = 100x)



*3dcm.inp*

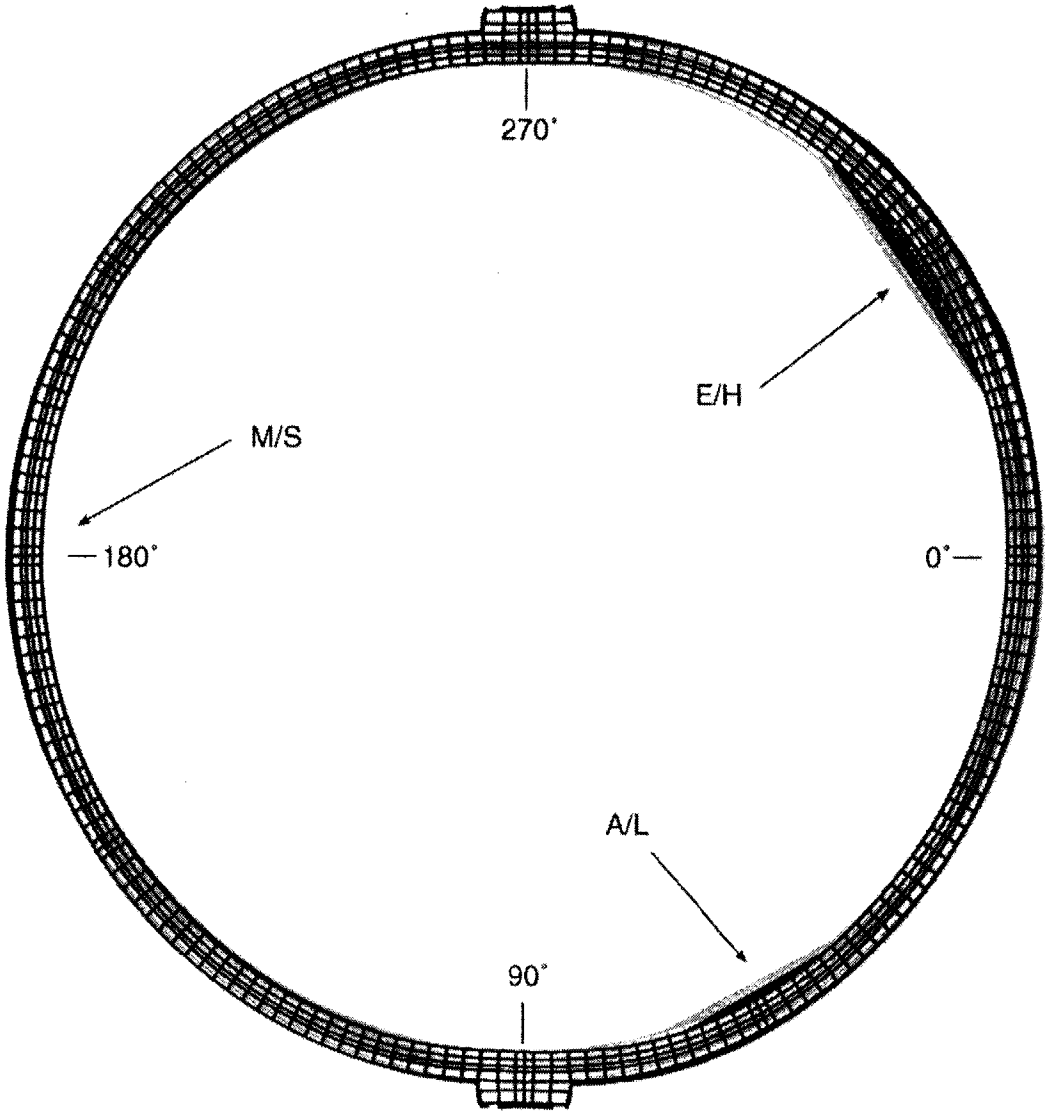


Figure 7-26. 3DCM Deformed Shape at P = 1.5 $P_d$ (mag. factor = 100x)

*3dcm.inp*

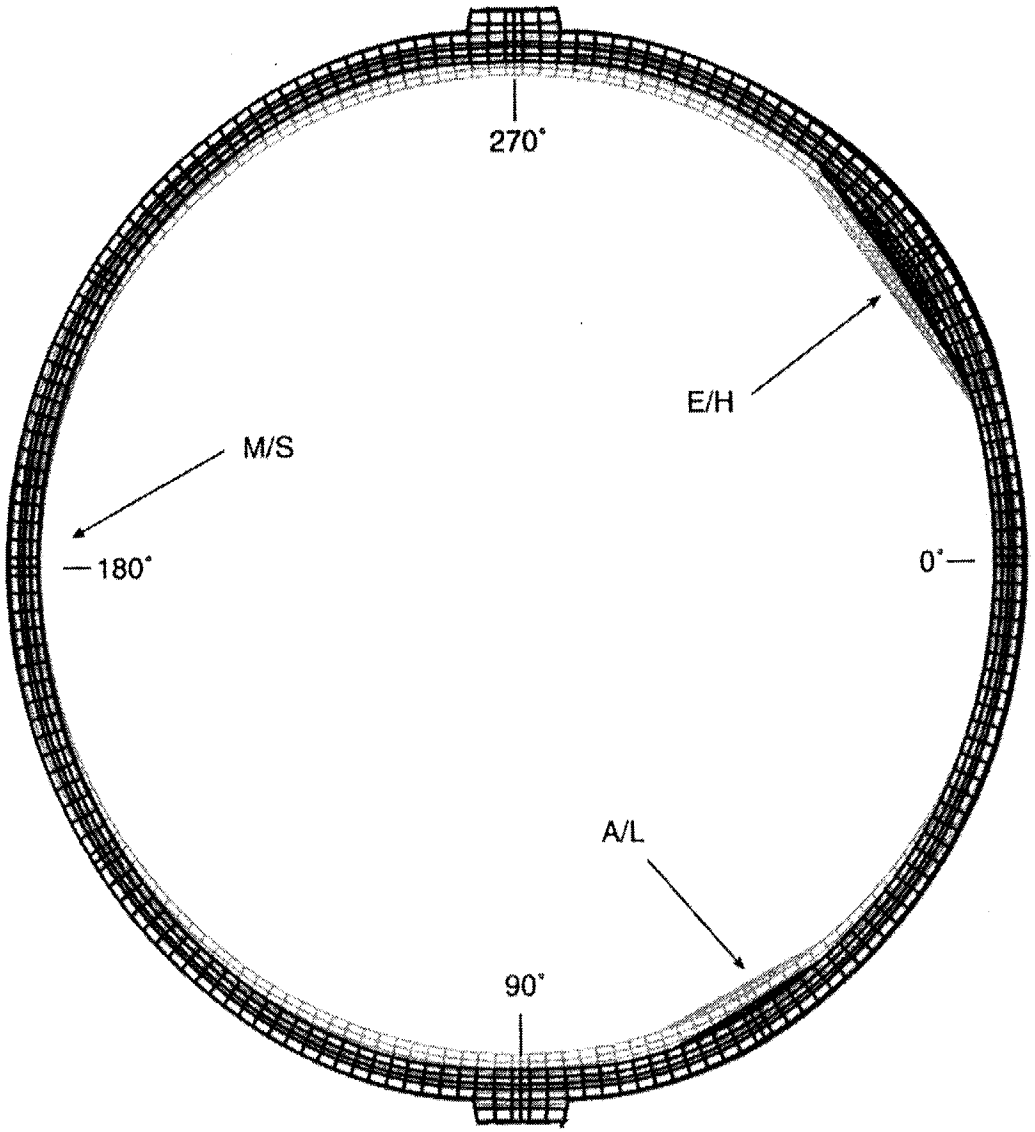


Figure 7-27. 3DCM Deformed Shape at P = 2.0 $P_d$ (mag. factor = 25x)

*3dcm.inp*

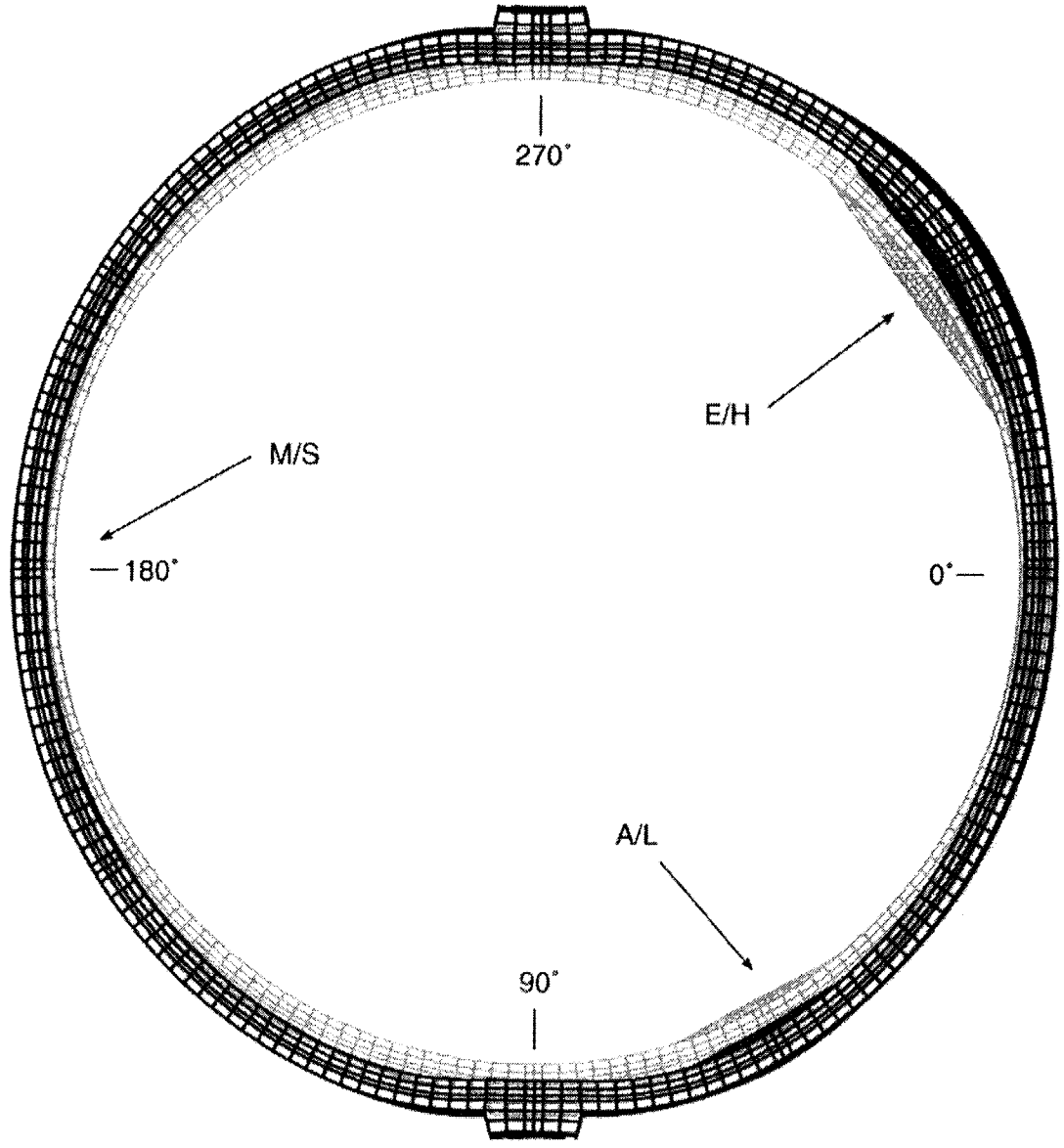


Figure 7-28. 3DCM Deformed Shape at P = 2.5 $P_d$ (mag. factor = 25x)

*3dcm.inp*

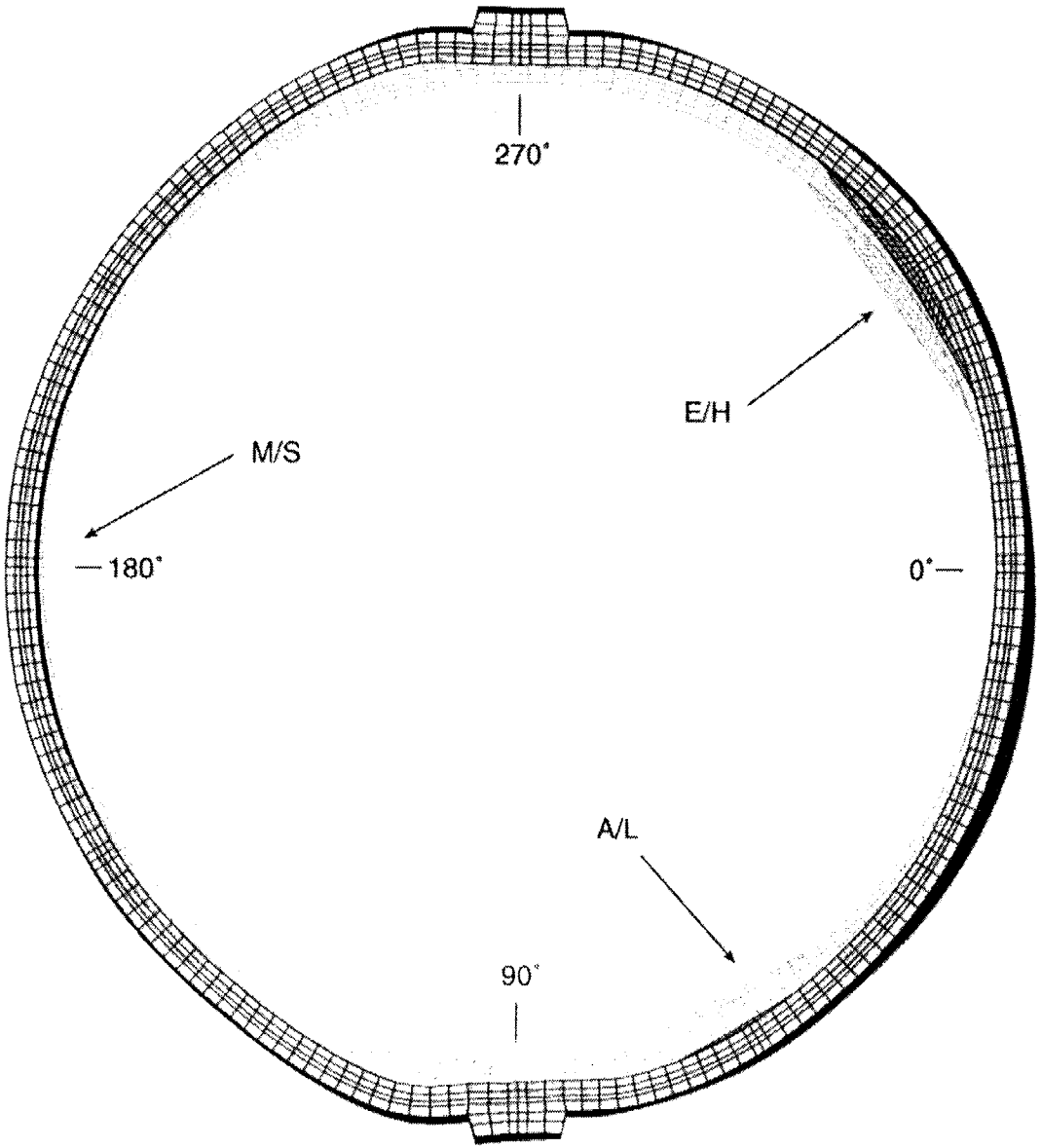


Figure 7-29. 3DCM Deformed Shape at P = 3.0 Pd (mag. factor = 10x)

*3dcm.inp*

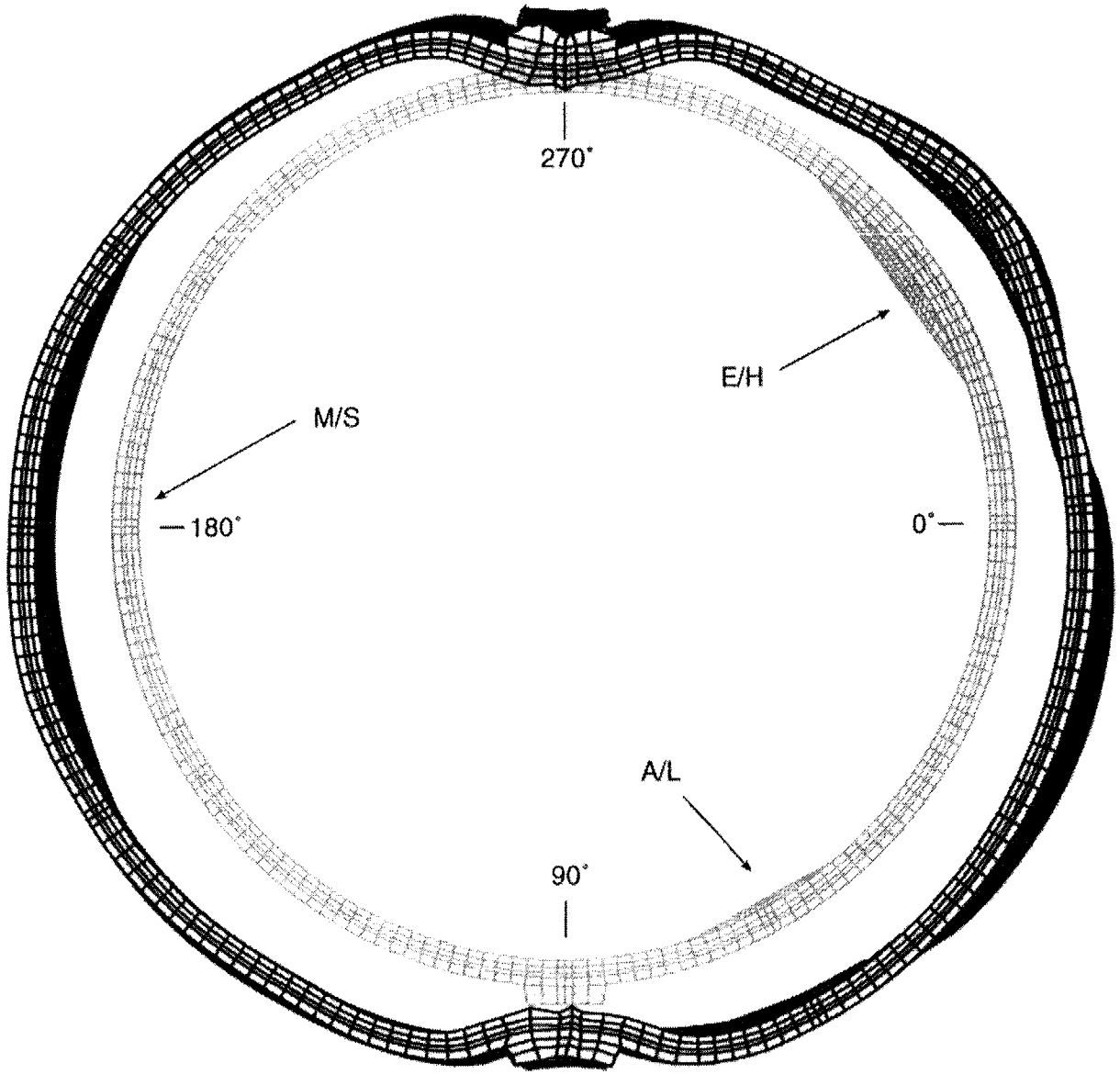


Figure 7-30. 3DCM Deformed Shape at P = 3.5 Pd (mag. factor = 10x)

*3dcm.inp*

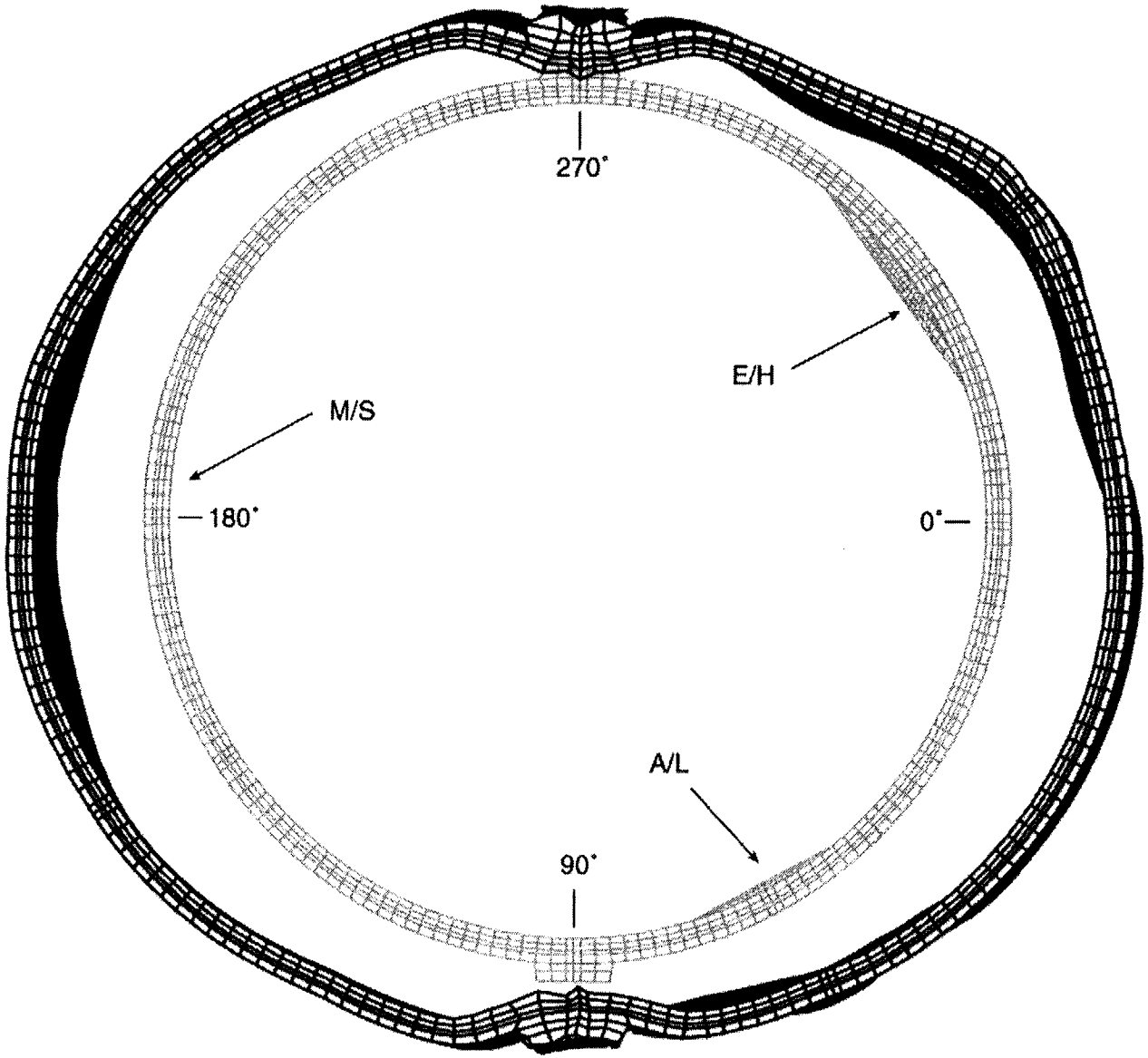


Figure 7-31. 3DCM Deformed Shape at P = 3.8 Pd (mag. factor = 5x)

*3dcm.inp*

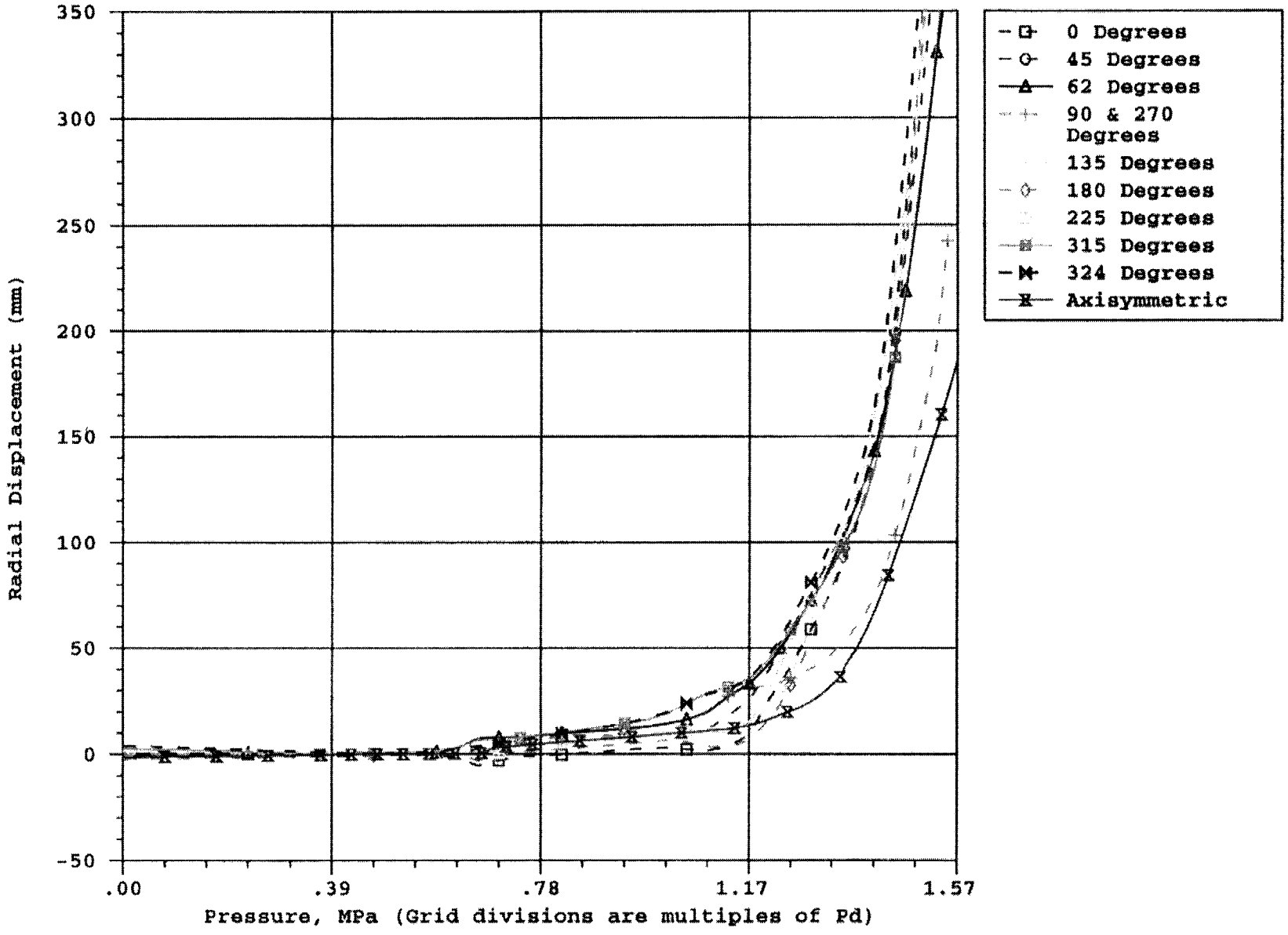


*3dcm.inp* Figure 7-32. 3DCM and Axisymmetric Radial Displacement Comparison vs. Pressure at Elevation 4.6752m

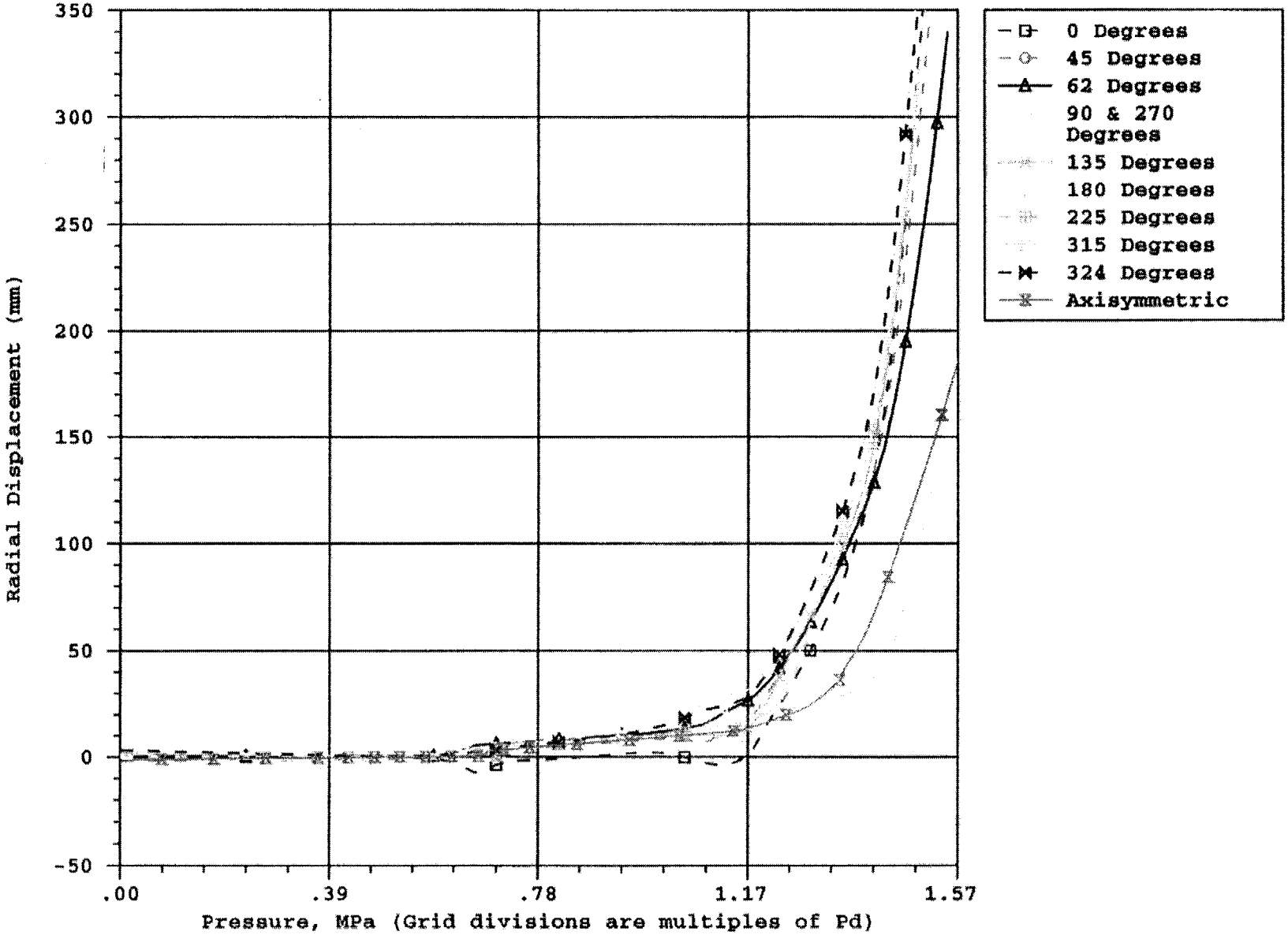


Figure 7-33. 3DCM and Axisymmetric Radial Displacement Comparisons vs. Pressure at Elevation 8.9567m

*3dcm.inp, model14.inp*

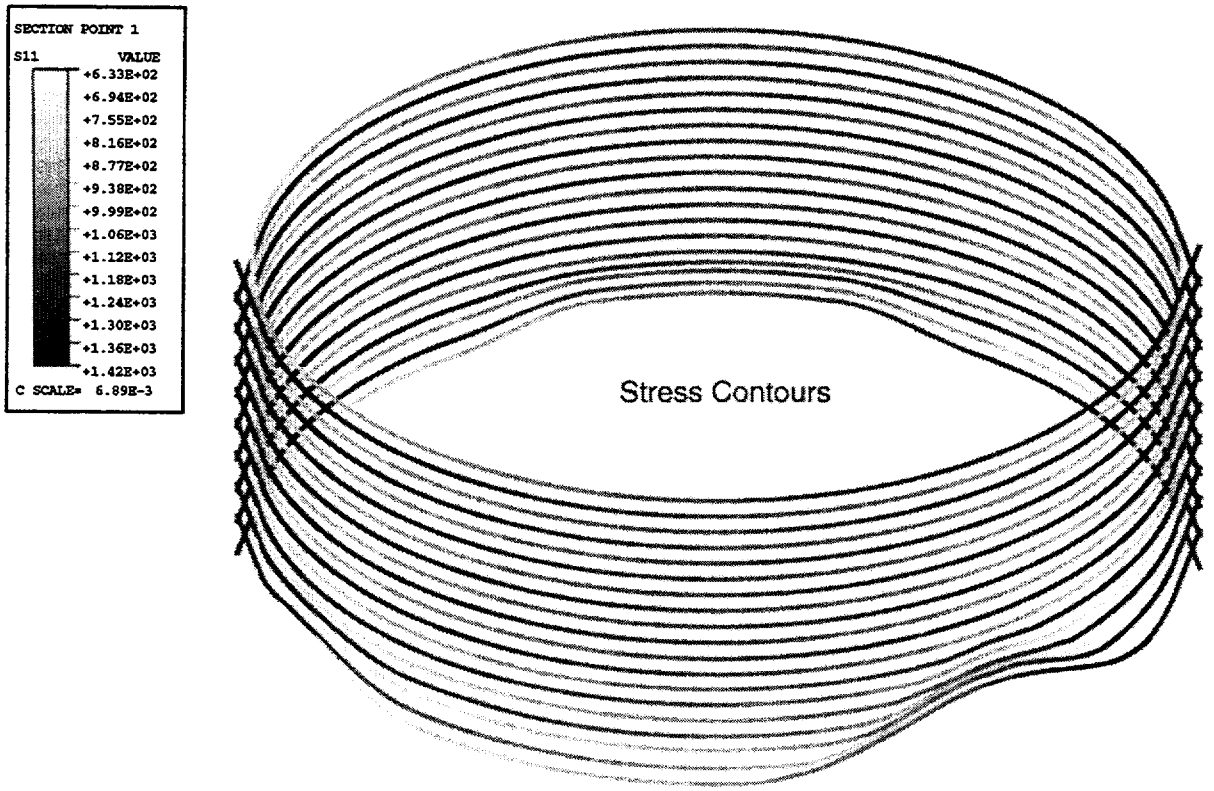


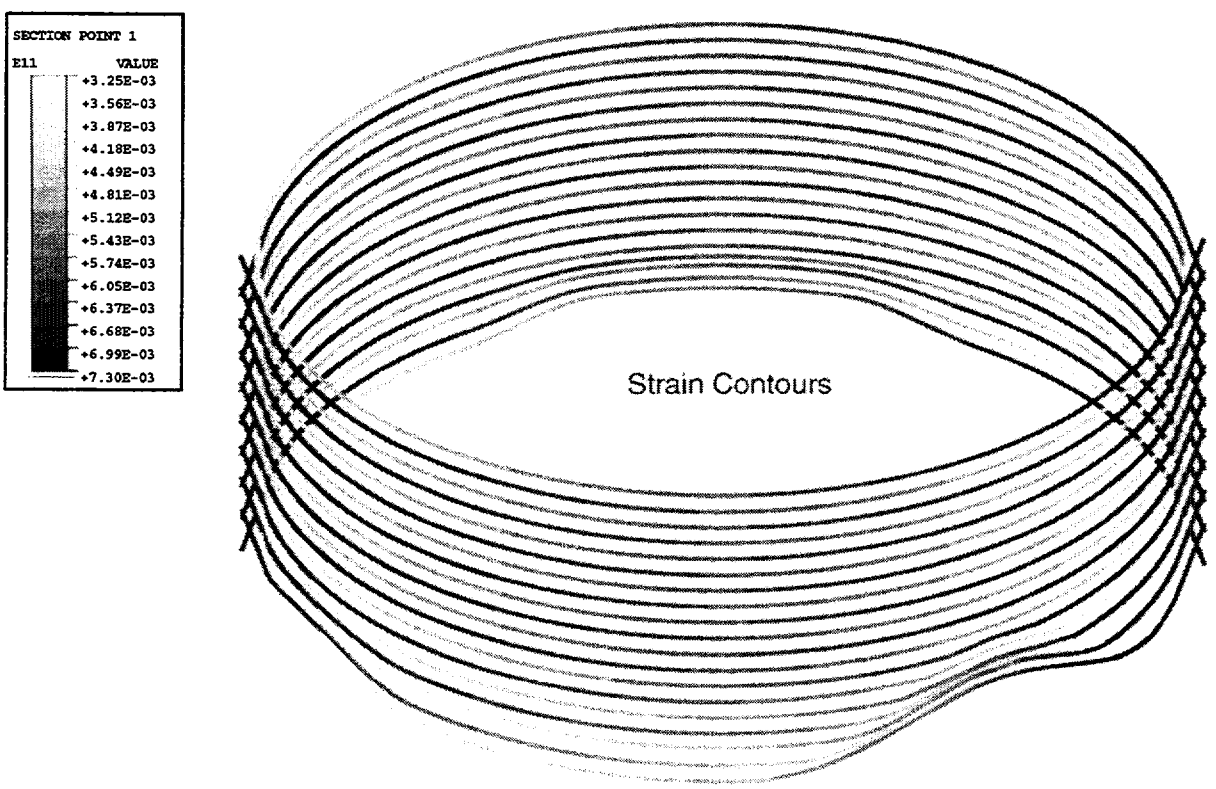


*3dcm.inp* Figure 7-34. Stress and Strain Contour Plots of Hoop Tendons at P = 2.0 Pd

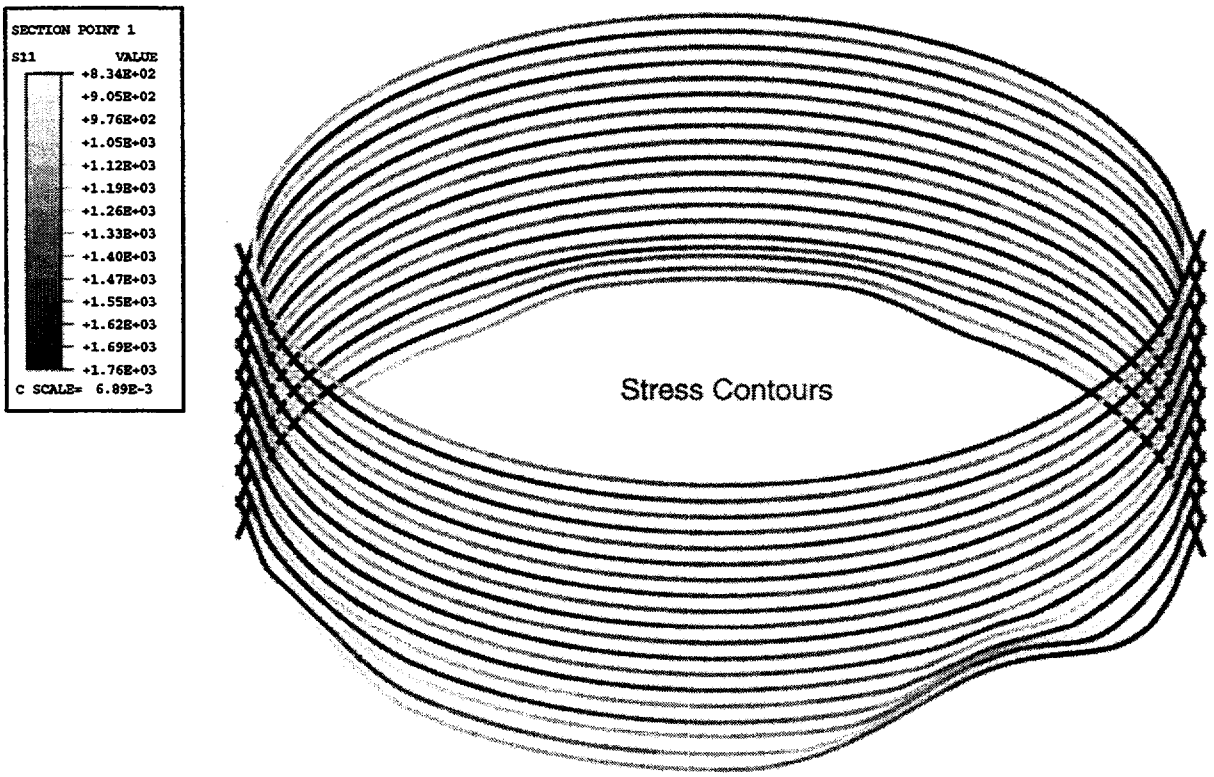


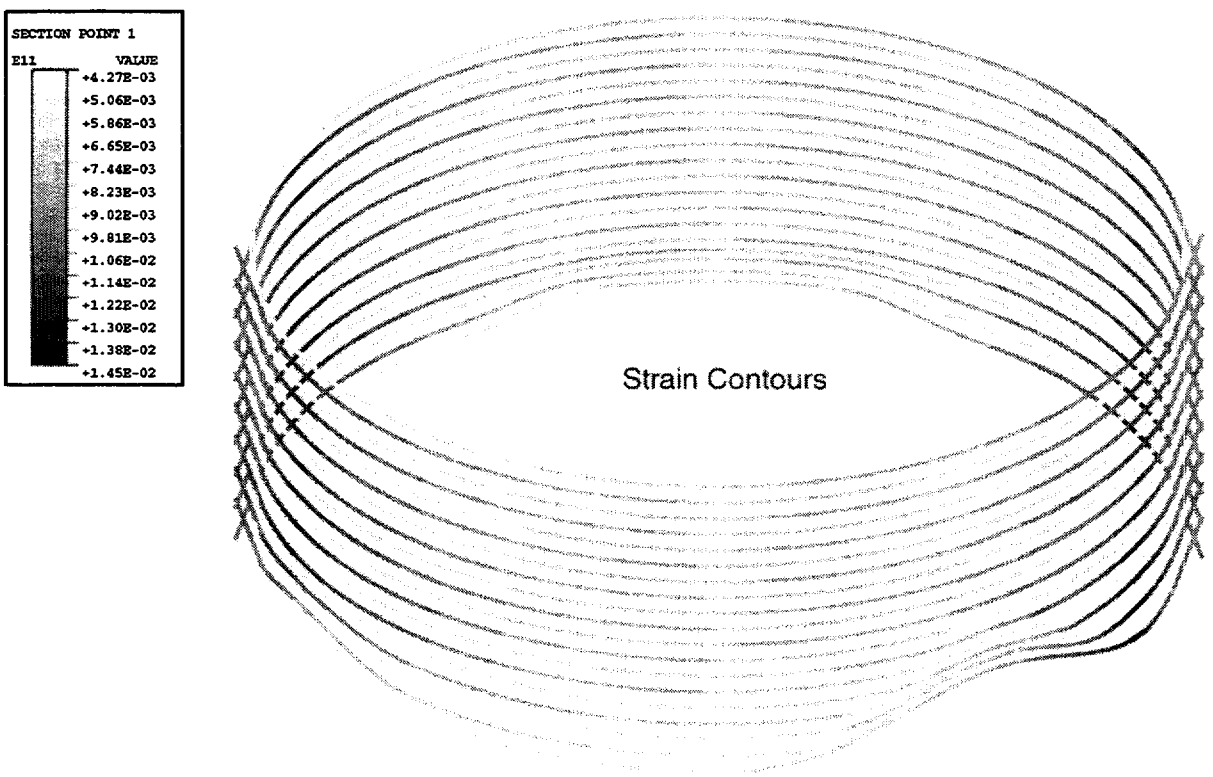


*3dcm.inp* Figure 7-35. Stress and Strain Contour Plots of Hoop Tendons at P = 3.0 Pd

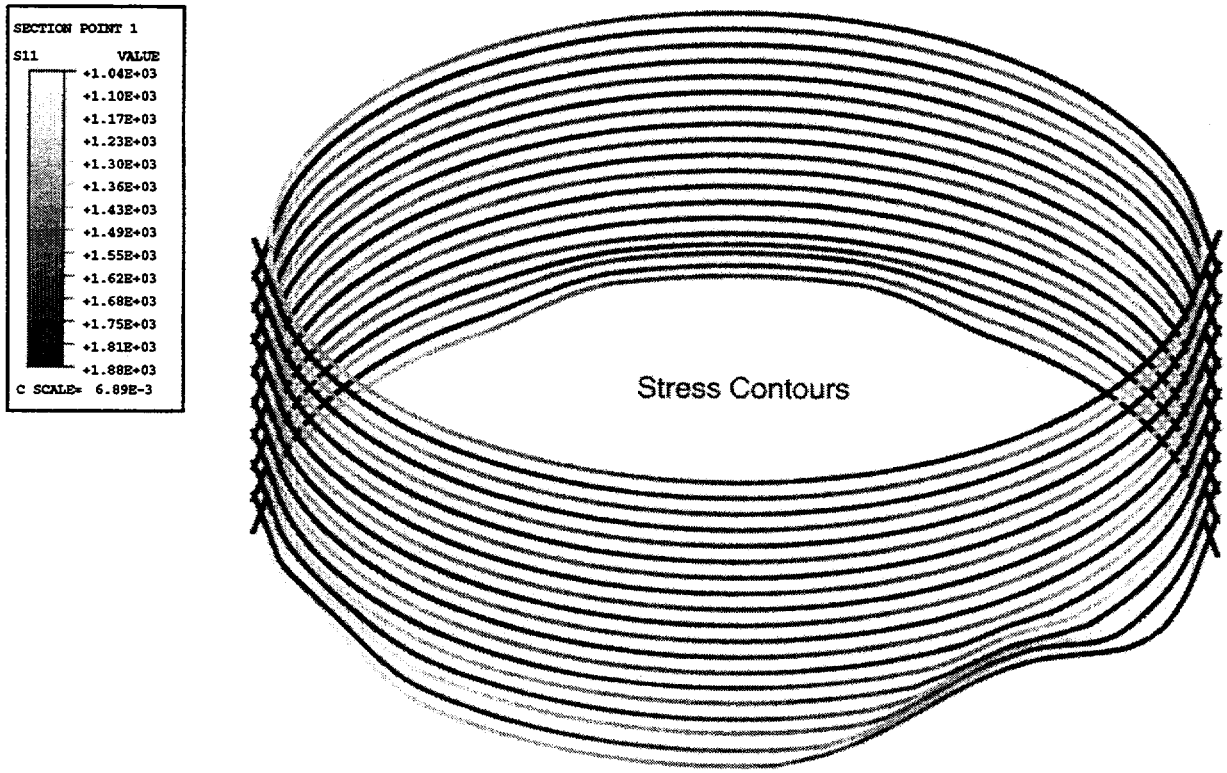


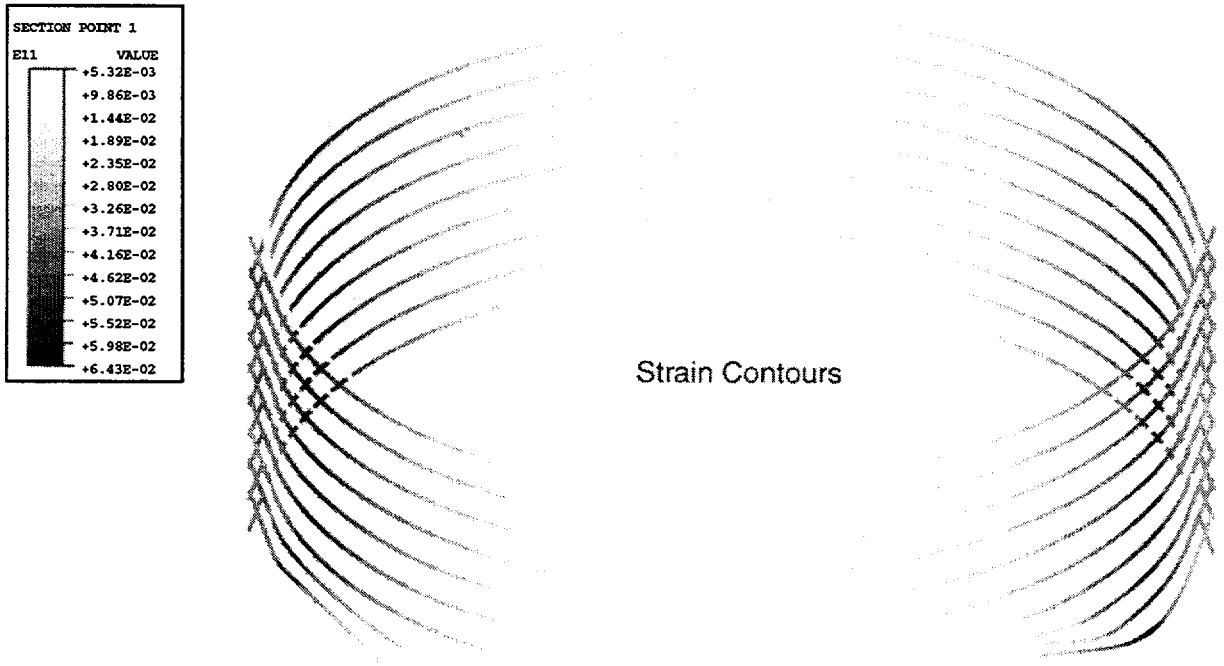


Figure 7-36. Stress and Strain Contour Plots of Hoop Tendons at P = 3.5 Pd

*3dcm.inp*

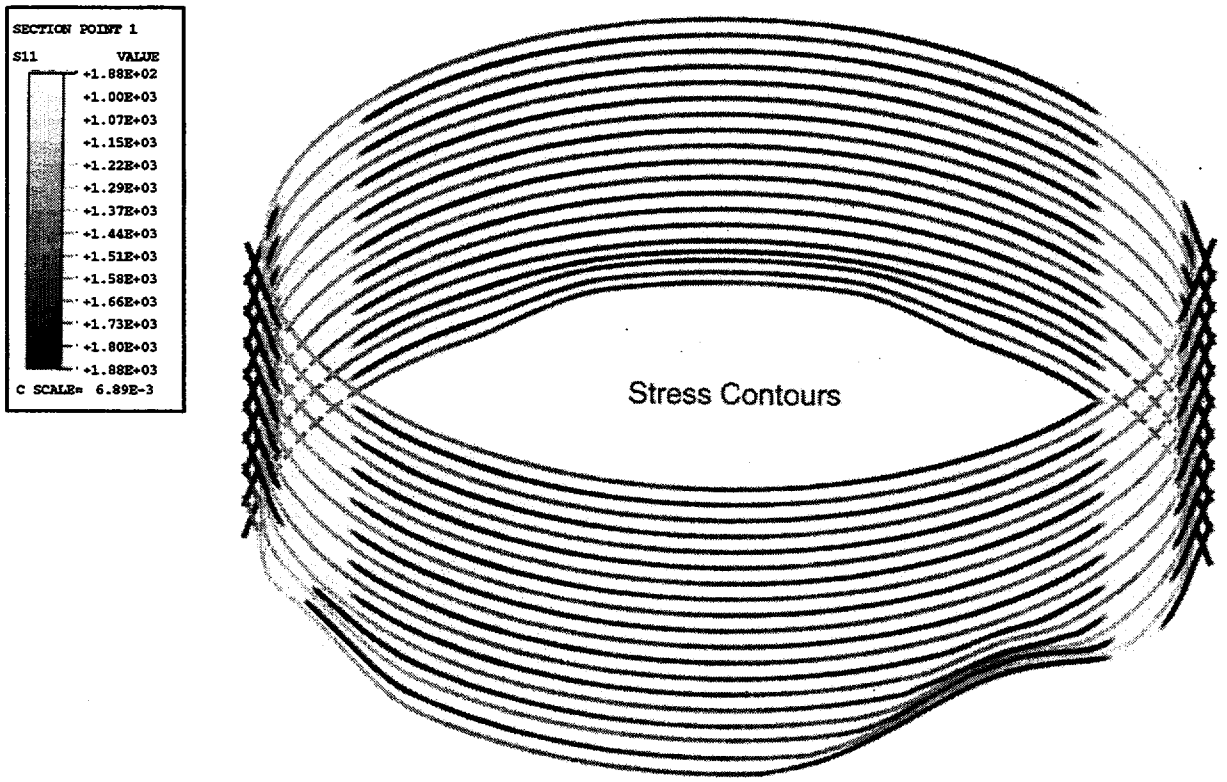


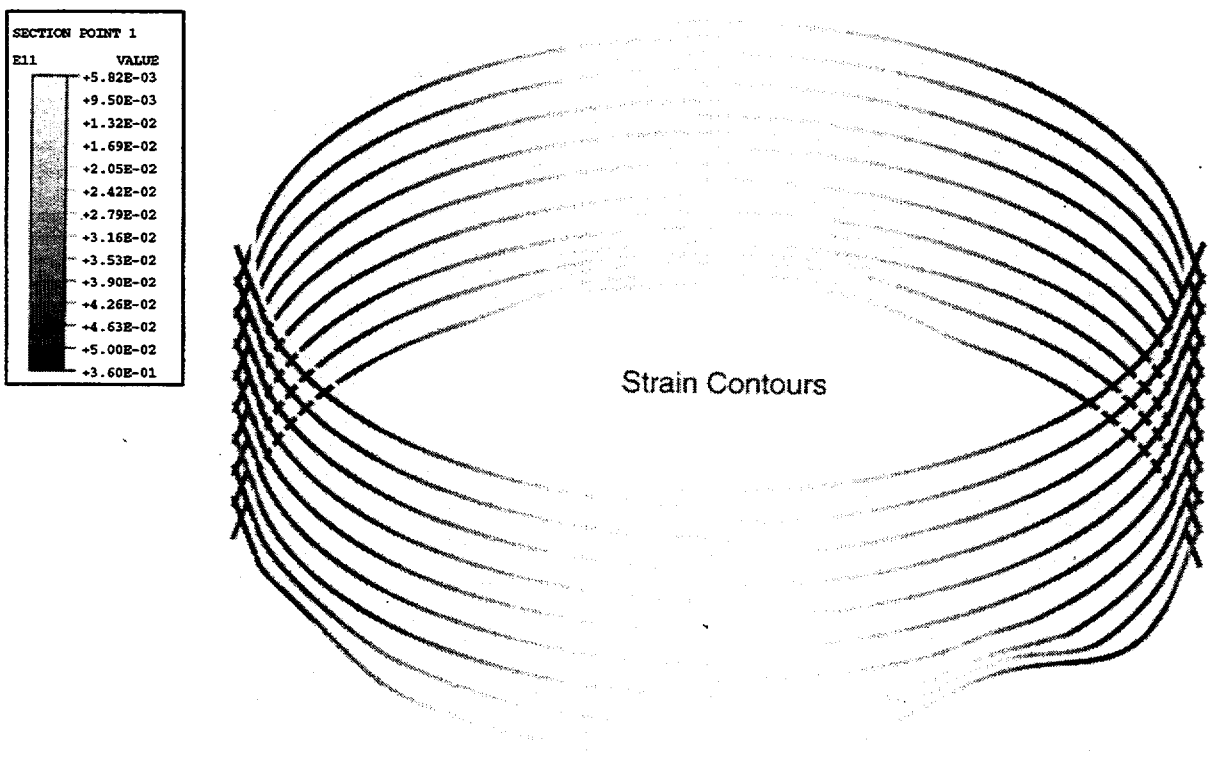


*3dcm.inp* Figure 7-37. Stress and Strain Contour Plots of Hoop Tendons at P = 3.8 Pd

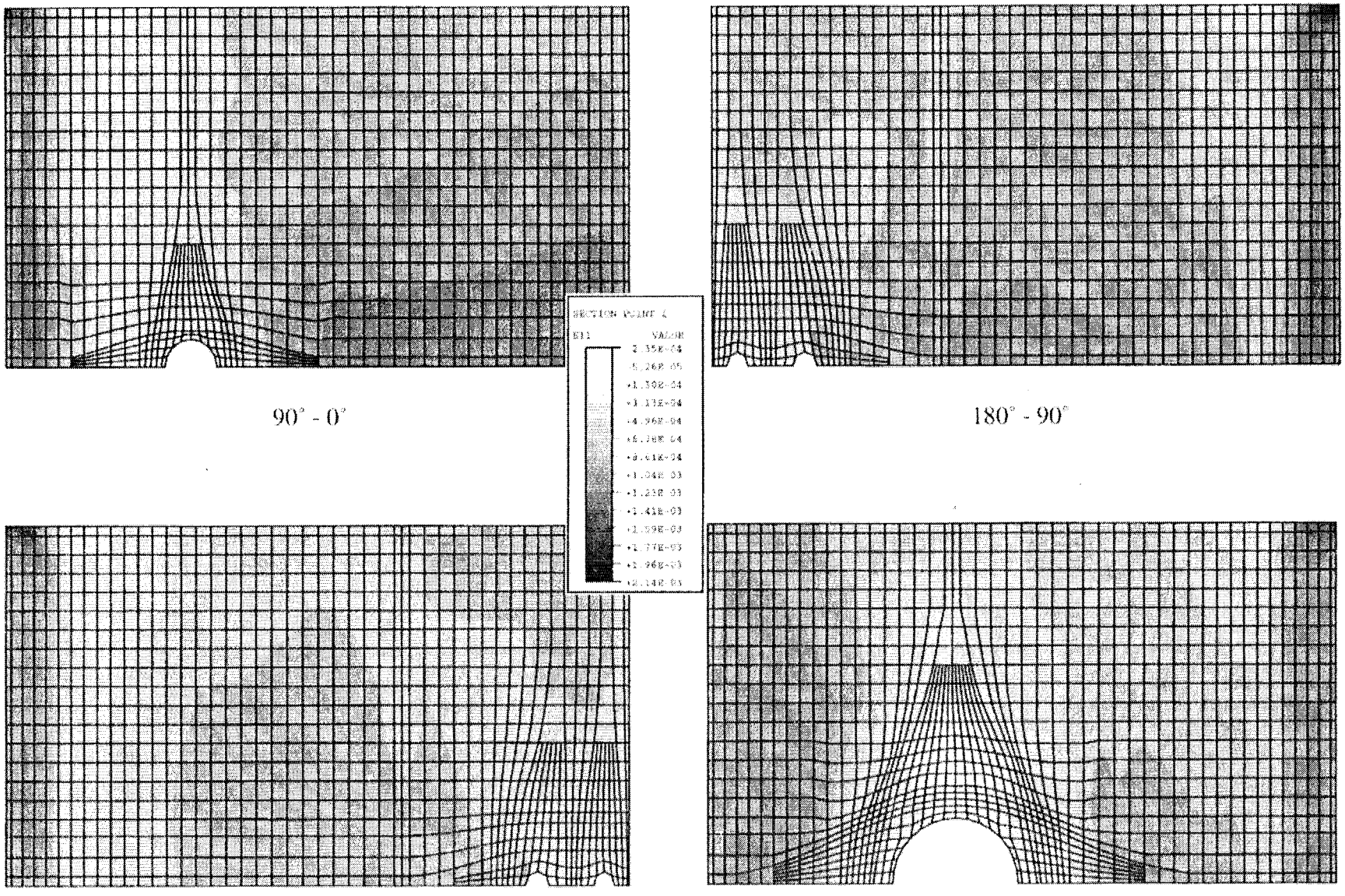


*3dcm.inp*

Figure 7-38. 3DCM Inside Hoop Strains at 2.0 Pd

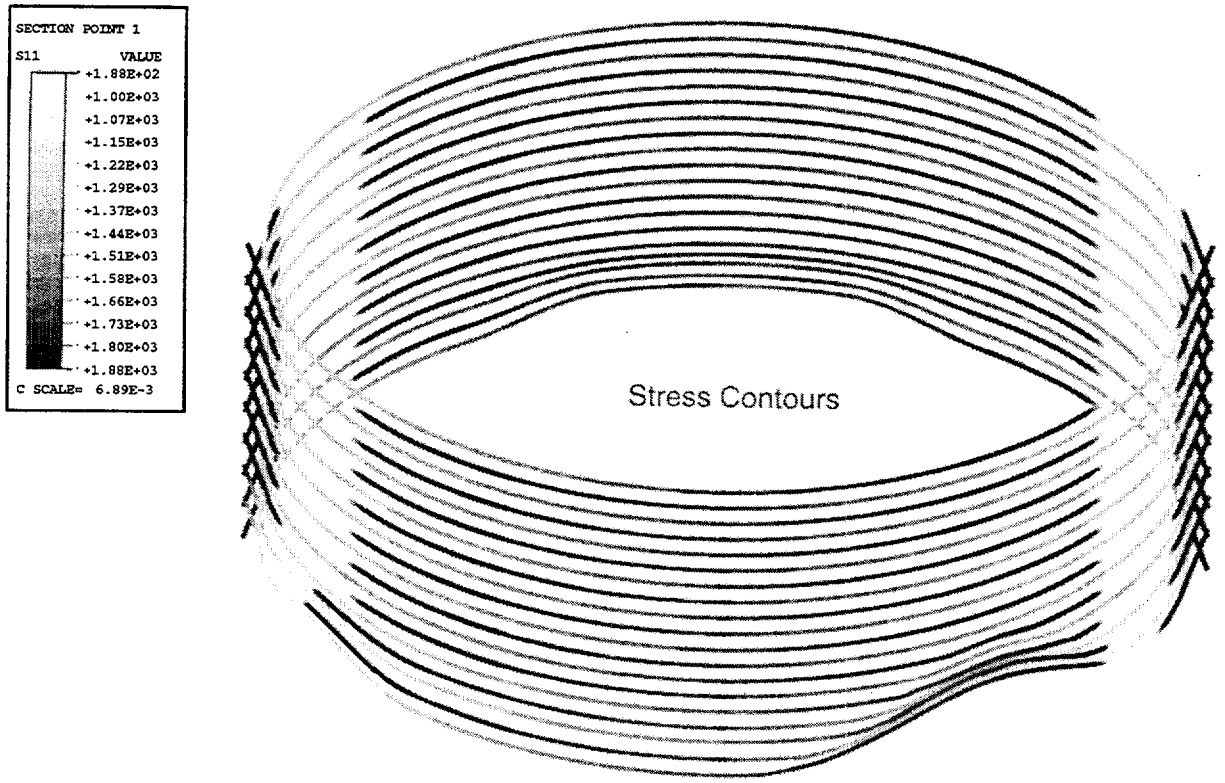


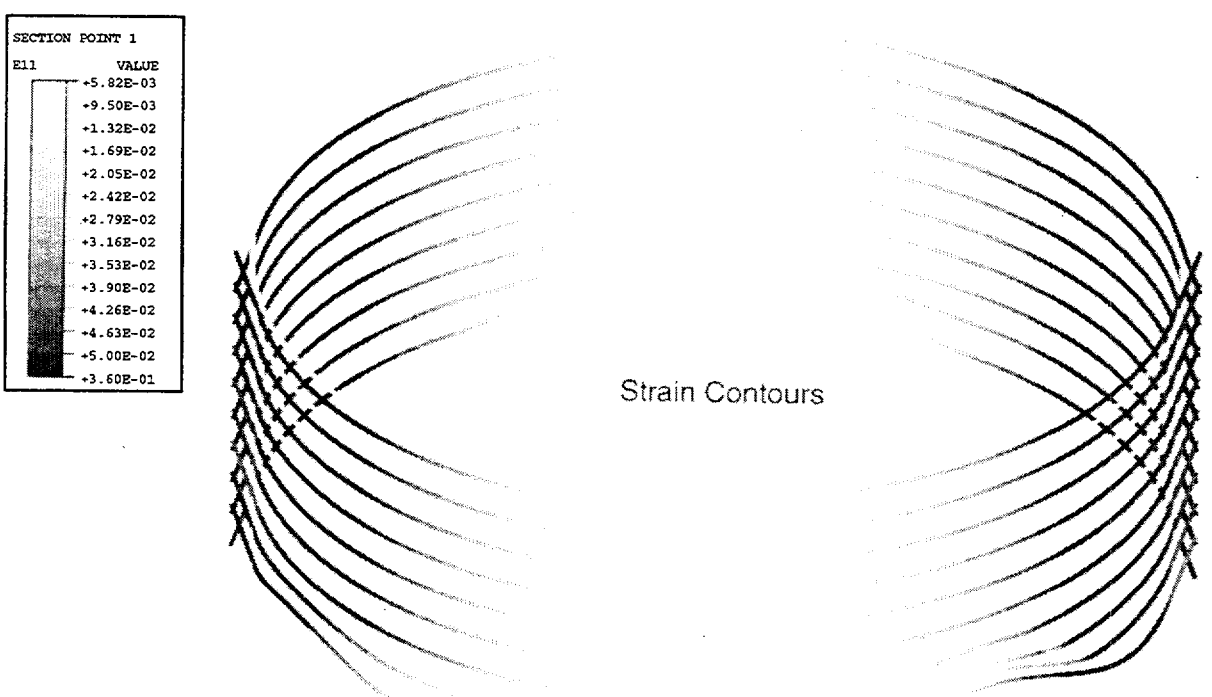


*3dcm.inp* Figure 7-37. Stress and Strain Contour Plots of Hoop Tendons at P = 3.8 Pd

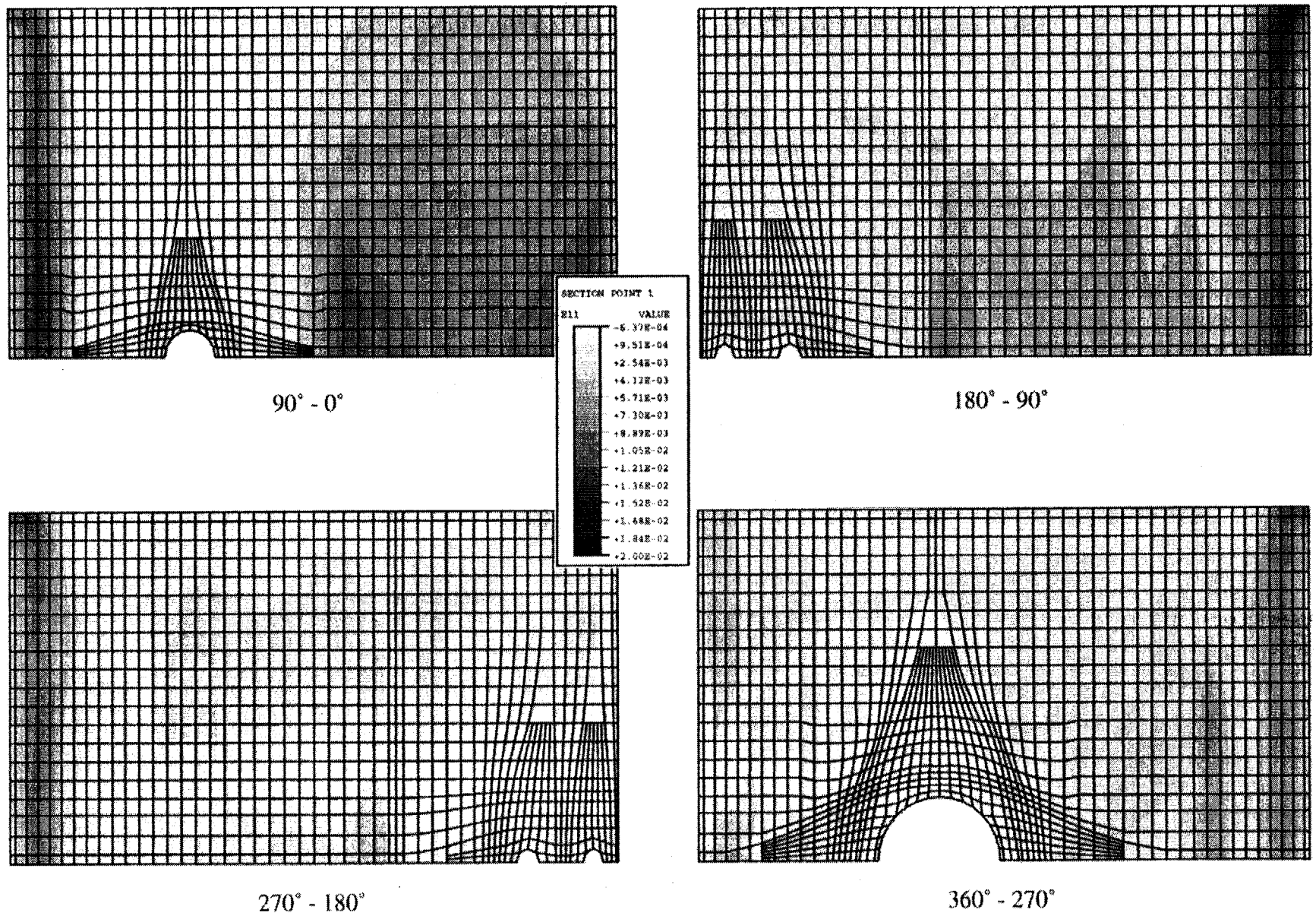


*3dcm.inp*

Figure 7-39. 3DCM Inside Hoop Strains at 3.0 Pd

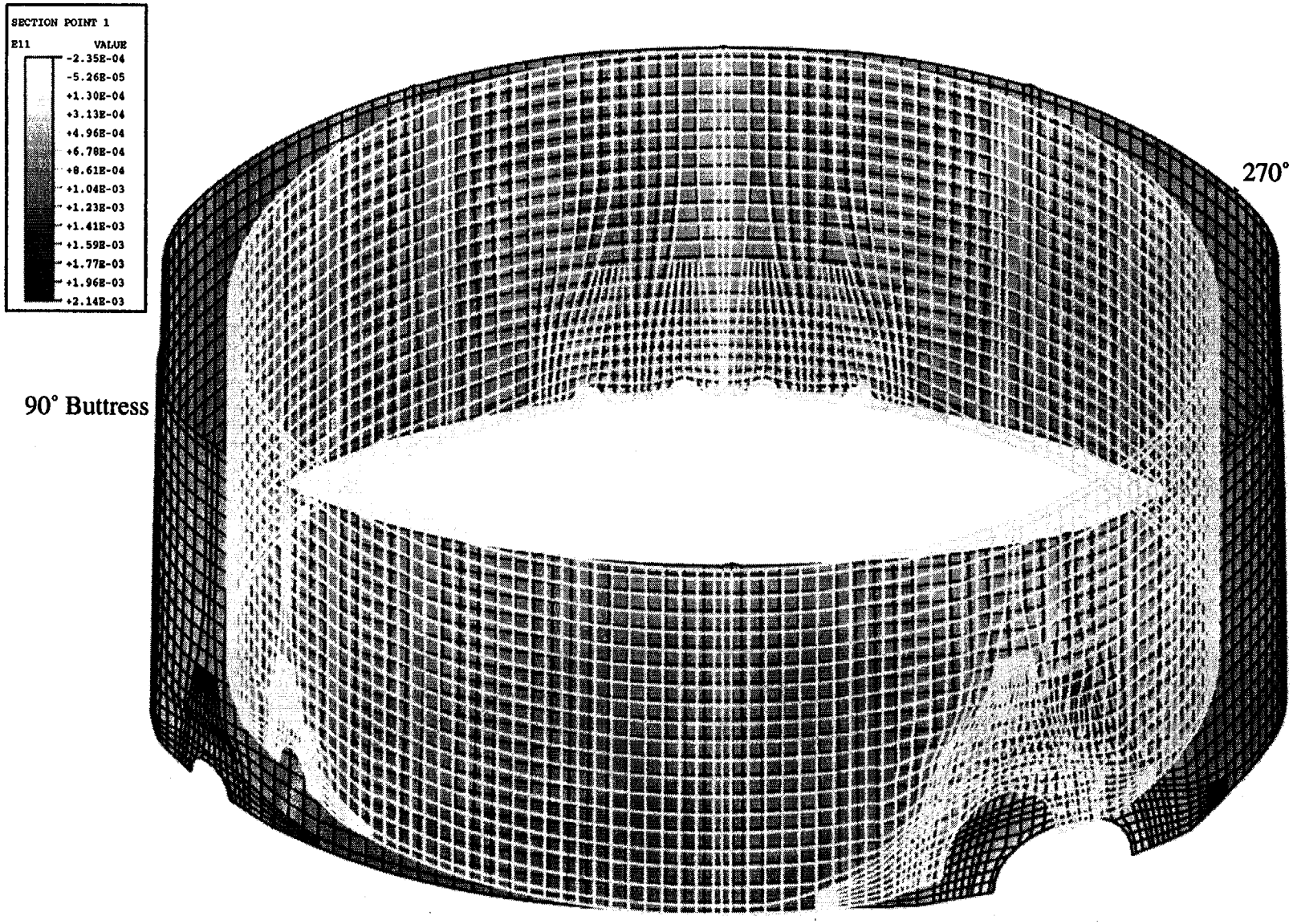


*3dcm.inp*

Figure 7-40. 3DCM Liner Hoop Strains at 2.0 Pd (Magnification factor = 100x)

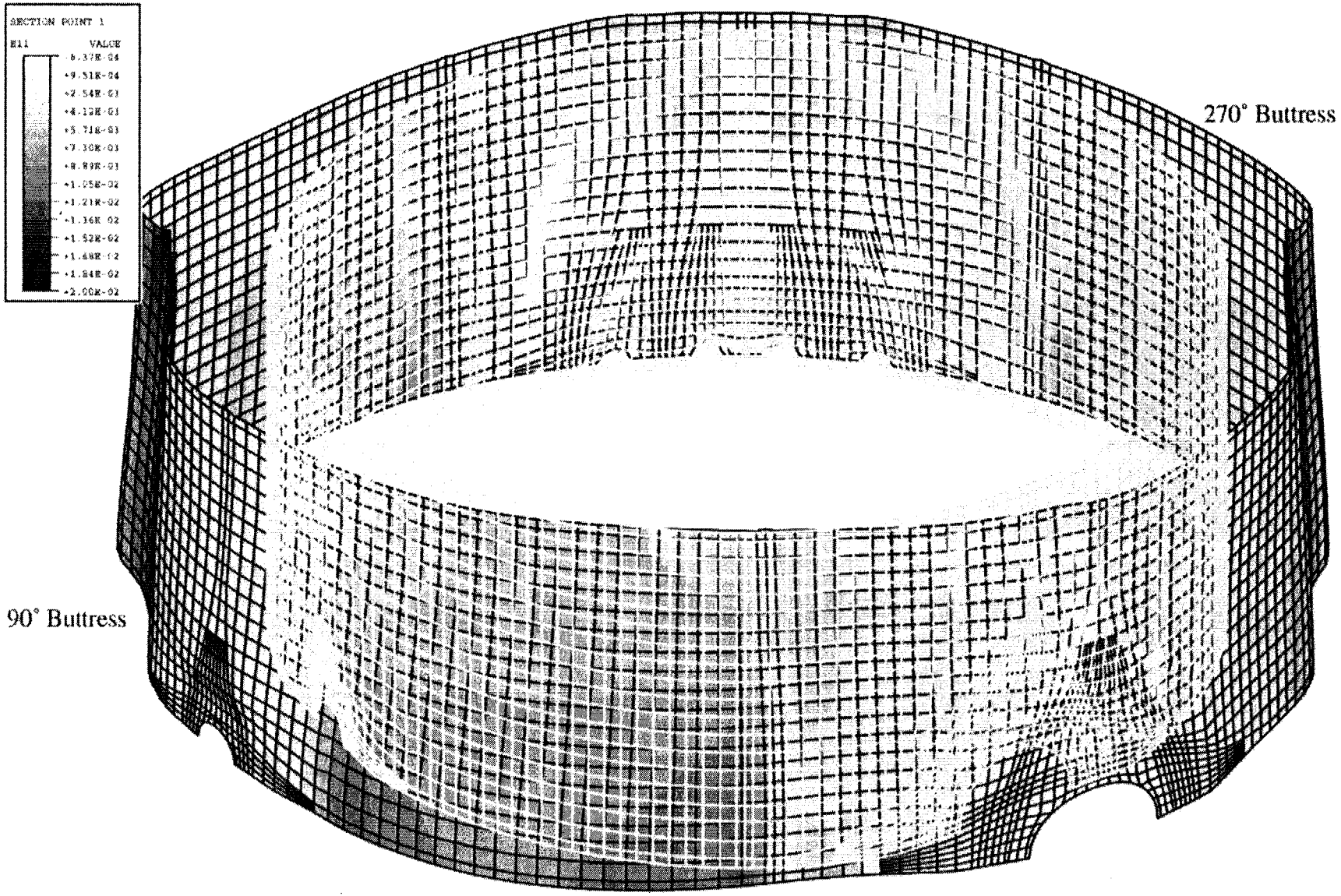


*3dcm.inp*

Figure 7-41. 3DCM Liner Hoop Strains at 3.0 Pd (Magnification factor = 35x)

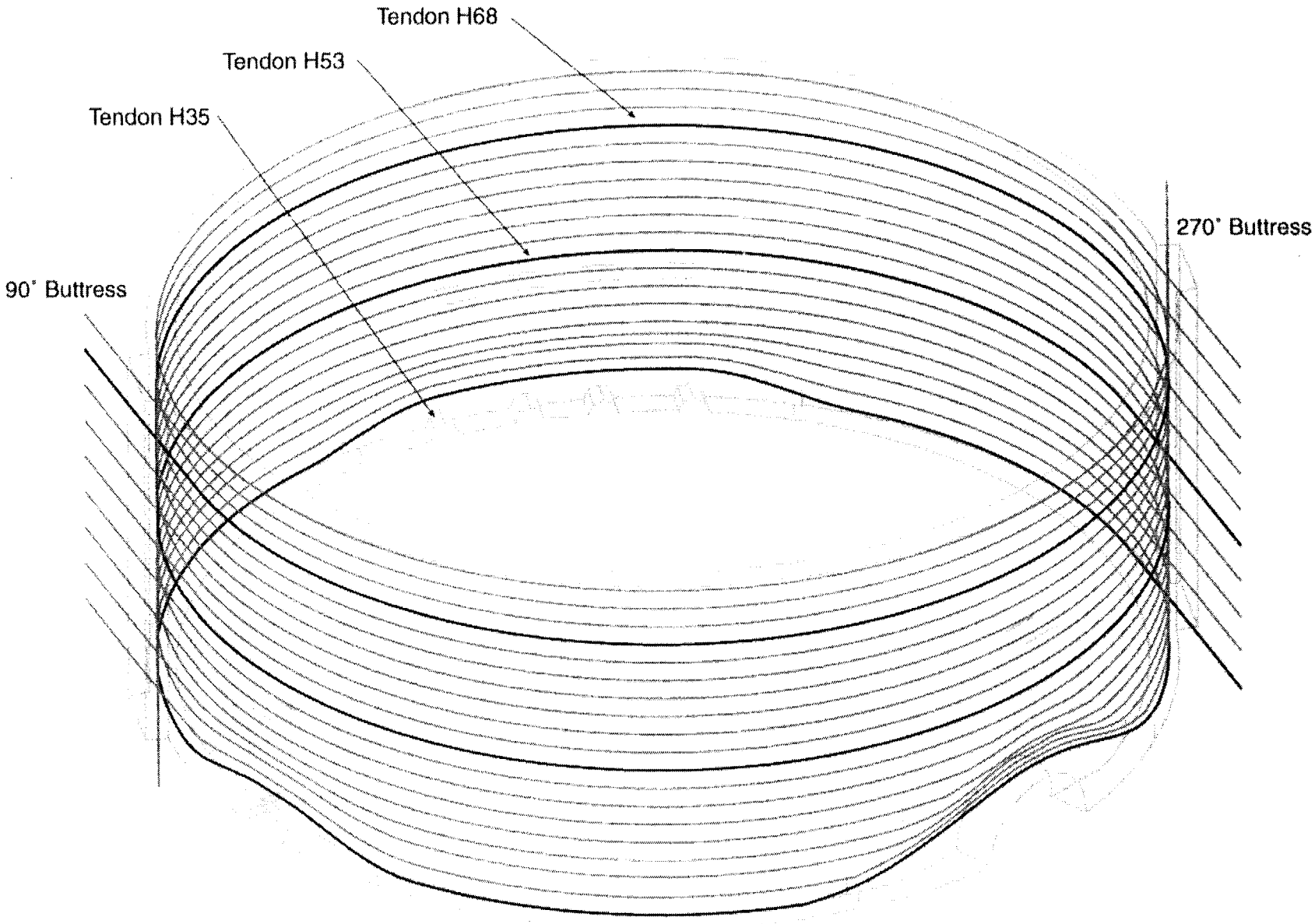


Figure 7-42. Location of Instrumented Tendons H35, H53, and H68

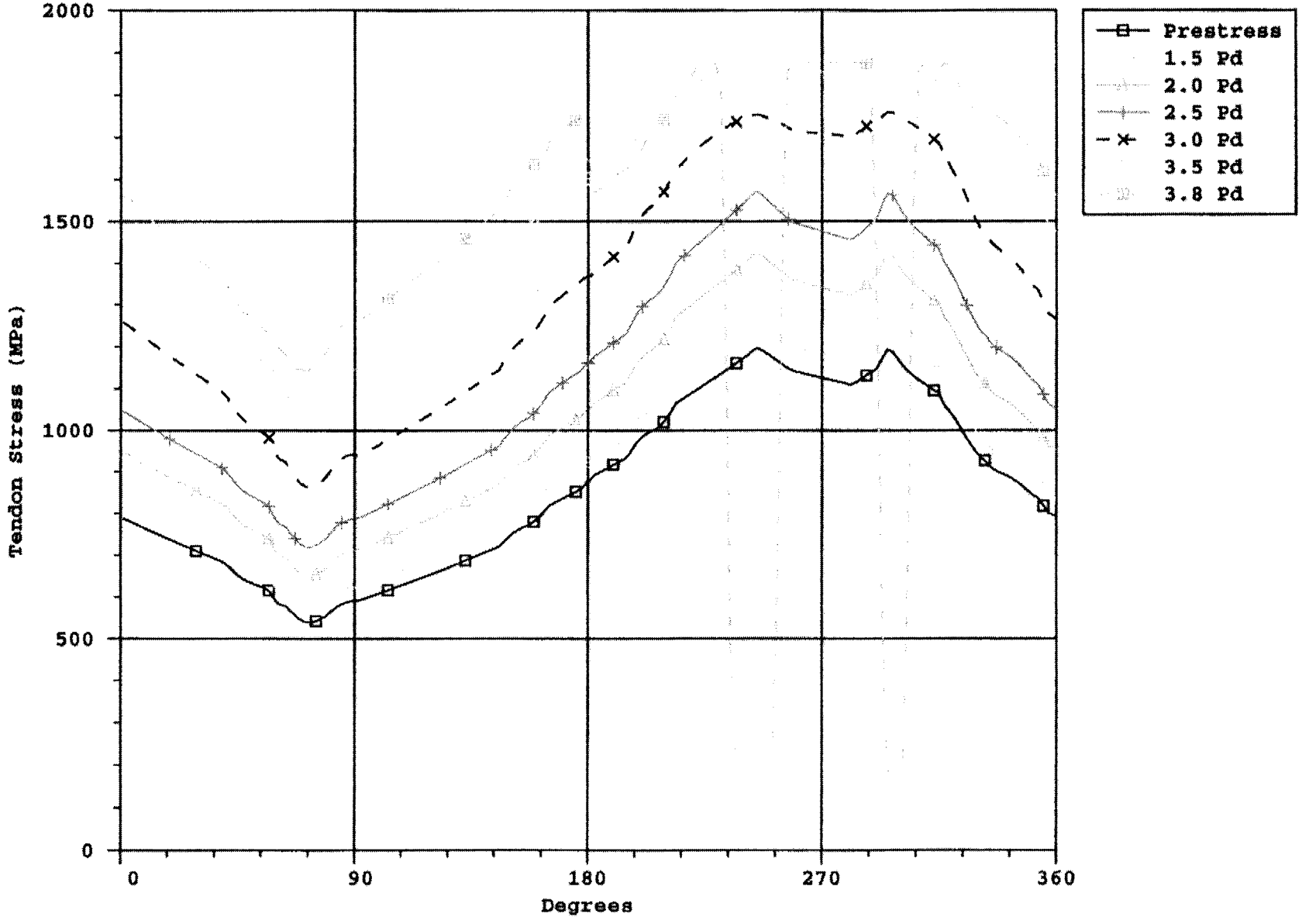


*3dcm.inp*

Figure 7-43. Tendon Stress Profile for Instrumented Hoop Tendon #H35

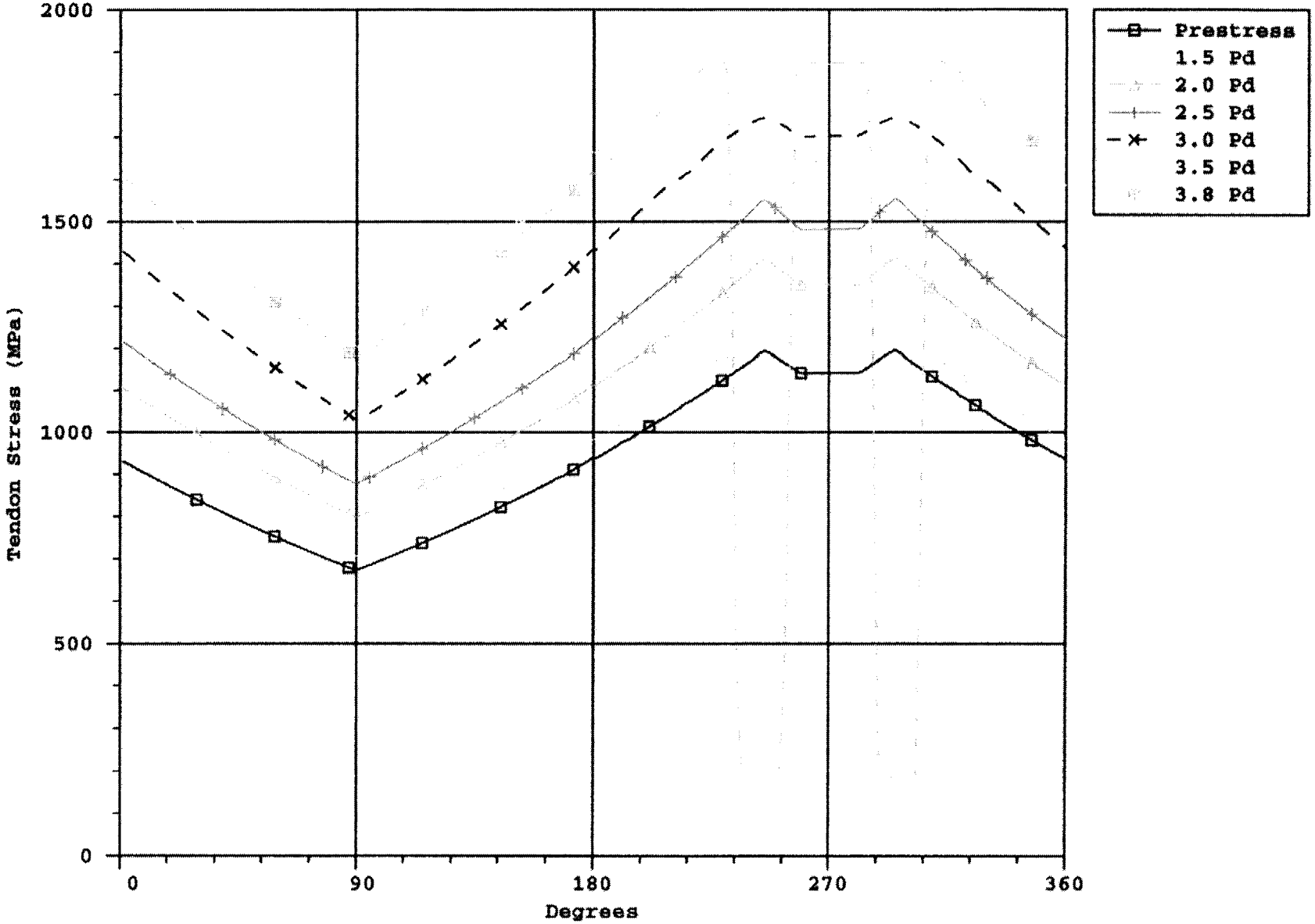


*3dcm.inp*

Figure 7-44. Tendon Stress Profile for Instrumented Hoop Tendon #H53

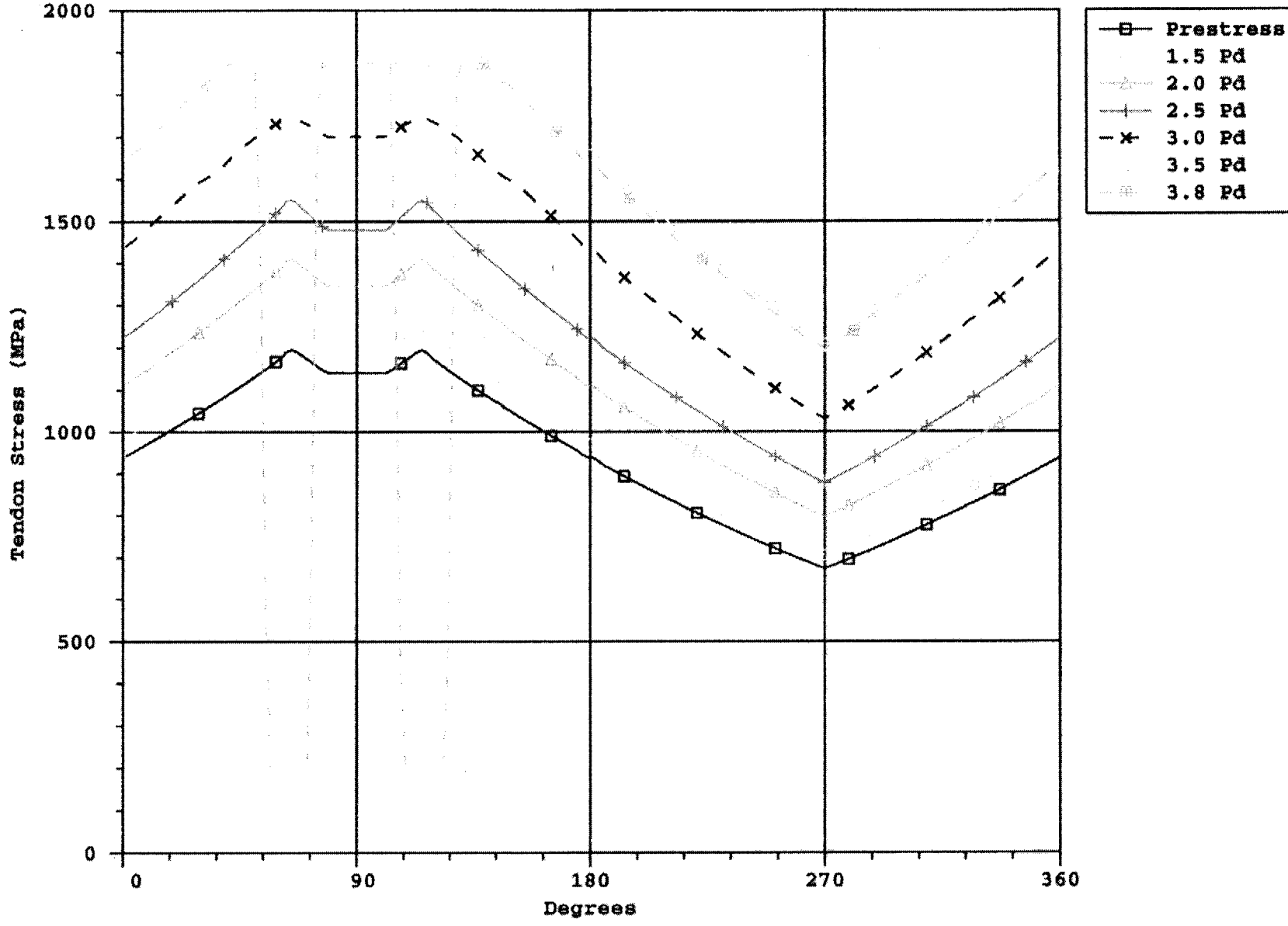


*3dcm.inp*

Figure 7-45. Tendon Stress Profile for Instrumented Hoop Tendon #H68

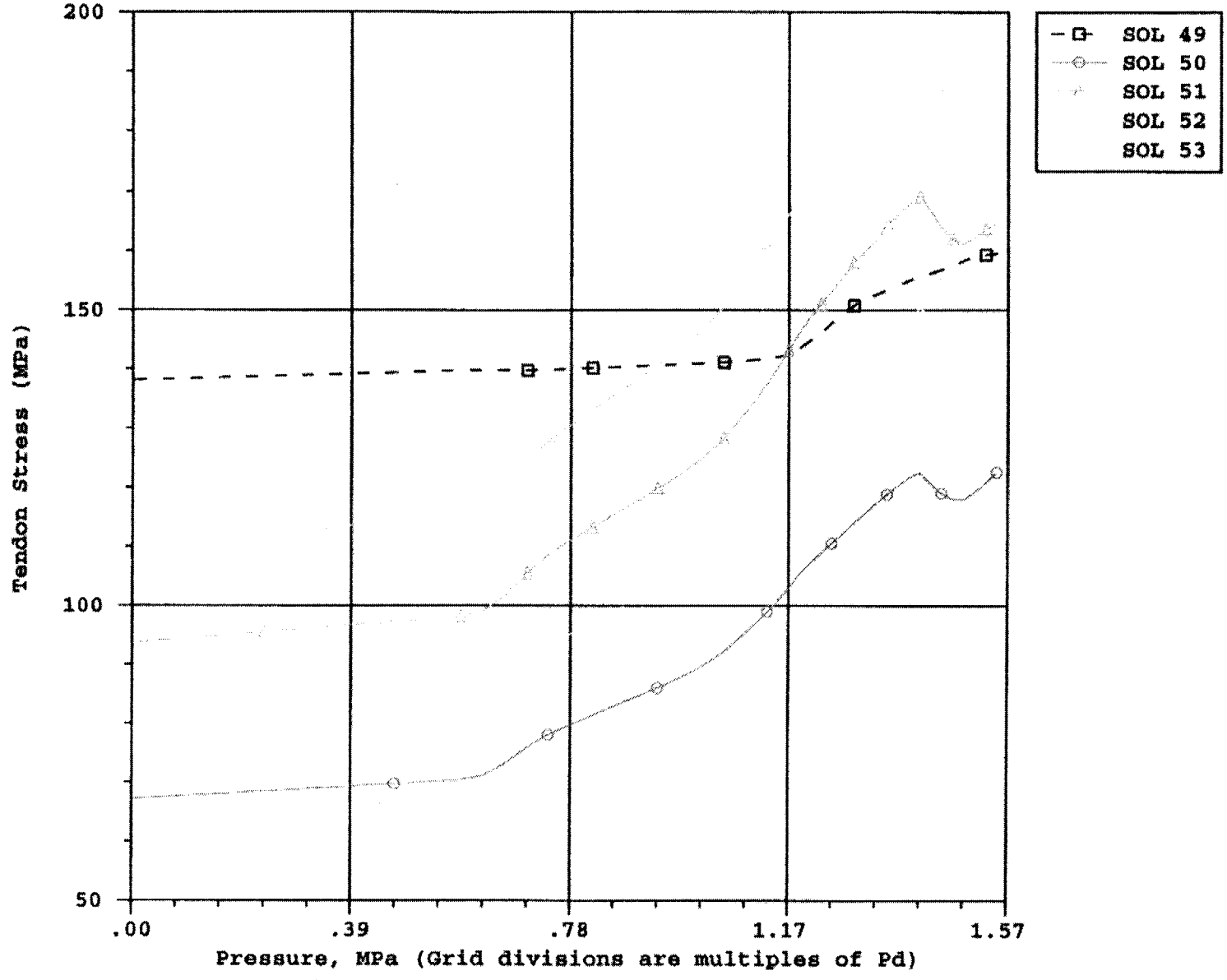


Figure 7-46. Tendon Stress Histories at Standard Output Locations 49-53



*3dcm.inp*

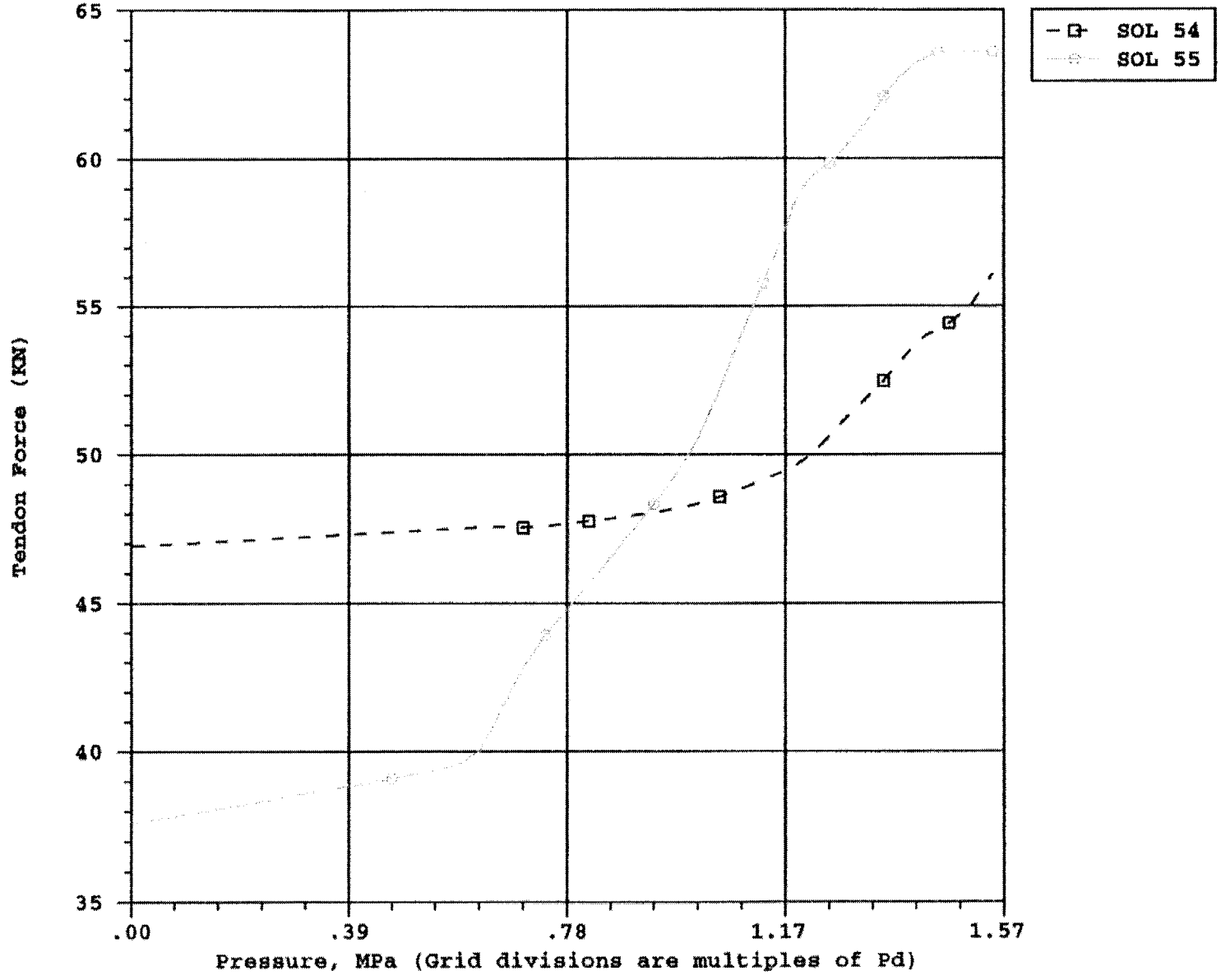


Figure 7-47. Tendon Stress Histories at Standard Output Locations 54 and 55

# 8. POTENTIAL FAILURE NEAR THE EQUIPMENT HATCH

## 8.1 Preliminary Analysis Summary

A study of the equipment hatch (E/H) region was conducted in the Preliminary Analysis Phase. Figures 8-1 and 8-2 show the area of the prestressed concrete containment vessel (PCCV) model liner that was considered in the study. Figure 8-1 is an elevation view from the drawings of the E/H region, while Figure 8-2 is a schematic of the analysis model. A liner model was originally planned to be loaded at boundary nodes with the displacement histories obtained directly from global analysis. Initial trials using this approach showed, however, that these boundary conditions alone could not reasonably produce the 3D displacement field that was expected in the interior of a liner-only model. Therefore, an intermediate modeling step was required. A composite shell model was produced (Figure 8-3) to approximate the 3D displacement field. Then displacement histories along the nodes coinciding with the T-anchor lines were applied to the heads of the T-anchors in the detailed liner model. The point of application of these boundary conditions is shown in Figure 8-4.

Details of the preliminary liner-only model are shown in Figure 8-5, and the mesh is shown in Figure 8-6. Different shell thicknesses were assigned for the collar ring and the tapered section as shown, and a beam was used for the pipe sleeve.

Only the stems of the line anchors were modeled. The stems of the anchor elements to which the displacements were applied displace as if they were firmly embedded in the concrete (in a manner similar to R. Weatherby's post-1:6-scale model test liner analysis [Clauss 1989]). The shear force-deflection behavior of the stem in the hoop direction then distributes the deformations to the liner in a manner consistent with the overall wall deformation. Pressure was applied to the inner liner surface. The displacement and pressure conditions were ramped up to those corresponding to 1.57 MPa ($4P_d$).

Results of the preliminary liner-only model are illustrated in Figure 8-7, which shows hoop strain contours at applied pressure of $3.6P_d$. The "mid-thickness" strain is shown, i.e., the membrane component of strain, which is the most reliable for predicting liner tearing. The strain results in the preliminary study were very revealing, especially after observing the relatively benign behavior of the wall-basemat juncture study. The strain concentrations occur in two general areas: (1) in the thin liner immediately adjacent to the collar plate transition and (2) at the liner "bend" point. There are also small pockets of "strain risers" between each of the T-anchor lines, but these are not nearly as elevated as the main concentration areas.

The two main concentration zones are compared quantitatively to each other and to far-field behavior in Figure 8-8, a set of peak strain histories versus pressure. This plot shows that strains adjacent to the collar plate are generally larger than at the bend point and that the largest strain (location that first tearing should occur) is near the collar and near the 2:30 position just up from the equator and adjacent to the termination of a vertical T-anchor.

Before quantifying these strain concentrations and making formal pretest predictions, however, several large areas of uncertainty remained from the Preliminary Analysis Phase liner-only study:

(1) boundary conditions applied to the edges of the model,

(2) way that the tendon stress distribution is affected by friction behavior,

(3) influence of the concrete wall on the liner strain state, and

(4) liner anchor shear behavior.

In particular, the boundary conditions from the preliminary work were driven by the composite shell model that had a number of modeling uncertainties.

The E/H liner analysis also did not investigate any E/H failure modes other than liner tearing, although other modes could include shear or flexure failure of the wall at the edge of the embossment or failure of a tendon or rebar. The goal of the next analysis step was to refine the calculation of liner strains in the E/H region and address some of these uncertainties. While the E/H represents only one penetration geometry, lessons learned from the E/H task were also applicable to modeling the other penetrations.

## 8.2 Computational Grid

The 3D concrete and liner model for the Pretest Analysis Phase studies is illustrated in Figures 8-9 and 8-10. The grid was developed by generating a concrete mesh

based on the tendon layout and then joining the embedded edges of the T-anchor webs to the concrete mesh with the *SURFACE attachment command in ABAQUS. The upper quadrant around the hatch was selected for modeling in order to have a local model completely encompassed by the 3D cylinder midheight (3DCM) model. Five layers of concrete elements through the wall thickness were used, and the liner was modeled with shell elements so that the liner bending and membrane behavior could be studied. Rebar in the concrete wall was modeled with ABAQUS rebar subelements, but tendons were modeled explicitly with truss elements and friction truss-tie elements as described in the next subsection.

The loading and boundary conditions applied to the 3D E/H model are shown in Figure 8-10. The conditions are similar to what they were for the liner-only studies except that, in 3D, shear and bending of the wall become important. This requires conditions of $\Delta_z=0$ at the vertical edges of the model.

## 8.3 Tendon Modeling

One of the most complex aspects of the 3D E/H model is tendon modeling. As previously mentioned, significant effort was exercised in the tendon representation in order to:

1. calculate the tendon stress distribution throughout the pressurization sequence, including the effects of friction; and

2. calculate the displacements of the concrete wall correctly, because this drives the liner, and thereby refine the prediction of liner strain concentrations.

Each meridional tendon was modeled with a truss element and with friction truss-ties to adjacent concrete nodes as shown in Figure 8-11. The tie elements (also truss elements) have length equal to the half-diameter of the tendon ducts. When the tendon is curved, the truss ties are oriented at an angle of $\tan^{-1}(0.21)$. By assigning this system of tendon elements small displacement theory, the friction truss-ties always transmit the exact amount of theoretical angular friction force from the tendon to the concrete. When the tendon segment being tied is straight, the tie element is oriented perpendicularly to the tendon (no friction). Thus, within the E/H model, wobble friction along straight runs of tendon is not considered. Wobble friction is considered, however, in estimating tendon stresses at the boundaries of the models. These estimates of tendon stress at the boundaries are identified in Figure 4-1. The friction losses for segments of tendons outside the boundaries of the model were based on

$$f_t = f_{je}^{-(\mu\alpha+ks)}, \text{where} \qquad (8\text{-}1)$$

$f_t$ = tendon stress reduced due to friction
$f_j$ = tendon stress at the jack after setting losses
$\mu = 0.21$
$s$ = length along tendon (cm)
$k = 6.575 \times 10^{-6}$ cm$^{-1}$
$\alpha$ = angle change along tendon length (radians)

The generation of the friction tie mesh required development of a special preprocessor. First, each tendon was located in space by location of the design points of tangency from the PCCV drawings. (Generally there are three points that define the path of a tendon sweeping around the penetration.) Then, the program used a least squares fit to compute the equation of each tendon path. For example, for the lowermost hoop tendon shown in Figure 8-11, an equation for the path was found to be:

$$0.001838x^3 - 0.09050x^2 - 0.02493x=147.8$$

(x is in radians; the dependent variable is the vertical dimension.)

Next, the program located mathematical points of intersection of each of the tendon equations and placed a finite element node at each point. As shown in Figure 8-12, the vertical tendons were modeled individually (one-for-one), but for purposes of reducing the size of the preliminary analysis, the hoop tendons were modeled two-for-one. Because the hoop tendons are laid out in pairs, this approximation is believed to result in negligible loss of accuracy. The program then located a friction tie node adjacent to each tendon node according to the following mathematical constraints:

1. tie node lies in plane defined by tendon node$_{i-1}$, node$_i$, and node$_{i+1}$,

2. vector from tendon node$_i$ to tie node has length equal to the radius of the duct, and

3. vector from tendon node$_i$ to tie node makes angle of $\tan^{-1}(0.21)$ with the chord subtended through node$_{i-1}$, node$_i$, and node$_{i+1}$.

The remainder of the concrete nodes were then generated "around the tendon nodes" with ANAGEN, an ANATECH-developed mesh generator that serves as a preprocessor to ABAQUS.

## 8.4 Analysis Results

To address the first objective of "coupling" the results of the 3DCM model to that of the local E/H model, an algorithm was developed whereby the local E/H model was subjected to the same average hoop strain versus pressure history across the local model as was exhibited in the 3DCM model. This provides the pressure versus "boundary condition" correlation that was a goal of the 3DCM model and the local modeling. This average hoop strain in the 3DCM model was computed as follows:

$$\varepsilon_{\theta_{avg}} = \frac{U_{R_{270}} + U_{R_{324}}}{2R} + \frac{U_{\theta 324}}{\frac{54^\circ}{180^\circ} \times \Pi R} \qquad (8\text{-}2)$$

$\varepsilon_{\theta avg.}$ = average hoop strain (circumferential length change divided by original length) across the local E/H model, which extends from azimuth 270° to 324°

$U_{R_{270}}$ = radial displacement at 270° azimuth

R = inside radius = 538 cm

The same average hoop strain versus pressure was then assumed for the local E/H model.

Deformation and strain results of the 3D analysis of the E/H are shown in Figures 8-13 through 8-21. The deformed shape plots (Figure 8-13 and 8-14) show that the wall in the E/H region moves out fairly uniformly, except that the displacement at the hatch is less than at the buttress. This result contradicts the 3DCM model results, but the overall displacement behavior of the 3DCM model governs that of the local model.

The tendon stress distributions in Figures 8-15 through 8-18 show the friction losses in the vicinity of the E/H and the build-up of tendon stress at high pressure.

The liner strain contours in Figures 8-19 through 8-21 generally show similar strain trends as the liner-only analysis. However, even more details in the local E/H model have been introduced, such as the hoop stiffeners which terminate near the 3:00 position of the edge of the insert plate. Strains near the vertical stiffener reach 17% at $3.25P_d$, which, as described in Chapter 11, has become the best-estimate failure pressure for the PCCV model.

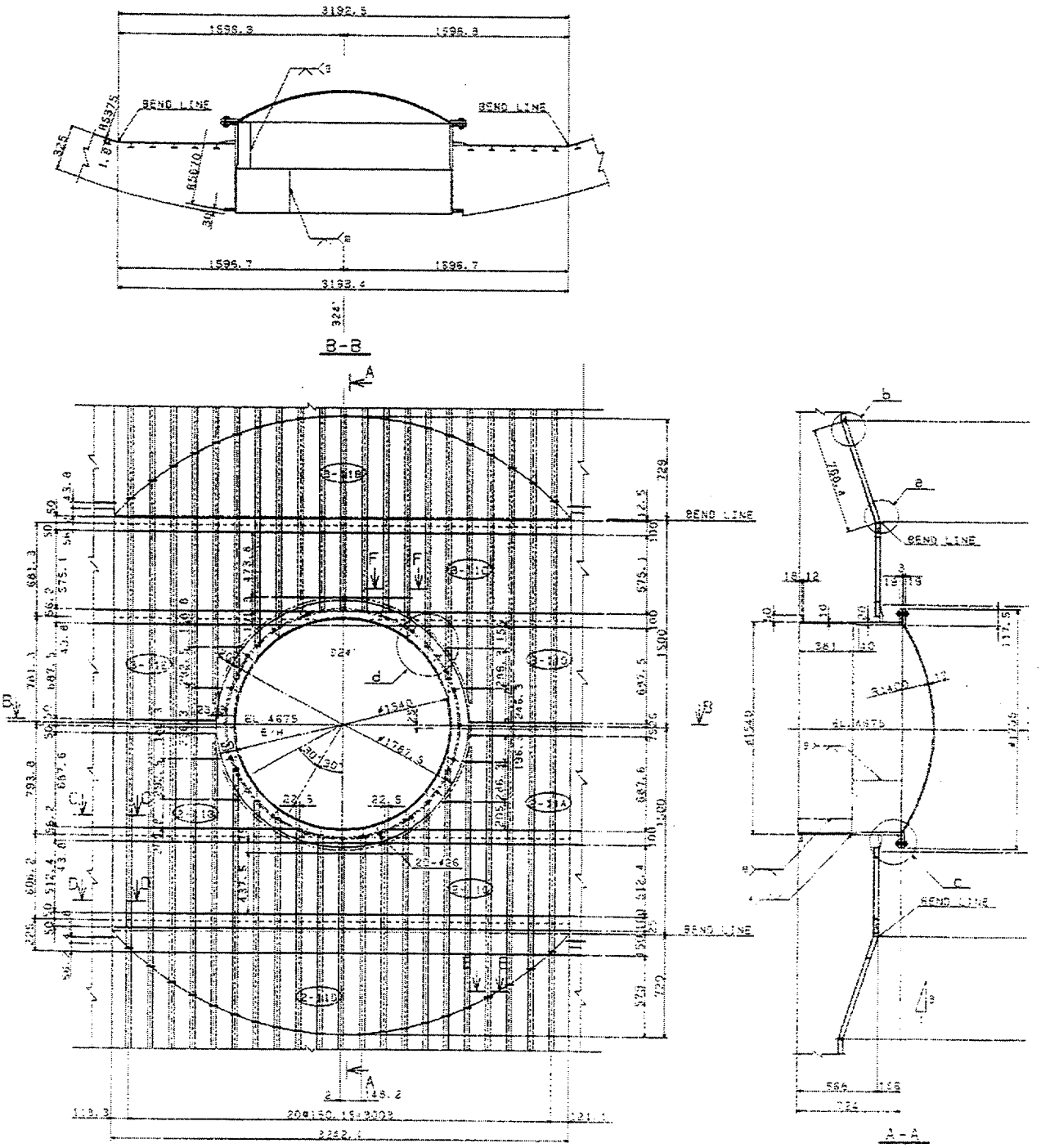


Figure 8-1. Equipment Hatch Liner Details.

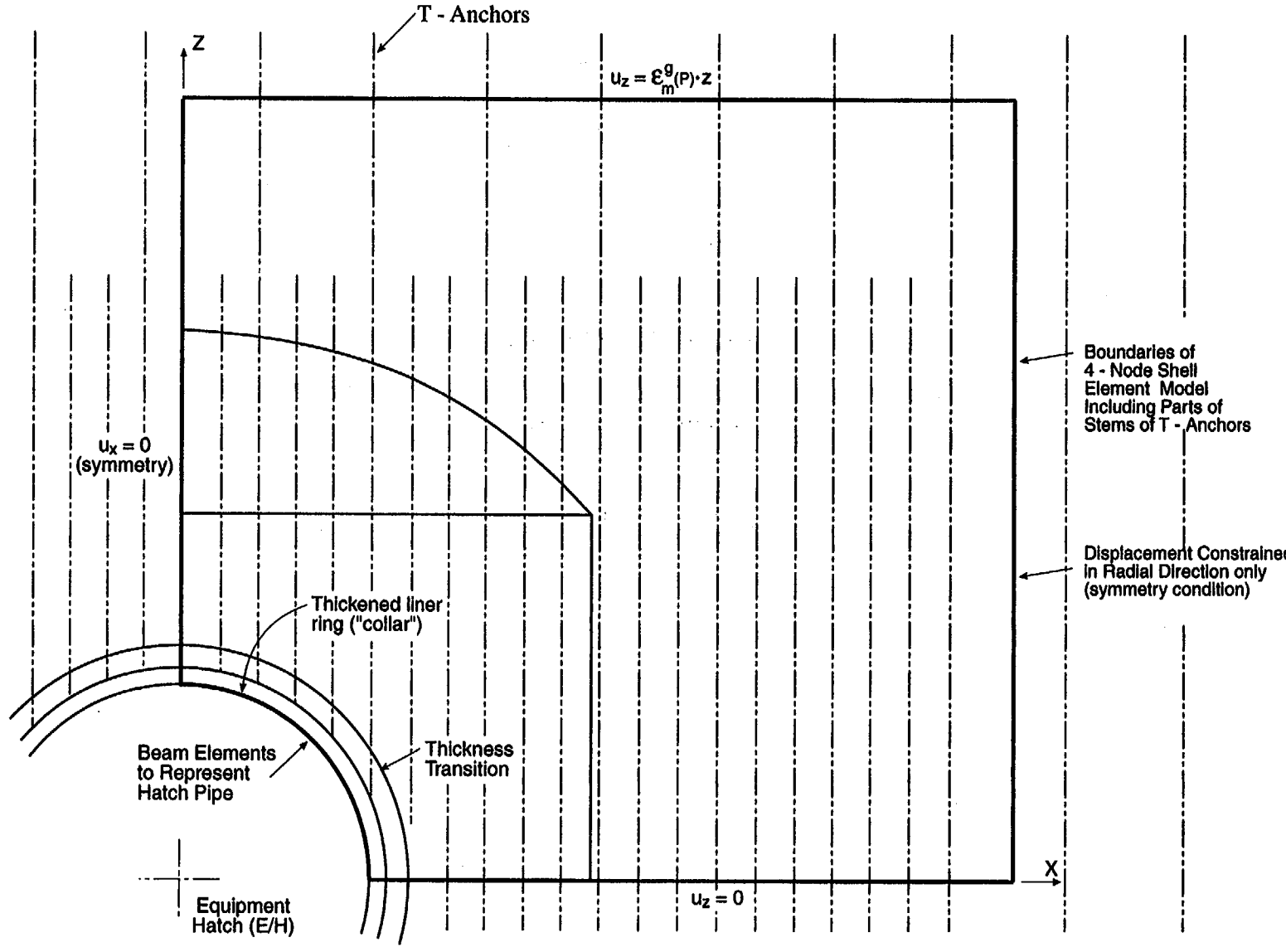


Figure 8-2. Detailed Liner Analysis Near E/H (View from Inside Prestressed Concrete Containment Vessel [PCCV] Looking Out Radially)

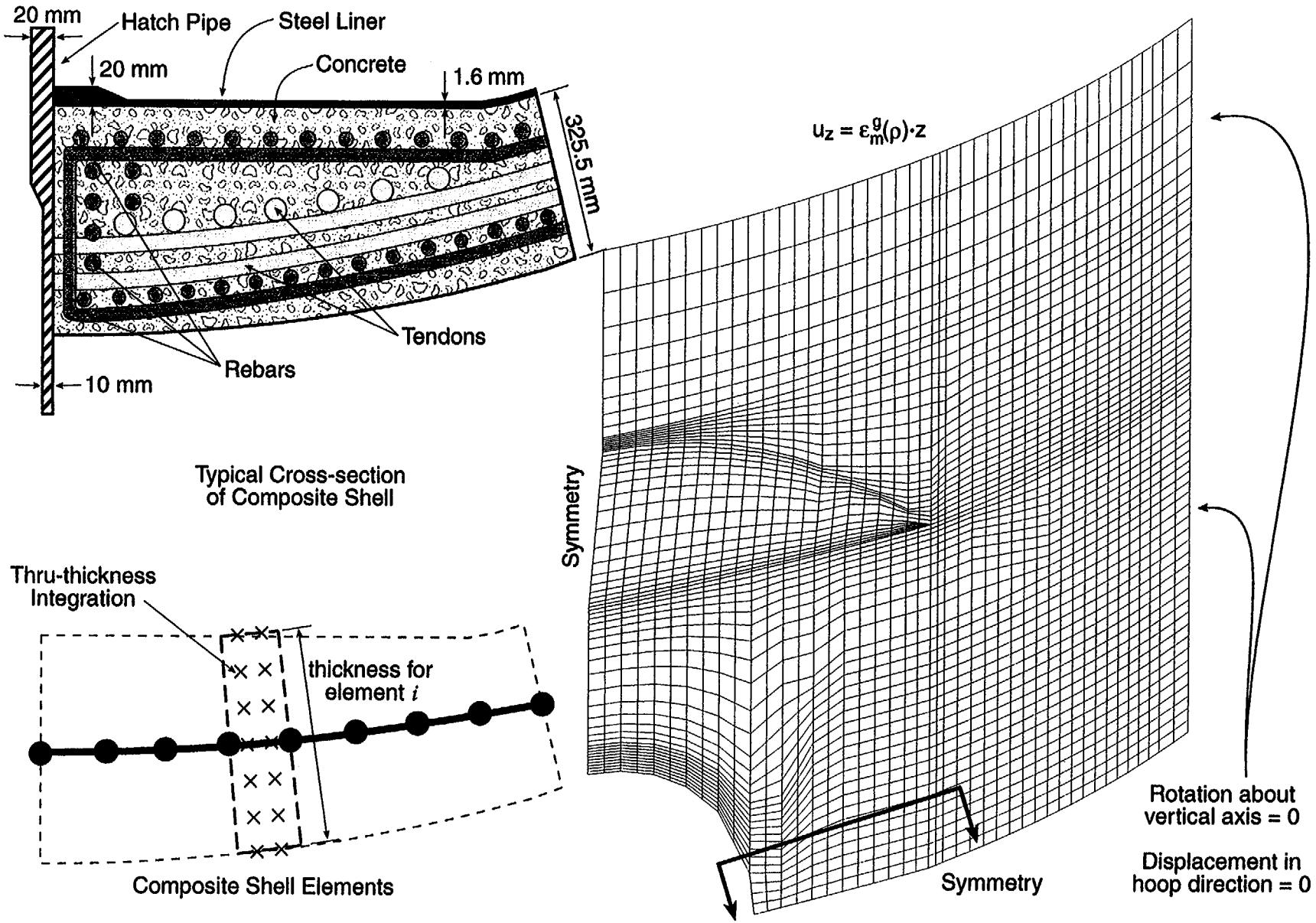


Figure 8-3. Composite Shell Model Used in E/H Liner Study

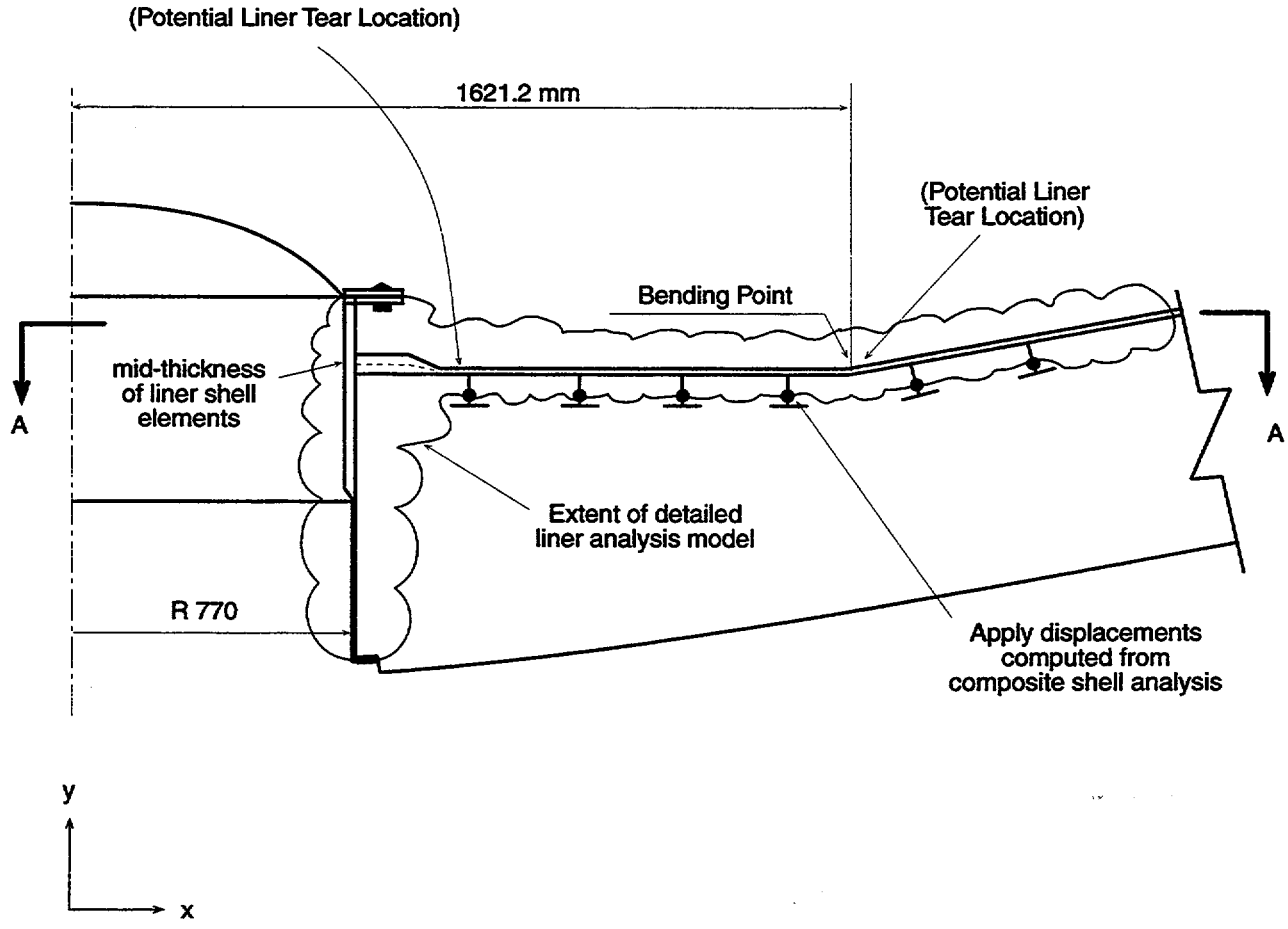


Figure 8-4. Plan Section Schematic of E/H Region

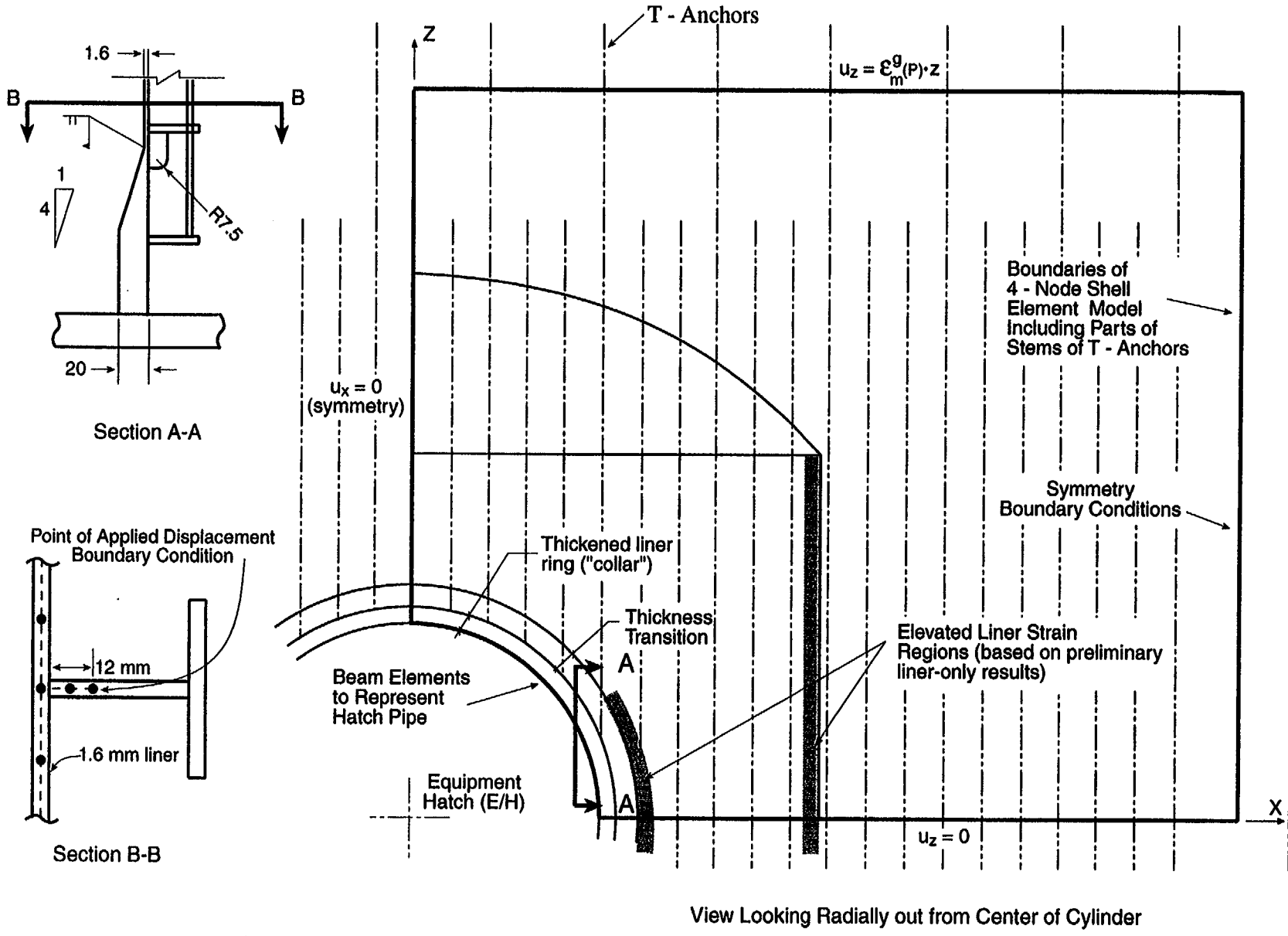


Figure 8-5. Detailed Liner Analysis Near E/H (View from Inside Prestressed Concrete Containment Vessel [PCCV] Looking Out Radially)

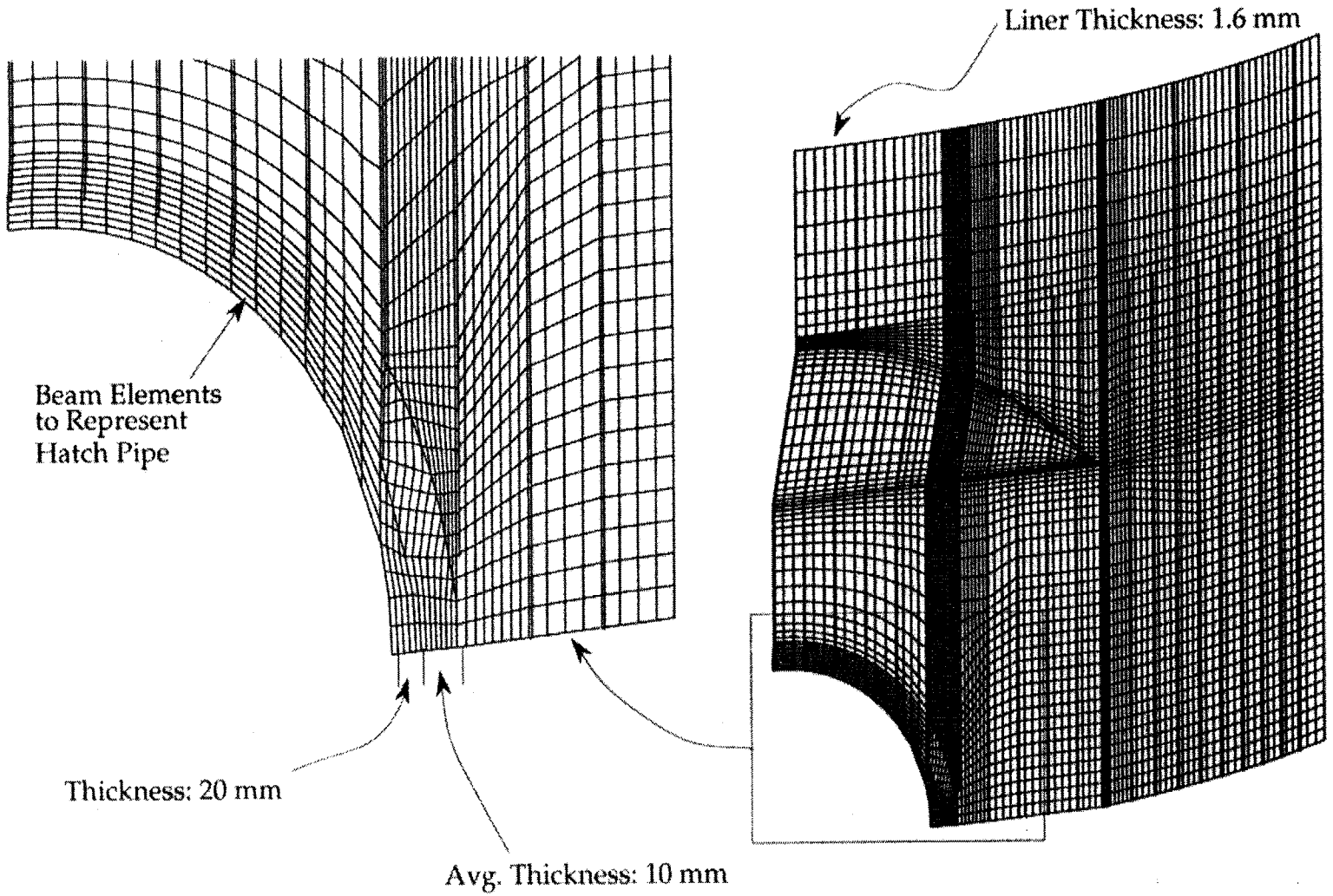


**Figure 8-6. Finite Element Model of Steel Liner**

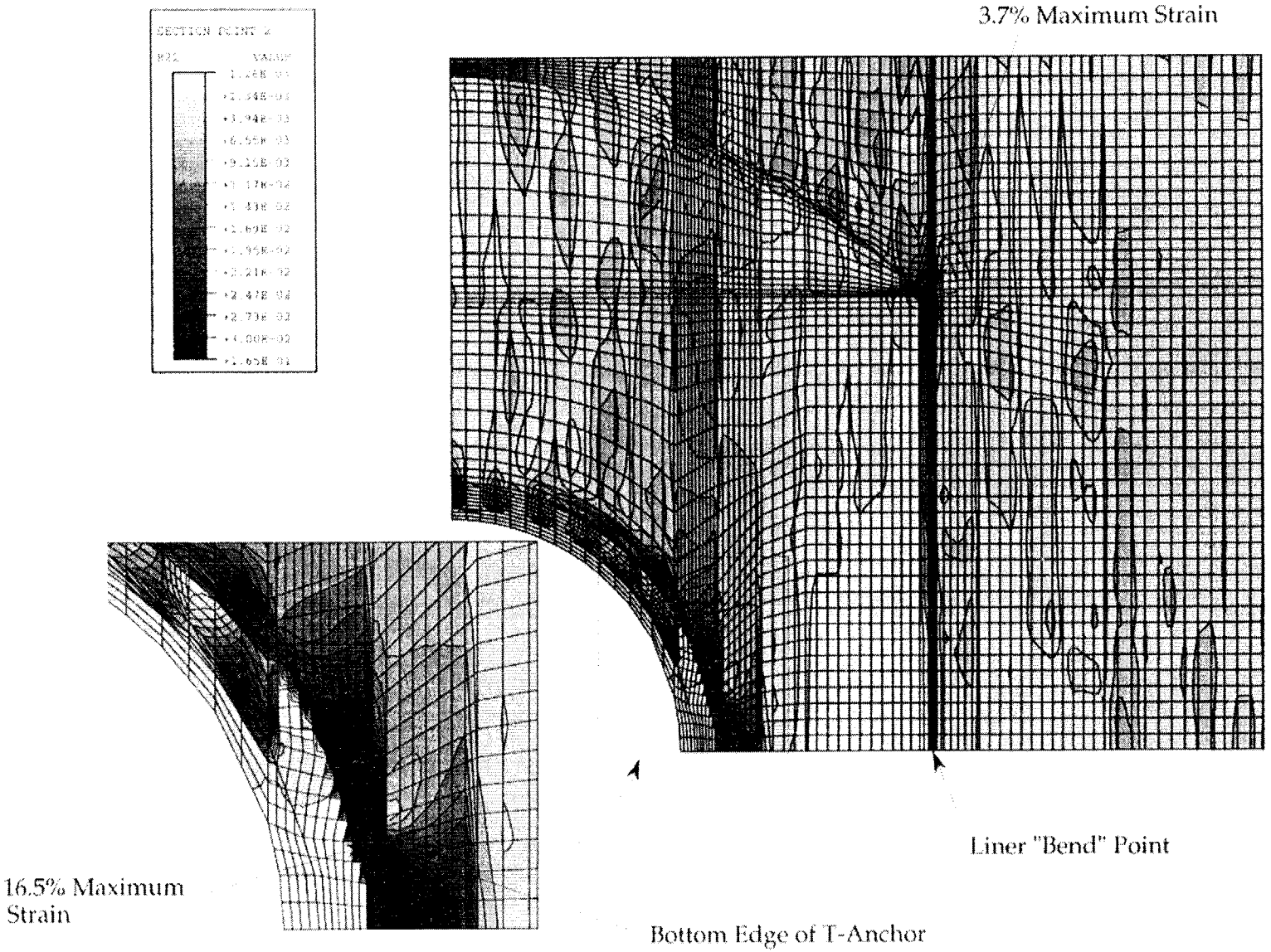


Figure 8-7. Liner Hoop Strains at Pressure of Approximately 3.6 Pd

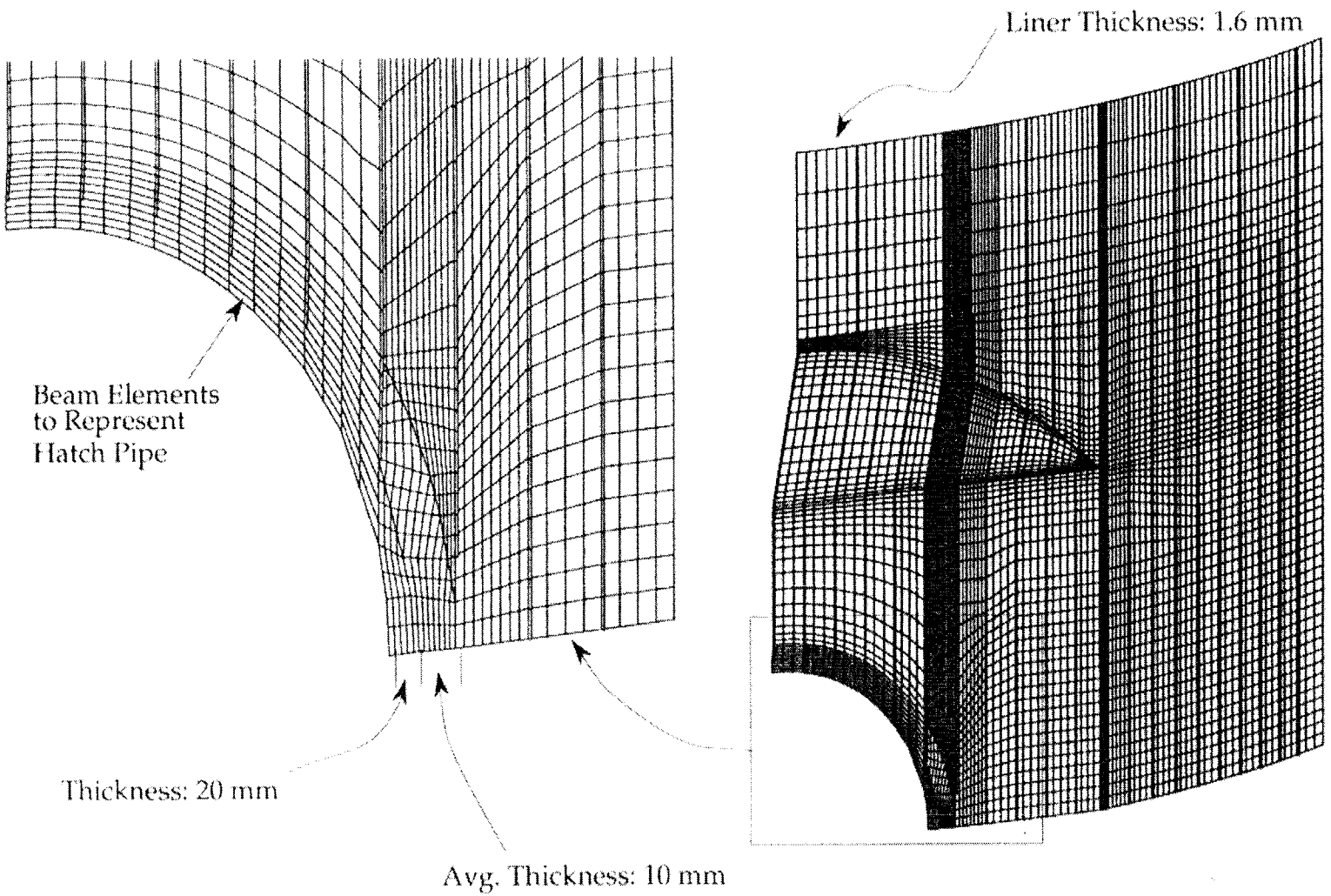


**Figure 8-6. Finite Element Model of Steel Liner**

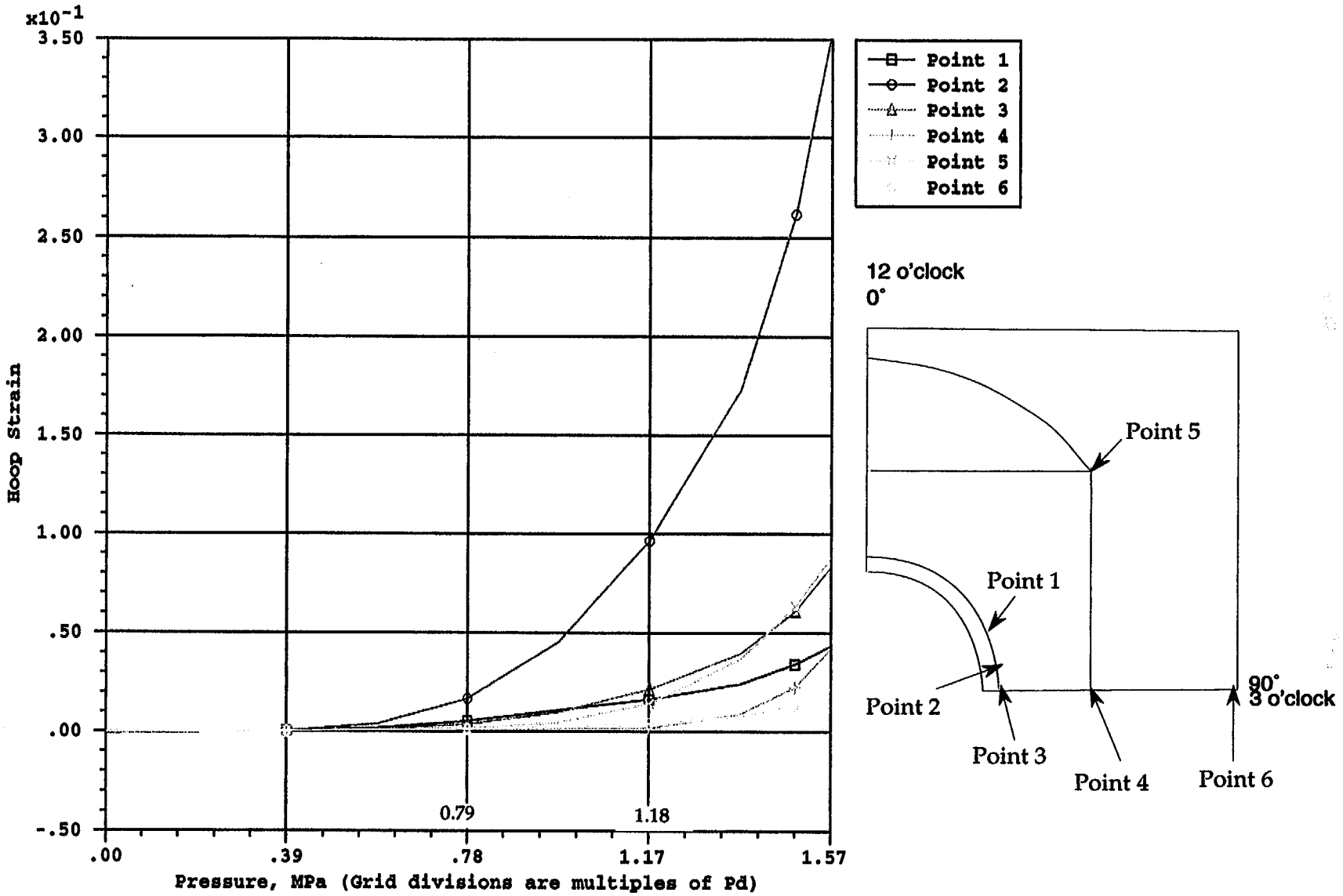




*3dcm.inp*

Figure 8-8. Liner Hoop Strain History as a Function of Internal Pressure

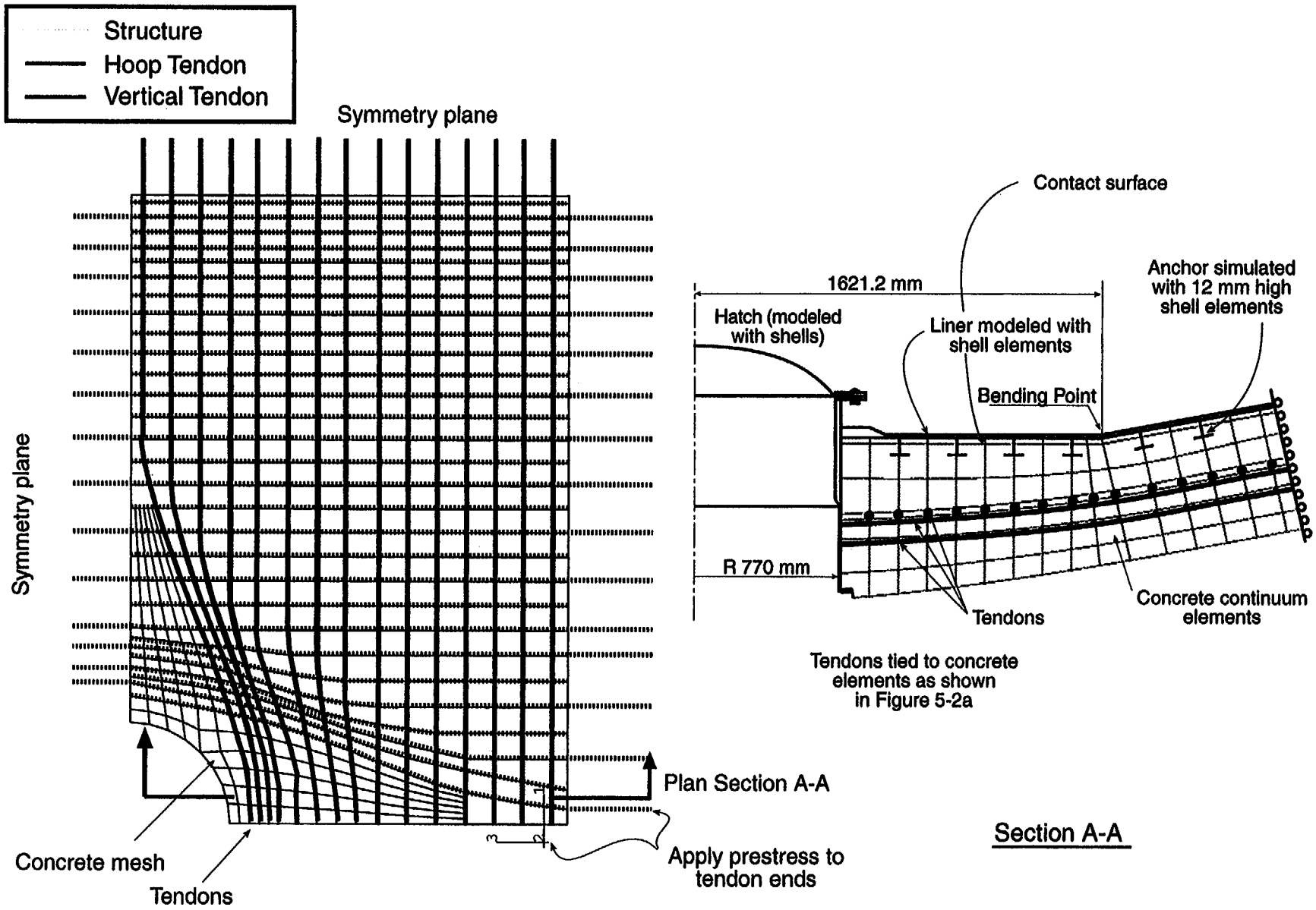


Figure 8-9. 3D Equipment Hatch Model Looking Radially In (left) and a Plane Section (right)

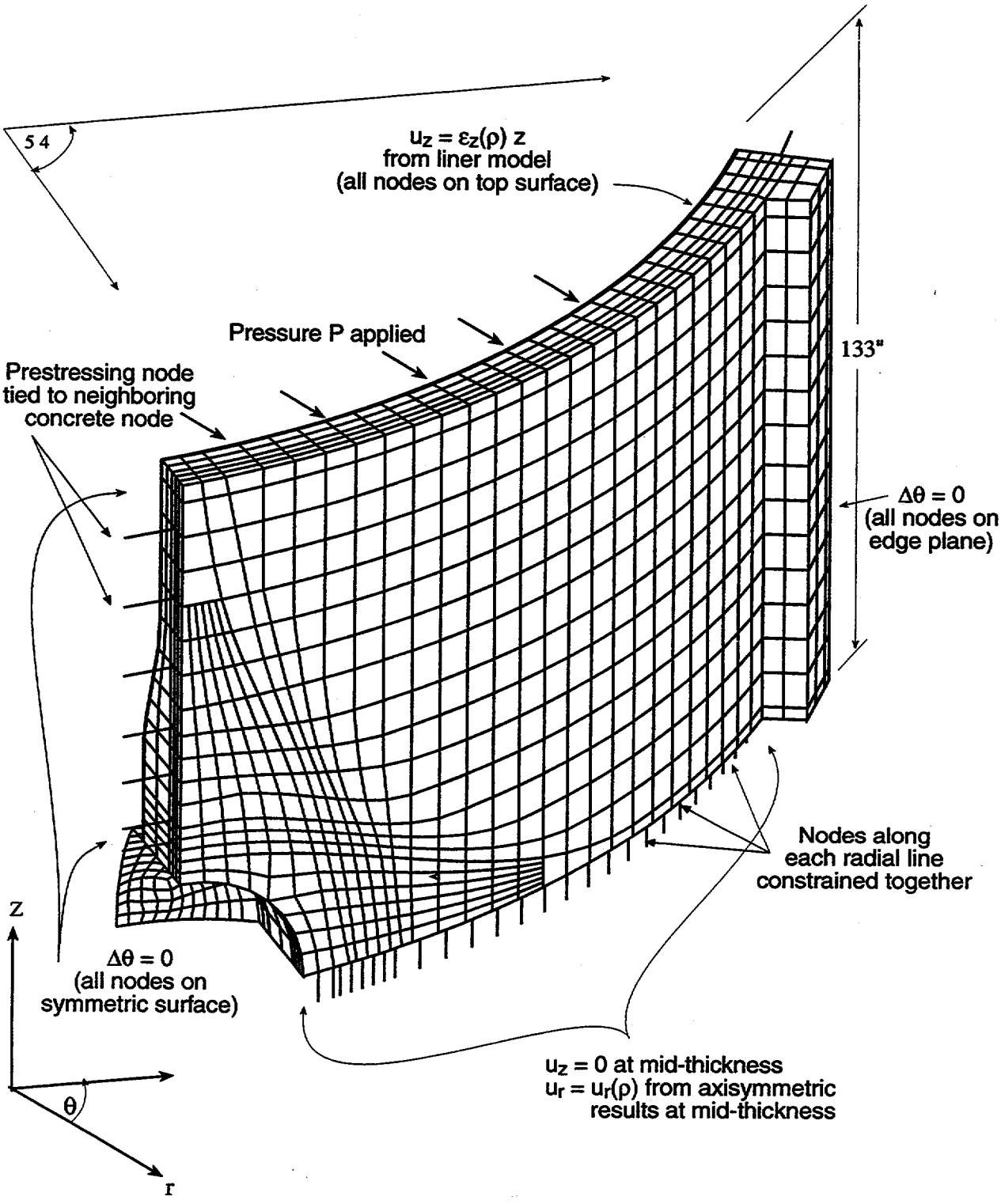


Figure 8-10. Boundary Conditions and Geometry for 3D E/H Model

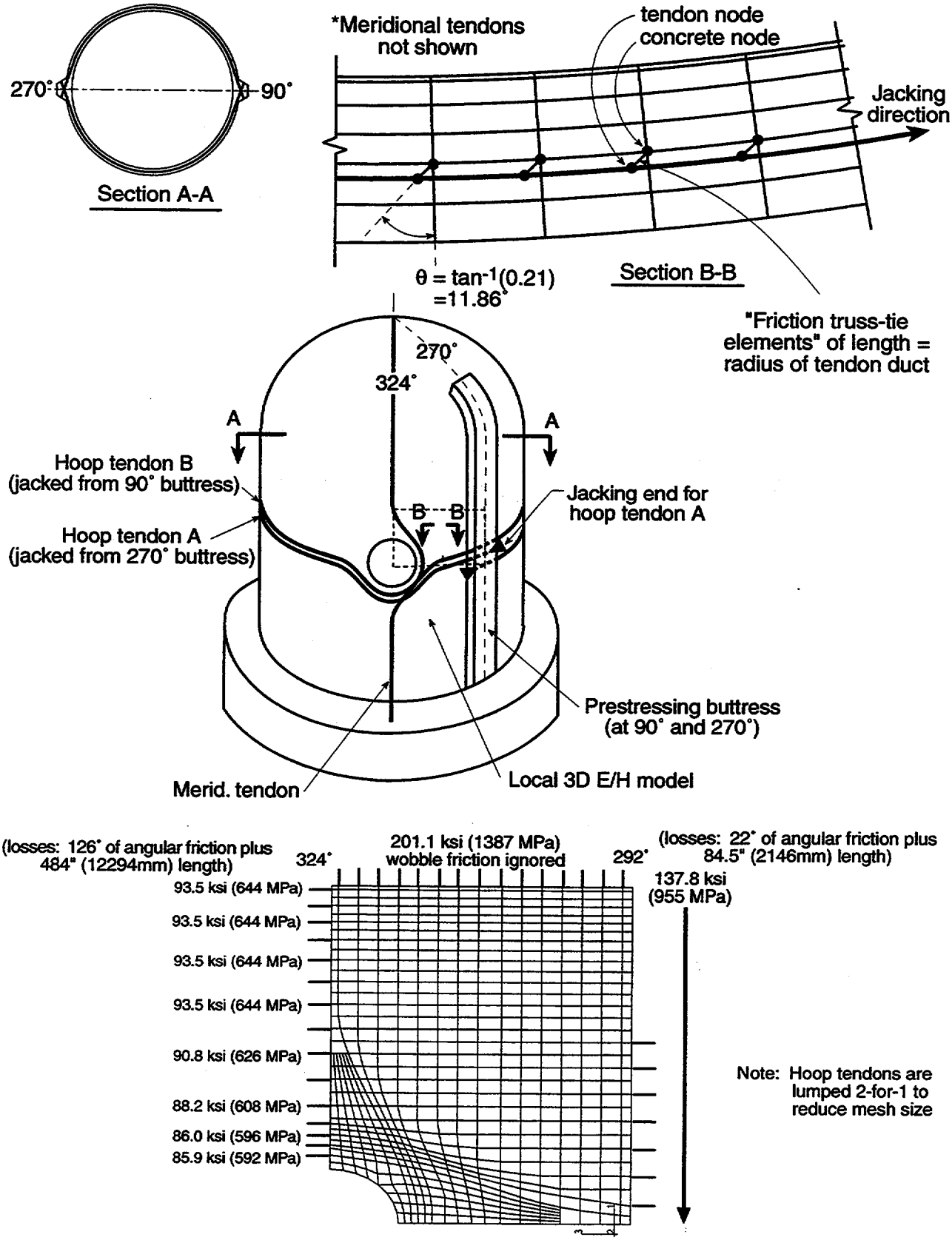


Figure 8-11. Tendon Stressing for 3D E/H Model

Figure 8-12. Finite Element Mesh Including Tendons, Liner, Anchors, and Stiffeners

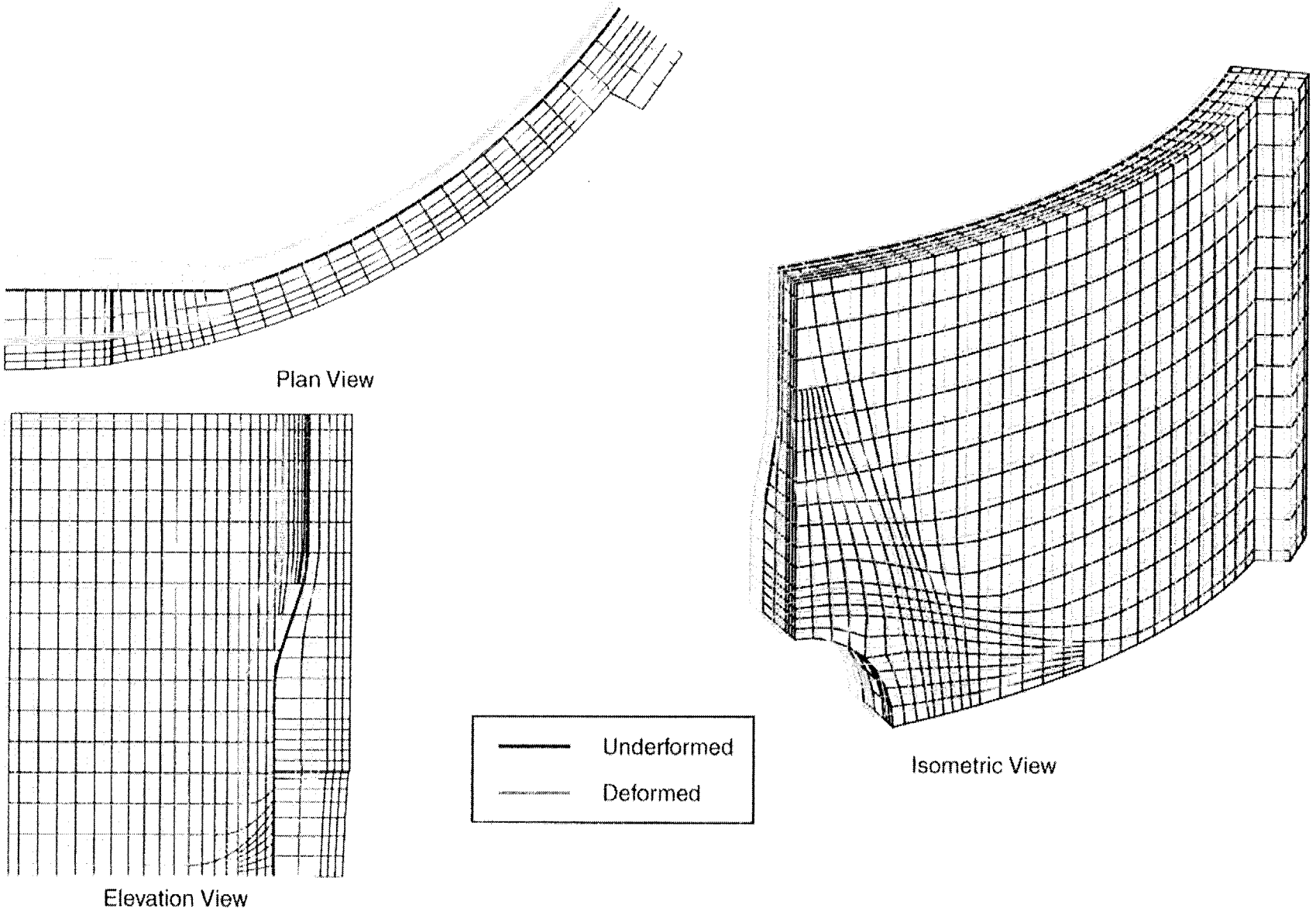


Figure 8-13. Prestress Deformed Shape of E/H Model at Pressure = 2.75 Pd (Magnification factor = 100x)

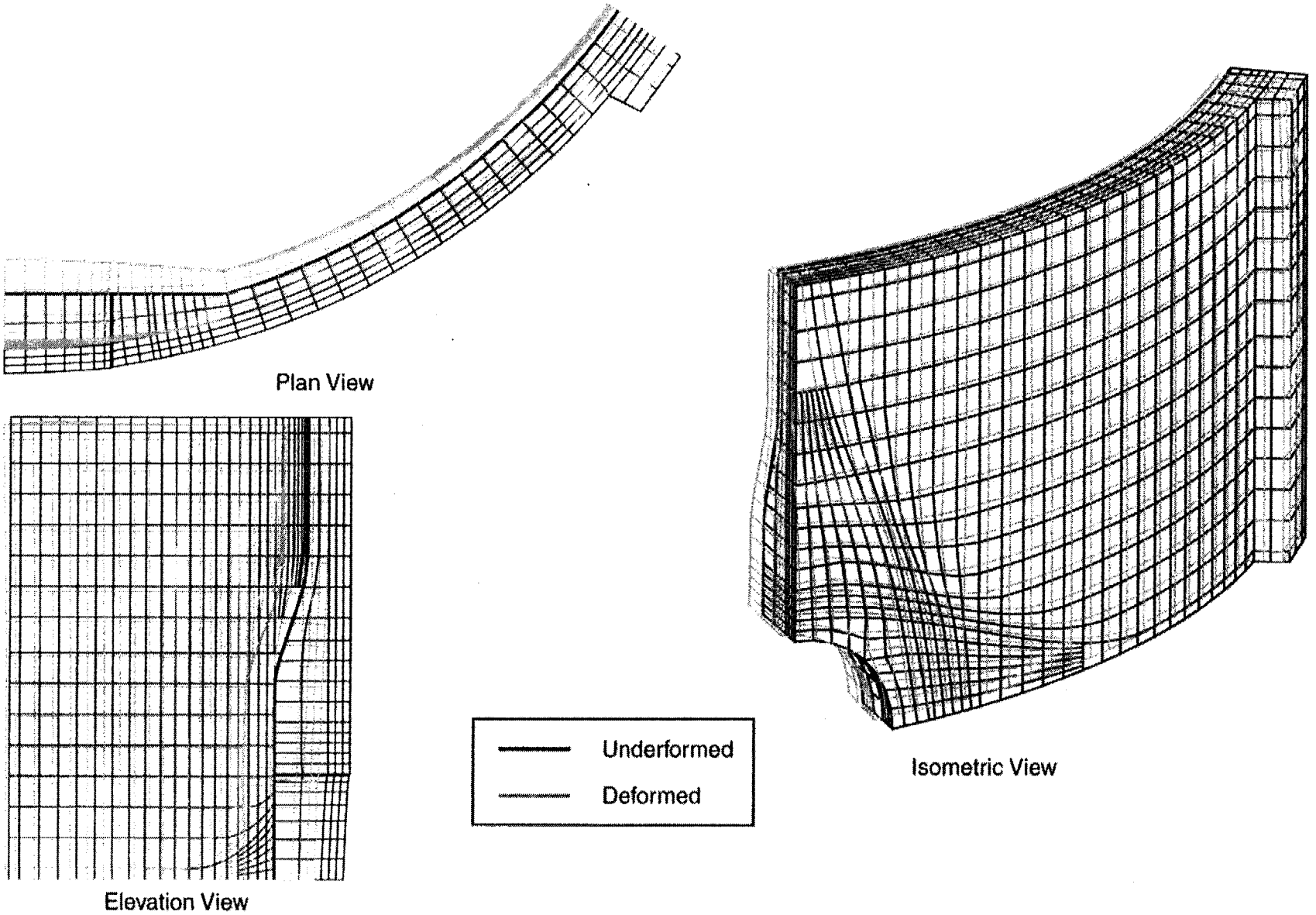


Figure 8-13. Prestress Deformed Shape of E/H Model at Pressure = 2.75 Pd (Magnification factor = 100x)

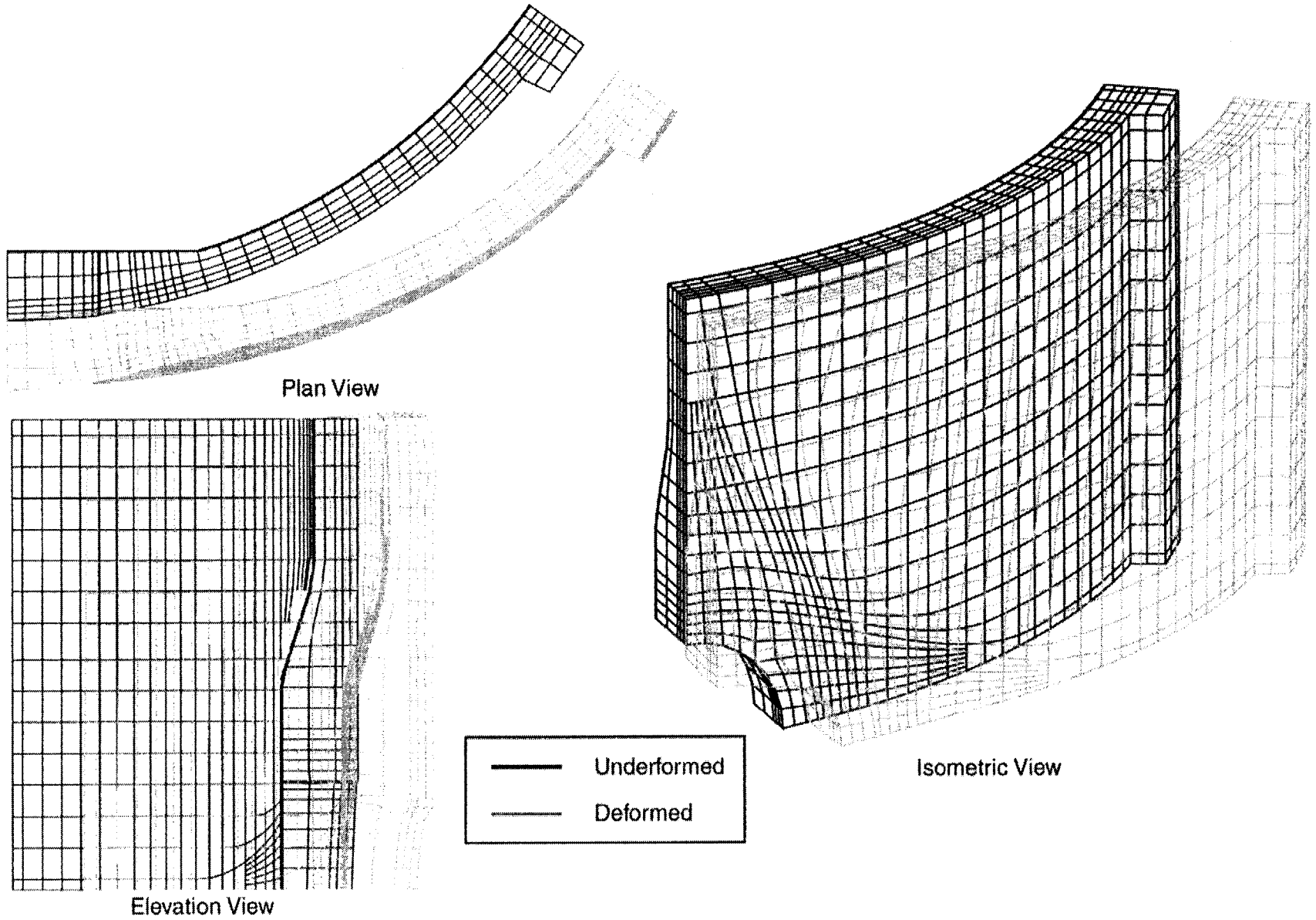


Figure 8-14. Deformed Shape of E/H Model at Pressure = 3.25 Pd (Magnification factor = 20x)

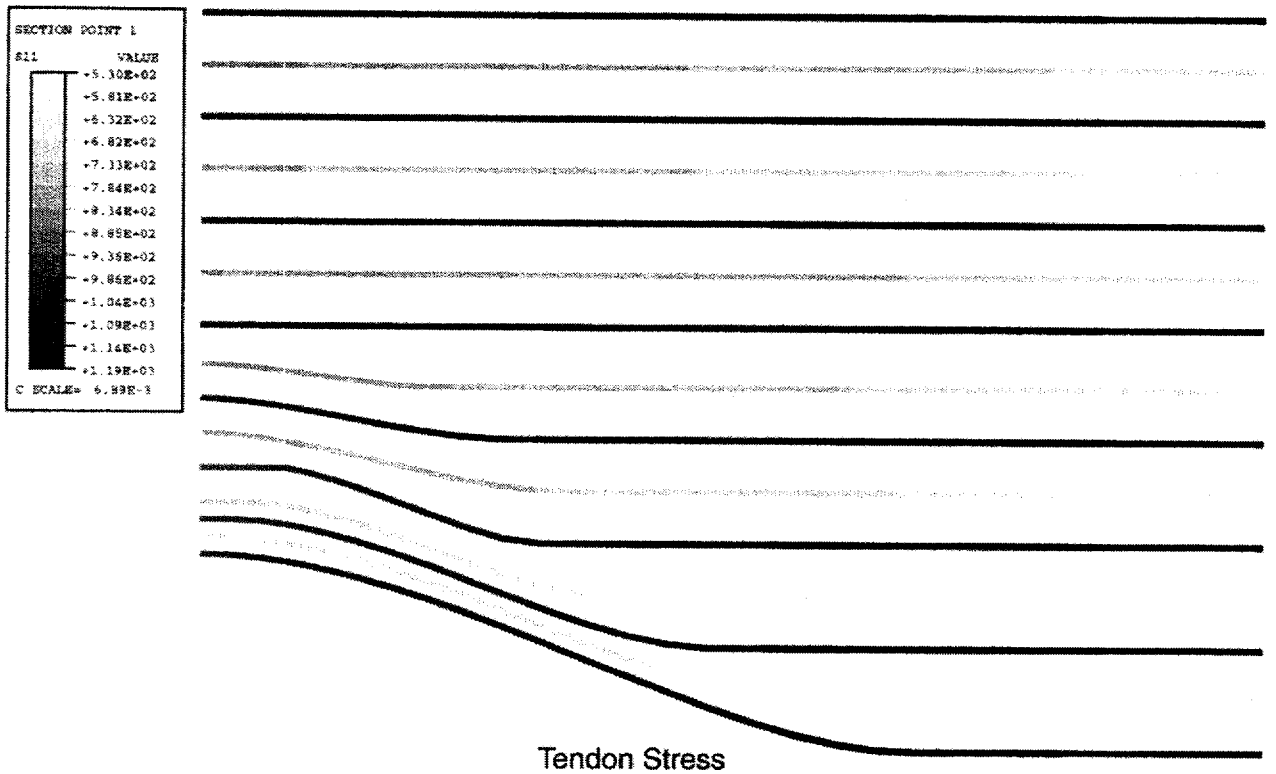


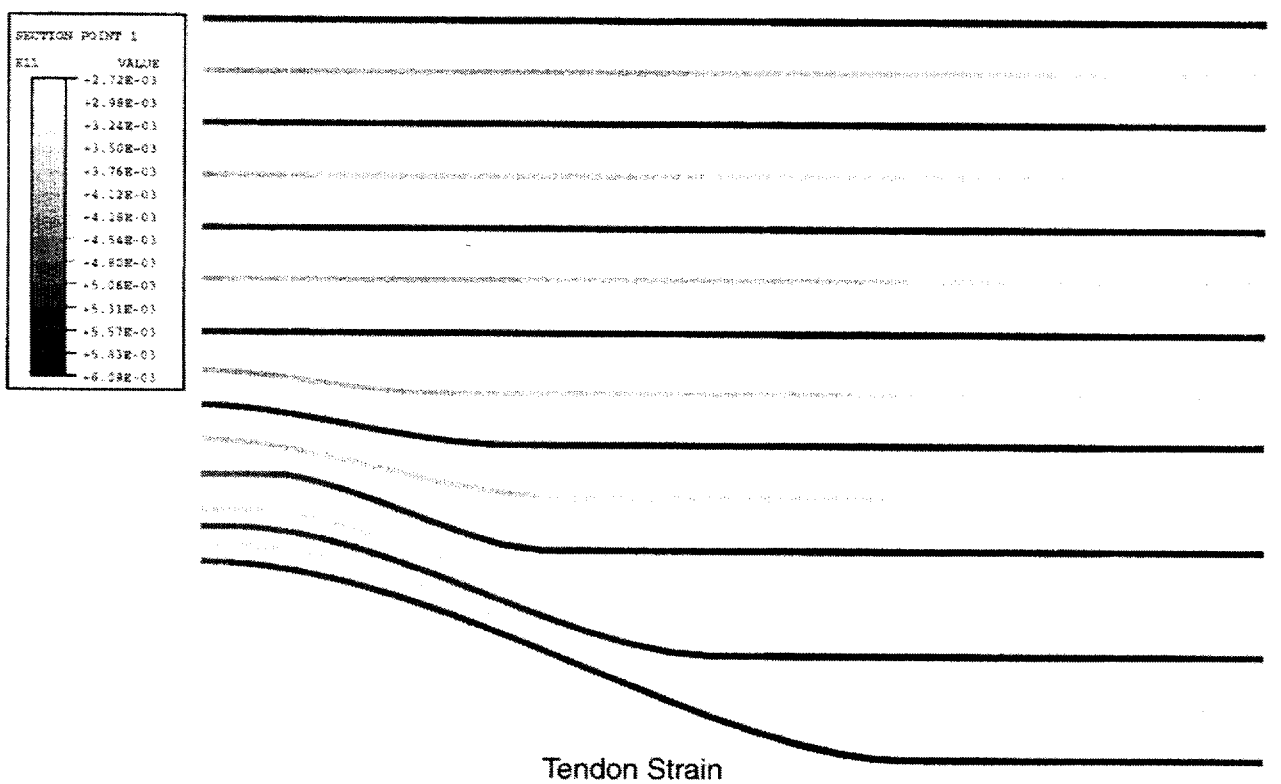


Figure 8-15. E/H Hoop Tendon Stress and Strain Contours at Prestress

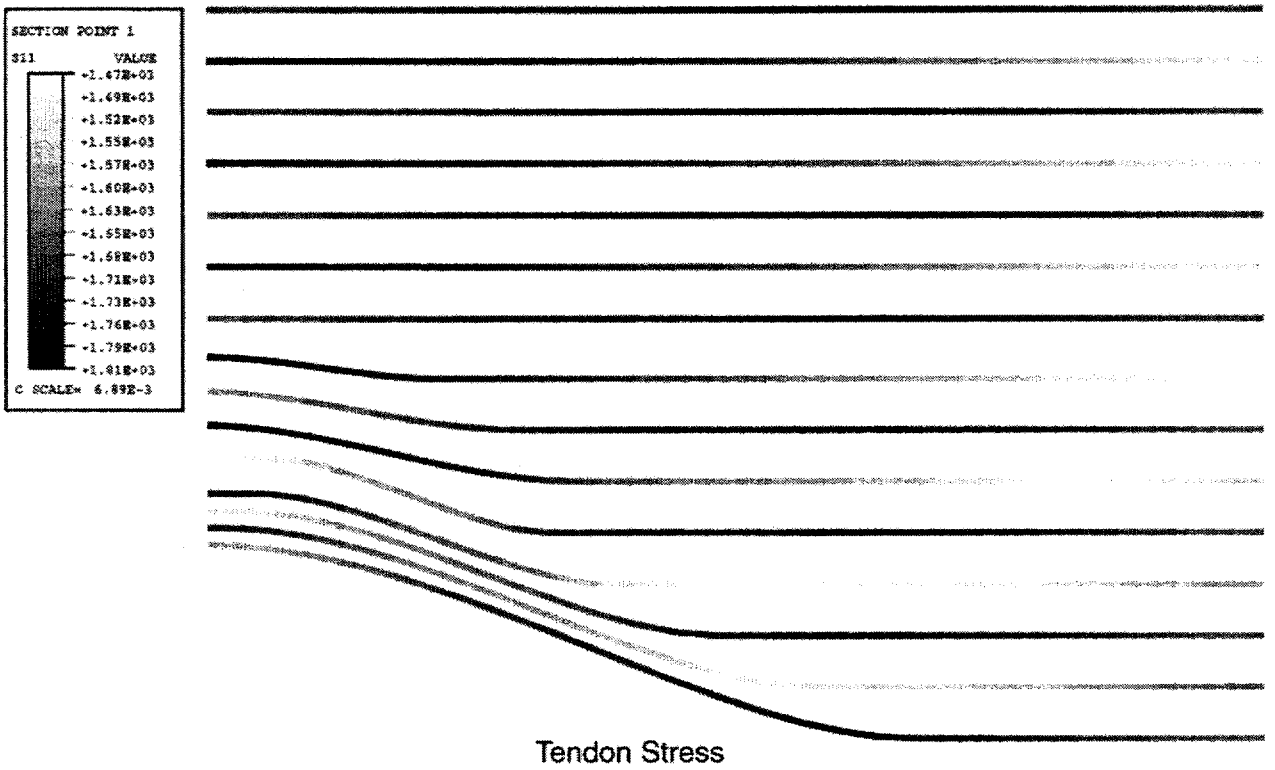


Tendon Stress

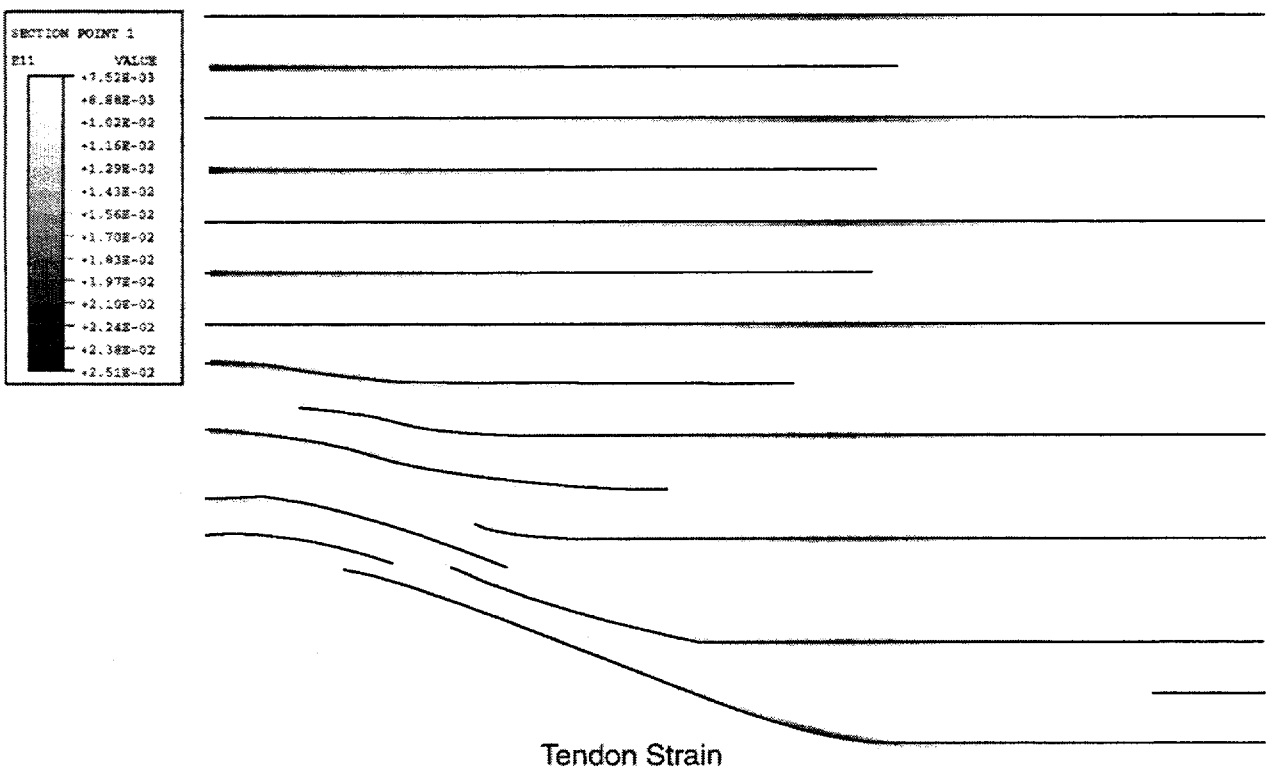


Tendon Strain

Figure 8-16. E/H Hoop Tendon Stress and Strain Contours at Pressure = 3.25 $P_d$

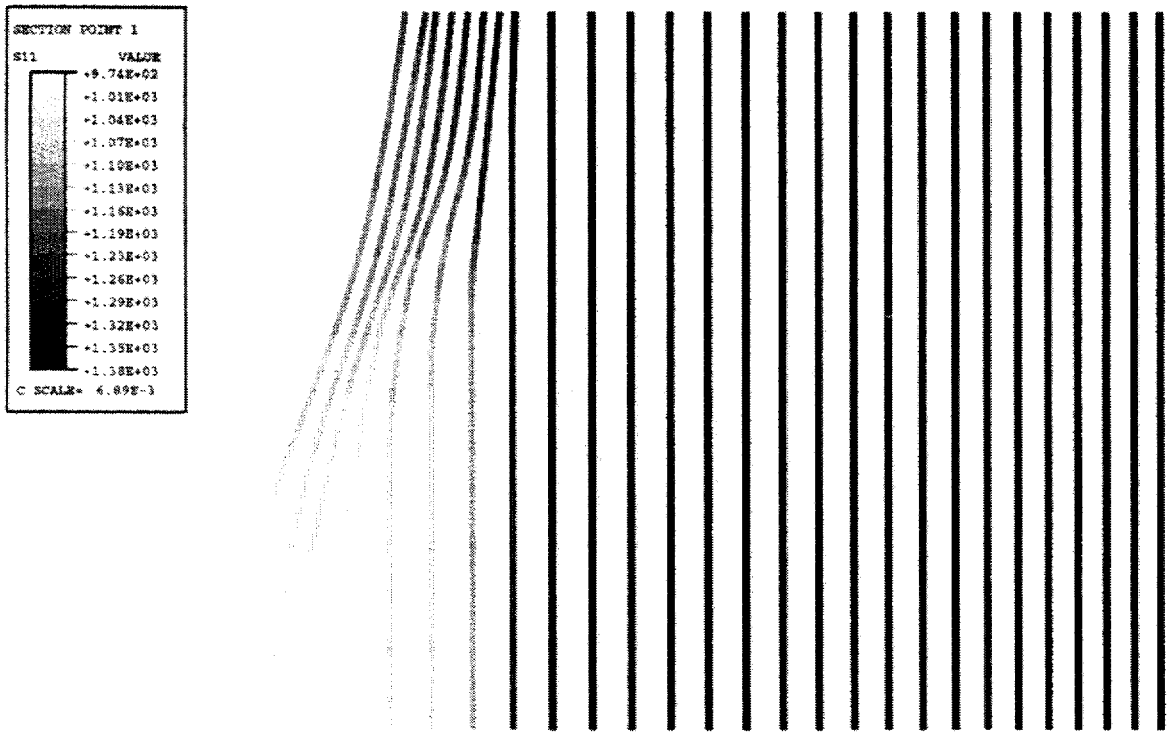


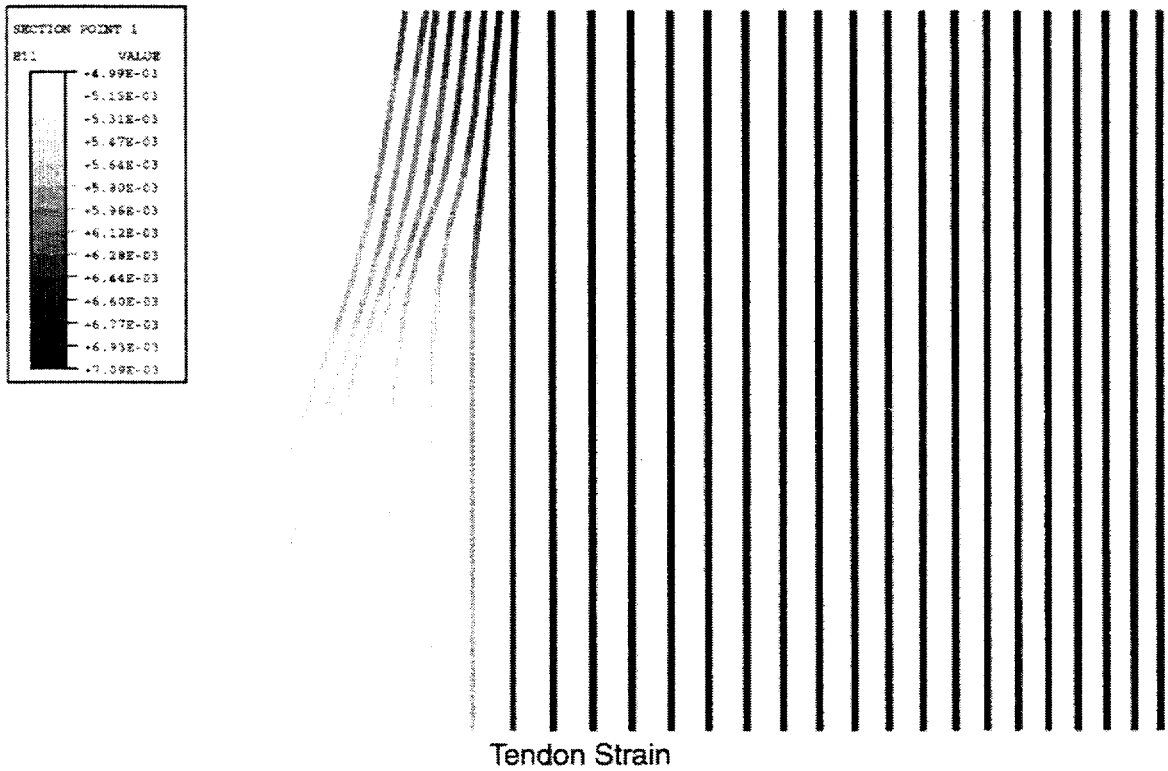


Figure 8-17. E/H Vertical Tendon Stress and Strain Contours at Prestress

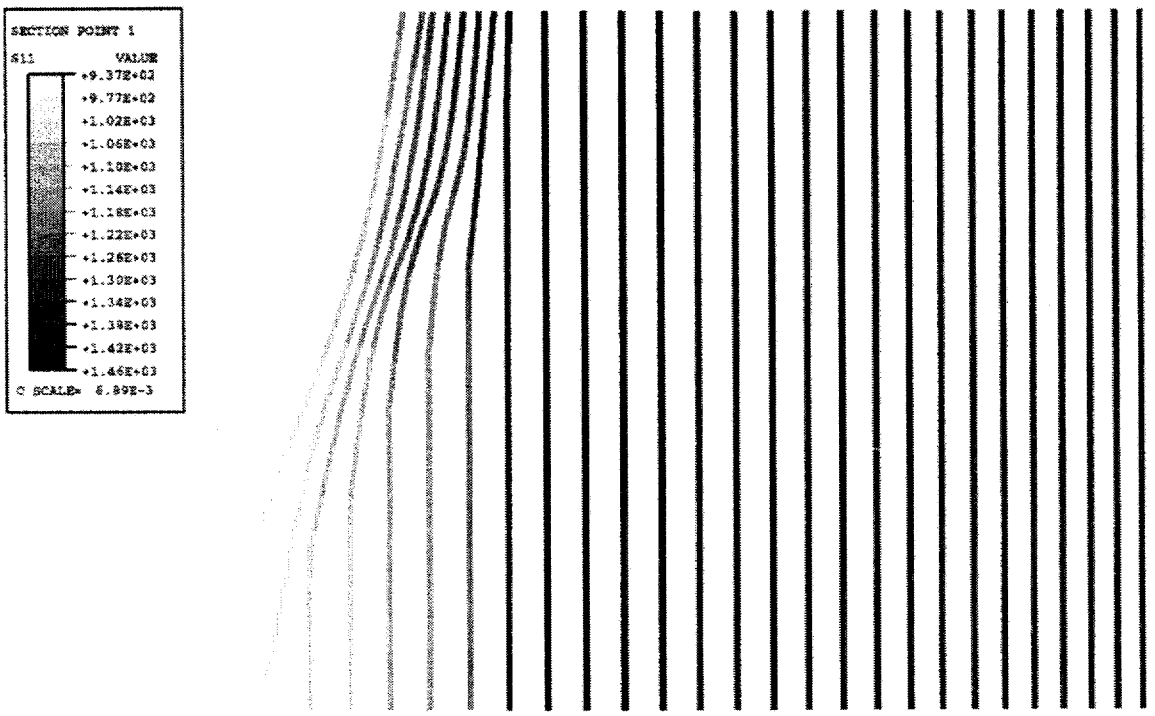


Tendon Stress

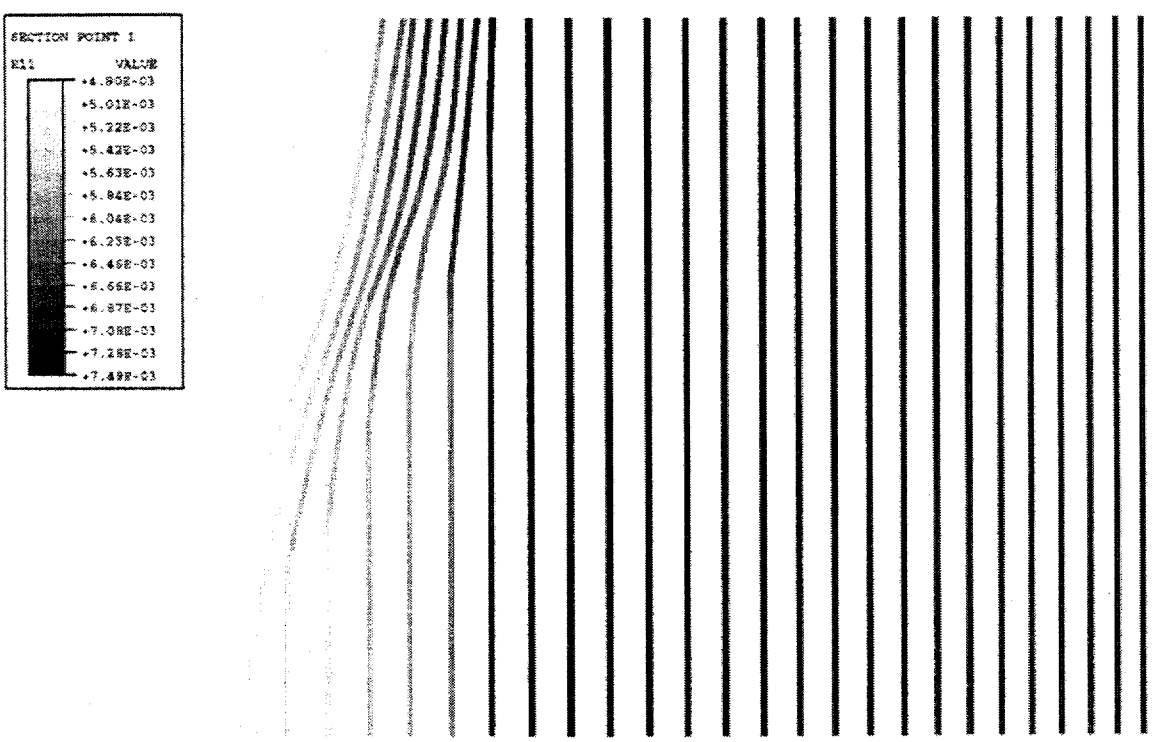


Tendon Strain

Figure 8-18. E/H Vertical Tendon Stress and Strain Contours at Pressure = 3.25 $P_d$

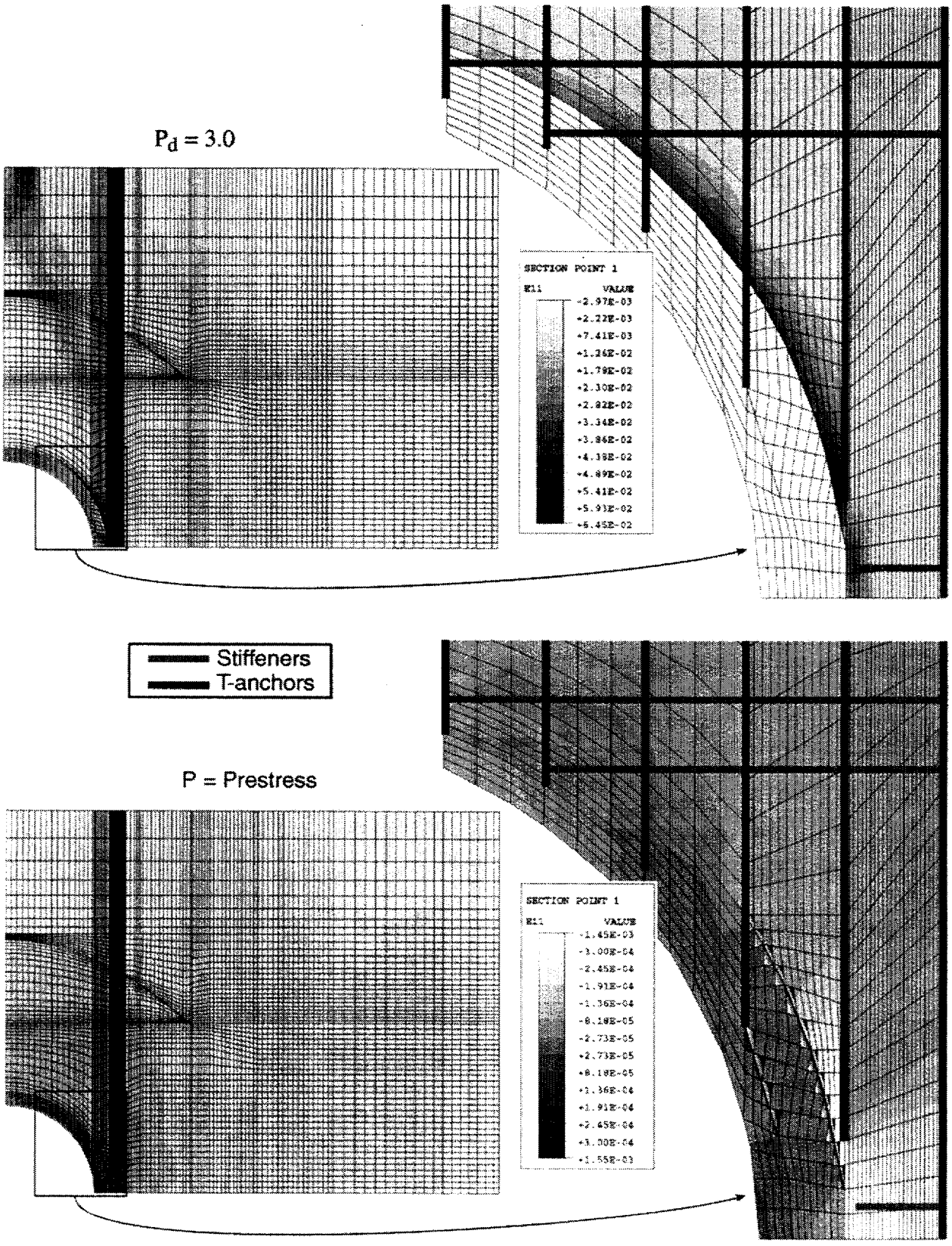


Figure 8-19. Liner Contour Hoop Strain Plots

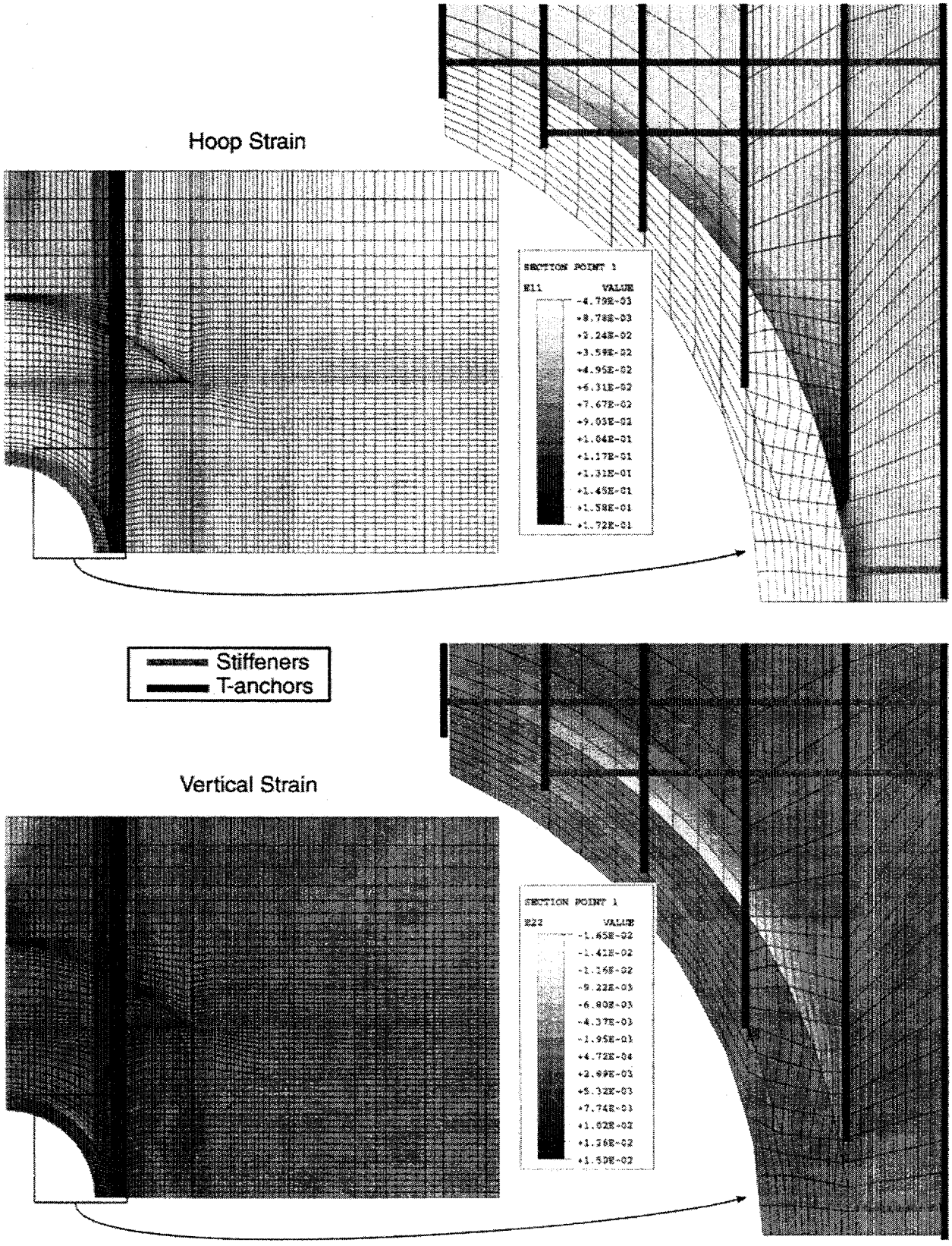


Figure 8-20. Liner Contour Strain Plots at P = 3.25 Pd

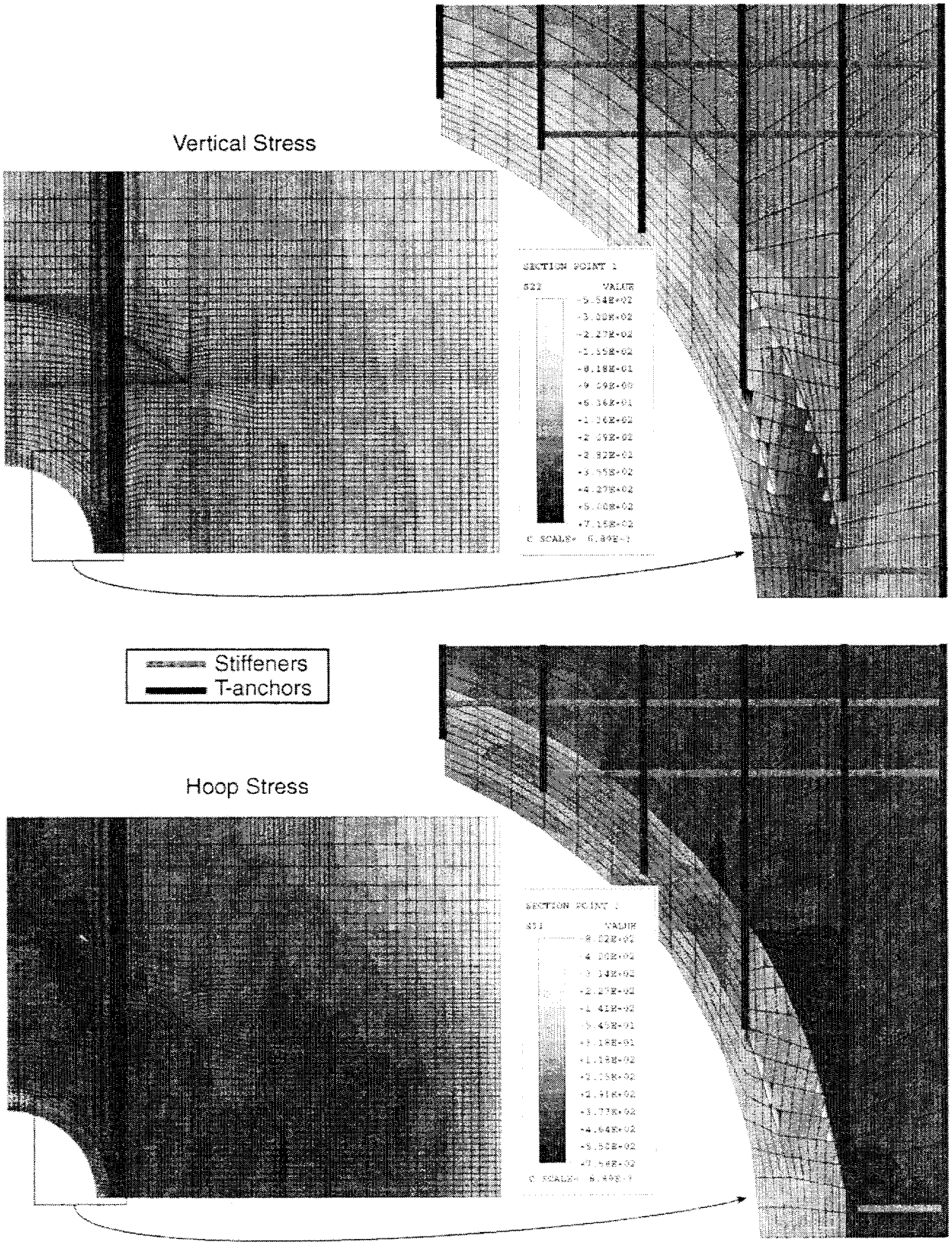


Figure 8-21. Liner Contour Stress Plots at P = 3.25 $P_d$

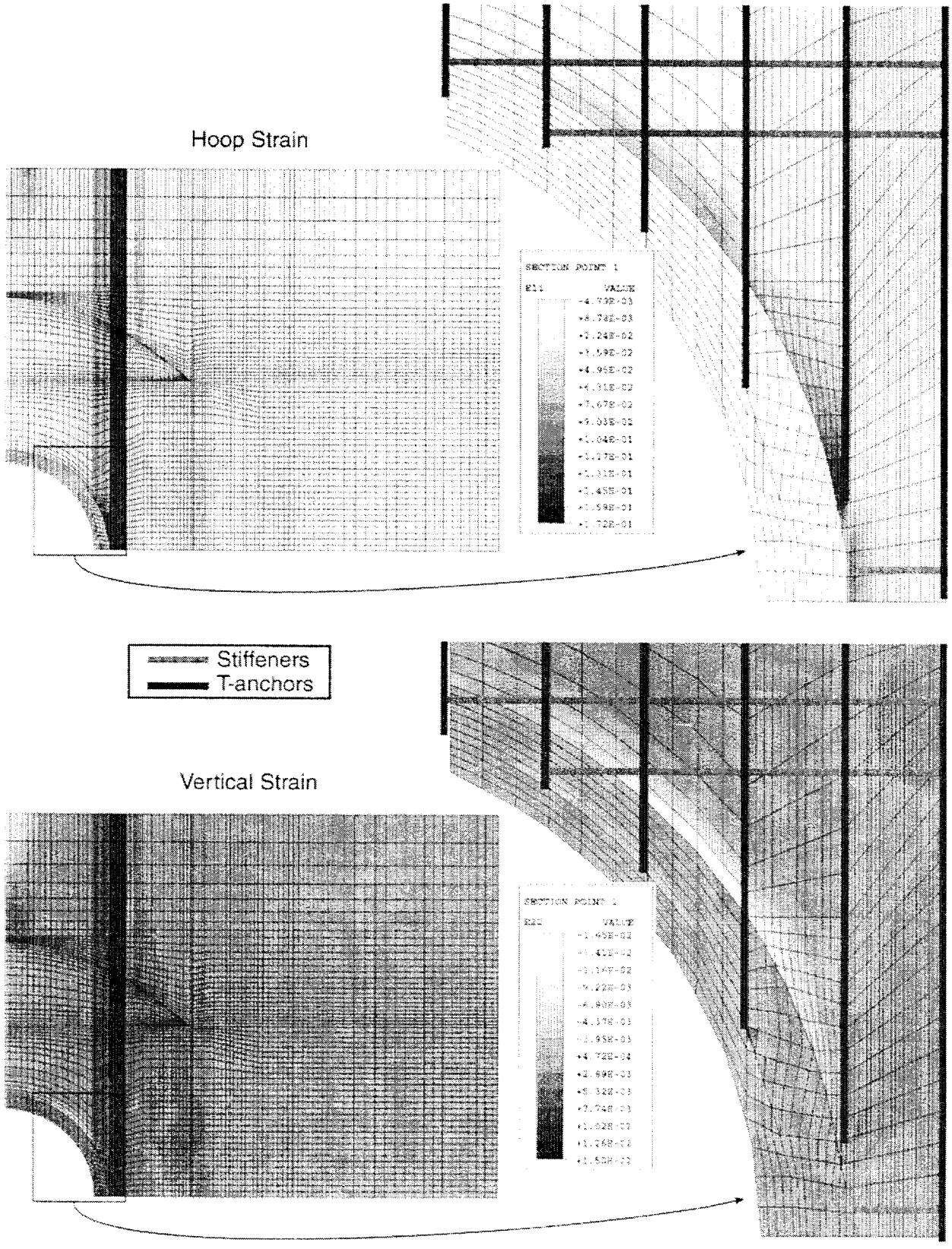


Figure 8-20. Liner Contour Strain Plots at P = 3.25 Pd

# 9. PERSONNEL AIRLOCK ANALYSIS

The personnel airlock (A/L) is the second largest penetration in the prestressed concrete containment vessel (PCCV) model, and it is located at the 62° azimuth, at Elev. 4.525 m. As with the equipment hatch (E/H), there are liner connection and anchorage details near the A/L that cause large strain concentrations, which makes the region near the A/L a candidate for a liner-tearing failure mode. Figure 9-1 shows the details of liner construction near the A/L.

A photograph of the region, taken prior to final welding, installation of some vertical anchors, and prestressing sheaths or rebar, are shown in Figure 9-2. Figure 9-2 identifies two specific kinds of large strain concentration locations associated with the A/L: the zone near the end of a vertical T-anchor (at about the 2:00 position) and at the end of a horizontal stiffener (near the 3:00 position). Both these details and the tendon and rebar geometries are similar to the E/H, so much of the modeling discussion in this chapter refers to the more detailed description of the modeling that is found in Chapter 8.

## 9.1 Computational Model

The A/L 3D local model is illustrated in Figure 9-3. In the Preliminary Analysis Phase, the lower quadrant (below Elev. 4.525m) was modeled, but the final prediction model was changed to the upper quadrant for two reasons:

1. so that the model would be encompassed by the 3D cylinder midheight (3DCM) model and, thereby, have appropriate boundary conditions at all edges; and

2. because the hoop stiffeners occur only in the upper quadrant.

Because the A/L is close to a buttress, the local model was extended to the buttress centerline, allowing study of the local strain concentrations near the buttress, in addition to those near the E/H. The modeling details for the local A/L model are similar to those developed for the E/H model. The liner-anchor interaction (shear-force deflection behavior of the anchors) is modeled identically to the E/H, as is the method of attaching the liner/anchor mesh to the concrete mesh. The concrete mesh and prestressing tendon element layouts are shown in Figures 9-4 and 9-5. The hoop tendons are modeled two-for-one just as in the 3DCM and in the E/H local model, and the meridional tendons are modeled one-for-one. The rebar generated for the local A/L model is identical to the 3DCM model.

## 9.2 Analysis Results

A similar hoop strain versus pressure, boundary condition correlation was used for the A/L local model as was used for the E/H model. Here the average hoop strain obtained from the 3DCM model was the hoop strain at Elev. 4.525 m, occurring along the 28° arc between the A/L centerline at 62° and the 90° buttress. This provides the pressure correlation for all the local A/L analysis results.

The 3D local model analysis results for the A/L are shown in Figures 9-6 through 9-14. Figures 9-6 and 9-7 show deformed shape results These plots show that the A/L deforms radially outward about the same amount as the buttress. The A/L moves out more than the buttress in the 3DCM model analysis, and this deformation profile is deemed to be the more complete prediction.

Figures 9-8 through 9-11 show tendon stress and strain contours at $3.75P_d$. Figures 9-12 through 9-14 show liner strain and stress contours at $3.75P_d$, which indicate where the elevated liner strain concentrations ("hot spots") are predicted to occur in this region. The most elevated liner strain concentration is predicted to occur adjacent to the hoop stiffener and vertical T-anchor termination points, which is similar to E/H analysis results.

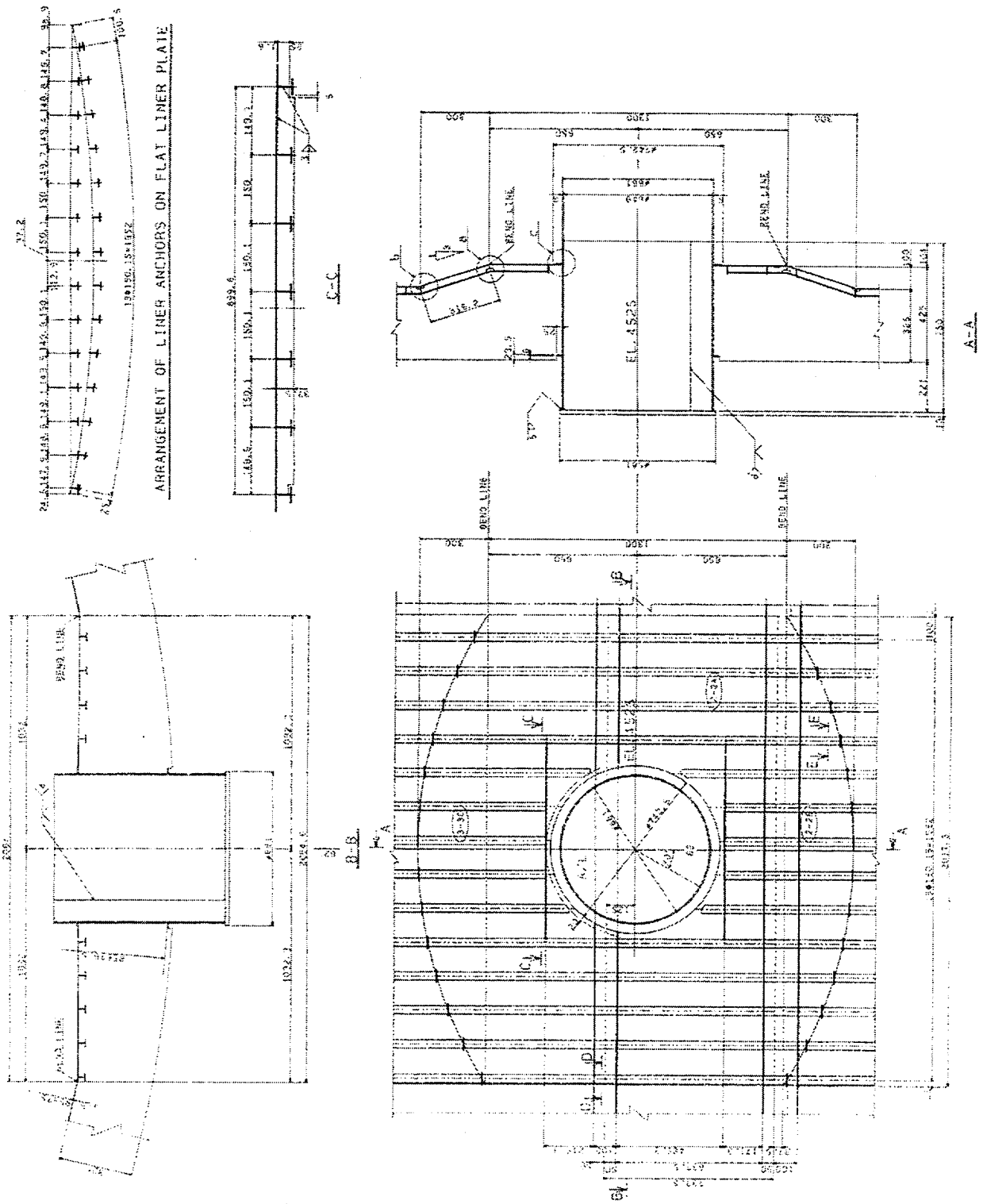


Figure 9-1. Personnel Airlock Liner Details

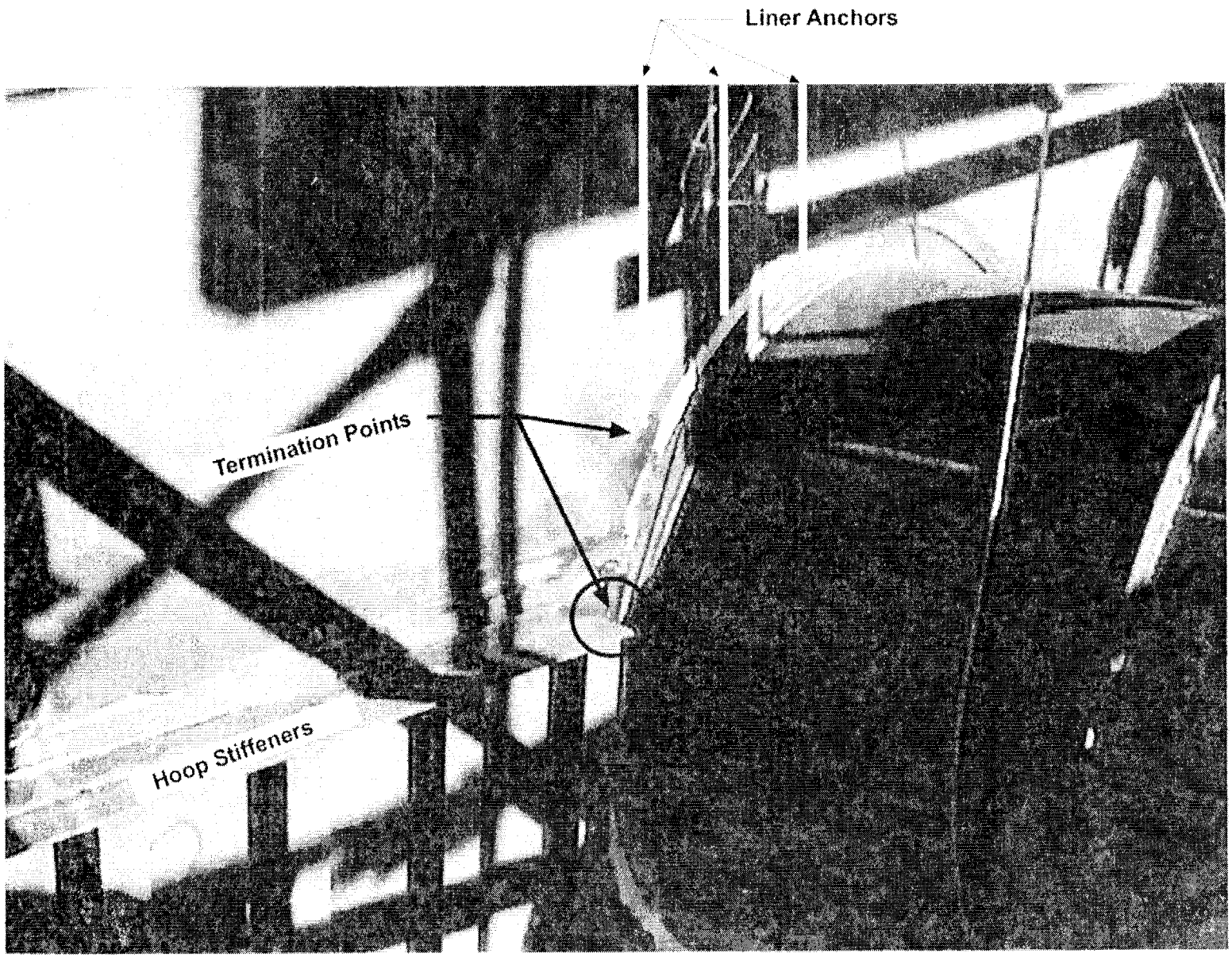


Figure 9-2. Personnel Airlock - Potential Liner Strain Concentrations

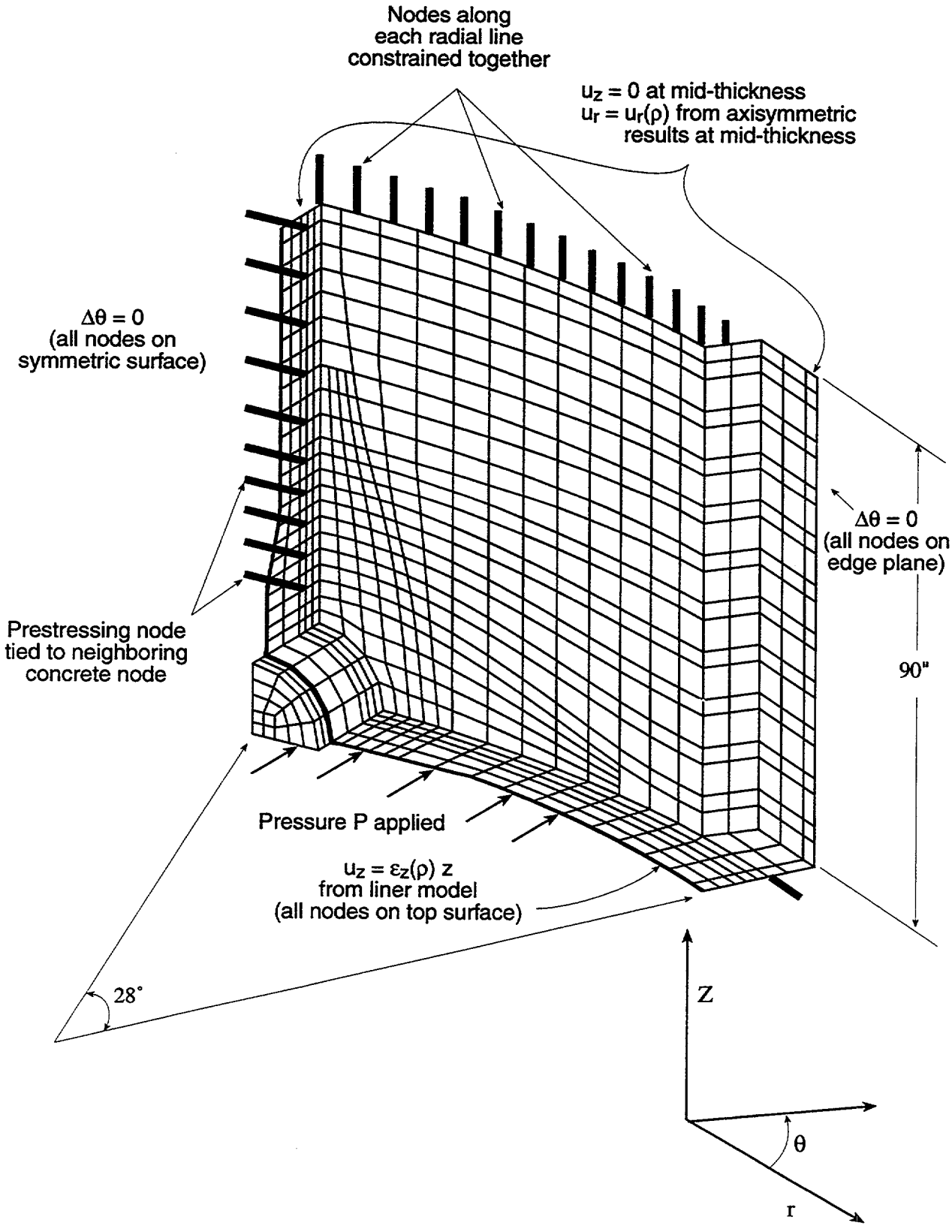


Figure 9-3. Boundary Conditions and Geometry for 3D Airlock Model

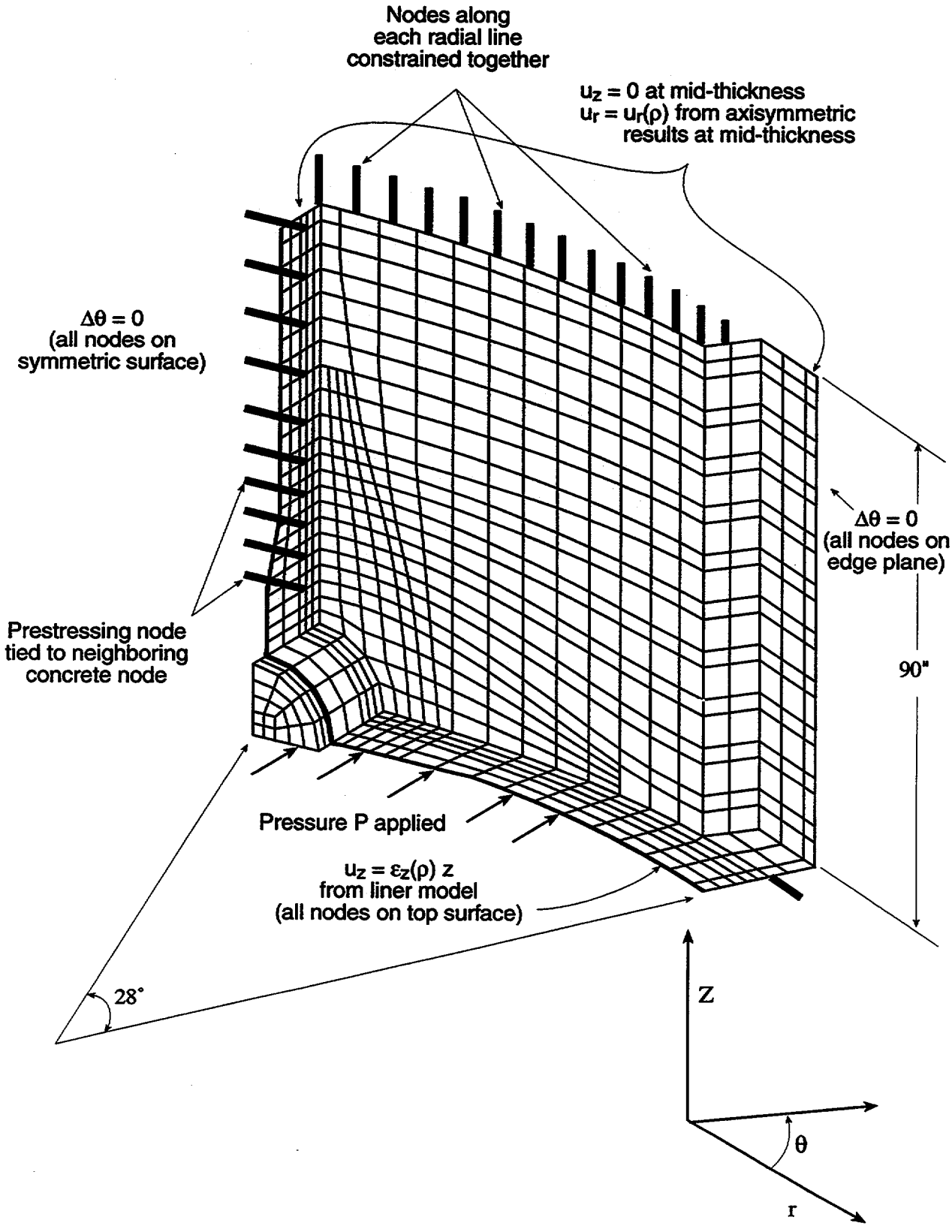


Figure 9-3. Boundary Conditions and Geometry for 3D Airlock Model

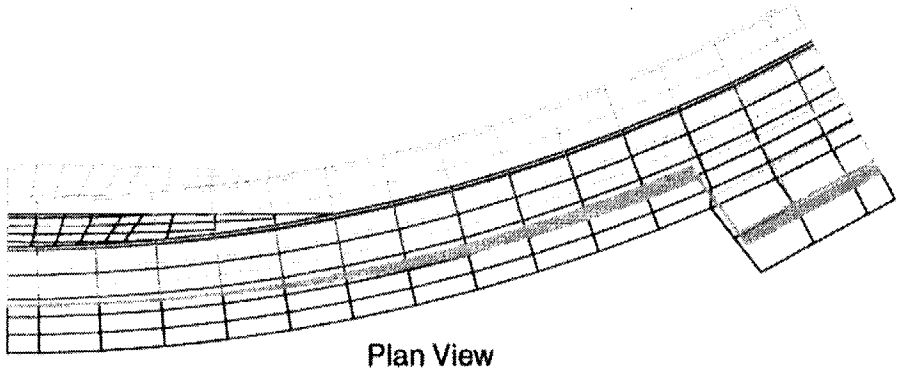


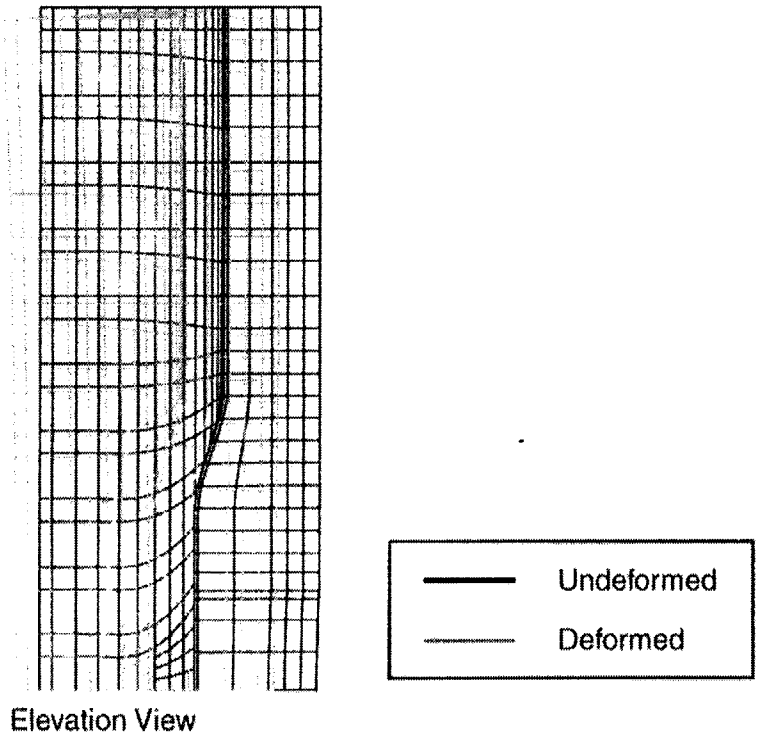




*al.inp*

Figure 9-4. Deformed Shape of A/L Model at Pressure = Prestress (Magnification factor = 100x)
Plan and Elevation View

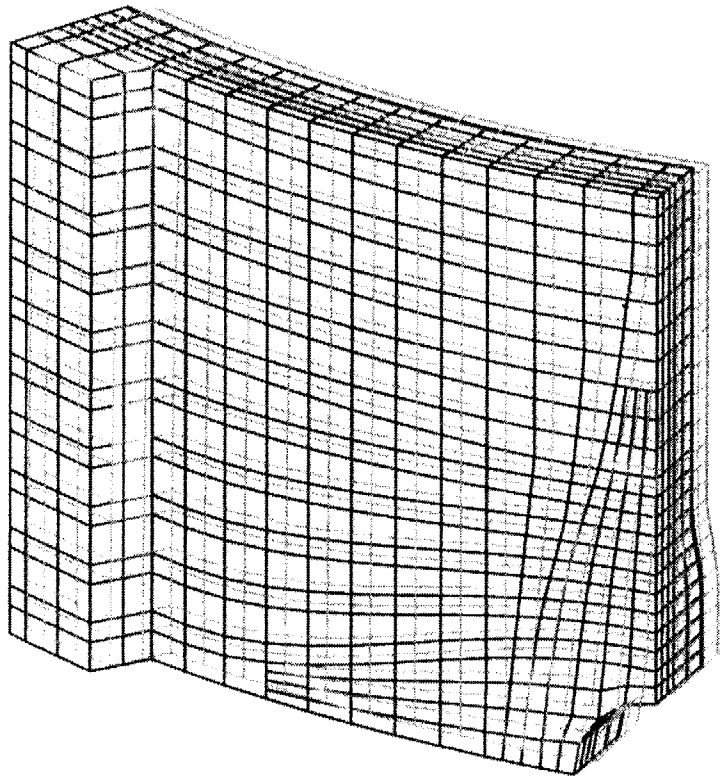

Isometric View

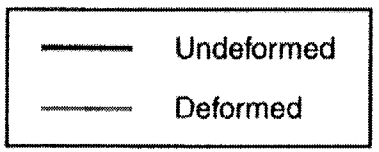


*al.inp*

Figure 9-5. Deformed Shape of A/L Model at Pressure = Prestress (Magnification factor = 100x)
Isometric View

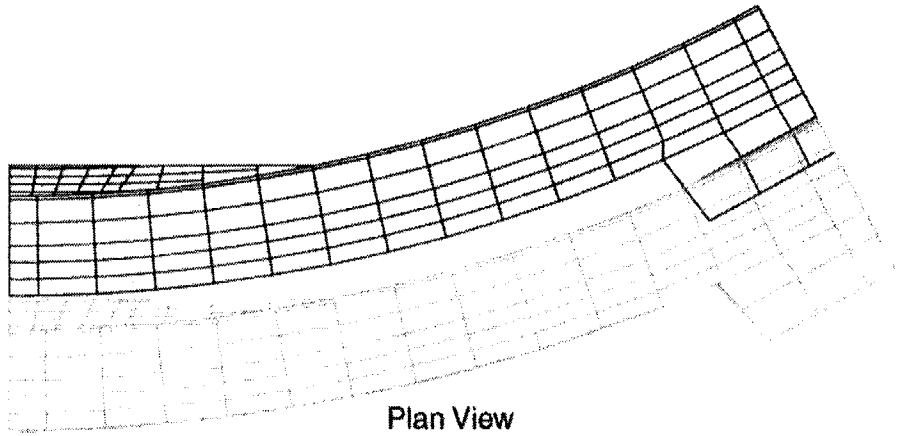


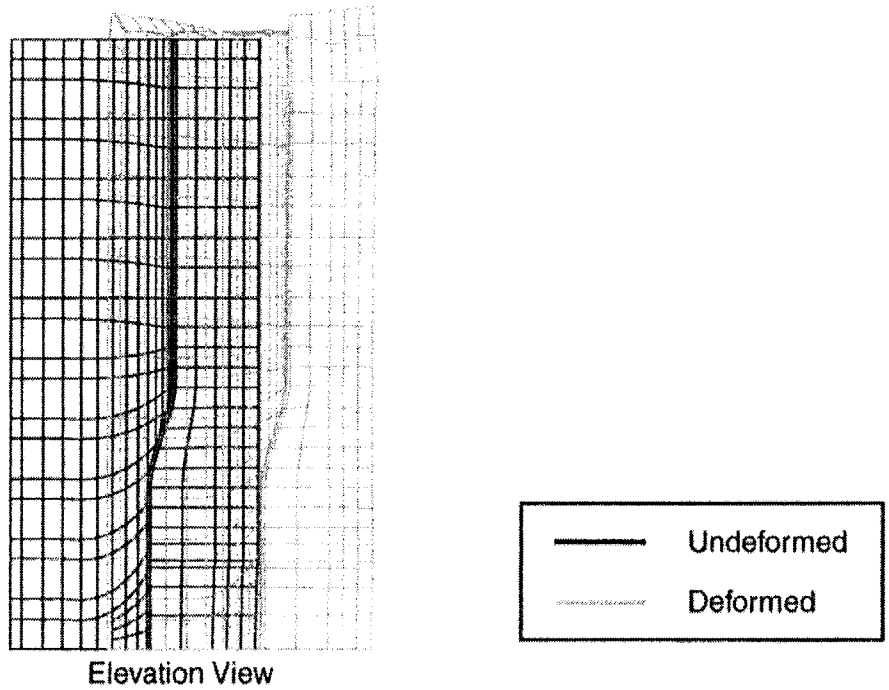




*al.inp*

Figure 9-6. Deformed Shape of A/L Model at Pressure = 3.75 $P_d$ (Magnification factor = 2x)
Plan and Elevation View

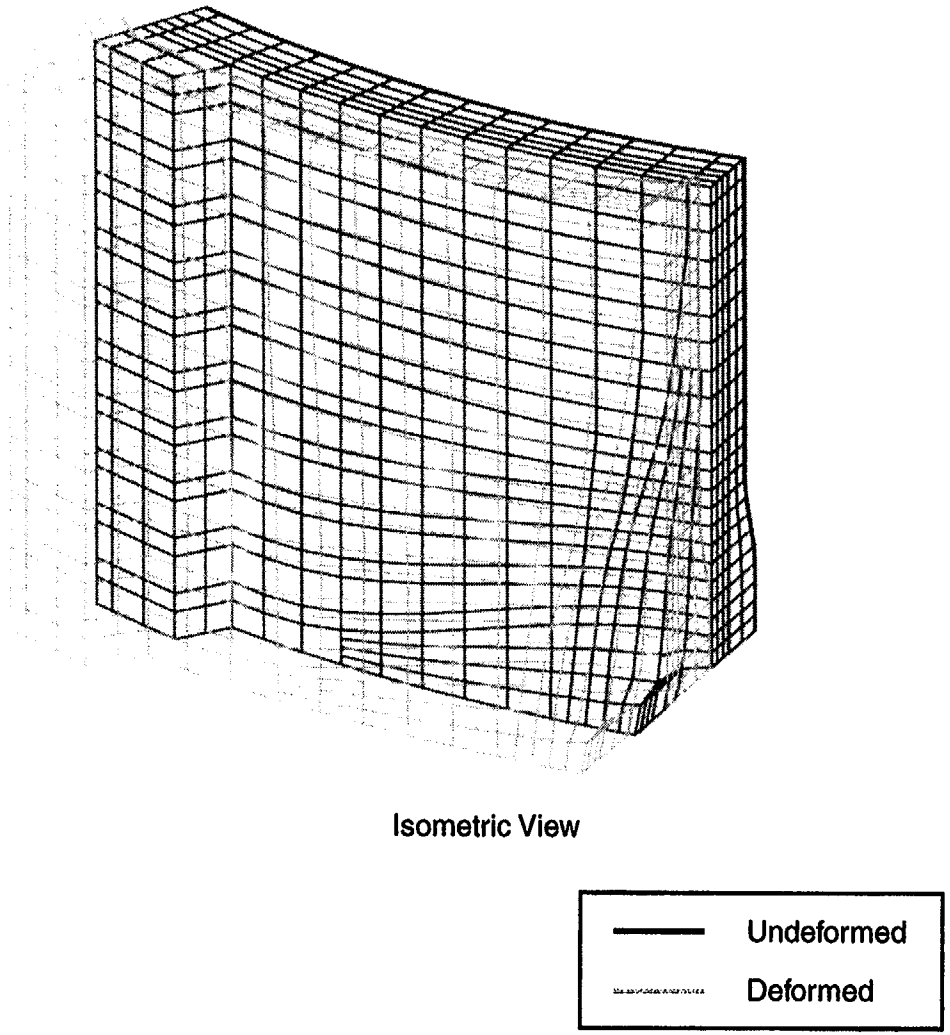


*al.inp*

Figure 9-7. Deformed Shape of A/L Model at Pressure = 3.75 $P_d$ (Magnification factor = 2x)
Isometric View

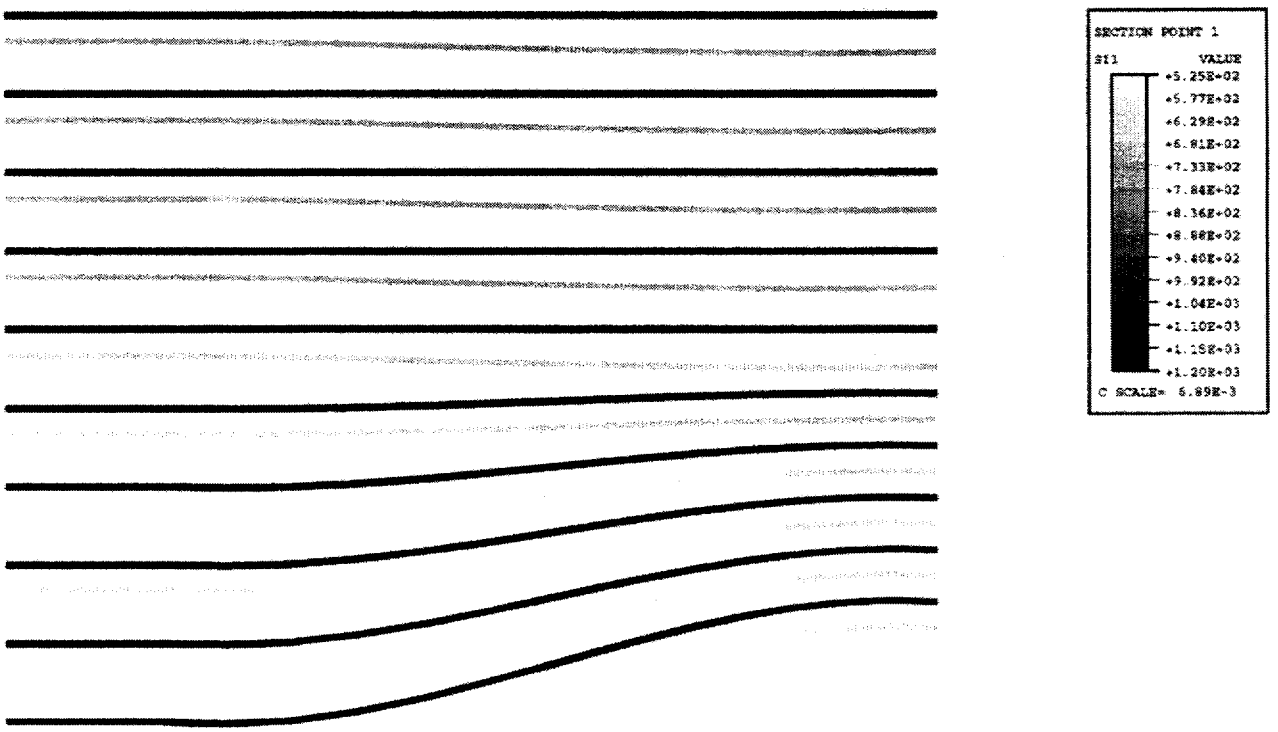


Tendon Stress

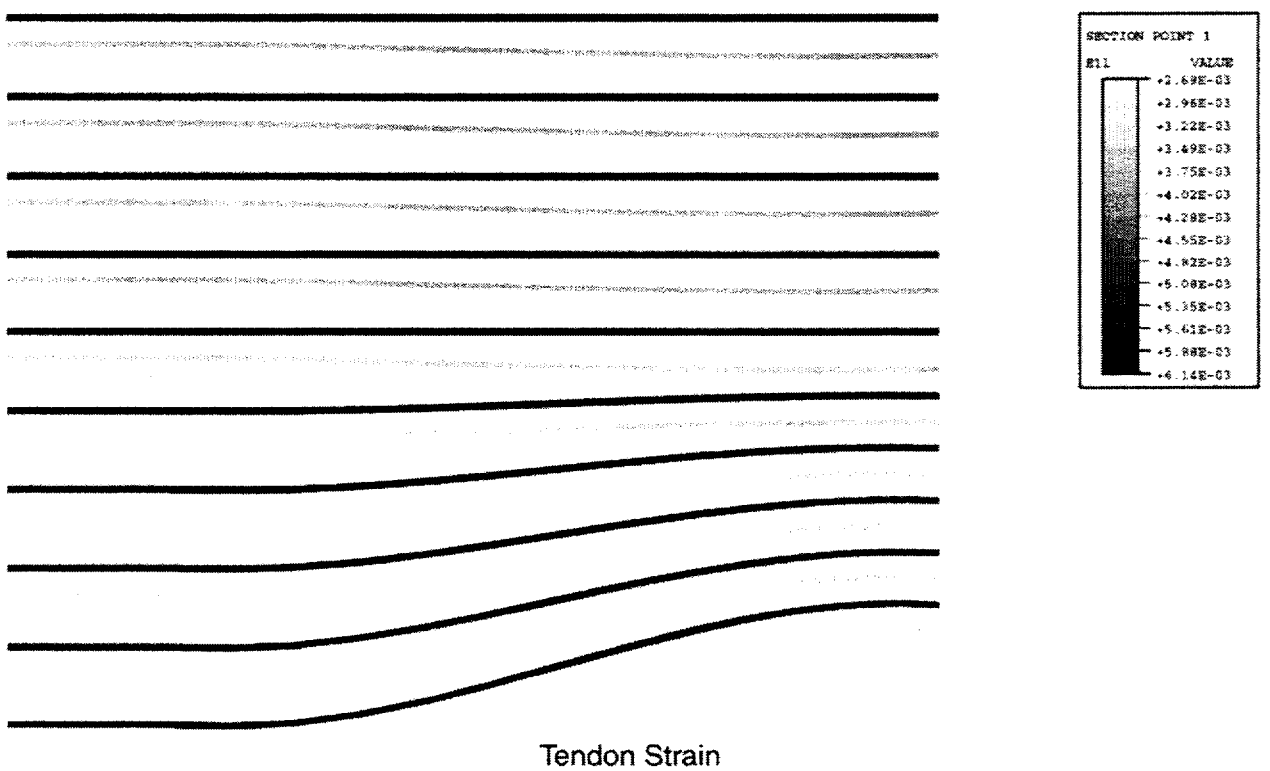


Tendon Strain

*al.inp* Figure 9-8. A/L Hoop Tendon Stress and Strain Contours at Prestress

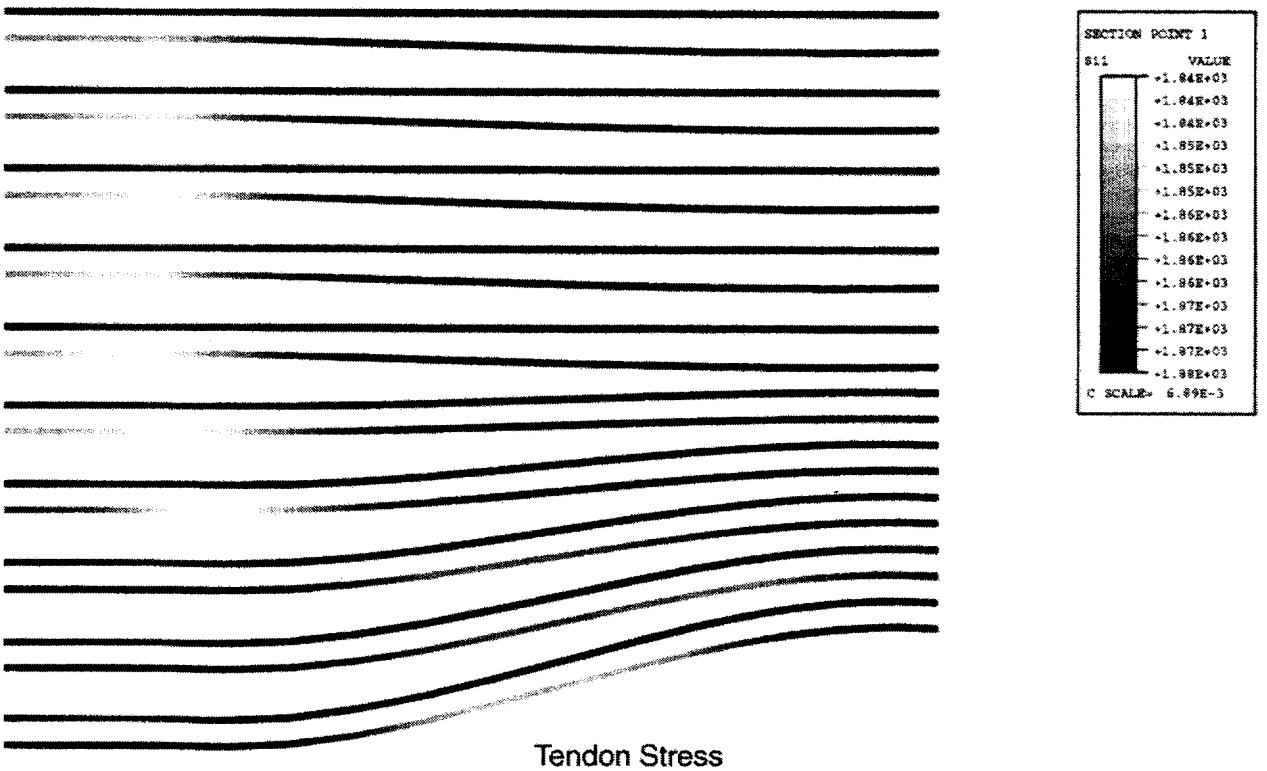


*al.inp* Figure 9-9. A/L Hoop Tendon Stress and Strain Contours at Pressure = 3.75 $P_d$

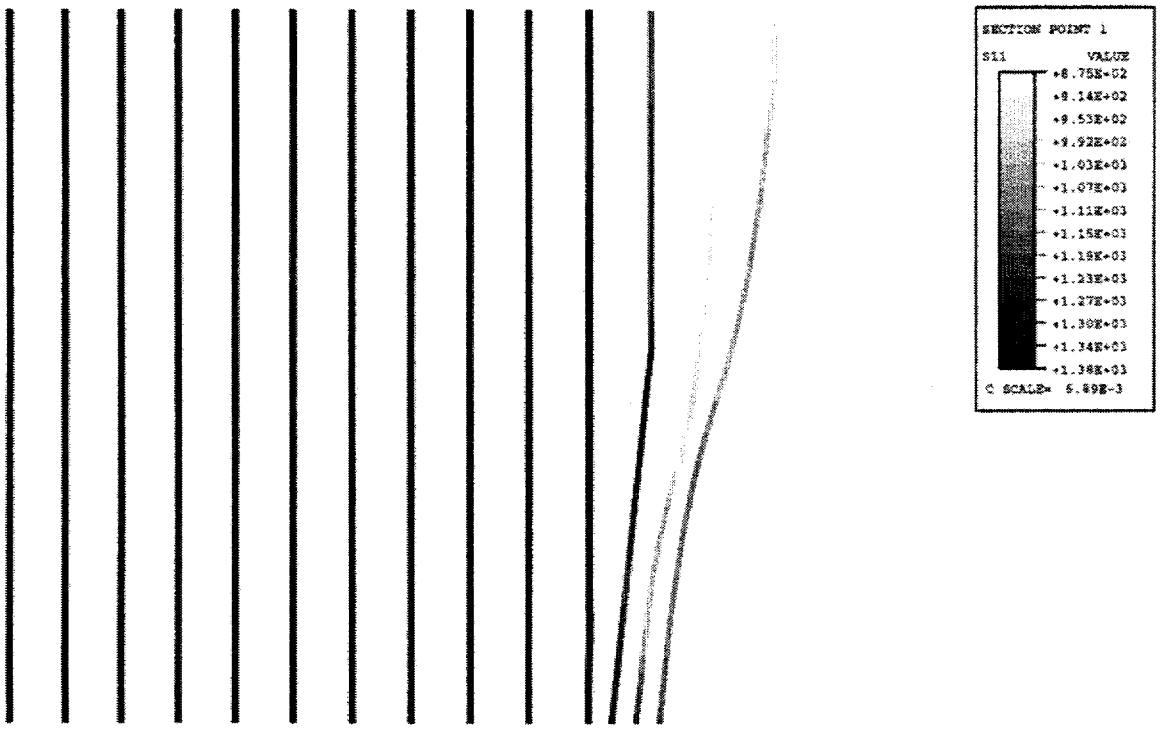


Tendon Stress

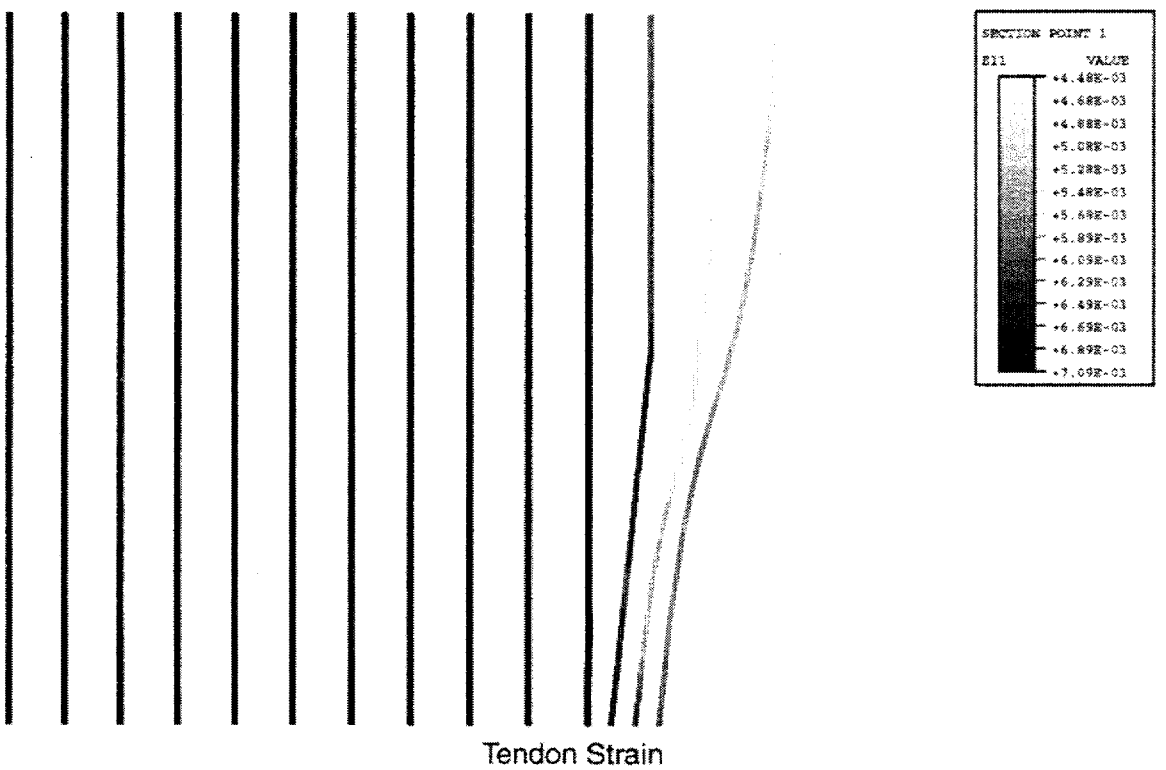


Tendon Strain

*al.inp* Figure 9-10. A/L Vertical Tendon Stress and Strain Contours at Prestress

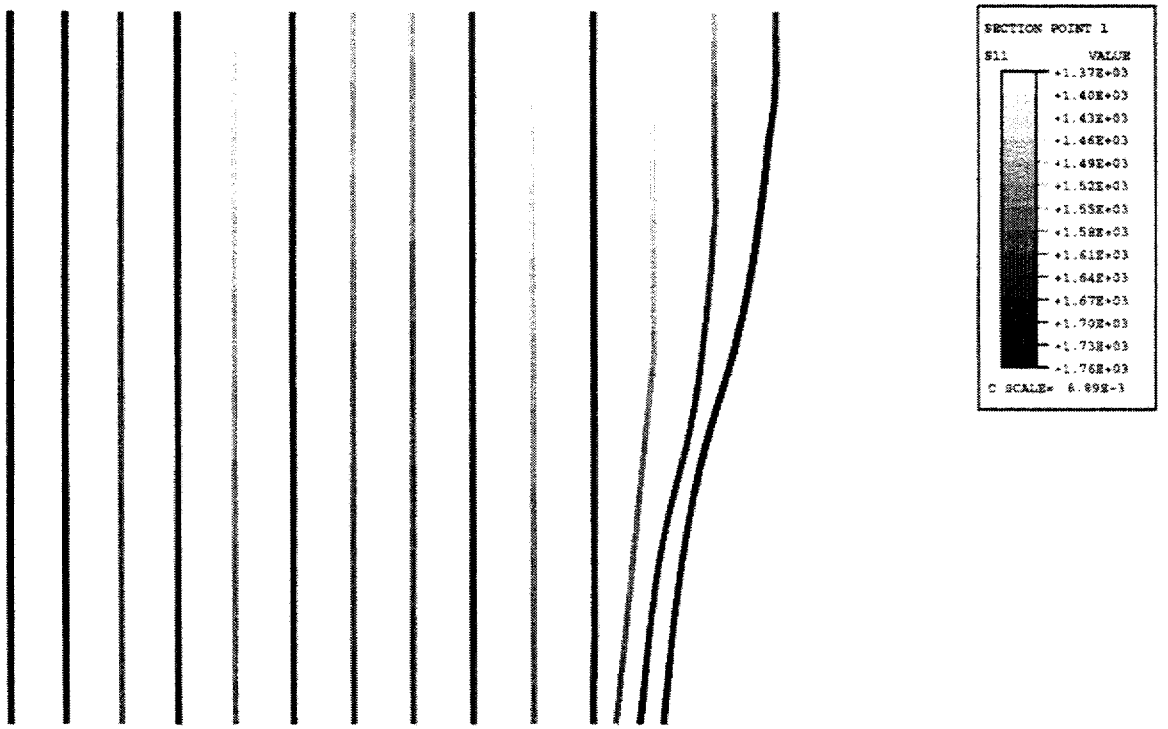


Tendon Stress

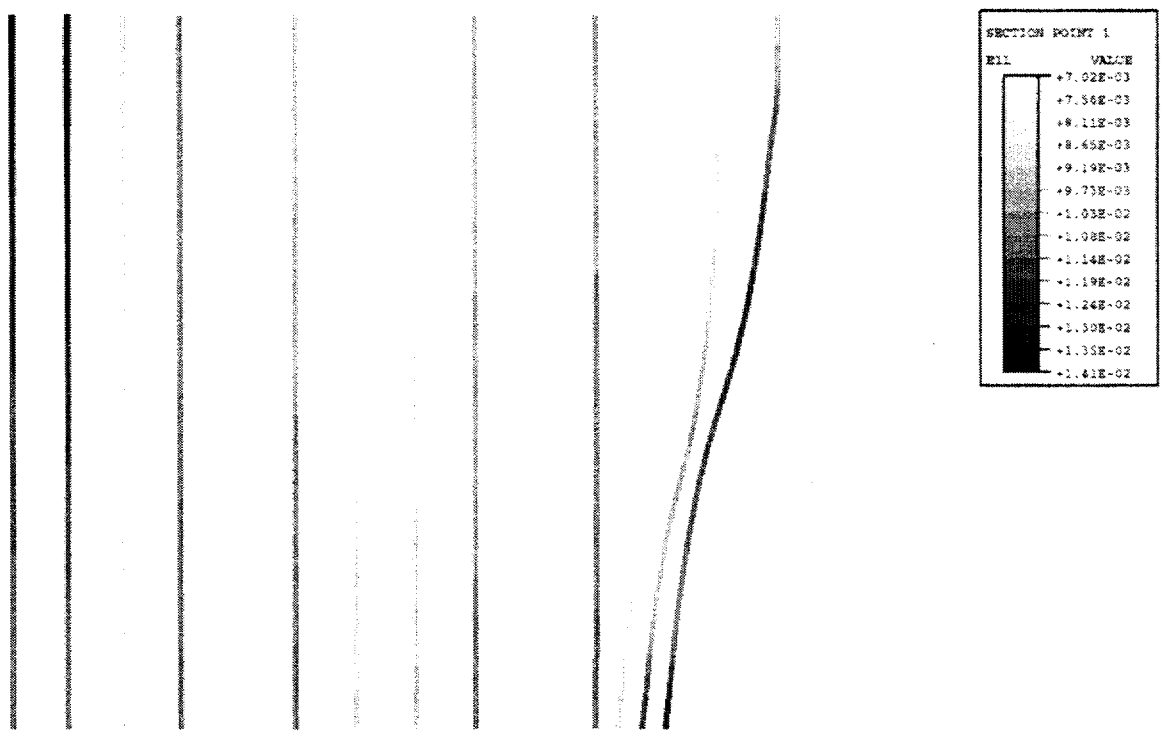


Tendon Strain

*al.inp* Figure 9-11. A/L Vertical Tendon Stress and Strain Contours at Pressure=3.75 $P_d$

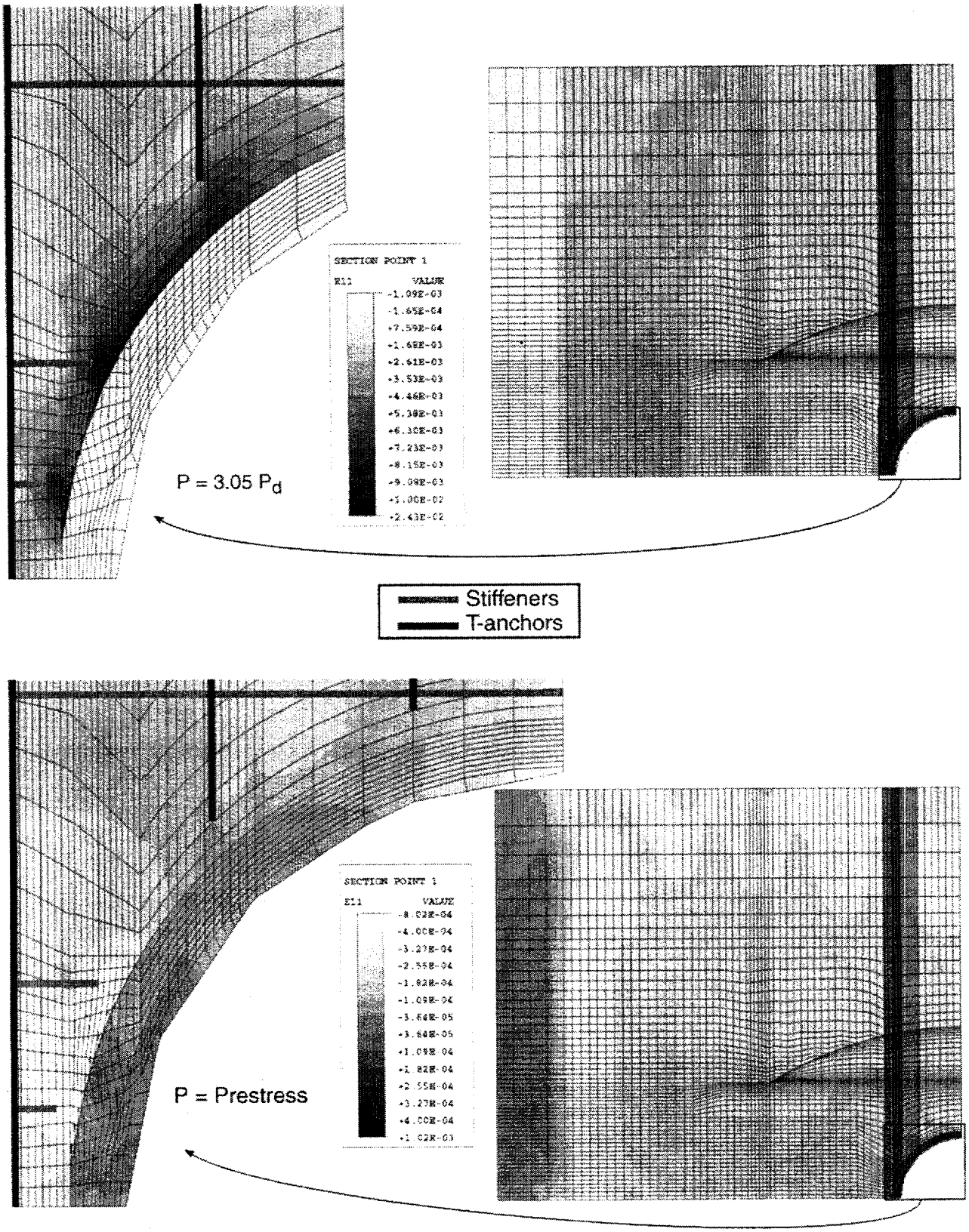


*al.inp*

Figure 9-12. Liner Contour Hoop Strain Plots

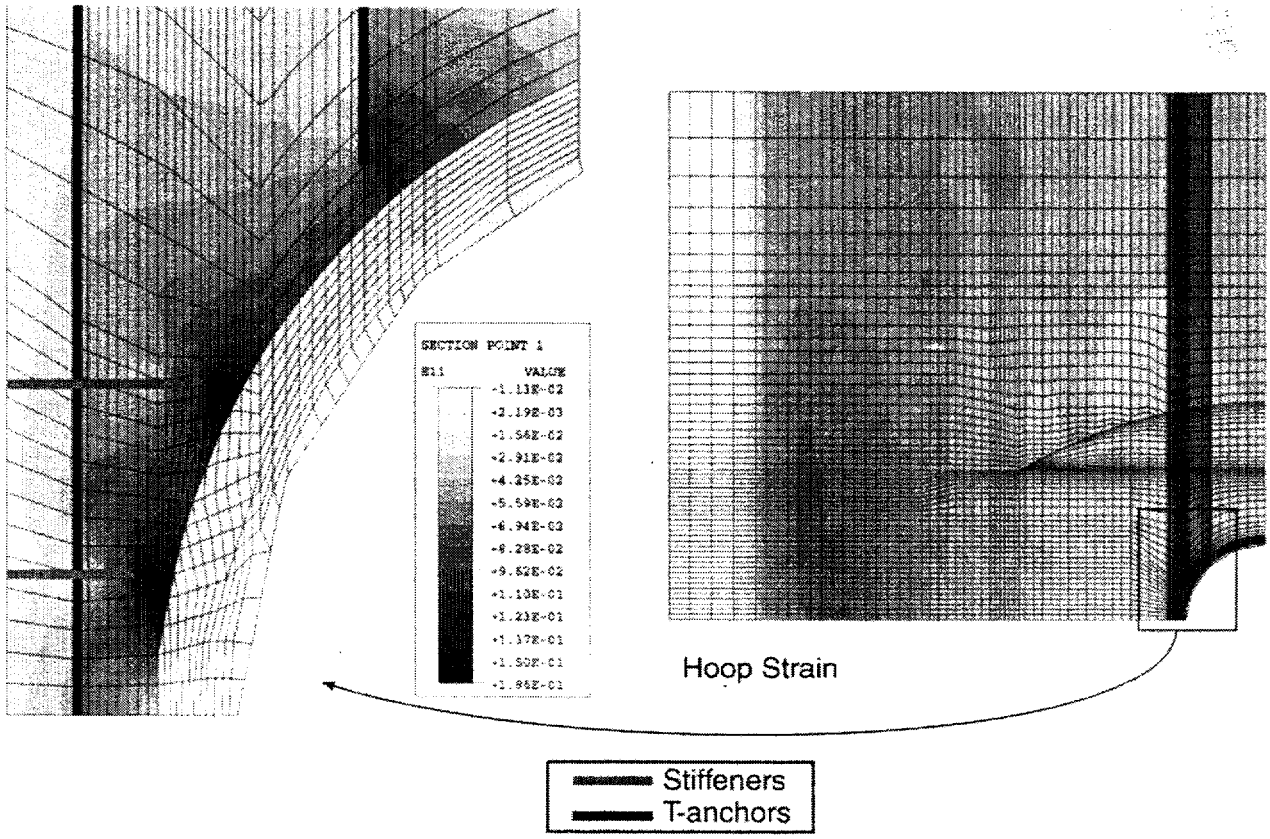


*al.inp*

Figure 9-13. Liner Contour Strain Plots at P = 3.75 $P_d$

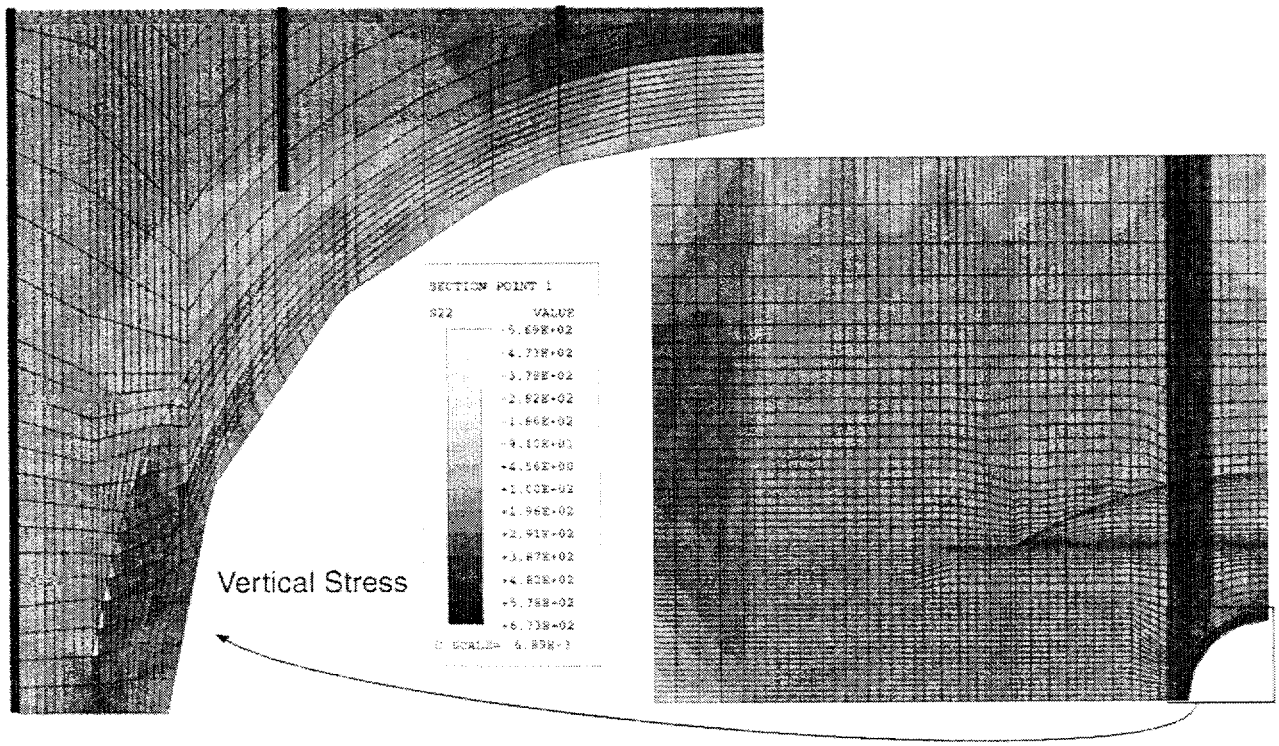


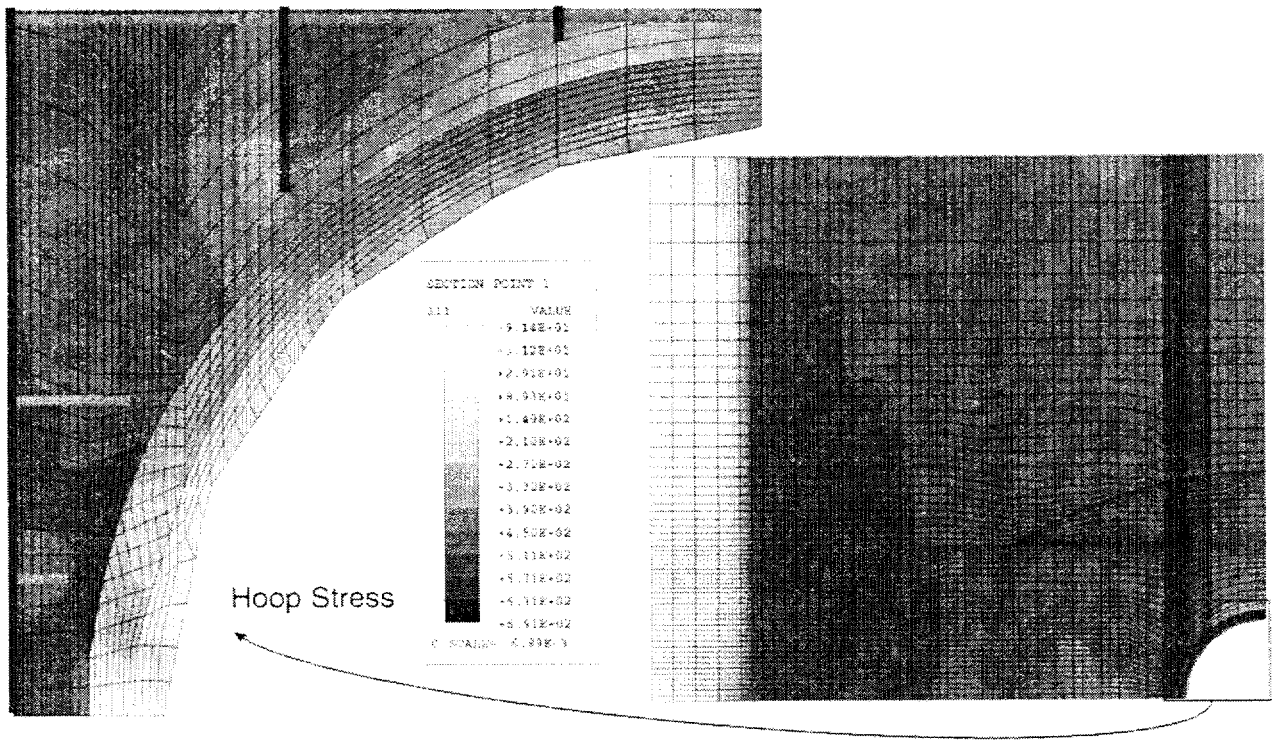


*al.inp*

Figure 9-14. Liner Contour Stress Plots at P=3.75 $P_d$

# 10. MAINSTEAM PENETRATION GROUP ANALYSIS

The mainsteam (M/S) penetration, the third largest penetration in the prestressed concrete containment vessel (PCCV) model, consists of a group of four penetrations located at the 180° azimuth. As with the equipment hatch (E/H), there are liner connection and anchorage details near the M/S that cause strain concentrations, which makes the region near the M/S another candidate for a liner-tearing failure mode. Details of liner construction near the M/S are shown in Figures 10-1 and 10-2.

Figure 10-2 identifies one specific kind of large strain concentration location similar to that associated with the A/L and E/H, namely, the zone near the end of a vertical T-anchor (at about the 1:30 position). There are no terminations of hoop stiffeners on the 1.6 mm liner plate in this region, so this strain concentration does not exist for the M/S. Much of the modeling discussion in this chapter refers to the more detailed description of similar modeling described in Chapters 3 and 8.

## 10.1 Computational Model

The local M/S 3D model is illustrated in Figure 10-3. Extent and modeling strategy for the local M/S model follow.

1. Upper quadrant was chosen so that the local model would be encompassed by the 3D cylinder midheight (3DCM) model and, thereby, have appropriate boundary conditions at all edges.

2. In addition, the critical liner anchor terminations occur only in the upper quadrant.

3. No tendons pass through this section yet the edges of the model are still sufficiently far away to appropriately capture to the strain concentrations.

The modeling details for the local M/S model are similar to those developed for the E/H model. The grid of the liner and anchors, is shown in Figures 10-4 and 10-5. The liner-anchor interaction (shear-force deflection behavior of the anchors) is modeled identically to the E/H, as is the method of attaching the liner/anchor mesh to the concrete mesh.

The rebar generated for the local M/S model is identical to the 3DCM model.

Unlike the E/H and A/L models, which were given symmetry boundary conditions on both vertical boundary planes, the M/S was loaded directly with displacement versus pressure histories at every node along the boundaries of the model. These pressure histories (different at every node and in all three degrees of freedom) were obtained directly from the 3DCM. The end result of the average hoop strain correlation approach used for the E/H and A/L is thought to be nearly the same as with the direct application of displacements to nodes used in the M/S model.

## 10.2 Analysis Results

The 3D local model analysis results for the M/S are shown in Figures 10-6 through 10-10. Figures 10-6 and 10-7 show deformed shape results These plots show that the M/S model deforms radially outward fairly uniformly across the model.

Figures 10-8 through 10-10 depict liner strain and stress contours, which show where the elevated liner strain concentrations are predicted to occur in this region. The "hot spots" for this model are near the vertical T-anchor termination. Peak strains at $3.8P_d$ are only about 5%, and these are generally lower than for the E/H or the A/L.

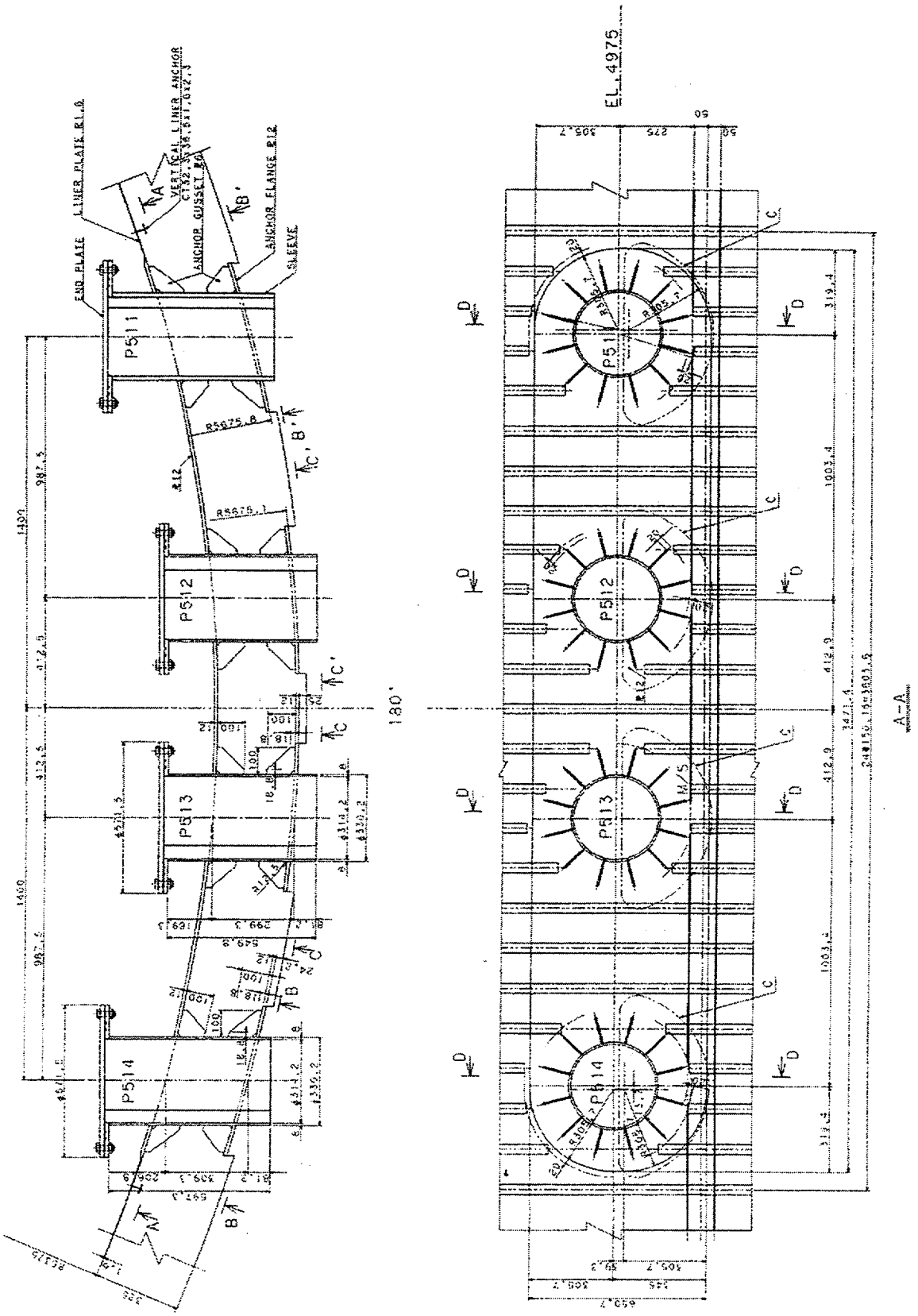


Figure 10-1. Mainsteam Penetration Liner Details

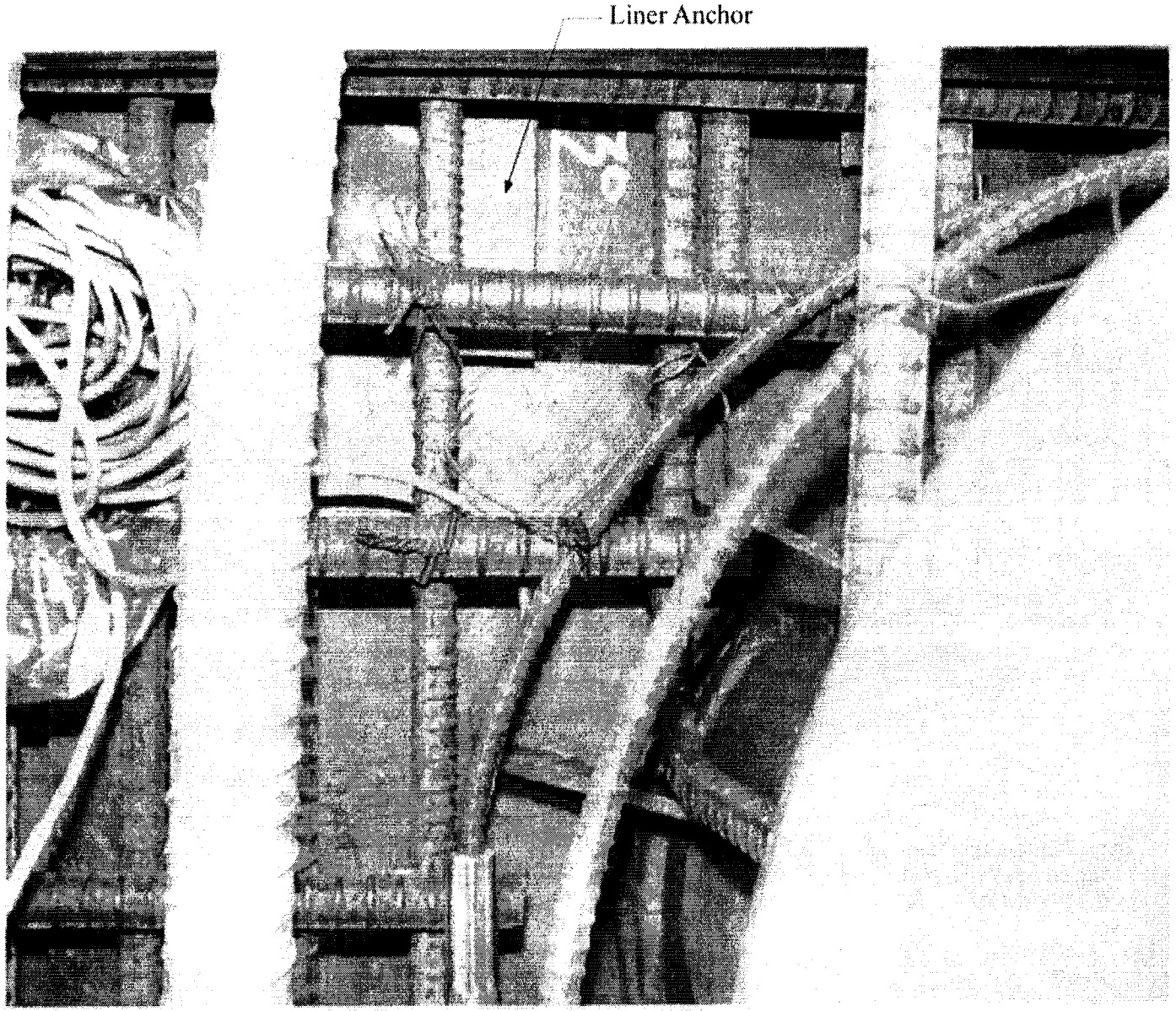


Figure 10-2. Liner Details Near Mainsteam Penetration

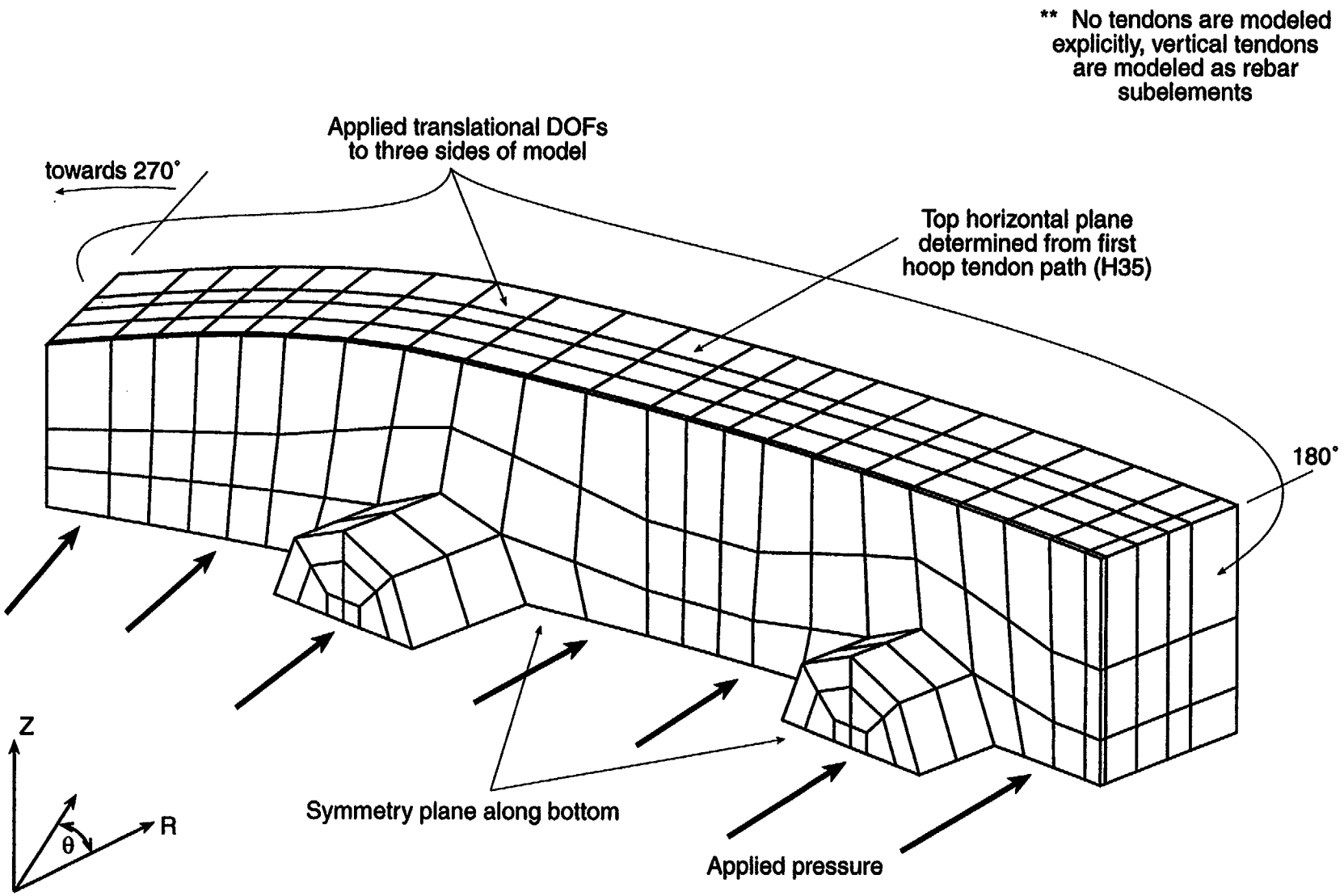


Figure 10-3. M/S Local Model Geometry and Boundary Conditions

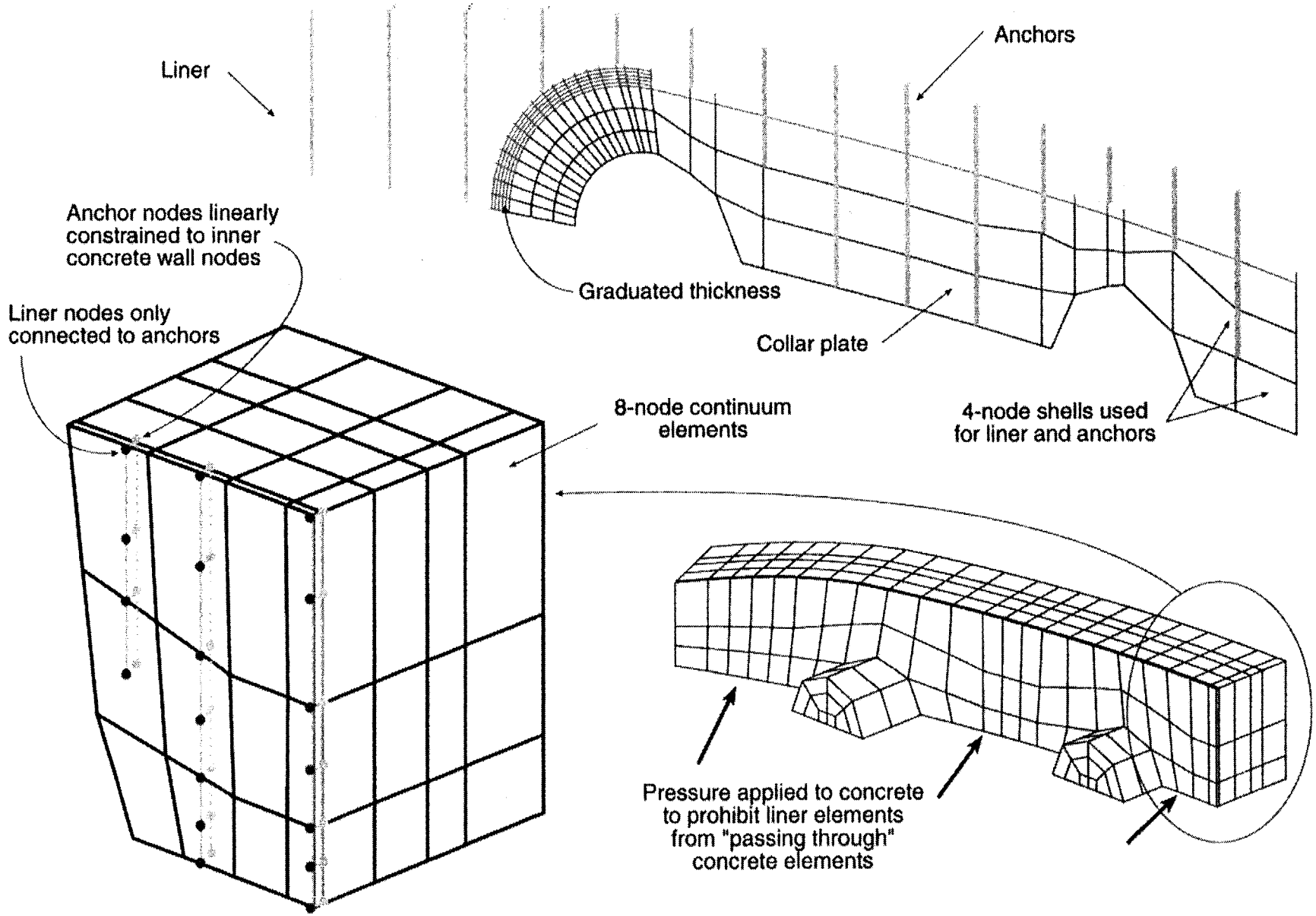


Figure 10-4. M/S Local Model Liner Details

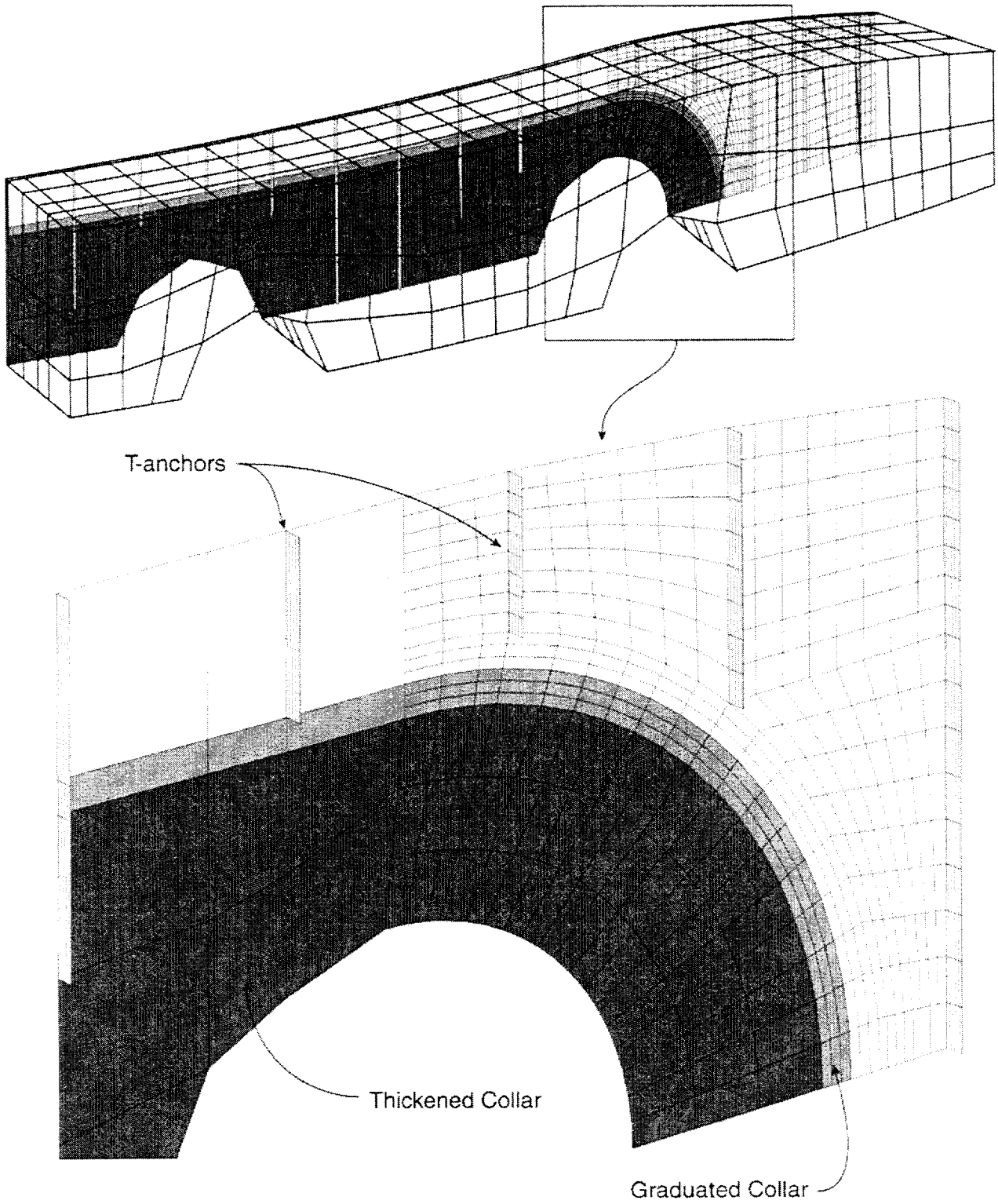


Figure 10-5. Finite Element Mesh Including Liner and Anchors

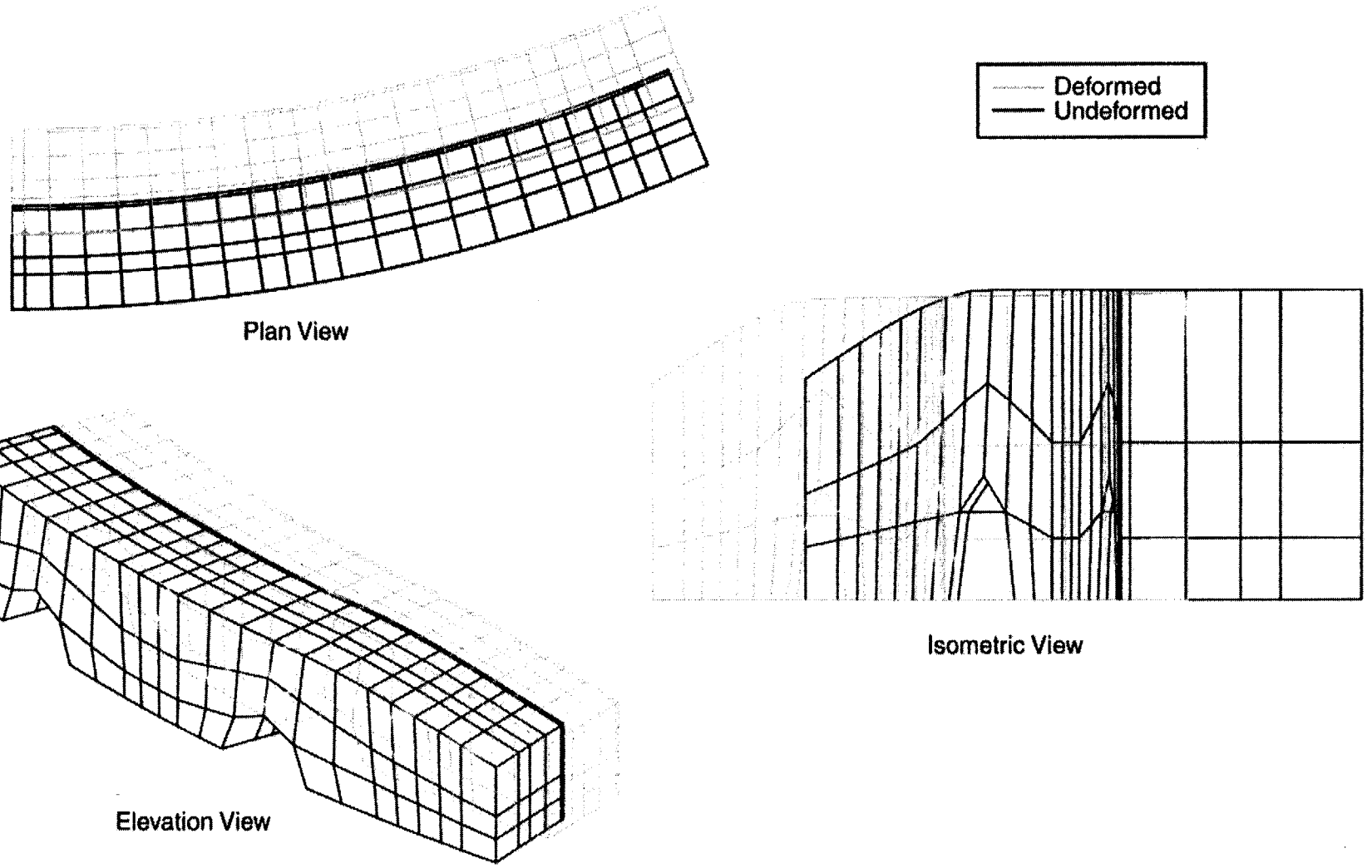




*ms.inp*

Figure 10-6. Deformed Shape of M/S Model at Prestress (Magnification factor = 100x)

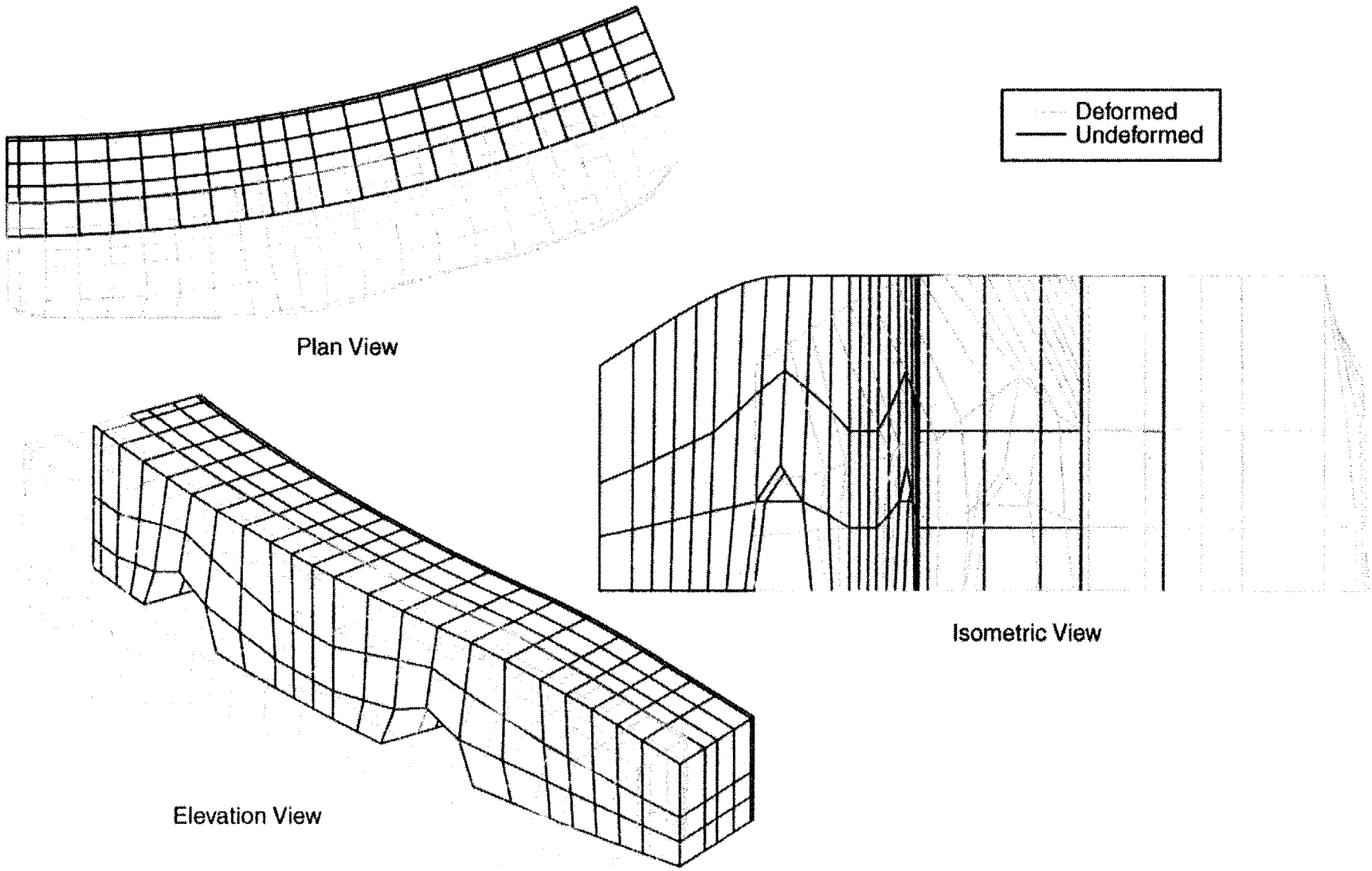




*ms.inp*

Figure 10-7. Deformed Shape of M/S Model at Pressure = 3.8 $P_d$ (Magnification factor = 2x)

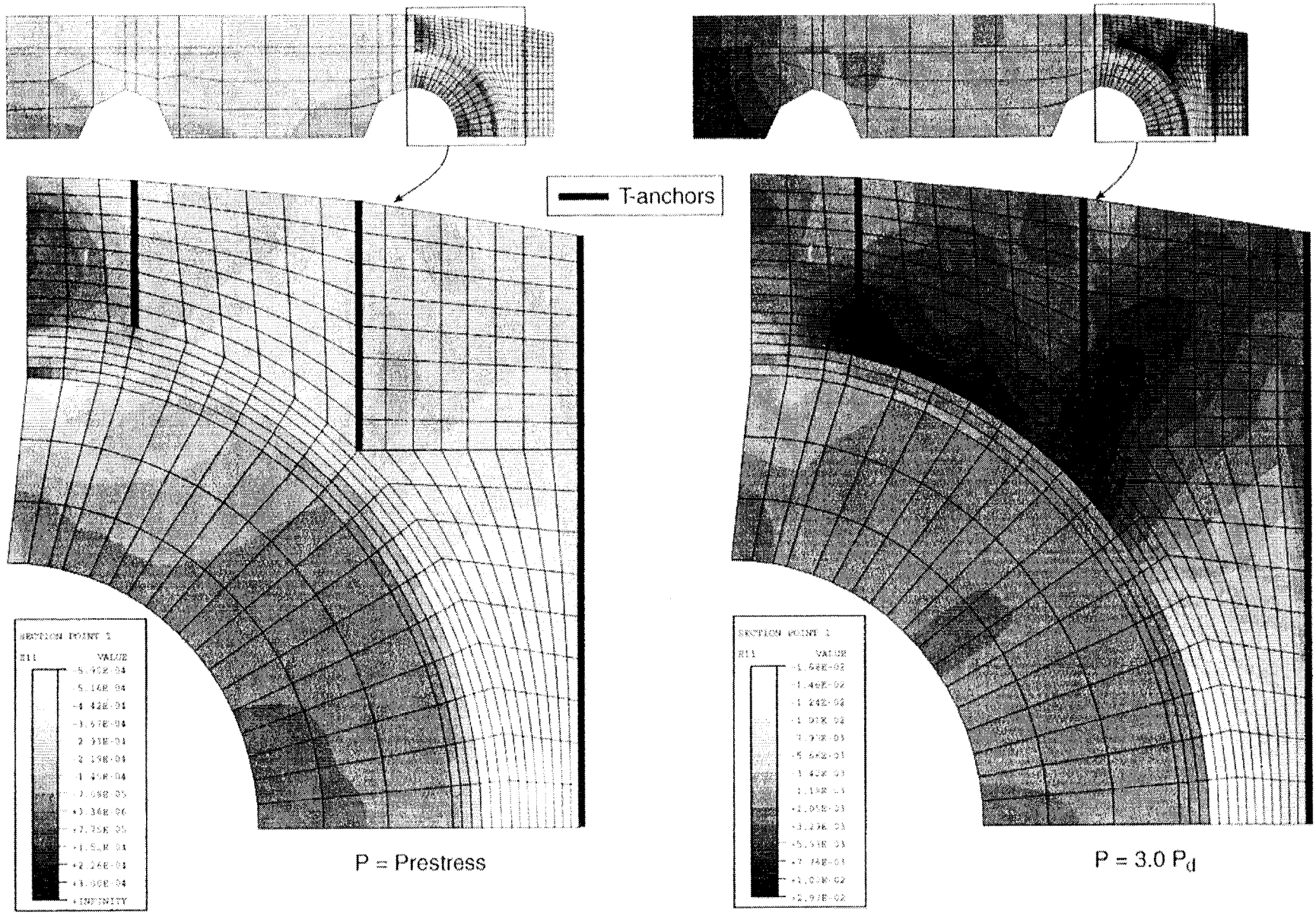


*ms.inp*

Figure 10-8. Liner Contour Strain Plots

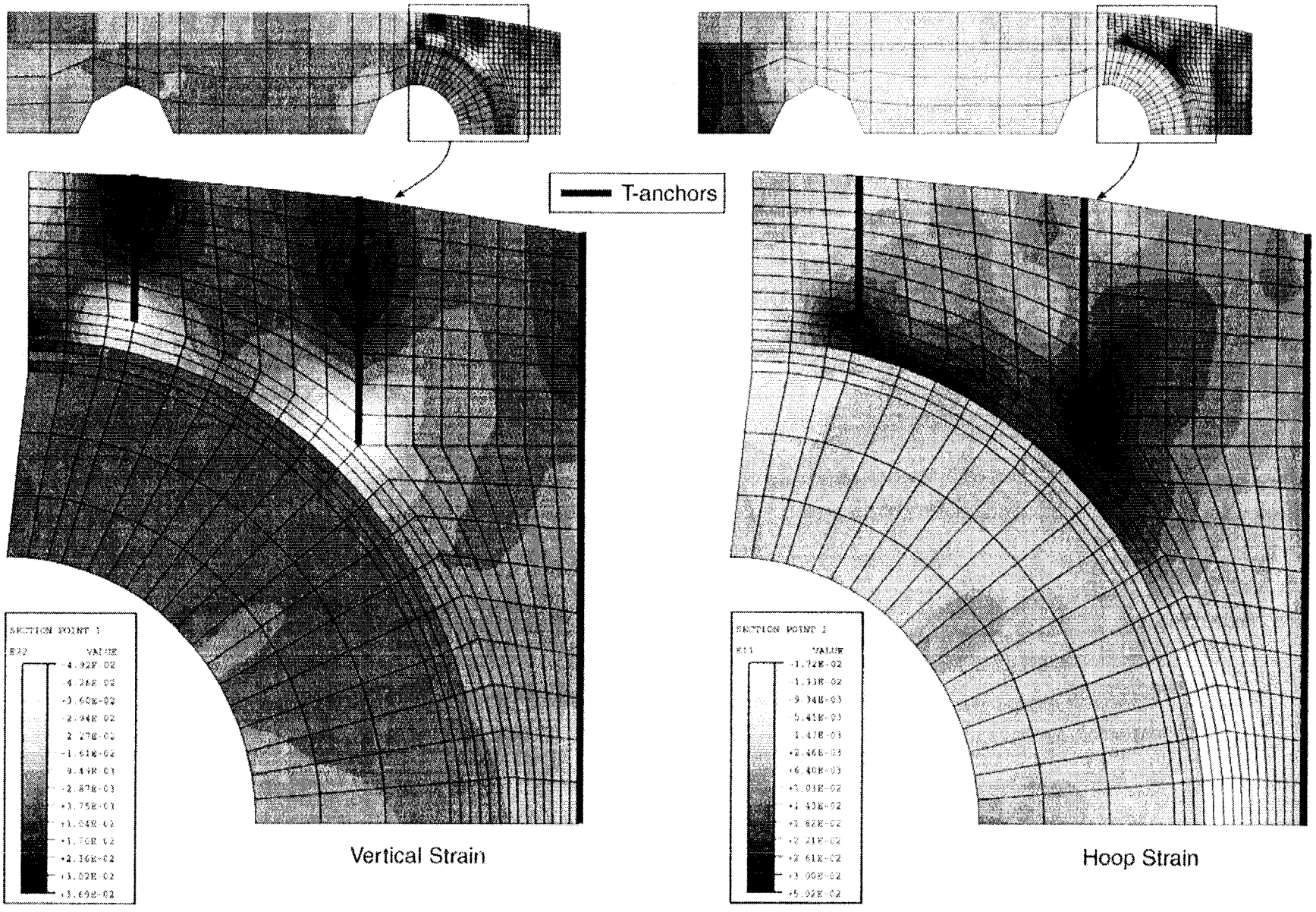


*ms.inp*

Figure 10-9. Liner Contour Strain Plots at P = 3.8 $P_d$

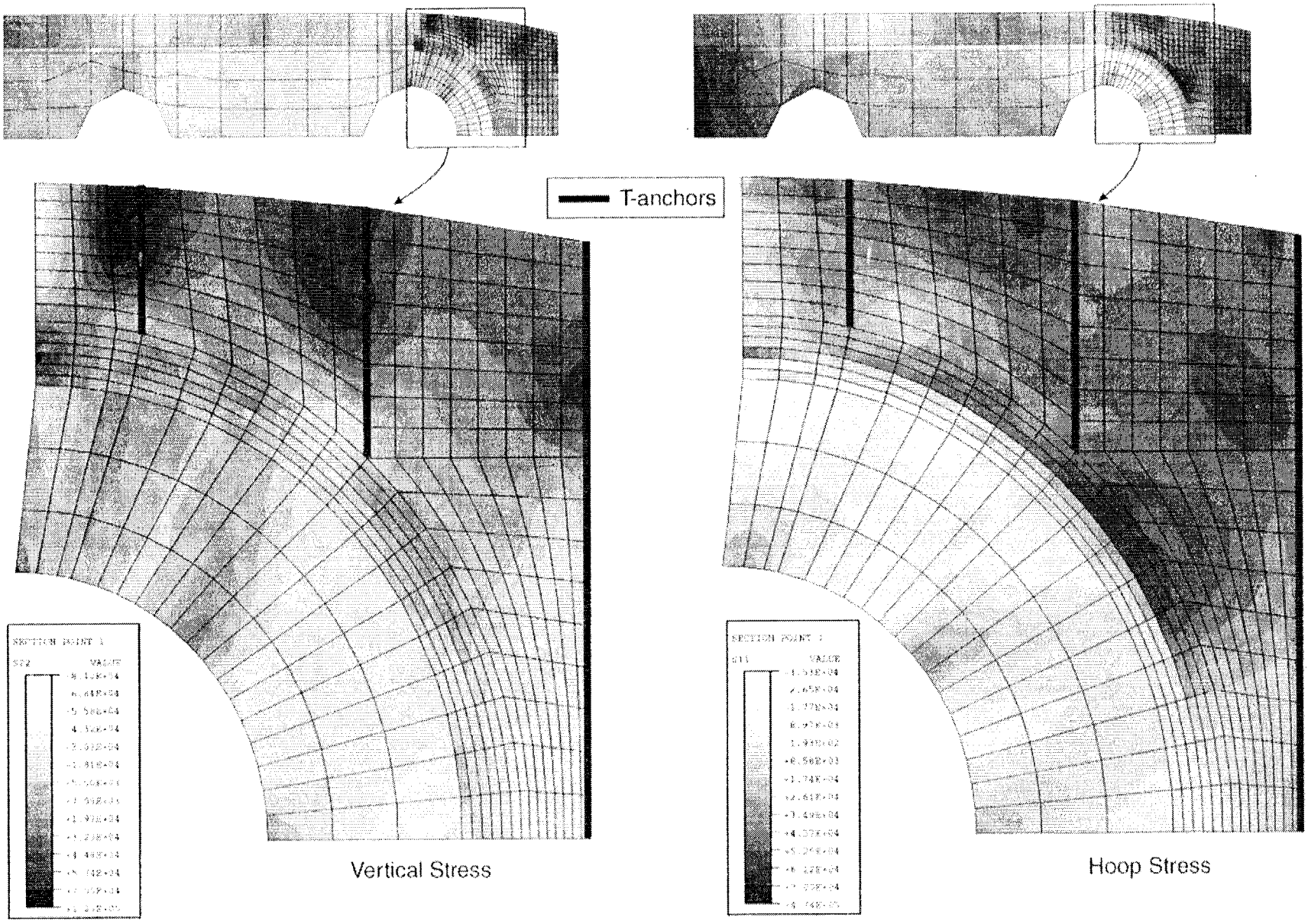


*ms.inp*

Figure 10-10. Liner Contour Stress Plots at P = 3.8 $P_d$

# 11. COMPARISONS AND CONCLUSIONS

## 11.1 Comparisons of Strains and Displacements in All Models

Chapters 5 through 10 discuss results of a different models draw conclusions about the failure modes for particular regions of the prestressed concrete containment vessel (PCCV). This chapter merges those analyses and merges the local and global behaviors into a response prediction for the whole structure. This process requires comparison of the different model results and ranking of the possible failure modes.

### 11.1.1 Comparisons of Global Axisymmetric to 3DCM Results

The first comparisons between models and conclusions on predicted behavior are the table of response events and pressure milestones shown in Appendix B. These results were requested of all Round Robin pretest analysts.

The most fundamental response component which is likely to drive the failure of the PCCV model is the radial expansion of the cylinder. The radial displacement behavior of the 3DCM is compared to the radial displacement of the axisymmetric analysis in Figures 11-1 and 11-2. This comparison shows a similar trend and, up to a pressure of three times $P_d$, close agreement between the 135° azimuth of the 3D cylinder midheight (3DCM) and the axisymmetric prediction. There are two important differences, however, that directly influence the failure prediction.

1. By modeling the 360° cylinder in three dimensions, the 3DCM shows the large variation of radial displacement with azimuth (large non-axisymmetry), and large local circumferential bending near the buttresses which are not represented by the axisymmetric model. This causes locally earlier yielding and plastic deformation than the axisymmetric model predicts, and, therefore, larger displacements at some azimuths than the axisymmetric solution.

2. Representing the complete tendon paths allows the 3DCM to represent anchor set losses and the tendon stress distribution along the length, which has allowed simulation the regions of larger than average stress/strain in the tendon. Thus, earlier yielding and an earlier rupture are calculated than are predicted in the axisymmetric model.

Based on these comparisons, the axisymmetric analysis results are judged to provide a very accurate representation of behavior up to about three times $P_d$ and then a reasonable representation of the average response of the vessel when "averaged" around all azimuths. Therefore, for most of the standard output location predictions (see Appendix B), the axisymmetric analysis is used. For predictions at azimuths other than 135° and at elevations included within the 3DCM, the 3DCM results were used for the standard analysis output predictions.

Because there are uncertainties with either analysis, but the 3DCM model reaches a limit state at lower pressure than the axisymmetric model because of the inclusion of 3D effects, the authors believe the failure predictions based on the two distinct models make reasonable upper and lower confidence bands on failure pressure as follows:

- minimum pressure reachable with 90% confidence: 1.08MPa, $2.75P_d$ (based on 3DCM model and local models); and

- maximum pressure reachable with 90% confidence: 1.38MPa, $3.51P_d$ (based on the global axisymmetric analysis and a 2% global hoop strain criteria as an upper limit).

### 11.1.2 Comparisons of the Local Models

To compare the high liner strain locations requires comparisons of the driving displacement and strains of the local models. This comparison is provided in Figures 11-3 and 11-4. The term "driving displacement/strains" is used here because containment vessel liner tearing tends to be a deformation-controlled process, rather than a strength-controlled process. The liner is firmly attached to the containment wall, so the liner, between attachment points is "driven" by the displacement and strain field that occurs in the containment wall. Figure 11-3 shows an estimate of the "driving strain" at the peak liner strain locations. The curves are constructed as follows:

- E/H: average hoop strain across the E/H local model, or the equivalent hoop strain driving the E/H region;

- A/L: average hoop strain across the A/L local model;
- M/S: radial displacement of the M/S, $u_{ms}$ divided by R;
- meridional strain at the wall-basemat juncture, including severe bending effects; and
- hoop strain at the edge of the 90° buttress, including severe bending effects.

The formula for deriving the "average hoop strains" of the local models was described in Chapter 8. The buttress location is actually the largest of the "driving strains" in the model.

Figure 11-4 compares the peak strains at the same locations. For the personnel airlock (A/L) and equipment hatch (E/H), there are two curves each because there are two kinds of strain concentration geometries at each location (described in more detail in the next subsection). The peak strain at edges of buttresses is amplified by the presence of hoop stiffener splices at vertical weld seams in the liner. While this detail has not been specifically modeled, from experience with similar details in other structures, the strain concentration factor at such details is approximately equal to three. Also, based on preliminary analysis work, a strain concentration exists at the wall-basemat juncture with a strain concentration factor of approximately two. This is based on the 5.9% strain predicted at $4P_d$ in the detailed liner-only model versus the 3% strain predicted in the global axisymmetric analysis. Thus, the peak strains near penetrations are pulled directly from local model analysis, and the curves for locations 1 and 5 are created by amplifying appropriate curves of Figure 11-3 by concentration factors of two and three, respectively. Figures 11-3 and 11-4 support the following observations:

1. At high pressures, the E/H has the strongest strain concentrations and the largest peak strain.
2. The concentrations near the ends of the hoop stiffeners are nearly equal to those near the ends of the T-anchors, but the concentration is largest near the T-anchor (Location 3).
3. At pressures greater than $3P_d$, the A/L locations rank third and the M/S locations rank fourth. The A/L strain concentration is largest at the vertical T-anchor.

## 11.2 Comparisons and Ranking of Potential Failure Modes

With the analyses completed and results tabulated and plotted, final comparison and ranking of failure modes requires a return to the structural drawings and a review of observations of the as-built structural details. This review is summarized in the drawing excerpts in Figures 11-5 through 11-12. Figure 11-6 shows sample locations of the liner strain concentration locations (SCLs) that have been identified, and categorizes them as follows:

Potential Liner Failure Locations

SCL Description

1. Horizontal Stiffeners Splice Straddling a Vertical Liner Seam: These occur at dozens of locations in the model. They can be a straight connection or at a slight-angle re-entrant corner as shown in D-D of Figure 11-6. The sudden gap in the hoop stiffener at the "rat-hole" needed for welding electrode access tends to cause a strain riser near the liner seam weld zone, which is already somewhat less ductile than the virgin liner material.
2. Horizontal Stiffener Termination on the 1.6 mm Liner Near Thickened Insert Plate: This is a "double" concentration caused by the hoop stiffener termination in a zone already subject to strain concentrations from the adjacent material thickness change. These locations are always further exacerbated by the presence of the weld to the insert plate and the weld of the stiffener to the 1.6 mm liner.
3. Vertical T-Anchor Termination on the 1.6 mm Liner Near Thickened Insert Plate: Similar to SCL 2, except the vertical T-anchor is a stronger embedment (because of the T-flange) than that of the hoop stiffener. The T-anchor, however, does not carry any hoop stress, which is an additional source of strain concentration in SCL 2.
4. Severe Acute Angle Weld Splices: These occur at the confluence of normal splicing of liner segments with the edge of a penetration, such as is shown for the mainsteam penetrations in Figure 11-6 or as occurs at the corners of the embossed regions of the E/H and A/L.

5. Wall-basemat Juncture Liner Connection Detail: Proximity to vertical T-anchor termination and to rigid basemat embedment cause strain concentration. The liner is not spliced here, however, so presumably, it retains its full ductility.

Note that this list is incomplete, e.g., strain concentrations are also known to occur at the crane rail attachment points and at the many horizontal welded seams coincident with vertical T-anchor splices. Locations such as these were eliminated from consideration early in the Preliminary Analysis Phase because of the relatively low "driving strains" that occur at these locations. Thus, to be placed on the list of competing failure locations requires a strain concentration detail *and* a significant driving strain.

Figures 11-7 through 11-12 inventory the occurrences of these SCLs. Again, only locations with significant driving strains coincident with the SCL detail are identified. The locations shown in the figures are itemized below.

| Figure | Description |
|---|---|
| 11-7 | three Type 1 located at 95° azimuth (edge of buttress), and two (times two for other side) Type 1 at edge of A/L embossment |
| 11-8 | six (times two for symmetry) Type 1 at edge of E/H Embossment, and eight Type 1 at 275°/265° azimuth (edge of buttress) |
| 11-9 | four Type 2 near 3:00 position of A/L; three Type 3 near 2:00 and 1:39 positions of A/L; four Type 4 at corners of embossment |
| 11-10 | four Type 2 near 3:00 position of A/L; three Type 3 near 2:00 and 1:39 positions of A/L; four Type 4 at corners of embossment |
| 11-11 | two Type 3 and two Type 4 near mainsteam (M/S) penetrations |
| 11-12 | two Type 3 and one of Types 1, 2, and 4 near feedwater (F/W) penetrations |

## 11.3 Final Failure Predictions

This chapter has itemized the locations on the liner where high strains occur and has shown that Strain Concentration Type 3 (near the termination of the vertical stiffener) at the E/H develops the highest strain during the pressure range, $3.0P_d$ to $3.4P_d$. In addition to this itemization, a thorough review of rebar strains, concrete strains and shear damage, and tendon stresses and strains has been conducted vis-a-vis the failure criteria described in Chapter 4. The result of this review did not reveal any failures in any structural components except in the liner. The liner failure pressure is calculated by comparing the strain versus pressure history in Figure 11-4 to the failure strain calculated from Equations 4-7 and 4-9. An additional factor of 0.6 is also applied to the Davis triaxiality criteria because the peak liner strains are located in the vicinity of full-penetration welds of the 1.6 mm liner to the thickened insert plate. (Development of this factor was also described in Chapter 4.) The final failure strain at the E/H location which coincides with the strain prediction is

Failure Strain = Calculated Strain = 0.162

This strain is calculated to occur at Pressure = $3.2P_d$, 1.25 MPa (185 psig).

This chapter has also presented a list of other candidate strain concentration locations. These are ranked in order of the pressure at which the analyses predict them to occur in Table 11-1.

The analysis also shows that a tendon rupture is likely at $3.5P_d$ for the tendon closest to the E/H, so this event/pressure milestone is predicted to be an upper bound on the failure pressure prediction. Note, however, that a tendon rupture failure mode is predicted to be precluded by one or more of the liner tears which will occur first and lead to very large leakage rates and depressurization of the vessel.

**Table 11-1. Possible Line-Tearing Locations in Descending Order of Probability of Occurrence**

| Probability of Occurrence | Possible Line-Tearing Locations |
|---|---|
| 1 | E/H near vertical T-anchor termination (four locations, Type 3) |
| 2 | E/H near horizontal stiffener termination (four locations, Type 2) |
| 3 | near a weld seam with hoop stiffener rat-hole, 5° from the centerline of 90° buttress (i.e., 95°; occurs in roughly six locations) |
| 4 and 5 | similar to 1 and 2, but near the A/L (seven locations, Types 3 and 2) |
| 6 | similar to 1, but near the M/S penetration (two locations, Type 3) |
| 7 | similar to 1 and 2, but near the F/W penetration (three locations, Types 3 and 2) |
| 8 | strain concentration Location Type 4 near F/W penetrations, M/S penetrations, and near E/H and A/L as shown in Figures 11-6 through 11-12 |
| 9 | liner tear at wall-basemat juncture |

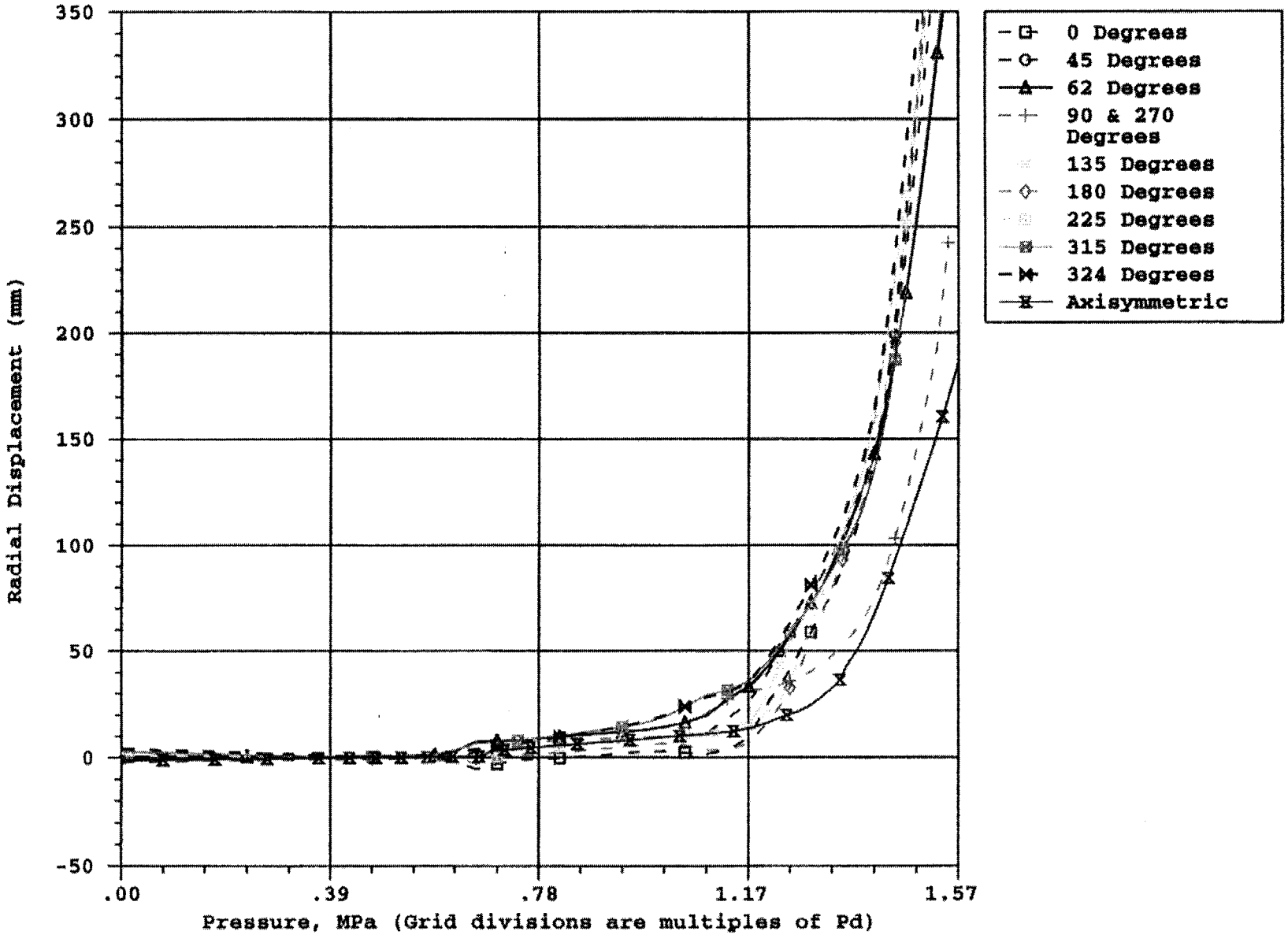


*3dcm.inp* Figure 11-1. 3DCM and Axisymmetric Radial Displacement Comparison vs. Pressure at Elevation 4.6752 m

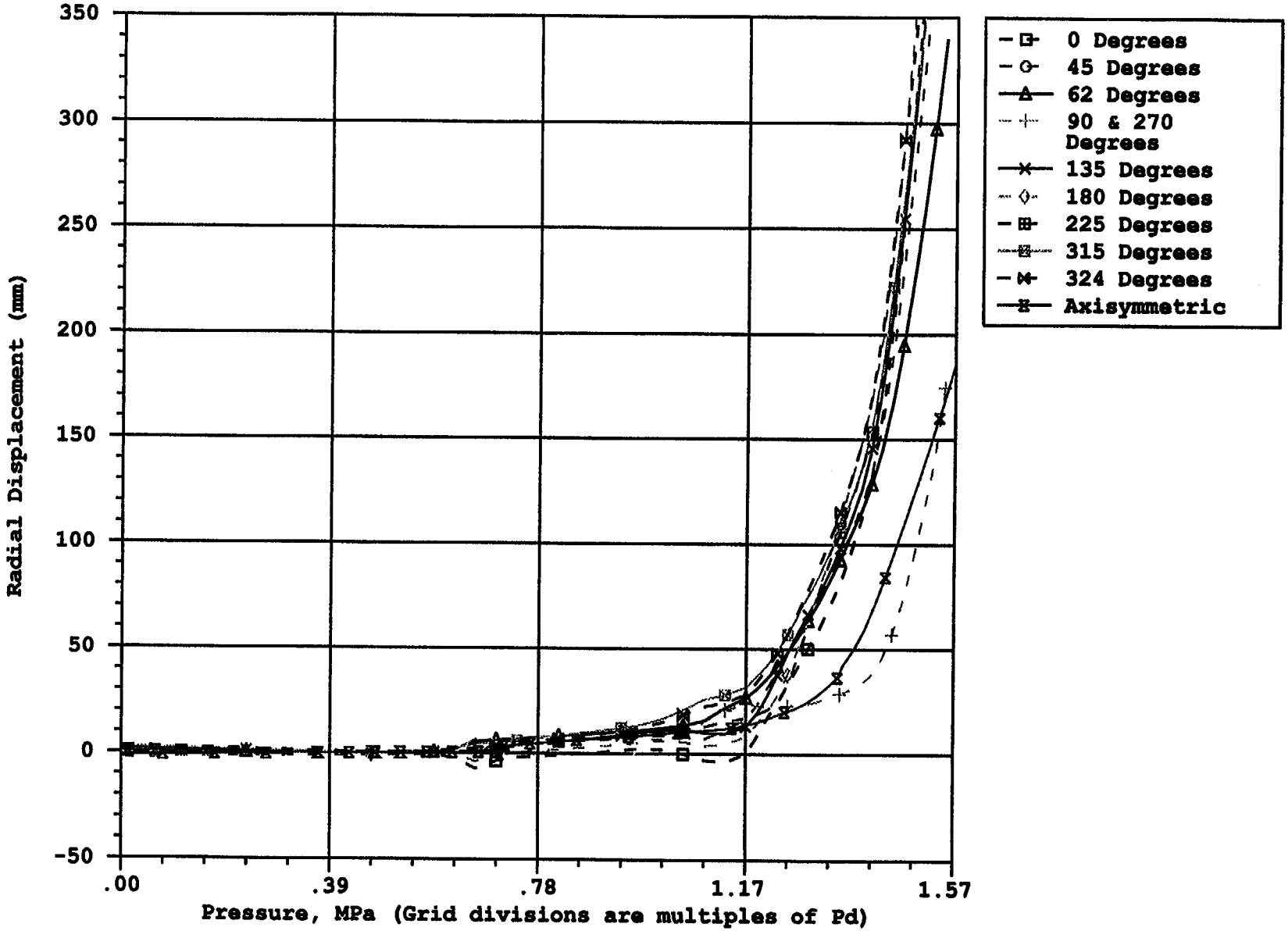


Figure 11-2. 3DCM and Axisymmetric Radial Displacement Comparison vs. Pressure at Elevation 8.9567 m

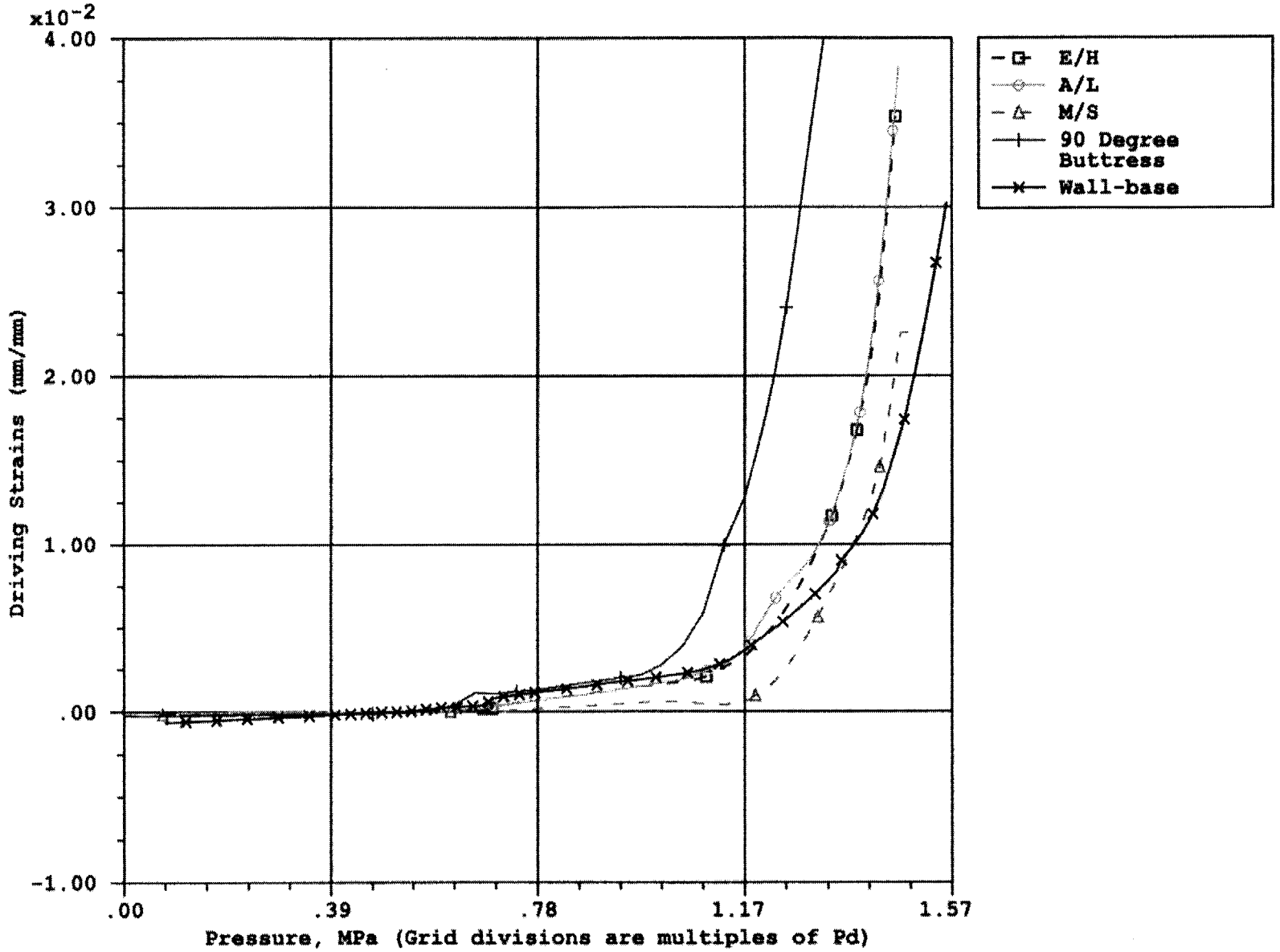


*eh.inp, al.inp, ms.inp, 3dcm.inp, model14.inp*

Figure 11-3. Driving Strains at Concentration Locations

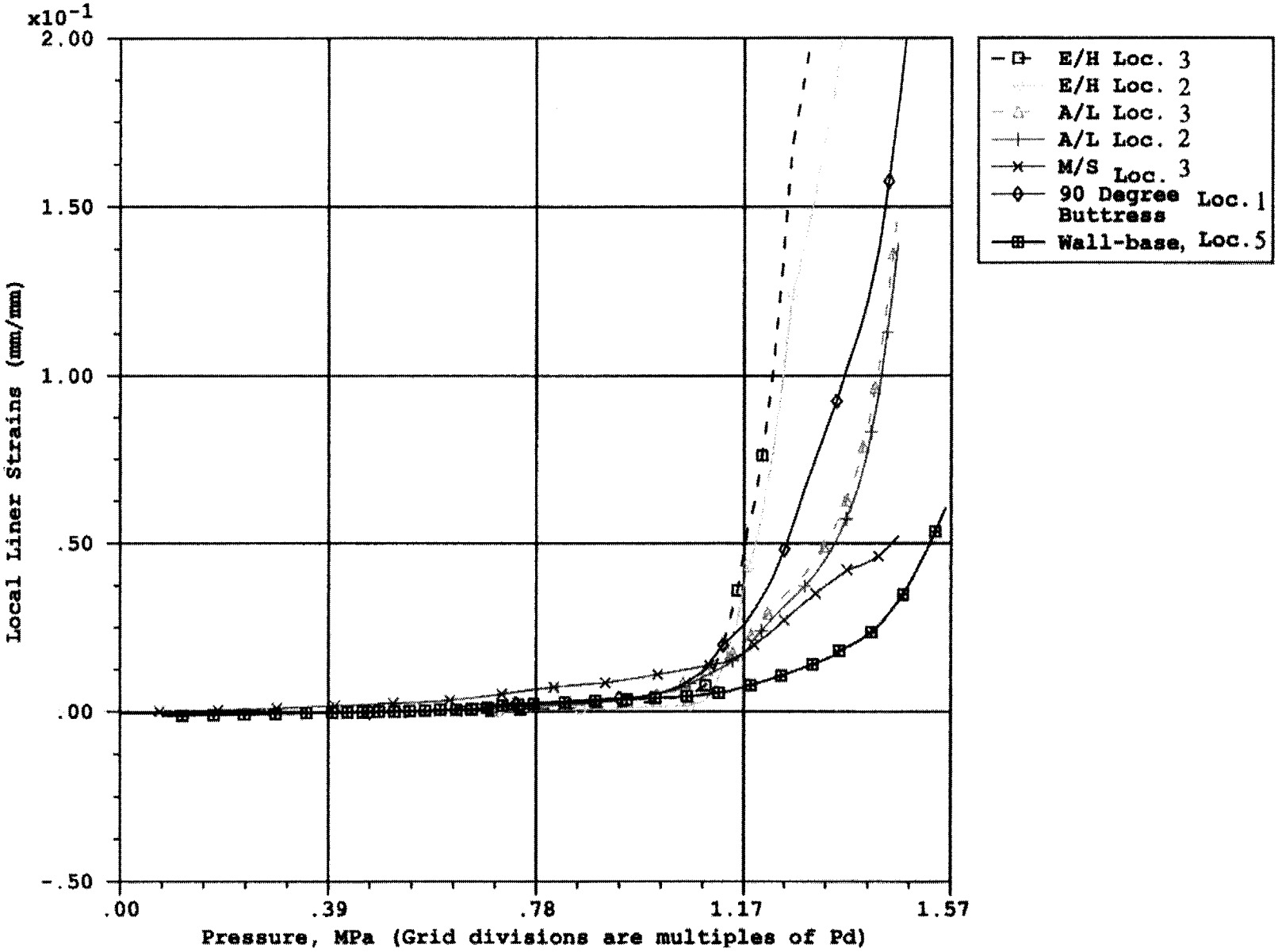


*eh.inp, al.inp, ms.inp, 3dcm.inp, model14.inp*

Figure 11-4. Peak Strains of Location Models at Possible Failure Locations

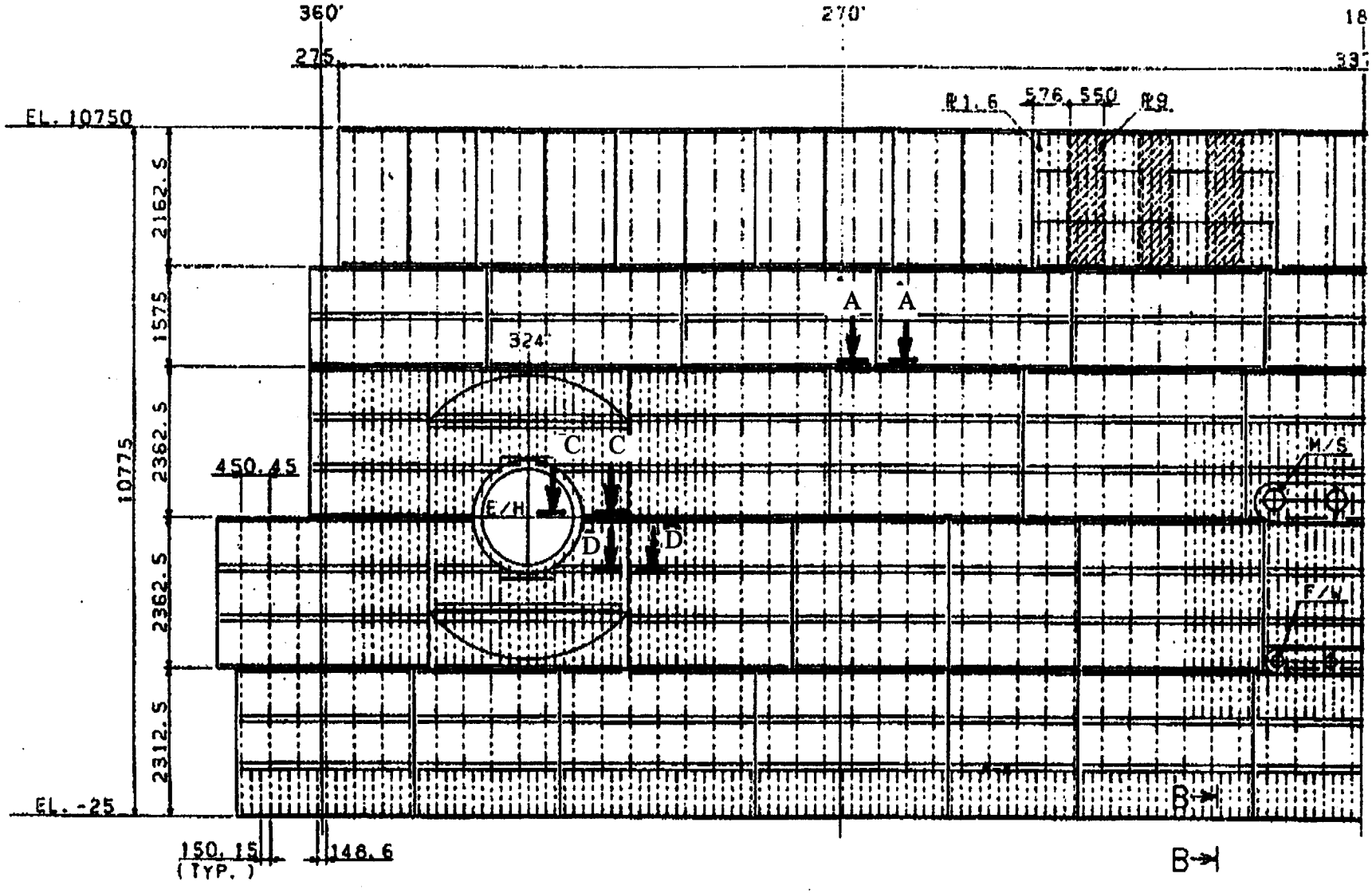


Figure 11-5. Categorization of Liner Strain Concentration Locations (Part 1)

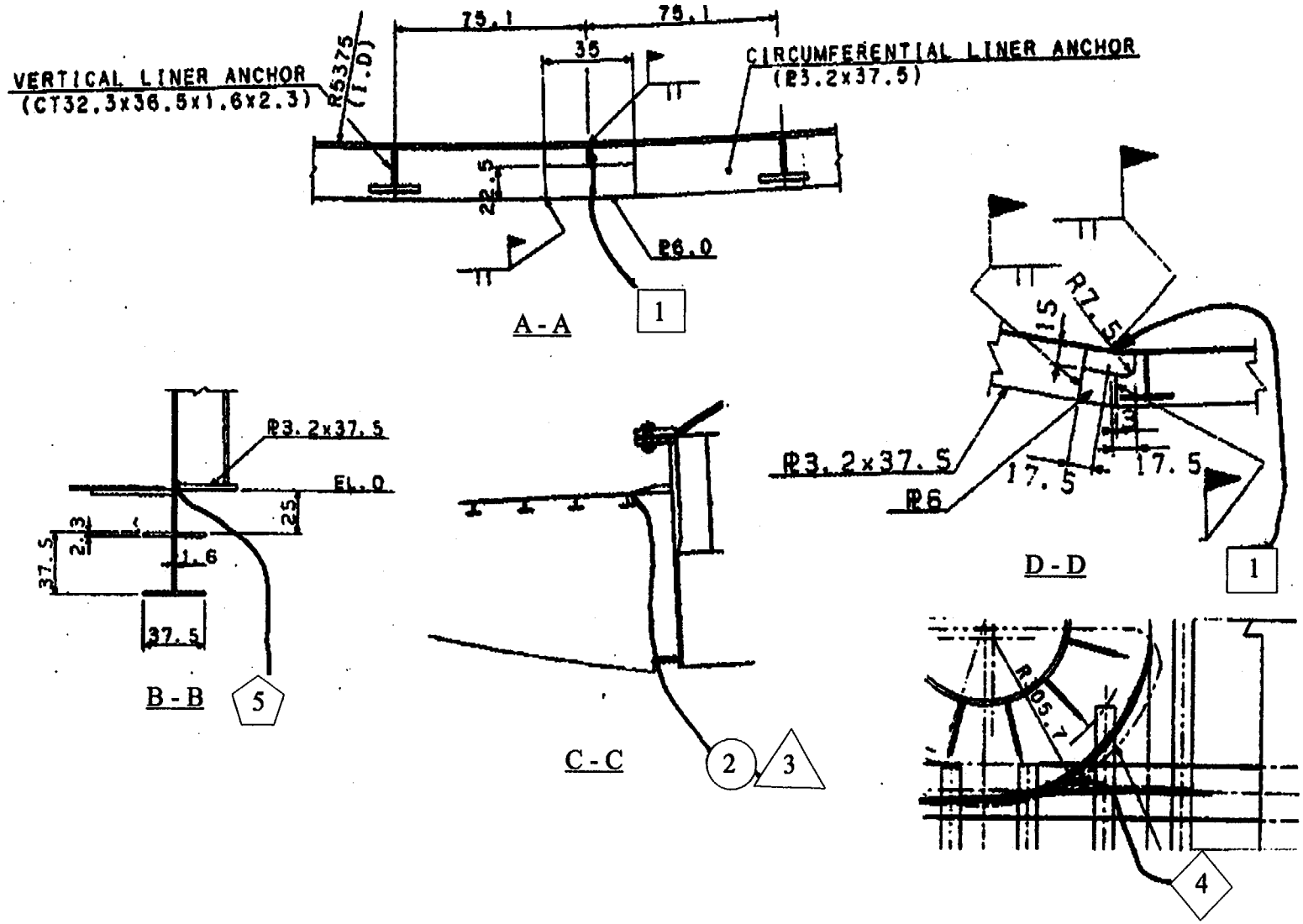


Figure 11-6. Categorization of Liner Strain Concentration Locations (Part 2)

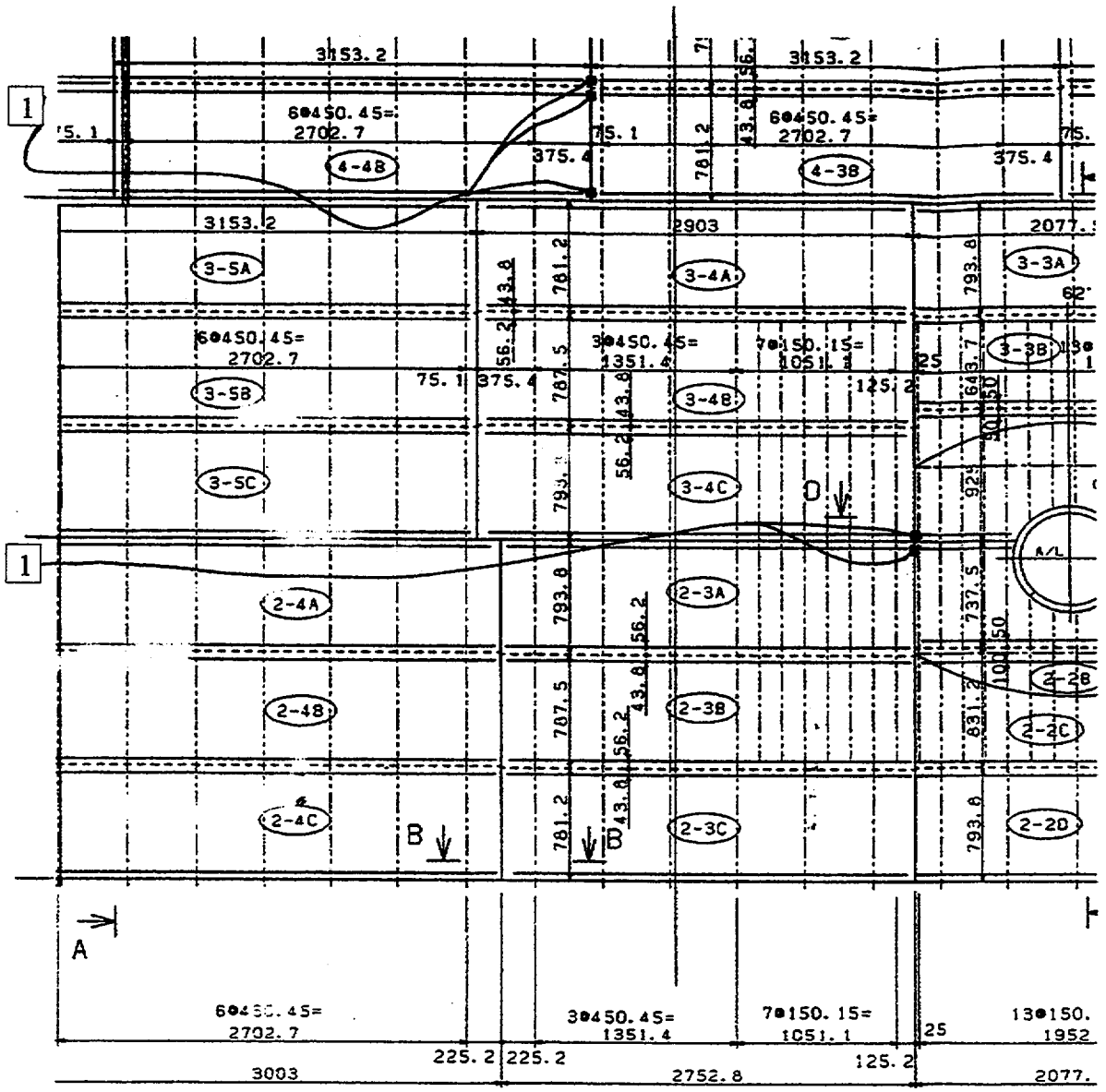


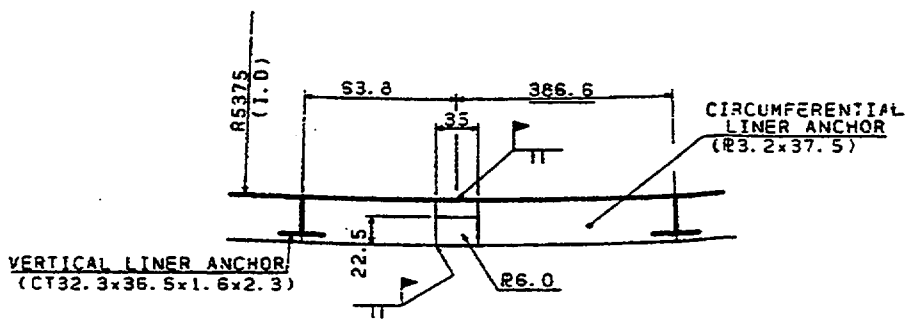


Figure 11-7. Strain Concentration Type 1 Near 90° Buttress and Near A/L

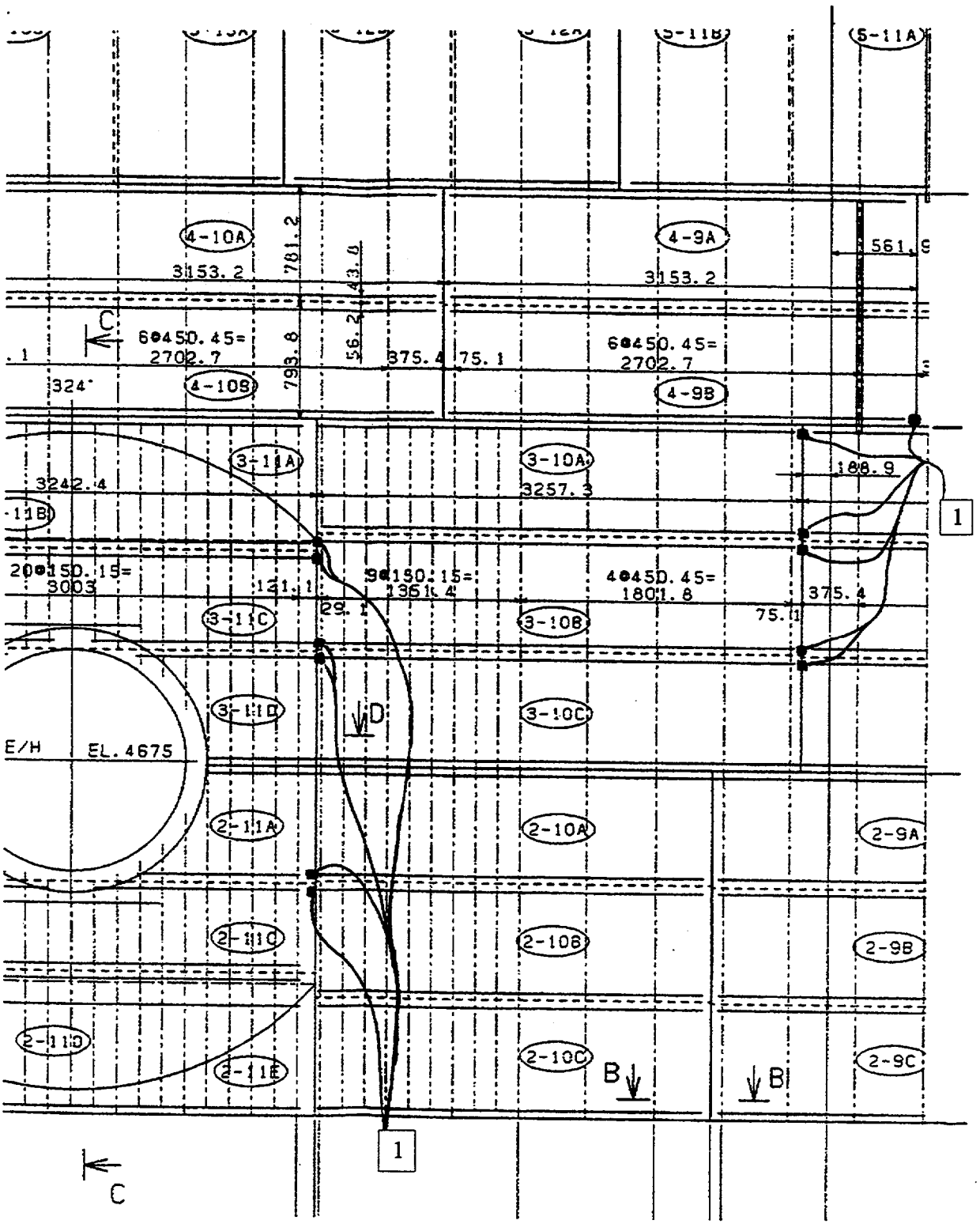


Figure 11-8. Strain Concentration Type 1 Near 270° Buttress and Near E/H

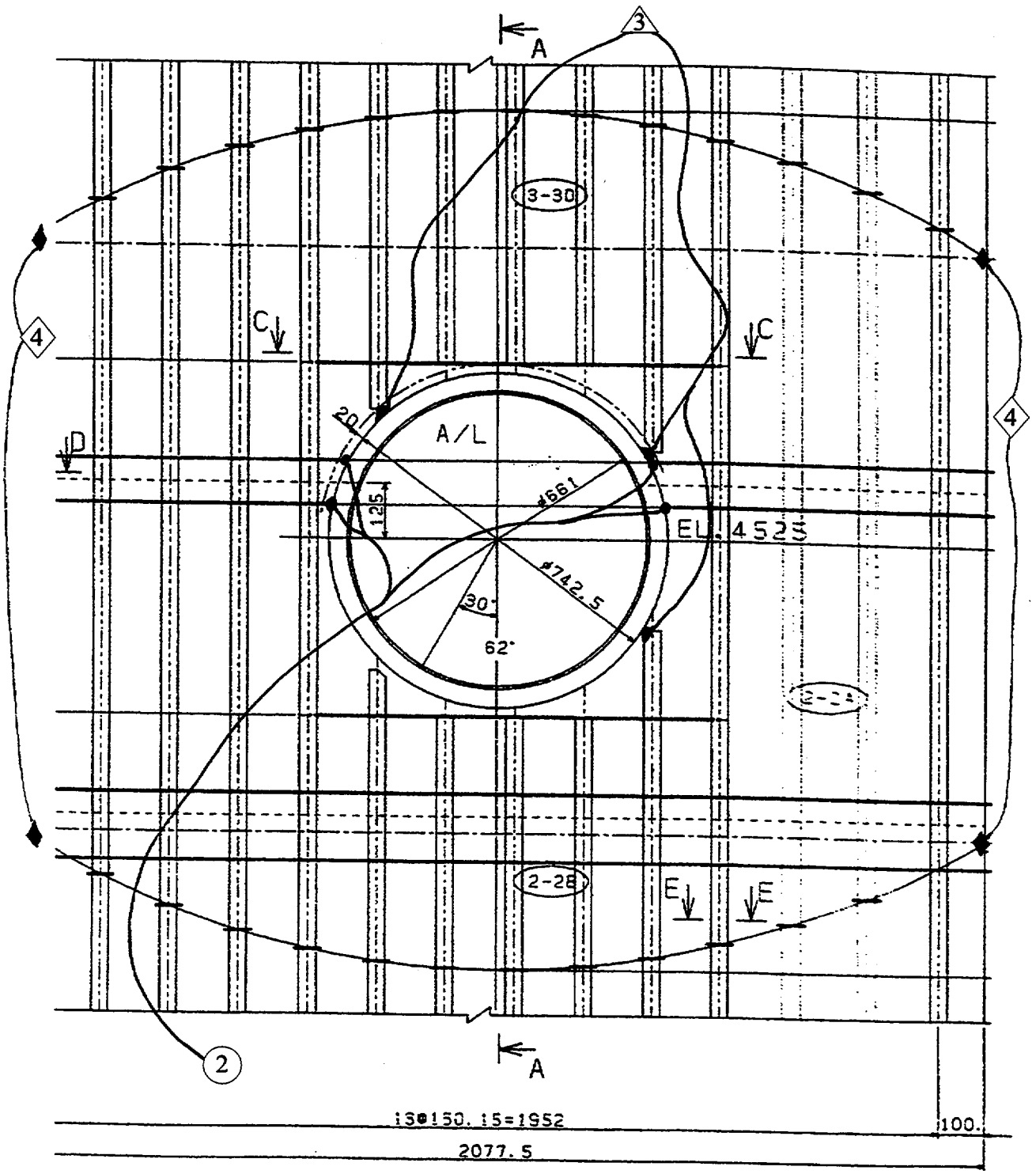


Figure 11-9. Strain Concentration Type 2,3,4 Near A/L

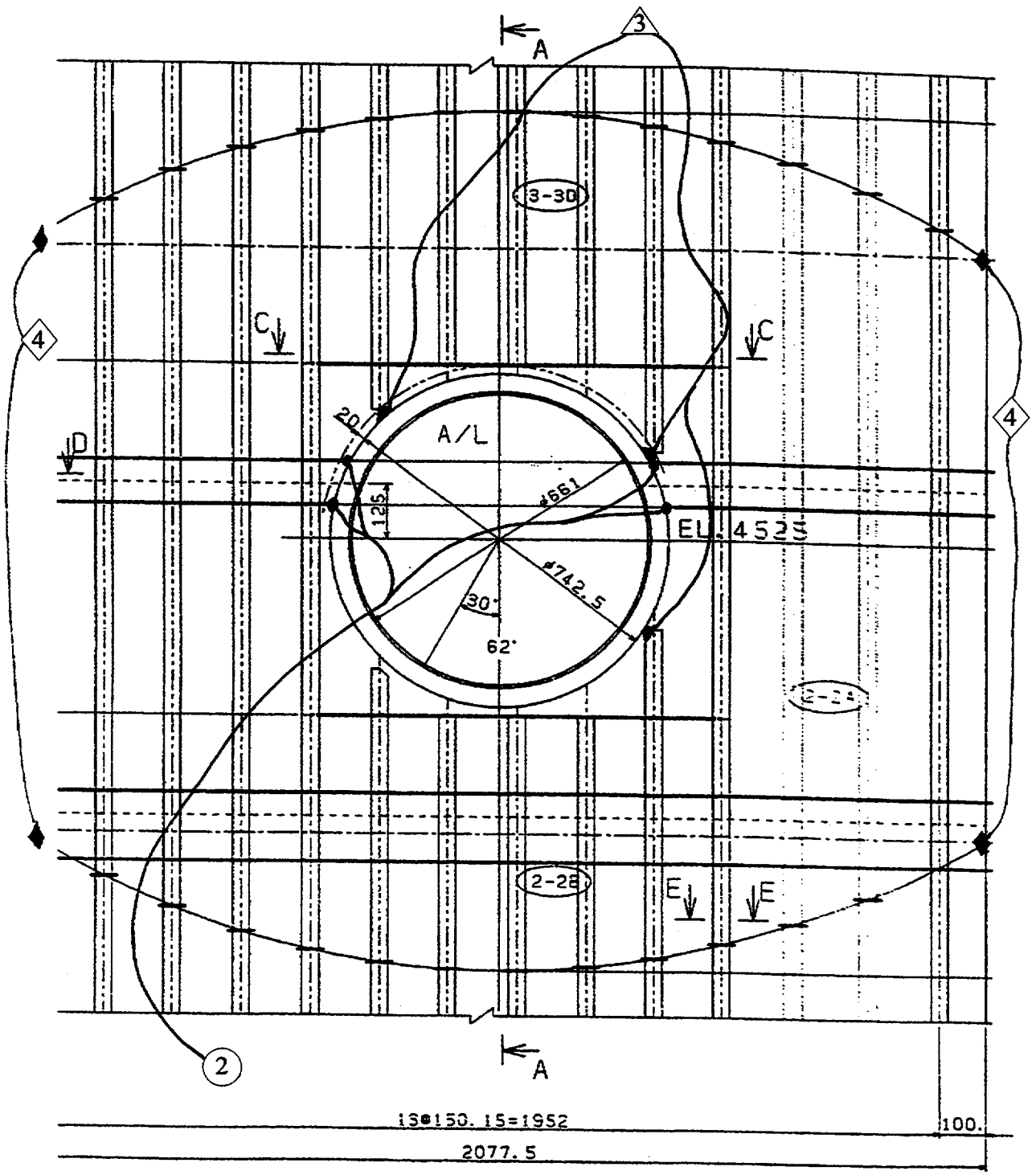


Figure 11-10. Strain Concentration Type 2,3,4 Near E/H

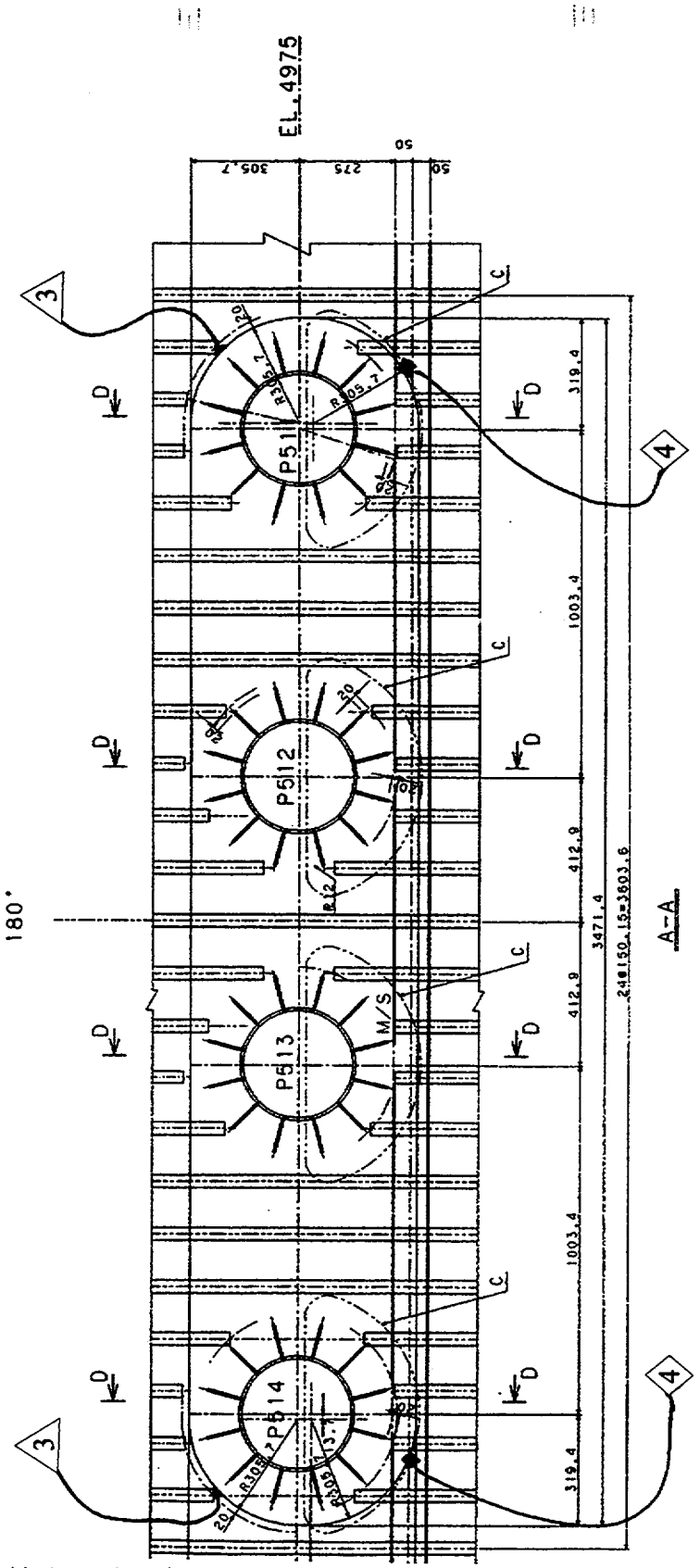


Figure 11-11. Strain Concentration Type 3,4 Near M/S Penetrations

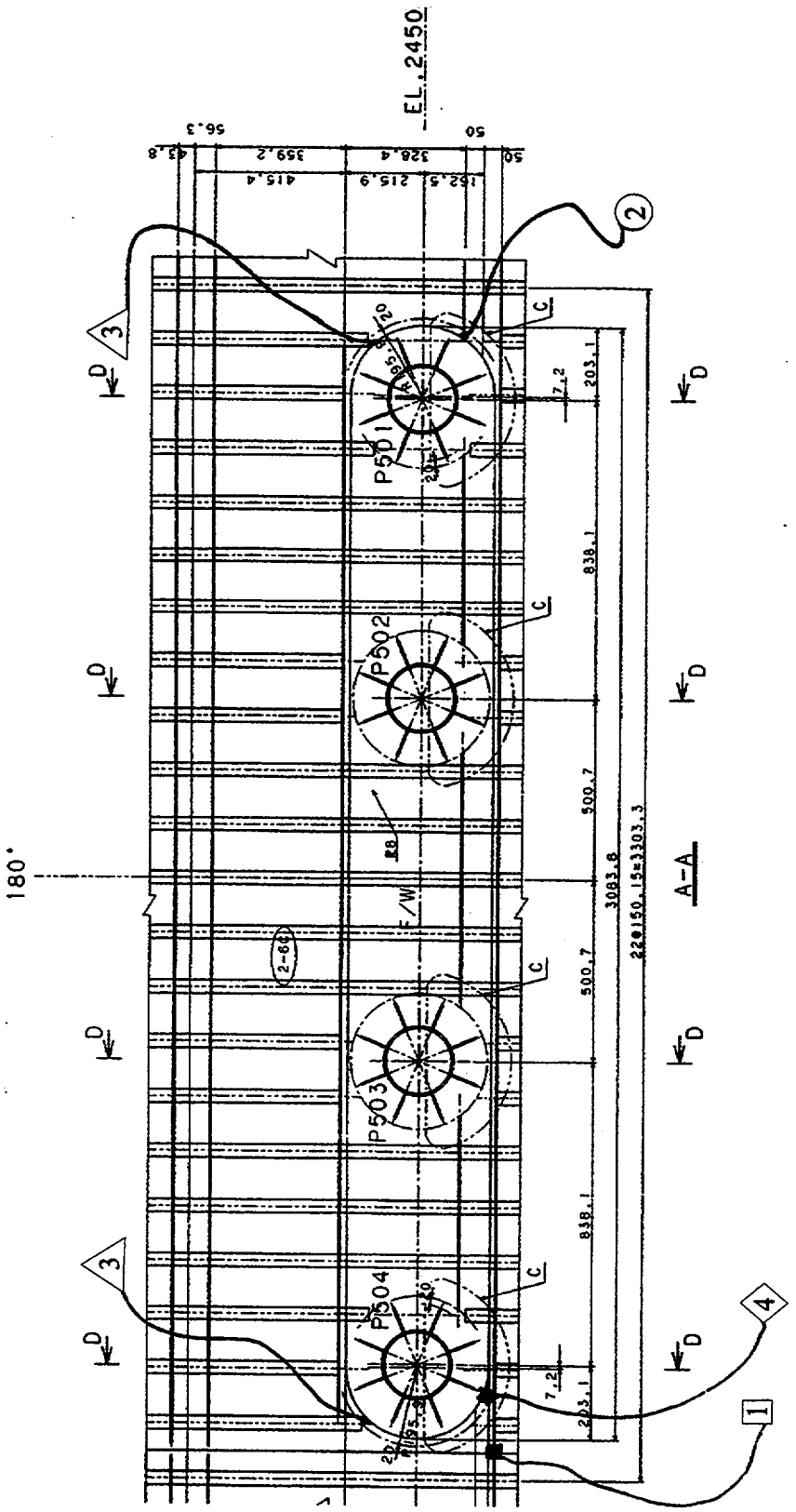


Figure 11-12. Strain Concentration Type 1,2,3,4 Near F/W Penetrations

# 12. AS-BUILT CONDITIONS AND UNCERTAINTIES

This chapter discusses some of the as-built conditions in the prestressed concrete containment vessel (PCCV) model that may influence the test results and the analytical uncertainties that these conditions may cause. The focus of the discussion is to demonstrate by example how these conditions might influence the test results and suggest a framework for how these effects might be evaluated and quantified after the test.

The analysis work comprising the pretest predictions of the PCCV model test behavior have been based on several major assumptions. This is out of necessity due to project schedule constraints and based on engineering judgment of the "diminishing returns" of making ever-increasing refinements to analytical detail. With regard to schedule, the predictions documented in this report also form the basis for the round-robin analysis submittal which was assembled for publication in fall 1999; thus the predictive analyses were conducted about a year before the scheduled pressure test. With regard to detail, the analysis could not include certain conditions which are unknown a year prior to testing. These limitations can be summarized in the following list of items that were not considered in the analytical predictions documented in the preceding chapters of this report.

Items not considered in analytical predictions

1. geometric and structural imperfections;
2. actual prestressing (as opposed to designers' planned values);
3. temperature effects;
4. material property variability; and
5. as-built stress and strain state in the model at test-time, including time-dependent effects.

## 12.1 Geometric and Structural Imperfections

No structure can be built to exact dimensions. This is true of a full-scale prototype and of the 1:4-scale model. Detailed identification and discussion of the consequences of these flaws is beyond the scope of this analysis report. A point worth mentioning, however, is that as dimensions of structural components get smaller, normally accepted construction deviations can have an increasing influence (in percentage terms). This can be restated construction tolerances do not scale the same as structure dimensions do. For the 1:4-scale PCCV this may hold true for such things as liner welding and rebar placement. The "cover" dimension on rebar placement is difficult to scale 1:4 and still fit all the rebar in using normal construction methods. Liner "fit-up" and welding tolerances may also have more significant consequences on a 1.6 mm-scaled liner than on the 6.4 mm-prototype.

In probabilistic risk assessment studies of reactor containments of the 1980s and early 1990s (Rang et al. 1995) it was typical to attempt to quantify randomness, variabilities, and uncertainties. The uncertainty and randomness values typically used for geometric and structural imperfections of containments typically range from 0.05 to 0.15. (Use of these numbers is described in more detail later in this chapter.) It would be difficult to estimate randomness and uncertainty figures related to the 1:4-scale PCCV, but for the reasons cited, suffice it to say that the numbers would be at the high end of the range. No accounting for geometric or structural imperfections has been included in the pretest prediction analysis, but this may be worth pursuing after the test data are available.

## 12.2 Actual Prestressing

Detailed discussion of prestressing, with particular attention to anchor set losses, was provided in Chapter 7, because the radial displacement behavior of the cylinder was found to be sensitive to the anchor set loss assumptions. At the time of publication of this report, actual setting losses experienced during prestressing had become available, although with insufficient time to repeat and re-document all of the analyses for this report. The parameter study in Chapter 7 predicts that differences between the assumed and actual setting losses could affect the radial response versus pressure of the cylinder, particularly the degree of ovalization that occurs relative to the buttresses. Preliminary review of the actual tendon stressing data indicates that the set losses may be larger than assumed in the pretest prediction analysis and close to the specified values. While it is not possible to quantify these effects for this report, the analysis predicts that the larger setting loss may tend to:

1. increase the radial expansion versus pressure of the response curves at the buttresses;

2. generally decrease the radial expansion versus pressure of the response curves at the penetration azimuths (180°, 324°, 296°); and

3. reduce the degree of circumferential bending of the wall near the buttress and reduce the liner tension predicted to occur at this juncture.

It is the opinion of the authors, however, that the degree of sensitivity of radial expansion related to setting losses, will, in the actual test, be self-limiting. The 3DCM model tendon friction modeling strategy "locks in" the tendon angular friction relationship and the orientation direction of setting loss distributions. In the actual model test, as the cylinder expands, tendon stresses will probably become more uniform through local slippage and stress redistribution, a phenomenon that the analytical model is unable to capture. These stress redistributions are likely to make the cylinder expansion more uniform with azimuth and generally limit the difference in behavior that might be associated with setting losses. The degree to which this occurs is unknown and generally adds to the level of pretest prediction uncertainty. Our understanding of the actual behavior should be improved after the test data are available.

## 12.3 Updated Creep Properties

As described in Chapter 5, the original design losses due to concrete creep were approximately 5% (i.e., about 55 MPa out of a vertical tendon stress of 1386 MPa). This is based on standard practice and on the design standards that were used. The vertical stress in the concrete wall, based on equilibrium considerations is approximately 7.5 MPa. The specific creep associated with these stresses can be calculated as follows:

Tendon strain lost = $\varepsilon = 55\text{MPa}/200{,}000 = 0.28 \times 10^{-3}$

Specific creep =

$$S_c = \frac{\varepsilon}{\sigma_{concrete}} = 0.28\text{x}10^{-3} / 7.5\text{MPa} = 37.3\text{x}10^{-6}$$

mm/mm/MPa

(0.257 in/in/psi)

As shown in Figure 12-1, this value agrees fairly well with the early creep measurements performed for the PCCV test program trial mixes (the CTL data). More recently, the creep behavior of the as-built model concrete has been measured and is also plotted in Figure 12-1. The specific creep derived from this data is

$$S_c = 39.56\text{x}10^{-6} + 18.73\text{x}10^{-6}\,\ell_n\,(t+1)\ \text{mm/mm/MPa}$$

(elastic part) (creep part)

$$(2.728 \times 10^{-7} + 1.292 \times 10^{-7}\,\ell n\,(t+1)\ \text{in/in/psi} \quad (12\text{-}1)$$

where t is the time that the load (prestress) is "on" in days. With prestressing completed during the months of March and April 2000 and the test date set for approximately October 1, 2000, the time with prestress is approximately 7 months or 180 days. The actual creep expected to occur, therefore, is

$$\varepsilon = S_c\,\sigma = (39.56 \times 10^{-6} + 18.73\text{x}10^{-6}\,\ell_n\,(181))\ 7.5\ \text{MPa}$$

(elastic part) (creep part)

This represents an actual tendon stress loss associated with creep of

$$\sigma_{tendon} = \varepsilon E = 0.73 \times 10^{-3}\,(200{,}000) = 146\ \text{MPa or } 10\%!$$

An additional 5% creep loss (a total of 10%) was used in the pretest prediction analysis based on initial observations of the larger than usual creep phenomena. The effects of larger than anticipated creep and of temperature are examined in the next subsection.

## 12.4 Analysis of Temperature and Creep Effects

The 2D axisymmetric model was run to include temperature loadings, prestress and creep. Shrinkage was ignored, assuming that these effects had already "saturated" prior to prestressing. This analysis was performed to assist in instrumentation decisions including the initial offset and range of travel of important gages and potentiometers, during the time between when the gages were mounted and turned on (which was prior to prestressing) and the time of the high pressure test.

The time-dependent analysis parameters were assigned as follows:

1. Global properties were modeled with the same material properties and prestress levels as in the previously documented prediction analysis;

2. Creep properties measured by the University of New Mexico (Eq. 12-1) were used;

3. Shrinkage was ignored (assumed already saturated);

4. Coefficients of thermal expansion were $\alpha_{concrete} = 5.5E^{-6}/°F$, $\alpha_{steel} = 6.5E^{-6}/°F$;

5. All nodes were assumed to have equal temperature at each step except for Step 15, where a temperature gradient was introduced through the wall and no heat transfer solutions were performed.

A scenario for time dependent effects analysis from the approximate time of gage activation to the time of the pressure test was developed, including estimated temperature variations, as shown in Table 12-1. Nonlinear analysis was conducted in stepwise fashion, using the 16 "states" identified in Table 12-1 and a total of 162 load increments to capture the effects of creep, etc.

Some results of the temperature and creep effects analysis are shown in Table 12-2 (maximum range of results for particular gages) and plotted in Figures 12-2 through 12-4. The results shown are displacements (Standard Output Locations 1 through 11) and meridional tendon stress (SOL 54).

The conclusions of the time-dependent effects analysis are summarized below:

1. The analysis predicted creep displacements of about 0.6 cm radially and 1.2 cm vertically in the cylinder.

2. The analysis predicted creep strains (hoop) of 0.1% in the liner and rebar at the cylinder midheight.

3. The total hoop strains at the cylinder midheight, including the results of prestress and creep, cause the liner to nearly reach yield.

4. Prestress losses due to creep are larger than was originally anticipated by the designers; losses due to creep are approximately 10% of initial tendon stress.

## 12.5 Further Discussion of Pretest Prediction Uncertainties

The discussions in this chapter and the time-dependent effects analysis help to identify the range of uncertainties that may exist for the pretest analysis. This subsection suggests a framework for quantifying uncertainties and their influence on the prediction of failure pressure that might be used after the test during posttest correlation to analysis. The methodology summarized below is an abbreviated version of the methodology originally published in Tang et al. (1995).

In Tang et al. (1995) a liner tearing criterion is presented in the context of a simplified analysis approach that takes the form

$$\varepsilon_p = KB\varepsilon_{global} \tag{12-2}$$

where $\varepsilon_p$ is the equivalent peak uniaxial strain at a discontinuity location, K is a strain concentration factor, B is a stress biaxiality factor and $\varepsilon_{global}$ is the global strain quantity that corresponds to the location where the local peak strain is being evaluated. Eq. (12-2) as originally developed provides a simplified criterion for concrete containment liner failure prediction. However, in the context of probabilistic risk assessment (PRA), one not only needs to predict leakage (liner tearing) but also to quantify probabilities and uncertainties. Thus, a deterministic leakage prediction methodology has to be combined with a probabilistic evaluation procedure to enable risk assessments for containment structures. This involves the characterization of probability distribution and uncertainty bands for the terms of Eq. (12-2) and the convolving of these into final probability distributions.

In the deterministic framework, the terms on the right-hand side of Eq. (12-2) are considered to be best estimates or median values. Thus, in the probabilistic framework, Eq. (12-2) is more appropriately recast as

$$\hat{\varepsilon}_p = \hat{K}\hat{B}\hat{\varepsilon}_{global} \tag{12-3}$$

and the probabilistic tearing criterion equation becomes $\varepsilon_p = KB\varepsilon_{global}$ in which

$$\varepsilon_{global} = \hat{\varepsilon}_{global}\gamma_u\gamma_R \tag{12-4}$$

$$K = \hat{K}\lambda_u\lambda_R \tag{12-5}$$

$$B = \hat{B}\xi_u\xi_R \tag{12-6}$$

K, B and $\varepsilon_{global}$ are now lognormally distributed random variables, and $\gamma_u$, $\gamma_R$, $\lambda_u$, $\lambda_R$, $\xi_u$ and $\xi_R$ are lognormally distributed variables with unit median and logarithmic standard deviation $\beta_u$ and $\beta_R$. The randomness of a calculated quantity is relatively low, for example

$$\beta_R \Big| \varepsilon_g = 0.05$$

represents inherent randomness in the finite element representation of actual structural details. As with any calculated quantity, the uncertainty is based on incomplete knowledge of actual material properties and actual structural details, and uncertainty in the mathematical idealization and discretization of a complex 3D structure with axisymmetric modeling. $\beta_u$ of 0.15 is normally assigned because of the standardization of the axisymmetric analysis procedure. A sample $\varepsilon_{global}$ curve showing graphical representation of the formula given in Eq. (12-4) is shown in Figure 12-5. Assuming that randomness and uncertainty on the local modeling can also be defined, the assignment of randomness and uncertainty factors for the terms in the liner tearing criterion formula can be summarized below.

$\varepsilon_{global}$ (global strain)

$\beta_u = 0.15$
$\beta_R = 0.05$

B (biaxiality)

$\beta_u = 0.10$
$\beta_R = 0.16$

K (strain concentration)

$\beta_u = 0.1$ to 0.2 depending on geometry
$\beta_u = 0.1$ default
$\beta_R = 0.05$

With the further assumption of variable independency, the randomness and uncertainty factors are combined for the default values listed above as follows:

$$\beta_c=(0.15^2+0.05^2+0.10^2+0.16^2+0.10^2+0.05^2)^{1/2}=0.27$$

This gives the dispersion of the entire right-hand side of Eq. (12-2). Since $\varepsilon_{global}$, K and B are assumed to be lognormally distributed random variables at a particular pressure, they can be calculated from the properties of lognormal random variables.

While the scope and objectives of the pretest analysis work for the 1:4 Scale-PCCV did not include a probabilistic risk assessment (PRA) of the failure (leakage) pressure prediction, if a PRA were needed, it could be constructed using the evaluation framework presented here. An illustration of how the final probability of leakage versus pressure might look for the 1:4 Scale PCCV model is shown in Figure 12-6. The purpose of this figure is to illustrate the methodology, not to present results of a detailed probability calculation. The figure is constructed with reference to Table 11-1 and the methodology described herein. It combines probabilities by location and by the number of occurrences at each location. Using the location numbering and the number of locations from Table 11-1, the probability calculation becomes

$$P_{leakage}=1-[(1-P_1)^4(1-P_2)^4(1-P_3)^6(1-P_4)^3(1-P_5)^4(1-P_6)^2 (1-P_7)^3] \quad (12\text{-}7)$$

Combining probabilities and locations produces leakage pressure predictions as presented in Chapter 11, but now with probabilities associated with pressure.

Best estimate (P-0.5), $P_{leakage} = 3.2P_d = 1.28$ MPa

Upper bound (P=0.9), $P_{leakage} = 3.60P_d = 1.44$ MPa

Lower bound (P=0.1), $P_{leakage} = 3.0P_d = 1.20$ MPa

**Table 12-1. Temperature, Load and Time Assumptions for Thermal, Creep, and Time-Dependent Effects Analysis**

| Results Point | Date/Time | Cumulative time (days) | Temp (°F) | Load |
|---|---|---|---|---|
| 1. | 2/23/2000, 2am | 0 | 30 | Dead Load |
| 2. | 2/23/2000, 2pm | 0.5 | 60 | Dead Load |
| 3. | 2/23/2000, 2pm | 0.5 | 60 | Dead + Prestress |
| 4. | 2/24/2000, 2am | 1.0 | 30 | Dead + Prestress |
| 5. | 2/24/2000, 2pm | 1.5 | 70 | Dead + Prestress |
| 6. | 8/21/2000, 2pm | 179.5 | 70 | Dead + Prestress |
| 7. | 8/22/2000, 2am | 180.0 | 40 (cold night) | Dead + Prestress |
| 8. | 8/22/2000, 2pm | 180.5 | 100 (hot day) | Dead + Prestress |
| 9. | 8/23/2000, 2pm | 181.5 | 70 | Dead + Prestress |
| 10. | 8/23/2000, 2pm | 181.6 | 70 | Dead + Prestress + 1.15xPd |
| 11. | 8/24/2000, 2pm | 182.5 | 70 (hold 1 day) | Dead + Prestress + 1.15xPd |
| 12. | 8/24/2000, 2pm | 182.6 | 70 | Dead + Prestress |
| 13. | 9/26/2000, 2pm | 215.5 | 60 | Dead + Prestress |
| 14. | 9/27/2000 2am | 216.0 | 20 (cold night) | Dead + Prestress |
| 15. | 9/27/2000, 10am | 216.33 | 100 out/40 in (warm morning) | Dead + Prestress |
| 16. | 9/27/2000, 2pm | 216.50 | 100 out/100 in (warm afternoon) | Dead + Prestress |

**Table 12-2. Range of Results for Thermal, Creep, and Time-Dependent Effects Analysis**

| | Starting Location (cm) | Ending Location (cm) | Maximum Distance from Starting Location (cm) | Minimum Distance from Starting Location (cm) | Range (cm) |
|---|---|---|---|---|---|
| SOL 1 | 0.0000 | 0.0501 | 0.0607 | -0.1129 | 0.1736 |
| SOL 2 | 0.0000 | 0.1190 | 0.1299 | -0.1215 | 0.2515 |
| SOL 3 | 0.0000 | -0.4186 | 0.0745 | -0.6703 | 0.7448 |
| SOL 4 | 0.0000 | -0.6251 | 0.0755 | -0.8903 | 0.9658 |
| SOL 5 | 0.0000 | -0.7135 | 0.0752 | -0.9754 | 1.0506 |
| SOL 6 | 0.0000 | -0.7452 | 0.0750 | -1.0041 | 1.0790 |
| SOL 7 | 0.0000 | -0.6241 | 0.0760 | -0.8768 | 0.9528 |
| SOL 8 | 0.0000 | -1.0594 | 0.1754 | -1.7188 | 1.8943 |
| SOL 9 | 0.0000 | -0.5712 | 0.0523 | -0.7526 | 0.8049 |
| SOL 10 | 0.0000 | -1.7071 | 0.2223 | -2.5286 | 2.7509 |
| SOL 11 | 0.0000 | -1.8059 | 0.2405 | -2.6975 | 2.9380 |

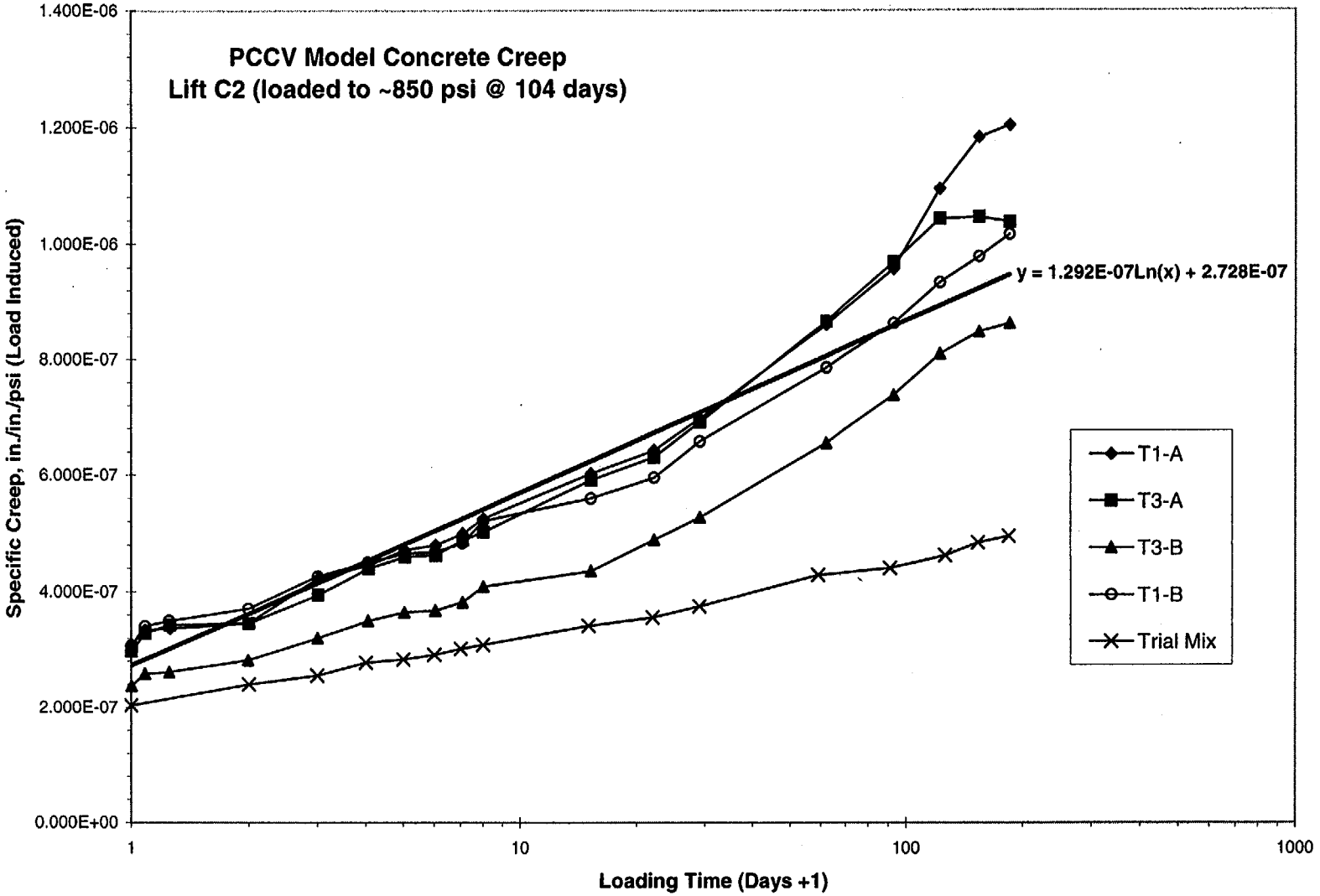


Figure 12-1. Typical Creep Data for the Prestressed Concrete Containment Vessel (PCCV) Model Concrete (i.e., Concrete Pour C-2).

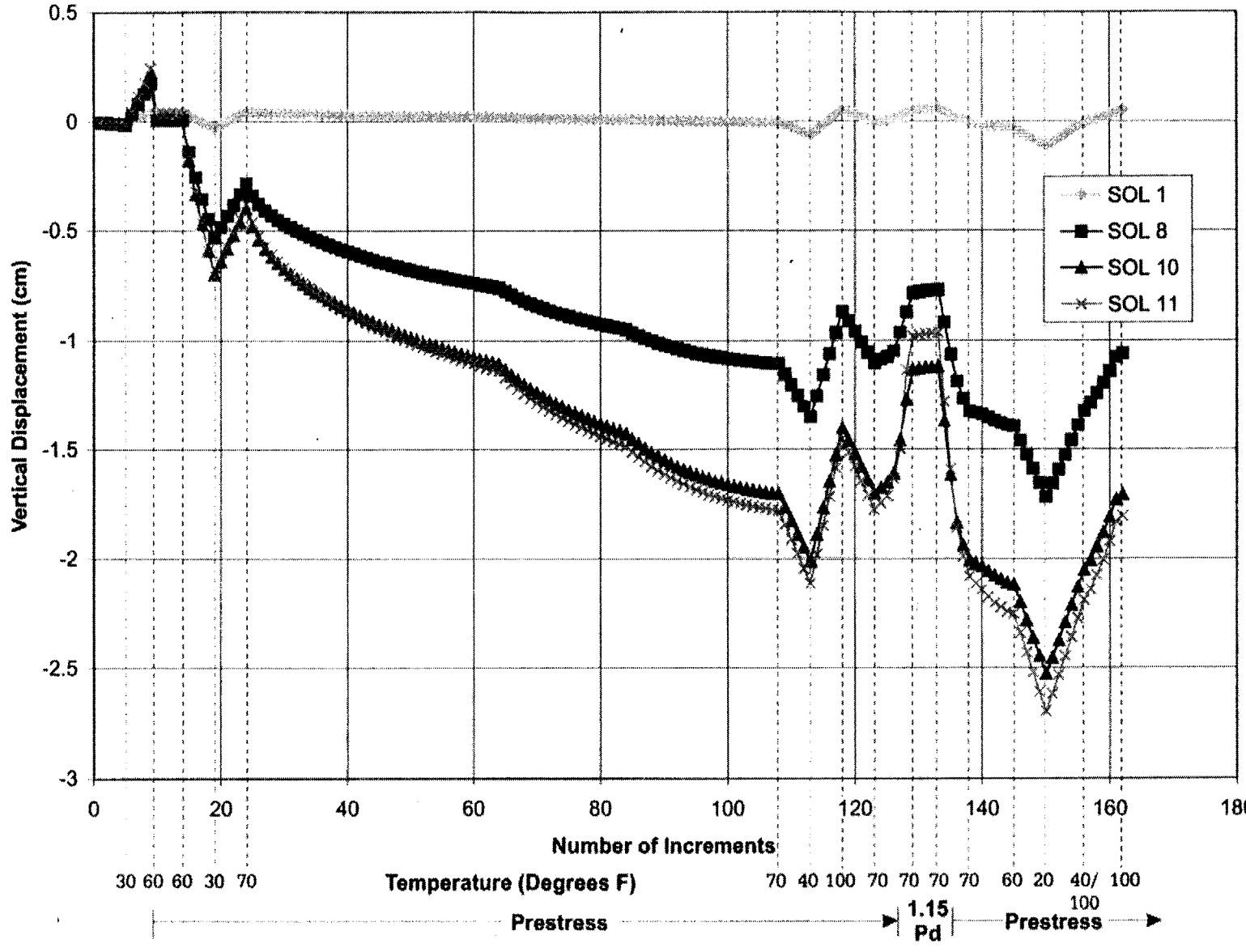


Figure 12-2. Prestressed Concrete Containment Vessel (PCCV) Thermal/Creep Analysis (Standard Output Locations 1,8,10,11)

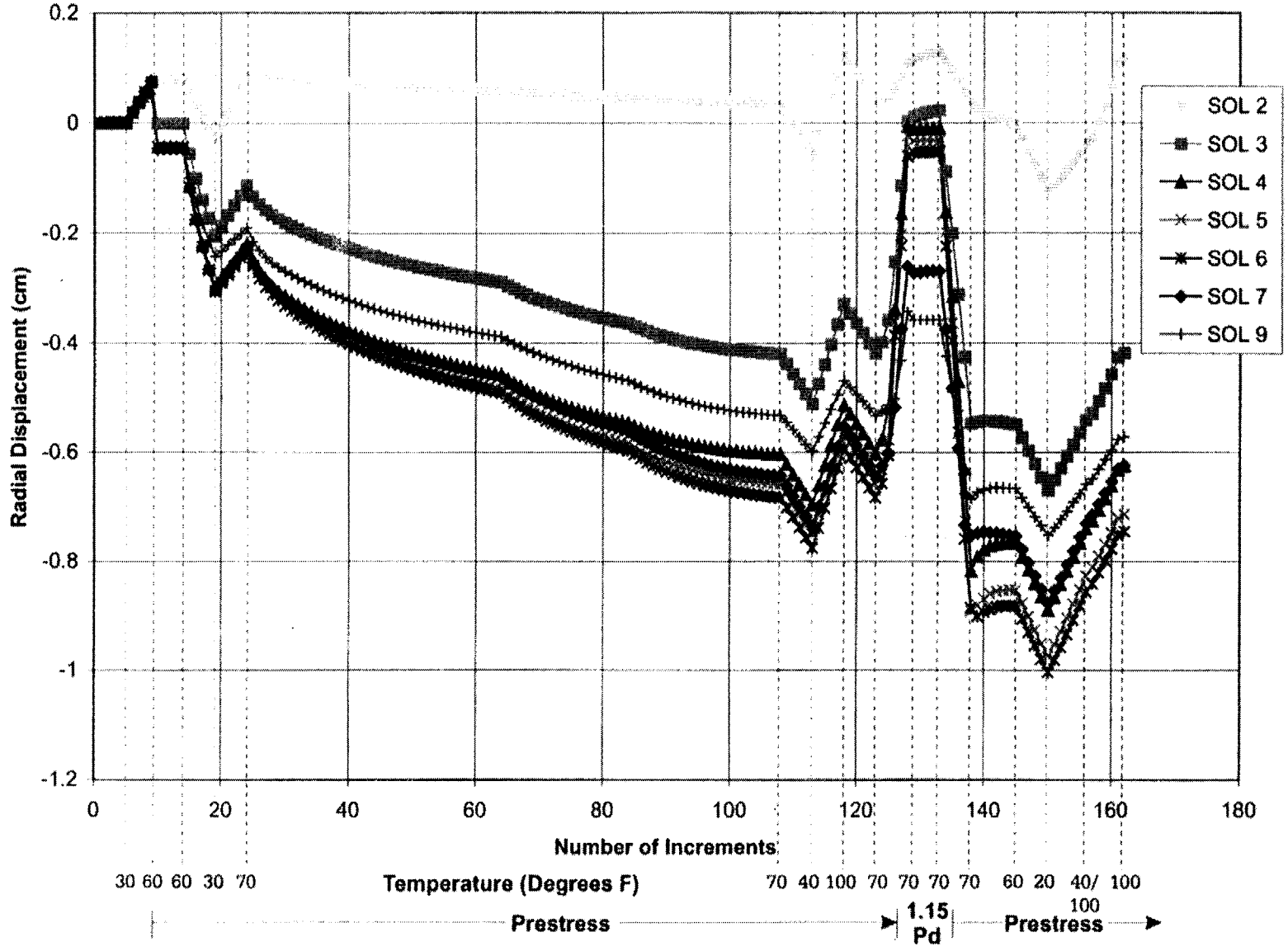


Figure 12-3. Prestressed Concrete Containment Vessel (PCCV) Thermal/Creep Analysis (Standard Output Locations 2-9)

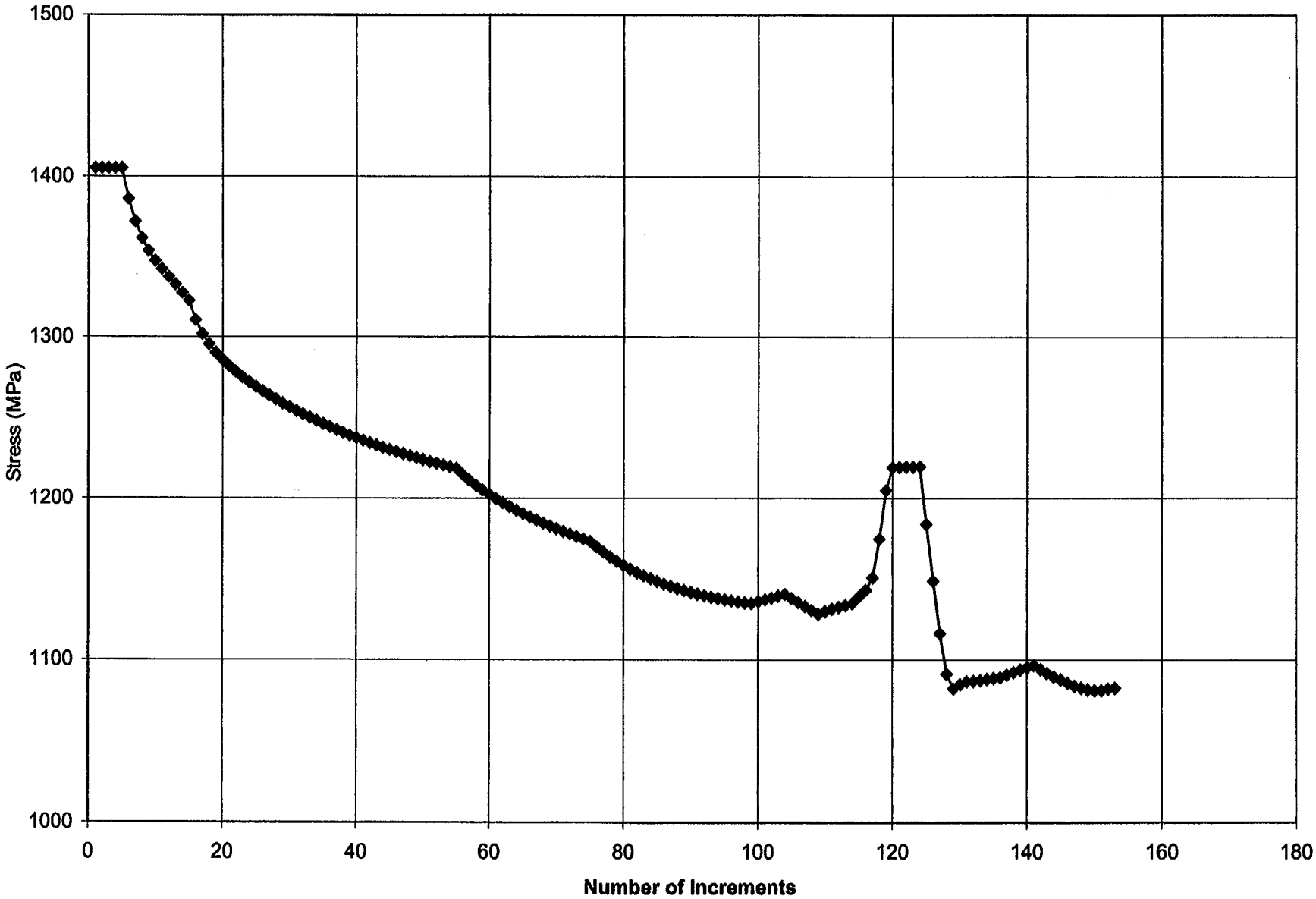


Figure 12-4. Meridional Tendon Stress at Tendon Gallery (Standard Ouput Location 54)

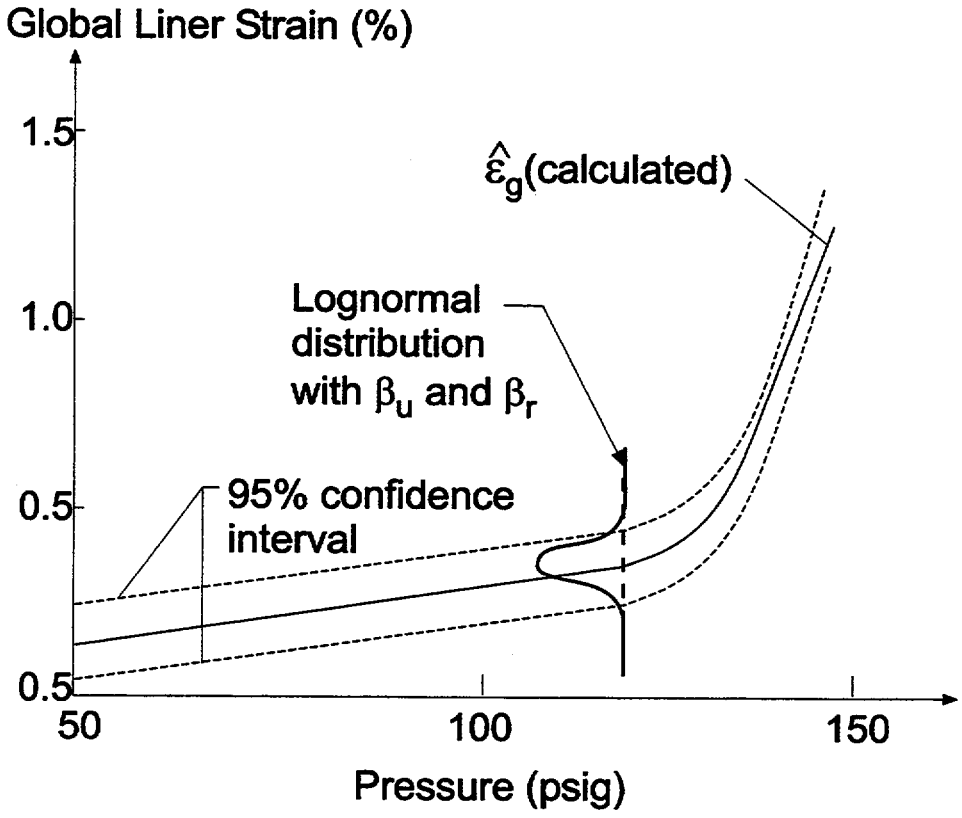


Figure 12-5. Typical Confidence Intervals Assigned to Prediction of Global Strain Versus Pressure

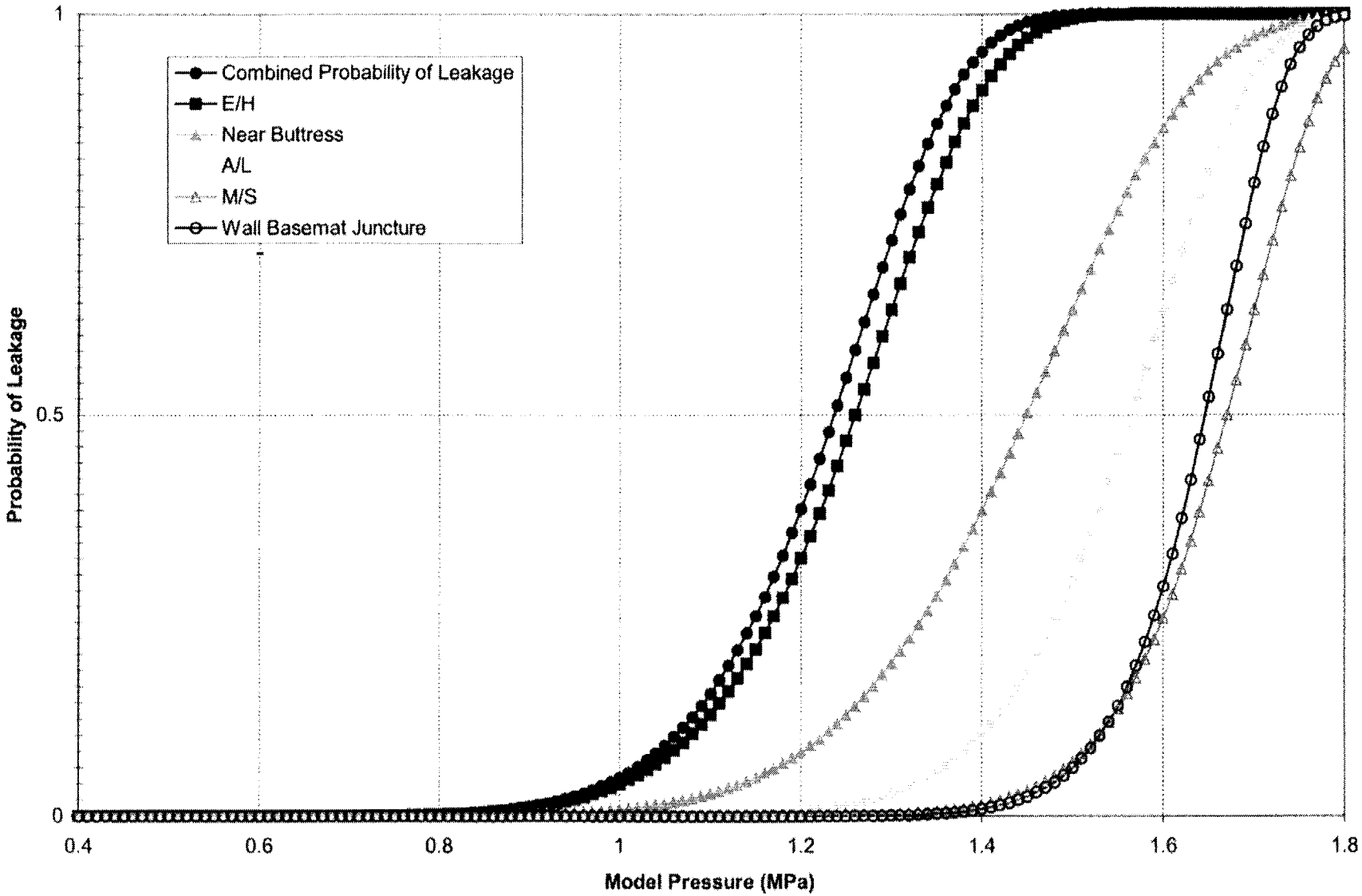


Figure 12-6. Example of How Probabilities of Liner Tearing at Discrete Locations Can be Combined to Obtain an Overall Probability of Leakage

# 13. REFERENCES


*ABAQUS User's Manual*, Version 4.7. 1988. Providence, RI: Hibbitt, Karlsson & Sorensen, Inc.

Clauss, D.B. 1987. *Round-Robin Pretest Analyses of a 1:6 Scale Reinforced Concrete Containment Model Subject to Static Internal Pressurization.* NUREG/CR-4913, SAND87-0891. Albuquerque, NM: Sandia National Laboratories.

Clauss, D.B. 1989. *Round-Robin Analysis of the Behavior of a 1:6 Scale Reinforced Concrete Containment Model Pressurized to Failure: Post-test Evaluations.* NUREG/CR-5341, SAND89-0349. Albuquerque, NM: Sandia National Laboratories.

Collins, M.P., and D. Mitchell. 1997. *Prestressed Concrete Structures*. Toronto, Ontario, Canada: Response Publications.

Dameron, R.A., Y.R. Rashid, and M.F. Sullaway. 1990. *Pretest Prediction of a 1:10 Scale Model Test of the Sizewell-B Containment Building.* NUREG/CR-5671. Albuquerque, NM: Sandia National Laboratories.

Dameron, R.A., Y.R. Rashid, V.K. Luk, and M.F. Hessheimer. 1997. "Preliminary Analysis of a 1:4 Scale Prestressed Concrete Containment Vessel Model," *Proceedings of the 14th International Conference on Structural Mechanics in Reactor Technology*, Lyon, France, August 17–22, 1997. Vol. 5: 89–96.

Dameron, R.A., Y.R. Rashid, V.K. Luk, and M.F. Hessheimer. 1998. "Investigation of Radial Shear in the Wall-Base Juncture of a 1:4 Scale Prestressed Concrete Containment Vessel Model," *Proceedings of ASME/JSME Joint Pressure Vessels and Piping Conference*, San Diego, California, July 26–30, 1998. PVP-Vol. 362: 189–198.

Hessheimer, M.F., R.A. Dameron, W.A. Von-Reisemann. 1997. "A Summary of Containment Integrity Research," *Proceedings of the Seminar on Containment of Nuclear Reactors Weld in Conjunction with 14th SMiRT*, August 25–26, 1997, Saclay, France.

Rashid, Y.R. 1968. "Ultimate Strength Analysis of Prestressed Concrete Pressure Vessels," *Nuclear Engineering and Design*, 7: 334–344.

Tang, H.T., R.A. Dameron, and Y.R. Rashid. 1995. "Probabilistic Evaluation of Concrete Containment Capacity for Beyond Design Basis Internal Pressures," *Nuclear Engineering and Design*, 157: 455–467.

# APPENDIX A

# DRAWINGS AND MATERIAL PROPERTY REFERENCES

## Table A-1. Liner Drawings Used in Model Generation

| DRAWING # | REVISION # | NAME |
|---|---|---|
| M1-ZCD1001A | 3 | Liner General Arrangement |
| M1-ZCD1002A | 0 | Cylinder Liner Anchor Details #1 Tiers |
| M1-ZCD1006A | 0 | Liner Plate Block Layout of Cylinder Portion |
| M1-ZCD1007A | 2 | Cylinder Liner Anchor Details #2~5 Blocks (0°~90°) |
| M1-ZCD1008A | 2 | Cylinder Liner Anchor Details #2~5 Blocks (90°~270°) |
| M1-ZCD1009A | 2 | Cylinder Liner Anchor Details #2~5 Blocks (270°~360°) |
| M1-ZCD1010A | 0 | Cylinder Liner Anchor Details (E/H) |
| M1-ZCD1011A | 0 | Cylinder Liner Anchor Details (A/L) |
| M1-ZCD1012A | 0 | Cylinder Liner Anchor Details (M/S) |
| M1-ZCD1013A | 0 | Cylinder Liner Anchor Details (F/W) |
| M1-ZCD1014A | 0 | Cylinder Liner Anchor Details and Pola Crane Bracket Details |
| M1-ZCD1015A | 1 | Liner Plate Block Layout of Dome Portion |
| M1-ZCD1016A | 0 | Stud Layout of Dome Portion |
| M1-ZCD1018A | 0 | Liner Plate Block and Stud Details of Dome Portion #6 Tiers |
| M1-ZCD1019A | 0 | Liner Plate Block and Stud Details of Dome Portion #7-8 Tiers |
| M1-ZCD1020A | 0 | Liner Plate Block and Stud Details of Dome Portion #9-10 Tiers |
| M1-ZCD1025A | 1 | Base Liner Plate Detail |

## Table A-2. Concrete, Reinforcement, and Tendon Drawings Used in Model Generation

| DRAWING # | REVISION # | NAME |
|---|---|---|
| PCCV-QCON-01 | R2 | Model-Generation Arrangement |
| PCCV-QCON-02 | R1 | Basemat Rebar Arrangement |
| PCCV-QCON-03 | R1 | Basemat Tendon Gallery Access Tunnel Rebar Arrangement |
| PCCVQCON-04 | R1 | Prestressing Tendon General Arrangement |
| PCCV-QCON-05 | R1 | Cylinder Prestressing Tendon Arrangement (270°~90°) |
| PCCV-QCON-06 | R1 | Cylinder Prestressing Tendon Arrangement (90°~270°) |
| PCCV-QCON-07 | R1 | Prestressing Tendon Details (E/H) (Vertical Dome) |
| PCCV-QCON-08 | R1 | Prestressing Tendon Details (E/H) (HOOP) |
| PCCV-QCON-09 | R1 | Prestressing Tendon Details (A/L) |
| PCCV-QCON-10 | R1 | Prestressing Tendon Details (M/S-F/W) |
| PCCV-QCON-11 | R1 | Dome Prestressing Tendon Arrangement- Prestressing System Hardware |
| PCCV-QCON-12 | R1 | Cylinder Dome and Rebar General Arrangement (1) |
| PCCV-QCON-13 | R1 | Cylinder Dome and Rebar General Arrangement (2) |
| PCCV-QCON-14 | R1 | Cylinder Dome and Rebar Details |
| PCCV-QCON-15 | R1 | Buttress Rebar Details |
| PCCV-QCON-16 | R1 | Opening Rebar Details (E/H) |
| PCCV-QCON-17 | R2 | Opening Rebar Details (A/L) |
| PCCV-QCON-18 | R3 | Penetration Rebar Details (M/S-F/W) |
| PCCV-QCON-19 | R2 | Crane Bracket Rebar Details – Rebar Arrangement Standards |

## Table A-3. Sheath Supporting Frame Details

| | | |
|---|---|---|
| PCCV-TS-1 | 0 | Sheath Supporting Frame (Cylinder) |
| PCCV-TS-2 | 0 | Sheath Supporting Frame (Cylinder) |
| PCCV-TS-3 | 0 | Sheath Supporting Frame (Cylinder) |
| PCCV-TS-4 | 0 | Sheath Supporting Frame (Cylinder) |
| PCCV-TS-5 | 0 | Sheath Supporting Frame (Cylinder) |
| PCCV-TS-6 | 0 | Sheath Supporting Frame (Cylinder) |
| PCCV-TS-7 | 0 | Sheath Supporting Frame (Cylinder) |
| PCCV-TS-8 | 0 | Sheath Supporting Frame (Cylinder) |
| PCCV-TS-9 | 0 | Sheath Supporting Frame (Cylinder) |
| PCCV-TS-10 | 0 | Sheath Supporting Frame (Cylinder) |
| PCCV-TS-11 | 0 | Sheath Supporting Frame (Cylinder) |
| PCCV-TS-12 | 0 | Sheath Supporting Frame (Cylinder) |
| PCCV-TS-13 | 0 | Sheath Supporting Frame (Cylinder) |
| PCCV-TS-14 | 0 | Sheath Supporting Frame (Cylinder) |
| PCCV-TS-15 | 0 | Sheath Supporting Frame (Cylinder) |
| PCCV-TS-16 | 0 | Sheath Supporting Frame (Cylinder) |
| PCCV-TS-17 | 0 | Sheath Supporting Frame (Cylinder) |
| PCCV-TS-18 | 0 | Sheath Supporting Frame (Cylinder) |
| PCCV-TS-19 | 0 | Sheath Supporting Frame (Cylinder) |
| PCCV-TS-20 | 0 | Sheath Supporting Frame (Cylinder) |
| PCCV-TS-21 | 0 | Sheath Supporting Frame (Dome) |

## Table A-4. Sources of Geometry and Material Property Information

| Preliminary Analysis Material | Reference/Source |
|---|---|
| Concrete $f_c'$ (used specified + 10%) | Drawings M1-ZCD1001A |
| Tendons | NUPEC report "The Report of Trial Manufacturing of Tendon System," JPN-12-T-3, 3/16/94. |
| Reinforcement | Data for "Typical Reinforcement" provided by Cascade Steel Rolling Mill, McMinnville, Oregon; provided by Sandia National Laboratories to ANATECH, 3/96 |
| Liner | Liner stress-strain data, excerpt from NUPEC report/Mill Test Report provided by Sandia National Laboratories to ANATECH, 2/96 |

Final Pretest Analyses

1. PCCV Round Robin Analysis-Reuse of Design Package, Sandia letter SO-97-047 with attachments, 11/17/97.
2. PCCV Round Robin Analysis - Updated Information Package, Sandia letter SO-98-052 with attachments, 8/27/98.
3. PCCV-Summary of Discussions with Round Robin Participants, Sandia letter SO-99-001 with attachments, 1/8/99.

# APPENDIX B

# ANATECH/SANDIA PRETEST ANALYSIS RESULTS FOR 1:4-SCALE PRESTRESSED CONCRETE CONTAINMENT VESSEL MODEL PRESSURE TEST

This submittal provides the pretest analysis results at the 55 standard output locations requested of the Round Robin analysts in Sandia letter SO-99-010, dated 3/30/99. The submittal includes the following:

1. A paper copy of the plots and a table for the pretest predictions versus internal gage (not atmospheric) pressure.
2. The analysis results stored in Microsoft Excel files on a 1.44 MB diskette. The files are arranged in one workbook with 55 sheets according to the plot ID entitling each sheet. The files consist of two columns of results with the first column for the internal gage pressure and the second column of the analysis results, specific for each standard output location.
3. The units used for all analysis results:
   - Internal gage pressure in MPa
   - Strains in mm/mm
   - Displacements in mm
   - Forces in kN
4. A table with description of pressure levels corresponding to the following event milestones and an explanation of how they were derived:
   - First cracking of concrete in cylinder primarily in the hoop direction
   - First cracking of concrete in cylinder primarily in the meridional direction
   - First yield of hoop rebar in cylinder
   - First yield of meridional rebar in wall-basemat juncture
   - First cracking of dome concrete above 45° dome angle
   - First cracking of dome concrete below 45° dome angle
   - First hoop tendon in cylinder reaching 1% strain
   - First hoop tendon in cylinder reaching 2% strain
   - First hoop tendon in cylinder reaching 3% strain
   - A qualitative assessment of the lower and upper limits of the prestressed concrete containment vessel (PCCV) model failure pressure range:
     - Minimum pressure reachable with 90% confidence level
       - this is the predicted pressure, with a high degree of confidence, that the model will achieve without failing
     - Maximum pressure reachable with 90% confidence level
       - this is the predicted pressure, with a high degree of confidence, that the model will not exceed 1:4-scale PCCV pretest prediction analysis

**Table B-1. Events and Pressure Milestones**

| Response Event | | How Derived | MPa | (psig) | $P_d$ Multiple |
|---|---|---|---|---|---|
| (1) | First cracking of concrete in cylinder due to hoop stresses (occurs adjacent to buttresses) | 3DCM model | 0.59 | (86) | 1.50 |
| (2) | First cracking of concrete in cylinder due to meridional stresses (occurs at wall-basemat juncture) | global axisym. model | 0.57 | (82) | 1.4 |
| (3) | First yield of rebar in hoop direction of cylinder (occurs near buttresses) | 3DCM model | 0.86 | (125) | 2.2 |

## Table B-1. Events and Pressure Milestones (continued)

| Response Event | How Derived | MPa | (psig) | $P_d$ Multiple |
|---|---|---|---|---|
| (4) First yield of rebar in meridional direction at wall-basemat juncture | global axisym. | 1.10 | (160) | 2.8 |
| (5) First cracking of concrete in dome above 45° dome angle | global axisym. | 0.86 | (125) | 2.2 |
| (6) First cracking of concrete in dome below 45° dome angle | global axisym. | 0.94 | (137) | 2.4 |
| (7) Hoop tendons reaching 1% strain (barrel mid-height) | 3DCM model | 1.18 | (171) | 3.0 |
| (8) " " " 2% strain " " | 3DCM model | 1.27 | (185) | 3.2 |
| (9) " " " 3% strain " " | 3DCM model | 1.32 | (192) | 3.4 |

Qualitative Assessment of Failure Pressure

The ANATECH/Sandia analysis and failure predictions hinge on two distinct models and analysis of each: a global axisymmetric analysis and the 3DCM. Because there are uncertainties with either analysis, but the 3DCM "fails" at lower pressure than the axisymmetric because of the inclusion of three-dimensional effects, we believe the failure predictions based on the two distinct models make reasonable upper and lower bound confidence bands on failure pressure.

- Minimum pressure reachable with 90% confidence is 1.08 MPa, 2.75 $P_d$ (based on the 3DCM and local models).
- Maximum pressure reachable with 90% confidence is 1.38 MPa, 3.51 $P_d$ (based on the global axisymmetric analysis and a 2% global hoop-strain criteria as an upper limit on what the model will survive).

NRC FORM 335 (2-89) NRCM 1102, 3201, 3202

U.S. NUCLEAR REGULATORY COMMISSION

**BIBLIOGRAPHIC DATA SHEET**

*(See instructions on the reverse)*

1. REPORT NUMBER (Assigned by NRC, Add Vol., Supp., Rev., and Addendum Numbers, if any)
NUREG/CR-6685
SAND2000-2093

2. TITLE AND SUBTITLE

Pretest Analysis of a 1:4-Scale Prestressed Concrete Containment Vessel Model

3. DATE REPORT PUBLISHED

| MONTH | YEAR |
|---|---|
| October | 2000 |

4. FIN OR GRANT NUMBER

JCN Y6131

5. AUTHOR(S)

R. A. Dameron*
L. Zhang *
Y. R. Rashid *
M. S. Vargas *

6. TYPE OF REPORT

Technical

7. PERIOD COVERED *(Inclusive Dates)*

Sept. 95 - Sept. 00

8. PERFORMING ORGANIZATION – NAME AND ADDRESS *(If NRC, provide Division, Office or Region, U.S. Nuclear Regulatory Commission, and mailing address; if contractor, provide name and mailing address.)*

Sandia National Laboratories , Principal Contractor
P. O. Box 5800; MS-0744
Albuquerque, NM 87185-0744

Subcontractor:
*ANATECH Corporation
5435 Oberlin Drive
San Diego, CA 92121

9. SPONSORING ORGANIZATION – NAME AND ADDRESS *(If NRC, type "Same as above", if contractor, provide NRC Division, Office or Region, U.S. Nuclear Regulatory Commission, and mailing address.)*

Division of Engineering Technology
Office of Nuclear Regulatory Research
U.S. Nuclear Regulatory Commission
Washington, D.C. 20555-0001

10. SUPPLEMENTARY NOTES

J. F. Costello, NRC Project Manager

11. ABSTRACT *(200 words or less)*

The Nuclear Power Engineering Corporation of Japan and the U.S. Nuclear Regulatory Commission, Office of Nuclear Regulatory Research, are co-sponsoring and jointly funding a Cooperative Containment Research Program at Sandia National Laboratories in Albuquerque, New Mexico. As a part of the program, a prestressed concrete containment vessel model will be tested to failure at Sandia in September 2000. The model, uniformly scaled at 1:4, is representative of the containment structure of an actual pressurized-water reactor plan (OHI-3) in Japan. The objectives of the internal pressurization test are to obtain measurement data of the structural response of the model to pressure loading beyond design basis accident in order to validate analytical modeling, to find pressure capacity of the model, and to observe its failure mechanisms.

This report describes results of pretest analytical studies of the prestressed concrete containment vessel model performed by ANATECH Corp. under contract with Sandia National Laboratories.

The principal objectives of the pretest analyses are to (1) obtain validation of analytical methods for predicting the structural response and failure modes of a prestressed concrete containment and (2) provide information useful for planning test procedures and instrumentation.

12. KEY WORDS/DESCRIPTORS *(List words or phrases that will assist researchers in locating the report.)*

- *Prestressed Concrete Containment Vessel*
- *Failure Test*
- *Structural Analysis*
- *Failure Pressure Mechanisms*

13. AVAILABILITY STATEMENT
Unlimited

14. SECURITY CLASSIFICATION
*(This Page)*
Unclassified

*(This Report)*
Unclassified

15. NUMBER OF PAGES

16. PRICE

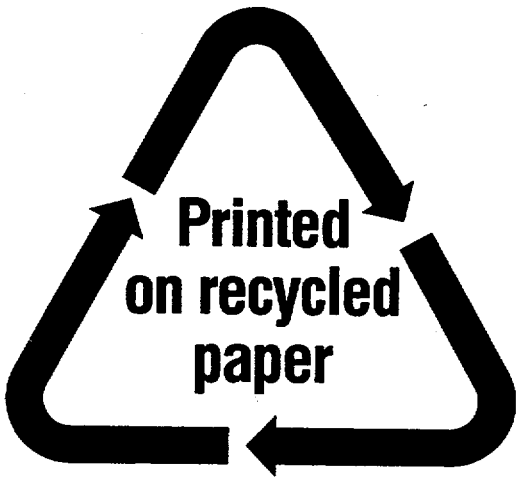


Federal Recycling Program

**UNITED STATES**
**NUCLEAR REGULATORY COMMISSION**
WASHINGTON, D.C. 20555-0001